



HAL
open science

High-energy gamma-ray emission in compact binaries

Benoît Cerutti

► **To cite this version:**

Benoît Cerutti. High-energy gamma-ray emission in compact binaries. Astrophysics [astro-ph]. Université de Grenoble, 2010. English. NNT: . tel-00499281

HAL Id: tel-00499281

<https://theses.hal.science/tel-00499281v1>

Submitted on 9 Jul 2010

HAL is a multi-disciplinary open access archive for the deposit and dissemination of scientific research documents, whether they are published or not. The documents may come from teaching and research institutions in France or abroad, or from public or private research centers.

L'archive ouverte pluridisciplinaire **HAL**, est destinée au dépôt et à la diffusion de documents scientifiques de niveau recherche, publiés ou non, émanant des établissements d'enseignement et de recherche français ou étrangers, des laboratoires publics ou privés.

THÈSE
présentée par

Benoît CERUTTI

pour obtenir le diplôme de Docteur en sciences de l'Université de Grenoble

(Arrêté ministériel du 7 août 2006)

Spécialité : ASTROPHYSIQUE & MILIEUX DILUÉS

High-energy gamma-ray emission in compact binaries
-
**Emission gamma de haute énergie dans les systèmes
binaires compacts**

Dirigée par

Guillaume DUBUS & Gilles HENRI

Soutenue publiquement le 10 juin 2010 devant le jury composé de

M.	Frédéric DAIGNE	Rapporteur
M.	Guillaume DUBUS	Examineur
Mme	Isabelle GRENIER	Examineur
M.	Gilles HENRI	Examineur
M.	John KIRK	Rapporteur
M.	Julien MALZAC	Examineur
M.	François MONTANET	Président

Thèse préparée au sein de l'Équipe



Laboratoire d'Astrophysique de Grenoble

UMR-5571 (OSUG/UJF/CNRS), BP 53, F-38041 Grenoble Cedex 9

Benoît CERUTTI

**High-energy gamma-ray emission in compact
binaries**

-

**Emission gamma de haute énergie dans les
systèmes binaires compacts**

PhD thesis — Université de Grenoble

— Juin 2010 —

Remerciements

Je voudrais commencer par remercier sincèrement Guillaume Dubus avec qui j'ai vécu trois années passionnantes et très stimulantes. Ce fut un réel plaisir et une chance de travailler avec Guillaume. Merci à Gilles Henri pour sa gentillesse et ses conseils avisés, en particulier sur les aspects les plus théoriques de ma thèse. J'ai également eu la chance de collaborer avec Julien Malzac avec qui j'ai également beaucoup appris. Je souhaiterais remercier les deux rapporteurs de ma thèse, John Kirk et Frédéric Daigne qui ont accepté cette tâche malgré les courts délais imposés et la longueur du manuscrit. J'ai beaucoup apprécié de travailler et de discuter avec Adam Hill et Anna Szostek. Merci à Anna pour son aide et ses commentaires sur le manuscrit de thèse. L'accueil très chaleureux de l'équipe Sherpas et de l'ensemble du laboratoire a aussi grandement contribué à mon bien-être au cours de cette thèse. J'en profite d'ailleurs pour remercier l'ensemble des thésards que j'ai connu au laboratoire, en particulier Timothé Boutelier et Astrid Lamberts avec qui j'ai partagé le même bureau. J'ai été également ravi de travailler avec Sarkis Rastikian. Merci à mes amis, qui sont venu parfois de loin (même de Suède!) pour assister à ma soutenance. Enfin, mes dernières pensées vont à mes parents et à mon frère qui m'ont toujours soutenu et qui ont toujours été présents.

Table of contents

Remerciements	i
Table of contents	ix
List of figures	ix
List of tables	xxi
Part 1. INTRODUCTION	1
CHAPTER 1. What is this thesis about?	3
1. The cosmic accelerators uncovered by the gamma-ray astronomy	3
2. Binary systems in the gamma-ray sky!	4
§ 1. Gamma-ray binaries	4
§ 2. Microquasars	6
3. Objectives of this thesis: What we want to understand	7
4. Guidelines: How is this thesis constructed?	8
[Français] De quoi parle cette thèse?	11
5. Les accélérateurs cosmiques découverts par l’astronomie gamma	11
6. Des systèmes binaires dans le ciel gamma!	11
§ 3. Les binaires gamma	12
§ 4. Microquasars	13
7. Objectifs de cette thèse: Ce que nous voulons comprendre	13
8. Comment cette thèse est-elle construite?	14
CHAPTER 2. Relevant high-energy processes	15
1. What we want to know	18
2. High-energy leptonic processes	18
§ 5. Inverse Compton scattering	18
§ 6. Bremsstrahlung	21
§ 7. Synchrotron radiation	23
§ 8. Triplet pair production	25
§ 9. Relevant leptonic processes in binaries	27
3. High-energy hadronic processes	28
§ 10. Proton-proton collision	29
§ 11. Photomeson production	31
4. Photon-photon annihilation	32

5. The cooling of relativistic particles	33
§ 12. The continuity equation	33
§ 13. General solution	34
§ 14. Some simple solutions	34
6. What we have learned	35
7. [Français] Résumé du chapitre	35
§ 15. Contexte et objectifs	35
§ 16. Ce que nous avons appris	36
Part 2. GAMMA-RAY EMISSION IN GAMMA-RAY BINARIES	37
CHAPTER 3. Anisotropic inverse Compton scattering	39
1. What we want to know	40
2. Kinematics and geometrical quantities	40
3. Differential cross sections	41
4. Anisotropic inverse Compton scattering in the Thomson approximation	42
§ 17. Soft photon density	42
§ 18. Anisotropic Thomson kernel	43
§ 19. Anisotropic scattering rate	44
§ 20. Beamed emission	45
§ 21. Isotropic Thomson kernel	45
§ 22. Integration over electron energy for a power law distribution	46
§ 23. Integration over soft photon energy for a black-body distribution	47
§ 24. Final check: Integration over an isotropic distribution of soft radiation	49
5. Anisotropic inverse Compton scattering in the general case	50
§ 25. General anisotropic kernel	50
§ 26. Integration over a power law for electrons and a black body for soft photons	51
§ 27. Final check: Comparison with Jones' isotropic solution	51
6. What we have learned	52
7. [Français] Résumé du chapitre	53
§ 28. Contexte et objectifs	53
§ 29. Ce que nous avons appris	54
CHAPTER 4. Gamma-ray modulation in gamma-ray binaries	55
1. What we want to know	56
2. The model	57
§ 30. The magnetic field	57
§ 31. The electron distribution	57
§ 32. Gamma-ray emission and pair production	59
3. Application to gamma-ray binaries	60
§ 33. LS 5039	60
§ 34. LS I +61 303 and PSR B1259-63	63
4. What we have learned	64
5. [Français] Résumé du chapitre	67

§ 35. Contexte et objectifs	67
§ 36. Ce que nous avons appris	68
6. Paper: The modulation of the gamma-ray emission from the binary LS 5039	69
CHAPTER 5. High-energy emission from the unshocked pulsar wind	83
1. Direct emission from the pulsar wind in gamma-ray binaries?	84
2. What we want to know	85
3. Compton drag of the pulsar wind	85
§ 37. Assumptions and geometry	85
§ 38. Anisotropic inverse Compton cooling of pairs	86
§ 39. Calculation of the cooled Lorentz factor in binaries	87
§ 40. Lorentz factor profiles and maps in LS 5039 and LS I +61 303	90
§ 41. Finite-size star and thermal spectrum	91
4. Inverse Compton emission	92
§ 42. The density of pairs	92
§ 43. Inverse Compton spectrum	94
§ 44. Pair production	96
5. Size and geometry of the pulsar wind nebula	96
6. What if the pulsar wind is anisotropic?	98
§ 45. Anisotropic pulsar wind	98
§ 46. The pulsar orientation	99
§ 47. Lorentz factor maps	101
§ 48. What are the odds to observe a low Lorentz factor?	101
7. Free pulsar wind emission in LS 5039 and LS I +61 303	103
8. Signature of the unshocked wind seen by <i>Fermi</i> ?	104
9. Striped pulsar wind	107
10. What we have learned	108
11. [Français] Résumé du chapitre	109
§ 49. Contexte et objectifs	109
§ 50. Ce que nous avons appris	110
12. Paper: Spectral signature of a free pulsar wind in the gamma-ray binaries LS 5039 and LS I +61 303	112
Part 3. PAIR CASCADE EMISSION IN GAMMA-RAY BINARIES	125
CHAPTER 6. Anisotropic pair production	127
1. What we want to know	127
2. Kinematics and threshold energy	128
3. Cross sections	129
4. Construction of the center-of-mass frame	130
§ 51. Geometrical construction	130
§ 52. Lorentz transform parameters	131
5. Rate of gamma-ray absorption	131

6. The spectrum of the produced pair	132
§ 53. General solution	132
§ 54. Anisotropic pair production kernel	133
§ 55. Integration over a power-law energy distribution and anisotropic effects	134
§ 56. Comparison with the isotropic and mono-energetic solution	134
§ 57. Comparison with Böttcher & Schlickeiser solution	135
7. The density of pairs	136
8. What we have learned	138
9. [Français] Résumé du chapitre	138
§ 58. Contexte et objectifs	138
§ 59. Ce que nous avons appris	138
CHAPTER 7. One-dimensional pair cascading	141
1. What we want to know	142
2. Assumptions and approximations for 1D cascade	143
3. Equations for anisotropic 1D cascade	144
§ 60. Equation for photons	144
§ 61. Equation for pairs	145
§ 62. Numerical integration	147
4. The development of 1D pair cascade in binaries	147
5. Anisotropic effects	149
6. 1D cascade emission in LS 5039	149
7. The density of escaping pairs	151
8. Pair cascading in the free pulsar wind	152
9. What we have learned	154
10. [Français] Résumé du chapitre	154
§ 63. Contexte et objectifs	154
§ 64. Ce que nous avons appris	155
11. Paper: One dimensional pair cascade emission in gamma-ray binaries	157
CHAPTER 8. Three-dimensional pair cascading	169
1. Assumptions on the ambient magnetic field	170
2. The first generation of pairs in binaries	171
§ 65. Spectrum and energy of pairs	172
§ 66. Absorption and spatial distribution of pairs	173
3. The first generation of gamma rays in binaries	174
§ 67. Geometry	174
§ 68. Equations for the first generation of gamma rays in the cascade	175
§ 69. Anisotropic effects	178
§ 70. Spatial distribution in LS 5039	179
4. Beyond the first generation approximation	180
§ 71. Semi-analytical approach	180
§ 72. The Monte Carlo approach	182

§ 73. The effect of the magnetic field	183
5. 3D pair cascade emission in LS 5039	184
§ 74. Modulation and spectra	185
§ 75. The location of the TeV source	185
§ 76. The ambient magnetic field in LS 5039	187
6. What we have learned	187
7. [Français] Résumé du chapitre	189
§ 77. Contexte et objectifs	189
§ 78. Ce que nous avons appris	191
8. Paper: Modeling the three-dimensional pair cascade in binaries	193
Part 4. HIGH-ENERGY EMISSION FROM RELATIVISTIC OUTFLOW	205
CHAPTER 9. Anisotropic Doppler-boosted emission	207
1. What we want to know	207
2. Geometry and assumptions	208
3. Boosted synchrotron radiation	209
4. Boosted anisotropic inverse Compton scattering	210
§ 79. Soft photon density in the comoving frame	211
§ 80. Doppler-boosted Compton spectrum	212
5. What we have learned	214
6. [Français] Résumé du chapitre	215
§ 81. Contexte et objectifs	215
§ 82. Ce que nous avons appris	215
CHAPTER 10. Doppler-boosted emission in gamma-ray binaries	217
1. Observational backdrop	217
2. The model and the geometry	218
3. LS 5039	218
4. LSI +61 303	219
5. PSR B1259-63	221
6. What we have learned	221
7. [Français] Résumé du chapitre	223
§ 83. Contexte et objectifs	223
§ 84. Ce que nous avons appris	224
8. Paper: Relativistic Doppler-boosted emission in gamma-ray binaries	225
CHAPTER 11. Doppler-boosted emission in the relativistic jet of Cygnus X-3	237
1. Observational backdrop	237
2. The model and the geometry	238
3. Results	240
4. Absorption and location of the gamma-ray source	240
§ 85. Soft photon density from the disk	241

§ 86. Gamma-ray absorption and application to Cygnus X-3	244
5. What we have learned	245
6. [Français] Résumé du chapitre	247
§ 87. Contexte et objectifs	247
§ 88. Ce que nous avons appris	248
7. Paper: The relativistic jet of Cygnus X-3 in gamma rays	249
Part 5. CONCLUSION	257
CHAPTER 12. Conclusion	259
1. What we have learned	259
§ 89. Gamma-ray emission in gamma-ray binaries	259
§ 90. Pair cascade emission in gamma-ray binaries	260
§ 91. High-energy emission from relativistic outflows	261
2. Open questions and looking forwards	262
[Français] Conclusion	265
3. Ce que nous avons appris	265
§ 92. L'émission gamma dans les binaires gamma	265
§ 93. Emission d'une cascade de paires dans les binaires gamma	266
§ 94. Emission de haute énergie dans les écoulement relativistes	267
4. Questions ouvertes et perspectives	268
Part 6. REFERENCES	271
Bibliography	273

List of figures

- 1 Top view of the compact object orbit (blue line) in Cygnus X-3 (*top left*), LS 5039 (*top right*), LS I +61°303 (*bottom left*) and PSR B1259 – 63 (*bottom right*). The red filled disk represents the massive star at scale in the system and the back solid line indicates periastron. The observer sees the orbit from the bottom. 5
- 2 This sketch depicts the main components in gamma-ray binaries involved in the non-thermal emission mechanism, in the pulsar wind nebula scenario (see the text for explanations). 7
- 3 Sketch of a microquasar and of its different components. Energetic particles are accelerated in the relativistic jet and radiate high-energy emission. 8
- 4 Total cross section for inverse Compton scattering as a function of $x = \epsilon'_0/m_e c^2$. The dashed line separates the Thomson ($x \ll 1$) to the Klein-Nishina regime ($x \gg 1$). The approximate formula given in Eq. (5.3) is shown with a red dashed line. 19
- 5 Numerically integrated inverse Compton energy losses (Eq. 5.8, blue solid line) of an electron of energy $E_e = \gamma_e m_e c^2$ bathed in a isotropic gas of photons with a black body energy distribution of effective temperature $T_* = 40\,000$ K. The analytical formula in the Thomson (red dashed line) and Klein-Nishina (red dashed-dotted line) regimes are overplotted for comparison. 20
- 6 Variations of ϕ_1 (blue line) and ϕ_2 (red line) as a function of Δ for the neutral hydrogen atom. 22
- 7 Bremsstrahlung spectrum (plot of the function f_b defined in Eq. 6.13) emitted by one electron of Lorentz factor $\gamma_e = 10$ (*bottom curve*), 100, 1000, and $= \infty$ (*top curve*) as a function of the ratio $\epsilon_1/\gamma_e m_e c^2$. The medium is composed of neutral hydrogen atoms only. 23
- 8 Variations of f_s defined in Eq. (7.23) as a function of ϵ_1/ϵ_c . 24
- 9 Total triplet pair production cross section as a function of x . The blue line corresponds to the expression valid for $x > 16$. The Bethe-Heitler formula Δ_{BH} , valid for $x > 10^4$, is shown by the red dashed line. The total inverse Compton cross section is also shown for comparison (green solid line). 26
- 10 Triplet pair production energy losses as a function of x for $\theta_0 = \pi/2$ given in Eq. (8.39). One should trust only the domain where $x \gtrsim 10^3$, below the energy losses are overestimated but the variations are still qualitatively correct. Inverse Compton losses are shown for comparison (red dashed line). 27
- 11 Leptonic cooling timescales: inverse Compton (solid line, "Th." in the Thomson limit and "KN" in the Klein-Nishina regime), synchrotron (dotted line, "Syn."), TPP (dashed line),

- and Bremsstrahlung (dot-dashed line, "Brem."), as a function of the electron Lorentz factor γ_e . This plot shows also the total cooling timescale t_{tot} (red dashed line) defined as $t_{tot}^{-1} = t_{ic}^{-1} + t_{syn}^{-1} + t_{TTP}^{-1} + t_B^{-1}$. The parameters used here are compatible with LS 5039: $T_\star = 39\,000$ K, $R_\star = 9.3R_\odot$, $v_\infty = 2400$ km s $^{-1}$, $\dot{M} = 10^{-7}M_\odot$ yr $^{-1}$ and $d \approx 0.1$ AU at periastron. The magnetic field is unknown but is chosen here as $B = 1$ G. 29
- 12 Inclusive cross section of the production of neutral pions in proton-proton collision σ_{pp} , as a function of the high-energy proton energy E_p . 30
- 13 Total cross section for pair production $\sigma_{\gamma\gamma}$ as a function of β (*left panel*) and as a function of the gamma-ray photon energy ϵ_1 (*right panel*) for $\epsilon_0 = 1$ eV and $\theta_0 = \pi$. The pair is mostly produced close to threshold (maximum for $\beta \approx 0.7$). 32
- 14 Inverse Compton scattering seen in the observer frame (*left panel*) and in the rest frame of the electron (*right panel*). Waves represent photons and the green thick arrow shows the direction of motion of the electron of total energy $E_e = \gamma_e m_e c^2$. The Lorentz boost from the observer to the rest frame of the electron is along the z-axis. 41
- 15 Second order Feynman diagram for Compton scattering. 42
- 16 Geometrical configuration for the computation of the anisotropic inverse Compton kernel. 42
- 17 Variations of the functions $f_{anis}(x)$ (red line) and $f_{iso}(x)$ (blue line) that appear in the computation of the Compton kernel in the Thomson approximation. 46
- 18 Comparison of the analytical solution (red dashed line) to the numerically integrated solution (blue solid line) for electrons with a power energy distribution and mono-energetic soft photons. Parameters used: $\epsilon_0 = 10$ eV, $\theta_0 = \pi$, $p = 2$. The effect of the low and high energy cut-off are shown on the numerical solution where $\gamma_- = 10^2$ and $\gamma_+ = 10^4$. 47
- 19 The same as in Fig. 18, but where the kernel is integrated over a black-body energy distribution of effective temperature $T_\star = 39000$ K, with $\theta_0 = 180^\circ$ (*top*), 120° , 90° , 60° , and 30° (*bottom*). 48
- 20 Variation of the term responsible for the angular dependence in the Thomson spectrum $(1 - \mu_0)^{p+1/2}$ (see Eq. 23.124) as a function of μ_0 , with indices $p = 0.5, 1, 2$ and 3 . 49
- 21 The same as in Fig. 19, with $\gamma_- = 10^2$ and $\gamma_+ = 10^7$. $\theta_0 = 180^\circ$ (*top*), 120° , 90° , 60° , and 30° (*bottom*). 52
- 22 The same as in Fig. 21 if the gas of target photons is isotropic. The Compton emission is computed with the isotropic kernel of Jones (1968) (blue solid line) and comparison with the anisotropic solution averaged over all the angles (red dashed line). 53
- 23 *Left panel*: This diagram shows the orbit of the compact object (blue line) and the massive companion star (red disk) in LS 5039 (top view). The distant observer is at bottom (indicated by the arrow). The orbital parameters are taken from Casares *et al.* (2005b). The orbital phases ϕ are given by the numbers where $\phi \equiv 0$ at periastron. Superior conjunction corresponds to $\phi \approx 0.06$ and inferior conjunction to $\phi \approx 0.72$. *Right panel*: The angle ψ between the unit vector \mathbf{e}_\star and \mathbf{e}_{obs} varies between $\psi_{sup} = \pi/2 + i$ at

- superior conjunction and $\psi_{inf} = \pi/2 - i$ at inferior conjunction, where i is the inclination of the orbit. The green disk indicates the position of the compact object in the orbit. 56
- 24 *Top panel:* Steady-state cooled electron energy distribution for $B = 0.1$ (*top*), 1 and 10 G (*bottom*). The compact object injects electrons with a constant -2 power law energy distribution. The massive star produces stellar photons with an energy $\epsilon_0 \approx 10$ eV. The orbital separation is $d \approx 0.1$ AU. *Bottom panel:* Resulting synchrotron spectrum emitted by the cooled distribution of electrons given in the *Top* panel. 59
- 25 Anisotropic inverse Compton spectrum (blue solid lines) and the effect of the gamma-ray absorption (red dashed line) in LS 5039 at the orbital phases ϕ (*left* panel from *top* to *bottom*): $\phi = 0.03, 0.09, 0.15, 0.24, 0.34, 0.44, 0.56, 0.66$, (*right* panel from *bottom* to *top*): $0.66, 0.76, 0.85, 0.91, 0.97$, and 0.03 . $\phi = 0$ at periastron, $\phi \approx 0.06$ at superior conjunction and $\phi \approx 0.72$ at inferior conjunction. Electrons are constantly injected with a power law energy distribution with $p = 2$ and $B = 1$ G at the pulsar position for an inclination $i = 60^\circ$. 61
- 26 *Top panel:* Theoretical anisotropic inverse Compton emission ("unabsorbed flux", black solid line) and pair production (" $\exp(-\tau)$ ", dashed grey line) above 100 GeV as a function of the orbital phase in LS 5039. Orbital parameters are taken from Casares *et al.* (2005b). *Bottom panel:* Gamma-ray light curves expected in the HESS energy band (red solid line, > 100 GeV) and in the *Fermi* energy band (blue solid line, > 1 GeV). HESS data points are shown for comparison and are taken from Aharonian *et al.* (2006). 62
- 27 The same as in Fig. 26 (*bottom* panel) if the compact object is a black hole ($i = 20^\circ$). 63
- 28 Theoretical gamma-ray spectra averaged along the full orbit (black solid line), over SUPC ($\phi \leq 0.45$ and $\phi > 0.9$, blue dashed line) and over INFC state ($0.45 < \phi \leq 0.9$, blue solid line). The contribution of synchrotron radiation alone is shown as well in dotted line (black: full orbit, *top* blue: SUPC and *bottom* blue: INFC). HESS (filled red bowties) and *Fermi* (red empty bowtie and black data points) observations are overplotted for comparison. Parameters: $i = 60^\circ$, $p = 2$, $B = 0.8 d_{0.1}^{-1}$ G and $L_p = 10^{36}$ erg s $^{-1}$. 64
- 29 Very-high energy lightcurve observed in LS I +61 $^\circ$ 303 (*top* panel) and PSR B1259 – 63 (*bottom* panel). Extracted from Albert *et al.* (2009) and Aharonian *et al.* (2009). 65
- 30 Orbit-averaged spectra (blue line, *left* panels) and phase-resolved gamma-ray lightcurves (blue line > 1 GeV, red line > 100 GeV, *right* panels) in LS I +61 $^\circ$ 303 (*top* panels) and PSR B1259 – 63 (*bottom* panels). Electrons are injected with a power law of index $p = 2.5$ in both binaries. There is no magnetic field. *Fermi* (black crosses) and MAGIC observations (red bowtie) are shown for LS I +61 $^\circ$ 303, EGRET (grey arrows, upper limits) and HESS (red bowtie) measurements are also shown for PSR B1259 – 63. The orbital parameters are taken from Aragona *et al.* (2009) for LS I +61 $^\circ$ 303 and from Manchester *et al.* (1995) for PSR B1259 – 63. 66
- 31 Simplistic drawing of a pulsar wind. Relativistic pairs of electrons and positrons are generated and accelerated in the pulsar magnetosphere. The wind of pairs is released at the light cylinder radius (R_L) and expands radially and freely ("unshocked" pulsar wind) up to the termination shock ("shocked" pulsar wind) at a distance R_s . At the shock, pairs are re-accelerated and isotropized. 84

- 32 This diagram depicts the binary system and the geometrical quantities used in the following. An electron from the wind with a Lorentz factor γ_e situated at a distance r from the pulsar and R from the companion star, interacts with a stellar photon of energy ϵ_0 . 86
- 33 Total energy losses per electron (blue solid line) as a function of the energy, where $\epsilon_0 = 1$ eV and $\theta_0 = 30^\circ$ (*bottom*), 60° , 90° , 90° and 150° (*top*). The analytical formula in the Thomson regime Eq. (38.162) is shown for comparison (red dashed line). 87
- 34 Lorentz factor of the pairs in the pulsar wind as a function of ψ_r for $\psi = 30^\circ$ (*bottom* lines), 60° , 90° , 120° and 150° (*top* lines), applied to LS 5039 (*left* panels) and LS I +61°303 (*right* panels). Pairs are injected by the pulsar at a Lorentz factor $\gamma_0 = 10^4$ (*top* panels), 10^5 and 10^6 (*bottom* panels). The massive star is assumed point-like and mono-energetic and both winds (pulsar and star) are assumed spherical and isotropic. 89
- 35 These maps show the spatial distribution of the cooled Lorentz factor of the wind in LS 5039 (*left* panels) and LS I +61°303 (*right* panels) at periastron. Each line gives the fraction of the energy left in the pairs after Compton cooling: 90% (*left* lines), 50%, 10% and 1% (*right* lines) of the injected Lorentz factor γ_0 . The massive star is shown by a red semi disk. 90
- 36 For a finite-size star, the relativistic electron (at the distance r) sees stellar photons originating within a cone of semi-aperture angle $\alpha_* = \arcsin(R_*/R)$ (red dashed line). 91
- 37 Cooling of the pulsar wind in LS 5039 for $\gamma_0 = 10^4$ (*left* panels) and 10^6 (*right* panels). The solutions for a mono-energetic and point-like star (blue solid lines) are compared with the solutions for a black-body star (red dashed lines, *top* panels) and a finite-size star (red dashed lines, *bottom* panels). 93
- 38 The observer sees only the radiation from the pairs aligned with the line of sight due to relativistic Doppler beaming effect. Because of the anisotropy of the radiation field set by the massive star, the gamma-ray emission depends strongly on the viewing angle ψ . 94
- 39 Inverse Compton spectrum emitted by an unterminated and mono-energetic pulsar wind in LS 5039 at periastron ($d \approx 0.1$ AU) with $L_p = 10^{36}$ erg s $^{-1}$ at a distance of 2.5 kpc. Pairs are injected with a Lorentz factor $\gamma_0 = 10^4$ (*top left*), 10^5 (*top right*), 10^6 (*bottom left*) and 10^7 (*bottom right*). For each energy, the wind is seen with a viewing angle $\psi = 30^\circ$ (*top* line), 60° , 90° , 120° , and 150° (*bottom* line). Pair production is ignored. 95
- 40 Absorbed inverse Compton spectrum emitted (blue solid lines) by an unterminated and mono-energetic pulsar wind with $\gamma_0 = 10^6$ in LS 5039 (*left*) and LS I +61°303 (*right*) at superior (*top*, $\psi = 30^\circ$) and inferior (*bottom*, $\psi = 150^\circ$) conjunctions. The non-absorbed spectrum is shown for comparison (dashed red line). Pair cascade emission is ignored. 97
- 41 The collision between the pulsar wind and the massive star wind produces a bow shock structure. The shocked stellar wind (red area) and the shocked pulsar wind (green area) are separated by the contact discontinuity (black solid line). The unshocked pulsar wind is limited by the relativistic shock wave front (green solid line) and has an asymptotic half opening angle α . 98

-
- 42 X-ray images of the Crab nebula (*left*, Weisskopf *et al.* 2000) and the pulsar wind nebula 3C 58 (*right*, Slane *et al.* 2004) obtained with *Chandra* where a jet-torus structure appears clearly. Images Extracted from Gaensler & Slane (2006). 99
- 43 Angular distribution of the Lorentz factor following Eq. (45.189) normalized to γ_m where $\gamma_m/\gamma_i \sim 10^4$. The pulsar pole is oriented along the x-axis where the Lorentz factor reaches its minimum value γ_0 and is maximum in the equator plane (y,z) where $\gamma_0 \approx \gamma_m$. 100
- 44 The pulsar axis (x'') is inclined with respect to the observer at an angle θ . The anisotropic pulsar wind is represented by the green loops. 101
- 45 Same as in Fig. 35 for an anisotropic pulsar wind in LS 5039 at periastron. Parameters used: $\gamma_i = 10^3$, $\gamma_m = 10^6$, $\phi = 0$ for four different orientations *top left* ($\phi_y = 0, \phi_z = \pi/20$), *top right* ($\phi_y = \pi/2, \phi_z = 0$), *bottom left* ($\phi_y = \pi/3, \phi_z = \pi/20$) and *bottom right* ($\phi_y = \pi/4, \phi_z = \pi/4$). The star is point-like and mono-energetic. The dotted lines indicate the position of the pulsar, the red dashed line the orientation of the equator and the red disk depicts the massive companion star. 102
- 46 Same as in Fig. 45 for LS I +61°303 at periastron. 103
- 47 Orbit-averaged emission from the free pulsar wind in LS 5039 (*top panel*) and LS I +61°303 (*bottom panel*). The wind is assumed radial, isotropic and mono-energetic with $\gamma_0 = 10^4$ (*left*), 10^5 , 10^6 and 10^7 (*right*). The gamma-ray emission is calculated for a terminated ($\eta = 2 \times 10^{-2}$, solid lines) and unterminated wind (dashed lines) for $L_p = 10^{36}$ erg s⁻¹, assuming that the systems are located at 2.5 kpc for LS 5039 and 2 kpc for LS I +61°303. *Fermi* (black data points), HESS and MAGIC (red bowties) observations are overplotted. 105
- 48 Inverse Compton emission in the gamma-ray binaries LS 5039 (*left*) and LS I +61°303 from an unshocked pulsar wind. *Top*: Theoretical orbit-averaged spectrum (blue solid line) for an inclination $i = 60^\circ$. Bowties are HESS and MAGIC observations (red, Aharonian *et al.* 2006; Albert *et al.* 2006), black data points show *Fermi* measurements (Abdo *et al.* 2009a,b). *Middle*: Gamma-ray flux integrated over 100 MeV as a function of the orbital phase ϕ (two full orbits), the *Fermi* light curve is overplotted for LS I +61°303. *Bottom*: Expected spectral index in the GeV energy band along the orbit. 106
- 49 The striped current sheet produced by an oblique rotator obtained with the split monopole model by Bogovalov (1999). Picture extracted from Kirk *et al.* (2009). 107
- 50 Kinematics for pair production. The photons annihilate and produce a pair electron-positron if the total energy available in the center-of-mass frame is greater than the rest mass energy of the pair. 128
- 51 Second order Feynman diagram for pair production. 129
- 52 Variation of the differential cross section $d\sigma_{\gamma\gamma}/d(\cos\theta'_1)$ for pair production as a function of $\cos\theta'_1$ for $\beta = 0.3, 0.7, 0.9$ and 0.99 . 130
- 53 Geometrical construction of the center-of-mass frame direction of motion (x_{cm} -axis). 130
- 54 Geometrical configuration for the computation of the anisotropic pair production kernel. 133
- 55 Spectrum the pair produced in the interaction of a gamma-ray photon of energy $\epsilon_1 = 265$ GeV, 300 GeV, 500 GeV, 1 TeV and 10 TeV with a mono-energetic beam of soft

- radiation ($\epsilon_0 = 1$ eV). The collision is head-on here ($\theta_0 = \pi$). The threshold energy for pair production is ≈ 260 GeV in this configuration. 134
- 56 Spectrum of pairs created by absorption of primary gamma rays following a power law energy distribution (photon index -2) and a mono-energetic beam of soft radiation (with $\epsilon_0 = 1$ eV). Spectra are computed for $\theta_0 = 10^\circ, 20^\circ, 30^\circ, 45^\circ, 60^\circ, 90^\circ$ and 180° . 135
- 57 Comparison between the analytical (blue line) and the numerically integrated (red dashed line) kernels for an isotropic source of soft radiation. $\epsilon_0 = 1$ eV and $\epsilon_1 = 300$ GeV, 500 GeV, 1 TeV and 10 TeV. 136
- 58 Comparison between the kernel found in Eq. (54.239) and the kernel found by Böttcher & Schlickeiser (1997), Eq. (57.245) where $\epsilon_0 = 1$ eV, and $\epsilon_1 = 300$ GeV, 500 GeV and 1 TeV for a head-on collision. 137
- 59 Cascade of pairs initiated by a primary high-energy gamma ray propagating in a soft photon field. 142
- 60 Geometrical quantities used in the model. The primary source injects gamma rays of energy ϵ_1 at a viewing angle ψ . These photons are absorbed by the stellar photon of energy $\epsilon_0 \approx 2.7kT_*$ at a distance r from the source and yield electron positron pairs focused along the line of sight due to relativistic beaming effect. 143
- 61 If the trajectory of the electron deviated by the magnetic field along the Compton interaction length λ_{ic} remains within a cone of half opening angle $\alpha = 1/\gamma_e$, the cascade is one-dimensional. 144
- 62 The primary source injects a density of gamma rays n_γ . Between r and $r + dr$, part of these photons are absorbed and new are emitted by the pairs produced in the cascade. 145
- 63 This diagrams depicts qualitatively the depopulation of the energy level E_e to the benefit of lower energy levels $m_e c^2 < E'_e < E_e$. 146
- 64 This diagrams depicts qualitatively the population of the energy level E_e by higher energy levels $E'_e \geq E_e$. 146
- 65 Development of the 1D cascade along the line of sight joining the primary source to the observer. The primary source is point-like, isotropic and injects gamma rays with a -2 power law energy distribution between 100 MeV and 100 TeV at the location of the compact object in LS 5039. The viewing angle is $\psi = 30^\circ$. On the left panels are shown the full escaping gamma-ray spectra (blue line), the radiation from the cascade only (green line) and the pure absorbed spectrum (red dashed line) for $r = R_*/4$ (*top*), R_* (*middle*) and $+\infty$ (*bottom*). The corresponding total unabsorbed emission from the cascade pairs is shown in the right panels. 148
- 66 The same as Fig. 65 with $r \rightarrow +\infty$ and $\psi = 30^\circ, 60^\circ, 90^\circ, 120^\circ$, and 150° . The radiation from the cascade only is not shown for more readability. 149
- 67 TeV orbital modulation of 1D pair cascade emission in LS 5039 (red line) as a function of the orbital phase (two full orbits shown here), and comparison with the primary absorbed flux (blue line). The injection of primary gamma rays is isotropic and constant along the orbit. Both conjunctions are shown with vertical dashed lines (with the orbital parameters found by Casares *et al.* 2005b). 150

-
- 68 Same as in Fig. 67 for LS I +61°303. The orbital parameters are taken from Casares *et al.* 2005a). 150
- 69 Theoretical gamma-ray lightcurves in LS 5039, in the *Fermi* energy range (flux > 1 GeV *left* panel) and HESS energy range (flux > 100 GeV, *right* panel). HESS data points are taken from Aharonian *et al.* (2006). The 1D cascade component (red line) is compared with the primary absorbed contribution (blue line). The sum of both component is shown by the green line. 151
- 70 Definition of the geometrical quantities useful for the computation of the density of escaping pairs in binaries. From the compact object point of view (origin), the massive star covers a solid angle Ω_* . Pairs propagating in the direction of the star (*i.e.* within Ω_*) are not considered in the calculation of the escaping density of pairs. 152
- 71 *Left* panel: Mean energy of escaping pairs at infinity as a function of the viewing angle ψ . *Right* panel: Density of escaping pairs in the cone of semi-aperture angle ψ as a function of ψ . 152
- 72 Emission from a mono-energetic free pulsar wind in LS 5039 at superior conjunction ($\psi = 30^\circ$) for $\gamma_0 = 10^4$ (*left*) and 10^6 (*right*) with $L_p = 10^{36}$ erg s⁻¹. The exact solution (*i.e.* keeping track of stochastic losses for the electrons, green line) is compared with the approximate solution (continuous losses approximation, red dashed line). The solution with 1D pair cascading is shown by the blue line. 153
- 73 Three-dimensional "isotropic" pair cascade (grey domain) is initiated if the magnetic field is strong enough to confine locally pairs $B > B_{min}$ or the cascade would be "anisotropic", but it should not exceed $B < B_{max}$ or pairs will emit mainly synchrotron radiation and the cascade would be "quenched". Pairs remain in the system if the magnetic field is above the dashed line. *Left*: LS 5039, *right*: LS I +61°303, at periastron for both systems. 171
- 74 Primary gamma rays injected at $r \equiv 0$ in the direction (θ, ϕ) produce pairs at r from the source and R from the massive star center. 172
- 75 Density of pairs produced by the annihilation of the primary gamma rays (injected at $r \equiv 0$ with a -2 power law energy distribution) with stellar photons at $r = R_*/4$ (*top left*), $R_*/2$, R_* and $2R_*$ (*bottom right*) in LS 5039. In each panel, the spectrum of pairs is computed for $\theta = 30^\circ$ (*top*, dashed line), 60° , 90° , 120° and 150° (*bottom*, dotted line). 173
- 76 This map gives the mean Lorentz factor of the pairs at their creation in LS 5039 at superior conjunction. The primary source is a -2 power law with a high energy cut-off at 100 TeV. The star (red disk) is assumed mono-energetic and point-like but the eclipse is taken into account (black region behind the star with respect to the source). 174
- 77 *Top* panels: This map shows the fraction of the gamma-ray flux left after pair production $e^{-\tau_{\gamma\gamma}(r,\theta)}$. Bright region are transparent and black regions are opaque. *Bottom* panels: Density of secondary pairs given by Eq. (66.278). The white lines gives the fraction of the absorbed primary gamma-ray flux. In both maps, the primary source injects photons of energy $\epsilon_1 = 100$ GeV at the compact object location ($r \equiv 0$) in LS 5039 (*left* panels) and LS I +61°303 (*right* panels), at periastron for both systems. The eclipsed region by the massive star (red semi disk) is delimited by a white dashed line. Distances are normalized to the orbital separation d . 175

-
- 78 Same as Fig. 77 with $\epsilon_1 = 1$ TeV. 176
- 79 Same as Fig. 77 with $\epsilon_1 = 10$ TeV. 176
- 80 The binary system is seen by a distant observer with a viewing angle ψ . Secondary pairs are secondary sources of gamma rays seen at an angle ψ_{obs} . 177
- 81 The massive star excludes part of the volume to the primary gamma-ray source (grey area) and to the observer (red area). 177
- 82 *Left panel*: Escaping radiation spectrum (blue line) for $\psi = 30^\circ, 60^\circ, 90^\circ, 120^\circ$ and 150° . The primary source is point-like, isotropic and injects gamma rays with a -2 power law energy distribution between 100 MeV and 100 TeV at the location of the compact object in LS 5039 (dotted line). The radiation from the pure absorbed spectrum (red dashed line) is shown for comparison. The emission from secondary pairs only is shown in the *right panel*. 179
- 83 TeV orbital modulation of 3D pair cascade emission in LS 5039 (red line) as a function of the orbital phase (two full orbits shown here), and comparison with the primary absorbed flux (blue line) and the full 1D cascade flux (red dashed line). The injection of primary gamma rays is isotropic and constant along the orbit. Both conjunctions are shown with vertical dashed lines (with the orbital parameters found by Casares *et al.* 2005b). 180
- 84 Spatial distribution and intensity of the very high-energy (> 100 GeV) radiation produced by the first generation of pairs in the 3D cascade in LS 5039 as observed by a distant observer (whose direction is indicated by a white solid line, *top panels*). Distances are normalized to the orbital separation d . The system is viewed at superior (*left*) and inferior conjunctions (*right*). Each map is a slice of the 3D cloud of gamma rays in the three orthogonal planes: front view (plane containing the observer and both stars, *top panels*), top view (*middle*) and right view (*bottom*). The primary source lies at the origin. The eclipsed regions by the massive star (red disk) are delimited by white dashed lines. The injection of the primary gamma rays is the same as in Fig. 82. 181
- 85 *Left panel*: The same as in Fig. 82 (*right panel*) for the second generation of pairs in the cascade only. *Right panel*: ratio of the second generation to the first generation gamma-ray flux in the cascade as a function of energy. 182
- 86 *Left panel*: Full cascade emission computed with the Monte Carlo code (blue solid line) in LS 5039 for $\psi = 30^\circ$ and 150° . Comparison between the semi-analytical (red dashed line) and the Monte Carlo (red solid line) results for the first generation of gamma rays only. The primary source is shown with a dotted line. *Right panel*: This plot shows the relative contribution from the primary absorbed flux (red dashed line), the first generation (red solid line) and from extra-generations (*i.e.* > 1 , green line) to the total escaping gamma-ray flux (blue line) in LS 5039 for $\psi = 30^\circ$. The right panel uses only results from the Monte Carlo code. Synchrotron radiation is ignored. 183
- 87 The same as in Fig. 83 where the 3D cascade radiation is computed with the Monte Carlo approach for all the generations (red solid line). The radiation from the first generation (Monte Carlo result) is plotted as well for comparison (red dotted line). 183

- 88 *Left panel*: Effect of the ambient magnetic field on the cascade radiation (first generation). The cascade is computed with the same parameters (semi-analytical approach) as used in Fig. 82 for $\psi = 30^\circ$ with an uniform magnetic field $B = 0$ (top), 1, 3, and 10 G (bottom). The cascade radiation (dashed red line) is compared with the injected (dotted line) and the full escaping gamma-ray spectra (blue solid line). *Right panel*: Effect of the magnetic field on the contribution from extra-generations in the cascade for $B = 0, 3,$ and 10 G and $\psi = 90^\circ$. The full escaping gamma-ray spectrum (Monte Carlo approach) with all generation (solid blue line) is compared with the one-generation cascade approximation (red dashed line). 184
- 89 Theoretical TeV lightcurve in LS 5039 (two full orbits, blue solid line) for $i = 60^\circ$ (*top panel*) and $i = 40^\circ$ (*bottom panel*), where 3D pair cascade radiation is computed with the Monte Carlo code for a finite-size and black-body companion star. The contribution from the cascade only (red solid line) and HESS data points are shown for comparison. Lightcurves are averaged in phase interval of width $\Delta\phi = 0.1$. The orbital parameters are taken from Casares *et al.* (2005b). Conjunctions are indicated by dotted lines. 186
- 90 Theoretical gamma-ray spectra in LS 5039 with $i = 40^\circ$. Spectra are averaged over the "SUPC" ($0.45 < \phi < 0.9$, green dashed line) and "INFC" ($\phi < 0.45$ or $\phi > 0.9$, green solid line) states as defined in Aharonian *et al.* (2006), and over the whole orbit (blue line). *Fermi* (data points and red contours) and HESS (red bowties) measurements are overplotted. The full 3D pair cascade emission is included (Monte Carlo calculations). The ambient magnetic field is chosen small $B < 1$ G. 187
- 91 Spatial distribution of the gamma-ray flux in LS 5039 at periastron (*top panels*), superior conjunction, apastron and inferior conjunction (*bottom panels*). These maps show the cascade gamma-ray emission in the high-energy (flux > 1 GeV, *middle panels*) and very-high energy bands (flux > 100 GeV, *right panels*) from the first generation only. These calculations were performed with the semi-analytical method. Each maps are centered to the massive star center. The orbit seen with an inclination $i = 60^\circ$ is shown on the left panel. The position of the compact object in the orbit is indicated by red solid line and a black dot. 188
- 92 The gamma-ray source may not coincide with the compact object location (green circle) but could be localized further away at a distance d' from the massive star center in the orbital plane (blue circle in the "pulsar wind"), or above the orbital plane at an altitude h (blue circle in the "jet"). 189
- 93 Same as in Fig. 89 for $i = 60^\circ$, where the TeV primary source is located in the orbital plane with $d' = 3d$ (*top panel*) or above and perpendicular to the orbital plane at an altitude $h = R_*$ (*bottom panel*). 190
- 94 Theoretical spectrum of the cascade radiation (first generation) averaged over the orbit with a uniform ambient magnetic field $B = 0.1, 1, 5$ and 10 G. Suzaku (Takahashi *et al.* 2009), *Fermi* (Abdo *et al.* 2009b) and HESS (Aharonian *et al.* 2006) observations are shown for comparison. 191
- 95 Emission processes seen in the observer frame (*left panel*) and in the comoving frame of the flow (*right panel*). Waves represent photons and the green thick arrow shows the

- direction of motion of the flow with a bulk Lorentz factor $\Gamma > 1$. The boost from the observer to the comoving frame is along the z-axis. 208
- 96 Effect of the Doppler boost on synchrotron radiation flux for a power law spectrum. The flux is increased by a factor \mathcal{D}_{obs}^3 and the power law is shifted in energy by a factor \mathcal{D}_{obs} . 210
- 97 Doppler factor \mathcal{D}_{obs} as a function of the cosine of the angle between the observer and the flow μ_{obs} for $\beta = 0$ (red dashed line), 0.1, 0.5 and 0.9 (*top*). The flux is forward boosted by the flow ($\mathcal{D}_{obs} > 1$) in a cone of semi aperture angle $\sim 1/\Gamma$, otherwise the flux is deboosted ($\mathcal{D}_{obs} < 1$). 210
- 98 Doppler factor \mathcal{D}_{obs} as a function of β for $\psi_{obs} = 0^\circ$ (dashed blue line) 20° , 30° , 60° , 90° and 180° . The flux is deboosted ($\mathcal{D}_{obs} < 1$) if $\Gamma \gtrsim 1/\psi_{obs}$. 211
- 99 Boosted anisotropic inverse Compton emission in the observer frame (blue solid lines) for $\psi_{obs} = 180^\circ$ and $\theta_{flow} = 0^\circ$ for a bulk velocity of the flow (from *top* to *bottom*) $\beta = 0, 0.1, 0.3, 0.5$ and 0.9 . Pairs are injected with an isotropic power law energy distribution with $\gamma_- = 10^2$ and $\gamma_+ = 10^7$, and with an index $p = 2$. The red dashed lines give the analytical solution found in Eq. (80.316) valid in the Thomson limit. The source of soft photon is point like with a black body spectrum of temperature $T_\star = 39\,000$ K in the observer frame. 213
- 100 Inverse Compton flux as a function of ψ_{obs} for $\theta_{flow} = 0^\circ$ and for a bulk velocity of the flow $\beta = 0$ (*top left* panel), 0.1 (*top right* panel), 0.3 (*bottom left* panel) and 0.5 (*bottom right* panel). The orbital phase is defined here as $\psi_{obs}/2\pi$ so that $\psi_{obs} = 180^\circ$ corresponds to 0.5 . Curves are normalized and integrated over energies above 100 MeV (blue lines) and above 100 GeV (red lines), with $T_\star = 39\,000$ K. 214
- 101 Geometry in gamma-ray binaries for the calculation of the Doppler-boosted emission. The shocked pulsar wind is collimated, inclined at an angle θ_{flow} with respect to the massive star-pulsar direction and is contained in the orbital plane. A distant observer sees the system with a viewing angle ψ_{obs} . The emission originates from a very small region (blue disk) at the pulsar location. 219
- 102 Orientation of the shocked pulsar wind in LS 5039. In this system, the flow is assumed radial. 220
- 103 *Left* panels: Theoretical non-thermal radiation expected in the one-zone leptonic model Dubus *et al.* (2008) with no Doppler boost $\beta = 0$. SUPC and INFC spectra are compared with *Suzaku* (Takahashi *et al.* 2009), *Fermi* (Abdo *et al.* 2009b) and HESS (Aharonian *et al.* 2006) bowties on the *top* panel. The expected very-high energy (*middle* panel) and X-ray (*bottom* panel) lightcurves are also shown. *Right* panels: The same as in the *left* panels with a Doppler boost $\beta = 1/3$ and $\theta_{flow} = 0^\circ$. 221
- 104 Orientation of the shocked pulsar wind in LS I +61°303. In this system, the flow is assumed tangent to the orbit in the opposite direction of the orbital motion. 222
- 105 *Left* panels: Theoretical synchrotron (red lines) and inverse Compton radiation (blue lines) expected in a one-zone leptonic model as a function of the orbital phase in LS I +61°303 (two full orbits). Electrons are injected with a constant power law energy distribution of index $p = 2$ and are bathed in a constant magnetic field along the orbit. In the *top* panel, synchrotron and the inverse Compton fluxes are calculated with $\beta = 0$. In the last two

- panels, $\beta = 1/3$ and the flow is assumed tangent to the orbit. Inverse Compton emission is computed with the analytical formula found in Eq. (80.316) (Thomson limit). The exact inverse Compton flux (with Klein-Nishina effects) computed above 100 GeV is shown in the *bottom* panel. The absorbed Compton gamma-ray lightcurve is shown with dashed line. The orbital parameters are taken from Aragona *et al.* (2009) and the origin $\phi = 0$ was chosen at periastron for this plot, *i.e.* 0.275 should be added to the phasing used in Aragona *et al.* (2009) and in the text. *Right panels:* Application to PSR B1259 – 63 with $\beta = 0$ (*top*), $1/3$ (*middle*) and 0.9 (*bottom*). 223
- 106 *Left panel:* Geometry of the jet in Cygnus X–3. The compact object produces a two-sided inclined jet with a relativistic velocity $\boldsymbol{\beta} = \pm\beta\mathbf{e}_j$. Stellar photons are upscattered to high energies by energetic electrons localized at two symmetric positions at an altitude H in the jet (blue disk) and counter-jet (red dashed disk). *Right panel:* Top view of the compact object orbit. 239
- 107 High-energy gamma-ray flux (> 100 MeV) in Cygnus X–3 as a function of the orbital phase (two full orbits here) for the black hole solution. The solution shown (blue solid line) has a $\chi^2 = 2.9$ for a set of parameters $\beta = 0.45$, $H = 8.5 \times 10^{11}$ cm, $\phi_j = 12^\circ$, $\theta_j = 106^\circ$ and with a total power in electrons $P_e = 1.12 \times 10^{38}$ erg s $^{-1}$ (where $\gamma_- = 10^3$). The contributions from the jet (red solid line) and the counter-jet (red dashed line) are shown as well for comparison. The folded *Fermi* lightcurve data points are taken from Fermi LAT Collaboration (2009). 241
- 108 Distribution of good fit models in the 90% of confidence region of the χ^2 statistics for the black hole solution (*left panels*) and for the neutron star solution (*right panels*) for the parameters β (*top panels*), H , ϕ_j and θ_j (*bottom panels*). The filled regions give the number of models such as the total power injected into pairs P_e is $\lesssim L_{edd}$ (light grey region), $\lesssim 10^{-1}L_{edd}$ (grey region) and $\lesssim 10^{-2}L_{edd}$ (dark grey region). The Eddington luminosity is $L_{edd} = 2 \times 10^{39}$ erg s $^{-1}$ for the black hole and $L_{edd} = 2 \times 10^{38}$ erg s $^{-1}$ for the neutron star. 242
- 109 Effect of the precession of the jet on the high-energy emission and modulation in Cygnus X–3. From the best fit solution (black solid line) with $\theta_j = 319^\circ$, only the azimuth angle is changed to (from dark to light grey line) $\theta_j = 31^\circ, 103^\circ, 175^\circ$ and 247° . 243
- 110 Geometry of a standard accretion disk. The compact object is located at the origin and the gamma-ray source above the accretion disk. Gamma-ray photons propagating towards the observer can be absorbed by thermal photons from the disk. 244
- 111 Gamma-ray opacity map $\exp(-\tau_{\gamma\gamma})$ as a function of the viewing angle ψ and the altitude of the gamma-ray source z in the jet, for $r = 0$ (along the axis of the accretion disk). Bright regions indicate low opacity $\tau_{\gamma\gamma} \ll 1$ and dark regions high opacity ($\tau_{\gamma\gamma} \gg 1$). The gamma-ray photons have an energy $\epsilon_1 = 1$ GeV and propagate above an accretion of inner radius $R_{in} = 10^7$ cm and external radius $R_{ext} = 10^{11}$ cm with $\dot{M} = 10^{-8}M_\odot$ yr $^{-1}$. The white dotted line indicates $z = R_{in}$ and the black dotted line $z = d$. 245
- 112 Same as in Fig. 111 in the (r, z) plane for a viewing angle $\psi = 0^\circ$ (*left panel*) and $\psi = 45^\circ$ (*right panel*). The black dashed lines indicate $r = R_{in}$ and $r = R_{ext}$. 246

113 Gamma-ray opacity as a function of the gamma-ray energy ϵ_1 for $z = 100R_{in}$ on axis ($r = 0$) and $\psi = 0^\circ, 30^\circ, 60^\circ$, and 90° .

List of tables

- | | | |
|---|--|-----|
| 1 | Physical and orbital parameters in gamma-ray emitting binaries adopted in this thesis. | 5 |
| 2 | Parameters used for the modeling of the Compton emission shown in Fig. 48. | 107 |

Part I

Introduction

1	What is this thesis about?	3
2	Relevant high-energy processes	15

1

What is this thesis about?

Outline

1. The cosmic accelerators uncovered by the gamma-ray astronomy.....	3
2. Binary systems in the gamma-ray sky!	4
§ 1. <i>Gamma-ray binaries</i>	4
§ 2. <i>Microquasars</i>	6
3. Objectives of this thesis: What we want to understand	7
4. Guidelines: How is this thesis constructed?	8

1. The cosmic accelerators uncovered by the gamma-ray astronomy

THERE IS EVIDENCE that particles are accelerated up to ultra-high energies ($> 10^{19}$ eV) in our Universe. How and where these energetic particles are accelerated are still highly debated questions. Thanks to space and ground-based facilities, gamma-ray astronomy has firmly identified during the last couple of years many astrophysical objects where particles are accelerated to high (> 100 MeV) and very-high (> 100 GeV) energies. Gamma rays are very energetic photons ($\gtrsim 100$ keV) produced when these high-energy particles interact or decay. Gamma-ray astronomy reveals the most energetic phenomena taking place in our Universe related to extreme physical conditions, as for instance high-energy densities, relativistic outflows or strong gravitational fields. The gamma-ray sky is also highly variable. This behavior is associated with the activity and the physics of compact objects such as neutron stars or black holes.

Gamma-ray astronomy is undoubtedly living its golden age today where space and ground based telescopes cover the sky simultaneously over 6 orders of magnitude in energy range (from 100 MeV to 100 TeV) with unprecedented sensitivity and angular resolution. We are facing a period in the history of high-energy astrophysics when the gamma-ray astronomy is mature enough to make reliable and direct observations of the cosmic accelerators. More than a hundred sources¹ have been detected by the third generation of Atmospheric Cherenkov telescopes such as HESS, MAGIC and VERITAS above 1 TeV and more than a thousand sources

¹See the TeVCat at <http://tevcap.uchicago.edu/> for an updated catalog.

have been detected at GeV energies by the space gamma-ray telescopes *Fermi* and *AGILE* (see e.g. the first *Fermi* LAT source catalog, The Fermi-LAT Collaboration 2010). The extragalactic gamma-ray sky is dominated by Active Galactic Nuclei (or AGN). The detection of gamma-ray bursts (or GRBs) and a few starburst Galaxies have also been reported. In our Galaxy, most of gamma-ray sources are pulsars, pulsar wind nebulae and supernova remnants but many other sources remain unidentified. Amongst the Galactic gamma-ray sources, there are a few of binary systems. This thesis is focused on these systems.

2. Binary systems in the gamma-ray sky!

Four gamma-ray sources have been firmly associated with Galactic binary systems, namely: LS I +61°303, LS 5039, PSR B1259 – 63 and Cygnus X–3. These identifications are definitively established thanks to the good localisations of the sources in the sky and to the very-high detection significance level (high signal/noise ratio). These gamma-ray sources are time-variable and demonstrably modulated on the orbital period in some cases (Aharonian *et al.* 2006; Albert *et al.* 2009; Aharonian *et al.* 2009; Abdo *et al.* 2009a,b; Fermi LAT Collaboration 2009). This is the main observational signature of these systems. These gamma-ray emitting binaries are composed of a massive non-degenerated star (Be, O or Wolf-Rayet) and a compact object. The parameters of these binaries (orbit, distance, companion star, ...) are known from optical spectroscopy and are summarized in Tab. 1 (see also the orbits in Fig. 1).

The TeV gamma-ray source HESS J0632 + 057, serendipitously discovered by HESS (Aharonian *et al.* 2007), might be also associated with a binary system (Hinton *et al.* 2009), but no orbital modulation has been reported yet even though the source exhibits some variability (Acciari *et al.* 2009). A TeV gamma-ray flare from Cygnus X–1 has been reported by the MAGIC collaboration (Albert *et al.* 2007) but with a low significance. In addition, the detection of GeV gamma-ray flares have been claimed by the *AGILE* collaboration (Sabatini *et al.* 2010), but these observations have not been confirmed by *Fermi*. I will not consider these two binary systems as firmly established gamma-ray emitting binaries in this thesis.

In this sample of binaries, we have two distinct classes of objects:

- Gamma-ray binaries: LS 5039, LS I +61°303 and PSR B1259 – 63 (and HESS J0632 + 057 ?).
- Microquasars: Cygnus X–3 (and Cygnus X–1 ?).

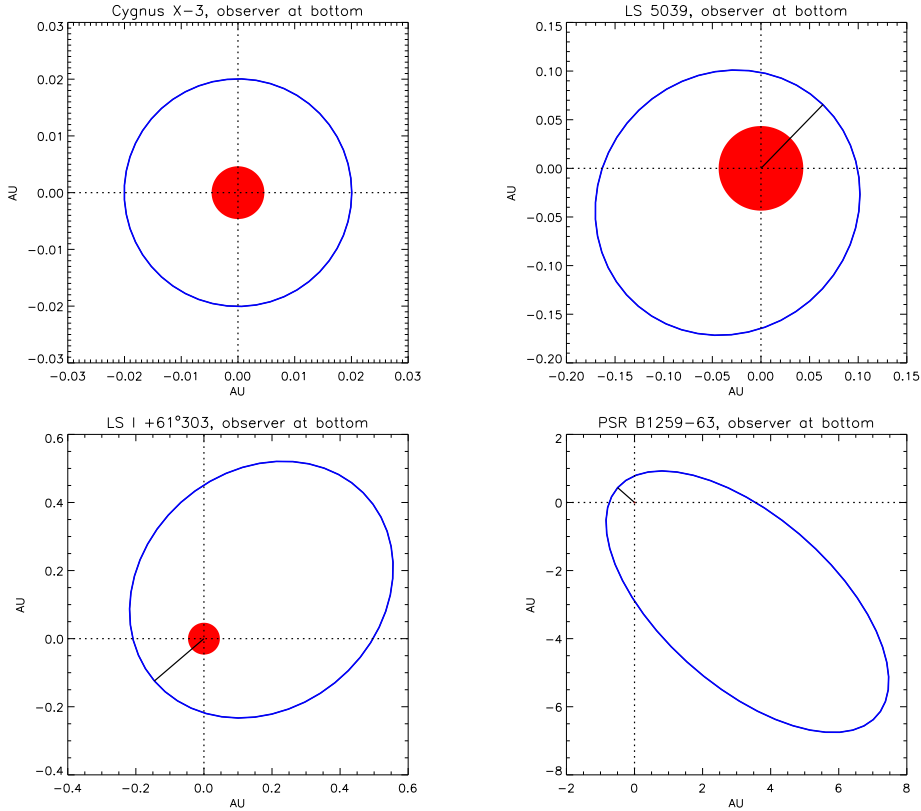
I give below the main properties of these objects and intend to depict the scenario of emission considered in this thesis for "gamma-ray binaries" and for "microquasars".

§ 1. Gamma-ray binaries

These systems emit non-thermal radiation from radio up to 10 TeV. Their non-stellar luminosity is maximum above 1 MeV, hence the name given to these systems "Gamma-ray binaries" (Dubus 2006b). The gamma-ray emission observed is steady with a low orbit-to-orbit variability. The TeV luminosity measured in these systems is high $L_\gamma \sim 10^{32}$ - 10^{33} erg s⁻¹ and is of the order of the X-ray luminosity. In PSR B1259 – 63, the compact object is a young 48 ms pulsar. Radio pulses are detectable but vanish near the passage to periastron, probably due to free-free absorption in

TAB. 1. Physical and orbital parameters in gamma-ray emitting binaries adopted in this thesis.

System	PSR B1259 – 63	LS I +61°303	LS 5039	Cygnus X–3
GeV or TeV emission?	TeV	GeV and TeV	GeV and TeV	GeV
Companion star type	Be	Be	O	WR
Stellar Temperature T_* (in K)	27 000	22 500	39 000	100 000
Stellar radius R_* (in R_\odot)	10	10	9.3	0.6 – 2.3 (?)
Star mass M_* (in M_\odot)	10	12	23	5 – 50 (?)
Distances (in kpc)	1.5	2	2.5	7
Compact object ¹	NS	NS or BH	NS or BH	NS or BH
Orbital period P_{orb} (days)	1237	26.5	3.9	0.2
Eccentricity e	0.87	0.537	0.337	0
Inclination i (degree)	35	?	?	?
Periastron angle ω (degree)	139	40.5	236	0

**FIG. 1.** Top view of the compact object orbit (blue line) in Cygnus X–3 (*top left*), LS 5039 (*top right*), LS I +61°303 (*bottom left*) and PSR B1259 – 63 (*bottom right*). The red filled disk represents the massive star at scale in the system and the back solid line indicates periastron. The observer sees the orbit from the bottom.

the Be stellar wind (Johnston *et al.* 1992). In LS 5039 and LS I +61°303, the nature of the compact object is still unknown.

¹NS: Neutron star, BH: Black Hole.

Maraschi & Treves (1981) suggested that the non-thermal emission in LS I +61°303 arises from the interaction of the relativistic wind generated by a young fast-rotating pulsar with the companion star wind (note that this scenario has been first proposed for Cygnus X–3 by Bignami *et al.* 1977). A small-scale pulsar-wind nebula is formed in the system. In PSR B1259 – 63, this scenario is most probably at work regarding the nature of the compact object in this system (Tavani *et al.* 1994; Kirk *et al.* 1999), but this is not clear for the other two binaries. However, the three systems share the same spectral and temporal features as depicted above. This argues in favor of a common scenario (Dubus 2006b). Gamma-ray binaries may all harbor a young fast-rotating pulsar. This is the "pulsar wind nebula" scenario. In addition, LS 5039 and LS I +61°303 do not show any sign of accretion (see the discussion in Dubus 2006b), arguing against accretion-power scenario. However, some models have been proposed in the "microquasar" scenario (see next section) *i.e.* where the high-energy emission originates from a relativistic jet powered by accretion on a black hole (see *e.g.* the works by Dermer & Böttcher 2006; Paredes *et al.* 2006; Romero *et al.* 2007).

In the pulsar wind nebula scenario (see the sketch in Fig. 2), high-energy electron-positron pairs are injected by the pulsar in a cold relativistic wind ("unshocked", green area in Fig. 2). The wind propagates freely up to the termination shock created by the collision with the stellar wind. In the "shocked" pulsar wind (red area in Fig. 2), pairs are randomized, accelerated and radiate non-thermal radiation. If the massive star wind is strong, the pulsar wind may be confined in a collimated outflow. A comet-like tail spiraling around the system forms in the system due to the orbital motion of the pulsar. This scenario provides a common framework to interpret the spectral and temporal behaviors in these systems.

The study of gamma-ray binaries has important implications. The wind of isolated pulsars is confined by the material of its supernova remnant on parsec scales. In gamma-ray binaries, the pulsar wind is confined to sub-AU scales by the massive star wind. These systems provide a novel environment for the study of pulsar winds at very small scales. The formation, the composition and the acceleration processes in pulsar winds are still poorly understood today. These important issues will undoubtedly benefit from the study of gamma-ray binaries.

§ 2. Microquasars

Microquasars are accreting binary systems with relativistic jets which are similar to those found in AGN or GRBs but on Galactic scales. In spite of the huge different spatial scales, AGN and microquasars exhibit many similarities in their temporal and spectral behaviors, suggesting that the same underlying physics is at work. In such systems, the primary source of energy is gravitational. Material from the normal star is accreted on the compact object (neutron star or black hole). Part of the accretion power is channeled in the formation and acceleration of a relativistic jet (see the diagram in Fig. 3). The observation of non-thermal radiation in radio up to X-rays from microquasar jets provides good evidence for particle acceleration up to 10 TeV (Corbel *et al.* 2002). The firm detection of Cygnus X–3 in gamma rays by *Fermi* gives the definitive evidence that microquasars emit high-energy gamma rays. Contrary to gamma-ray binaries, the gamma-ray luminosity is lower than the X-ray luminosity ($L_\gamma \lesssim 10^{-2}L_X$ in Cygnus X–3). In addition, the gamma-ray emission is transient and related to major ejections events in the relativistic jet. The study of microquasars in gamma rays is particularly interesting as these

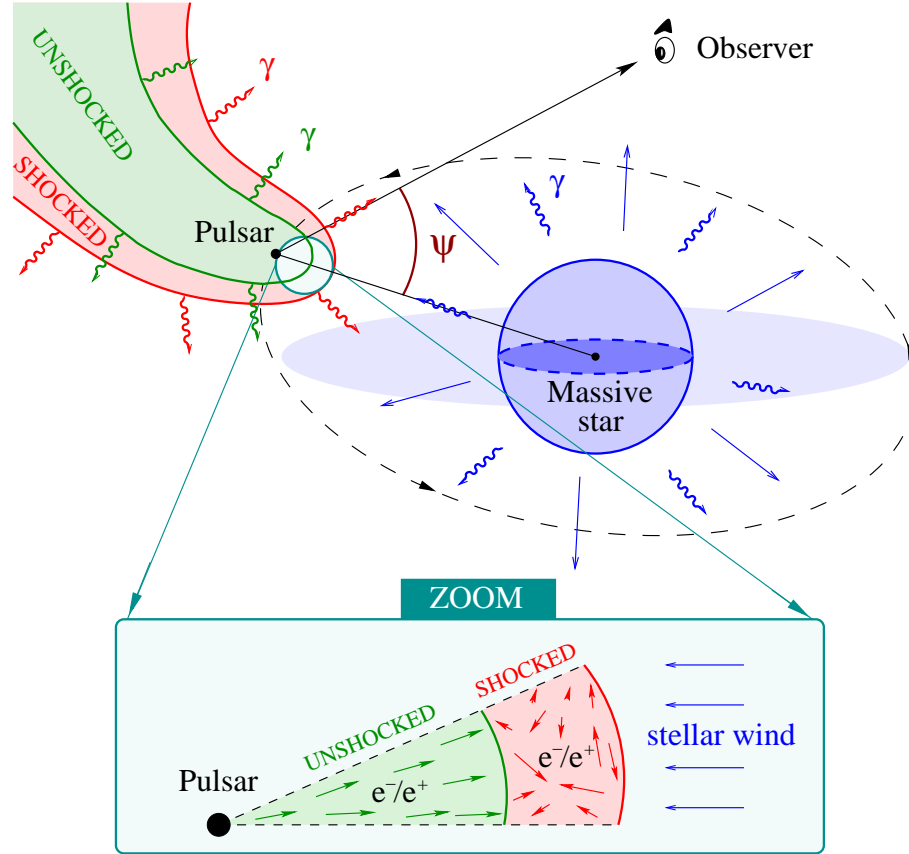


FIG. 2. This sketch depicts the main components in gamma-ray binaries involved in the non-thermal emission mechanism, in the pulsar wind nebula scenario (see the text for explanations).

systems provide a nearby and well constrained laboratory to understand the accretion-ejection mechanisms and the acceleration processes in relativistic jets. This also benefits to the study of AGN.

3. Objectives of this thesis: What we want to understand

This thesis is dedicated to the modeling of the high-energy radiation emitted by gamma-ray binaries and microquasars. The study presented here was triggered by the intriguing HESS observations of the gamma-ray modulation in LS 5039. My thesis focuses on the theoretical modeling of the gamma-ray variability (flux and spectrum) in gamma-ray emitting binaries. For this, it is important to take into account the full complexity of the geometry in all the relevant high-energy processes. The ultimate goal of this thesis would be to answer the following questions:

1. What are the relevant processes in compact binaries at high energies?
2. Where does the gamma-ray orbital modulation come from?
3. What is the nature of the compact object in these systems?
4. Where does particle acceleration take place?
5. What fraction of the total power (rotation, accretion) is channeled into non-thermal particles?

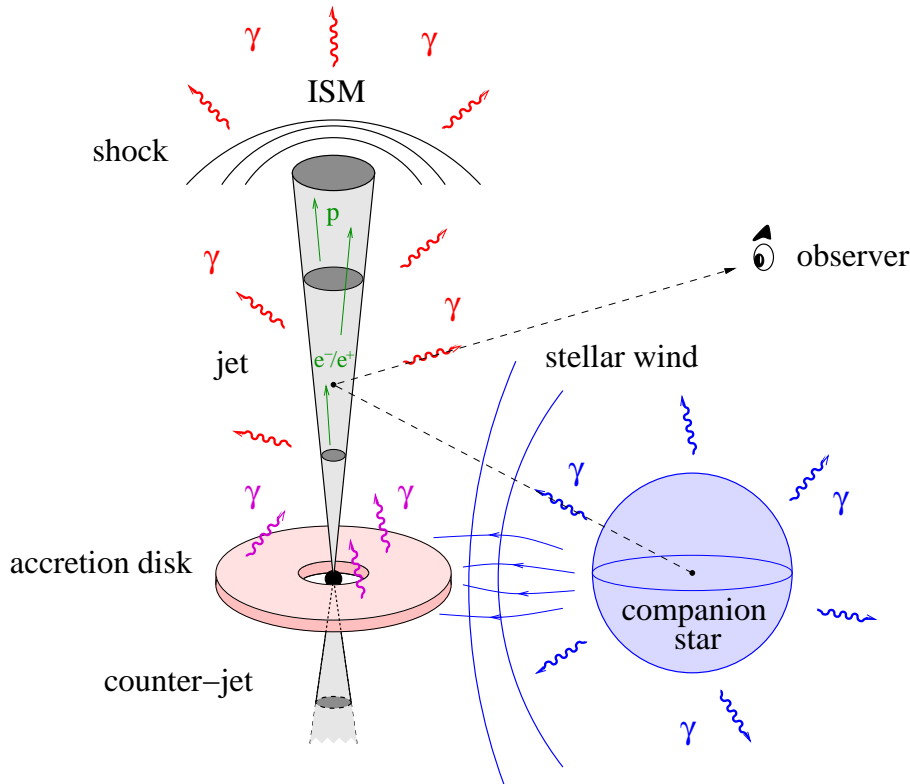


FIG. 3. Sketch of a microquasar and of its different components. Energetic particles are accelerated in the relativistic jet and radiate high-energy emission.

6. What is the physics at work in pulsar winds?
7. What is the emission from relativistic outflows?

4. Guidelines: How is this thesis constructed?

The manuscript is divided into 5 distinct parts and 12 chapters. Below, I give an overview of each part and indicate the related questions (out of the ones listed in the previous section) for which it aims to answer.

Part I presents the main objectives of this thesis (this Chapter) and introduces the main processes considered in high-energy astrophysics (Chapter 2). The main objective of this part is to distinguish amongst the known high-energy processes which one are the most relevant in binaries (Question 1). Hadronic and leptonic origin of the high-energy gamma rays are discussed. Chapter 2 provides the main equations for the computation of high-energy processes which will be useful throughout this thesis. This toolbox is however incomplete and is not always appropriate in our context. In consequence, I had to develop specific theoretical tools adapted for the modeling of the high-energy emission in a binary environment. These tools are presented in Chapter 3, 6 and 9 at the beginning of each part (II, III and IV).

Part II is dedicated to the modeling of the gamma-ray emission from gamma-ray binaries, in the framework of the pulsar wind nebula scenario. Chapter 4 will focus on the emission from the "shocked" pulsar wind and Chapter 5 on the emission from the "unshocked" wind. The goal of this part is to see whether the pulsar wind nebula model provides a viable scenario to account

for gamma-ray observations and in particular the modulation (Question 2). The objective is also to formulate new constraints on the physics of pulsar winds such as the magnetic field or the particle energy distribution (Question 5, 6 & 7).

In LS 5039, gamma-ray absorption is very high and leads to the creation of many electron-positron pairs. These particles can initiate a cascade of new pairs and contribute significantly to the total gamma-ray flux. The model of the shocked pulsar wind (Chapter 4) fails to account for the observed TeV gamma-ray flux where gamma-ray absorption is very high. The high-energy radiation reprocessed by the cascade could reduce significantly the gamma-ray opacity in LS 5039, and could explain the observed TeV gamma-ray flux.

Part III focuses on the modeling of pair cascade emission in gamma-ray binaries, particularly in LS 5039. As a first attempt and in order to quantify the relevance of this process, I present a one-dimensional model for the cascade radiation in binaries (Chapter 7). I will show that this type of cascade is not realistic but provides an upper limit of the cascade emission where absorption is very high. In LS 5039, a more realistic assessment of the gamma-ray emission from the cascade is required. I developed a three-dimensional model for the cascade in gamma-ray binaries in collaboration with Julien Malzac which I apply to the case of LS 5039 (Chapter 8). The main objective is to explain the amplitude of the TeV gamma-ray modulation (Question 2). I investigate also in this part the effect the ambient magnetic field and the effect of the location of the gamma-ray emitter in LS 5039 (Question 4).

Part IV describes the effects of a relativistic bulk motion on radiative processes (Question 7) in the context of pulsar winds in gamma-ray binaries (Chapter 10). In the classical model of pulsar winds, the shocked pulsar wind has a mildly relativistic bulk velocity. Relativistic Doppler-boosting effects should change the high-energy emission and change the modulation (Question 2). These effects are precisely investigated in this part. I formulate constraints on the bulk velocity of the flow (Question 6).

In Part IV, I present also a new model for the gamma-ray emission in the microquasar Cygnus X-3 (Chapter 11). The main objective is to explain the origin of the GeV gamma-ray orbital modulation in this system (Question 2). The fit of the theoretical to the observed lightcurve constrains the geometry and the physics of the jet in Cygnus X-3 (Question 3, 4, 5 & 7).

Part V briefly summarizes the main results obtained in this thesis. The list of questions given in the first chapter is updated and addressed to future investigations.

[Français] De quoi parle cette thèse?

5. Les accélérateurs cosmiques découverts par l'astronomie gamma

Nous savons que des particules sont accélérées jusqu'à ultra haute énergie ($> 10^{19}$ eV) dans notre Univers. Comment et où ces particules énergétiques sont accélérées sont des questions encore très débattues aujourd'hui. Grâce aux instruments spatiaux et au sol, l'astronomie gamma a fermement identifiée au cours de ces dernières années beaucoup d'objets astrophysiques où des particules de haute (> 100 MeV) et très haute (> 100 GeV) énergie sont accélérées. Les rayons gamma sont des photons très énergétiques ($\gtrsim 100$ keV) produits lorsque ces particules de très haute énergie interagissent ou décroissent. L'astronomie gamma révèle les phénomènes les plus énergétiques qui se passent dans notre Univers, phénomènes reliés à des conditions physiques extrêmes (densités d'énergies élevées, écoulements relativistes, champs gravitationnels intenses, ...). Le ciel gamma est aussi extrêmement variable. Cette propriété est associée à l'activité et à la physique des objets compacts tels que les étoiles à neutrons ou les trous noirs.

L'astronomie gamma vit aujourd'hui son âge d'or au cours duquel des télescopes au sol et dans l'espace couvrent simultanément le ciel sur plus de 6 ordres de grandeur en énergie (de 100 MeV à 100 TeV) avec une sensibilité et une résolution angulaire sans précédent. Nous vivons une période de l'histoire de l'astrophysique des hautes énergies au cours de laquelle l'astronomie gamma est suffisamment mature pour produire des observations directes et fiables des accélérateurs cosmiques. Plus d'une centaine de sources² ont été détectées par la troisième génération de télescopes atmosphérique Cherenkov tels que HESS, MAGIC et VERITAS au-dessus de 1 TeV et plus d'un millier de sources ont été détectées au GeV par les satellites gamma *Fermi* et *AGILE* (voir *e.g.* le premier catalogue *Fermi* des sources détectées par le LAT, The Fermi-LAT Collaboration 2010). Le ciel gamma extragalactique est dominé par les noyaux actifs de Galaxies (ou AGN). Les détections de sursauts gamma (ou GRBs) et de quelques galaxies "starburst" ont été également rapportées. Dans notre galaxie, la plupart des sources gamma sont des pulsars, des nébuleuses de pulsar et des restes de supernovae mais beaucoup d'autres restent encore non identifiées. Parmi les sources galactiques, il y a quelques systèmes binaires. Toute notre attention sera portée sur ces systèmes dans cette thèse.

6. Des systèmes binaires dans le ciel gamma!

Quatre sources gamma ont été fermement associées à des systèmes binaires: LS I +61°303, LS 5039, PSR B1259 – 63 et Cygnus X–3. Ces identifications sont définitivement établies grâce à la très bonne localisation des sources dans le ciel et au niveau de détection très élevé (grand

²Voir le TeVCat à l'adresse <http://tevcat.uchicago.edu/> pour un catalogue mis à jour.

rapport signal/bruit). Ces sources gamma sont variables dans le temps et présentent une modulation orbitale de leur flux dans certains cas (Aharonian *et al.* 2006; Albert *et al.* 2009; Aharonian *et al.* 2009; Abdo *et al.* 2009a,b; Fermi LAT Collaboration 2009). C'est la principale signature observationnelle de ces systèmes. Ces binaires qui émettent du rayonnement gamma sont toutes composées d'une étoile massive non dégénérée (Be, O ou Wolf-Rayet) et d'un objet compact. Les paramètres de ces binaires (orbite, distance, étoile compagnon, ...) sont connus par spectroscopie optique et sont résumés dans Tab. 1 (voir aussi les orbites sur Fig. 1).

La source gamma TeV HESS J0632 + 057, découverte fortuitement par HESS (Aharonian *et al.* 2007), pourrait être aussi associée à un système binaire (Hinton *et al.* 2009), mais aucune modulation orbitale n'a été observée pour l'instant même si la source présente une certaine variabilité (Acciari *et al.* 2009). Une éruption gamma au TeV en provenance de Cygnus X-1 a été rapportée par la collaboration MAGIC (Albert *et al.* 2007) mais avec une faible significativité. De plus, la détection d'éruptions gamma au GeV a été annoncée par la collaboration *AGILE* (Sabatini *et al.* 2010), mais ces observations n'ont pas été confirmées par *Fermi*. Je ne considérerai donc pas ces deux systèmes binaires comme étant des émetteurs de rayons gamma dans cette thèse.

Dans cet échantillon de binaires, nous avons deux classes d'objets:

- Binaires gamma: LS 5039, LS I +61°303 et PSR B1259 – 63 (et HESS J0632 + 057 ?).
- Microquasars: Cygnus X-3 (et Cygnus X-1 ?).

Je présente ci-dessous les principales propriétés de ces objets et j'essaie de décrire les scénarios d'émission considérés dans cette thèse pour les "binaires gamma" et pour les "microquasars".

§ 3. Les binaires gamma

Ces systèmes émettent du rayonnement non-thermique de la radio jusqu'à 10 TeV. Leur luminosité non stellaire est maximale au-dessus de 1 MeV, d'où le nom donné à ces systèmes de "binaires gamma" (Dubus 2006b). L'émission gamma observée est stationnaire avec une faible variabilité inter-orbitale. La luminosité TeV mesurée dans ces systèmes est élevée $L_\gamma \sim 10^{32}$ - 10^{33} erg s⁻¹ et est de l'ordre de la luminosité X. Dans PSR B1259 – 63, l'objet compact est une pulsar jeune de période 48 ms. Les pulses radio sont observés mais disparaissent à proximité du passage au périastre, probablement à cause de l'absorption dans le vent de l'étoile Be (Johnston *et al.* 1992). Dans LS 5039 et LS I +61°303, la nature de l'objet compact reste toujours inconnue.

Maraschi & Treves (1981) suggérèrent que l'émission non-thermique dans LS I +61°303 provient de l'interaction entre le vent relativiste généré par un pulsar jeune en rotation rapide et le vent de l'étoile compagnon (remarquons ici que ce scénario a été pour la première fois proposé pour Cygnus X-3 par Bignami *et al.* 1977). Une nébuleuse de pulsar à petite échelle se forme dans le système. Dans PSR B1259 – 63, ce scénario est très probablement à l'oeuvre étant donné la nature de l'objet compact dans le système (Tavani *et al.* 1994; Kirk *et al.* 1999), mais cela n'est pas clair pour les deux autres binaires. Cependant, les trois systèmes partagent les mêmes propriétés spectrales et temporelles comme décrit ci-dessus, supportant ainsi l'idée d'un scénario commun (Dubus 2006b). Les binaires gamma contiendraient toutes un pulsar jeune en rotation rapide. C'est le scénario de la "nébuleuse de vent de pulsar". De plus, LS 5039 et LS I +61°303 ne présentent aucun signe d'accrétion (voir la discussion dans Dubus 2006b), allant ainsi à l'encontre d'un scénario de type accrétion. Cependant, quelques modèles ont été

proposés dans le scénario "microquasar" (voir la section suivante) *i.e.* dans lequel l'émission gamma de haute énergie provient d'un jet relativiste alimenté par accrétion sur un trou noir (voir *e.g.* les travaux par Dermer & Böttcher 2006; Paredes *et al.* 2006; Romero *et al.* 2007).

Dans le scénario du vent de pulsar (voir le schéma sur Fig. 2), des paires électron-positron de haute énergie sont injectées par le pulsar dans un vent relativiste ("unshocked", zone verte dans Fig. 2). Le vent se propage librement jusqu'au choc terminal créé par la collision avec le vent stellaire. Dans le vent choqué du pulsar ("shocked", zone rouge dans Fig. 2), les paires sont isotropisées, accélérées et rayonnent de l'émission non-thermique. Si le vent de l'étoile massive est fort, le vent du pulsar peut être confiné en un écoulement collimaté. Une structure en queue cométaire spiralant autour du système se forme dûe au mouvement orbital du pulsar. Ce scénario fournit un cadre commun pour interpréter le comportement spectral et temporel dans ces systèmes.

L'étude des binaires gamma a des implications importantes. Le vent d'un pulsar isolé est confiné par la matière du reste de supernova sur une échelle de l'ordre du parsec. Dans les binaires gamma, le vent du pulsar est confiné à des échelles bien plus faibles (sub UA) par le vent de l'étoile massive. Ces systèmes fournissent un environnement nouveau pour l'étude des vents de pulsar à de très petites échelles spatiales. La formation, la composition et les processus d'accélération dans les vents de pulsar sont toujours mal compris aujourd'hui. Les binaires gamma contribueront sans doute à répondre à ces importantes questions.

§ 4. Microquasars

Les microquasars sont des systèmes binaires accrétants avec des jets relativistes, similaires à ceux rencontrés dans les AGN ou les GRBs mais à des échelles galactiques. Malgré l'énorme différence d'échelle spatiale, les AGN et les microquasars présentent beaucoup de similarités dans leur comportement temporel et spectral, suggérant qu'une même physique sous-jacente est à l'oeuvre. Dans de tels systèmes, la source primaire d'énergie est gravitationnelle. La matière en provenance de l'étoile normale est accrétée par l'objet compact (étoile à neutron ou trou noir). Une partie de l'énergie d'accrétion est canalisée pour former et accélérer un jet relativiste (voir le schéma dans Fig. 3). L'observation d'émission non-thermique de la radio jusqu'en X en provenance du jet dans certains microquasars apporte la preuve que des particules sont accélérées jusqu'à 10 TeV (Corbel *et al.* 2002). La détection de Cygnus X-3 en gamma par *Fermi* apporte la preuve définitive que les microquasars peuvent émettre des rayons gamma de haute énergie. Contrairement aux binaires gamma, la luminosité gamma est plus faible que la luminosité X ($L_\gamma \lesssim 10^{-2}L_X$ dans Cygnus X-3). De plus, l'émission gamma est transitoire et reliée à des événements d'éjection importants dans le jet relativiste. L'étude des microquasars en gamma est particulièrement intéressante car ces systèmes sont des laboratoires proches et bien contraints qui permettent de mieux comprendre les mécanismes d'accrétion-éjection et les processus d'accélération dans les jets relativistes. Ces objets sont également intéressants pour l'étude des AGN.

7. Objectifs de cette thèse: Ce que nous voulons comprendre

Cette thèse est dédiée à la modélisation du rayonnement de haute énergie dans les binaires gamma et les microquasars. L'étude présentée ici a été motivée par la curieuse modulation

gamma observée par HESS dans LS 5039. Cette thèse se concentre sur la modélisation théorique de la variabilité gamma (flux et spectre) des binaires émettant en gamma. Pour cela, il est primordial de tenir compte de toute la complexité géométrique dans tous les processus pertinents à haute énergie. Le but ultime de cette thèse serait de répondre aux questions suivantes:

1. Quels sont les processus pertinents à haute énergie dans les binaires compactes?
2. Quelle est l'origine de la modulation orbitale gamma?
3. Quelle est la nature de l'objet compact dans ces systèmes?
4. Où est-ce que l'accélération des particules a lieu?
5. Quelle fraction de la puissance totale (rotationnelle, accrétion) est canalisée sous forme de particules non-thermique?
6. Quelle est la physique des vents de pulsar?
7. Quelle est l'émission produite dans les écoulements relativistes?

8. Comment cette thèse est-elle construite?

Le manuscrit est découpé en 5 parties distinctes et 12 chapitres. Ci-dessous, je donne une vue d'ensemble de chaque partie et indique l'ensemble des questions (parmi celles listées dans la section précédente) auquel nous allons tenter de répondre.

La première partie présente les principaux objectifs de cette thèse (ce Chapitre) et présente les principaux processus de haute énergie considérés en astrophysique des hautes énergies (Chapitre 2). Le principal objectif de cette partie est de sélectionner parmi l'ensemble des processus de haute énergie connus ceux qui sont les plus pertinents dans les binaires (Question 1). L'origine hadronique ou leptonique de l'émission gamma de haute énergie est discutée. Le Chapitre 2 donne les principales équations pour décrire les processus de haute énergie qui seront utiles tout au long de cette thèse. Cette boîte à outil reste néanmoins incomplète et n'est pas toujours appropriée dans notre contexte. C'est pourquoi j'ai développé des outils théoriques spécifiques adaptés à la modélisation de l'émission de haute énergie dans l'environnement d'une binaire. Ces outils sont présentés dans les Chapitres 3, 6 et 9 au début de chaque partie (II, III et IV).

La deuxième partie est dédiée à la modélisation de l'émission gamma en provenance des binaires gamma, dans le cadre du scénario du vent de pulsar. Le Chapitre 4 se concentrera sur l'émission du vent "choqué" du pulsar et le Chapitre 5 sur l'émission du vent "non-choqué". Le but de cette partie est de voir si le modèle du vent de pulsar constitue un scénario viable pour rendre compte des observations gamma et en particulier de la modulation (Question 2). L'objectif est aussi de formuler de nouvelles contraintes sur les paramètres physiques des vents de pulsar tels que le champ magnétique ou la distribution en énergie des particules (Question 5, 6 & 7).

Dans LS 5039, l'absorption gamma est très forte et conduit à la création d'un grand nombre de paires électron-positron. Ces particules peuvent alors initier une cascade de nouvelles paires et contribuer de manière significative au flux gamma total. Le modèle du vent choqué de pulsar (Chapitre 4) ne permet pas d'expliquer le flux observé au TeV où l'absorption gamma est très élevée. Le rayonnement de haute énergie recyclé par la cascade pourrait réduire considérablement l'opacité gamma dans LS 5039 et pourrait ainsi expliquer le flux gamma au TeV.

La troisième partie se concentre sur la modélisation de l'émission d'une cascade de paires dans les binaires gamma, en particulier dans LS 5039. En premier lieu et dans le but de quantifier la pertinence de ce phénomène, je présente un modèle 1D pour le rayonnement de la cascade dans les binaires (Chapitre 7). Je montrerai que ce type de cascade n'est pas réaliste mais qu'il permet néanmoins de mettre une limite supérieure sur l'émission de la cascade lorsque l'absorption est très forte. Dans LS 5039, un traitement plus réaliste de l'émission gamma en provenance de la cascade est nécessaire. J'ai développé un modèle tridimensionnel de cascade dans les binaires gamma en collaboration avec Julien Malzac que j'ai appliqué à LS 5039 (Chapitre 8). L'objectif principal est d'expliquer l'amplitude de la modulation gamma au TeV (Question 2). J'étudie également dans cette partie l'effet du champ magnétique ambiant et l'effet de la position de l'émetteur gamma dans LS 5039 (Question 4).

La partie IV décrit les effets d'un mouvement d'ensemble relativiste sur les processus radiatifs (Question 7) dans le contexte des vents de pulsars dans les binaires gamma (Chapitre 10). Dans le modèle classique des vents de pulsar, le vent choqué a une vitesse d'ensemble modérément relativiste. Les effets d'amplification Doppler relativiste devraient changer l'émission de haute énergie et la modulation (Question 2). Ces effets sont précisément étudiés dans cette partie. Je formule des contraintes sur les vitesses d'ensemble de l'écoulement (Question 6).

Dans la partie IV, je présente aussi un nouveau modèle pour l'émission gamma dans le microquasar Cygnus X-3 (Chapitre 11). L'objectif principal est d'expliquer l'origine de la modulation orbitale gamma au GeV dans ce système (Question 2). L'ajustement de la courbe de lumière théorique à celle observée permet de contraindre la géométrie et la physique du jet dans Cygnus X-3 (Questions 3, 4, 5 & 7).

La dernière partie (Part V) résume brièvement les principaux résultats obtenus dans cette thèse. La liste des questions donnée dans ce premier chapitre est actualisée et destinée à de futures recherches.

2

Relevant high-energy processes

Outline

1. What we want to know	18
2. High-energy leptonic processes	18
§ 3. <i>Inverse Compton scattering</i>	18
§ 4. <i>Bremsstrahlung</i>	21
§ 5. <i>Synchrotron radiation</i>	23
§ 6. <i>Triplet pair production</i>	25
§ 7. <i>Relevant leptonic processes in binaries</i>	27
3. High-energy hadronic processes	28
§ 8. <i>Proton-proton collision</i>	29
§ 9. <i>Photomeson production</i>	31
4. Photon-photon annihilation	32
5. The cooling of relativistic particles	33
§ 10. <i>The continuity equation</i>	33
§ 11. <i>General solution</i>	34
§ 12. <i>Some simple solutions</i>	34
6. What we have learned	35
7. [Français] Résumé du chapitre	35
§ 13. <i>Contexte et objectifs</i>	35
§ 14. <i>Ce que nous avons appris</i>	36

HIGH-ENERGY CHARGED PARTICLES going through a gas of material and bathed in a magnetic and radiation fields cool down and radiate in some cases high-energy gamma rays. I briefly review in this chapter the main high-energy processes that involve highly relativistic electrons and protons (*i.e.* particles with a total energy much greater than their rest mass energy $E \gg mc^2$). I intend to present the main features of each interaction and provide references where more technical details can be found. The main objective here is to single out what are the relevant processes occurring in compact binaries. For this, I compute the cooling timescale of each interaction for typical physical conditions found in binaries, as a function of the energy of the particles. First, I review the high-energy processes involving high-energy electrons or "leptonic processes", namely:

- Inverse Compton scattering (§ 5).
- Bremsstrahlung (§ 6).
- Synchrotron radiation or "magnetic Bremsstrahlung" (§ 7).
- Triplet pair production (§ 8).

In a second part, I investigate whether high-energy gamma rays could be produced also by energetic protons in a binary environment. I review here two "hadronic processes", namely:

- Proton-proton collision (§ 10).
- Photomeson production (§ 11).

High-energy gamma rays can also be absorbed by low energy radiation and produce electron-positron pairs (Sect. 4). The high-energy processes listed above cool electrons. In consequence, the initial energy distribution of particles can be changed by the cooling. In Sect. 5, I provide the main equation that describes the cooling of particles and derive analytical solutions in some simple cases.

1. What we want to know

- What are the relevant high-energy processes at work in compact binaries?
- Does the gamma-ray emission has a leptonic or hadronic origin?

2. High-energy leptonic processes

§ 5. Inverse Compton scattering

Inverse Compton scattering has been studied in great details in the astrophysical context for many years now. I recommend to the reader interested into the technical details to refer to *e.g.* Ginzburg & Syrovatskii (1964), Jones (1965, 1968), Blumenthal & Gould (1970), Rybicki & Lightman (1979), or Longair (1992).

Basically, inverse Compton scattering is the interaction of an energetic electron (or positron) of energy $E_e = \gamma_e m_e c^2$ (γ_e is the Lorentz factor of the electron) with low energy (or "soft") photons of energy ϵ_0 . In the collision, the electron loses energy and upscatters the low energy photon to high energy ϵ_1 . This interaction can be written as

$$e^\pm (E_e) + \gamma (\epsilon_0) \rightarrow e^\pm (E'_e) + \gamma (\epsilon_1). \quad (5.1)$$

Inverse Compton scattering can be seen as a "normal" Compton scattering, *i.e.* where an energetic photon transfers momentum to an electron at rest and is scattered at lower energy, in the rest frame of the electron. In the observer frame, the energy transfer is reversed due to the relativistic motion of the electron, hence the name "inverse" Compton scattering. If the energy of the soft photon in the rest frame of the electron is smaller than the rest mass energy of the electron ($\epsilon'_0 \ll m_e c^2$), then the recoil of the electron can be ignored and the photon is scattered with no loss of energy *i.e.* the outgoing photon energy is $\epsilon'_1 \approx \epsilon'_0$. This is known as the *Thomson limit*. In this case, the low energy photon can be upscattered up to an energy $\epsilon_1 \approx 4\gamma_e^2 \epsilon_0$ (for a head-on collision, see next chapter). If $\gamma_e = 10^4$ and $\epsilon_0 = 1$ eV, a $\epsilon_1 = 100$ MeV gamma-ray photon can be produced. Note that even if the low energy photon is boosted by a large factor, the scattered photon energy remains a small fraction of the total energy of the electron $\epsilon_1 \ll \gamma_e m_e c^2$

in the Thomson limit. This is not the case if $\epsilon'_0 \gg m_e c^2$, where the recoil of the electron cannot be ignored. This is the *Klein-Nishina regime*. In this regime, the electron loses almost all its energy so that $\epsilon_1 \approx \gamma_e m_e c^2$.

Defining $x = \epsilon'_0 / m_e c^2$, the total cross section of this process is (Rybicki & Lightman 1979)

$$\sigma_{ic} = \frac{3}{4} \sigma_T \left[\frac{1+x}{x^3} \left\{ \frac{2x(1+x)}{1+2x} - \ln(1+2x) \right\} + \frac{1}{2x} \ln(1+2x) - \frac{1+3x}{(1+2x)^2} \right], \quad (5.2)$$

where $\sigma_T = (8/3)\pi r_e^2$ is the Thomson cross section and $r_e = e^2/m_e c^2 = 2.82 \times 10^{-13}$ cm is the classical radius of the electron. For $x \ll 1$ (Thomson regime), the cross section is constant and $\sigma_{ic} \approx \sigma_T$. If $x \gg 1$ (Klein-Nishina regime), the cross section declines (Fig. 4) and can be approximated by the expression

$$\sigma_{ic} \approx \frac{3}{8} \sigma_T \frac{1}{x} \left(\ln 2x + \frac{1}{2} \right). \quad (5.3)$$

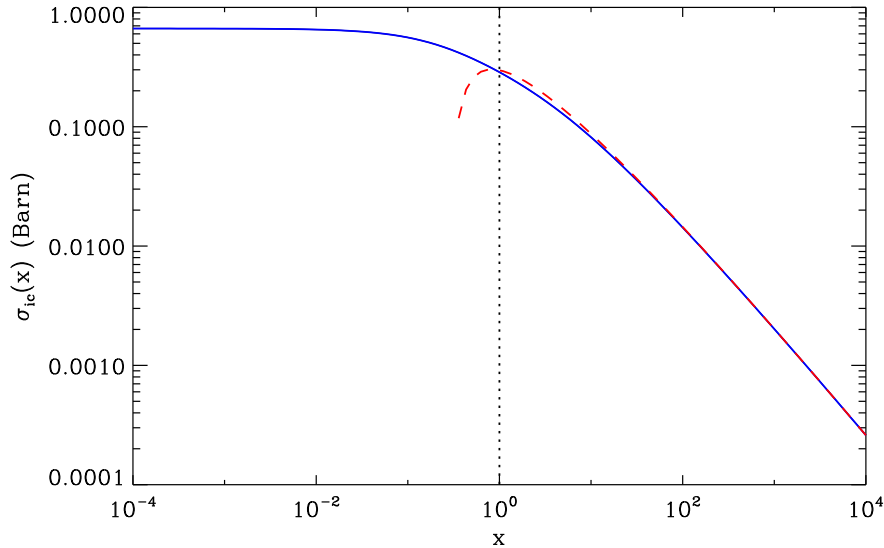


FIG. 4. Total cross section for inverse Compton scattering as a function of $x = \epsilon'_0 / m_e c^2$. The dashed line separates the Thomson ($x \ll 1$) to the Klein-Nishina regime ($x \gg 1$). The approximate formula given in Eq. (5.3) is shown with a red dashed line.

The spectrum of the scattered photons by an electron going through an isotropic gas of soft photon was first derived by Jones (1968). The density of gamma rays scattered per electron, per unit of energy and per unit of time is given by Jones' kernel (in the general case, *i.e.* including Klein-Nishina effects)

$$\frac{dN}{dt d\epsilon_1} = \frac{2\pi r_e^2 c}{\gamma_e^2 \epsilon_0} f_{jones}(q), \quad (5.4)$$

where

$$f_{jones}(q) = 2q \ln q + (1+2q)(1-q) + \frac{1}{2} \frac{(\Gamma_{\epsilon_0} q)^2}{1 + \Gamma_{\epsilon_0} q} (1-q), \quad (5.5)$$

and

$$\Gamma_{\epsilon_0} = \frac{4\epsilon_0 \gamma_e}{m_e c^2} \quad q = \frac{\epsilon_1}{\Gamma_{\epsilon_0} (\gamma_e m_e c^2 - \epsilon_1)}. \quad (5.6)$$

Relativistic kinematics gives

$$\epsilon_0 \leq \epsilon_1 \leq \gamma_e m_e c^2 \frac{\Gamma_{\epsilon_0}}{1 + \Gamma_{\epsilon_0}}. \quad (5.7)$$

The total power lost per electron is given in the general case by

$$-\frac{dE_e}{dt} = \int_{\epsilon_1} (\epsilon_1 - \epsilon_0) n_{ph} \frac{dN}{dt d\epsilon_1} d\epsilon_1, \quad (5.8)$$

where n_{ph} is the soft photon density (number of photons per unit of volume). In the Thomson limit, for an isotropic gas of photon and assuming that $\epsilon_0 \ll \epsilon_1$, we have (Blumenthal & Gould 1970)

$$-\frac{dE_e}{dt} = \frac{4}{3} \sigma_{TC} \gamma_e^2 U_{ph}, \quad (5.9)$$

where U_{ph} is the soft photon energy density (erg cm^{-3}). For a star of luminosity L_* , the energy density of soft photon at a distance d from its center is $U_* = L_*/4\pi c d^2$, with $L_* = 4\pi R_*^2 \sigma_{SB} T_*^4$ where R_* is the stellar radius T_* the stellar temperature and σ_{SB} , the Stefan-Boltzmann constant. In the deep Klein-Nishina regime (*i.e.* if $\Gamma_{\epsilon_0} \gg 1$), the Compton losses are less efficient than in the Thomson limit and are given by (Blumenthal & Gould 1970)

$$-\frac{dE_e}{dt} = \frac{\pi r_e^2}{3} \left(\frac{\pi}{h}\right)^3 (m_e c k T_*)^2 \left(\frac{R_*}{d}\right)^2 \left[\ln \frac{4\gamma_e k T_*}{m_e c^2} - \frac{5}{6} - C_e - C_l \right] \quad (5.10)$$

where k is the Boltzmann constant and $C_e = 0.5772$ and $C_l = 0.5700$. This expression is valid for an isotropic gas of soft photons generated by a star with a black body spectrum of temperature T_* and radius R_* at a distance d . Fig. 5 gives the Compton energy losses in the general case and shows the analytical results for comparison.

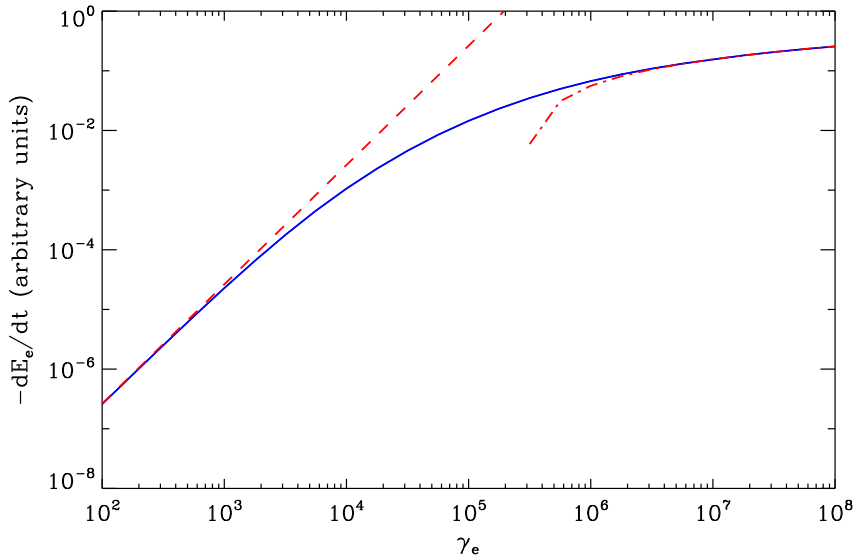


FIG. 5. Numerically integrated inverse Compton energy losses (Eq. 5.8, blue solid line) of an electron of energy $E_e = \gamma_e m_e c^2$ bathed in a isotropic gas of photons with a black body energy distribution of effective temperature $T_* = 40\,000$ K. The analytical formula in the Thomson (red dashed line) and Klein-Nishina (red dashed-dotted line) regimes are overplotted for comparison.

We can now define and derive the typical Compton cooling timescale of an electron of energy E_e bathed in a soft photon density as

$$t_{ic} = -\frac{E_e}{\dot{E}_e} = \frac{3m_e c^2}{4\sigma_T c U_{ph} \gamma_e} \propto \gamma_e^{-1}, \quad (5.11)$$

in the Thomson regime, with $\dot{E}_e = dE_e/dt$. I will use this key quantity in the following to compare with the other processes. Note that inverse Compton emission could be produced also by energetic protons. However, since the cross section is $\sigma_T \propto r_e^2 \propto m_e^{-2}$ (in the Thomson limit, Eq. 5.2), the cooling and the gamma-ray emission will be reduced by a factor $\gtrsim 10^6$ ($m_p/m_e \sim 2000$).

Before finishing with this part, I would like to mention the "double inverse Compton scattering" where two gamma rays are produced in one interaction so that

$$\gamma + e^\pm \rightarrow \gamma + \gamma + e^\pm. \quad (5.12)$$

The cross section of this process σ_d first computed by Ram & Wang (1971), remains extremely small and becomes comparable to the "simple" inverse Compton scattering ($\sigma_d/\sigma_{ic} \approx 0.5$) only if $x > 10^8$ *i.e.* at ultra-high energy (Mastichiadis 1986). Hence, this process will be ignored in the following.

§ 6. Bremsstrahlung

Bremsstrahlung emission is produced by high-energy charged particles interacting with the Coulomb electric field generated by the surrounding charges present in the crossed medium (considered at rest in the observer frame). This process can be treated as inverse Compton scattering of virtual photons from the Coulomb electric field on the high-energy particle. I will consider here the case of a relativistic electron of energy E_e crossing a plasma composed of atoms and ions with an atomic number Z of density n_Z (cm^{-3}).

The differential cross section for the emission of a Bremsstrahlung photon of energy ϵ_1 between an electron of energy E_e and a charge Ze is given by (Bethe & Mott 1934; Blumenthal & Gould 1970)

$$\frac{d\sigma}{d\epsilon_1} = \frac{\alpha r_e^2}{\epsilon_1} \left(\left[1 + \left(1 - \frac{\epsilon_1}{E_e} \right)^2 \right] \phi_1 - \frac{2}{3} \left(1 - \frac{\epsilon_1}{E_e} \right) \phi_2 \right) = \frac{\alpha r_e^2}{\epsilon_1} f_b, \quad (6.13)$$

where $\alpha \approx 1/137$ is the fine-structure constant, ϕ_1 and ϕ_2 are functions of E_e and ϵ_1 and depend on the scattering charge Ze . If the charge is unshielded (*i.e.* the atom is completely ionized), we have

$$\phi_1 = \phi_2 = 4Z^2 \left(\ln \left[\frac{2E_e}{m_e c^2} \left(\frac{E_e}{\epsilon_1} - 1 \right) \right] - \frac{1}{2} \right), \quad (6.14)$$

otherwise, these functions should be calculated for each species. For the atomic neutral hydrogen $Z = 1$, and defining

$$\Delta = \frac{\epsilon_1 m_e c^2}{4\alpha E_e (E_e - \epsilon_1)}, \quad (6.15)$$

we have $\phi_1 \approx 45.79$, $\phi_2 \approx 44.46$ if $\Delta \ll 1$ (strong shielding) and $\phi_1 \approx \phi_2 \approx 8 [\ln(1/2\alpha\Delta) - 1/2]$ if $\Delta \gg 1$ (weak shielding, see Gould 1969 for more details and for $Z > 1$). The full variation of these functions are shown in Fig. 6.

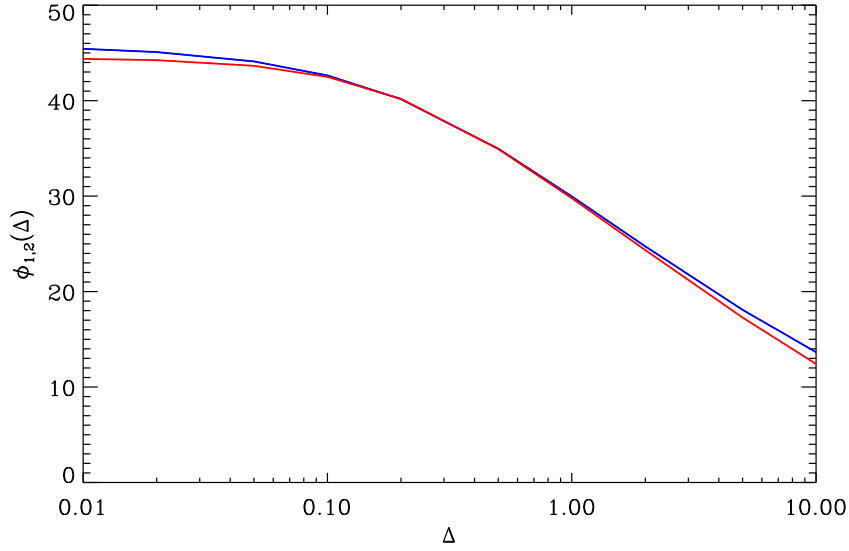


FIG. 6. Variations of ϕ_1 (blue line) and ϕ_2 (red line) as a function of Δ for the neutral hydrogen atom.

The Bremsstrahlung spectrum emitted by one electron of energy E_e going through a gas containing s different species of density n_s is

$$\frac{dN}{dt d\epsilon_1} = \sum_s n_s c \frac{d\sigma_s}{d\epsilon_1}. \quad (6.16)$$

Fig. 7 shows the variations of the differential cross section given in Eq. 6.13 if the target material is neutral hydrogen only, for various electron energy E_e . This plot shows that the emitted gamma-ray spectrum is broad and rather flat particularly for ultra-relativistic electrons $E_e \gg m_e c^2$. In addition, the electron can lose almost all of its energy as inverse Compton scattering in the deep Klein-Nishina regime.

The total power lost by the electron is obtained with

$$-\frac{dE_e}{dt} = \int_{\epsilon_1} \epsilon_1 \frac{dN}{dt d\epsilon_1} d\epsilon_1. \quad (6.17)$$

Performing this integral yields

$$-\frac{dE_e}{dt} = 4\alpha r_e^2 c \sum_Z n_Z Z(Z+1) \left(\ln \frac{2E_e}{m_e c^2} - \frac{1}{3} \right) E_e, \quad (6.18)$$

for a completely ionized (or weakly shielded) medium, and

$$-\frac{dE_e}{dt} = \alpha r_e^2 c \sum_s n_s \left(\frac{4}{3} \phi_{1,s} - \frac{1}{3} \phi_{2,s} \right) E_e \propto E_e, \quad (6.19)$$

for a highly shielded medium ($\Delta \ll 1$), where the functions $\phi_{1,s}$, $\phi_{2,s}$ are constant which depends on the species s . For a neutral gas of hydrogen of density n_H we have

$$-\frac{dE_e}{dt} \approx 0.34 r_e^2 c n_H E_e. \quad (6.20)$$

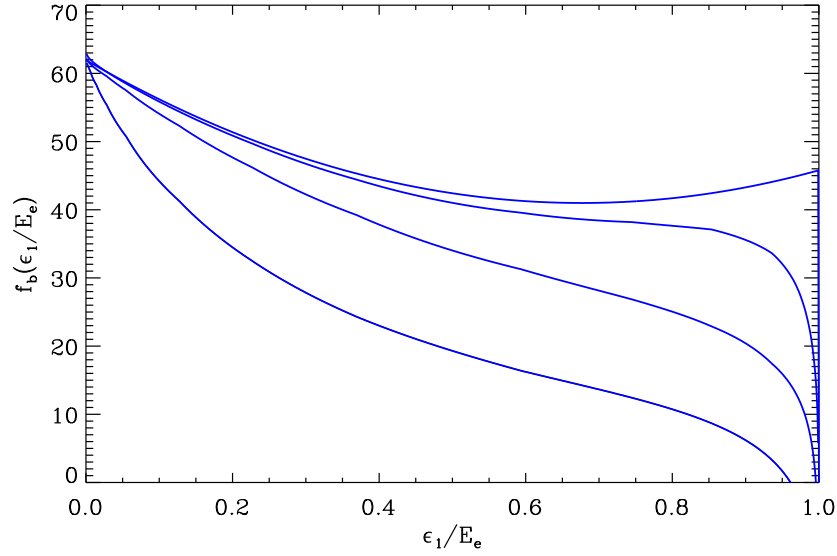


FIG. 7. Bremsstrahlung spectrum (plot of the function f_b defined in Eq. 6.13) emitted by one electron of Lorentz factor $\gamma_e = 10$ (*bottom curve*), 100, 1000, and $= \infty$ (*top curve*) as a function of the ratio $\epsilon_1/\gamma_e m_e c^2$. The medium is composed of neutral hydrogen atoms only.

Then the typical cooling timescale of an electron radiating *via* Bremsstrahlung in a neutral gas of hydrogen is

$$t_B = -\frac{E_e}{\dot{E}_e} \approx \frac{1}{0.34 r_e^2 c n_H} \propto n_H^{-1}, \quad (6.21)$$

e.g. depends only on the density of material crossed by the electron. This expression is correct if the strong shielding approximation is valid, *i.e.* for electrons with $\gamma_e \gtrsim 10^3$ (see Fig. 7).

§ 7. Synchrotron radiation

Synchrotron radiation is emitted by relativistic charged particles spiraling along a magnetic field line. As for bremsstrahlung, this process can be seen as the Compton scattering of virtual soft photons of the magnetic field on the relativistic charged particle. Let's consider here the case of a relativistic electron of energy E_e with a constant pitch angle α to the magnetic field line. The spectrum emitted by the electron is given by (for technical details, see *e.g.* Ginzburg & Syrovatskii 1965, Blumenthal & Gould 1970, Longair 1992)

$$\frac{dN}{dt d\epsilon_1} = \frac{\sqrt{3} e^3 B \sin \alpha}{h m_e c^2 \epsilon_1} f_s \left(\frac{\epsilon_1}{\epsilon_c} \right), \quad (7.22)$$

with

$$f_s(x) = x \int_x^{+\infty} K_{5/3}(t) dt, \quad (7.23)$$

where e is the fundamental charge of the electron, h is the Planck constant, $K_{5/3}$ is the modified Bessel function of 5/3 order and

$$\epsilon_c = \left(\frac{3heB\gamma_e^2}{4\pi m_e c} \right) \sin \alpha \quad (7.24)$$

is the critical energy. The synchrotron radiation spectrum emitted by a relativistic electron is broad and peaks at $\epsilon_1 \approx \epsilon_c$ (Fig. 8). Above the critical energy $\epsilon_1 \gg \epsilon_c$, the spectrum presents an exponential cut-off. In this case, f_s can be approximated by

$$f_s(x) = \sqrt{\frac{\pi}{2}} x^{1/2} e^{-x}. \quad (7.25)$$

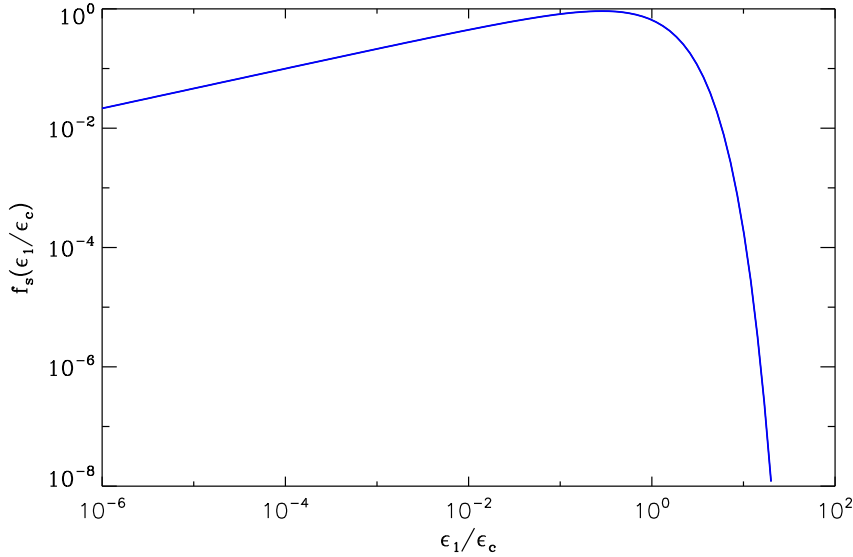


FIG. 8. Variations of f_s defined in Eq. (7.23) as a function of ϵ_1/ϵ_c .

The power lost by a relativistic electron ($\gamma_e \gg 1$) is

$$-\frac{dE_e}{dt} = \frac{2}{3} r_e^2 c \gamma_e^2 B^2 \sin^2 \alpha. \quad (7.26)$$

If the magnetic field is randomly oriented with respect to the electron direction of motion, the average power lost over an isotropic distribution of pitch angle α yields

$$-\frac{dE_e}{dt} = \frac{4}{3} \sigma_{TC} \gamma_e^2 \left(\frac{B^2}{8\pi} \right). \quad (7.27)$$

We can note that this formula is identical to the Compton energy losses in the Thomson limit (see Eq. 5.9) where the energy density of the soft radiation field is given by the magnetic energy density $U_B \equiv B^2/8\pi$. The synchrotron cooling timescale is then

$$t_{syn} = -\frac{E_e}{\dot{E}_e} = \frac{3m_e c^2}{4\sigma_{TC} U_B \gamma_e} \propto \gamma_e^{-1} B^{-2}. \quad (7.28)$$

The radiated energy remains a small fraction of the total energy of the electron $\epsilon_1 \ll \gamma_e m_e c^2$ (as for inverse Compton scattering in the Thomson limit). We can note also that synchrotron radiation photons are mostly emitted with an energy $\epsilon_1 \approx \epsilon_c$. This energy cannot however exceed ~ 70 MeV or the electron would lose most of its energy in one turn of its orbit along the magnetic field line (Blumenthal & Gould 1970).

In addition, one should be aware that the treatment of synchrotron radiation presented above is classical in the sense that quantum effects have not been considered in the calculations.

This approximation holds as long as the magnetic field strength is below the critical value $B_{QED} = m_e^2 c^3 / \hbar e \approx 4.4 \times 10^{13}$ G. Beyond this value, quantum synchrotron spectra have to be calculated as in *e.g.* Brainerd & Petrosian (1987) (see also the full quantum treatment by Erber 1966). This effect can be interpreted as the Klein-Nishina regime as found in inverse Compton scattering. Other exotic phenomena occur for such strong magnetic fields $B > B_{QED}$ (see for instance Duncan 2000). Super critical magnetic fields can be found at the surface of magnetars, which are highly magnetized neutron star with $B \gtrsim 10^{13}$ - 10^{15} G (*e.g.* Duncan & Thompson 1992), and possibly in the central engine of gamma-ray bursts. Quantum synchrotron radiation is irrelevant in our context and will be ignored in the following.

§ 8. Triplet pair production

The study presented in this section was carried out under my supervision by Sarkis Rastikian, at that time (June 2009) an undergraduate student at the University of Grenoble ("Licence 2" level). I briefly summarize the results of our investigations below.

Triplet pair production (TPP) is the annihilation of a soft photon of energy ϵ_0 in the Coulomb electric field of a relativistic electron of energy E_e (or positron). In this interaction, one electron-positron pair is created and the electron loses energy. This process can be written as

$$\gamma(\epsilon_0) + e^\pm(E_e) \rightarrow e^\pm(E'_e) + e^+(E_+) + e^-(E_-). \quad (8.29)$$

TPP occurs if there is enough energy available in the center-of-mass frame to create the electron-positron pair. The threshold energy for TPP is given by the relativistic kinematics which yields

$$2E_e\epsilon_0(1 - \beta_e \cos \theta_0) = 8m_e^2 c^4, \quad (8.30)$$

where θ_0 is the angle between the incoming photon and the electron direction of motion. Defining $x = \gamma_e \epsilon_0 (1 - \beta_e \cos \theta_0) / m_e c^2 = \epsilon'_0 / m_e c^2$ as for inverse Compton scattering (see § 5), TPP is kinematically possible if $x \geq 4$.

The TPP cross section can be accurately calculated with Quantum Electrodynamics, but this is a fairly difficult task (see Joseph & Rohrlich 1958 for a review of the first attempts on this issue). However, there is in the literature several analytical formula available for the total cross section of this process but valid only in specific range for x . For $4 < x < 16$, the total cross section can be written as (Motz *et al.* 1969)

$$\sigma_{TPP} = (\Delta_{BH} + \Delta_B + \Delta_{BG})(1 - \Delta_M), \quad (8.31)$$

where

$$\Delta_{BH} = \alpha r_e^2 \left[\frac{28}{9} \ln(2x) - \frac{218}{27} \right] \quad (8.32)$$

$$\Delta_B = -\frac{\alpha r_e^2}{x} \left[\frac{4}{3} (\ln 2x)^3 - 3 (\ln 2x)^2 + 6.84 \ln 2x - 21.51 \right] \quad (8.33)$$

$$\Delta_{BG} = \frac{\alpha r_e^2}{x^2} \left[\frac{8}{3} (\ln 2x)^3 - \left(4 - \frac{1}{x} \right) (\ln 2x)^2 - \frac{1}{18} \left(168 + \frac{106}{x} + \frac{49}{x^2} \right) \ln 2x - 11.8 - \frac{16.8}{x} - \frac{0.27}{x^2} \right], \quad (8.34)$$

and where Δ_M is a correction factor defined by Mork (1967). For $x > 16$ the cross section is $\sigma_{TPP} = \Delta_{BH} + \Delta_B + \Delta_{BG}$, for $x > 100$ $\sigma_{TPP} = \Delta_{BH} + \Delta_B$ and for $x > 10^4$, the expression simplifies into the Bethe-Heitler formula $\sigma_{TPP} = \Delta_{BH}$. The total cross section increases roughly

logarithmically (far from threshold) with energy and exceeds the inverse Compton cross section (which declines as $\propto \ln x/x$ for $x \gtrsim 10$, see Eq. 5.3) for $x \approx 250$. For $\epsilon_0 = 10$ eV, an electron interacts preferentially by TPP rather than inverse Compton if $E_e \gtrsim 6$ TeV.

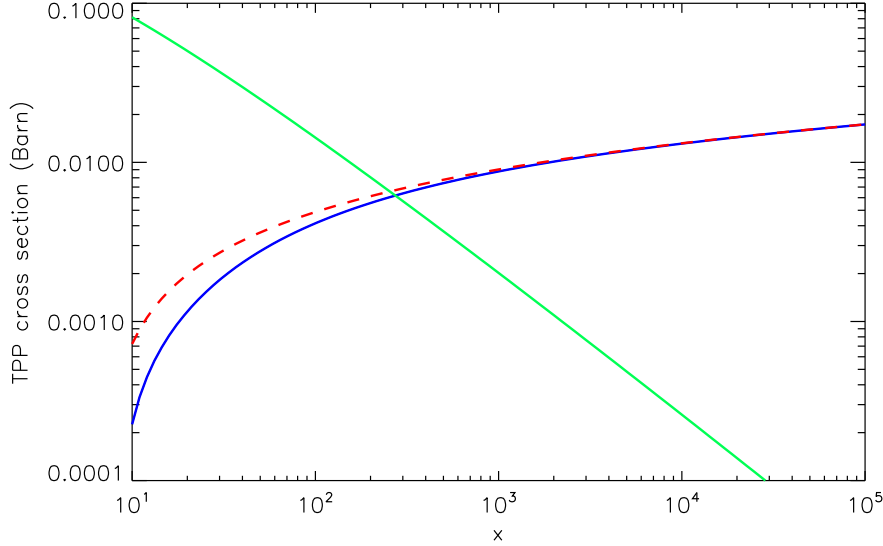


FIG. 9. Total triplet pair production cross section as a function of x . The blue line corresponds to the expression valid for $x > 16$. The Bethe-Heitler formula Δ_{BH} , valid for $x > 10^4$, is shown by the red dashed line. The total inverse Compton cross section is also shown for comparison (green solid line).

The energy losses by TPP of the initial electron is given by

$$-\frac{dE_e}{dt} = \int_{E'_e} (E_e - E'_e) n_{ph} c (1 - \beta_e \cos \theta_0) \frac{d\sigma}{dE'_e} dE'_e, \quad (8.35)$$

where E'_e is the energy of the electron after the collision, n_{ph} is the soft photon density, and $d\sigma/dE'_e$ is the differential cross section which gives the energy distribution of the cooled electron. There is unfortunately no analytical formula for $d\sigma/dE'_e$ (to my knowledge) and the computation of this quantity is pretty technical (see *e.g.* Jarp & Mork 1973; Mastichiadis *et al.* 1986; Anguelov *et al.* 1999). Following Mastichiadis (1991), we approximate the integral in Eq. (8.35) by

$$-\frac{dE_e}{dt} \approx \langle \Delta E_e \rangle \frac{dN}{dt}, \quad (8.36)$$

where $\langle \Delta E_e \rangle = \langle E_e - E'_e \rangle$ is the mean energy left in the interaction and dN/dt is the TPP scattering rate. Because of energy conservation, we have $E_e + \epsilon_0 = E'_e + E_+ + E_-$. Assuming that $\epsilon_0 \ll E_e$ we have $\Delta E_e \approx E_+ + E_-$. Hence, $\langle \Delta E_e \rangle = \langle E_+ \rangle + \langle E_- \rangle = 2\langle E_+ \rangle$ for symmetry reasons. Mastichiadis (1991) derived from his Monte Carlo calculation an analytical fit for the mean energy of the created pair, provided that the product $E_e \epsilon_0 / m_e^2 c^4 \gtrsim 10^3$ so that

$$\langle E_+ \rangle \approx \frac{2.5 m_e^2 c^4}{\epsilon_0} \left(\frac{E_e \epsilon_0}{m_e^2 c^4} \right)^{1/4}. \quad (8.37)$$

The scattering rate is defined as

$$\frac{dN}{dt} = n_{ph} c \sigma_{TPP} (1 - \beta_e \cos \theta_0). \quad (8.38)$$

With Eqs. (8.35)-(8.38) and using the Bethe-Heitler formula, we have

$$-\frac{dE_e}{dt} \approx \frac{5\alpha r_e^2 m_e^2 c^5 n_{ph}}{\epsilon_0} \left(\frac{E_e \epsilon_0}{m_e^2 c^4}\right)^{1/4} \left[\frac{28}{9} \ln\left(\frac{2E_e \epsilon_0}{m_e^2 c^4}\right) - \frac{218}{27}\right] \propto x^{1/4} \ln x, \quad (8.39)$$

if $\theta_0 = \pi/2$ (the average over angles does not change qualitatively the result). This expression is valid only if $x \gtrsim 10^3$ (Fig. 10), otherwise the energy losses are slightly overestimated (Mastichiadis 1991). Dermer & Schlickeiser (1991) did also a rough estimate of the TPP energy losses and found a simple analytical solution. The TPP cooling timescale is

$$t_{TPP} = -\frac{E_e}{\dot{E}_e} \propto \frac{E_e^{3/4}}{\ln E_e}. \quad (8.40)$$

It is worthwhile to note at this stage that the energy lost by the electron per TPP interaction is a small fraction of its total energy. In addition, this fraction decreases with energy ($\langle \Delta E_e \rangle / E_e \propto E_e^{-3/4}$). Meanwhile, this effect is compensated by an increase of the scattering rate with energy ($dN/dt \propto \ln E_e$). This is exactly the opposite behaviour observed in the inverse Compton cooling, since the electron undergoes only few scatterings but loses almost all its energy in one interaction (for $x \gg 1$, see § 5). TPP losses exceed inverse Compton losses if $x \gtrsim 10^6$ (see Fig. 10) even though electrons interact preferentially *via* TPP than inverse Compton scattering for $x \gtrsim 250$ (where $\sigma_{TPP} > \sigma_{ic}$, see Fig. 9).

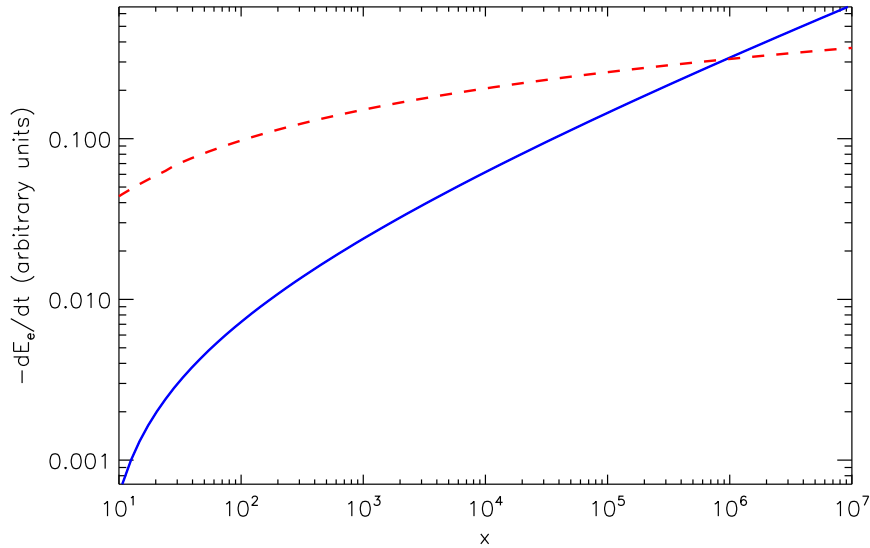


FIG. 10. Triplet pair production energy losses as a function of x for $\theta_0 = \pi/2$ given in Eq. (8.39). One should trust only the domain where $x \gtrsim 10^3$, below the energy losses are overestimated but the variations are still qualitatively correct. Inverse Compton losses are shown for comparison (red dashed line).

§ 9. Relevant leptonic processes in binaries

A simple way to select the relevant leptonic processes at work in binaries is to compare the cooling timescale of an electron *via* each interaction. In binaries, the soft photon density is provided by the massive star of temperature T_* and radius R_* . For an electron of Lorentz factor

γ_e situated at a distance d from the massive star center, the Compton cooling timescale in the Thomson regime is (Eq. 5.11)

$$t_{Th} \approx 30 \gamma_3^{-1} d_{0.1}^2 T_{*,4}^{-4} R_{*,10}^{-2} \text{ s}, \quad (9.41)$$

writing $\gamma_3 = \gamma_e/10^3$, $d_{0.1} = d/0.1 \text{ AU}$, $T_{*,4} = T_*/40\,000 \text{ K}$ and $R_{*,10} = R_*/10R_\odot$. These parameters corresponds roughly to LS 5039 at periastron. In the Klein-Nishina regime we have (Eq. 5.10)

$$t_{KN} \approx 20 \gamma_6 d_{0.1}^2 T_{*,4}^{-2} R_{*,10}^{-2} [\ln(\gamma_6 T_{*,4}) + 1.3]^{-1} \text{ s}, \quad (9.42)$$

with $\gamma_6 = \gamma_e/10^6$. The inverse Compton cooling timescale decreases with energy in the Thomson regime but increases with energy in the Klein-Nishina regime due to the decline of the cross section (Fig. 11, solid line). Similarly, TPP cooling timescale can be rewritten as (Eq. 8.40)

$$t_{TPP} \approx 1.5 \times 10^4 \gamma_8^{3/4} d_{0.1}^2 T_{*,4}^{-9/4} R_{*,10}^{-2} [\ln(\gamma_8 T_{*,4}) + 5.6]^{-1} \text{ s}, \quad (9.43)$$

where $\gamma_8 = \gamma_e/10^8$. The synchrotron cooling timescale is

$$t_{syn} \approx 774 \gamma_6^{-1} B_1^{-2} \text{ s}, \quad (9.44)$$

with $B_1 = B/1 \text{ G}$. The density of the stellar wind gives the density of material crossed by the electron. Assuming that the wind is composed exclusively of hydrogen atoms, the density of scattering charge for Bremsstrahlung is $n_H = \dot{M}/4\pi d^2 v_\infty m_p$, where \dot{M} is the mass loss rate of the star, v_∞ is the terminal velocity of the wind and m_p the mass of the proton. The Bremsstrahlung cooling timescale is (Eq. 6.21)

$$t_B \approx 2.2 \times 10^6 \dot{M}_7^{-1} v_{2400} d_{0.1}^2 \text{ s}, \quad (9.45)$$

with $\dot{M}_7^{-1} = \dot{M}/10^{-7} M_\odot \text{ yr}^{-1}$ and $v_{2400} = v_\infty/2400 \text{ km s}^{-1}$. Fig. 11 shows the variation of the leptonic cooling timescales as a function of the energy of the electron. This plot shows that inverse Compton scattering and synchrotron radiation are the two main cooling channels in binaries. Even if the electron crosses the dense equatorial wind of a Be star where the equivalent mass-loss rate is $1\text{-}2 \times 10^{-7} M_\odot \text{ yr}^{-1}$ with typical velocity of a few hundred km s^{-1} (Waters *et al.* 1988), the effect of Bremsstrahlung cooling remains small compared with inverse Compton and synchrotron radiation for highly relativistic electrons ($\gamma_e \gg 1$). The ambient magnetic field is unknown in binaries, but if $B \gtrsim 1 \text{ G}$ synchrotron radiation could be the dominant cooling processes at very-high energy (in LS 5039 $\gamma_e \gtrsim 10^7$, see Fig. 11). TPP would dominate over inverse Compton at ultra-high energy ($\gamma_e \gtrsim 10^{11}$ in LS 5039) provided that the magnetic field is very low ($B \lesssim 10^{-4} \text{ G}$).

Hence, inverse Compton scattering and synchrotron radiation appear as the dominant leptonic processes at work in binaries in the high-energy range ($10^3 \lesssim \gamma_e \lesssim 10^{10}$). I neglected the other two processes.

3. High-energy hadronic processes

High-energy gamma rays could also be produced by the decay of neutral pions $\pi^0 \rightarrow \gamma + \gamma$. Pions are produced by the cooling of relativistic nuclei. I briefly review below the pion production by proton-proton and photon-proton collisions and discuss the relevance of these processes in compact binaries.

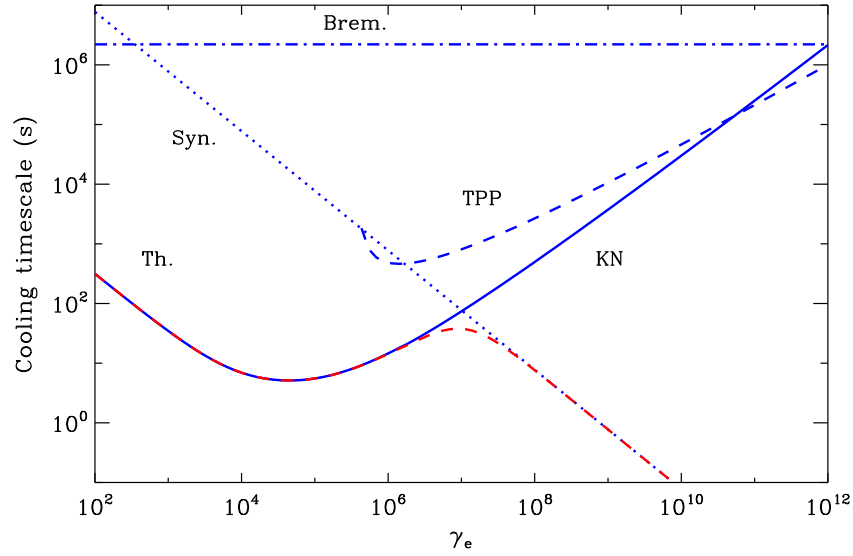


FIG. 11. Leptonic cooling timescales: inverse Compton (solid line, "Th." in the Thomson limit and "KN" in the Klein-Nishina regime), synchrotron (dotted line, "Syn."), TPP (dashed line), and Bremsstrahlung (dot-dashed line, "Brem."), as a function of the electron Lorentz factor γ_e . This plot shows also the total cooling timescale t_{tot} (red dashed line) defined as $t_{tot}^{-1} = t_{ic}^{-1} + t_{syn}^{-1} + t_{TPP}^{-1} + t_B^{-1}$. The parameters used here are compatible with LS 5039: $T_* = 39\,000$ K, $R_* = 9.3R_\odot$, $v_\infty = 2400$ km s $^{-1}$, $\dot{M} = 10^{-7}M_\odot$ yr $^{-1}$ and $d \approx 0.1$ AU at periastron. The magnetic field is unknown but is chosen here as $B = 1$ G.

§ 10. Proton-proton collision

We consider here the case of a relativistic proton colliding with target proton at rest (*e.g.* from the massive star wind in our context) in the observer frame. In this interaction, many mesons (*i.e.* particles composed of a quark and an anti-quark) are produced and in particular neutral pions π^0 with an energy E_π as

$$p(E_p) + p(m_p c^2) \rightarrow p + p + \pi^0(E_\pi) + \dots \quad (10.46)$$

The minimum energy of the proton E_p required for the production of a neutral pion is given by the relativistic kinematics. A simple calculation yields

$$E_p \geq \frac{m_\pi^2 c^4 + 2m_p^2 c^4 + 4m_p m_\pi c^4}{2m_p c^2} \approx 1.22 \text{ GeV}, \quad (10.47)$$

where $m_p c^2 \approx 938$ MeV and $m_\pi c^2 \approx 135$ MeV are the rest mass energy of the proton and of the pion. The density of neutral pions produced depends on the density of target protons n_H (cm $^{-3}$), on the density of high-energy protons $n_p \equiv dN_p/dE_p(E_p)$ and on the inclusive cross section of the reaction $\sigma_{pp}(E_\pi, E_p)$ (*i.e.* for the production of pions only, other particles created in the interaction are not considered). Following Aharonian & Atoyan (2000), the density of neutral pions created

is given by

$$\frac{dN_\pi}{dt dE_\pi} \approx cn_H \int_{E_p} \delta(E_\pi - K_\pi E_{kin}) \sigma_{pp}(E_p) n_p(E_p) dE_p \quad (10.48)$$

$$\approx \frac{cn_H}{K_\pi} \sigma_{pp} \left(m_p c^2 + \frac{E_\pi}{K_\pi} \right) n_p \left(m_p c^2 + \frac{E_\pi}{K_\pi} \right), \quad (10.49)$$

where $E_{kin} = E_p - m_p c^2$ is the kinetic energy of the proton and K_π is the mean fraction of the kinetic energy of the proton transferred to the pions, per proton-proton collision. In the GeV-TeV energy band, $K_\pi \approx 0.17$ according to accelerator measurements including also a contribution of about $\sim 6\%$ from the mesons η in the production of π^0 (Gaisser 1990). The expression in Eq. (10.49) is correct only if the energy distribution of the high-energy protons is broad (*e.g.* power law). Otherwise (*e.g.* for pile-up, or close to exponential cut-off), a more complex calculation is necessary (see Kelner *et al.* 2006), but this case is not considered in the following. The cross section is well approximated by (Aharonian & Atoyan 2000)

$$\sigma_{pp}(E_p) = 30 \left[0.95 + 0.06 \ln \left(\frac{E_{kin}}{1 \text{ GeV}} \right) \right] \text{ mb}, \quad (10.50)$$

for $E_{kin} > 1 \text{ GeV}$ and $\sigma_{pp}(E_p) = 0$ for $E_{kin} < 1 \text{ GeV}$. The cross section increases slowly with energy (see Fig. 12).

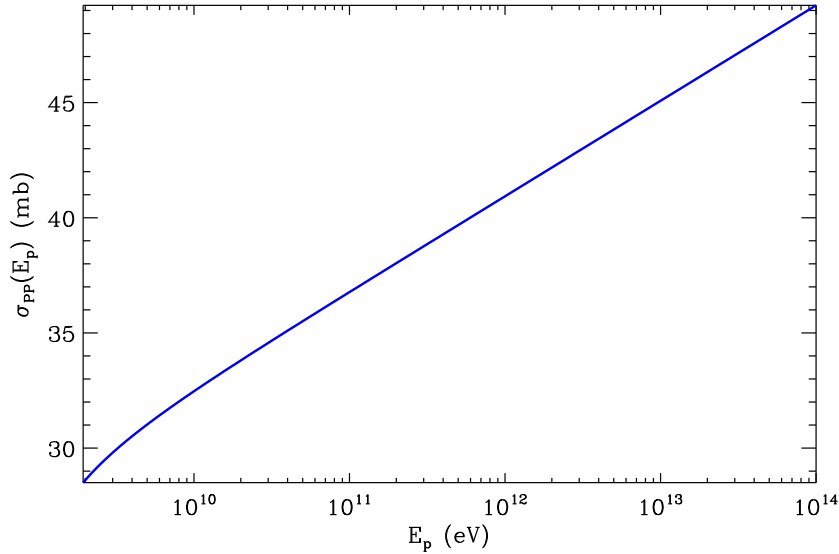


FIG. 12. Inclusive cross section of the production of neutral pions in proton-proton collision σ_{pp} , as a function of the high-energy proton energy E_p .

The spectrum of the gamma rays produced by the decay of neutral pions is given by (see Stecker 1966 for the technical details, see also Dermer 1986)

$$\frac{dN}{dt d\epsilon_1} = 2 \int_{\epsilon_1 + \frac{m_\pi^2 c^4}{4\epsilon_1}}^{+\infty} \frac{dN_\pi}{dt dE_\pi} \frac{dE_\pi}{(E_\pi^2 - m_\pi^2 c^4)^{1/2}}, \quad (10.51)$$

where the boundaries in the integral are given by the kinematics, and the distribution $1/(E_\pi^2 - m_\pi^2 c^4)^{1/2}$ gives the spectrum of gamma rays produced in the decay of one pion

(isotropic in the rest frame of the pion). The factor 2 indicates that two gamma rays are produced per decay. Note that the lifetime of the neutral pion is very small $\tau' = 8.3 \pm 0.6 \times 10^{-17}$ s in the rest frame (Particle Data Group *et al.* 2008). Even for highly relativistic pions, say $\gamma_\pi = 10^8$, the life time in the observer frame $\tau \sim \gamma_\pi \tau' \sim 10^{-8}$ s remains very small compared with the typical escaping timescale ($t_{esc} = d/c \gtrsim 10^2$ s) or proton cooling in binaries (see below).

The characteristic timescale to create a neutral pion by proton-proton collision is

$$t_{pp} = \frac{1}{n_H c \sigma_{pp}}. \quad (10.52)$$

In LS 5039 at periastron, a pion is produced at threshold after $t_{pp} \gtrsim 10^5$ s $\gg t_{esc} \sim 100$ s. Because $t_{pp} \gg t_{esc}$, only the fraction $t_{esc}/t_{pp} \ll 1$ of the high-energy protons will have enough time to produce pions with an efficiency of $K_\pi \approx 10\%$ for each interaction. If the gamma-ray luminosity L_γ observed in gamma-ray binaries are produced by the decay of pions only, then the luminosity in protons should be

$$L_p \gtrsim \frac{t_{pp}}{t_{esc} K_\pi} L_\gamma \approx 10^4 L_\gamma \quad (10.53)$$

(see also the discussion in *e.g.* Aharonian *et al.* 2005a; Bosch-Ramon & Khangulyan 2009). A hadronic origin of the high-energy gamma rays in binaries would then require a larger energy budget compared with a leptonic origin (where L_e , the luminosity in electrons is $\approx L_\gamma$, because $t_{ic} \ll t_{esc}$ and a large fraction of the electron energy can be transferred to gamma rays in the Klein-Nishina regime). Hence, this scenario appears less favorable and will not be considered in our modeling (see however the model in Romero *et al.* 2003).

§ 11. Photomeson production

The interaction of a low energy photon of energy ϵ_0 with an ultra relativistic proton of energy E_p can produce pions *i.e.*

$$\gamma(\epsilon_0) + p(E_p) \rightarrow \pi^0(E_\pi) + p \quad (11.54)$$

if

$$2\epsilon_0 E_p (1 - \beta_p \cos \theta_0) \geq m_\pi c^2 (m_\pi c^2 + 2m_p c^2), \quad (11.55)$$

where θ_0 is the angle between both particles direction of motion. For $\epsilon_0 = 10$ eV, $\beta_p \approx 1$ and for a head-on collision $\cos \theta_0 = -1$, pions are produced if the proton energy exceeds $E_p \gtrsim 7.5$ PeV. The total cross section for this process is about $\sigma_{\gamma p} \sim 0.5$ mb at threshold (Particle Data Group *et al.* 2008). The characteristic timescale for pion production is then

$$t_{\gamma p} = \frac{1}{n_{ph} c \sigma_{\gamma p}}. \quad (11.56)$$

In LS 5039, with $n_{ph} \sim 10^{14}$ ph cm $^{-3}$, $t_{\gamma p} \gtrsim 10^3$ s $\gtrsim t_{esc}$. This processes appears then to be more relevant than pion production by proton-proton collision, because of the dense stellar photon field provided by the massive companion star in compact binaries, but the threshold energy remains too high for our investigations in the GeV-TeV energy band. We will ignore this process as well in our modeling.

4. Photon-photon annihilation

The photon-photon annihilation $\gamma(\epsilon_1) + \gamma(\epsilon_0) \rightarrow e^+ + e^-$ is the main absorption process for high-energy gamma rays produced by the radiative processes described above. A high-energy gamma-ray of energy ϵ_1 interacting with a low energy photon of energy ϵ_0 produces an electron-positron pair if the total energy available in the center-of-mass frame is bigger than the rest mass energy of the pair, *i.e.* (see Chapter 6 for more details)

$$2\epsilon_1\epsilon_0(1 - \cos\theta_0) \geq 4m_e^2c^4, \quad (11.57)$$

with θ_0 the angle between the direction of propagation of the two photons. For a photon of energy $\epsilon_0 = 10$ eV and for a head-on collision ($\cos\theta_0 = -1$), a pair is produced if $\epsilon_1 \gtrsim m_e^2c^4/\epsilon_0 \approx 25$ GeV. The total cross section is given by (see *e.g.* Gould & Schröder 1967)

$$\sigma_{\gamma\gamma} = \frac{\pi r_e^2}{2} (1 - \beta^2) \left[(3 - \beta^4) \ln\left(\frac{1 + \beta}{1 - \beta}\right) - 2\beta(2 - \beta^2) \right], \quad (11.58)$$

where $\beta = v_e/c$ is the velocity of the electron-positron pair in the center-of-mass frame. This formula is also known as the "Breit-Wheeler" cross section named after two physicists who pioneered the pair creation process (Breit & Wheeler 1934). In the non-relativistic limit ($\beta \ll 1$), the cross section simplifies as

$$\sigma_{\gamma\gamma} = \pi r_e^2 \beta. \quad (11.59)$$

The total cross section is maximum for $\beta \approx 0.7$. At the threshold energy for pair production ($\beta = 0$), the cross section equals 0 and increases almost linearly up to $\beta \approx 0.7$ and decreases exponentially towards 0 for $\beta \approx 1$ (Fig. 13).

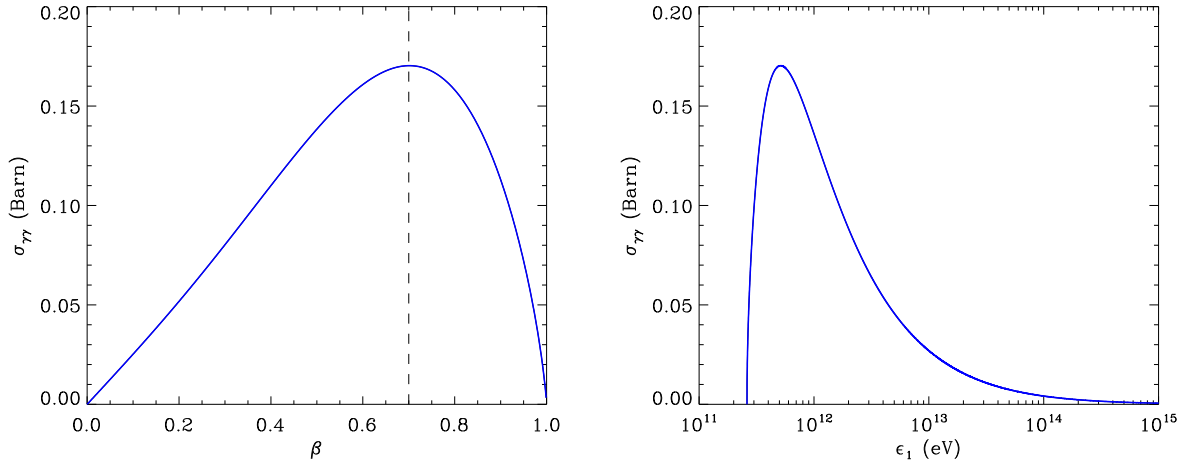


FIG. 13. Total cross section for pair production $\sigma_{\gamma\gamma}$ as a function of β (*left panel*) and as a function of the gamma-ray photon energy ϵ_1 (*right panel*) for $\epsilon_0 = 1$ eV and $\theta_0 = \pi$. The pair is mostly produced close to threshold (maximum for $\beta \approx 0.7$).

The gamma-ray opacity $\tau_{\gamma\gamma}$ is given by (Gould & Schröder 1967)

$$\tau_{\gamma\gamma} = \iiint \frac{dn_{ph}}{d\Omega_0 d\epsilon_0} (1 - \cos\theta_0) \sigma_{\gamma\gamma} d\Omega_0 d\epsilon_0 dl, \quad (11.60)$$

where l is the path length of the gamma-ray photon in a soft photon gas of density $dn_{ph}/d\Omega_0 d\epsilon_0$ per unit of energy ϵ_0 and solid angle Ω_0 . In gamma-ray binaries, the opacity of a gamma-ray photon of energy 100 GeV is roughly $\tau_{\gamma\gamma} \approx \sigma_{\gamma\gamma} n_{ph} d \approx 20 \gg 1$ in LS 5039 where the soft photon density is very high at the compact object location ($d \approx 0.1$ AU and $n_{ph} \approx 10^{14}$ ph cm $^{-3}$). Hence, pair production is a relevant process in gamma-ray binaries in the GeV-TeV energy band (see Dubus 2006a). We will always consider this effect in our modeling. Chapter 6 is dedicated to the full calculation of pair production in binaries.

Pair production could also occur between curvature radiation and the magnetic field in the magnetosphere of pulsars (see *e.g.* Sturrock 1971). This effect will not be discussed in this thesis but this is an important issue for the modeling of the pulsed high-energy emission in pulsars.

Before we move on the next section, I would like to mention that high-energy gamma rays can also undergo "double pair production", *i.e.*

$$\gamma(\epsilon_1) + \gamma(\epsilon_0) \rightarrow e^+ + e^- + e^+ + e^-, \quad (11.61)$$

if

$$2\epsilon_1\epsilon_0(1 - \cos\theta_0) \geq 16m_e^2c^4. \quad (11.62)$$

The full Quantum Electrodynamics treatment of this process indicates that the cross section has a maximum asymptotic value $\sigma_{dpp} \approx 6.45 \mu\text{b}$ (Brown *et al.* 1973). This cross section equals the "simple" pair production cross section $\sigma_{\gamma\gamma}$ for $\epsilon_1\epsilon_0(1 - \cos\theta_0) \gtrsim 4 \times 10^4 m_e^2 c^4$ (Mastichiadis 1986). Hence this process would be important for ultra-high energy gamma rays only, and will not be considered in the following.

5. The cooling of relativistic particles

§ 12. The continuity equation

In this section, I describe the changes in the energy distribution of particles over time, and energy due to cooling (via processes described in previous sections), the escape and injection of particles in the region of interest. The cooled energy distribution $n \equiv dN/dE$ as a function of time t and energy E is given by the following continuity equation (Ginzburg & Syrovatskii 1964; Blumenthal & Gould 1970)

$$\frac{\partial n}{\partial t} + \frac{\partial}{\partial E}(\dot{E}n) + \frac{n}{T} = Q_i(E_0, t_0). \quad (12.63)$$

This equation is a simplified form of the general Fokker-Planck equation which describes the transport of particles. The second term in Eq. (12.63) is an advection term in the energy space due to the cooling (*via e.g.* the processes described above). The third term describes the escaping of particles from the cooling region with a typical timescale T . In the right side of Eq. (12.63) are the source terms which inject fresh particles at an energy E_0 at t_0 . This equation is valid as long as the energy lost per collision is a small fraction of the total energy of the electron. In other words, this condition holds if

$$-\dot{E}/E \ll N\sigma c, \quad (12.64)$$

where N is the density of scattering particles and σ the cross section of the process considered. For high-energy electrons (positrons), Synchrotron radiation, TPP and inverse Compton scattering in the Thomson regime satisfy this condition. This is not the case for Bremsstrahlung or inverse Compton scattering in the deep Klein-Nishina regime where the fraction of energy

lost in the interaction can be large $\Delta E_e \approx E_e$. Zdziarski (1989) showed that the continuous losses approximation is rather good in the Klein-Nishina regime if the electron and or soft photon distributions are broad in energy. We will do this assumption in the following. In Chapter 7 (see Sect. 8), I perform the exact calculation of the Klein-Nishina energy losses and compare with the continuous losses approximation.

Eq. (12.63) should also contain a diffusion term in energy but this effect can be neglected in the our context where only synchrotron and inverse Compton emission are relevant cooling processes (Blumenthal & Gould 1970).

§ 13. General solution

The Green kernel G should satisfy the equation

$$\frac{\partial G}{\partial t} + \frac{\partial}{\partial E} (\dot{E}G) + \frac{G}{T} = \delta(E - E_0) \delta(t - t_0). \quad (13.65)$$

The solution to this equation is (Ginzburg & Syrovatskii 1964)

$$G(E, t; E_0, t_0) = \frac{1}{|\dot{E}|} e^{-\frac{t-t_0}{T}} \delta(t - t_0 - \tau) \Theta(t - t_0) \Theta(E_0 - E), \quad (13.66)$$

where δ and Θ are respectively the Dirac and the step distribution, and where

$$\tau(E_0, E) = \int_{E_0}^E \frac{dE'}{\dot{E}'} \quad (13.67)$$

is the characteristic timescale for the energy change of the particle from E_0 to E . The general solution of Eq. (12.63) is

$$n(E, t) = \int_{-\infty}^{+\infty} \int_{-\infty}^{+\infty} G(E, t; E_0, t_0) Q_i(E_0, t_0) dt_0 dE_0. \quad (13.68)$$

Substituting Eq. (13.66) in the above equation yields

$$n(E, t) = \frac{1}{|\dot{E}|} \int_E^{+\infty} \exp\left(-\frac{1}{T} \int_{E_0}^E \frac{dE'}{\dot{E}'}\right) Q_i\left(E_0, t - \int_{E_0}^E \frac{dE'}{\dot{E}'}\right) dE_0. \quad (13.69)$$

§ 14. Some simple solutions

It is possible to derive from Eq. (13.69) simple solutions for a steady injection of particles (*i.e.* $\partial n / \partial t = 0$) with no escaping term (T is much greater than the characteristic timescale τ). If the source injects fresh particles with energies distributed as a power law such as $Q_i = Q_0 E_0^{-p}$, then we have (if $p \neq 1$)

$$n(E) = \frac{Q_0}{|\dot{E}|(p-1)} E^{-(p-1)}. \quad (14.70)$$

For electrons cooling down in the Thomson regime or *via* synchrotron radiation, we have (Eq. 5.9, 7.27) $\dot{E} \propto E^2$ then

$$n(E) \propto E^{-(p+1)}. \quad (14.71)$$

For a monoenergetic injection of new particles so that $Q_i = Q_0 \delta(E_0 - E_i)$ and if electrons cool down in the Thomson regime or by synchrotron radiation, the steady cooled distribution of electrons is

$$n(E) \propto E^{-2} \Theta(E_i - E). \quad (14.72)$$

6. What we have learned

In this introductory chapter, I have presented the main high-energy cooling processes of relativistic electrons (positrons) and protons usually considered in high-energy astrophysics. I found that inverse Compton scattering and synchrotron radiation are the most relevant high-energy leptonic processes in the typical environment of compact binaries. Bremsstrahlung could be relevant in denser environments than those found in binaries. Triplet pair production is unimportant in the cooling except if the system accelerates electrons to energies \gtrsim PeV. Hadronic processes are not favored as the energy budget in protons required to account for the full gamma-ray luminosity should be very high, *i.e.* 3 or 4 orders of magnitude higher than the power injected in leptons. High-energy gamma rays can be highly absorbed by the large density of target photons provided the massive companion star.

For the modeling of the high-energy radiation in compact binaries, I will consider only inverse Compton scattering, synchrotron radiation and pair production.

7. [Français] Résumé du chapitre

§ 15. Contexte et objectifs

Une particule chargée de haute énergie traversant un milieu matériel baigné dans un champ de rayonnement et un champ magnétique se refroidit et émet, dans certain cas, des rayons gamma de haute énergie. Dans ce chapitre, je passe brièvement en revue les processus de haute énergie dans lesquels des électrons et des protons hautement relativistes sont impliqués (*i.e.* particules dont l'énergie totale est bien plus grande que leur énergie de masse $E \gg mc^2$). Je présente les caractéristiques essentielles de chaque interaction. Je fournis également quelques références dans lesquelles plus de détails techniques se trouvent.

L'objectif principal de ce chapitre est de distinguer parmi tous les processus de haute énergie quels sont ceux qui sont les plus susceptibles de se produire dans les binaires compactes. Pour cela, je calcule le temps caractéristique de refroidissement des particules en fonction de leur énergie pour chaque interaction dans des conditions physiques typiques rencontrées dans les binaires considérés dans cette thèse. Dans une première partie, je présente les processus de haute énergie impliquant des électrons (ou positrons) relativistes ou "processus leptoniques" suivants:

- La diffusion Compton inverse (§ 5).
- Bremsstrahlung (ou rayonnement de freinage) (§ 6).
- Rayonnement synchrotron ou "Bremsstrahlung magnétique" (§ 7).
- Production d'un triplet de paires (§ 8).

Des rayons gamma de haute énergie peuvent être aussi produits par des protons relativistes. Cette possibilité est envisagée et discutée dans le contexte des binaires compactes. Je présente ici les deux "processus hadroniques" suivant:

- La diffusion proton-proton (§ 10).
- La diffusion photon-proton (§ 11).

Les photons gamma de haute énergie peuvent être absorbés par des photons de bien plus basse énergie et produire des paires électron-positron. J'expose brièvement ici le processus de production de paire par annihilation à deux photons (Sect. 4). Les processus de haute

énergie donnés ci-dessus refroidissent les particules. Le spectre initial des particules peut être alors fortement modifié par le refroidissement. Dans une dernière partie (Sect. 5), je donne la principale équation qui régit le refroidissement des particules et je dérive quelques solutions analytiques simples.

§ 16. Ce que nous avons appris

Dans ce chapitre introductif, j'ai trouvé que la diffusion Compton inverse et le rayonnement synchrotron sont les processus leptoniques les plus pertinents dans l'environnement typique d'une binaire compacte. Le refroidissement par Bremsstrahlung pourrait être un processus important si le milieu ambiant était plus dense que celui observé dans les binaires étudiées ici. Le refroidissement des paires par le processus de production d'un triplet de paires peut être négligé sauf si des électrons sont accélérés à des énergies jusqu'au PeV. La production de photons gamma par des processus hadroniques ne semble pas être la solution privilégiée. En effet, l'énergie totale dans les protons nécessaire pour expliquer la luminosité gamma observée doit être très élevée, *i.e.* environ de 3 à 4 ordres de grandeurs au dessus de l'énergie injectée dans des électrons. Par ailleurs, les rayons gamma peuvent être presque totalement absorbés dans le champ de photons thermiques généré par l'étoile massive.

Dans cette thèse, je ne considérerai que la diffusion Compton inverse, l'émission synchrotron et le processus de production de paires.

Part II

Gamma-ray emission in gamma-ray binaries

3	Anisotropic inverse Compton scattering	39
4	Gamma-ray modulation in gamma-ray binaries	55
5	High-energy emission from the unshocked pulsar wind	83

3

Anisotropic inverse Compton scattering

Outline

1. What we want to know	40
2. Kinematics and geometrical quantities	40
3. Differential cross sections	41
4. Anisotropic inverse Compton scattering in the Thomson approximation	42
§ 15. <i>Soft photon density</i>	42
§ 16. <i>Anisotropic Thomson kernel</i>	43
§ 17. <i>Anisotropic scattering rate</i>	44
§ 18. <i>Beamed emission</i>	45
§ 19. <i>Isotropic Thomson kernel</i>	45
§ 20. <i>Integration over electron energy for a power law distribution</i>	46
§ 21. <i>Integration over soft photon energy for a black-body distribution</i>	47
§ 22. <i>Final check: Integration over an isotropic distribution of soft radiation</i>	49
5. Anisotropic inverse Compton scattering in the general case	50
§ 23. <i>General anisotropic kernel</i>	50
§ 24. <i>Integration over a power law for electrons and a black body for soft photons</i>	51
§ 25. <i>Final check: Comparison with Jones' isotropic solution</i>	51
6. What we have learned	52
7. [Français] Résumé du chapitre	53
§ 26. <i>Contexte et objectifs</i>	53
§ 27. <i>Ce que nous avons appris</i>	54

THIS CHAPTER is dedicated to the detailed study of inverse Compton scattering in the case where the ambient source of target photons is anisotropic. I provide here the full equations and calculations of the radiated spectrum in the Thomson limit (Sect. 4) and in the general case (Sect. 5), including Klein-Nishina effects. More specifically, this part focuses on the angular dependence of the emitted inverse Compton spectrum. Results are also compared with known formulae derived for an isotropic source of soft photons (see *e.g.* Ginzburg & Syrovatskii 1964; Jones 1968; Blumenthal & Gould 1970; Rybicki & Lightman 1979).

A significant part of the work exposed here has been done during my Master degree. I add to this previous study new analytical formulae.

1. What we want to know

- What is the angular dependence of the inverse Compton emission?
- What are the main features of anisotropic inverse Compton scattering?
- How does this compare with known results in the isotropic case?

2. Kinematics and geometrical quantities

To study inverse Compton scattering, it is worthwhile to consider the interaction in the frame where the electron is at rest. Primed quantities are defined in the rest frame of the electron and unprimed quantities are defined in the observer frame where the electron is moving at relativistic speed ($\gamma_e \gg 1$). In the rest frame of the electron, the photon of energy ϵ'_0 transfers momentum to the electron and is scattered with an energy ϵ'_1 at an angle Θ' with respect to its initial direction of propagation (Fig. 14). Let's define the 4-momentum for each particles in the rest frame of the electron

$$k'_0 = \begin{pmatrix} \epsilon'_0 \\ \mathbf{k}'_0 \end{pmatrix} \quad k'_1 = \begin{pmatrix} \epsilon'_1 \\ \mathbf{k}'_1 \end{pmatrix} \quad p'_0 = \begin{pmatrix} m_e c^2 \\ \mathbf{0} \end{pmatrix} \quad p' = \begin{pmatrix} E'_e \\ \mathbf{p}' \end{pmatrix}. \quad (16.73)$$

The conservation of the total 4-momentum before and after the interaction yields

$$k'_0 + p'_0 = k'_1 + p'. \quad (16.74)$$

Then we have

$$\begin{pmatrix} E'_e \\ \mathbf{p}' \end{pmatrix} = \begin{pmatrix} \epsilon'_0 - \epsilon'_1 + m_e c^2 \\ \mathbf{k}'_0 - \mathbf{k}'_1 \end{pmatrix}, \quad (16.75)$$

and using $E_e'^2 = \mathbf{p}'^2 c^2 + m_e^2 c^4$, we obtain the Compton formula

$$\epsilon'_1 = \frac{\epsilon'_0}{1 + \frac{\epsilon'_0}{m_e c^2} (1 - \cos \Theta')}, \quad (16.76)$$

which links the energy of the scattered photon with the angle Θ' and the energy of the incoming photon. The angle between both photons can be expressed as a function of the spherical angles of each photons in the (x', y', z') coordinate system shown in Fig. 14. If \mathbf{e}'_0 and \mathbf{e}'_1 are unit vectors in the direction of the incoming respectively outgoing photon, we have

$$\cos \Theta' = \mathbf{e}'_0 \cdot \mathbf{e}'_1 = \cos \theta'_1 \cos \theta'_0 + \sin \theta'_1 \sin \theta'_0 \cos (\phi'_1 - \phi'_0). \quad (16.77)$$

The relativistic Doppler shift formulae provide the relations between energies and angles in both frames. From the observer frame to the rest frame of the electron, the boost along the electron direction of motion (z-axis) gives

$$\epsilon'_0 = \gamma_e (1 - \beta_e \cos \theta_0) \epsilon_0 \quad \epsilon_0 = \gamma_e (1 + \beta_e \cos \theta'_0) \epsilon'_0 \quad (16.78)$$

$$\epsilon'_1 = \gamma_e (1 - \beta_e \cos \theta_1) \epsilon_1 \quad \epsilon_1 = \gamma_e (1 + \beta_e \cos \theta'_1) \epsilon'_1, \quad (16.79)$$

and angles change as

$$\cos \theta'_0 = \frac{\cos \theta_0 - \beta_e}{1 - \beta_e \cos \theta_0} \quad \cos \theta_0 = \frac{\cos \theta'_0 + \beta_e}{1 + \beta_e \cos \theta'_0}. \quad (16.80)$$

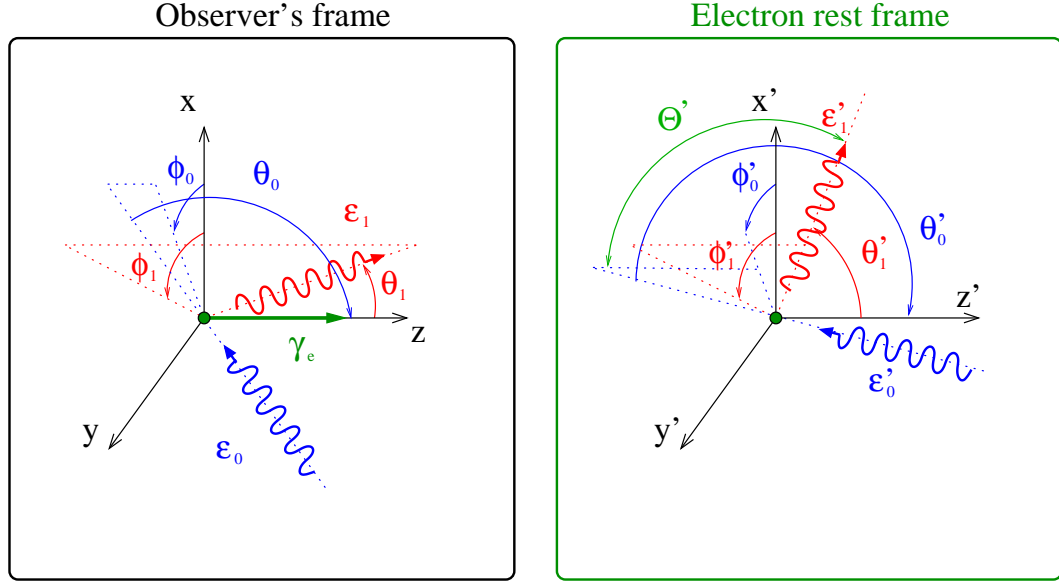


FIG. 14. Inverse Compton scattering seen in the observer frame (*left panel*) and in the rest frame of the electron (*right panel*). Waves represent photons and the green thick arrow shows the direction of motion of the electron of total energy $E_e = \gamma_e m_e c^2$. The Lorentz boost from the observer to the rest frame of the electron is along the z-axis.

for θ_0 as well as for θ_1 . The azimuthal angles ϕ_0 and ϕ_1 are invariant as they are defined in the plane perpendicular to the boost direction.

3. Differential cross sections

In Quantum ElectroDynamics theory, the full differential cross section of Compton scattering in the rest frame of the electron (for unpolarized photons, see Feynman diagrams in Fig. 15) is given by the Klein-Nishina formula (see *e.g.* Heitler 1954; Rybicki & Lightman 1979)

$$\frac{d\sigma}{d\Omega'_1 d\epsilon'_1} = \frac{r_e^2}{2} \left(\frac{\epsilon'_1}{\epsilon'_0} \right)^2 \left(\frac{\epsilon'_1}{\epsilon'_0} + \frac{\epsilon'_0}{\epsilon'_1} - \sin^2 \Theta' \right) \delta \left(\epsilon'_1 - \frac{\epsilon'_0}{1 + \frac{\epsilon'_0}{m_e c^2} (1 - \cos \Theta')} \right), \quad (16.81)$$

where r_e is the classical radius of the electron and δ is the Dirac distribution.

The full quantum and relativistic corrections are included in Eq. (16.81). These effects appear at very high-energy when the recoil of the electron in the rest frame is significant ($\epsilon'_0 \gg m_e c^2$), *i.e.* in the *Klein-Nishina regime*. If $\epsilon'_0 \ll m_e c^2$, the recoil of the electron can be ignored (see Eq. 16.76) and the photon is scattered with no loss of energy $\epsilon'_0 = \epsilon'_1$. This is the *Thomson limit*. In this case, the differential cross section is given by

$$\frac{d\sigma}{d\Omega'_1 d\epsilon'_1} = \frac{r_e^2}{2} (1 + \cos^2 \Theta') \delta(\epsilon'_1 - \epsilon'_0). \quad (16.82)$$

The total cross section given in Eq. (5.2) is obtained by integrating the differential cross section, such as

$$\sigma_{ic} = \iint \frac{d\sigma}{d\Omega'_1 d\epsilon'_1} d\Omega'_1 d\epsilon'_1. \quad (16.83)$$

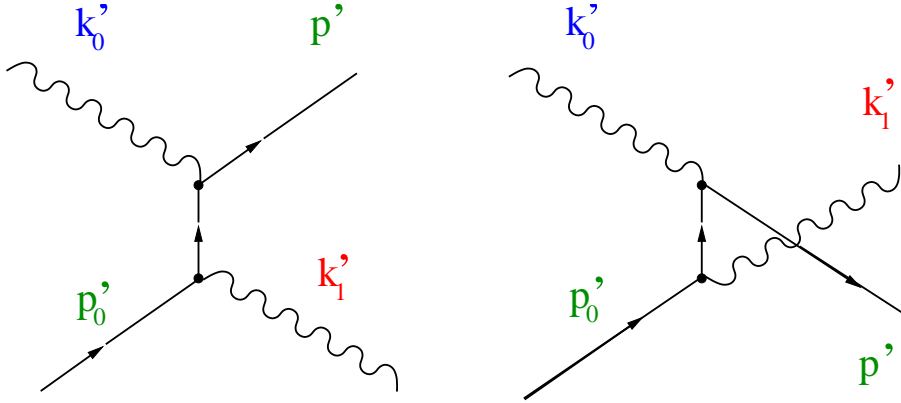


FIG. 15. Second order Feynman diagram for Compton scattering.

4. Anisotropic inverse Compton scattering in the Thomson approximation

In this part, we aim to derive the spectrum of the photons scattered by a relativistic electron interacting with a gas of soft radiation in the Thomson regime ($\epsilon'_0 \ll m_e c^2$). We first compute the spectrum in the case of a mono-energetic beam of soft photons. This elementary spectrum or "anisotropic inverse Compton kernel" is then integrated over simple distributions for electrons and photons and analytical formulae are presented below. We will focus on the angular dependence of the emitted spectrum. Our solutions are compared with known formulae in the case of an isotropic source of soft radiation.

§ 17. Soft photon density

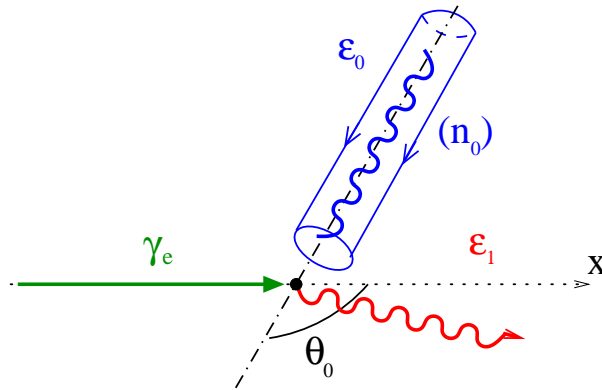


FIG. 16. Geometrical configuration for the computation of the anisotropic inverse Compton kernel.

Following Fargion *et al.* (1997), we consider a mono-energetic beam of soft photons interacting with an electron of energy $E_e = \gamma_e m_e c^2$ (Fig. 16). The normalized soft photon density ($\text{ph cm}^{-3} \text{erg}^{-1} \text{sr}^{-1}$) in the observer frame is

$$\frac{dn}{d\epsilon d\Omega} = \delta(\epsilon - \epsilon_0) \delta(\mu - \mu_0) \delta(\phi - \phi_0), \quad (17.84)$$

where $\mu_{(0)} \equiv \cos\theta_{(0)}$. Using the relativistic invariant $dn/d\epsilon$ (Blumenthal & Gould 1970), the photon density in the rest frame of the electron is

$$\frac{dn'}{d\epsilon' d\Omega'} = \frac{dn}{d\epsilon d\Omega} \frac{d\Omega}{d\Omega'} \quad (17.85)$$

With Eqs. (16.78)-(16.80), we have

$$\frac{d\Omega}{d\Omega'} = \gamma_e^2 (1 - \beta_e \mu)^2 \quad (17.86)$$

$$\delta(\epsilon - \epsilon_0) = \gamma_e (1 - \beta_e \mu) \delta(\epsilon' - \epsilon'_0) \quad (17.87)$$

$$\delta(\mu - \mu_0) = \frac{1}{\gamma_e^2 (1 - \beta_e \mu)^2} \delta(\mu' - \mu'_0) \quad (17.88)$$

$$\delta(\phi - \phi_0) = \delta(\phi' - \phi'_0). \quad (17.89)$$

The Dirac distribution were re-arranged using the formula

$$\delta[f(x)] = \sum_i \frac{1}{|df/dx|_{x=x_i}} \delta(x - x_i), \quad (17.90)$$

where f is a function of x and $f(x_i) = 0$. Hence, the soft photon density in the electron frame is

$$\frac{dn}{d\epsilon d\Omega} = \gamma_e (1 - \beta_e \mu) \delta(\epsilon' - \epsilon'_0) \delta(\mu' - \mu'_0) \delta(\phi' - \phi'_0). \quad (17.91)$$

This transform changes the energy and the direction of the incoming radiation but the density is also changed by the Doppler factor $\gamma_e (1 - \beta_e \mu)$.

§ 18. Anisotropic Thomson kernel

The number of photons scattered per electron, per unit of time, energy, and solid angle in the rest frame of the electron is (Jones 1968; Blumenthal & Gould 1970)

$$\frac{dN}{dt' d\epsilon'_1 d\Omega'_1} = \iint \frac{dn'}{d\epsilon' d\Omega'} c \frac{d\sigma}{d\epsilon'_1 d\Omega'_1} d\epsilon' d\Omega', \quad (18.92)$$

where c is the relative velocity between the electron (at rest) and the incoming photon. Since the total number of photons is invariant, the density of scattered photons in the observer frame is given by

$$\frac{dN}{dt d\epsilon_1 d\Omega_1} = \frac{dN}{dt' d\epsilon'_1 d\Omega'_1} \frac{dt'}{dt} \frac{d\Omega'_1}{d\Omega_1} \frac{d\epsilon'_1}{d\epsilon_1}, \quad (18.93)$$

so that (with $dt'/dt = 1/\gamma_e$ as we are looking at the *emitted* spectrum)

$$\frac{dN}{dt d\epsilon_1 d\Omega_1} = \frac{1}{\gamma_e^2 (1 - \beta_e \mu_1)} \iint \frac{dn'}{d\epsilon' d\Omega'} c \frac{d\sigma}{d\epsilon'_1 d\Omega'_1} d\epsilon' d\Omega'. \quad (18.94)$$

Injecting Eq. (16.82) and (17.91) into Eq. (18.94), we obtain after integration

$$\frac{dN}{dt d\epsilon_1 d\Omega_1} = \frac{r_e^2 c (1 - \beta_e \mu_0)}{2\gamma_e (1 - \beta_e \mu_1)} \left(1 + \left[\mu'_1 \mu'_0 + (1 - \mu_1'^2)^{1/2} (1 - \mu_0'^2)^{1/2} \cos(\phi_1 - \phi_0) \right]^2 \right) \delta(\epsilon'_1 - \epsilon'_0). \quad (18.95)$$

The last integration over Ω_1 requires one more rearrangement of the remaining Dirac distribution such as

$$\delta(\epsilon'_1 - \epsilon'_0) = \frac{1}{\beta_e \gamma_e \epsilon_1} \delta \left(\mu_1 - \frac{1}{\beta_e} \left[1 - \frac{\epsilon_0}{\epsilon_1} (1 - \beta_e \mu_0) \right] \right). \quad (18.96)$$

In addition, we have

$$\int_0^{2\pi} \cos \phi_1 d\phi_1 = 0 \quad \int_0^{2\pi} \cos^2 \phi_1 d\phi_1 = \pi. \quad (18.97)$$

The anisotropic inverse Compton kernel in the Thomson approximation is then given by (Fargion *et al.* 1997)

$$\boxed{\frac{dN}{dt d\epsilon_1} = \frac{\pi r_e^2 c}{2\beta_e \gamma_e^2 \epsilon_0} \left[3 - \mu_0'^2 + (3\mu_0'^2 - 1) \frac{1}{\beta_e^2} \left(\frac{\epsilon_1}{\gamma_e^2 \epsilon_0 (1 - \beta_e \mu_0)} - 1 \right)^2 \right]}. \quad (18.98)$$

Relativistic kinematics (Eqs. 16.78-16.79) yields the energy range for the scattered photons so that

$$\frac{1 - \beta_e \mu_0}{1 + \beta_e} < \frac{\epsilon_1}{\epsilon_0} < \frac{1 - \beta_e \mu_0}{1 - \beta_e}. \quad (18.99)$$

For "head-on" collisions ($\theta_0 = \pi$), the scattered photon is at least as energetic as the soft radiation $\epsilon_1 \geq \epsilon_0$ and can be scattered at the maximum energy $\gamma_e^2 (1 + \beta_e)^2 \epsilon_0 \approx 4\gamma_e^2 \epsilon_0$ (if $\beta \approx 1$). For "rear-end" collisions ($\theta_0 = 0$), the interaction becomes a "normal" Compton scattering since the soft photon loses energy Eq. (18.99) $\epsilon_1 \leq \epsilon_0$. The expression in Eq. (18.98) is exact in the Thomson limit, but this formula can be substantially simplified in the ultra-relativistic limit $\gamma_e \gg 1$. With $\mu_0' \approx -1$ ("head-on approximation") and $\beta_e \approx 1$, the kernel can be rewritten as

$$\frac{dN}{dt d\epsilon_1} = \frac{2\pi r_e^2 c}{\gamma_e^2 \epsilon_0} f_{anis}(x), \quad (18.100)$$

where

$$f_{anis}(x) = 2x^2 - 2x + 1 \quad (18.101)$$

and

$$x = \frac{\epsilon_1}{2\gamma_e^2 (1 - \mu_0) \epsilon_0}, \quad (18.102)$$

with

$$1/4\gamma_e^2 \leq x \leq 1. \quad (18.103)$$

Note that this formula is not valid for $\theta_0 = 0$ but this case is not important in our context as it corresponds to the "normal" Compton scattering regime $\epsilon_1 \leq \epsilon_0$. However, this formula is exact in a sense if one is interested only in the contribution of photons with energy greater than ϵ_0 since no photon is expected beyond this energy in the exact solution. The function $f(x)$ is shown in Fig. 17. Thanks to this simplified expression for the kernel, we are now able to derive simple and analytical formulae in some useful and simple cases.

§ 19. Anisotropic scattering rate

The inverse Compton scattering rate gives the number of collision per electron per unit of time. This quantity is defined as

$$\frac{dN}{dt} = \int_{\epsilon_-}^{\epsilon_+} \frac{dN}{dt d\epsilon_1} d\epsilon_1. \quad (19.104)$$

Using Eqs. (18.100, 18.103) we have $0 \leq x \leq 1$ (for $\gamma_e \gg 1$)

$$\frac{dN}{dt} = \sigma_{TC} (1 - \mu_0). \quad (19.105)$$

The scattering rate is maximum for head-on collisions. No scattering are expected for rear-end collisions. The term $(1 - \mu_0)$ is due to the Doppler effect in the Lorentz transform which changes the density of soft radiation seen by the electron in the rest frame (Eq. 17.91).

§ 20. Beamed emission

We investigate in this section the angular distribution of the scattered emission in the observer frame. Integrating Eq. (18.95) over ϵ_1 yields

$$\frac{dN}{dt d\Omega_1} = \frac{r_e^2 c (1 - \beta_e \mu_0)}{2\gamma_e^2 (1 - \beta_e \mu_1)^2} \left(1 + \left[\mu_1' \mu_0' + (1 - \mu_1'^2)^{1/2} (1 - \mu_0'^2)^{1/2} \cos(\phi_1 - \phi_0) \right]^2 \right). \quad (20.106)$$

For $\gamma_e \gg 1$, the emission is boosted within a cone of semi aperture angle $\theta_1 \sim 1/\gamma_e \ll 1$ in the observer frame. Hence, the angular distribution of the scattered photon is highly beamed along the direction of motion of the electron.

§ 21. Isotropic Thomson kernel

We would like to compute the Thomson kernel averaged over an isotropic source of soft radiation and compare our solution to known formulae. For an isotropic source of radiation, the kernel is

$$\frac{dN_{iso}}{dt d\epsilon_1} = \frac{1}{4\pi} \iint \frac{dN}{dt d\epsilon_1} d\Omega_0 = \frac{1}{2} \int_{-1}^{+1} \frac{dN}{dt d\epsilon_1} d\mu_0. \quad (21.107)$$

However, we have the following constraint from kinematics (Eq. 18.103)

$$\frac{\epsilon_1}{2\gamma_e^2 \epsilon_0} \leq 1 - \mu_0 \leq \frac{2\epsilon_1}{\epsilon_0}. \quad (21.108)$$

Also, $-1 \leq \mu_0 \leq +1$ and since $\epsilon_1/\epsilon_0 \geq 1$ we have

$$\frac{\epsilon_1}{2\gamma_e^2 \epsilon_0} \leq 1 - \mu_0 \leq 2. \quad (21.109)$$

Defining $y = 1 - \mu_0$, $x = \epsilon_1/2\gamma_e^2 \epsilon_0 y$, Eq. (21.107) can be rewritten as

$$\frac{dN_{iso}}{dt d\epsilon_1} = \frac{\pi r_e^2 c}{\gamma_e^2 \epsilon_0} \int_{\frac{\epsilon_1}{2\gamma_e^2 \epsilon_0}}^2 (2x^2 - 2x + 1) dy. \quad (21.110)$$

Performing this integral yields

$$\frac{dN_{iso}}{dt d\epsilon_1} = \frac{2\pi r_e^2 c}{\gamma_e^2 \epsilon_0} f_{iso}(x') \quad (21.111)$$

with

$$f_{iso}(x') = 2x' \ln x' + x' + 1 - 2x'^2 \quad (21.112)$$

and

$$x' = \frac{\epsilon_1}{4\gamma_e^2 \epsilon_0}. \quad (21.113)$$

This expression coincides with the known formula of the isotropic kernel in the Thomson limit (see e.g. Eq. 2.42 in Blumenthal & Gould 1970). $f_{iso}(x')$ is shown in Fig. 17.

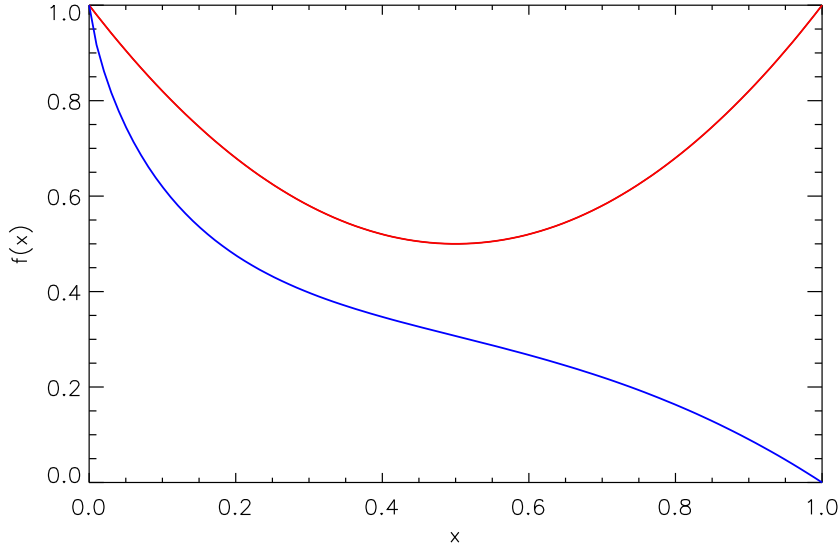


FIG. 17. Variations of the functions $f_{anis}(x)$ (red line) and $f_{iso}(x)$ (blue line) that appear in the computation of the Compton kernel in the Thomson approximation.

§ 22. Integration over electron energy for a power law distribution

We now consider an isotropic population of electrons with a power-law energy distribution in the observer frame such as

$$\frac{dN_e}{d\gamma_e} = K_e \gamma_e^{-p} \quad (22.114)$$

$$\gamma_- < \gamma_e < \gamma_+,$$

with K_e a normalisation constant and p the spectral index. The anisotropic kernel integrated over this population of electrons is given by

$$\frac{dN}{dt d\epsilon_1} = 2\pi r_e^2 c K_e \int_{\gamma_-}^{\gamma_+} \frac{\gamma_e^{-p-2}}{\epsilon_0} f_{anis}(x) d\gamma_e. \quad (22.115)$$

It is more convenient to perform this integration over x rather than γ_e . With

$$\gamma_e = \left(\frac{\epsilon_1}{2(1-\mu_0)\epsilon_0} \right)^{1/2} x^{-1/2}, \quad (22.116)$$

Eq. (22.115) can be rewritten like

$$\frac{dN}{dt d\epsilon_1} = \pi r_e^2 c K_e 2^{\frac{p+1}{2}} (1-\mu_0)^{\frac{p+1}{2}} \epsilon_0^{\frac{p-1}{2}} \epsilon_1^{-\frac{(p+1)}{2}} \int_{x_-}^{x_+} x^{\frac{p-1}{2}} f_{anis}(x) dx. \quad (22.117)$$

For energies far from the low and high energy cut-off ($\gamma_- \ll \gamma_e \ll \gamma_+$), the integral in Eq. (22.117) is

$$\int_0^1 x^{\frac{p-1}{2}} f_{anis}(x) dx = \frac{2(p^2 + 4p + 11)}{(p+1)(p+3)(p+5)}. \quad (22.118)$$

The integrated kernel can then be expressed as

$$\frac{dN}{dt d\epsilon_1} = \pi r_e^2 c K_e \frac{2^{\frac{p+3}{2}} (p^2 + 4p + 11)}{(p+1)(p+3)(p+5)} (1 - \mu_0)^{\frac{p+1}{2}} \epsilon_0^{\frac{p-1}{2}} \epsilon_1^{-\left(\frac{p+1}{2}\right)}. \quad (22.119)$$

We find the well-known result that the emitted Compton spectrum is a power-law of index $(p+1)/2$ in the Thomson limit (see *e.g.* Blumenthal & Gould 1970; Rybicki & Lightman 1979). The analytical result matches very well the numerically integrated solution with less than 1% of error (see Fig. 18).

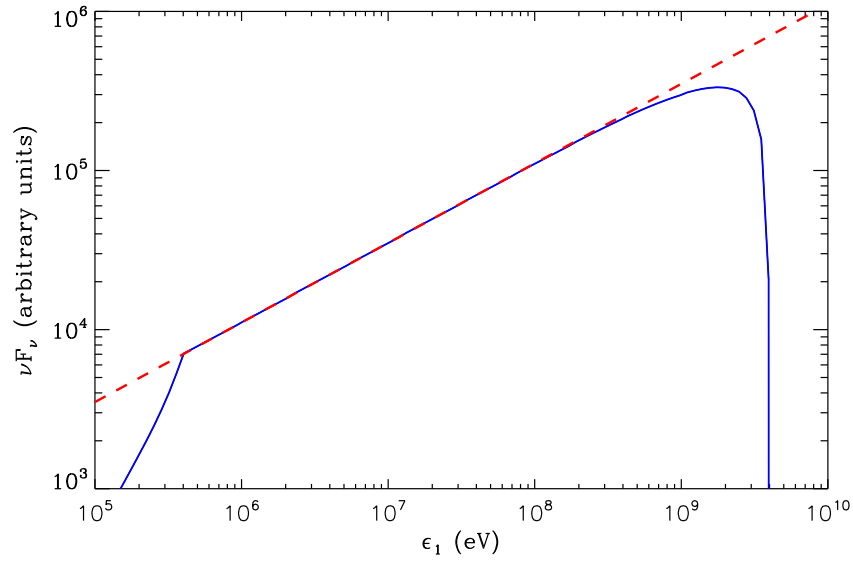


FIG. 18. Comparison of the analytical solution (red dashed line) to the numerically integrated solution (blue solid line) for electrons with a power energy distribution and mono-energetic soft photons. Parameters used: $\epsilon_0 = 10$ eV, $\theta_0 = \pi$, $p = 2$. The effect of the low and high energy cut-off are shown on the numerical solution where $\gamma_- = 10^2$ and $\gamma_+ = 10^4$.

§ 23. Integration over soft photon energy for a black-body distribution

We would like here to integrate the solution found in the previous section (Eq. 22.119) over a black-body spectrum for the soft photons. For a Planck distribution produced by for instance a star, the density of soft photon (in cm^{-3}) is

$$dn_* = \pi \left(\frac{R_*}{R} \right)^2 \frac{2}{h^3 c^3} \frac{\epsilon_0^2}{\exp\left(\frac{\epsilon_0}{kT_*}\right) - 1} d\epsilon_0 \quad (23.120)$$

where $\pi (R_*/R)^2$ is the solid angle covered by the star of radius R_* and of temperature T_* observed at a distance R from its center. However, the source of thermal photons is assumed point like here in the sense that all photons come from the same direction. The integration of the kernel in Eq. (22.119) over the soft photon density in Eq. (23.120) can be written as follows

$$\frac{dN}{dt d\epsilon_1} = \pi r_e^2 c K_e \frac{2^{\frac{p+3}{2}} (p^2 + 4p + 11)}{(p+1)(p+3)(p+5)} (1 - \mu_0)^{\frac{p+1}{2}} \epsilon_1^{-\left(\frac{p+1}{2}\right)} \pi \left(\frac{R_*}{R} \right)^2 \frac{2}{h^3 c^3} \times I, \quad (23.121)$$

with

$$I = \int_0^{+\infty} \frac{\epsilon_0^{\frac{p+3}{2}}}{\exp\left(\frac{\epsilon_0}{kT_\star}\right) - 1} d\epsilon_0. \quad (23.122)$$

Assuming $X = \epsilon_0/kT_\star$, we have (Abramowitz & Stegun 1972)

$$I = (kT_\star)^{\frac{p+5}{2}} \int_0^{+\infty} \frac{X^{\frac{p+3}{2}}}{\exp X - 1} dX = (kT_\star)^{\frac{p+5}{2}} \Gamma\left(\frac{p+5}{2}\right) \zeta\left(\frac{p+5}{2}\right), \quad (23.123)$$

where Γ is the gamma function and ζ the Riemann function. The anisotropic inverse Compton spectrum integrated over a power-law energy distribution of pairs and over the soft photon energy black-body distribution is given by the formula

$$\boxed{\frac{dN}{dt d\epsilon_1} = \frac{\pi r_e^2 c K_e}{h^3 c^3} \pi \left(\frac{R_\star}{R}\right)^2 2^{\frac{p+5}{2}} \frac{(p^2 + 4p + 11) \Gamma\left(\frac{p+5}{2}\right) \zeta\left(\frac{p+5}{2}\right)}{(p+1)(p+3)(p+5)} (kT_\star)^{\frac{p+5}{2}} (1 - \mu_0)^{\frac{p+1}{2}} \epsilon_1^{-\left(\frac{p+1}{2}\right)}}. \quad (23.124)$$

Both analytical and numerical solutions agree with an error smaller than 1% (Fig. 19). Fig. 19 presents also the scattered spectrum for various angles θ_0 and shows the strong angular dependence of the emitted Compton spectrum in the Thomson limit (see also Fig. 20). The maximum energy of the scattered radiation decreases with the angle as $\epsilon_+ \approx 2\gamma_e^2(1 - \mu_0)\epsilon_0$ (see the numerical integrated solution in Fig. 20) and can be as low as $\epsilon_+ = \epsilon_0$ if $\theta = 0^\circ$ (see Eq. 18.99), independently to the energy of the electron. The emitted flux decreases for lower angles as well because the Compton scattering rate diminishes (Eq. 19.105). More emission is expected when electrons and photons undergo head-on collisions in the observer frame.

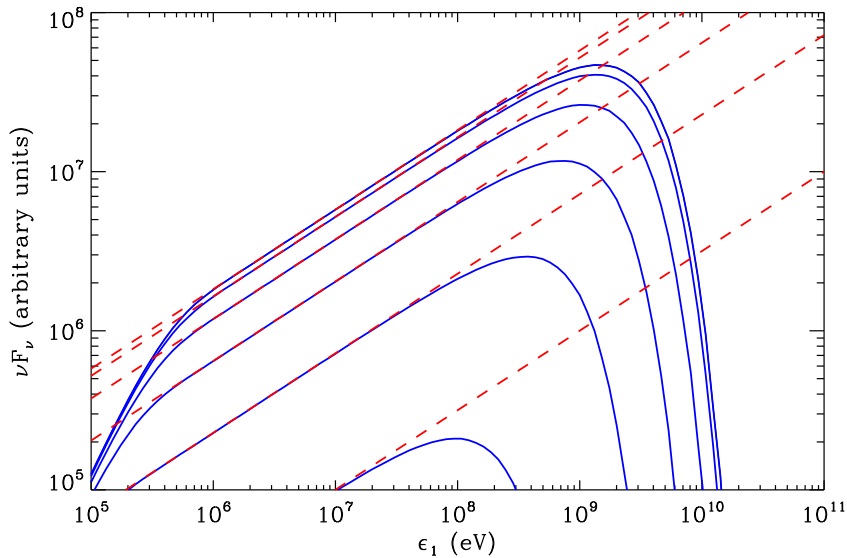


FIG. 19. The same as in Fig. 18, but where the kernel is integrated over a black-body energy distribution of effective temperature $T_\star = 39000$ K, with $\theta_0 = 180^\circ$ (top), 120° , 90° , 60° , and 30° (bottom).

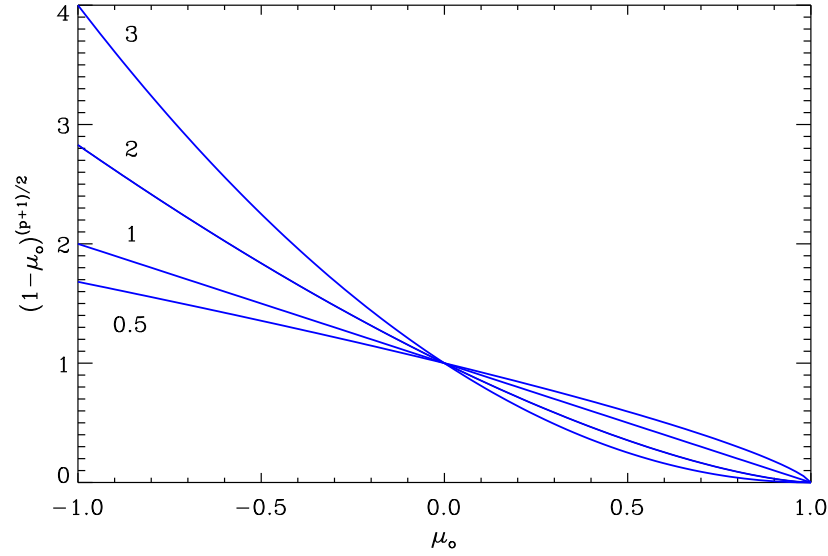


FIG. 20. Variation of the term responsible for the angular dependence in the Thomson spectrum $(1 - \mu_0)^{p+1/2}$ (see Eq. 23.124) as a function of μ_0 , with indices $p = 0.5, 1, 2$ and 3 .

§ 24. Final check: Integration over an isotropic distribution of soft radiation

The aim of this part is to check if the formula found in Eq. (23.124) is compatible with the formula found by Ginzburg & Syrovatskii (1964) integrated over a power law for electrons and an isotropic black body spectrum for photons. Let's integrate here the kernel found in the previous section over an isotropic source of soft radiation. The isotropic kernel is given by performing the following integrals

$$\frac{dN_{iso}}{dt d\epsilon_1} = \frac{1}{4\pi} \int_0^{2\pi} \int_0^\pi \frac{dN}{dt d\epsilon_1} \sin \theta_0 d\theta_0 d\phi_0 = \frac{1}{2} \int_{-1}^{+1} \frac{dN}{dt d\epsilon_1} d\mu_0. \quad (24.125)$$

Changing the covered solid angle $\pi (R_*/R)^2$ (star) by 4π (isotropic source) and writing $h = 2\pi\hbar$, the kernel is

$$\frac{dN_{iso}}{dt d\epsilon_1} = \frac{\pi r_e^2 c K_e}{8\pi^3 \hbar^3 c^3} 4\pi \frac{2^{\frac{p+5}{2}} (p^2 + 4p + 11) \Gamma\left(\frac{p+5}{2}\right) \zeta\left(\frac{p+5}{2}\right)}{(p+1)(p+3)(p+5)} (kT_*)^{\frac{p+5}{2}} \epsilon_1^{-\left(\frac{p+1}{2}\right)} \times I', \quad (24.126)$$

where

$$I' = \frac{1}{2} \int_{-1}^{+1} (1 - \mu_0)^{\frac{p+1}{2}} d\mu_0 = \frac{2^{\frac{p+3}{2}}}{p+3}. \quad (24.127)$$

Hence, the isotropic inverse Compton kernel for an isotropic gas of soft radiation is

$$\frac{dN_{iso}}{dt d\epsilon_1} = \frac{r_e^2}{\pi \hbar^3 c^2} K_e \frac{2^{p+3} (p^2 + 4p + 11) \Gamma\left(\frac{p+5}{2}\right) \zeta\left(\frac{p+5}{2}\right)}{(p+3)^2 (p+1)(p+5)} (kT_*)^{\frac{p+5}{2}} \epsilon_1^{-\left(\frac{p+1}{2}\right)}. \quad (24.128)$$

This final solution coincides with the isotropic solution given in Blumenthal & Gould (1970), Eq. (2.65).

5. Anisotropic inverse Compton scattering in the general case

In this part we follow the same method as exposed in Sect. 4 in the general case, including the Klein-Nishina effects that appear at very-high energy ($\epsilon'_0 \gg m_e c^2$). I first derive an analytical formula for the anisotropic kernel following the same step as in the Thomson limit. Then, I compare this solution with the known Jones' kernel in the isotropic case. At the end of this section, I investigate the angular dependence of the emitted spectrum by electrons with a power law energy distribution propagating in an anisotropic black body photon gas.

§ 25. General anisotropic kernel

The anisotropic kernel is obtained by injecting Eq. (17.91) and the full differential cross section (Eq. 16.81) in Eq. (18.94) so that we have

$$\frac{dN}{dt d\epsilon_1 d\Omega_1} = \frac{r_e^2 c (1 - \beta_e \mu_0)}{2\gamma_e (1 - \beta_e \mu_1)} \iiint \left(\frac{\epsilon'_1}{\epsilon'} \right)^2 \left(\frac{\epsilon'_1}{\epsilon'} + \frac{\epsilon'}{\epsilon'_1} - \sin^2 \Theta' \right) \times \\ \delta \left(\epsilon'_1 - \frac{\epsilon'}{1 + \frac{\epsilon'}{m_e c^2} (1 - \cos \Theta')} \right) \delta(\epsilon' - \epsilon'_0) \delta(\mu' - \mu'_0) \delta(\phi' - \phi'_0) d\epsilon' d\mu' d\phi'. \quad (25.129)$$

If we write (using Eq. 17.90)

$$\delta \left(\epsilon'_1 - \frac{\epsilon'}{1 + \frac{\epsilon'}{m_e c^2} (1 - \cos \Theta')} \right) = \frac{1}{\left[1 - \frac{\epsilon'_1}{m_e c^2} (1 - \cos \Theta') \right]^2} \delta \left(\epsilon' - \frac{\epsilon'_1}{1 - \frac{\epsilon'_1}{m_e c^2} (1 - \cos \Theta')} \right), \quad (25.130)$$

we obtain

$$\frac{dN}{dt d\epsilon_1 d\Omega_1} = \frac{r_e^2 c (1 - \beta_e \mu_0)}{2\gamma_e (1 - \beta_e \mu_1)} \left[1 + \cos^2 \Theta'_0 + \left(\frac{\epsilon'_1}{m_e c^2} \right)^2 \frac{(1 - \cos \Theta'_0)^2}{1 - \frac{\epsilon'_1}{m_e c^2} (1 - \cos \Theta'_0)} \right] \\ \times \delta \left(\frac{\epsilon'_1}{1 - \frac{\epsilon'_1}{m_e c^2} (1 - \cos \Theta'_0)} - \epsilon'_0 \right), \quad (25.131)$$

where $\cos \Theta'_0 = \mu'_0 \mu'_1 + \sin \theta'_0 \sin \theta'_1 \cos(\phi'_1 - \phi'_0)$. The last integration over Ω_1 can be simplified if $\gamma_e \gg 1$ since

$$\cos \Theta'_0 = \frac{\mu_0 - \beta_e}{1 - \beta_e \mu_0} \frac{\mu_1 - \beta_e}{1 - \beta_e \mu_1} + \frac{1}{\gamma_e^2} \frac{\sin \theta_1}{1 - \beta \mu_1} \frac{\sin \theta_0}{1 - \beta \mu_0} \cos(\phi'_1 - \phi'_0) \approx \mu'_0 \mu'_1. \quad (25.132)$$

The last Dirac distribution can be rewritten as

$$\delta \left(\frac{\epsilon'_1}{1 - \frac{\epsilon'_1}{m_e c^2} (1 - \cos \Theta'_0)} - \epsilon'_0 \right) = \frac{\left[1 - \frac{\gamma_e \epsilon_1}{m_e c^2} (1 + \beta_e \mu'_0 - (\beta_e + \mu'_0) \mu_1) \right]^2}{\left| \beta_e \gamma_e \epsilon_1 + \frac{\epsilon_1^2}{m_e c^2} \mu'_0 \right|} \delta(\mu_1 - x) \\ = K \delta(\mu_1 - x), \quad (25.133)$$

with

$$x = \frac{1 - \frac{\epsilon_0}{\epsilon_1} (1 - \beta_e \mu_0) + \frac{\epsilon_0}{\gamma_e m_e c^2}}{\beta_e + \frac{\epsilon_0}{\gamma_e m_e c^2} \mu_0}. \quad (25.134)$$

The last integration over Ω_1 is now easy to perform. Because of the approximation $\gamma_e \gg 1$, the expression does not depend on ϕ_1 anymore. The integration over μ_1 is straightforward and μ_1 is changed into x . The general expression for the anisotropic inverse Compton scattering is

$$\left. \frac{dN}{dt d\epsilon_1} = \frac{\pi r_e^2 c (1 - \beta_e \mu_0)}{\gamma_e (1 - \beta_e x)} K \left[1 + \left(\frac{x - \beta_e}{1 - \beta_e x} \right)^2 \mu_0^2 + \left(\frac{\gamma_e \epsilon_1}{m_e c^2} \right)^2 \frac{[1 + \beta_e \mu_0' - (\beta_e + \mu_0') x]^2}{1 - \frac{\gamma_e \epsilon_1}{m_e c^2} [1 + \beta_e \mu_0' - (\beta_e + \mu_0') x]} \right] \right| \quad (25.135)$$

The emitted spectrum in the observer frame is limited in energy by the relativistic kinematics. Using Eqs. (16.78)-(16.80) we have $\epsilon_- \leq \epsilon_1 \leq \epsilon_+$ with

$$\epsilon_{\pm} = \frac{(1 - \beta_e \mu_0) \epsilon_0}{1 + \frac{\epsilon_0}{\gamma_e m_e c^2} \mp \left[\beta_e^2 + 2\beta_e \mu_0 \left(\frac{\epsilon_0}{\gamma_e m_e c^2} \right) + \left(\frac{\epsilon_0}{\gamma_e m_e c^2} \right)^2 \right]^{1/2}}. \quad (25.136)$$

In the Klein-Nishina regime, the scattered photon can carry away almost all the energy of the electron $\epsilon_+ \approx \gamma_e m_e c^2$. Also, this maximum energy becomes almost independent of the angle θ_0 (see next section, Fig. 21).

§ 26. Integration over a power law for electrons and a black body for soft photons

Contrary to what I have done in the Thomson limit, it is not easy to obtain analytical formula in the general case even for energy distribution as simple as power laws or black body. Instead, I provide here numerically integrated solutions in the case where electrons are injected with a power law energy distribution and soft radiation with a black body spectrum as in § 22 - § 23. We would like also to focus on the angular dependence of the emitted spectrum in the deep Klein-Nishina regime. The full anisotropic inverse Compton spectrum is obtained with

$$\frac{dN}{dt d\epsilon_1} = \iint \frac{dN_e}{d\gamma_e} \frac{dn_{*}}{d\epsilon_0} \frac{dN}{dt d\epsilon_1} d\gamma_e d\epsilon_0, \quad (26.137)$$

where $dN_e/d\gamma_e$ and $dn_{*}/d\epsilon_0$ are given by Eqs. (22.115), (23.120). This equation is numerically solved and some spectra are shown for different angles of interaction in Fig. 21. The same features as presented and discussed in § 23 appear in the general case as well but new effect appear in the Klein-Nishina regime. Indeed, at very high-energy the spectrum becomes much softer due to the decline of the total cross section (see Fig. 4). The angular dependence on the emitted spectrum is weaker in the Klein-Nishina regime than in the Thomson limit. Also, the maximum energy of the scattered photon reach almost $\epsilon_1 \approx \gamma_e m_e c^2$ and does not depend on the angle. It is interesting to note that the Klein-Nishina energy cut-off has an angular dependence since the condition $\epsilon_0'/m_e c^2 = \gamma_e \epsilon_0 (1 - \beta_e \cos \theta_0) / m_e c^2$ depends on θ_0 . The spectrum remains Thomson-like at higher energy for small angles. For the same injection of particles, the emitted spectrum can have a different amplitude but also a different spectral index depending on the angle at a given energy in the Klein-Nishina domain.

§ 27. Final check: Comparison with Jones' isotropic solution

Jones (1968) found an analytical solution in the general case for an isotropic source of soft radiation. Jones' kernel is given by Eq. (5.4) (see Chapter 2). The Compton emission produced

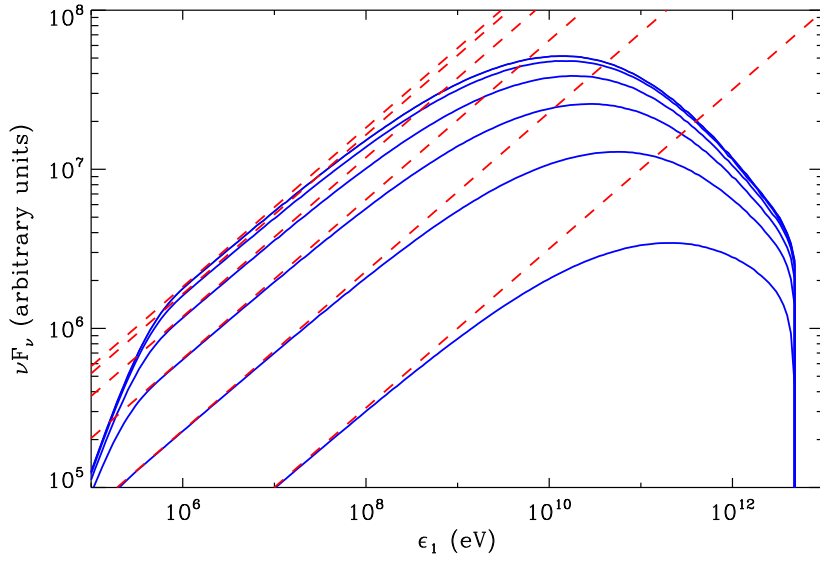


FIG. 21. The same as in Fig. 19, with $\gamma_- = 10^2$ and $\gamma_+ = 10^7$. $\theta_0 = 180^\circ$ (top), 120° , 90° , 60° , and 30° (bottom).

by electrons with a power law energy distribution bathed in a black-body, isotropic gas of soft radiation is

$$\frac{dN_{iso}}{dt d\epsilon_1} = \iint \frac{dN_e}{d\gamma_e} \frac{dn_\star}{d\epsilon_0} \frac{dN_{jones}}{dt d\epsilon_1} d\gamma_e d\epsilon_0. \quad (27.138)$$

We would like here to compare our solution in Eq. (25.135) with Jones kernel and see whether both solutions give compatible results. We perform the full inverse Compton calculation as in § 26 but averaged over the all the solid angle Ω_0 such as

$$\frac{dN_{iso}}{dt d\epsilon_1} = \frac{1}{4\pi} \iiint \frac{dN_e}{d\gamma_e} \frac{dn_\star}{d\epsilon_0} \frac{dN}{dt d\epsilon_1} d\gamma_e d\epsilon_0 d\Omega_0. \quad (27.139)$$

Both solutions gives the same result (Fig. 22).

6. What we have learned

I derived analytical expression for the anisotropic inverse Compton kernel both in the Thomson limit and in the general case. The kernel represents the spectrum emitted by one electron of energy $E_e = \gamma_e m_e c^2$ interacting with a mono-energetic beam of soft radiation. This distribution includes all the feature of inverse Compton scattering and is very useful to compute the emission from any given distribution of electrons and photons. Because of relativistic beaming effect, photons are scattered within a cone of semi-aperture angle $1/\gamma_e \ll 1$ *i.e.* almost in the direction of motion of the radiating electron.

In the Thomson limit, the energy of the soft radiation is multiplied at most by a factor $\approx 4\gamma_e^2$ for head-on collisions. The emitted spectrum has a strong angular dependence. The inverse Compton flux is maximum if electrons and photons collide head-on in the observer frame. I found new analytical formulae for the spectrum emitted by a population of electrons with a power law energy distribution and soft photons produced by a black body. All the results are compatible with known solutions in the isotropic case. The formula in Eq. (23.124) is particularly

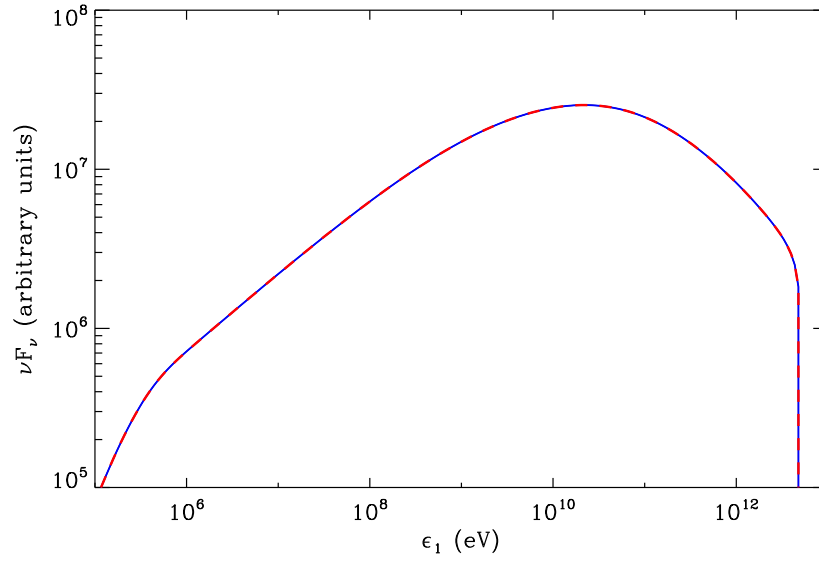


FIG. 22. The same as in Fig. 21 if the gas of target photons is isotropic. The Compton emission is computed with the isotropic kernel of Jones (1968) (blue solid line) and comparison with the anisotropic solution averaged over all the angles (red dashed line).

useful for the study of Doppler boosted inverse Compton emission in gamma-ray binaries and microquasars (see Chapters 9, 10 and 11). Even though this expression is not valid in the Klein-Nishina regime, it depicts the main feature of anisotropic inverse Compton scattering.

In the general case, the kernel has a complicated expression but I found an analytical formula provided that electrons are ultra-relativistic ($\gamma_e \gg 1$). In the Klein-Nishina regime, the electron can give almost all of its energy to the soft photon $\epsilon_1 \approx \gamma_e m_e c^2$, though the scattering rate decreases due to the decline of the cross section. Also, the angular dependence of the emitted spectrum is dampened in this regime. The numerically integrated solution over an isotropic gas of photons is compatible with Jones' solution.

These investigations have been partly published in Dubus *et al.* (2008) where we studied the gamma-ray modulation in LS 5039. This work is presented in the following chapter (Chapter 4).

7. [Français] Résumé du chapitre

§ 28. Contexte et objectifs

Ce chapitre est dédié à l'étude détaillée de la diffusion Compton inverse dans le cas où la source de photon est anisotrope. Je donne ici l'ensemble des équations qui permet d'aboutir au spectre des photons émis dans l'approximation de Thomson (Sect. 4) et dans le cas général (Sect. 5) où les effets Klein-Nishina sont pris en compte. Plus précisément, ce chapitre se concentre sur l'étude de la dépendance angulaire du spectre Compton inverse émis. Les résultats sont comparés avec les formules bien connues obtenues dans les cas où la source de photon est isotrope (voir *e.g.* Ginzburg & Syrovatskii 1964; Jones 1968; Blumenthal & Gould 1970; Rybicki & Lightman 1979). Le travail présenté ici repose en grande partie sur les études que j'ai mené au cours de mon Master 2. Je rajoute à cette précédente étude de nouvelles formules analytiques.

§ 29. Ce que nous avons appris

J'ai dérivé une expression analytique du noyau Compton inverse anisotrope dans l'approximation Thomson et dans le cas général. Le noyau donne le spectre Compton inverse émis par un électron d'énergie $E_e = \gamma_e m_e c^2$ interagissant avec un faisceau monochromatique de photons mous. Cette quantité contient toutes les caractéristiques physiques de la diffusion Compton inverse et se trouve être fort utile pour calculer l'émission en provenance d'une distribution quelconque d'électrons et de photons cibles. A cause des effets relativistes, les photons sont diffusés dans un cône avec un angle d'ouverture $1/\gamma_e \ll 1$, *i.e.* presque dans la direction du déplacement de l'électron diffuseur (avant l'interaction).

Dans l'approximation de Thomson, l'énergie du photon mou est amplifiée par un facteur $\approx 4\gamma_e^2$ dans le cas où la collision avec l'électron est frontale. Le spectre a une forte dépendance angulaire. Le flux Compton inverse est maximum si la collision entre l'électron et le photon est frontale dans le référentiel de l'observateur. J'ai trouvé de nouvelles formules analytiques pour une distribution des électrons en loi de puissance et pour une distribution de photons mous suivant une loi de corps noir. Tous mes résultats, intégrés sur une distribution isotrope de photons, concordent avec les solutions connues. La formule dans Eq. (23.124) est particulièrement utile pour l'étude de l'émission Compton inverse amplifiée par effet Doppler relativiste dans les binaires gamma et les microquasars (voir les Chapitres 9, 10 et 11). Même si cette expression n'est pas valide dans le regime Klein-Nishina, elle décrit tout de même bien les effets d'anisotropie de la diffusion Compton inverse.

Sous sa forme générale, le noyau a une expression compliquée. J'ai trouvé une expression analytique dans le cas où les électrons sont ultra relativistes ($\gamma_e \gg 1$). Dans le régime Klein-Nishina, l'électron peut transférer presque toute son énergie au photon mou $\epsilon_1 \approx \gamma_e m_e c^2$, bien que le taux de diffusion diminue en raison de la chute de la section efficace. Aussi, la dépendance angulaire du spectre émis est atténuée dans ce regime. La solution numériquement intégrée sur une distribution isotrope de photons est compatible avec la solution de Jones.

Ces recherches ont été en partie publiées dans Dubus *et al.* (2008) où nous avons étudié la modulation gamma dans LS 5039. Ce travail est présenté dans le chapitre suivant (Chapitre 4).

4

Gamma-ray modulation in gamma-ray binaries

Outline

1. What we want to know	56
2. The model	57
§ 28. The magnetic field	57
§ 29. The electron distribution	57
§ 30. Gamma-ray emission and pair production	59
3. Application to gamma-ray binaries	60
§ 31. LS 5039	60
§ 32. LS I +61 303 and PSR B1259-63	63
4. What we have learned	64
5. [Français] Résumé du chapitre	67
§ 33. Contexte et objectifs	67
§ 34. Ce que nous avons appris	68
6. The modulation of the gamma-ray emission from the binary LS 5039	69

GAMMA-RAY BINARIES exhibit a stable³ orbital modulation of their gamma-ray flux. In LS 5039, HESS observations (Aharonian *et al.* 2006) show that the TeV emission is minimum at superior conjunction (*i.e.* where the compact object is behind the massive star with respect to the observer) and maximum close to inferior conjunction (*i.e.* where the compact object lies between the massive star and the observer, see Fig. 23). *Fermi* observations of LS 5039 at GeV energies present also a stable orbital modulation anti-correlated with the TeV lightcurve, with a maximum at superior conjunction (Abdo *et al.* 2009b). The escaping gamma-ray emission appears to be related to the peculiar orientation of the system with respect to the observer.

³Note that orbit-to-orbit variability in LS I +61°303 has been observed at GeV energies by *Fermi* (Abdo *et al.* 2009a). In addition, recent TeV observations failed to redetect this system (Holder 2009). The gamma-ray emission in LS I +61°303 is not steady.

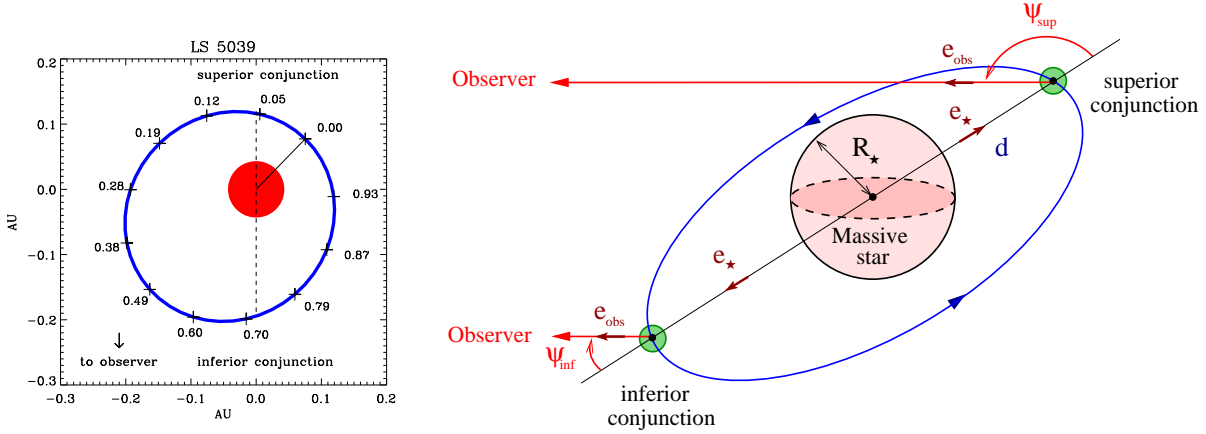


FIG. 23. *Left panel:* This diagram shows the orbit of the compact object (blue line) and the massive companion star (red disk) in LS 5039 (top view). The distant observer is at bottom (indicated by the arrow). The orbital parameters are taken from Casares *et al.* (2005b). The orbital phases ϕ are given by the numbers where $\phi \equiv 0$ at periastron. Superior conjunction corresponds to $\phi \approx 0.06$ and inferior conjunction to $\phi \approx 0.72$. *Right panel:* The angle ψ between the unit vector \mathbf{e}_* and \mathbf{e}_{obs} varies between $\psi_{\text{sup}} = \pi/2 + i$ at superior conjunction and $\psi_{\text{inf}} = \pi/2 - i$ at inferior conjunction, where i is the inclination of the orbit. The green disk indicates the position of the compact object in the orbit.

In gamma-ray binaries, a high-density of low energy photons are provided by the luminous companion star ($n_* \sim 10^{14} \text{ ph cm}^{-3}$ in LS 5039 at periastron). The inverse Compton cooling of a population of energetic electron-positron pairs injected at the compact object location produces gamma rays. In addition, because of the relative position of the observer with respect to the companion star and the pulsar, the emitted flux depends on the orbital phase due to anisotropic effects in the inverse Compton emission as shown in the previous chapter (see Chapter 3). Pair production is also important in gamma-ray binaries for gamma-ray photon of energy $\epsilon_1 \gtrsim m_e^2 c^4 / kT_* \approx 75 T_{*,4}^{-1} \text{ GeV}$ (see Chapter 2) and depends on the orbital phase as well (Dubus 2006a). Kirk *et al.* (1999) first combined the effects of both processes in the context of binaries and applied their model to PSR B1259 – 63. Inverse Compton emission and pair production are both maximum at orbital phases where the angle ψ between the massive star-pulsar direction and the pulsar-observer direction is maximum, *i.e.* at superior conjunction. On the contrary, these processes are minimum where ψ is minimum *i.e.* at inferior conjunction (see Fig. 23).

I briefly present below a simple model which combines anisotropic inverse Compton emission and pair production in gamma-ray binaries (Sect. 2), and focus on the system LS 5039 (Sect. 3). This model is a first attempt to explain the GeV and the TeV orbital modulation in gamma-ray binaries, in the framework of the pulsar wind nebula scenario. The model is also applied to LS I +61°303 and PSR B1259 – 63 (Sect. 3). This study partly relies on my investigations carried out during my Master 2 degree, and was published in Dubus *et al.* (2008) (Sect. 6).

1. What we want to know

- Can anisotropic inverse Compton and pair production explain the GeV and TeV orbital modulation in gamma-ray binaries?
- What are the constraints on the particle energy distribution?

2. The model

We propose here a prototype model for the high-energy emission in gamma-ray binaries, where non-thermal electron-positron pairs are injected by a young rotation-powered pulsar. This plasma of ultra-relativistic pairs models the shocked pulsar wind region where pairs are randomized at the termination shock between the pulsar wind and the massive star wind (see Chapter 1). I derive in this part, the different ingredients required to model the high-energy emission in binaries which are the magnetic field (§ 30), the particle energy distribution (§ 31) and the emission and absorption processes (§ 32).

§ 30. The magnetic field

Following the MHD model of Kennel & Coroniti (1984b), the magnetic field downstream the termination shock in the pulsar wind is

$$B = 3(1 - 4\sigma) \left(\frac{L_p}{cR_s^2} \frac{\sigma}{1 + \sigma} \right)^{1/2} \propto R_s^{-1}, \quad (30.140)$$

where σ is the magnetisation of the wind (ratio of the magnetic to kinetic energy), R_s is the distance from the pulsar to the termination shock, and L_p is the spin down power of the pulsar. This expression is valid only for kinetic energy dominated wind ($\sigma \ll 1$), *i.e.* most of the energy in the wind is carried by particles. R_s is the distance where the pulsar and the massive star wind momenta are balanced, *i.e.* if

$$\frac{L_p}{4\pi R_s^2 c} = \rho_w v_w^2, \quad (30.141)$$

where ρ_w is the density and v_w the velocity of the massive star wind (the orbital velocity of the pulsar is neglected with respect to the wind velocity). Then,

$$R_s = \frac{d}{1 + (\dot{M} v_w c / L_p)^{1/2}}, \quad (30.142)$$

where \dot{M} is the mass loss rate of the massive star. We conclude that in this model, the magnetic field in the wind depends only on the orbital separation such as $B \propto d^{-1}$ (see Eq. 30.140).

§ 31. The electron distribution

Non-thermal electrons are assumed to be injected at a constant rate at the compact object location with a single power-law energy distribution. We assume for simplicity that the pairs radiate in a compact region of radius R_s close to the compact object much smaller than the orbital separation d , before the particles escape the cooling zone. This assumption is correct if the Compton cooling timescale t_{ic} remains much smaller than the escaping timescale $t_{esc} = d/c$. Using Eq. (9.41) (see Chapter 2), we have

$$t_{ic} = t_{esc} \quad (31.143)$$

$$\gamma_- = 6 \times 10^2 d_{0.1} T_{*,4}^{-4} R_{*,10}^{-2}. \quad (31.144)$$

This condition gives a lower limit for the energy for the electron $E_- = \gamma_- m_e c^2$. The maximum energy reached by the electrons $E_+ = \gamma_+ m_e c^2$ depends on the acceleration timescale t_{acc} in the

system. This timescale is unlikely to be shorter than

$$\begin{aligned} t_{acc} &\approx \frac{R_L}{c} = \frac{\gamma_e m_e c}{eB} \\ t_{acc} &\approx 0.06 \gamma_6 B_1^{-1} \text{ s}, \end{aligned} \quad (31.145)$$

where $R_L = \gamma_e m_e c^2 / eB$ is the Larmor radius of an electron and B the magnetic field in the zone considered (see above). If the particles lose energy more rapidly than they are accelerated, then the condition $t_{acc} = t_{cool}$ yields the upper-limit for the electron distribution γ_+ . Comparing the acceleration timescale with the synchrotron timescale $t_{syn} = t_{acc}$ (the dominant cooling timescale at very-high energy, see Fig. 11) gives (using Eq. 7.28)

$$\begin{aligned} \gamma_+ &= \left(\frac{9m_e^2 c^4}{4e^3 B} \right)^{1/2} \\ \gamma_+ &\approx 10^8 B_1^{-1/2}. \end{aligned} \quad (31.146)$$

The injected particle energy distribution is then

$$\frac{dn_{inj}}{dtd\gamma_e} = K_e \gamma_e^{-p} \exp\left(-\frac{\gamma}{\gamma_+}\right), \quad (31.147)$$

where K_e is a normalisation constant, p is the spectral index and $\gamma_e \geq \gamma_-$. Taking into account synchrotron and inverse Compton cooling for an isotropic distribution of electrons, the steady-state cooled electron distribution in the system is (see Eq. 13.69)

$$\boxed{\frac{dn_e}{d\gamma_e} = \frac{1}{|\dot{\gamma}_e|} \int_{\gamma_e}^{+\infty} \frac{dn_{inj}}{dtd\gamma_0} d\gamma_0}, \quad (31.148)$$

where $\dot{\gamma}_e = \dot{\gamma}_{syn} + \dot{\gamma}_{ic}$, is the total energy losses per electron *via* synchrotron radiation and inverse Compton scattering. Fig. 24 gives the cooled electron energy distribution for a system like LS 5039 for different magnetic field intensity. In the Thomson regime, the cooled electron distribution is $\propto \gamma_e^{-(p+1)}$ according to Eq. (14.71). Klein-Nishina effects are significant as soon as $\gamma_e \epsilon_0 / m_e c^2 \gtrsim 1$, then the Compton losses decline and the cooled particle distribution becomes harder (if $p = 2$, $\propto \gamma_e^{-1.3}$, see Fig. 24). Then, when $t_{syn} \lesssim t_{ic}$ synchrotron losses dominate and the cooled electron distribution is $\propto \gamma_e^{-(p+1)}$ as in the Thomson limit, according to Eq. (14.71). Note that this steady-state electron distribution is a very good approximation as long as $\gamma_e \gtrsim 10^3$. Hence, this model is appropriate to describe the high-energy radiation in gamma-ray binaries. At lower energies, a more detailed model taking into account the advection of pairs in the system would have to be considered as in Dubus (2006b).

We have three free parameters in the model to adjust the particle distribution:

- The magnetic field at the shock B : this parameter sets the maximum energy reached by pairs.
- The slope p .
- The total power injected into pairs L_p by the pulsar.

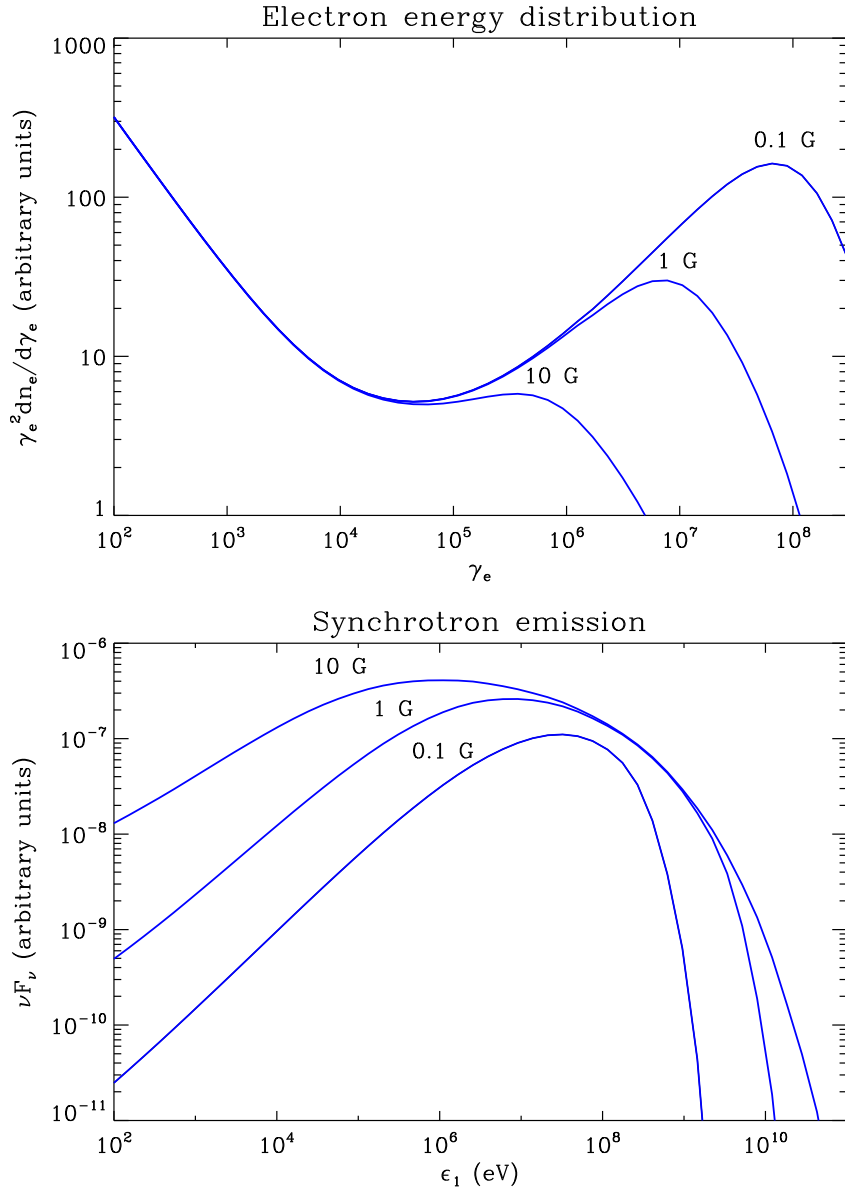


FIG. 24. *Top panel:* Steady-state cooled electron energy distribution for $B = 0.1$ (top), 1 and 10 G (bottom). The compact object injects electrons with a constant -2 power law energy distribution. The massive star produces stellar photons with an energy $\epsilon_0 \approx 10$ eV. The orbital separation is $d \approx 0.1$ AU. *Bottom panel:* Resulting synchrotron spectrum emitted by the cooled distribution of electrons given in the *Top* panel.

§ 32. Gamma-ray emission and pair production

Following the procedure described in Chapter 3, the anisotropic inverse Compton emission is given by (see Eq. 26.137)

$$\boxed{\frac{dN_{ic}}{dt d\epsilon_1} = \iiint \frac{dn_e}{d\gamma_e} \frac{dn_\star}{d\epsilon_0 d\Omega_0} \frac{dN}{dt d\epsilon_1} d\gamma_e d\epsilon_0 d\Omega_0}, \quad (32.149)$$

where $dn_*/d\epsilon_0 d\Omega_0$ is the stellar photon density, and $dN/dt d\epsilon_1$ is the anisotropic Compton kernel (see Eq. 25.135). For a black body spectrum we have

$$\frac{dn_*}{d\epsilon_0 d\Omega_0} = \frac{2}{h^3 c^3} \frac{\epsilon_0^2}{\exp\left(\frac{\epsilon_0}{kT_*}\right) - 1}. \quad (32.150)$$

For a point-like star, the angle between the electron and the stellar photon θ_0 coincides with the viewing angle ψ (see Fig. 23). If \mathbf{e}_* is the unit vector in the star-pulsar direction and if \mathbf{e}_{obs} is in the pulsar-observer direction, we have $\cos \psi = \mathbf{e}_* \cdot \mathbf{e}_{\text{obs}}$.

Synchrotron radiation is calculated as follows

$$\boxed{\frac{dN_{\text{syn}}}{dt d\epsilon_1} = \int_{\gamma_e} \frac{dn_e}{d\gamma_e} \frac{dN'}{dt d\epsilon_1} d\gamma_e}, \quad (32.151)$$

where $dN'/dt d\epsilon_1$ is the synchrotron kernel (see Chapter 2, Eq. 7.22). For illustrative purpose, the synchrotron spectrum emitted by the cooled pairs is shown in Fig. 24 (*bottom panel*) for various magnetic field. Assuming that the gamma-ray source of photon is point-like and localized at the pulsar location ($R_s \ll d$), the absorbed gamma-ray spectrum is

$$\frac{dN_{\text{abs}}}{dt d\epsilon_1} = \frac{dN}{dt d\epsilon_1} e^{-\tau_{\gamma\gamma}}, \quad (32.152)$$

where $\tau_{\gamma\gamma}$ is the gamma-ray opacity integrated along the line of sight from the source to the observer (see Chapter 2, Eq. 11.60). We possess now all the elements to compute the high-energy emission in gamma-ray binaries.

3. Application to gamma-ray binaries

§ 33. LS 5039

This model was originally developed to explain the TeV orbital modulation in LS 5039 observed by HESS (Aharonian *et al.* 2006). Fig. 25 shows the expected Compton emission spectrum and the effect of gamma-ray absorption in LS 5039 for different orbital phases, using Eq. (32.149). Electrons are injected with $p = 2$ power law distribution with $B = 1 d_{0.1}^{-1}$ G at the pulsar location (at periastron) for an inclination of the orbit $i = 60^\circ$, so that the viewing angle ψ varies between $\pi/2 - i = 30^\circ$ at inferior conjunction and $\pi/2 + i = 150^\circ$ at superior conjunction. Close to superior conjunction, the Compton flux is high with a photon index of about -2 . In addition, pair production is also maximum and absorbs almost entirely the gamma-ray emission between 100 GeV and 1 TeV. Close to inferior conjunction, the Compton flux is smaller but harder because the scattering remains in the Thomson regime at higher energies since the condition $\gamma_e \epsilon_0 (1 - \beta_e \cos \psi) / m_e c^2$ depends on the viewing angle ψ as noted in Chapter 3 (see § 26). Even though the Compton emission is minimum at this phase, the gamma-ray flux is almost unaffected by gamma-ray absorption, minimum at this phase as well, and more flux than at superior conjunction escapes.

Fig. 26 (*top panel*) gives the modulation of gamma-ray emission and absorption in LS 5039, above 100 GeV. The combination of both components leads to the theoretical TeV lightcurve (Fig. 26, *bottom panel* red line). Absorption erases the Compton emission peak at superior conjunction ($\phi \approx 0.06$), and the interplay between both processes gives rise to a peak at the non

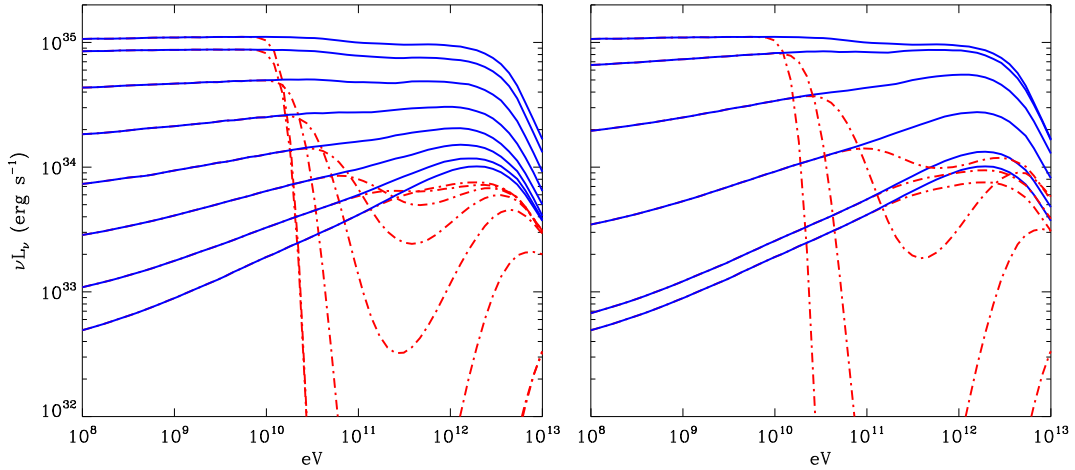


FIG. 25. Anisotropic inverse Compton spectrum (blue solid lines) and the effect of the gamma-ray absorption (red dashed line) in LS 5039 at the orbital phases ϕ (*left panel from top to bottom*): $\phi = 0.03, 0.09, 0.15, 0.24, 0.34, 0.44, 0.56, 0.66$, (*right panel from bottom to top*): $0.66, 0.76, 0.85, 0.91, 0.97$, and 0.03 . $\phi = 0$ at periastron, $\phi \approx 0.06$ at superior conjunction and $\phi \approx 0.72$ at inferior conjunction. Electrons are constantly injected with a power law energy distribution with $p = 2$ and $B = 1$ G at the pulsar position for an inclination $i = 60^\circ$.

trivial phase $\phi \approx 0.85$, precisely where HESS lightcurve is maximum. This peak is a key feature of this model and is very robust against changes in the magnetic field B or the index of the particle distribution p . The very-high energy lightcurve integrated above 100 GeV gamma-ray photons is a very good fit to HESS observation except close to superior conjunction ($0.0 < \phi < 0.2$) where the model underestimates the flux due to the high gamma-ray opacity. Pairs produced by gamma-ray absorption could reprocess a fraction of the absorbed energy and initiate a cascade of pairs in the system. We will come back to this important issue in Chapter 7 and 8. In the GeV energy band, the flux is not affected by the gamma-ray absorption and the gamma-ray modulation follows the anisotropic inverse Compton emission lightcurve. This model correctly reproduces the GeV lightcurve observed by *Fermi* (Abdo *et al.* 2009b), but the spectral shape cannot be reproduced as explained below.

The compact object in LS 5039 could be a black hole if the inclination of the system is $i \lesssim 30^\circ$. Taking $i = 20^\circ$, the angle ψ varies from 70° to 110° . Hence, the amplitude of the Compton modulation decreases. Fig. 27 presents the gamma-ray modulation expected in this case, using the same electron distribution as for the neutron star case localized at the compact object position. The GeV lightcurve shape is unchanged compared with the pulsar case and the amplitude of the modulation is smaller. However, the TeV lightcurve is substantially changed. The lightcurve presents one broad peak around $0.4 \lesssim \phi \lesssim 0.8$, with a maximum shifted to $\phi \approx 0.75$. The fit to HESS observations is less good. Low inclinations are not favored in this model.

This study might not be appropriate in the case of a black hole. The high-energy emission may not occur at the compact object location but further away, *e.g.* in a relativistic jet. However, the origin of the gamma-ray modulation and in particular the GeV-TeV anticorrelation appears unclear in this case. Indeed, if the gamma-ray emitter is too far from the compact object and the star (*i.e.* at distances $\gtrsim d$), gamma-ray absorption would be insufficient to anticorrelate the

TeV with the GeV flux (Dubus 2006a). Particles should be accelerated close to the compact object location in LS 5039. I investigate more quantitatively this possibility in Chapter 8.

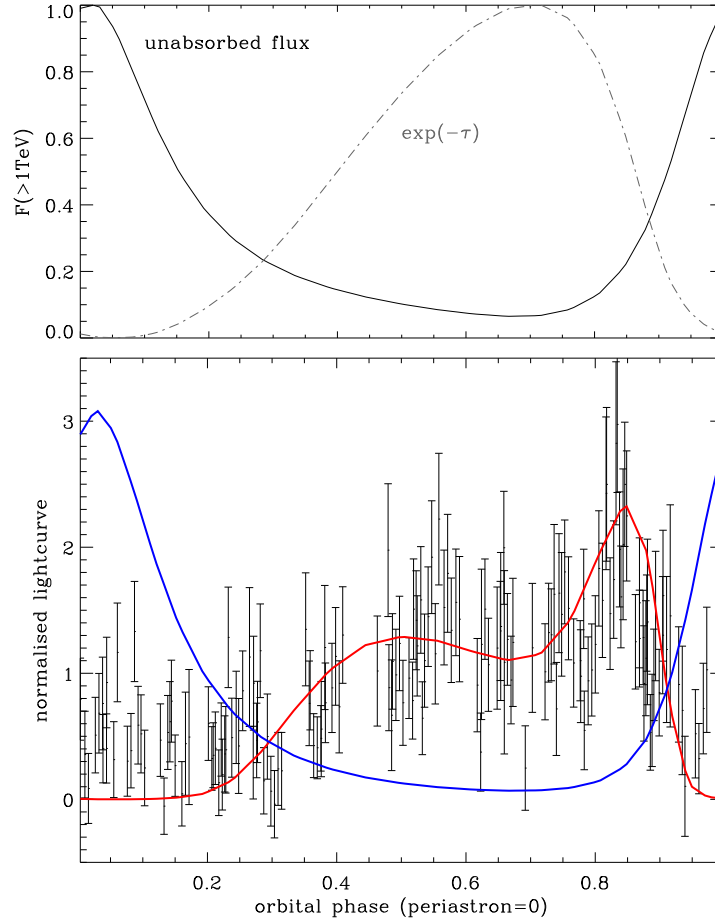


FIG. 26. *Top panel:* Theoretical anisotropic inverse Compton emission ("unabsorbed flux", black solid line) and pair production (" $\exp(-\tau)$ ", dashed grey line) above 100 GeV as a function of the orbital phase in LS 5039. Orbital parameters are taken from Casares *et al.* (2005b). *Bottom panel:* Gamma-ray light curves expected in the HESS energy band (red solid line, > 100 GeV) and in the *Fermi* energy band (blue solid line, > 1 GeV). HESS data points are shown for comparison and are taken from Aharonian *et al.* (2006).

Fig. 28 shows the gamma-ray spectra averaged over the orbit in LS 5039, corresponding to the modulation given in Fig. 26. Spectra are also averaged over two spectral states "SUPC" and "INFC" as defined in Aharonian *et al.* (2006). SUPC state is the averaged emission in the phase range $\phi \leq 0.45$ and $\phi > 0.9$ and INFC state is averaged over the phases $0.45 < \phi \leq 0.9$. In the INFC state, HESS observations shows an energy cut-off at about $\epsilon_1 \approx 10$ TeV. Reproducing the hard spectrum at INFC and the energy cut-off constraints tightly the injected slope to $p = 2 \pm 0.3$ and the magnetic field in the emitting region to $B = 0.8 \pm 0.2 d_{0.1}^{-1}$ G. Assuming that the system is at a distance 2.5 kpc from Earth, the measured gamma-ray luminosity constrains also the total power injected into pairs to 10^{36} erg s^{-1} . This is consistent with the spin-down power found in young pulsars, as for instance in PSR B1259 – 63 (Manchester *et al.* 1995). The SUPC state

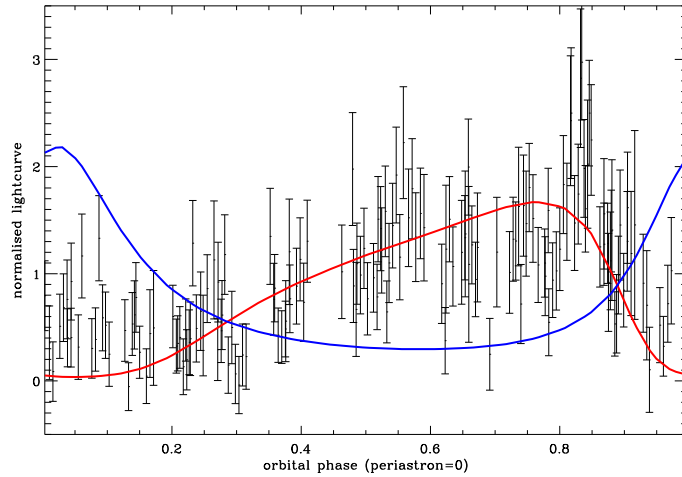


FIG. 27. The same as in Fig. 26 (*bottom panel*) if the compact object is a black hole ($i = 20^\circ$).

is not reproduced correctly by the model. In the GeV energy band, the model underestimates the gamma-ray flux by about a factor 3. In addition, the energy cut-off observed by *Fermi* at a few GeV is inconsistent with the energy cut-off expected due to pair production in the model. It appears clear today that another population of particles is required to explain the GeV excess (see the discussion in Chapter 5). Note that synchrotron radiation dominates over Compton emission below 100 MeV, hence it does not contribute significantly to the GeV modulation.

Note that other studies (see *e.g.* Bednarek 2007; Khangulyan *et al.* 2008; Sierpowska-Bartosik & Torres 2008), using also a combination of anisotropic inverse Compton and pair production, have shown similar patterns in the GeV and TeV lightcurves in LS 5039.

§ 34. LS I +61 303 and PSR B1259-63

LS I +61°303 and PSR B1259 – 63 present also an orbital modulated TeV emission (Aharonian *et al.* 2005b, 2009; Albert *et al.* 2009) (see Fig. 29).

Fig. 30 shows the expected gamma-ray modulation in LS I +61°303 and PSR B1259 – 63, combining the effect of pair production and anisotropic Compton emission. In both systems, the gamma-ray absorption does not play a significant role on the modulation and the GeV or TeV light curve are very similar. In LS I +61°303, the gamma-ray emission is maximum just after superior conjunction ($\phi \approx 0.25$, $\phi = 0.275$ at periastron Aragona *et al.* 2009) where both the seed photon density and the viewing angle are high. The peak is followed by a steep decline and a minimum at inferior conjunction ($\phi \approx 0.31$) (see Fig. 30). This result is inconsistent with *Fermi*, MAGIC and VERITAS observations (Abdo *et al.* 2009a; Albert *et al.* 2006; Acciari *et al.* 2008) where gamma rays are mainly produced between around $\phi \approx 0.4$ at GeV, and around 0.6 (*i.e.* close to apastron) at TeV (Fig. 29). In PSR B1259 – 63, the gamma-ray emission modulation is dominated by the distance of the pulsar to the massive star as the orbit is very eccentric. HESS detects this system at the periastron passage where the seed photon density for inverse Compton emission is high. The model reproduces only qualitatively the gamma-ray orbital modulation but cannot reproduce the detailed light curve (Fig. 30).

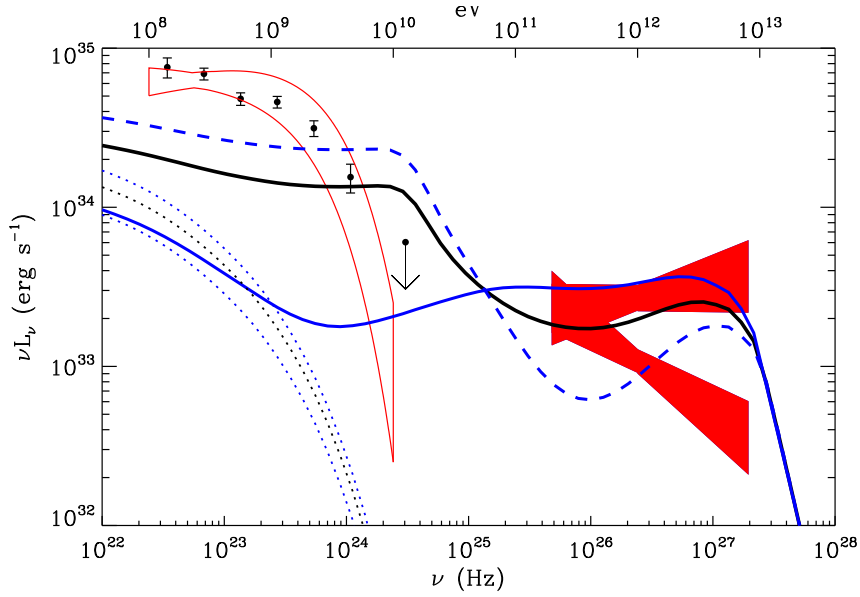


FIG. 28. Theoretical gamma-ray spectra averaged along the full orbit (black solid line), over SUPC ($\phi \leq 0.45$ and $\phi > 0.9$, blue dashed line) and over INFC state ($0.45 < \phi \leq 0.9$, blue solid line). The contribution of synchrotron radiation alone is shown as well in dotted line (black: full orbit, *top* blue: SUPC and *bottom* blue: INFC). HESS (filled red bowties) and *Fermi* (red empty bowtie and black data points) observations are overplotted for comparison. Parameters: $i = 60^\circ$, $p = 2$, $B = 0.8 d_{0.1}^{-1}$ G and $L_p = 10^{36}$ erg s⁻¹.

In both systems, the origin of the gamma-ray orbital modulation is not clear and cannot be interpreted with the simple model as shown here. Peaks and dips do not coincide with conjunctions. The orbit of the compact object in these systems is more eccentric and evolve in a more complex stellar wind environment than in LS 5039. The physical conditions at the collision site between the pulsar wind and the Be stellar wind are poorly understood and might change significantly along the orbit. Clearly, a more complex model would be required to explain in details the observed gamma-ray modulation. Note that some models have been proposed to explain the spectral and temporal features of these system (see *e.g.* Kirk *et al.* 1999; Khangulyan *et al.* 2007; Sierpowska-Bartosik & Bednarek 2008; Takata & Taam 2009; Sierpowska-Bartosik & Torres 2009; Zdziarski *et al.* 2010).

The puzzling phasing of the maximum TeV emission in LS I +61°303 (Fig. 29) might be due to relativistic Doppler-boosting effects in the pulsar wind outflow. I will come back to this issue in Chapter 10 where a full model is presented and applied to gamma-ray binaries.

4. What we have learned

I presented a simple model for the gamma-ray modulation in gamma-ray binaries, in which anisotropic inverse Compton emission and pair production are combined. Electrons are injected at a constant rate at the vicinity of the compact object, assumed here to be a young pulsar, and radiate inverse Compton and synchrotron radiation. A steady-state electron distribution is formed after Compton and synchrotron cooling, provided that pairs have enough time to radiate before escaping the system. In LS 5039, this is a very good approximation for high-

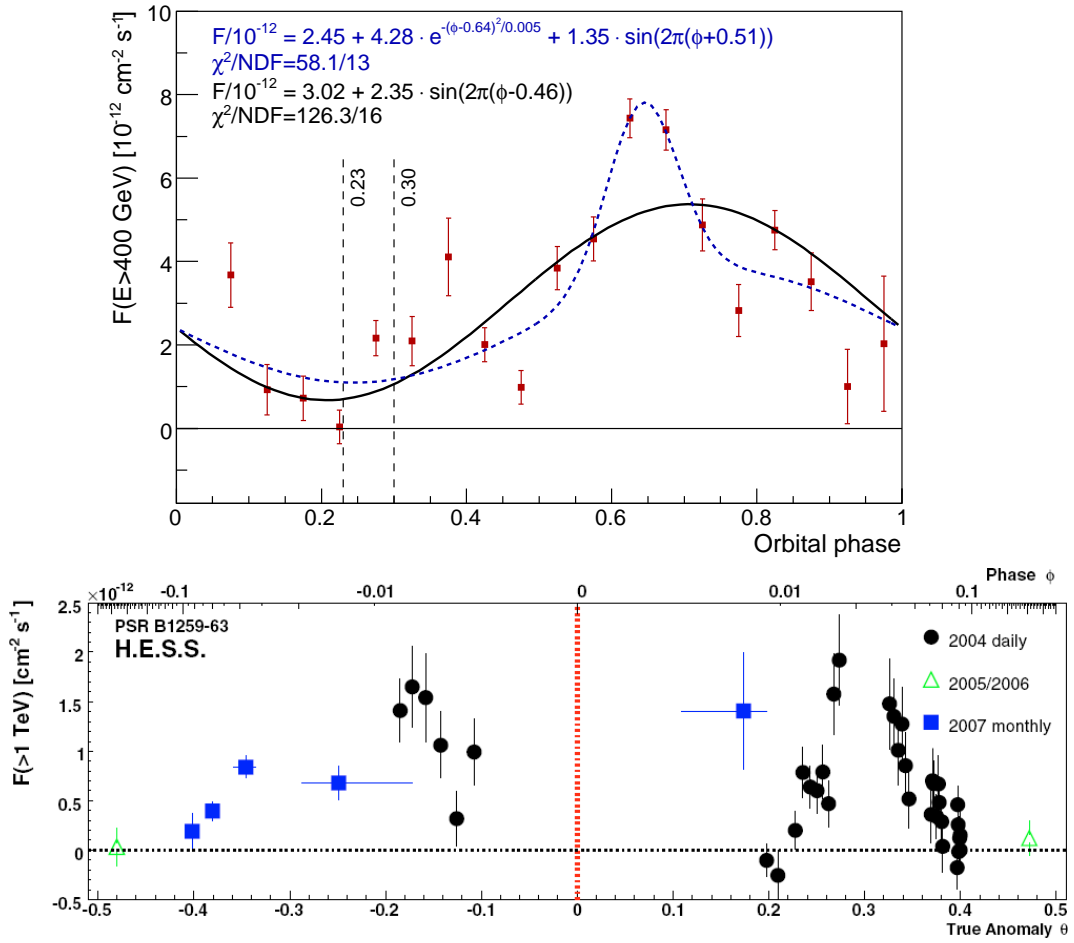


FIG. 29. Very-high energy lightcurve observed in LS I +61°303 (*top panel*) and PSR B1259 – 63 (*bottom panel*). Extracted from Albert *et al.* (2009) and Aharonian *et al.* (2009).

energy electrons $\gamma_e \gtrsim 10^3$. This approach is appropriate only for the modeling of the high-energy emission.

In this model, the electron distribution is defined by three free parameters: the index of the power-law p , the maximum energy reached by the electrons which is related to the magnetic field B in the cooling zone, and the total power injected by the pulsar into energetic pairs L_p . Then, the resulting gamma-ray emission and modulation depends only on the geometry of the system.

In LS 5039, the subtle interplay between pair production and anisotropic Compton emission explains well the TeV lightcurve observed by HESS, except close to superior conjunction where pair cascade emission could be significant (see Chapter 7 and 8). Fitting the model with HESS INFC state constrains tightly the injected particle energy distribution. Electrons should be injected with a spectral index $p = 2 \pm 0.3$ with a total power $L_p = 10^{36} \text{ erg s}^{-1}$ consistent with the spin-down power found in young pulsars. The high-energy cut-off observed by HESS at $\approx 10 \text{ TeV}$ is reproduced if the magnetic field in the cooling zone is $B = 0.8 \pm 0.2 \text{ G}$ at periastron.

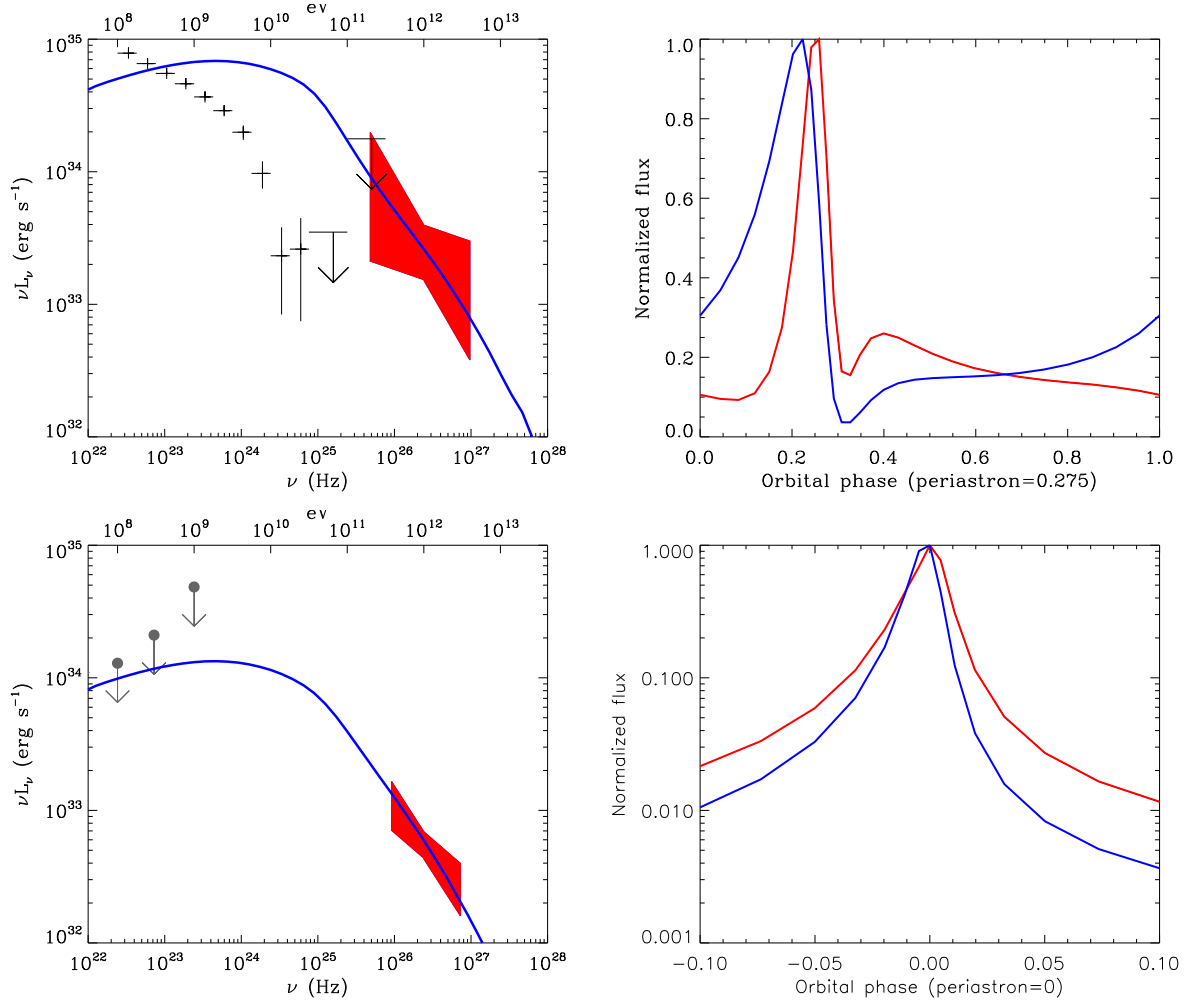


FIG. 30. Orbit-averaged spectra (blue line, *left panels*) and phase-resolved gamma-ray lightcurves (blue line > 1 GeV, red line > 100 GeV, *right panels*) in LS I +61°303 (*top panels*) and PSR B1259 - 63 (*bottom panels*). Electrons are injected with a power law of index $p = 2.5$ in both binaries. There is no magnetic field. *Fermi* (black crosses) and MAGIC observations (red bowtie) are shown for LS I +61°303, EGRET (grey arrows, upper limits) and HESS (red bowtie) measurements are also shown for PSR B1259 - 63. The orbital parameters are taken from Aragona *et al.* (2009) for LS I +61°303 and from Manchester *et al.* (1995) for PSR B1259 - 63.

The model cannot account for the GeV emission observed by *Fermi* (flux and spectrum). Low inclinations $i \lesssim 30^\circ$ are not favored.

The gamma-ray modulation in the other two gamma-ray binaries LS I +61°303 and PSR B1259 - 63 cannot be explained by the simple model presented here. The compact object evolves in a more complex environment than in LS 5039 (Be wind, highly eccentric orbit). Obviously, there are some missing ingredients for the modeling of the gamma-ray emission in these systems.

The results found with this model are the starting point of my other investigations in this thesis. The emission from the unshocked pulsar wind (Chapter 5), pair cascade emission (Chapter 7 and 8) and the study of the Doppler-boosted emission (Chapter 10) are extensions of this prototype model.

I exposed the main results of this work in a contributed talk at the "French Society of Astronomy and Astrophysics meeting 2007" (see the proceeding Cerutti *et al.* 2007). In addition, I had the opportunity to present this work in a contributed poster session at the "SLAC Summer Institute 2008: Cosmic accelerators". This work have been published in Dubus *et al.* (2008), given below. Also, I used this model to discuss the possible constraints on models that could allow hard X-ray observations in a contributed talk at the "Simbol-X Second International Symposium" in 2008 (see the proceeding Cerutti *et al.* 2009d).

5. [Français] Résumé du chapitre

§ 35. Contexte et objectifs

Les binaires gamma présentent une modulation orbitale stable⁴ de leur flux gamma. Dans LS 5039, les observations HESS (Aharonian *et al.* 2006) montrent que l'émission TeV est minimale à la conjonction supérieure (*i.e.* où l'objet compact est derrière l'étoile massive par rapport à l'observateur) et est maximale à proximité de la conjonction inférieure (*i.e.* où l'objet compact se situe entre l'étoile massive et l'observateur, voir Fig. 23). Les observations de LS 5039 par *Fermi* au GeV présentent aussi une modulation orbitale stable anticorrélée avec la courbe de lumière TeV, avec un maximum à la conjonction supérieure (Abdo *et al.* 2009b). L'émission gamma observée semble être reliée à l'orientation particulière du système par rapport à l'observateur.

Dans les binaires gamma, l'étoile massive génère une importante quantité de photons de basse énergie ($n_{\star} \sim 10^{14}$ ph cm⁻³ dans LS 5039 au périastre). Le refroidissement par diffusion Compton inverse d'une population de paires électron-positron relativistes injectée à la position de l'objet compact produit des rayons gamma. De plus, le flux émis dépend de la phase orbitale à cause des effets d'anisotropie dans le processus d'émission Compton inverse comme il a été démontré dans le chapitre précédent (voir Chapitre 3). La production de paires est aussi très importante dans les binaires gamma pour des photons gamma d'énergie $\epsilon_1 \gtrsim m_e^2 c^4 / kT_{\star} \approx 75 T_{\star,4}^{-1}$ GeV (voir Chapitre 2) et dépend également de la phase orbitale (Dubus 2006a). Kirk *et al.* (1999) ont été les premiers à combiner les effets des deux processus dans le contexte des binaires et ont appliqué leur modèle à PSR B1259 – 63. L'émission Compton inverse et la production de paires sont tous deux maximum à la phase orbitale où l'angle ψ entre la direction étoile massive-pulsar et la direction pulsar-observateur est maximum, *i.e.* à la conjonction supérieure. Au contraire, ces processus sont minimum lorsque ψ est minimum *i.e.* à la conjonction inférieure (voir Fig. 23).

Dans ce chapitre, je présente un modèle simple combinant l'émission Compton inverse anisotrope et la production de paires dans les binaires gamma (Sect. 2), et en particulier dans le système LS 5039 (Sect. 3). Ce modèle est un prototype pour expliquer la modulation orbitale GeV et TeV dans les binaires gamma, dans le cadre du scénario vent de pulsar. Ce modèle est aussi appliqué à LS I +61°303 et PSR B1259 – 63 (Sect. 3). Cette étude repose en partie sur les recherches menées au cours de mon stage de Master 2, et a été publiée dans Dubus *et al.* (2008) (Sect. 6).

⁴Notons qu'une variabilité orbite à orbite dans LS I +61°303 est clairement observée au GeV par *Fermi*. De plus, des observations récentes au TeV n'ont pas permises la redétection de ce système (Holder 2009). L'émission gamma dans LS I +61°303 n'est pas stationnaire.

§ 36. Ce que nous avons appris

J'ai présenté un modèle simple pour tenter d'expliquer la modulation gamma dans les binaires gamma. Dans ce modèle, des électrons sont injectés avec un taux constant à proximité de l'objet compact, supposé ici être un pulsar jeune, et rayonnent par diffusion Compton inverse et par synchrotron. Après refroidissement Compton et synchrotron, une distribution stationnaire d'électrons se forme à condition que les particules aient suffisamment de temps pour rayonner avant de s'échapper de la zone d'injection. Dans LS 5039, il s'agit d'une très bonne approximation pour des électrons de haute énergie $\gamma_e \gtrsim 10^3$. Cette approche est donc appropriée pour modéliser l'émission gamma de haute énergie.

Dans ce modèle, la distribution des électrons est complètement déterminée par trois paramètres libres que sont: l'indice de la loi de puissance p , l'énergie maximale atteinte par les électrons qui est reliée au champ magnétique dans la zone de refroidissement, et la puissance totale injectée par le pulsar dans les paires L_p . L'émission et la modulation gamma résultante ne dépendent alors plus que de la géométrie du système.

Dans LS 5039, la combinaison subtile entre la production de paires et l'émission Compton anisotrope permet d'expliquer correctement la courbe de lumière TeV observée par HESS, sauf autour de la conjonction supérieure où l'émission en provenance d'une cascade de paires pourrait être non négligeable (voir les Chapitres 7 et 8). L'ajustement du modèle au spectre INFC mesuré par HESS contraint fortement la distribution en énergie des particules injectées. Les électrons doivent être injectés avec un indice spectral $p = 2 \pm 0.3$ et une puissance totale $L_p = 10^{36}$ erg s⁻¹ cohérente avec les luminosités observées dans les pulsars jeunes. La coupure du spectre à haute énergie observée par HESS à ≈ 10 TeV est reproduite si le champ magnétique dans la zone de refroidissement est $B = 0.8 \pm 0.2$ G au périastre. Le modèle ne permet pas de rendre compte de l'émission au GeV observée par *Fermi* (flux et spectre). L'inclinaison de l'orbite ne doit pas être trop faible $i \lesssim 30^\circ$ ou la modulation n'est pas bien reproduite, favorisant ainsi la solution pulsar.

La modulation gamma dans les deux autres binaires gamma LSI +61°303 et PSR B1259 – 63 ne peut pas être expliquée simplement avec le modèle présenté ici. Dans ces systèmes, l'objet compact évolue dans un environnement bien plus complexe que dans LS 5039 (vent étoile Be, orbite très excentrique). Il apparaît clair que d'autres ingrédients manquent dans la modélisation de l'émission gamma dans ces systèmes.

Les résultats obtenus avec ce modèle constituent le point de départ des autres recherches que j'ai mené au cours de cette thèse. L'émission en provenance du vent non choqué de pulsar (Chapitre 5), l'émission d'une cascade (Chapitres 7 et 8) et l'étude de l'amplification Doppler de l'émission (Chapitre 10) sont des extensions de ce modèle prototype.

J'ai présenté les principaux résultats de ce travail lors d'une présentation orale à la réunion générale de la Société Française d'Astronomie et d'Astrophysique en 2007 (voir le compte rendu Cerutti *et al.* 2007). De plus, j'ai eu la chance de pouvoir promouvoir ces travaux lors d'une session poster à l'école d'été du SLAC en 2008 ("SLAC Summer Institute 2008: Cosmic accelerators"). Ces recherches ont été publiées dans Dubus *et al.* (2008), donné intégralement ci-dessous. Enfin, j'ai utilisé ce modèle pour discuter des éventuelles contraintes que pourrait apporter des observations en X durs dans une présentation orale au "Simbol-X Second International Symposium" en 2008 (voir le compte rendu Cerutti *et al.* 2009d).

6. Paper: The modulation of the gamma-ray emission from the binary LS 5039

The modulation of the gamma-ray emission from the binary LS 5039

Guillaume Dubus, Benoît Cerutti, and Gilles Henri

Laboratoire d'Astrophysique de Grenoble, UMR 5571 CNRS, Université Joseph Fourier, BP 53, 38041 Grenoble, France

Draft March 26, 2010

ABSTRACT

Context. Gamma-ray binaries have been established as a new class of sources of very high energy (VHE, >100 GeV) photons. These binaries are composed of a massive star and a compact object. The gamma-rays are probably produced by inverse Compton scattering of the stellar light by VHE electrons accelerated in the vicinity of the compact object. The VHE emission from LS 5039 displays an orbital modulation.

Aims. The inverse Compton spectrum depends on the angle between the incoming and outgoing photon in the rest frame of the electron. Since the angle at which an observer sees the star and electrons changes with the orbit, a phase dependence of the spectrum is expected.

Methods. A procedure to compute anisotropic inverse Compton emission is explained and applied to the case of LS 5039. The spectrum is calculated assuming the continuous injection of electrons close to the compact object: the shape of the steady-state distribution depends on the injected power-law and on the magnetic field intensity.

Results. Compared to the isotropic approximation, anisotropic scattering produces harder and fainter emission at inferior conjunction, crucially at a time when attenuation due to pair production of the VHE gamma-rays on star light is minimum. The computed lightcurve and spectra are very good fits to the HESS and EGRET observations, except at phases of maximum attenuation where pair cascade emission may be significant for HESS. Detailed predictions are made for a modulation in the GLAST energy range. The magnetic field intensity at periastron is 0.8 ± 0.2 G.

Conclusions. The anisotropy in inverse Compton scattering plays a major role in LS 5039. A simple model reproduces the observations, constraining the magnetic field intensity and injection spectrum. The comparison with observations, the derived magnetic field intensity, injection energy and slope suggest emission from a rotation-powered pulsar wind nebula. These results confirm gamma-ray binaries as promising sources to study the environment of pulsars on small scales.

Key words. radiation mechanisms: non-thermal — stars: individual (LS 5039) — gamma rays: theory — X-rays: binaries

1. Introduction

Gamma-ray binaries have been established in the past couple of years as a new class of sources of very high energy (VHE, >100 GeV) photons. They are characterized by a large gamma-ray luminosity above an MeV, at the level of or exceeding their X-ray luminosity. At present, all three such systems known (LS 5039, PSR B1259-63 and LSI +61°303, recently possibly joined by Cyg X-1) comprise a massive star (Aharonian et al. 2005a,b; Albert et al. 2006, 2007). The compact object in PSR B1259-63 is a 48-ms, young radio pulsar. The VHE emission arises from the interaction of the relativistic wind from this pulsar, extracting rotational energy from the neutron star, with the stellar wind from its companion (Tavani et al. 1994). Particles gain energy at the shock between the winds, resulting in a small-scale pulsar wind nebula (Maraschi & Treves 1981). The particles radiate away their energy as they are entrained in the shocked flow, forming a comet-like trail of emission behind the pulsar (Dubus 2006b).

The nature of the compact object and origin of the VHE emission remains controversial in LS 5039 and LSI +61°303, although recent observations indicate the radio emission of LSI +61°303 behaves like the comet tail expected in the pulsar scenario (Dhawan et al. 2006). Alternatively, the VHE emission could originate from particles accelerated in a relativistic jet, the energy source being accretion onto a black hole or neutron star

(Dermer & Böttcher 2006; Paredes et al. 2006). The rationale being that there is evidence for particle acceleration in the jets of microquasars and active galactic nuclei. However, hard evidence for accretion occurring in either LS 5039 or LSI +61°303 has been hard to come by (e.g. Martocchia et al. 2005) and the similarities between the three systems (and differences with the usual microquasars) do not argue in favour of the accretion/ejection scenario (Dubus 2006b).

Regardless of the actual powering mechanism, some particles must be accelerated to high energies to generate the VHE gamma-rays. If these particles are leptons, the only viable gamma-ray radiation mechanism is inverse Compton scattering on the stellar photons. The massive stars in gamma-ray binaries have effective temperatures of several tens of thousand K and radii of about $10 R_{\odot}$, yielding luminosities of the order of 10^{39} erg s^{-1} . This provides a huge density of stellar photons in the UV band that VHE leptons may up-scatter, much greater than any other possible source of target photons (e.g. synchrotron or bremsstrahlung emission).

The emitted VHE photons also have enough energy to produce e^+e^- pairs with the UV stellar photons. Most of the VHE flux may therefore be lost to the observer if the source is behind the star and VHE photons have to travel through the stellar light. Gamma-ray attenuation has been shown to lead to a modulation of the VHE flux with minimum absorption (maximum) at in-

ferior (superior) conjunction (Böttcher & Dermer 2005; Dubus 2006a).

HESS observations have indeed shown a stable modulation of the VHE flux from LS 5039 on the orbital period with a maximum around inferior conjunction. This suggests attenuation plays a role and that the source of VHE gamma-rays cannot be more than about an AU from the binary (or attenuation would be too weak to modulate the flux). However, a non-zero flux is detected at superior conjunction where a large attenuation is expected, possibly because of pair cascading. Moreover, the spectral changes that are reported do not fit with an interpretation based on pure attenuation of a constant VHE source spectrum (Aharonian et al. 2006).

Inverse Compton scattering also has a well-known dependence on the angle Θ between incoming and outgoing photon. The photon flux from the star being anisotropic, the resulting inverse Compton emission will depend on the angle at which it is observed. Hence, a phase-dependent VHE spectrum will be observed even if the distribution of particles is isotropic and remains constant throughout. This effect has previously been investigated in PSR B1259-63 by Ball & Kirk (2000) who calculated the radiative drag on the unshocked pulsar wind from scattering of stellar light, using results from Ho & Epstein (1989). The drag produces a Compton gamma-ray line with a strong dependence on viewing angle.

This work purports to explain the HESS observations of LS 5039 using a combination of anisotropic inverse Compton scattering and attenuation in the simplest way possible. The aim is to constrain the underlying particle distribution and/or powering mechanism. §2 derives the main equations governing anisotropic Compton scattering in the context of gamma-ray binaries and discusses the principal characteristics to expect. §3 presents the application to the case of LS 5039. The lightcurve and spectra observed by the HESS collaboration are reproduced by a model taking into account the photon field anisotropy and the attenuation due to pair creation. §4 concludes on the origin of the VHE emission from this system.

2. Anisotropic Compton scattering

Quantities in the electron rest frame are primed and quantities in the observer frame are left unprimed. The electron energy is $\gamma_e m_e c^2$, the energy of the incoming (stellar) photon is ϵ_0 and the outgoing photon energy is ϵ_1 . These quantities are related in the electron rest frame by the standard

$$\epsilon'_1 = \frac{\epsilon'_0}{1 + \frac{\epsilon'_0}{m_e c^2} (1 - \cos \Theta')} \quad (1)$$

with Θ' the angle between the incoming and outgoing photons. The incoming and outgoing photon energies are equal $\epsilon'_1 = \epsilon'_0$ in the Thomson scattering approximation $\epsilon'_0 \ll m_e c^2$, or $\epsilon_0 \ll m_e c^2 / [\gamma_e (1 - \beta \cos \theta_0)]$ when expressed in the observer frame (θ_0 is the photon angle with respect to the electron direction of motion). Scattering is also Thomson-like even if $\gamma_e \epsilon_0 > m_e c^2$ when the incoming and outgoing photon have almost the same direction ($\Theta' \ll (2m_e c^2 / \epsilon'_0)^{1/2}$). In the observer frame there is also an angle θ_{crit} below which scattering will be Thomson-like. This angle is defined by

$$\cos \theta_{\text{crit}} \approx \frac{1}{\beta} \left(1 - \frac{m_e c^2}{\gamma_e \epsilon_0} \right) \quad (2)$$

i.e. $\theta_{\text{crit}} \lesssim 60^\circ$ for $\gamma_e \epsilon_0 = 1$ MeV. The cross-section in the electron rest frame is

$$\frac{d\sigma}{d\epsilon'_1 d\Omega'_1}(\epsilon'_0, \epsilon'_1, \Theta') = \frac{r_e^2}{2} \left(\frac{\epsilon'_1}{\epsilon'_0} \right)^2 \left(\frac{\epsilon'_1}{\epsilon'_0} + \frac{\epsilon'_0}{\epsilon'_1} - \sin^2 \Theta' \right) \quad (3)$$

where r_e is the classical electron radius and the photon energies $\epsilon'_{0,1}$ are related through Eq. (1).

2.1. Monoenergetic beam

It is worthwhile to consider first the simple case of a monoenergetic beam of photons scattering off a single electron. The main steps are listed below and a detailed derivation may be found in Fargion et al. (1997).

In the observer frame, the incoming photon density (in $\text{sr}^{-1} \text{erg}^{-1}$), normalised to the (constant) total photon density n_0 (in photons cm^{-3}), is

$$\frac{dn}{d\epsilon d\Omega} = \delta(\epsilon - \epsilon_0) \delta(\cos \theta - \cos \theta_0) \delta(\phi - \phi_0) \quad (4)$$

with δ the Dirac function. The frame origin is at the location of the electron (the frame orientation is arbitrary). The photon density in the electron frame is found by using the invariance of $dn/d\epsilon$ (Blumenthal & Gould 1970).

The fraction of photons scattered per unit time, energy and solid angle in the electron frame is then given by (Jones 1968; Blumenthal & Gould 1970)

$$\frac{dN'}{dt' d\epsilon'_1 d\Omega'_1} = \iint c \frac{d\sigma}{d\epsilon'_1 d\Omega'_1} \frac{dn'}{d\epsilon' d\Omega'} d\Omega' d\epsilon' \quad (5)$$

which can be transformed to the observer frame using that the number of photons is invariant

$$\frac{dN}{dt d\epsilon_1 d\Omega_1} = \frac{dN'}{dt' d\epsilon'_1 d\Omega'_1} \frac{dt' d\epsilon'_1 d\Omega'_1}{dt d\epsilon_1 d\Omega_1}. \quad (6)$$

Ω'_1 denotes the solid angle into which the outgoing photon is emitted and $\cos \Theta' = \cos \theta' \cos \theta'_1 + \sin \theta' \sin \theta'_1 \cos(\phi'_1 - \phi')$. Defining the polar angles $\theta_{0,1}$ with respect to the direction of electron motion, the resulting differential photon spectrum is a function of γ_e , θ_0 , ϕ_0 , ϵ_0 , θ_1 , ϕ_1 and ϵ_1 . The integration gives a rather unwieldy expression that can be found in the Appendix (Eq. A.2).

In the Thomson regime ($\epsilon'_0 \ll m_e c^2$), the outgoing photon energy is unequivocally related to the incoming photon energy since $\epsilon'_1 = \epsilon'_0$. To each polar angle θ_1 corresponds a unique photon energy. In the general regime there is also a dependence on the azimuth (see Appendix). Staying in the Thomson regime, the total spectrum emitted by an electron follows from the integration over $d\Omega'_1$ of Eq. (5) and is (Fargion et al. 1997)

$$\frac{dN}{dt d\epsilon_1} = \frac{\pi r_e^2 c}{2\beta \gamma_e^2 \epsilon_0} \left[3 - \mu_0^2 + \frac{1}{\beta^2} (3\mu_0^2 - 1) \left(\frac{\epsilon_1}{\gamma_e \epsilon'_0} - 1 \right)^2 \right] \quad (7)$$

where $\mu'_0 = \cos \theta'_0$ and ϵ_1 varies between $\epsilon_0(1 - \beta\mu_0)/(1 \pm \beta)$. This expression shows how the emitted spectrum depends upon the angle θ_0 between the monochromatic point source and the direction of motion of the electron. A more general expression is given in the Appendix (Eq. A.6).

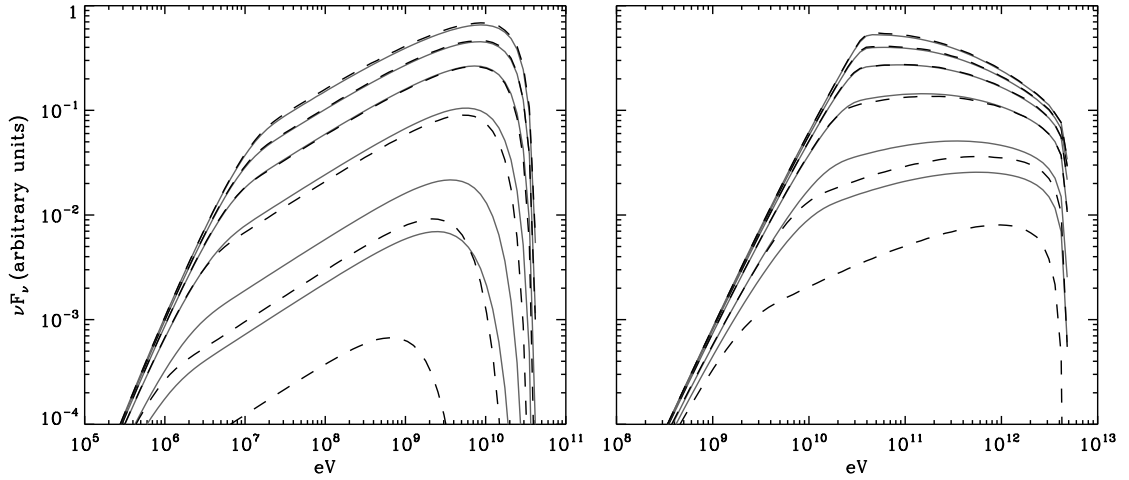


Fig. 1. Dependence of the viewing angle on the inverse Compton spectrum. The source of photons is a star with $kT=1$ eV. The electron cloud is situated at a distance $d = 2R_*$. The electrons are distributed according to a power-law $dn_e = \gamma_e^{-2} d\gamma_e$. The left panel shows the variation of the spectrum with angle when the interaction occurs in the Thomson regime (electron energy range $10^3 < \gamma_e < 10^5$). In the right panel the interaction occurs in the Klein-Nishina regime (electron range $10^5 < \gamma_e < 10^7$). In each panel, the spectrum is shown at viewing angles $\psi = 15^\circ$ (bottom), 30° , 60° , 90° , 120° and 180° (top). The observer sees the electron cloud in front of the seed photon source when the angle is small. Solid lines are calculated taking into account the finite star size (Eq. 13); dashed lines correspond to the point source approximation (Eq. 12).

2.2. Kernel for spectral calculations

The monochromatic, single photon result can be used as a kernel to integrate over general electron and incoming photon distributions. The total spectrum in photons $s^{-1} \text{ erg}^{-1} \text{ sr}^{-1}$ is then given by

$$\frac{dN_{\text{tot}}}{dt d\epsilon_1 d\Omega_1} = \iiint \frac{dN}{dt d\epsilon_1 d\Omega_1} n_0 d\Omega_0 d\epsilon_0 \frac{dn_e}{d\gamma_e d\Omega_e} d\Omega_e d\gamma_e \quad (8)$$

where the evaluation of the kernel must take into account the changes in electron direction with respect to the given direction. However, this expression can be simplified.

The electron energy must be very large $\gamma_e \gg 1$ in order to emit VHE photons. The emission is strongly forward boosted in the direction of the electron motion by relativistic aberrations. An observer looking at the inverse Compton emission from an isotropic cloud of relativistic electrons sees essentially only the emission emitted by those electrons moving within an angle $1/\gamma_e$ from the line-of-sight (see e.g. Ball & Kirk 2000). Their emission is almost entirely focused into the line-of-sight. Photons emitted slightly away from the line-of-sight and included in the integration compensate to order $1/\gamma_e$ for the emission from electrons moving at larger angles. Therefore, to a good approximation,

$$\int \frac{dN}{dt d\epsilon_1 d\Omega_1} \frac{dn_e}{d\gamma_e d\Omega_e} d\Omega_e \approx \left. \frac{dN}{dt d\epsilon_1} \right|_{\alpha} \frac{dn_e}{d\gamma_e d\Omega_e} \Big|_{\Omega_1} \quad (9)$$

and the spectrum will be given by

$$\frac{dN_{\text{tot}}}{dt d\epsilon_1 d\Omega_1} = \iiint n_0 d\Omega_0 d\epsilon_0 \left. \frac{dN}{dt d\epsilon_1} \right|_{\alpha} \frac{dn_e}{d\gamma_e d\Omega_e} \Big|_{\Omega_1} d\gamma_e \quad (10)$$

where the kernel is given by Eq. (7) or Eq. (A.6), evaluated at the angle α between the point-like photon source, the electron cloud and the observer. If \mathbf{e}_{obs} is a unit vector from the electron cloud to the observer and \mathbf{e}_0 is a unit vector from the photon

source to the electron cloud, expressed using θ_0 and ϕ_0 , then $\mu_\alpha \equiv \cos \alpha = \mathbf{e}_0 \cdot \mathbf{e}_{\text{obs}}$.

For scattering on an isotropic distribution of photons, \mathbf{e}_{obs} can be arbitrarily oriented so that $\alpha = \theta_0$. For a blackbody of temperature T_* ,

$$n_0 d\Omega_0 = \frac{2}{h^3 c^3} \frac{\epsilon_0^2}{\exp(\epsilon_0/kT_*) - 1} d\Omega_0 \equiv f_0 d\Omega_0 \quad (11)$$

For a point-like star of radius R_* at a distance d_* from the electrons, \mathbf{e}_{obs} can be defined on the plane containing the three locations so that, again, $\alpha = \theta_0$. The photon distribution is

$$n_0 d\Omega_0 = \pi \left(\frac{R_*}{d_*} \right)^2 f_0 \delta(\mu_0 - \mu_\psi) \delta(\phi_0) d\Omega_0 \quad (12)$$

with f_0 as defined in the previous equation and where ψ is the angle between the star centre, the cloud and the observer. The integral on Ω_0 is direct so the kernel only needs be numerically integrated on ϵ_0 and γ_e . Finally, for a star of finite size, the integration element is

$$n_0 d\Omega_0 = f_0 \cos \theta_0 d\Omega_0, \quad \phi_0 \in [0, 2\pi], \quad \sin \theta_0 \in [0, R_*/d_*] \quad (13)$$

and $\mu_\alpha = \cos \psi \cos \mu_0 + \sin \psi \sin \mu_0 \cos \phi_0$. This requires a quadruple numerical integral.

The electron distribution will be assumed to be isotropic in the following so that the expression in Eq. (9) is a function f_e of γ_e only and $\int f_e d\gamma_e$ gives the total number of electrons per steradian.

2.3. Anisotropic scattering of stellar photons

Figure 1 shows example calculations of the inverse Compton spectrum from a distribution of electrons scattering photons emitted by a star, as seen from different viewing angles. The incoming photons have a blackbody distribution and the electrons have a power-law distribution $dn_e = \gamma_e^{-2} d\gamma_e$. The viewing

angle ψ is defined as the angle between the star, electron cloud and observer ($\cos \psi = \mathbf{e}_\star \cdot \mathbf{e}_{\text{obs}}$ with \mathbf{e}_\star a unit vector from the star centre to the cloud). Two cases are shown: one corresponding to scattering in the Thomson regime and one for the Klein-Nishina regime. For each case, results obtained in the point source approximation and taking into account the finite size of the star are compared.

When scattering occurs in the Thomson regime ($\epsilon'_0 \ll m_e c^2$), the maximum energy $\gamma \epsilon'_0 (1 + \beta)(1 - \beta \cos \psi)$ decreases with decreasing viewing angle ψ , i.e. when the electrons move in front of the star as seen by the observer (left panel of Fig. 1). This is to be expected as the electrons are then forward scattering radiation that is less energetic in their rest-frame than in the head-on case because of the $1 - \beta \cos \psi$ term in the Lorentz transform. The other effect is a lower rate of emission for low ψ (as can be directly deduced from Eq. 6 and seen in the left panel of Fig. 1). This is also due to the decrease in the density of incoming photons in the electron rest frame when both particles move in the same direction. Scattering is more likely to occur when the particles collide head-on (e.g. Sazonov & Sunyaev 2000).

These effects are pronounced in the point source approximation and are diluted when taking into account the finite size of the star (see dashed lines compared to full lines in Fig. 1). With a star of finite size, electrons see incoming photons from a variety of angles, which contributes to raising the seed photon density in the electron rest frame when $\psi = 0$ (and to slightly decreasing it at $\psi = \pi$). Because the density is tied to $1 - \beta \cos \psi$, this suggests a simple rule-of-thumb, corroborated by numerical investigations: the effect of the finite star-size should be taken into account when $\sin \psi \lesssim R_\star/d_\star$ but can otherwise be neglected. If the observer is within the cone defined by the star with the electrons at apex, then the density of photons seen by the electrons moving towards the observer will be significantly greater than in the point source case. Outside of this cone, the difference with a point source approximation is minor. In Fig. 1, the star angular size seen by the electrons is 30° (defining the cone opening angle) and the point source approximation is indeed acceptable for $\psi > 30^\circ$.

When scattering occurs in the Klein-Nishina regime ($\epsilon'_0 > m_e c^2$), the maximum energy is almost constant at $\gamma_{\text{max}} m_e c^2$ regardless of viewing angle. For large viewing angles, the spectrum is soft due to the decrease in cross-section in this regime, just as in the isotropic case. At small viewing angles, the seed photon energy in the rest frame of the electron is lower than in the head-on case because of the angle dependence in the relativistic boost, as described above for the Thomson regime. Moreover, since the limit between Thomson and Klein-Nishina regimes is at $\epsilon_0 \gamma_e (1 - \beta \cos \psi) \approx m_e c^2$, scattering can reach back to the Thomson regime for small enough viewing angles, regardless of the electron energy (see Eq. 2 in §2). There are two consequences. First, the amplitude of the variations with viewing angle is smaller than in the Thomson regime, because at small ψ the decrease in photon density is compensated by the larger cross-section. Second, since there is no drop in cross-section at small ψ , there can be a significant hardening of the spectrum compared to the spectrum at larger ψ (right panel of Fig. 1). These spectral effects may play an important role in modelling the emission from gamma-ray binaries, for which scattering occurs mostly in the Klein-Nishina regime. This is investigated in the next section.

3. Application to LS 5039

The influence of anisotropic scattering on the emission from gamma-ray binaries can be sketched from the results of the previous section. If the high energy emission is due to inverse Compton scattering off electrons co-rotating with the binary, the viewing angle of the observer will vary with orbital phase, inducing changes in the observed spectrum — all other things being set equal (particle distribution and location, distance to the star etc).

Anisotropic scattering will most influence the emission from systems with high inclinations, if the electrons are located in the orbital plane. At low inclinations the changes are expected to be minor as the scattering angle ψ stays close to $\pi/2$. On the other hand, for high inclinations the inverse Compton spectrum may change significantly between inferior and superior conjunctions. The emission will be intense and soft at the time of maximum attenuation by pair production, and low and hard at the time of minimum attenuation. Anisotropic inverse Compton emission combined with attenuation of VHE photons can therefore play an important part in (1) reducing the amplitude of the variations expected from a simple attenuation model; (2) hardening the spectrum at high flux states compared to expectations from a calculation assuming an isotropic flux.

LS 5039 presents an ideal testbed. The massive star has an O6.5V spectrum ($T_\star = 39,000$ K, $R_\star = 9.3 R_\odot$, $M_\star = 23 M_\odot$) in a 3.9 day eccentric orbit ($e = 0.39$) with its compact companion (Casares et al. 2005). A diagram of the binary orbit oriented on the sky is shown in Fig. 2. The measured radial velocity of the O star constrains the inclination to about 60° for a neutron star companion and about 20° for a black hole. The compact star moves from one to three stellar radii from the surface of the massive star.

The intensity and spectral variations have been well-established in LS 5039 by HESS observations, concluding that pure attenuation of a constant VHE spectrum could not explain the observations to satisfaction (see §1). Given the above discussion, this section examines whether taking into account anisotropic scattering provides an improved agreement.

3.1. The radiating electrons

Two main assumptions are made to calculate the emission. First, the electrons are assumed to scatter radiation at the location of the compact object, in a small region compared to the orbital separation. This is a very good approximation in the pulsar wind nebula scenario where the highest energy electrons emit the gamma-ray radiation close to the shock. (The cooled electrons then emit in radio well away from the system.) This may or may not be appropriate in the case of a relativistic jet, where emission can occur at various distances along the outflow. This is further discussed §3.4.

Second, the adopted distribution of particles is the steady-state distribution for constant injection of particles, taking into account synchrotron and inverse Compton losses. The magnetic field in the radiating zone is assumed to be homogeneous. The radiative losses occur on very short timescales compared to the orbital timescale so the steady-state approximation is justified except for low energy particles whose radiative timescale becomes longer than their escape timescale from the radiating zone. This occurs at $\gamma_e \approx 10^3$ (see below). The injection spectrum is a power-law $dn_e \propto \gamma_e^{-p} d\gamma_e$ with an exponential cutoff at the maximum γ_{max} allowed by comparing acceleration and radiative timescales.

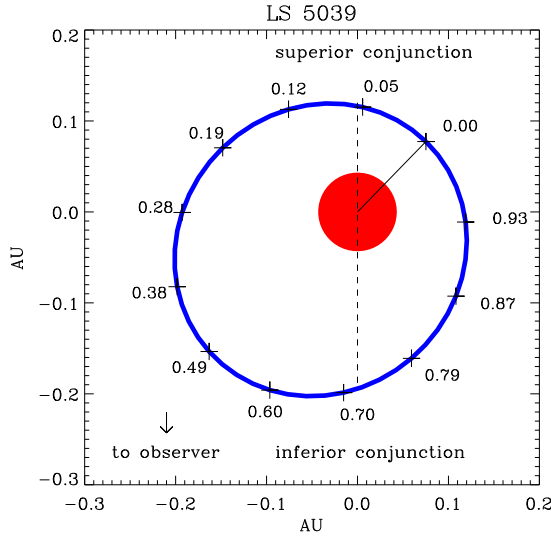


Fig. 2. The binary orbit of LS 5039 as seen from directly above. The O6.5V star radius is to scale. The binary orientation is set for an observer at the bottom of the diagram. The binary inclination on the plane of the sky is not taken into account. The numbers indicate the orbital phase (mean anomaly) at various positions. Periastron passage is indicated by a full line (orbital phase $\phi_{\text{orb}}=0$). The dashed line is the line of conjunctions ($\phi_{\text{sup}} \approx 0.06$, $\phi_{\text{inf}} \approx 0.72$). The orbital parameters are taken from Casares et al. (2005).

The minimum acceleration timescale for TeV electrons ($\gamma_6=10^6$) is set by the gyrofrequency and is $t_{\text{acc}} \approx 0.06 \gamma_6/B_1$ s with $B_1=1$ G the magnetic field intensity. The synchrotron cooling timescale is $t_S \approx 770/B_1^2 \gamma_6$ s. For electrons with Lorentz factors $\gamma_e > \gamma_{\text{KN}} \approx 6 \cdot 10^4 T_{\star,4}^{-1}$, inverse Compton scattering of stellar photons occurs in the Klein-Nishina regime. The corresponding timescale is $t_{\text{IC}} \approx 20 \gamma_6 d_{0,1}^2 / [\ln \gamma_6 + 1.4] (T_{\star,4} R_{\star,10})^2$ s (Blumenthal & Gould 1970) with $T_{\star,4}=40,000$ K, $R_{\star,10}=10 R_{\odot}$ and $d_{0,1}$ is the orbital separation in units of 0.1 AU (the LS 5039 orbital separation at periastron).

The steady-state distribution derives from a comparison of these three timescales. Synchrotron losses dominate over inverse Compton losses above a critical γ_S given by ($t_S=t_{\text{IC}}$):

$$\gamma_S \approx 6 \cdot 10^6 (T_{\star,4} R_{\star,10}) / (B_1 d_{0,1}). \quad (14)$$

At the highest energies, γ_{max} is therefore set by synchrotron losses ($t_{\text{acc}}=t_S$), which gives $\gamma_{\text{max}} \approx 1.2 \cdot 10^8 B_1^{-1/2}$. Assuming continuous injection of electrons with a γ_e^{-p} spectrum, the steady-state distribution is steepened by synchrotron losses between γ_S and γ_{max} to a γ_e^{-p-1} power-law. Inefficient Klein-Nishina losses dominate between γ_{KN} and γ_S , producing a hard spectrum mirroring the decrease in energy loss rate with increasing γ_e in the Klein-Nishina regime. Below γ_{KN} inverse Compton losses in the Thomson regime result in a γ_e^{-p-1} power-law as in the synchrotron case.

Steady-state distributions obtained using a full numerical calculation follow very well the main characteristics outlined above (Fig. 3, see also Moderski et al. 2005). The inverse Compton losses are treated in the isotropic approximation since the magnetic field will quickly randomize particle directions. The particles see, on average, the equivalent of an isotropic radi-

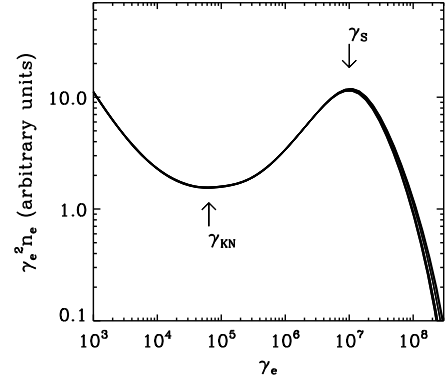


Fig. 3. Steady-state electron distribution N_e along the orbit of LS 5039. The injection spectrum is a γ_e^{-2} power-law with an exponential cutoff at $\gamma_e \approx 10^8$ (see §3.1). The magnetic field varies as $B = 0.8 d_{0,1}^{-1}$ G, where $d_{0,1}$ is the orbital separation in units of 0.1 AU. Inverse Compton losses in the Thomson regime ($\gamma_e < \gamma_{\text{KN}}$) and synchrotron losses ($\gamma_e > \gamma_S$) steepen the index of the injected distribution by one to $N_e \propto \gamma_e^{-3}$. Inverse Compton losses in the Klein-Nishina regime dominate between $\gamma_{\text{KN}} < \gamma_e < \gamma_S$, causing a hardening of the distribution (Moderski et al. 2005). The steady-state distribution varies little with orbital phase since $\gamma_S \propto (Bd)^{-1}$ stays constant: the changes with orbital phase produce only a slight thickening of the line in the above figure.

ation field; but the inverse Compton spectrum received by an observer at a fixed location changes with viewing angle. In Fig. 3, the injection is a power law γ_e^{-p} with $p = 2$ and the distribution between γ_{KN} and γ_S is roughly proportional to $\gamma_e^{-1.3}$. The slope of this distribution depends on the slope of the injected spectrum. For power-law injections γ_e^{-p} with hard indices ($p < 2$) the slope between γ_{KN} and γ_S tends to γ_e^{-1} . For soft indices $p > 2$, the hardening gradually disappears, reaching γ_e^{-2} between γ_{KN} and γ_S for an injection with $p = 3$. As discussed below, the observations of LS 5039 constrain p to about 2.

This steady-state distribution is a very good approximation to the more detailed pulsar wind model of Dubus (2006b) for electrons with $\gamma_e \gtrsim 10^3$: lower energy electrons escape from the vicinity of the pulsar without radiating much of their energy. More generally, this distribution should apply equally well to any leptonic model assuming a constant injection of non-thermal particles cooling in the vicinity of the compact object via synchrotron and inverse Compton radiation.

3.2. Compact pulsar wind nebula: orbital lightcurve

With the inverse Compton losses fixed by the geometry, the only remaining free parameters are the slope of the injected power-law, the total energy in radiating electrons and the value of the magnetic field. In the case of a compact pulsar wind nebula, the magnetic field is determined by the conditions at the pulsar wind termination shock. Its intensity sets γ_S , which in turn will fix the frequency above which a break will be seen in the VHE gamma-ray spectrum. In principle, B may vary with orbital phase as the eccentric orbit brings the pulsar at various radii in the stellar wind. However, the magnetic field intensity is inversely proportional to the shock distance from the pulsar, and the latter is roughly proportional to the orbital separation so that $B \propto 1/d$

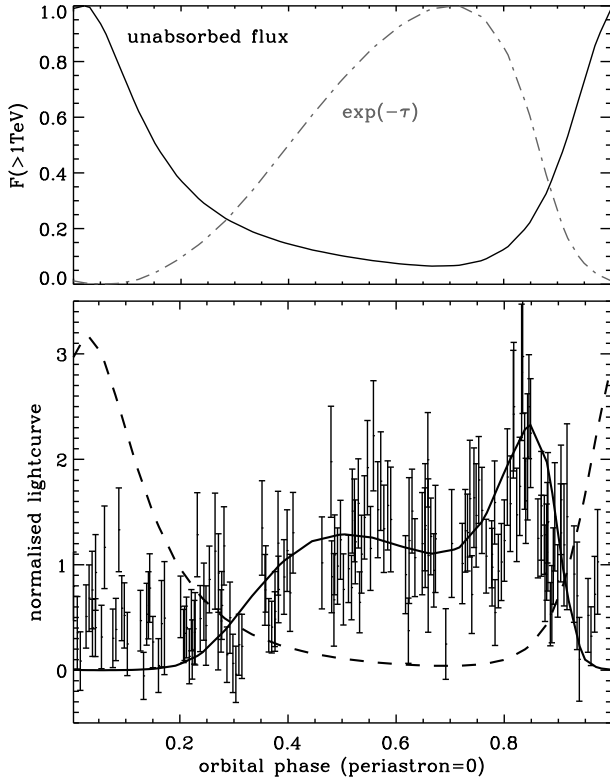


Fig. 4. Predicted orbital lightcurves for LS 5039 in the case of a neutron star ($i = 60^\circ$). Top panel: the integrated photon rate above 1 TeV (full line) due to anisotropic inverse Compton scattering and the transmission $\exp(-\tau_{\gamma\gamma})$ for the pair production process, also integrated above 1 TeV. Inverse Compton scattering is minimum at inferior conjunction ($\phi_{\text{orb}} \approx 0.72$, see Fig. 2). The absorption due to pair production is also minimum at this time. Bottom panel: the resulting orbital lightcurve (full line) compared to the HESS observations. Combining anisotropic inverse Compton emission and attenuation by pair production produces a peak at $\phi_{\text{orb}} \approx 0.8$ consistent with the observations. The agreement is good except at periastron where cascade emission (ignored here) may be important. The dashed line shows the photon rate in GLAST above 1 GeV ($\text{ph cm}^{-2} \text{s}^{-1}$). The model predicts a peak in the GLAST lightcurve close to periastron and a minimum at inferior conjunction. The normalizations are arbitrary. The lightcurves are calculated using the electron distributions shown in Fig. 3.

(see e.g. Dubus 2006b). In this case, the distribution of particles will not change along the orbit as $\gamma_s \propto (Bd)^{-1}$.

Figure 4 shows the expected lightcurve at different orbital phases with $B = 0.8$ G at periastron and $p = 2$ (using the electron distribution shown in Fig. 3). The orbital elements were computed as in Dubus (2006a). The unabsorbed intensity is high close to superior conjunction and small at inferior conjunction, as explained in §2.3. The angle to the observer varies between 30° and 149° whereas the angular size of the star at the compact object is 30° at most: the finite size of the star, taken into account in the calculation, has a minor effect on the results. The attenuation

lightcurve, computed following Dubus (2006a) is also shown. It peaks at inferior conjunction where attenuation is minimum.

The lightcurve including both anisotropic emission and attenuation by pair production reproduces very well the observed lightcurve. Most notably, the combination of low attenuation, increasing photon density and a hard inverse Compton spectrum produces a small peak after inferior conjunction that appears to be present in the HESS observations. The peak is a key feature of this model. This lightcurve is very robust against changes in the value of the magnetic field used, or even in the type of particle distribution used. At higher inclinations, a weaker peak appears before inferior conjunction as the variations in viewing angle cause a larger drop in inverse Compton emission at $\phi_{\text{orb}} = 0.72$. However, this model still predicts little to no flux at and after periastron because of the very strong attenuation of the emission emitted around the pulsar. A possible explanation is that a pair cascade develops.

The lightcurve above 1 GeV is also plotted in Fig. 4. Attenuation is negligible and the variations mostly follow the photon density modulo some modifications due to the anisotropy: for instance, the minimum is at inferior conjunction. GLAST should therefore see a modulation in the flux from LS 5039 with a peak close to periastron and a minimum at inferior conjunction, almost anti-correlated with the HESS modulation.

A similar lightcurve has been obtained by Bednarek (2007), using a complex Monte-Carlo code simulating the effects of anisotropic scattering and the development of cascades. However, Bednarek (2007) wrongly interpreted the GLAST modulation as being due to stronger cascade emission close to periastron. As described above, the modulation is due to a combination of increased seed photon density and anisotropic effects and not to cascade emission¹.

3.3. Compact pulsar wind nebula: phase-resolved spectra

Figure 5 shows the evolution of the attenuated and unattenuated spectra with orbital phase. These were used to produce the lightcurves shown in Fig. 4. The spectra display a complex interplay between the varying threshold for pair production, the high absorption it causes at superior conjunction when the inverse Compton flux is high, and the weaker but harder inverse Compton emission at inferior conjunction. The variations in the GeV (GLAST) range have a very large amplitude, with a flat spectrum at the highest intensities and a hard spectrum at low intensities. This should easily be accessible to GLAST in the very near future (Dubois 2006). Note that synchrotron emission contributes significantly to the emission below a GeV and that this is not taken into account in this lightcurve. Its impact is to soften the spectrum and reduce the amplitude of the variations below a GeV (see §3.4 below and Fig. 6).

The attenuated spectrum averaged over the full orbit is shown in Fig. 6. The hitherto puzzling drop between the EGRET and HESS spectra is very well reproduced by the model without invoking a cascade. The inverse Compton spectrum by itself underestimates the EGRET flux by factors of a few but, taking

¹ Bednarek (2007) also confused the phases of inferior and superior conjunctions (Fig. 2). The compact object is on the near side of the orbit (inferior conjunction) at phases 0.4-0.8 so that the broad maximum is not due to the stronger Compton scattering expected when the object is behind the star (see Fig. 5). Similarly, the dip at phase 0.7 is not due to stronger absorption (expected at superior conjunction): it actually occurs at the phase of minimum absorption and is due to the lower Compton emissivity at inferior conjunction, as described above.

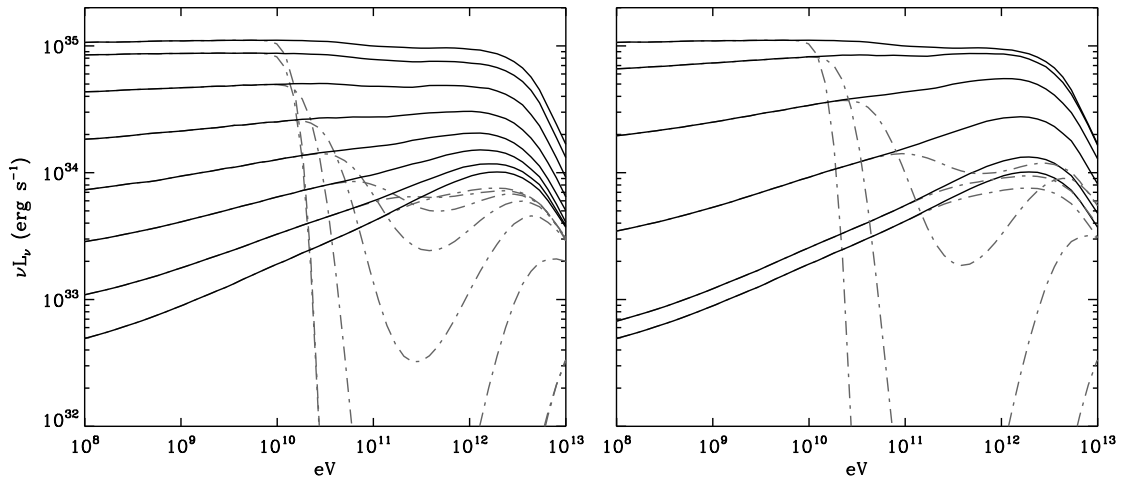


Fig. 5. Evolution of the model inverse Compton spectrum with orbital phase in LS 5039 (neutron star case). The intrinsic emission spectra are shown with full lines and the dashed lines show the spectra after attenuation by pair production on stellar photons during the propagation of the gamma-rays through the system. The underlying electron distributions are those shown in Fig. 3. Left panel: from top to bottom the spectra correspond to orbital phases $\phi_{\text{orb}}=0.03, 0.09, 0.15, 0.24, 0.34, 0.44, 0.56$ and 0.66 (see Fig. 2). Right panel: the plotted orbital phases from bottom to top are $0.66, 0.76, 0.85, 0.91, 0.97$ and 0.03 .

into account the synchrotron emission from the electrons using the adopted magnetic field intensity ($B=0.8$ G at periastron and varying as $1/d$), the calculated synchrotron emission produces a very good match to both the EGRET and HESS spectra. Note that the average HESS spectrum is not shown for reasons of clarity in Fig. 6 but is close to the ‘high’ state spectrum (see below), with a slightly higher luminosity.

The two average spectra for the phase intervals of the HESS ‘high’ ($0.45 < \phi_{\text{orb}} < 0.9$) and ‘low’ state ($\phi_{\text{orb}} < 0.45$ or $\phi_{\text{orb}} > 0.9$) spectra are also shown in Fig. 6 (Aharonian et al. 2006). Reproducing the cutoff in the high-state HESS spectrum strongly constrains the magnetic field intensity to ≈ 0.8 G at periastron. A higher magnetic field moves the cutoff to lower energies and is inconsistent with the data. A lower B moves the cutoff to higher energies and hardens the spectrum too much. The high-state spectrum is rather sensitive to the value of B : the acceptable range is only $B = 0.8 \pm 0.2 d_{0.1}^{-1}$ G. Outside of this range the fit does not go through the error bars of the HESS data points.

The synchrotron emission contributes significantly below 1 GeV, diluting the hardening of the spectrum around $\phi = 0.7$ expected from pure inverse Compton emission. Actually, a softening is predicted below a few GeV. The GLAST lightcurve shown in Fig. 4 is not noticeably changed (on a linear scale) by taking synchrotron emission into account. The hard electron distribution, naturally resulting from inefficient Klein-Nishina losses here, is instrumental in obtaining the flat spectrum in the HESS range. The range $\gamma_{\text{KN}} < \gamma_e < \gamma_S$ of this hard distribution depends upon the value of the magnetic field, but its shape is independently set by the index p of the injected power-law γ_e^{-p} . With $p \lesssim 1.7$ the predicted HESS spectrum is too hard and the emission in the EGRET band is too low. With $p \gtrsim 2.3$, the predicted HESS spectrum is too soft and the EGRET emission is too large. Therefore, the slope of the injected power-law is constrained to $p = 2 \pm 0.3$.

Besides the magnetic field intensity and slope of injected electrons, the other free parameter is the normalization of the electron distribution. The fit was obtained for a total energy in electrons from $\gamma_e = 10^3$ to $+\infty$ of $3 \cdot 10^{37}$ erg. This energy corre-

sponds to the injection of 10^{36} erg s^{-1} in particles, assuming an escape timescale from the radiative zone of 30 s (longer than the radiative timescale under consideration). In the pulsar wind nebula the shocked electrons have a bulk velocity $\approx c/3$ so that the escape timescale corresponds to a radiating zone of $3 \cdot 10^{11}$ cm, comparable to the shock size found for typical wind parameters in LS 5039 (Dubus 2006b). The estimated injection energy rate is consistent with a reasonable pulsar spindown power, such as that measured in PSR B1259-63 (Manchester et al. 1995).

The low-state spectrum is responsible for most of the orbit-averaged emission in the EGRET range, which is nicely fit by the model. However, the HESS low-state spectrum is not satisfactory. This spectrum corresponds to phases where the intrinsic inverse Compton emission is both soft, as the observed spectrum, and intense. The intrinsic emission is actually strongest at the times of highest attenuation so that the two effects compensate somewhat. However, the cross-section for pair production drops above a few TeV. Therefore, the predicted phase-averaged low-state is not a pure power-law but still shows hints of an attenuation line with a kink at high energies. Changes in the electron distribution may also help to reduce the discrepancy. A cutoff at a lower γ_e (i.e. a higher magnetic field) than that shown in Fig. 3 would yield a better agreement if it occurred at the appropriate orbital phases. However, at this stage it appears more reasonable to investigate first the impact of pair cascading on this spectrum, as this is required to explain the detection at periastron.

The model contains only three parameters: the slope of the injected power-law, the particle distribution normalization and the magnetic field intensity at periastron (or any other arbitrary orbital phase). The shape of the particle distribution and the associated emission along the orbit are then unequivocally predicted. The parameters were adjusted so as to fit the high-state HESS spectrum. That this choice also fits very well the EGRET observations gives strong support to this simple-minded model, even if the low-state HESS spectrum is not reproduced to satisfaction.

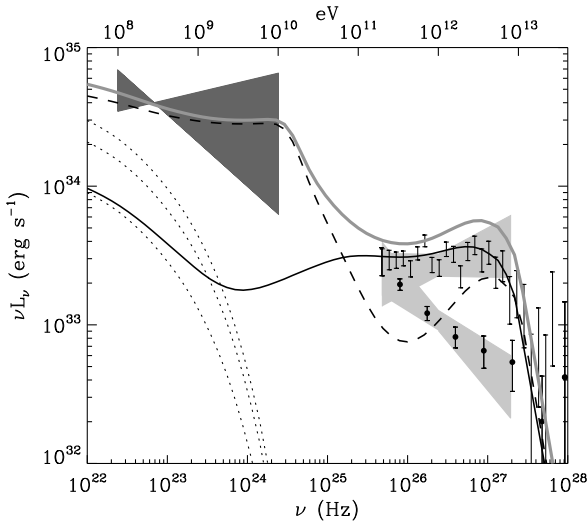


Fig. 6. Comparison with the EGRET and HESS observations of the LS 5039 model spectra for a neutron star. The EGRET bowtie is in dark grey and the HESS high-state and low-state bowties are in light grey (Hartman et al. 1999; Aharonian et al. 2006). The corresponding HESS deconvolved spectral points are also shown (with a dot identifying the low-state points). Fluxes have been transformed to luminosities assuming a distance of 2.5 kpc (Casares et al. 2005). The full grey line is the average spectrum calculated using the results of Fig. 5. It reproduces well the drop in flux from EGRET to HESS (the average HESS spectrum is close to the high-state spectrum shown). The high-state spectrum (full dark line) is very well reproduced provided the magnetic field at periastron is lower than 0.8 G. The low-state spectrum (dashed dark line) is not reproduced well, possibly because cascade emission contributes significantly at these orbital phases where pair production is very important or because the electron distribution varies along the orbit. Here, the synchrotron emission from the electrons is taken into account with $B = 0.8d_{0.1}^{-1}$ G as derived from the VHE spectrum. Its contribution to the spectra is shown by the dotted lines (from bottom to top: low-state, high-state, and orbital average).

3.4. Black hole jet?

This subsection examines how the results are changed if the compact object is a black hole. The main effect is that consistency with radial velocity curves require the inclination to change to 20° ($4.5 M_\odot$ black hole). The variation in viewing angle is then reduced to the interval 70° – 110° . The electrons are still assumed to be accelerated in the vicinity of the black hole and to reach a steady-state distribution such as the one described above. Here, the magnetic field has a fixed value as there is no *a priori* reason for it to change with the orbital separation. This gives a moderate change of a factor 2 in the break γ_S of the electron distribution, because the orbital separation varies by a factor 2, in contrast to the situation described in Fig. 3.

The orbital lightcurve and the spectra obtained with $B = 0.8$ G and $p = 2$ are shown in Figs. 7-8. In contrast with the neutron star case, there is only one broad peak in the predicted HESS lightcurve. This is because the reduced variation of the viewing angle does not lead to a large drop in scattered flux at inferior conjunction. The small peak predicted at high inclinations (neutron star) can therefore be used as a discriminant between

the two cases. The averaged spectra are much harder than in the neutron star case. The amplitude of the variation at GeV energies is less than for a neutron star and the average flux overestimates the EGRET emission. The poor fit of the low-state spectrum remains. Both the lightcurve and spectra are arguably not as good fits as those obtained in the neutron star case, but not so much as to exclude that LS 5039 is seen at a low inclination (and hence contains a black hole).

Emission from a relativistic jet may differ from the estimate above. Any Doppler boosting will change the observed spectrum. However, the resolved radio emission, if interpreted as a compact jet, implies only a moderate velocity and little boosting (Paredes et al. 2000). Modest Doppler (de)boosting may also be expected from the pulsar wind emission as its post-shock speed is approximately $c/3$. More importantly, emission may occur all along the jet and not just be localized near the black hole. Far from the compact object, the viewing angle tends to become the inclination angle ($\psi \rightarrow i$) regardless of orbital phase². Hence, emission at progressively higher altitudes in the jet is less and less influenced by anisotropic effects. The emission is also less attenuated by pair production, with $\tau_{\gamma\gamma}$ negligible at heights ≥ 1 AU. If most of the emission occurs far in the jet, and assuming the electron distribution stays constant, the flux modulation is only linked to the stellar photon density. The result is a constant spectral shape, peak flux at periastron and a trough at apastron. These are inconsistent with the observations. Therefore, a jet model for LS 5039 probably requires either (1) that most of the emission occurs close to the compact object in order to reproduce the orbital gamma-ray modulation via anisotropic scattering and attenuation or (2) that the emission occurs away in the jet and that some unspecified intrinsic mechanism changes the particle distribution and/or the radiation process.

4. Conclusion

The anisotropic behaviour of inverse Compton scattering has a major influence on the emission from gamma-ray binaries. In these sources, the massive star provides a large source of seed photons with energies around an electron-volt. If high energy electrons are accelerated in the vicinity of the compact object, then the angle between the star, compact object and observer changes with orbital phase. The variation in viewing angle leads to a strong modulation in both the intensity and spectral shape of the scattered radiation.

Scattering stellar photons to the TeV range requires very energetic electrons with Lorentz factors $\gamma_e \approx 10^6 - 10^7$. The scattering therefore occurs in the Klein-Nishina regime. In this case, the anisotropy results, at inferior conjunction, in a harder and fainter spectrum than predicted using an isotropic approximation for the incoming photons. Crucially, inferior conjunction also corresponds to the phase at which the produced VHE gamma-rays are less attenuated by pair production on stellar photons. At other phases the emitted spectrum is close to the one obtained using the isotropic photon field approximation and can be severely attenuated by pair production. The result is a complex interplay that reduces the amplitude of the variations expected from a pure attenuation model and a hardening at inferior conjunction.

² Note that two errors have slipped by in Dubus (2006a) when dealing with the case of a VHE source perpendicular to the orbital plane. In the last equation of A.2 the angle for emission perpendicular to the plane is given as $\cos \psi = (d_0/d) \cos \psi_0 = (d_0/d) \sin \theta \sin i$ but should be $\cos \psi = (d_0/d) \sin \theta \sin i - (z/d) \cos i$. The other is that Fig. 8 (attenuation with height) was calculated at a fixed viewing angle of 76° . The conclusions are unchanged.

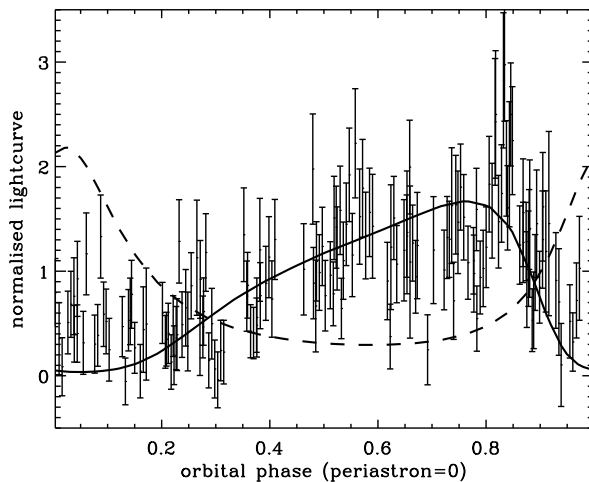


Fig. 7. Predicted orbital lightcurves for LS 5039 in the case of a black hole ($i = 20^\circ$). The full line is the integrated photon flux above 1 TeV (HESS), the dashed line is integrated above 1 GeV (GLAST). The variations in viewing angle are reduced compared to the high inclination (neutron star) case (Fig. 4) and there is only one broad maximum in the HESS lightcurve. The electron distribution is calculated as described in Fig. 3 but using a constant magnetic field intensity of 0.8 G.

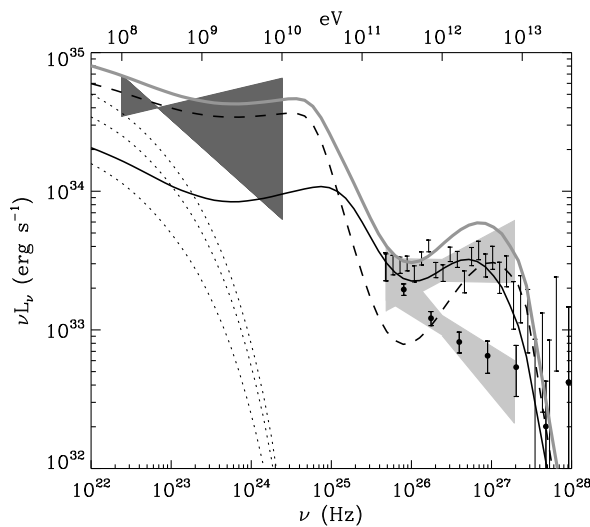


Fig. 8. Comparison with the EGRET and HESS observations of the LS 5039 model spectra for a black hole. The radiating electrons are injected in the immediate vicinity of the black hole. The magnetic field intensity used to fit the high-state spectrum is 0.8 G, constant throughout the orbit. The injected electrons have a power-law of index $p = 2$. The line coding is the same as in Fig. 6.

The LS 5039 lightcurve and spectra were modelled using a simple-minded leptonic model. The electrons are assumed to be accelerated efficiently in a small zone in the vicinity of the compact object with a standard γ_e^{-p} power-law. Radiative losses due to inverse Compton emission and synchrotron emission generate a distinctive steady-state electron distribution in this environment dominated by stellar photons. The distribution has a promi-

nent hardening between the energy at which inverse Compton losses enter the Klein-Nishina regime ($\gamma_{KN} \approx 6 \cdot 10^4$ in LS 5039) and the energy at which synchrotron losses take over ($\gamma_S \approx 10^7$ for a 1 G field). This is for instance the distribution found in the vicinity of the pulsar wind shock but it applies equally well to any leptonic model where particles are accelerated close to the compact object. The magnetic field was allowed to vary as the inverse of the orbital separation, as expected from a pulsar wind nebula. The model has only three parameters: the intensity of the magnetic field, the normalization of the electron distribution and the slope p of the injected power-law γ_e^{-p} .

The cutoff in the very high energy gamma-ray spectrum is very sensitive to the magnetic field intensity, via the location of γ_S in the electron distribution. Fitting the high-state spectrum seen by HESS gives a rather constrained magnetic field intensity at periastron of 0.8 ± 0.2 G. This value compares well with the values found using simple pulsar wind models which give $5 (\dot{E}_{36} \sigma_3)^{1/2} R_{11}^{-1}$ G, where \dot{E}_{36} is the pulsar spindown power in units of 10^{36} erg s^{-1} , σ_3 is the ratio of magnetic to kinetic energy in the pulsar wind in units of 10^{-3} and R_{11} is the distance of the shock to the pulsar in units of 10^{11} cm. Fitting the HESS high-state spectrum also sets the injection slope to $p = 2 \pm 0.3$, close to the canonical value for shock acceleration. The normalization of the electron distribution implies an injection rate of 10^{36} erg s^{-1} for a radiative zone of $3 \cdot 10^{11}$ cm. These results are remarkably consistent with the expectations for a pulsar wind model.

The spectrum is also found to fit extremely well the EGRET observations, adding credence to the reliability of this simple approach. The model predicts a strong variation in the GLAST band with a softening from high to low flux below a GeV (where synchrotron emission dominates the spectrum) but a hardening above a GeV (where inverse Compton emission dominates the spectrum). The HESS low-state spectrum is not explained to satisfaction. The model fits nicely the EGRET measurements but produces too many gamma-rays at 5-10 TeV. A possible solution is a more complex orbital phase-dependence of the electron distribution at selected phases. Another solution is that the low-state spectrum corresponds to phases of strong attenuation and that emission from the created pairs contribute significantly to the spectrum. Additional HESS observations near minimum flux would be welcomed.

The orbital modulation of the HESS emission is easily reproduced. A well-defined peak is predicted between phases 0.7-0.9 for which evidence may already be seen in the data. The lightcurve at GLAST energies is anti-correlated with the HESS lightcurve and has a peak at periastron, where the stellar photon density is maximum, and a minimum at inferior conjunction because of the anisotropic effects in inverse Compton scattering. The GLAST spectrum below 1 GeV should be influenced by the tail of the synchrotron emission from the highest energy electrons. The peak synchrotron emission is at about 100 MeV for maximally accelerated electrons, regardless of magnetic field. Hence, if this component is detected, it will provide evidence that electrons are indeed accelerated with extreme efficiency in this source.

Similar results for the magnetic field intensity and particle energy are found when a lower inclination is used, i.e. implying a black hole compact object rather than a neutron star. In this case, the emission is thought to arise from a relativistic jet powered by accretion onto the black hole. Within the assumptions of this work on the particle distribution, it is difficult to argue that a significant part of the emission occurs far along a jet since this does not naturally reproduce neither the spectrum nor the lightcurve measured by HESS. Most of the emission should

still occur close to the compact object. However, unlike in the case of a pulsar wind nebula, there is no independent theoretical expectations in support of the magnetic field intensity (certainly smaller than its equipartition value in the accretion flow) and particle energy that are derived. Therefore, the pulsar wind nebula model appears favoured independently of other possible considerations.

Despite the complexity of the phenomena involved in pulsar wind nebula emission, it is found that the peculiar environment of a gamma-ray binary, most prominently the enormous luminosity of the massive companion, severely constrains the number of degrees-of-freedom in the model. A simple model suffices to reproduce most of the observations. The value of the magnetic field at the shock is found to be tightly constrained by the HESS observations to 0.8 ± 0.2 G and the injection spectrum slope to $p = 2 \pm 0.3$. These results confirm that gamma-ray binaries are promising sources to study the environment of pulsars on very small scales.

Acknowledgements. GD acknowledges support from the *Agence Nationale de la Recherche* and comments on an early draft from B. Giebels.

References

- Aharonian, F., Akhperjanian, A. G., Aye, K.-M., et al. 2005a, *Science*, 309, 746
Aharonian, F., Akhperjanian, A. G., Aye, K.-M., et al. 2005b, *A&A*, 442, 1
Aharonian, F., Akhperjanian, A. G., Bazer-Bachi, A. R., et al. 2006, *A&A*, 460, 743
Albert, J., Aliu, E., Anderhub, H., et al. 2006, *Science*, 312, 1771
Albert, J., Aliu, E., Anderhub, H., et al. 2007, *ArXiv e-prints*, 706
Ball, L. & Kirk, J. G. 2000, *Astroparticle Physics*, 12, 335
Bednarek, W. 2007, *A&A*, 464, 259
Blumenthal, G. R. & Gould, R. J. 1970, *Reviews of Modern Physics*, 42, 237
Böttcher, M. & Dermer, C. D. 2005, *ApJ*, 634, L81
Casares, J., Ribó, M., Ribas, I., et al. 2005, *MNRAS*, 364, 899
Dermer, C. D. & Böttcher, M. 2006, *ApJ*, 643, 1081
Dhawan, V., Mioduszewski, A., & Rupen, M. 2006, in VI Microquasar Workshop: Microquasars and Beyond, PoS (MQW6) 52
Dubois, R. 2006, in VI Microquasar Workshop: Microquasars and Beyond, PoS (MQW6) 68
Dubus, G. 2006a, *A&A*, 451, 9
Dubus, G. 2006b, *A&A*, 456, 801
Fargion, D., Konoplich, R. V., & Salis, A. 1997, *Z. Phys. C.*, 74, 571
Hartman, R. C., Bertsch, D. L., Bloom, S. D., et al. 1999, *ApJS*, 123, 79
Ho, C. & Epstein, R. I. 1989, *ApJ*, 343, 277
Jones, F. C. 1968, *Physical Review*, 167, 1159
Manchester, R. N., Johnston, S., Lyne, A. G., et al. 1995, *ApJ*, 445, L137
Maraschi, L. & Treves, A. 1981, *MNRAS*, 194, 1P
Martocchia, A., Motch, C., & Negueruela, I. 2005, *A&A*, 430, 245
Moderski, R., Sikora, M., Coppi, P. S., & Aharonian, F. 2005, *MNRAS*, 363, 954
Paredes, J. M., Bosch-Ramon, V., & Romero, G. E. 2006, *A&A*, 451, 259
Paredes, J. M., Martí, J., Ribó, M., & Massi, M. 2000, *Science*, 288, 2340
Sazonov, S. Y. & Sunyaev, R. A. 2000, *A&A*, 354, L53
Tavani, M., Arons, J., & Kaspi, V. M. 1994, *ApJ*, 433, L37

Appendix A: Inverse Compton spectrum for a mono-energetic beam of photons

The purpose of this Appendix is first to carry out the integration set out in Eq. (5) and second to give an expression valid in the Klein-Nishina regime for the total spectrum emitted by a single electron scattering a mono-energetic beam of photons (Eq. 7). The fraction of scattered photons per time, energy and steradian is given by Eq. (6), which can be expanded using Eqs. (1-5)

$$\frac{dN}{dt d\epsilon_1 d\Omega_1} = \frac{r_e^2 c (1 - \beta\mu_0)}{2\gamma_e (1 - \beta\mu_1)} \iiint \left(\frac{\epsilon'_1}{\epsilon'} \right)^2 \left(\frac{\epsilon'_1}{\epsilon'} + \frac{\epsilon'}{\epsilon'_1} - \sin^2 \Theta' \right) \delta(\epsilon' - \epsilon'_0) \delta(\mu' - \mu'_0) \delta(\phi' - \phi'_0) \delta \left(\epsilon'_1 - \frac{\epsilon'}{1 + \frac{\epsilon'}{m_e c^2} (1 - \mu_{\Theta'})} \right) d\epsilon' d\mu' d\phi' \quad (\text{A.1})$$

where primed (unprimed) quantities are measured in the electron (observer) frame, $\mu_{\Theta'} \equiv \cos \Theta' = \mu' \mu'_1 + \sin \theta' \sin \theta'_1 \cos(\phi'_1 - \phi')$, $\mu' = \cos \theta'$, $\mu_0 = \cos \theta_0$, $\mu'_0 = \cos \theta'_0$ etc. Re-arranging the last Dirac and performing the three integrations yields

$$\frac{dN}{dt d\epsilon_1 d\Omega_1} = \frac{r_e^2 c (1 - \beta\mu_0)}{2\gamma_e (1 - \beta\mu_1)} \left[1 + \mu_{\Theta_0}^2 + \left(\frac{\epsilon'_1}{m_e c^2} \right)^2 \frac{(1 - \mu_{\Theta_0})^2}{1 - \frac{\epsilon'_1}{m_e c^2} (1 - \mu_{\Theta_0})} \right] \delta \left(\frac{\epsilon'_1}{1 - \frac{\epsilon'_1}{m_e c^2} (1 - \mu_{\Theta_0})} - \epsilon'_0 \right). \quad (\text{A.2})$$

The integration over Ω_1 to obtain the full spectrum of radiation emitted by the electron is simplified if $\gamma_e \gg 1$. In that case,

$$\mu_{\Theta_0} = \mu'_0 \mu'_1 + \sin \theta'_0 \sin \theta'_1 \cos(\phi'_1 - \phi'_0) = \frac{\mu_0 - \beta}{1 - \beta\mu_0} \frac{\mu_1 - \beta}{1 - \beta\mu_1} + \frac{1}{\gamma_e^2} \frac{\sin \theta_1}{1 - \beta\mu_1} \frac{\sin \theta_0}{1 - \beta\mu_0} \cos(\phi_1 - \phi_0) \approx \mu'_0 \mu'_1, \quad (\text{A.3})$$

which is equivalent to saying the outgoing photon is emitted along the direction of electron motion when $\gamma_e \gg 1$. The last Dirac can then be rewritten as a function of μ_1 :

$$\frac{dN}{dt d\epsilon_1 d\Omega_1} = \frac{r_e^2 c (1 - \beta\mu_0)}{2\gamma_e (1 - \beta\mu_1)} \left[1 + \mu_{\Theta_0}^2 + \left(\frac{\epsilon'_1}{m_e c^2} \right)^2 \frac{(1 - \mu_{\Theta_0})^2}{1 - \frac{\epsilon'_1}{m_e c^2} (1 - \mu_{\Theta_0})} \right] \frac{\left[1 - \frac{\gamma_e \epsilon_1}{m_e c^2} (1 + \beta\mu'_0 - (\beta + \mu'_0)\mu_1) \right]^2}{\left| \beta\gamma_e \epsilon_1 + \frac{\epsilon_1^2}{m_e c^2} \mu'_0 \right|} \delta(\mu_1 - x) \quad (\text{A.4})$$

$$\text{with } x = \frac{1 - \frac{\epsilon'_0}{\gamma_e \epsilon_1} + \frac{\epsilon'_0}{m_e c^2} (1 + \beta\mu'_0)}{\beta + \frac{\epsilon'_0}{m_e c^2} (\beta + \mu'_0)}. \quad (\text{A.5})$$

The integration over Ω_1 is now straightforward, giving for the total spectrum:

$$\frac{dN}{dt d\epsilon_1} = \frac{\pi r_e^2 c (1 - \beta\mu_0)}{\gamma_e (1 - \beta x)} \left[1 + \left(\frac{x - \beta}{1 - x\beta} \right)^2 \mu_0'^2 + \left(\frac{\gamma_e \epsilon_1}{m_e c^2} \right)^2 \frac{\left[1 + \beta\mu'_0 - (\beta + \mu'_0)x \right]^2}{1 - \frac{\gamma_e \epsilon_1}{m_e c^2} \left[1 + \beta\mu'_0 - (\beta + \mu'_0)x \right]} \right] \frac{\left[1 - \frac{\gamma_e \epsilon_1}{m_e c^2} (1 + \beta\mu'_0 - (\beta + \mu'_0)x) \right]^2}{\left| \beta\gamma_e \epsilon_1 + \frac{\epsilon_1^2}{m_e c^2} \mu'_0 \right|}. \quad (\text{A.6})$$

Relativistic kinematics gives the domain of variation of the scattered photon energy ϵ_1 in the observer frame. The maximum ϵ_+ and minimum ϵ_- energies in the spectrum are :

$$\epsilon_{\pm} = \frac{(1 - \beta\mu_0) \epsilon_0}{1 + \frac{\epsilon_0}{\gamma_e m_e c^2} \pm \left[\beta^2 + 2\beta\mu_0 \left(\frac{\epsilon_0}{\gamma_e m_e c^2} \right) + \left(\frac{\epsilon_0}{\gamma_e m_e c^2} \right)^2 \right]^{1/2}} \quad (\text{A.7})$$

The angle dependence of the maximum energy in the Thomson regime is $(1 - \beta\mu_0)$. For high electron energies, in the Klein-Nishina regime, the maximum photon energy is limited to $\gamma_e m_e c^2$ and becomes almost independent of angle.

List of Objects

- 'LS 5039' on page 1
- 'PSR B1259-63' on page 1
- 'LSI +61°303' on page 1
- 'Cyg X-1' on page 1

5

High-energy emission from the unshocked pulsar wind

Outline

1. Direct emission from the pulsar wind in gamma-ray binaries?	84
2. What we want to know	85
3. Compton drag of the pulsar wind	85
§ 35. Assumptions and geometry	85
§ 36. Anisotropic inverse Compton cooling of pairs	86
§ 37. Calculation of the cooled Lorentz factor in binaries	87
§ 38. Lorentz factor profiles and maps in LS 5039 and LS I +61 303	90
§ 39. Finite-size star and thermal spectrum	91
4. Inverse Compton emission	92
§ 40. The density of pairs	92
§ 41. Inverse Compton spectrum	94
§ 42. Pair production	96
5. Size and geometry of the pulsar wind nebula	96
6. What if the pulsar wind is anisotropic?	98
§ 43. Anisotropic pulsar wind	98
§ 44. The pulsar orientation	99
§ 45. Lorentz factor maps	101
§ 46. What are the odds to observe a low Lorentz factor?	101
7. Free pulsar wind emission in LS 5039 and LS I +61 303	103
8. Signature of the unshocked wind seen by <i>Fermi</i> ?	104
9. Striped pulsar wind	107
10. What we have learned	108
11. [Français] Résumé du chapitre	109
§ 47. Contexte et objectifs	109
§ 48. Ce que nous avons appris	110
12. Spectral signature of a free pulsar wind in gamma-ray binaries	112

1. Direct emission from the pulsar wind in gamma-ray binaries?

PULSARS are compact ($R_{NS} \sim 10$ km), fast rotating ($P_{NS} \lesssim 1$ s) and highly magnetized ($B_{NS} \sim 10^{12}$ G) stars. The huge electric field induced by the rotation of the neutron star extracts and accelerates charged particles in the magnetosphere. This plasma of particles is released in a relativistic wind at the light cylinder where the magnetic field lines open, *i.e.* at a radius where the corotation velocity equal the speed of light $R_L = cP_{NS}/2\pi$. In the classical model of isolated pulsars like the Crab (see *e.g.* Rees & Gunn 1974; Kennel & Coroniti 1984a), part of the rotational energy of the pulsar is thought to be dissipated by a relativistic wind of electron-positron pairs and possibly ions. This wind is assumed to be radial and mono-energetic with an ultra-relativistic bulk Lorentz factor $\gamma_0 \sim 10^6$. The structure and the formation of pulsar winds are not well constrained and fully understood today (the interested reader should refer to the reviews by Gaensler & Slane 2006; Kirk *et al.* 2009 and references therein). The pulsar wind expands freely up to the termination shock (radius R_s , see Fig. 31) where pairs are isotropized, re-accelerated and radiate synchrotron radiation and upscatter ambient low energy photons to high energies.

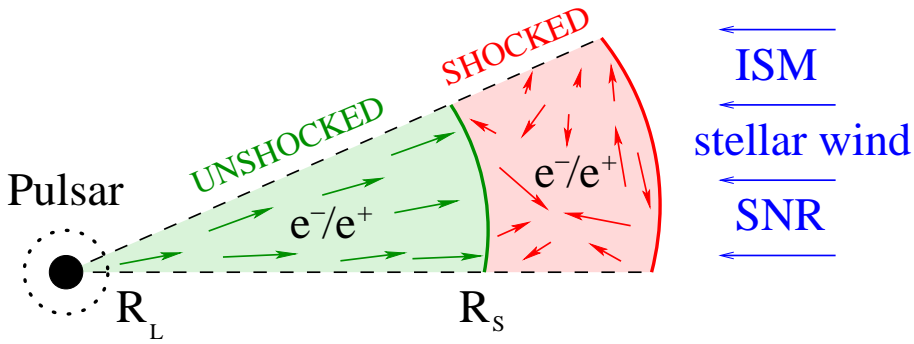


FIG. 31. Simplistic drawing of a pulsar wind. Relativistic pairs of electrons and positrons are generated and accelerated in the pulsar magnetosphere. The wind of pairs is released at the light cylinder radius (R_L) and expands radially and freely ("unshocked" pulsar wind) up to the termination shock ("shocked" pulsar wind) at a distance R_s . At the shock, pairs are re-accelerated and isotropized.

Upstream the termination shock, particles do not radiate synchrotron radiation because the magnetic field is frozen into the relativistic flow of pairs. For this reason, the unshocked pulsar wind region was thought to be non-observable. Nevertheless, inverse Compton scattering between the pairs and the ambient soft radiation should occur in this zone. Because of the high Lorentz factor of the wind, the spectral signature of an emitting free pulsar wind should be directly observed in the gamma-ray energy band. In isolated pulsars, soft radiation can come from the nebula itself (synchrotron, or thermal emission) or from the Cosmological Microwave Background (CMB) but these sources of photons are too tenuous to produce a detectable gamma-ray signal. Bogovalov & Aharonian (2000) considered the thermal radiation from the neutron star surface in the Crab nebula and predicted a line-like Compton signature in gamma rays and put constraints on the size of the kinetic energy dominated wind region.

In the pulsar wind nebula scenario, gamma-ray binaries are composed of an energetic pulsar (See Chapter 1). In such systems, the massive companion star provides a huge density of target soft radiation for inverse Compton scattering ($n_* \sim 10^{14}$ ph cm^{-3} at the compact object location

in LS 5039). The Compton emission from the unshocked pulsar wind should be very strong. The density of Cosmological Microwave Background (CMB) photons is very small compared with the stellar photon density ($n_{CMB} \sim 10^3 \text{ ph cm}^{-3} \ll n_*$) and can be ignored. Thermal X-ray photons from the neutron star surface can be ignored as well here ($n_{NS} < n_*$ at the light cylinder if $R_L > R_{NS}/R_* (T_{NS}/T_*)^{3/2} d$, i.e. if $P_{NS} \gtrsim 75 \text{ ms}$ in LS 5039). In addition, inverse Compton collisions with pairs in the wind would occur close to rear-end in this case, hence very inefficient.

Gamma-ray binaries appear as ideal objects for the study of pulsar winds at small scales (sub-AU scales, to be compared with $\sim 0.1 \text{ pc}$ for a typical isolated pulsar wind nebula). We investigate in this chapter whether the emission from an unshocked pulsar wind could be expected and observed today in gamma-ray binaries. Ball & Kirk (2000) studied the emission in the binary PSR B1259–63 and PSR J0045–73. We compute here the Compton emission in tighter systems which are LS 5039 and LS I +61°303 where the gamma-ray signal should be even stronger. The aim of this work is to put constraints on the parameters of the wind such as the energy of pairs, the size and structure of the wind.

This chapter is organized as follow. I first quantify the cooling of particles in the wind by anisotropic inverse Compton scattering (Sect. 3). The equations to compute the emitted spectrum seen by a distant observer are derived (Sect. 4). Then, I compute the expected gamma-ray spectrum from the unshocked pulsar wind in LS 5039 and LS I +61°303 (Sect. 7). These results are discussed in the context of *Fermi* observations (Sect. 8) and in the context of alternative models for the pulsar wind emission (Sect. 9). My results and conclusions of this study are presented in the paper Cerutti *et al.* (2008b), fully included here in Sect. 12.

2. What we want to know

- What is the signature of the free pulsar wind emission in gamma-ray binaries?
- Is this emission detected/detectable?
- What constraints can we put on the physics of pulsar winds?

3. Compton drag of the pulsar wind

§ 37. Assumptions and geometry

The pulsar is assumed to produce a radial and isotropic wind of electron-positron pairs with an initial (before cooling) bulk Lorentz factor γ_0 . Pairs cool down *via* inverse Compton scattering on photons from the massive star. Other sources of soft radiation are ignored (CMB, neutron star). The pulsar wind is decelerated and radiates high-energy photons whose energy depends on the energy of the injected pairs γ_0 . Because of the angular dependence of the inverse Compton scattering efficiency, the cooling of pairs depends strongly on the angle θ_0 between the line joining the star to the electron position in the wind and its direction of motion (see Fig. 32). The radiation from the unshocked pulsar wind will be highly anisotropic.

Let's define some geometrical quantities useful for the following calculations. The distance of the electron to the massive star R is

$$r + l_1 = d \cos \psi \quad l_2 = d \sin \psi \quad \Rightarrow \quad R^2 = d^2 + r^2 - 2rd \cos \psi, \quad (37.153)$$

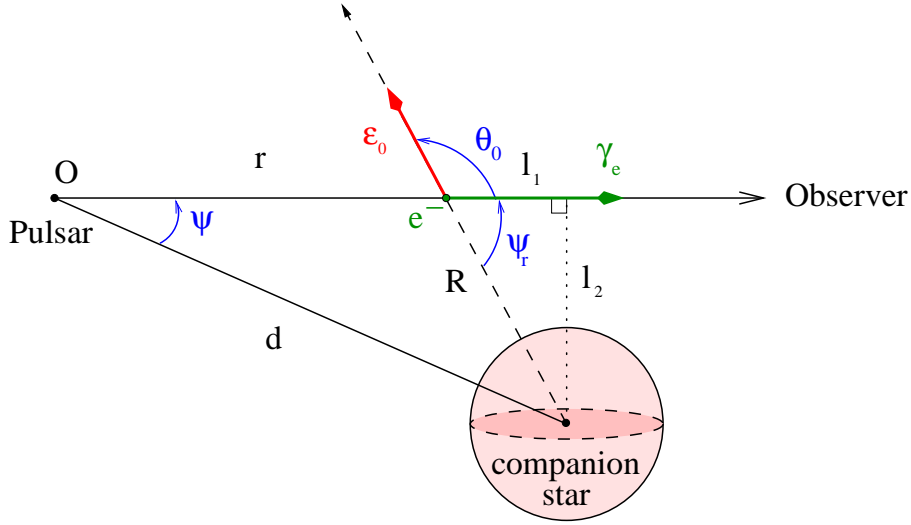


FIG. 32. This diagram depicts the binary system and the geometrical quantities used in the following. An electron from the wind with a Lorentz factor γ_e situated at a distance r from the pulsar and R from the companion star, interacts with a stellar photon of energy ϵ_0 .

and the cosine of the angle between the massive star center and the electron direction of motion can be expressed as (Fig. 32)

$$\cos(\pi - \theta_0) = \frac{l_1}{R} \quad \Rightarrow \quad \cos \theta_0 \equiv \mu_0 = \frac{r - d \cos \psi}{\sqrt{d^2 + r^2 - 2rd \cos \psi}}. \quad (37.154)$$

It is also convenient to define the angle $\psi_r = \pi - \theta_0$ such as

$$\psi_r = \arctan \left(\frac{d \sin \psi}{d \cos \psi - r} \right) \quad (37.155)$$

if $r < d \cos \psi$ and

$$\psi_r = \pi + \arctan \left(\frac{d \sin \psi}{d \cos \psi - r} \right) \quad (37.156)$$

if $r > d \cos \psi$.

§ 38. Anisotropic inverse Compton cooling of pairs

In this section, we aim to derive the energy loss of an electron of total energy E_e in an anisotropic and mono-energetic photon field of density n_* ph cm^{-3} and energy ϵ_0 . As presented in Chapter 2 (see Eq. 5.8), the power lost by the electron is

$$-\frac{dE_e}{dt} = -m_e c^2 \frac{d\gamma_e}{dt} = \int_{\epsilon_-}^{\epsilon_+} (\epsilon_1 - \epsilon_0) n_* \frac{dN}{dt d\epsilon_1} d\epsilon_1, \quad (38.157)$$

where $dN/dt d\epsilon_1$ is the Compton kernel. This formula can be extended as

$$-\frac{dE_e}{dt} = -\epsilon_0 n_* \int_{\epsilon_-}^{\epsilon_+} \frac{dN}{dt d\epsilon_1} d\epsilon_1 + n_* \int_{\epsilon_-}^{\epsilon_+} \epsilon_1 \frac{dN}{dt d\epsilon_1} d\epsilon_1. \quad (38.158)$$

In the Thomson regime, the power lost by the electron can be computed exactly. Using the exact anisotropic Thomson kernel (Eq. 18.98) and defining the $y = \epsilon_1/\epsilon_0 (1 - \beta\mu_0)$, the first term

(scattering rate) is given by

$$\int_{\epsilon_-}^{\epsilon_+} \frac{dN}{dt d\epsilon_1} d\epsilon_1 = \frac{\pi r_e^2 c}{2\beta\gamma_e^2} (1 - \beta\mu_0) \int_{\frac{1}{1+\beta}}^{\frac{1}{1-\beta}} \left[3 - \mu_0'^2 + \frac{1}{\beta^2} (3\mu_0'^2 - 1) \left(\frac{y}{\gamma_e^2} - 1 \right)^2 \right] dy. \quad (38.159)$$

Performing the integral leads to the expression of the anisotropic scattering rate

$$\frac{dN}{dt} = \sigma_{TC} (1 - \beta\mu_0). \quad (38.160)$$

Similarly, the computation of the second term (mean energy loss by collision) in Eq. (38.158) gives

$$\int_{\epsilon_-}^{\epsilon_+} \epsilon_1 \frac{dN}{dt d\epsilon_1} d\epsilon_1 = \sigma_{TC} (1 - \beta\mu_0)^2 \epsilon_0 \gamma_e^2. \quad (38.161)$$

The total anisotropic Compton losses for an electrons in the Thomson regime is

$$-\frac{dE_e}{dt} = \sigma_{TC} n_* (1 - \beta\mu_0) \epsilon_0 \{ (1 - \beta\mu_0) \gamma_e^2 - 1 \} \quad (38.162)$$

and is proportional to γ_e^2 as in the isotropic case (see Eq. 5.9). In the general case, including Klein-Nishina effects, Eq. (38.157) is solved numerically. In the deep Klein-Nishina regime, the Compton cooling of pairs is less efficient due to the decline of the cross-section (see Fig. 33).

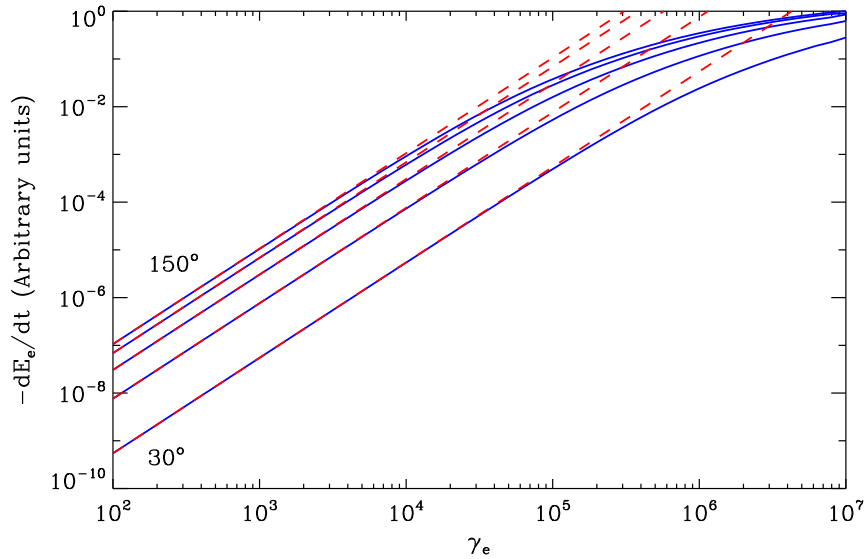


FIG. 33. Total energy losses per electron (blue solid line) as a function of the energy, where $\epsilon_0 = 1$ eV and $\theta_0 = 30^\circ$ (bottom), 60° , 90° , 90° and 150° (top). The analytical formula in the Thomson regime Eq. (38.162) is shown for comparison (red dashed line).

§ 39. Calculation of the cooled Lorentz factor in binaries

The Compton cooling of pairs decelerates the pulsar wind. Assuming that the pairs remain highly relativistic after the cooling $\gamma_e \gg 1$, the Lorentz factor of the wind at any position $\gamma_e(r, \psi)$

in the system can be obtained by solving the first order differential equation

$$\frac{d\gamma_e}{dt} = \frac{d\gamma_e}{dr} \underbrace{\frac{dr}{dt}}_{\approx c} \Rightarrow \frac{d\gamma_e}{dr} = -\frac{1}{m_e c^3} \int_{\epsilon_-}^{\epsilon_+} (\epsilon_1 - \epsilon_0) n_* \frac{dN}{dt d\epsilon_1} d\epsilon_1. \quad (39.163)$$

In the point-like and mono-energetic star approximation, the stellar density of photons is given by

$$n_* = \frac{L_*}{4\pi c \bar{\epsilon}_0 R^2}, \quad (39.164)$$

where $L_* = 4\pi R_*^2 \sigma_{SB} T_*^4$ is the luminosity of the massive star and $\bar{\epsilon}_0 \approx 2.7kT_*$ is the mean energy of the soft stellar radiation (for black-body distribution). Eq. (39.163) can be rewritten like

$$\boxed{\frac{d\gamma_e}{dr} = -\frac{1}{m_e c^3} \frac{L_*}{4\pi c R^2} \int_{\epsilon_-}^{\epsilon_+} \left(\frac{\epsilon_1 - \bar{\epsilon}_0}{\bar{\epsilon}_0} \right) \frac{dN}{dt d\epsilon_1} d\epsilon_1}. \quad (39.165)$$

Chernyakova & Illarionov (1999) found an analytical formula to this equation in the Thomson regime. This solution is compatible with the numerical calculation. Ball & Kirk (2000) found a simple expression for Eq. (39.165) in the general case including Klein-Nishina effects for $\gamma_e \gg 1$ given by

$$\frac{d\gamma_e}{dr} = -\frac{r_e^2 L_*}{4m_e c^3 d^2} \left(\frac{e'_0}{e_0} \right)^2 \left(\frac{1 - \mu_0^2}{\sin^2 \psi} \right) \left(1 - \frac{e_0}{\gamma_e e'_0} - \frac{e_0}{\gamma_e} \right) F_{loss}(e'_0) \quad (39.166)$$

in which

$$e_0 = \frac{\epsilon_0}{m_e c^2} \quad e'_0 = \gamma_e e_0 (1 - \beta \mu_0) \quad (39.167)$$

and where F_{loss} is a function defined by Jones (1965)

$$F_{loss}(x) = \frac{-2x(10x^4 - 51x^3 - 93x^2 - 51x - 9)}{3x^4(1+2x)^3} + \frac{(x^2 - 2x - 3) \ln(2x + 1)}{x^4}. \quad (39.168)$$

This expression was also found compatible with the numerical solution. To solve the differential equation in Eq. (39.165), I used a simple Runge-Kutta 4 method. It is more convenient and numerically more stable to perform the integration over the angle ψ_r (Fig. 32) rather than r such as

$$\frac{d\gamma_e}{d\psi_r} = \frac{d\gamma_e}{dr} \times \frac{dr}{d\psi_r} = \frac{d\gamma_e}{dr} \times \frac{\sin \psi}{\sin^2 \psi_r}. \quad (39.169)$$

Results are presented in the next section.

At this stage, it is important to note that we implicitly assumed that the Compton cooling of pairs is a continuous process. However, this assumption holds only in the Thomson regime ($\Delta E_e \ll E_e$). In the Klein-Nishina regime, pairs lose almost all their energy in a single collision ($\Delta E_e \sim E_e$). Our approach here is not appropriate at very high-energy and the full integro-differential equations given in *e.g.* Blumenthal & Gould (1970) should be used. The energy distribution of the cooled pairs will be broader. I thank the anonymous referee of the article Cerutti *et al.* (2008b) for drawing my attention to this effect. The calculation of continuous losses, though incorrect, remains a rather good approximation in the Klein-Nishina regime (Zdziarski 1989; Moderski *et al.* 2005), particularly if the energy distribution of the injected pairs is broad. We discuss this effect into more details in the chapter dedicated to one-dimensional pair cascade (see Chapter 7, Sect. 8).

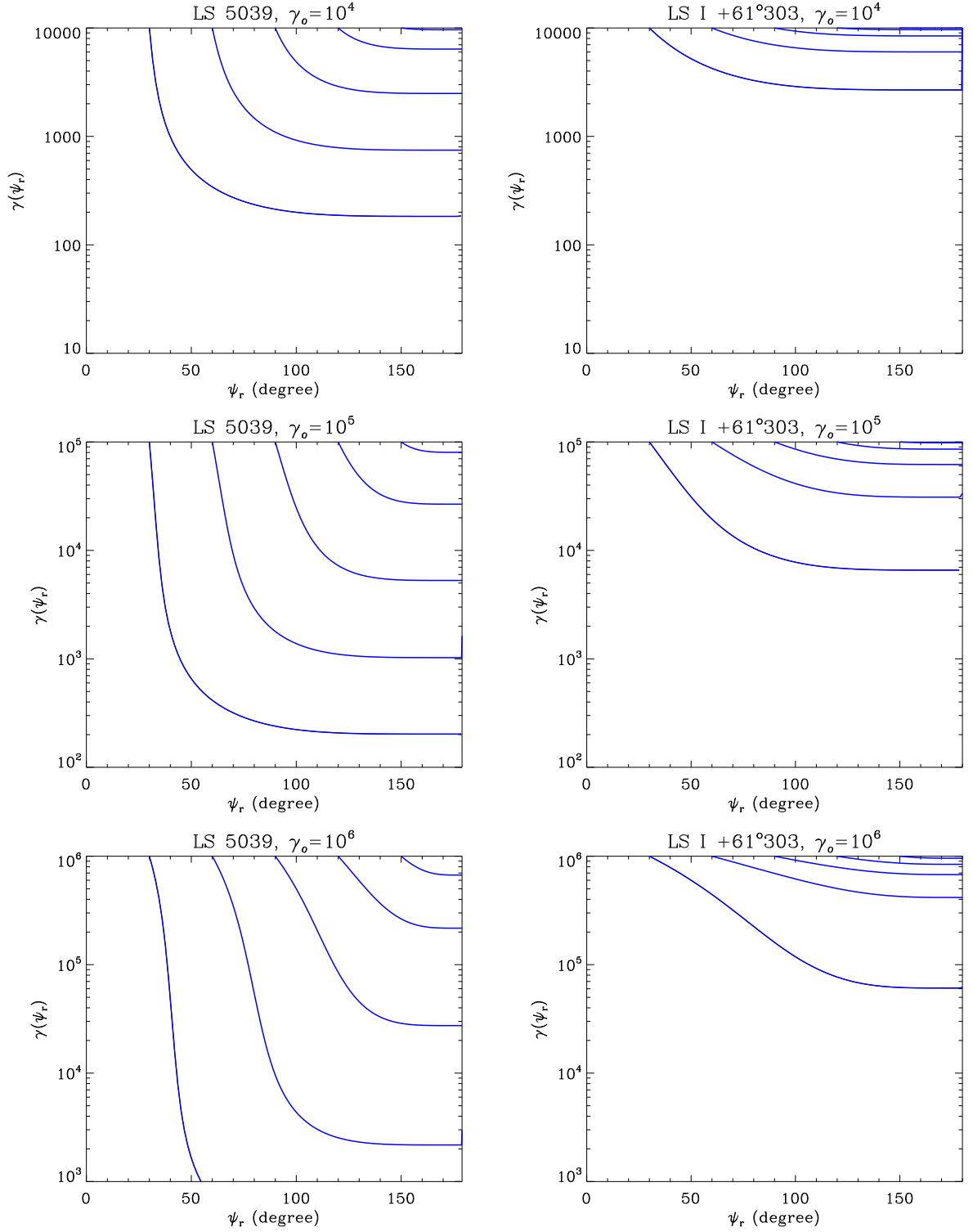


FIG. 34. Lorentz factor of the pairs in the pulsar wind as a function of ψ_r , for $\psi = 30^\circ$ (*bottom* lines), 60° , 90° , 120° and 150° (*top* lines), applied to LS 5039 (*left* panels) and LS I +61°303 (*right* panels). Pairs are injected by the pulsar at a Lorentz factor $\gamma_0 = 10^4$ (*top* panels), 10^5 and 10^6 (*bottom* panels). The massive star is assumed point-like and mono-energetic and both winds (pulsar and star) are assumed spherical and isotropic.

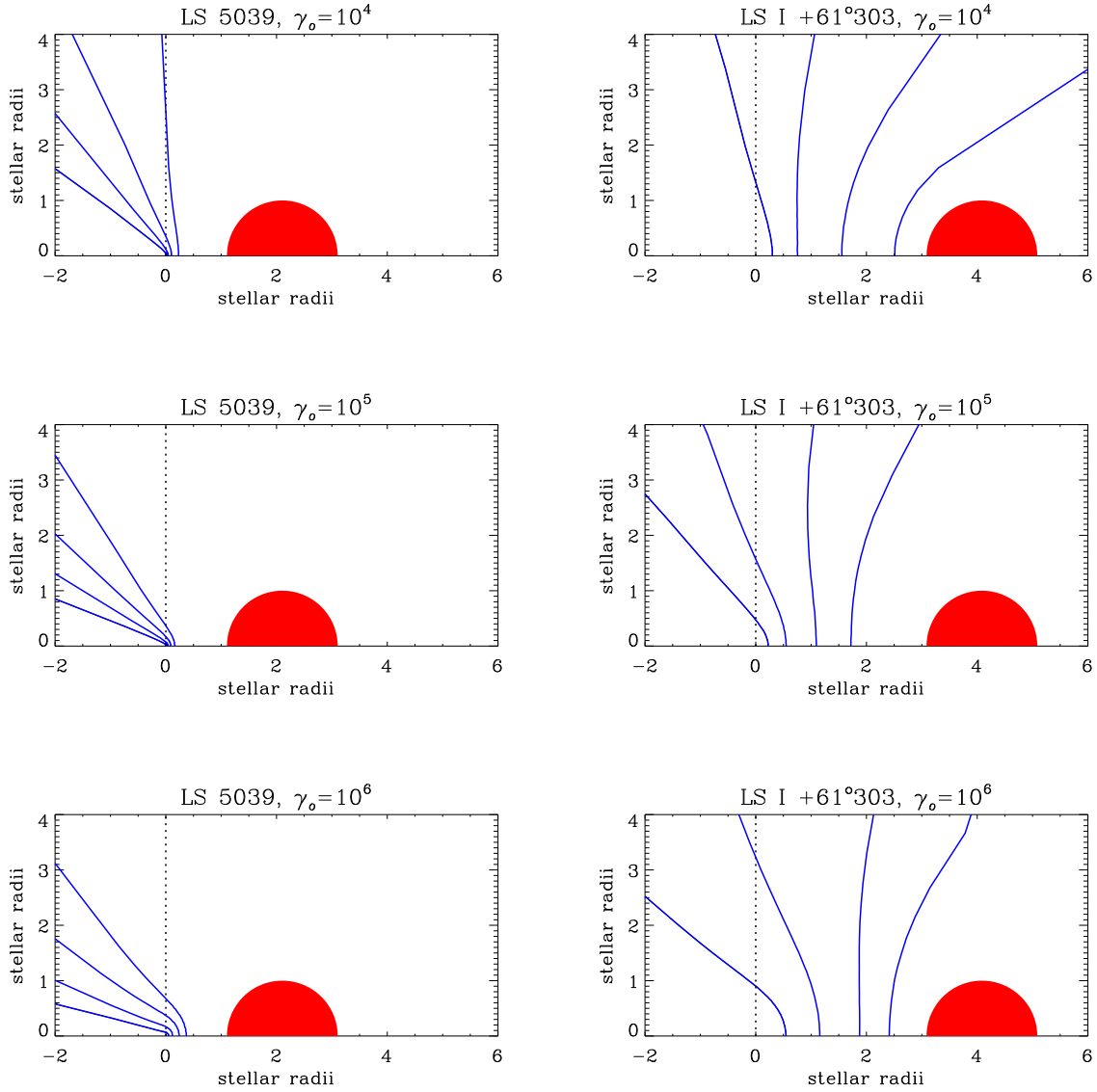


FIG. 35. These maps show the spatial distribution of the cooled Lorentz factor of the wind in LS 5039 (*left panels*) and LS I +61°303 (*right panels*) at periastron. Each line gives the fraction of the energy left in the pairs after Compton cooling: 90% (*left lines*), 50%, 10% and 1% (*right lines*) of the injected Lorentz factor γ_0 . The massive star is shown by a red semi disk.

§ 40. Lorentz factor profiles and maps in LS 5039 and LS I +61 303

The Lorentz factor of the pairs in the wind is shown in Fig. 34 as a function of the distance to the pulsar (indirectly given by ψ_r) for different viewing angles ψ applied to LS 5039 and LS I +61°303. For $\psi < \pi/2$, the Compton drag of the wind is very efficient since stellar photons collide with the pairs almost head-on. Also, as the electron propagates towards the massive star the density of soft photon increases. Most of the wind energy is radiated for $\psi_r < \pi/2$. The Compton cooling is stronger in LS 5039 as the massive star is more luminous and closer to the compact object than in LS I +61°303.

The maps in Fig. 35 gives a better idea of the effect of the Compton drag of the pulsar wind. These maps are computed by solving Eq. (39.165). Each line represents the fraction of energy left in the wind in both gamma-ray binaries. These calculations are similar to those carried out by Ball & Kirk (2000) for PSR B1259–63 and PSR J0045–73. The profiles are rotationally symmetric about the line joining the pulsar and the optical star because both winds are assumed spherical and isotropic. The effect of an anisotropic pulsar wind is discussed in Sect. 6.

These calculations show that a significant fraction of the energy of the pulsar wind can be lost in these tight systems if the wind is assumed unterminated. We will investigate the effect of a truncated wind in Sect. 5.

§ 41. Finite-size star and thermal spectrum

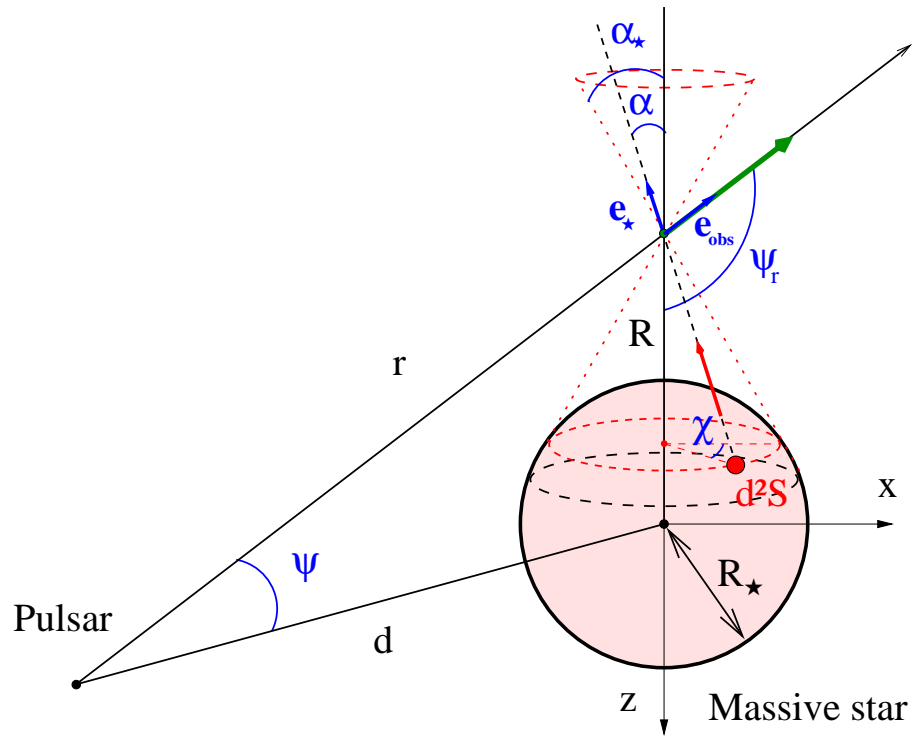


FIG. 36. For a finite-size star, the relativistic electron (at the distance r) sees stellar photons originating within a cone of semi-aperture angle $\alpha_* = \arcsin(R_*/R)$ (red dashed line).

It is more realistic to take into account the finite size and the thermal spectrum of the companion star. Eq. (39.165) should contain two extra integrations, one over the angular distribution of soft photons from the stellar surface and one over their energy distribution.

- In the black body approximation and neglecting emission and absorption lines, the stellar photon density $dn_*/d\epsilon_0 d\Omega_*$ (in $\text{ph cm}^{-3} \text{s}^{-1} \text{sr}^{-1}$) is

$$\frac{dn_*}{d\epsilon_0 d\Omega_*} = \frac{2}{h^3 c^3} \frac{\epsilon_0^2}{\exp\left(\frac{\epsilon_0}{kT_*}\right) - 1}. \quad (41.170)$$

- If the star is assumed spherical, stellar photons are distributed within the cone defined by the star with the electron at apex of semi-aperture angle $\alpha_* = \arcsin(R_*/R)$. The cosine of the

angle between the photons and the electrons μ_0 has to be expressed as a function of the spherical angle α and χ (see Fig. 36). Defining \mathbf{e}_{obs} the unit vector along the direction of motion of the electron directed towards the observer and \mathbf{e}_* the unit vector along the direction of propagation of the soft photon such as

$$\mathbf{e}_* = \begin{pmatrix} -\sin \alpha \cos \chi \\ -\sin \alpha \sin \chi \\ -\cos \alpha \end{pmatrix} \quad \mathbf{e}_{\text{obs}} = \begin{pmatrix} \sin \psi_r \\ 0 \\ \cos \psi_r \end{pmatrix}, \quad (41.171)$$

hence

$$\mu_0 = \mathbf{e}_* \cdot \mathbf{e}_{\text{obs}} = -\cos \psi_r \cos \alpha - \sin \psi_r \sin \alpha \cos \chi. \quad (41.172)$$

The massive star covers the solid angle

$$\Omega_* = \int_{\Omega_*} d\Omega_* = \int_0^{\alpha_*} \int_0^{2\pi} \cos \alpha \sin \alpha d\alpha d\chi = \pi \left(\frac{R_*}{R} \right)^2. \quad (41.173)$$

In the finite-size and black body star case, the complete differential equation to solve is given by

$$\frac{d\gamma_e}{dr} = -\frac{1}{m_e c^3} \iiint (\epsilon_1 - \epsilon_0) \frac{dn_*}{d\epsilon_0 d\Omega_*} \frac{dN}{dt d\epsilon_1} d\epsilon_1 d\epsilon_0 d\Omega_*. \quad (41.174)$$

Fig. 37 shows the effect of the black-body spectrum and the finite size of the star on the Compton drag of the pulsar wind. These calculations reveal that the simple case of a mono-energetic and point-like star is a good approximation as differences with the more realistic case are small. A more detailed discussion is provided in Cerutti *et al.* (2008b) (see Sect. 2.2 in this article) but is not essential in the following.

4. Inverse Compton emission

The previous section provides the amount of energy radiated by the electrons in the wind. We would like here to compute the full spectrum of the scattered radiation. We first need to know the density of pairs injected by the pulsar in the wind. The aim of this part is to derive the equations for spectral calculations. The results applied to LS 5039 and LS I +61°303 along the orbit are presented and discussed below in Sect. 7.

§ 42. The density of pairs

We assume here that the total luminosity of the pulsar L_p (in erg s^{-1}) is converted into a relativistic wind of pairs, so that

$$L_p = \iint E_e \frac{dN_e}{dE_e dt d\Omega_e} dE_e d\Omega_e, \quad (42.175)$$

where $dN_e/dE_e dt d\Omega_e$ is the density of pairs injected by the pulsar in $\text{erg}^{-1} \text{s}^{-1} \text{sr}^{-1}$. If the wind is radial and isotropic

$$L_p = 4\pi m_e c^3 \int \frac{dN_e}{d\gamma_e dr d\Omega_e} \beta_e \gamma_e d\gamma_e \quad (42.176)$$

In the mono-energetic pulsar wind approximation, the electron density is

$$\frac{dN_e}{d\gamma_e dr d\Omega_e} = K_e \delta(\gamma_e - \gamma_e(r)), \quad (42.177)$$

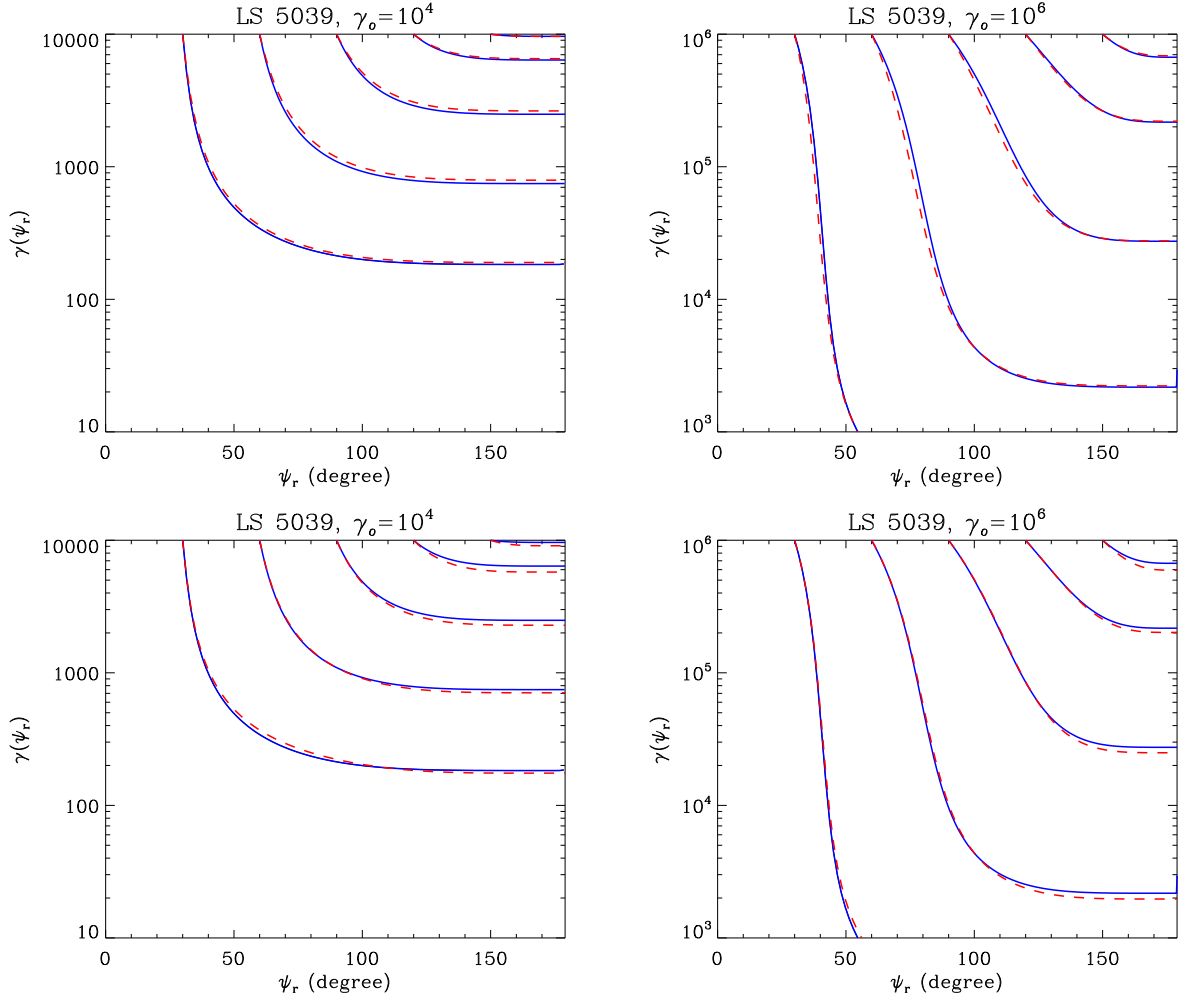


FIG. 37. Cooling of the pulsar wind in LS 5039 for $\gamma_0 = 10^4$ (left panels) and 10^6 (right panels). The solutions for a mono-energetic and point-like star (blue solid lines) are compared with the solutions for a black-body star (red dashed lines, top panels) and a finite-size star (red dashed lines, bottom panels).

where K is a normalization constant. Injecting this density in Eq. (42.176) and if at $r = 0$ we have $\gamma_e(0) = \gamma_0$, thus

$$K_e = \frac{L_p}{4\pi m_e c^3 \beta_0 \gamma_0}. \quad (42.178)$$

For an injection of pairs with a power-law energy distribution

$$\frac{dN_e}{d\gamma_e dr d\Omega_e}(r=0) = K_e \gamma_0^{-p}, \quad \gamma_- < \gamma_0 < \gamma_+, \quad (42.179)$$

the normalisation constant is (if $p \neq 2$ and $\gamma_e \gg 1$, $\beta_e \approx 1$)

$$K_e = \frac{(2-p)L_p}{4\pi m_e c^3 (\gamma_+^{2-p} - \gamma_-^{2-p})}, \quad (42.180)$$

and

$$K_e = \frac{L_p}{4\pi m_e c^3 \ln(\gamma_+/\gamma_-)} \quad (42.181)$$

if $p = 2$.

§ 43. Inverse Compton spectrum

For the computation of the gamma-ray emission from the wind, we assume that each electron scatters all photons in their direction of motion in the observer's frame (Fig. 38). This is a very good approximation since ultra-relativistic ($\gamma_e \gg 1$) pairs emit most of their radiation within a cone of semi-aperture angle $\theta \sim 1/\gamma_e \ll 1$ (see Chapter 3, § 20). This assumption will be always fulfilled in the following.

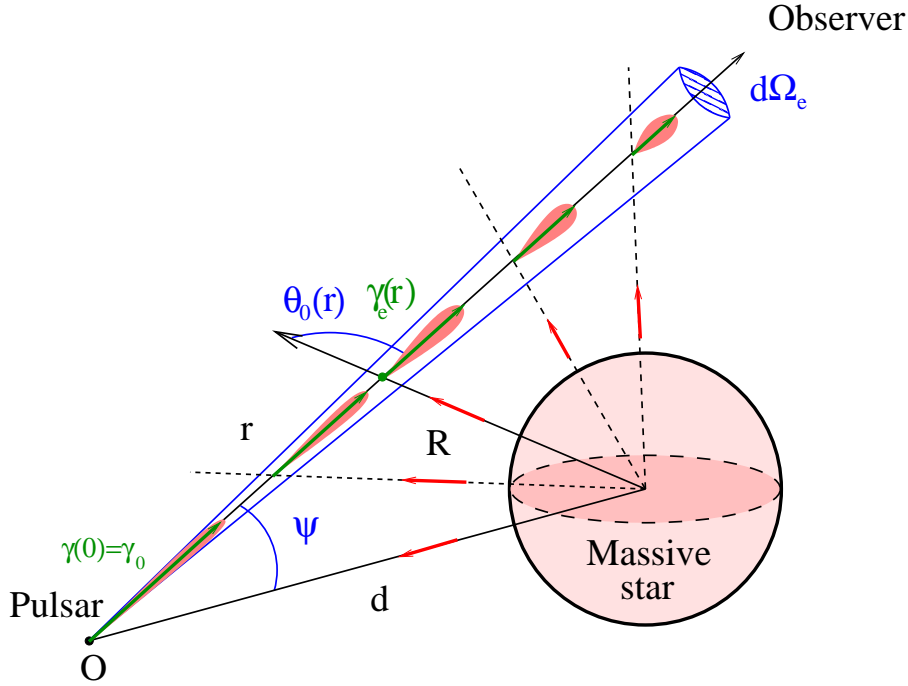


FIG. 38. The observer sees only the radiation from the pairs aligned with the line of sight due to relativistic Doppler beaming effect. Because of the anisotropy of the radiation field set by the massive star, the gamma-ray emission depends strongly on the viewing angle ψ .

Pairs in the wind radiate *via* inverse Compton scattering along the line of sight. In the collision, soft photons transfer transverse momentum to the electrons and heat the wind. This effect was shown to be small for an ultra-relativistic wind by Ball & Kirk (2000). We will assume that the wind remains cold. Thus, the number of pairs is kept constant along the line of sight (neglecting pair production). The overall observed emission from the unshocked pulsar wind is the superposition of the radiation from each electron along the line joining the pulsar to a distant observer (Fig. 38). The total number of photons scattered per unit of time, energy ϵ_1 and per unit of solid angle Ω_e depends on the density of electrons in the wind along the line of sight and on the soft photon density. As noticed in Sect. § 39, it is easier to perform the integration over ψ_r rather than r . In the point-like and mono-energetic star approximation, the emitted spectrum is (neglecting pair production)

$$\frac{dN}{dt d\epsilon_1 d\Omega_e} = \int_{\psi}^{\pi} \int_{\gamma_e} \frac{dN_e}{d\gamma_e dr d\Omega_e} n_* \frac{dN}{dt d\epsilon_1} \frac{\sin \psi d}{\sin^2 \psi_r} d\gamma_e d\psi_r. \quad (43.182)$$

If the pulsar wind is mono-energetic, the inverse Compton spectrum is line-like centered at an energy which depends on the injected Lorentz factor of the pairs γ_0 and whose amplitude

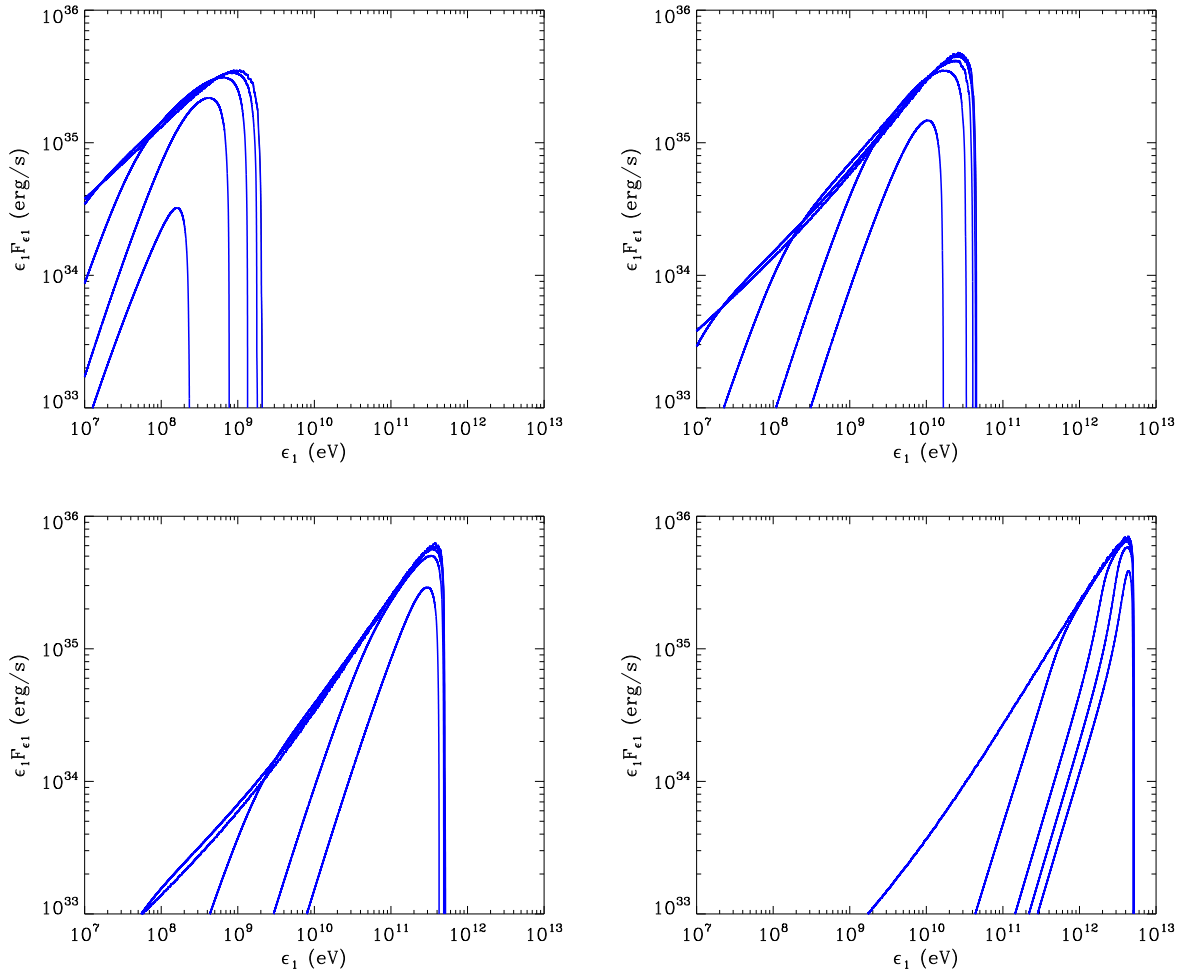


FIG. 39. Inverse Compton spectrum emitted by an unterminated and mono-energetic pulsar wind in LS 5039 at periastron ($d \approx 0.1$ AU) with $L_p = 10^{36} \text{ erg s}^{-1}$ at a distance of 2.5 kpc. Pairs are injected with a Lorentz factor $\gamma_0 = 10^4$ (top left), 10^5 (top right), 10^6 (bottom left) and 10^7 (bottom right). For each energy, the wind is seen with a viewing angle $\psi = 30^\circ$ (top line), 60° , 90° , 120° , and 150° (bottom line). Pair production is ignored.

depends on the pulsar luminosity L_p (Fig. 39). This peak is broadened by the cooling of pairs and becomes sharper with increasing energy. Also, the gamma-ray radiation depends strongly on the viewing angle. The Compton emission line is stronger for small viewing angles since Compton scattering is more efficient. This angular dependence is smaller in the Klein-Nishina regime ($\gamma_0 > 10^5$).

For $\psi < \pi/2$, a tail develops at lower energies where cooled particles re-radiate. For $\gamma_0 < 10^5$, these pairs cool down in the Thomson regime and form a power-law with an index in νF_ν close to 0.5. This is consistent with the cooling in the Thomson regime of a mono-energetic distribution of electrons (see Eq. 14.72). This power-law is harder if $\gamma_0 > 10^5$ because of Klein-Nishina effects. If the escaping timescale of the system $t_{esc} \sim d/c$ becomes smaller than the inverse Compton timescale t_{ic} , pairs have not enough time to radiate. This condition gives the low energy cut-off of the Compton emission from the wind. This feature appears clearly in Fig. 39 for $\psi = 90^\circ$ for instance at about 0.2 GeV for $\gamma_0 = 10^5$. If $\psi > \pi/2$, pairs escape directly

the system and have not enough time to re-radiate at lower energies and the low-energy cut-off reaches the high-energy cut-off, producing an even sharper line.

The effect of the finite size and the black-body spectrum of the companion star does not change significantly the emitted spectrum. In this case, the full inverse Compton spectrum is

$$\frac{dN}{dt d\epsilon_1 d\Omega_e} = \iiint \frac{dN_e}{d\gamma_e dr d\Omega_e} \frac{dn_\star}{d\epsilon_0 d\Omega_\star} \frac{dN}{dt d\epsilon_1} \frac{\sin \psi d}{\sin^2 \psi_r} d\gamma_e d\psi_r d\epsilon_0 d\Omega_\star. \quad (43.183)$$

§ 44. Pair production

Pair production between gamma rays produced in the wind and stellar photons acts if the energy of the emitted gamma rays are beyond the threshold energy for pair production (see Eq. 11.57), *i.e.* if $\epsilon_1 \geq 2m_e^2 c^4 / \epsilon_0 (1 - \cos \theta_0)$. The source of gamma rays under consideration here is spatially extended. Each point along the line of sight is a gamma-ray source. Pair production should then be computed at each point along the line of sight as well. The escaping gamma-ray spectrum seen by the observer is given by

$$\frac{dN_{abs}}{dt d\epsilon_1 d\Omega_e} = \iiint \frac{dN_e}{d\gamma_e dr d\Omega_e} \frac{dn_\star}{d\epsilon_0 d\Omega_\star} \frac{dN}{dt d\epsilon_1} e^{-\tau_{\gamma\gamma}(\psi_r)} \frac{\sin \psi d}{\sin^2 \psi_r} d\gamma_e d\psi_r d\epsilon_0 d\Omega_\star, \quad (44.184)$$

where $\tau_{\gamma\gamma}(\psi_r)$ is the gamma-ray opacity

$$\tau_{\gamma\gamma}(\psi_r) = \int_{\psi_r}^{\pi} \frac{d\tau_{\gamma\gamma}}{d\psi_r} d\psi_r. \quad (44.185)$$

Figure 40 shows the absorbed spectra in LS 5039 and LS I +61°303 at both conjunctions. The effect of pair production in PSR B1259–63 is very small (Dubus 2006a; Ball & Kirk 2000). The radiation from a cascade of pairs is neglected here but is fully considered and discussed in Chapter 7. $\gamma\gamma$ -absorption and inverse Compton emission are maximum at about the same orbital phases as both processes have almost the same angular dependence. In LS 5039 where pair production is very high, the very high-energy flux is maximum close to superior conjunction. This effect is weaker in LS I +61°303 and important only close to periastron where the soft photon density is maximum.

5. Size and geometry of the pulsar wind nebula

The pulsar wind has been considered as untruncated, *i.e.* propagating freely up to the observer. This assumption is probably incorrect in tight binaries. The interaction between the stellar and the pulsar wind leads to the formation of a shock separated by a contact discontinuity. If the stellar wind is strong, the pulsar wind can be confined close to the pulsar. The position and the shape of the shock depends on the ratio between the momentum of both winds. This quantity η is defined as (see *e.g.* Eichler & Usov 1993)

$$\eta = \frac{L_p/c}{\dot{M}_w v_\infty}, \quad (44.186)$$

where \dot{M}_w is the mass loss rate of the star and v_∞ the terminal velocity of the stellar wind. Both momenta are balanced at the standoff distance R_s to the pulsar so that

$$R_s = \frac{\sqrt{\eta}}{1 + \sqrt{\eta}} d. \quad (44.187)$$

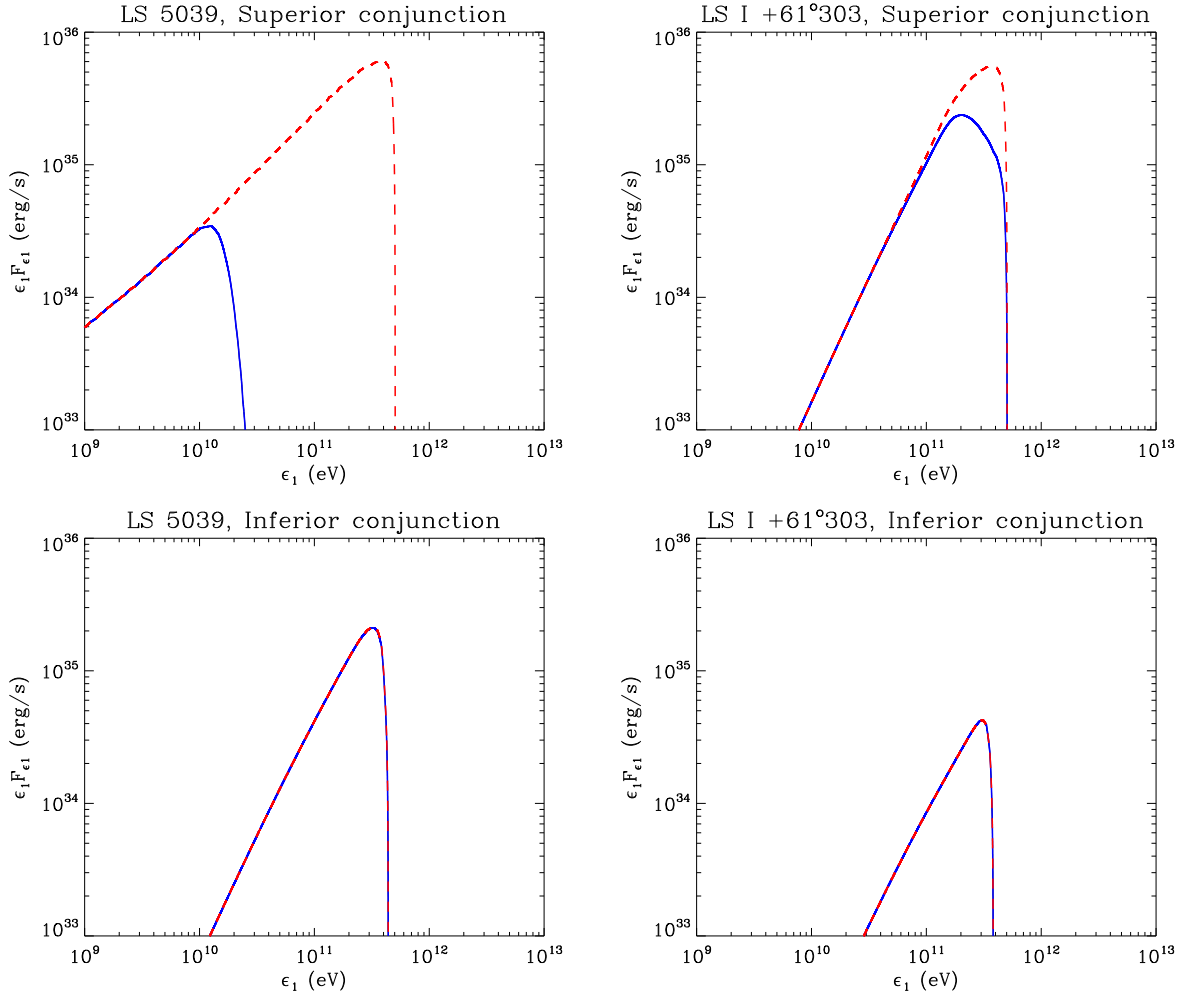


FIG. 40. Absorbed inverse Compton spectrum emitted (blue solid lines) by an unterminated and mono-energetic pulsar wind with $\gamma_0 = 10^6$ in LS 5039 (*left*) and LS I +61°303 (*right*) at superior (*top*, $\psi = 30^\circ$) and inferior (*bottom*, $\psi = 150^\circ$) conjunctions. The non-absorbed spectrum is shown for comparison (dashed red line). Pair cascade emission is ignored.

If $\eta \ll 1$, the stellar wind dominates and the pulsar wind is confined and collimated backward in the binary system. In LS 5039, where $\dot{M}_w \sim 10^{-7} M_\odot \text{ yr}^{-1}$, $v_\infty \sim 2400 \text{ km s}^{-1}$ (McSwain *et al.* 2004) and if the pulsar has a similar spin down power than in PSR B1259–63 *i.e.* $L_p = 10^{36} \text{ erg s}^{-1}$, then $\eta \approx 2 \times 10^{-2} \ll 1$. In LS I +61°303, the structure of the wind is more complex. It is composed of a slow and dense equatorial disk and a fast tenuous polar wind for which $\dot{M}_w \sim 10^{-8} M_\odot \text{ yr}^{-1}$ and $v_\infty \sim 2000 \text{ km s}^{-1}$ are usually assumed (Waters *et al.* 1988). In the polar wind, $\eta = 0.2-0.3$ ($L_p = 10^{36} \text{ erg s}^{-1}$) and is about $10^{-3}-10^{-2}$ in the equatorial wind (with $v_w \sim 100 \text{ km s}^{-1}$ and a mass flux a hundred times greater than the polar wind). In both cases, the pulsar wind is confined by the stellar wind. For this reason, we investigated the effect of a terminated pulsar wind on the high-energy emission.

The precise shape of the shock between a pulsar wind (relativistic and magnetized) and stellar wind (non-relativistic) is not well constrained today. A full treatment of the problem would require heavy relativistic MHD simulations. Some numerical models have been applied

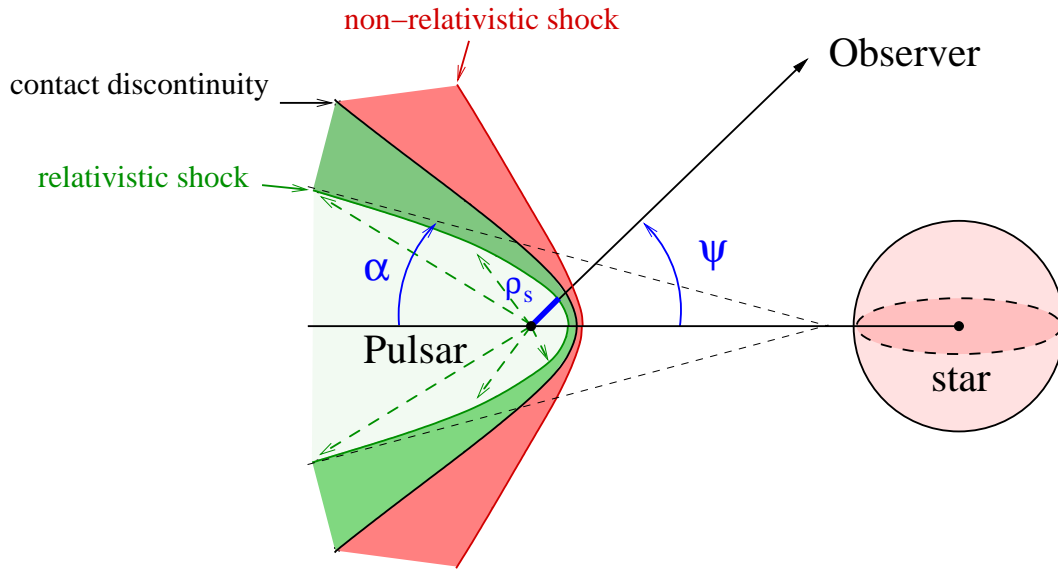


FIG. 41. The collision between the pulsar wind and the massive star wind produces a bow shock structure. The shocked stellar wind (red area) and the shocked pulsar wind (green area) are separated by the contact discontinuity (black solid line). The unshocked pulsar wind is limited by the relativistic shock wave front (green solid line) and has an asymptotic half opening angle α .

to isolated pulsars in interaction with the interstellar medium (see for instance the simulations by Bucciantini *et al.* 2005). Bogovalov *et al.* (2008) modeled the collision between a pulsar wind and the stellar wind in PSR B1259–63 for non-magnetized flows. In this article, the authors provide analytical fits to the dependence of the asymptotic half-opening angle α of the shock for both winds with the parameter η . For the pulsar wind (Bogovalov *et al.* 2008),

$$\alpha = 41.1 \log \eta + 71.7, \quad \text{in degrees.} \quad (44.188)$$

This formula is valid for $\eta > 1.25 \times 10^{-2}$. For lower values, the pulsar wind is closed. As a first attempt, we approximate the shape of the shock front of the pulsar wind to an hyperbola. The distance between the pulsar and the apex of the hyperbola is given by Eq. (44.187) and the asymptotic half-opening angle α by Eq. (44.188). We used these assumptions in the full calculation of the high-energy emission from the pulsar wind in LS 5039 and LS I +61°303 (see Sect. 7 and Cerutti *et al.* 2008b).

6. What if the pulsar wind is anisotropic?

§ 45. Anisotropic pulsar wind

High-resolution observations, particularly in X-rays with *Chandra* (Fig. 42), have revealed that some pulsar wind nebulae exhibit a jet-torus structure (see the review by Gaensler & Slane 2006 and references therein). This morphology can be interpreted in the framework of the classical model of Kennel & Coroniti (1984a) if the pulsar wind is anisotropic (Begelman & Li 1992; Bogovalov & Khangulyan 2002a). The solutions given by "split-monopole" type models for pulsars (Michel 1969; Bogovalov 1999) show that the energy flux in the wind should be axisymmetric. If θ is the polar angle of the pulsar, the injected Lorentz factor in the wind γ_0

(far from the light cylinder) is (Bogovalov & Aharonian 2000; Bogovalov & Khangulyan 2002b)

$$\gamma_0(\theta) = \gamma_i + \gamma_m \sin^2 \theta, \quad (45.189)$$

The wind is still assumed radial and the flux of electron isotropic. This assumption entails that the pulsar luminosity should have the same latitude dependence such as $L_p = L_i + L_m \sin^2 \theta$. To reproduce the Crab nebula morphology, Bogovalov & Khangulyan (2002a) suggest that the Lorentz factor values should be spread over four order of magnitudes with $\gamma_i = 200$ and $\gamma_m = 10^6$ - 10^7 .

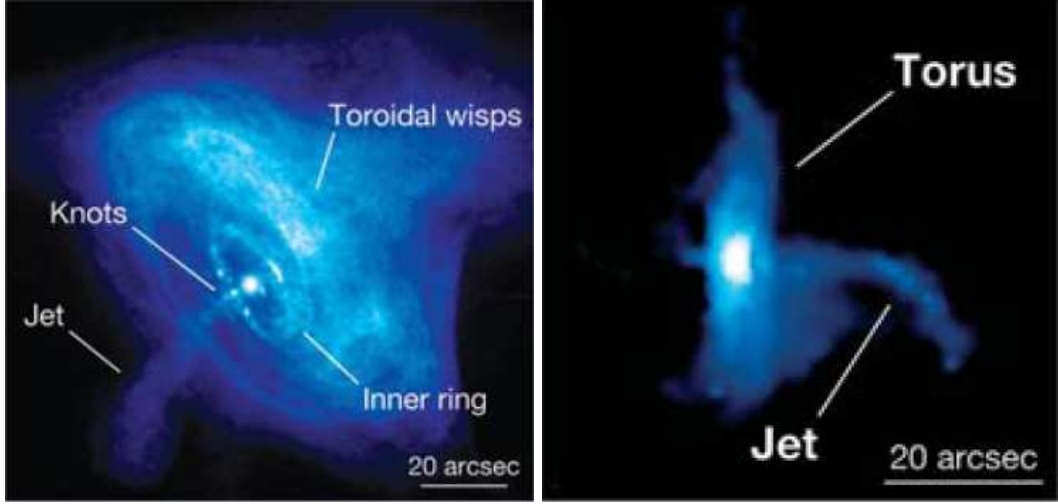


FIG. 42. X-ray images of the Crab nebula (*left*, Weisskopf *et al.* 2000) and the pulsar wind nebula 3C 58 (*right*, Slane *et al.* 2004) obtained with *Chandra* where a jet-torus structure appears clearly. Images Extracted from Gaensler & Slane (2006).

In this part, we would like to investigate whether an anisotropic pulsar wind could significantly change the high-energy emission from the unshocked pulsar wind. If the pulsar wind is indeed highly anisotropic, the emission seen by the observer (intensity and position) should depends strongly on its orientation (fixed, unless the neutron star axis precesses). The density of pairs (assumed isotropic) is (see Eq. 42.177)

$$\frac{dN_e}{d\gamma_e dr d\Omega_e} = \frac{L_p}{4\pi m_e c^3 \langle \beta_0 \rangle \langle \gamma_0 \rangle} \delta(\gamma_e - \gamma_e(r, \theta)), \quad (45.190)$$

where $\langle \gamma_0 \rangle$ is the Lorentz factor averaged over all the solid angles such as

$$\langle \gamma_0 \rangle = \frac{1}{4\pi} \int_0^\pi \int_0^{2\pi} \gamma_0(\theta) \sin \theta d\theta d\phi = \gamma_i + \frac{2}{3} \gamma_m. \quad (45.191)$$

§ 46. The pulsar orientation

Fig. 43 shows the angular distribution of the Lorentz factor. First, we have to determine the orientation of the pulsar with respect to the massive star and the observer for an arbitrary inclination. Let's define the Euler angles ϕ_x , ϕ_y and ϕ_z as the rotation angles along the x, y and the z-axis. Because of the rotation symmetry about the x axis, we consider only ϕ_y and ϕ_z . The observer probes the pulsar wind in the direction defined by the spherical angles ϕ and ψ (see Fig. 44).

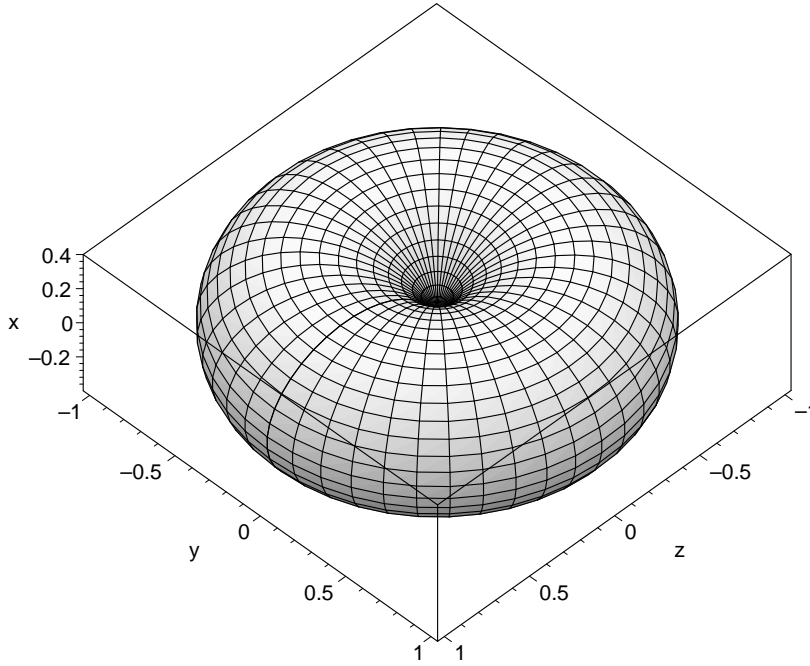


Fig. 43. Angular distribution of the Lorentz factor following Eq. (45.189) normalized to γ_m where $\gamma_m/\gamma_i \sim 10^4$. The pulsar pole is oriented along the x-axis where the Lorentz factor reaches its minimum value γ_0 and is maximum in the equator plane (y,z) where $\gamma_0 \approx \gamma_m$.

If the pulsar wind is turned by ϕ_y and ϕ_z , the rotation matrices are

$$M_y = \begin{pmatrix} \cos \phi_y & 0 & -\sin \phi_y \\ 0 & 1 & 0 \\ \sin \phi_y & 0 & \cos \phi_y \end{pmatrix} \quad M_z = \begin{pmatrix} \cos \phi_z & \sin \phi_z & 0 \\ -\sin \phi_z & \cos \phi_z & 0 \\ 0 & 0 & 1 \end{pmatrix} \quad (46.192)$$

$$\begin{pmatrix} x'' \\ y'' \\ z'' \end{pmatrix} = \underbrace{M_z M_y}_M \begin{pmatrix} x \\ y \\ z \end{pmatrix} \quad \text{with} \quad M = \begin{pmatrix} \cos \phi_y \cos \phi_z & \sin \phi_z & -\sin \phi_y \cos \phi_z \\ -\cos \phi_y \sin \phi_z & \cos \phi_z & \sin \phi_y \sin \phi_z \\ \sin \phi_y & 0 & \cos \phi_y \end{pmatrix}. \quad (46.193)$$

We are interested in the cosine of the polar angle of the pulsar defined in the coordinates of the pulsar (x'', y'', z'') as a function of the orientation to the observer. The cosine of the angle between the pulsar axis to the observer line of sight is given by the product $\cos \theta = \mathbf{e}_x'' \cdot \mathbf{e}_{\text{obs}}$ (see Fig. 44). With

$$\mathbf{e}_x'' = \cos \phi_y \cos \phi_z \mathbf{e}_x + \sin \phi_z \mathbf{e}_y - \sin \phi_y \cos \phi_z \mathbf{e}_z, \quad (46.194)$$

and

$$\mathbf{e}_{\text{obs}} = \sin \psi \cos \phi \mathbf{e}_x + \sin \psi \sin \phi \mathbf{e}_y + \cos \psi \mathbf{e}_z \quad (46.195)$$

we have

$$\cos \theta = \mathbf{e}_x'' \cdot \mathbf{e}_{\text{obs}} = \cos \phi_y \cos \phi_z \sin \psi \cos \phi + \sin \phi_z \sin \psi \sin \phi - \sin \phi_y \cos \phi_z \cos \psi. \quad (46.196)$$

The injected Lorentz factor probed by the observer is

$$\gamma_0(\psi, \phi) = \gamma_i + \gamma_m (1 - \cos^2 \theta), \quad (46.197)$$

formula in which ϕ_y and ϕ_z are free parameters. Note that Eq. (46.197) depends on ϕ since the symmetry about the line joining both stars is broken for an anisotropic pulsar wind. Once the orientation set, the calculation of the high-energy emission from the wind is analogous to the isotropic case described above. For a distant observer, the pulsar wind appears isotropic with a fixed Lorentz factor which depends on its orientation.

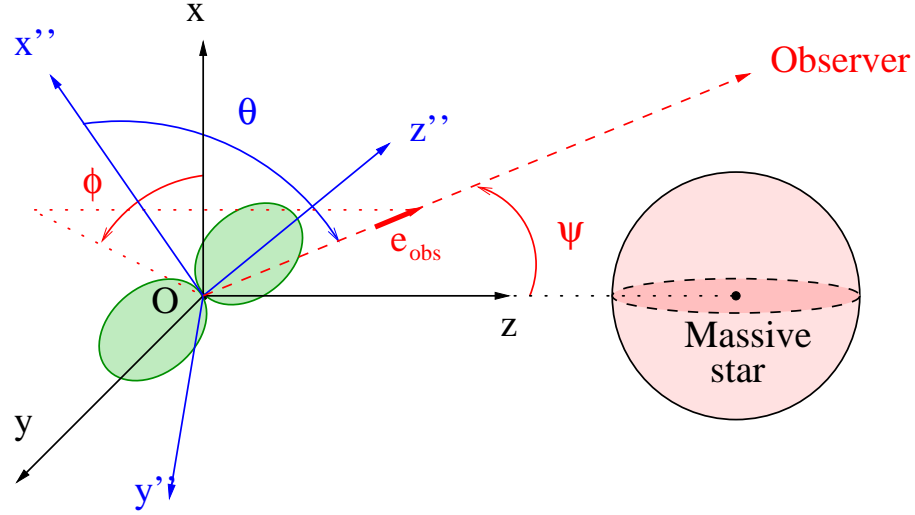


FIG. 44. The pulsar axis (x'') is inclined with respect to the observer at an angle θ . The anisotropic pulsar wind is represented by the green loops.

§ 47. Lorentz factor maps

Similarly to what we have done in the isotropic case, we perform here the calculation of the Lorentz factor distribution for an anisotropic pulsar wind (Figs. 45-46). A jet-like structure appears clearly in the direction of the poles of the pulsar as the Lorentz factor drops dramatically there.

§ 48. What are the odds to observe a low Lorentz factor?

In theory, the Lorentz factor of the wind and the luminosity of the pulsar probed by the observer can be very low but this is rather unlikely as we are going to show below. We aim to answer the following question: what is the probability to observe a pulsar with a Lorentz factor and luminosity lower than say 10% of the maximum value?

Let's take a pulsar with a completely random orientation to the observer. The probability for a unit vector to be in the direction (θ, ϕ) with $\theta \in [0, \pi/2]$ and $\phi \in [0, 2\pi]$ is

$$dp = C \sin \theta d\theta d\phi \Rightarrow \int dp = 1 \Rightarrow C = \frac{1}{2\pi}, \quad (48.198)$$

hence the random variable Θ is distributed as

$$\frac{dp}{d\theta} = f_{\Theta}(\theta) = \sin \theta. \quad (48.199)$$

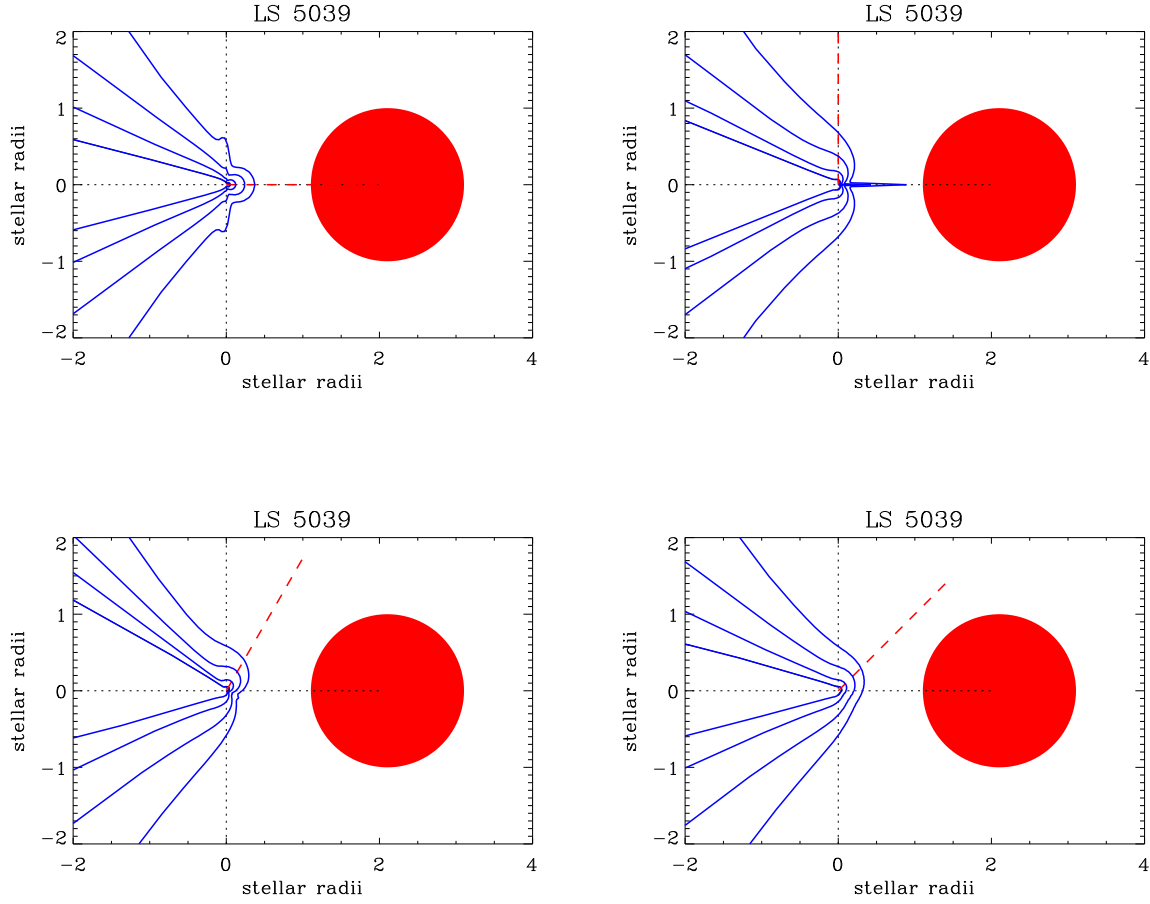


FIG. 45. Same as in Fig. 35 for an anisotropic pulsar wind in LS 5039 at periastron. Parameters used: $\gamma_i = 10^3$, $\gamma_m = 10^6$, $\phi = 0$ for four different orientations *top left* ($\phi_y = 0, \phi_z = \pi/20$), *top right* ($\phi_y = \pi/2, \phi_z = 0$), *bottom left* ($\phi_y = \pi/3, \phi_z = \pi/20$) and *bottom right* ($\phi_y = \pi/4, \phi_z = \pi/4$). The star is point-like and mono-energetic. The dotted lines indicate the position of the pulsar, the red dashed line the orientation of the equator and the red disk depicts the massive companion star.

The random variable $\Gamma = \gamma_i + \gamma_m \sin^2 \Theta$ then follows the distribution function given by

$$f_{\Gamma}(\gamma_0) = f_{\Theta}(\theta) \left| \frac{d\theta}{d\gamma_0} \right| = \frac{1}{2\sqrt{1 - \left(\frac{\gamma_0 - \gamma_i}{\gamma_m}\right)^2}}. \quad (48.200)$$

The probability to have a Lorentz factor γ'_0 lower than γ_0 is

$$F_{\Gamma}(\gamma_0) = \int_{\gamma_i}^{\gamma_0} f_{\Gamma}(\gamma'_0) d\gamma'_0 = 1 - \sqrt{1 - \left(\frac{\gamma_0 - \gamma_i}{\gamma_m}\right)^2}. \quad (48.201)$$

If we assume $\gamma_m = 10^6$, the probability to observe the pulsar more pole on and to observe less than 10% of γ_m (with $\gamma_i \ll 0.1 \gamma_m$) and so 10% of L_p is about 5%. Although unlikely, the emission from the pulsar wind would not be detected if the pulsar is seen close to pole-on.

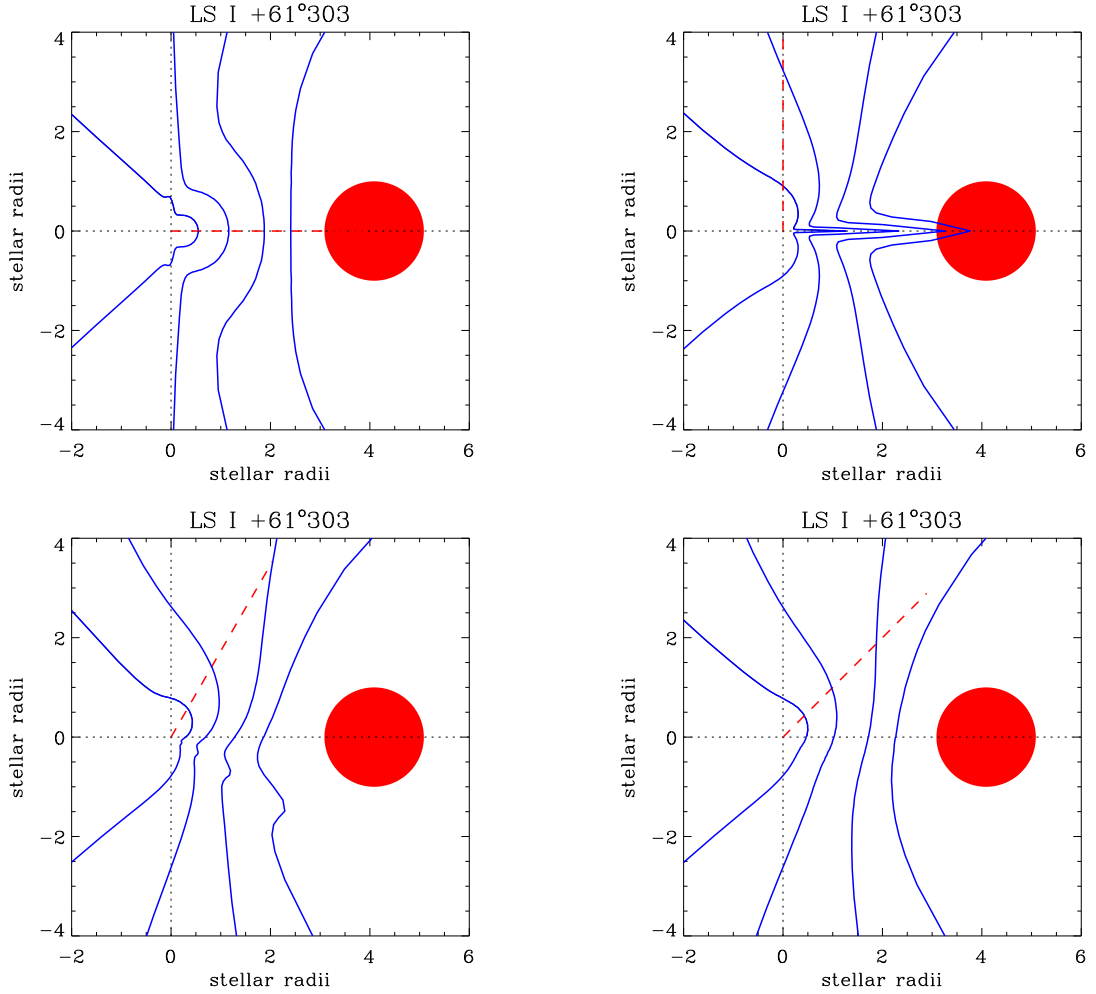


FIG. 46. Same as in Fig. 45 for LS I +61°303 at periastron.

I conclude from this study that it is not really relevant to consider an anisotropic pulsar wind in our model. I will ignore this effect in the following.

7. Free pulsar wind emission in LS 5039 and LS I +61 303

The results obtained in the previous sections are applied here for the computation of the pulsar wind emission in LS 5039 and LS I +61°303 along the orbit. The pulsar wind is isotropic, radial and mono-energetic and injects a power $L_p = 10^{36}$ erg s⁻¹ into pairs. A line-like gamma-ray spectrum is expected to be radiated by the free pulsar wind in both binaries (Fig. 47). Similar results were obtained in PSR B1259–63 by Ball & Kirk (2000) and Khangulyan *et al.* (2007).

Here, the gamma-ray signature of the free pulsar wind in LS 5039 and LS I +61°303 is too strong and can be excluded by the available observations. HESS and MAGIC measurements (Aharonian *et al.* 2006; Albert *et al.* 2006) clearly exclude the range $10^6 \lesssim \gamma_0 \lesssim 10^7$. *Fermi* observations (Abdo *et al.* 2009a,b) also rule out a mono-energetic pulsar wind with $10^4 \lesssim \gamma_0 \lesssim 10^6$. The Lorentz factor of the wind should be greater than 10^7 or lower than 10^4 . The size of the pulsar wind zone is not very constraining as it does not change much the results (see Fig. 47),

except if the pulsar wind size is unrealistically small ($\eta \ll 10^{-3}$). In addition, the termination shock cannot be too close to the pulsar or the magnetic field would be too high (as $B_s \propto 1/R_s$, see Chapter 4 or Kennel & Coroniti 1984a). Hence, no TeV emission could be sustained in this case.

If we reduce significantly the spin down luminosity of the pulsar $L_p < 10^{36} \text{ erg s}^{-1}$, the gamma-ray peak intensity can be reduced and found consistent with observations. This assumption would imply that less energy would be available for pairs radiating at the termination shock. The gamma-ray emission expected in our model for the shocked pulsar wind emission (see Chapter 4) would underestimate the TeV flux.

It is clear from this study that the classical model of pulsar winds is too simplistic. First, the mono-energetic pulsar wind assumption might be inaccurate. If pairs are injected with a broad power-law energy distribution, the line-like component is erased. This possibility could solve this discrepancy, and explain the puzzling *Fermi* observations in LS 5039 and LS I +61°303. This is discussed below in Sect. 8. Alternatively, the assumption that the wind is kinetic energy dominated might be wrong. It is possible that the conversion of the electromagnetic energy into kinetic energy in pairs is not completed in gamma-ray binaries where the pulsar wind size is $\sim 0.01\text{-}0.1 \text{ AU}$ (0.1 pc in isolated pulsars). Hence, the wind may remain highly magnetized up to the termination shock with only a small fraction of energy into the plasma of electrons. The "striped wind" model could provide a favorable theoretical framework to interpret our results. I briefly discussed about this alternative model in Sect. 9.

8. Signature of the unshocked wind seen by *Fermi*?

New observations at GeV energies by the *Fermi* Gamma-ray space Telescope of LS I +61°303 (Abdo *et al.* 2009a) and LS 5039 (Abdo *et al.* 2009b) provided the first detections of an orbital modulation of the GeV gamma-ray flux. The measured spectra are consistent with a power-law (photon index 2.2 for LS I +61°303 and 1.9 for LS 5039) plus an exponential cut-off at a few GeV (6.3 GeV for LS I +61°303 and 2.1 GeV for LS 5039). This energy cut-off is too low to be due to pair production of gamma rays on stellar radiation. Pair production should be effective at 30-50 GeV in LS 5039 and LS I +61°303. Particles responsible for the GeV component have probably a different origin than pairs radiating at TeV energies.

The high-energy emission from gamma-ray binaries could come from the magnetospheric emission of the pulsar itself (*i.e.* inside the light cylinder). Indeed, the observed (isolated) gamma-ray pulsars present similar spectral features with photon indexes clustered around 1-2 and with energy cut-off typically ranging from 1 to 5 GeV (see the first *Fermi* catalog of gamma-ray pulsars, *Fermi* LAT collaboration 2009). This scenario would provide a natural explanation for the spectral features but the origin of the orbital modulation remains unclear. Magnetospheric emission models should be revisited in the context of an additional external anisotropic source of radiation.

Alternatively, the GeV emission in gamma-ray binaries could be the signature of a Compton cooling unshocked pulsar wind. We explore here whether this possibility would provide a good explanation for the spectral and temporal features of the GeV component in LS 5039 and LS I +61°303. To reproduce accurately *Fermi* observations, pairs in the wind are injected with a constant soft power-law energy distribution (index p) with an exponential cut-off (E_{cut}). Spectra are computed with Eq. (43.182) along the orbit using the latest orbital parameters found by

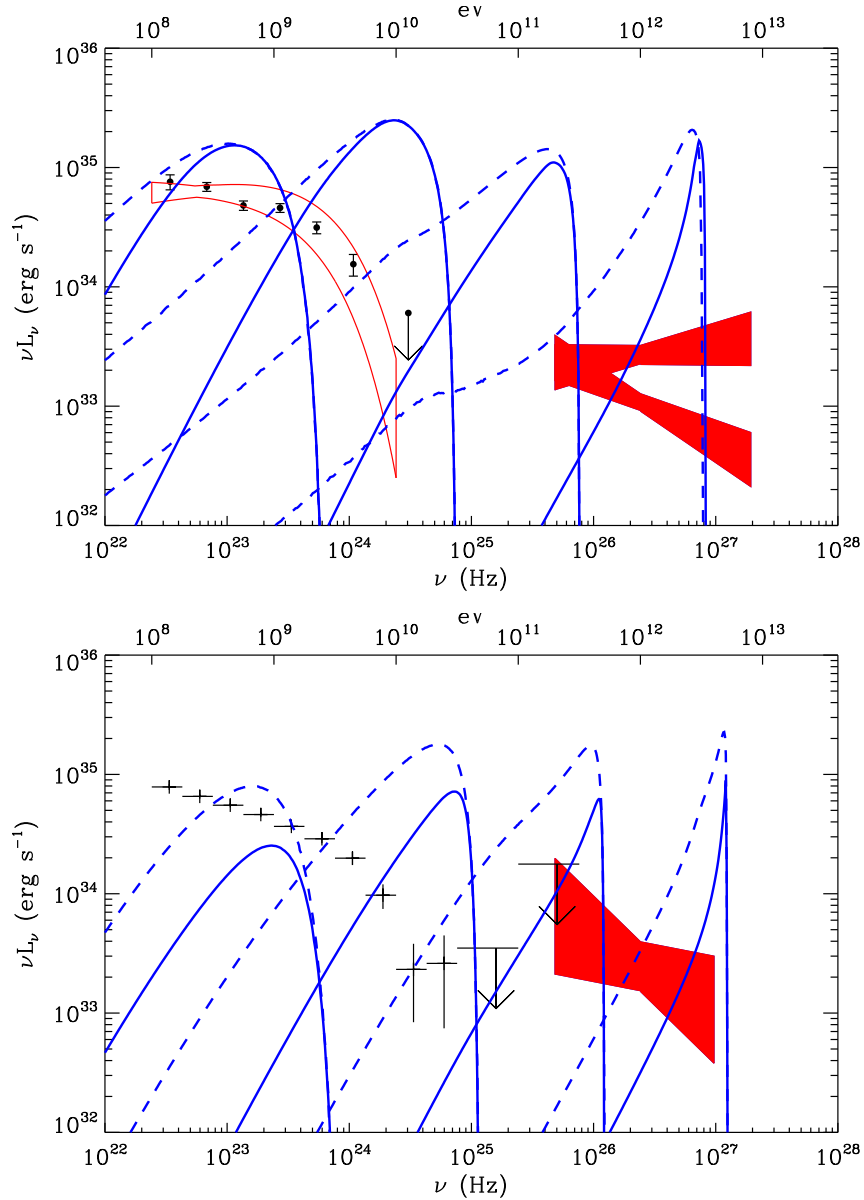


FIG. 47. Orbit-averaged emission from the free pulsar wind in LS 5039 (*top panel*) and LS I +61°303 (*bottom panel*). The wind is assumed radial, isotropic and mono-energetic with $\gamma_0 = 10^4$ (*left*), 10^5 , 10^6 and 10^7 (*right*). The gamma-ray emission is calculated for a terminated ($\eta = 2 \times 10^{-2}$, solid lines) and unterminated wind (dashed lines) for $L_p = 10^{36}$ erg s $^{-1}$, assuming that the systems are located at 2.5 kpc for LS 5039 and 2 kpc for LS I +61°303. *Fermi* (black data points), HESS and MAGIC (red bowties) observations are overplotted.

Aragona *et al.* (2009). Fig. 48 shows the expected inverse Compton emission in both binaries and the parameters used for the modeling are given in Tab. 2.

This model reproduces well both the spectrum and the modulation in LS 5039. The modulation of the spectral index is also explained. In LS I +61°303, the spectrum can be well reproduced as well if the luminosity for the pulsar is high ($L_p \geq 10^{37}$ erg s $^{-1}$) but the model fails to explain the observed GeV modulation. The theoretical light curve shape is correct but is shifted in phase by $\Delta\phi \approx -0.25$ with respect to observations. There is no obvious reason to explain this lag in this scenario. The spectral index is also expected to be orbital modulated.

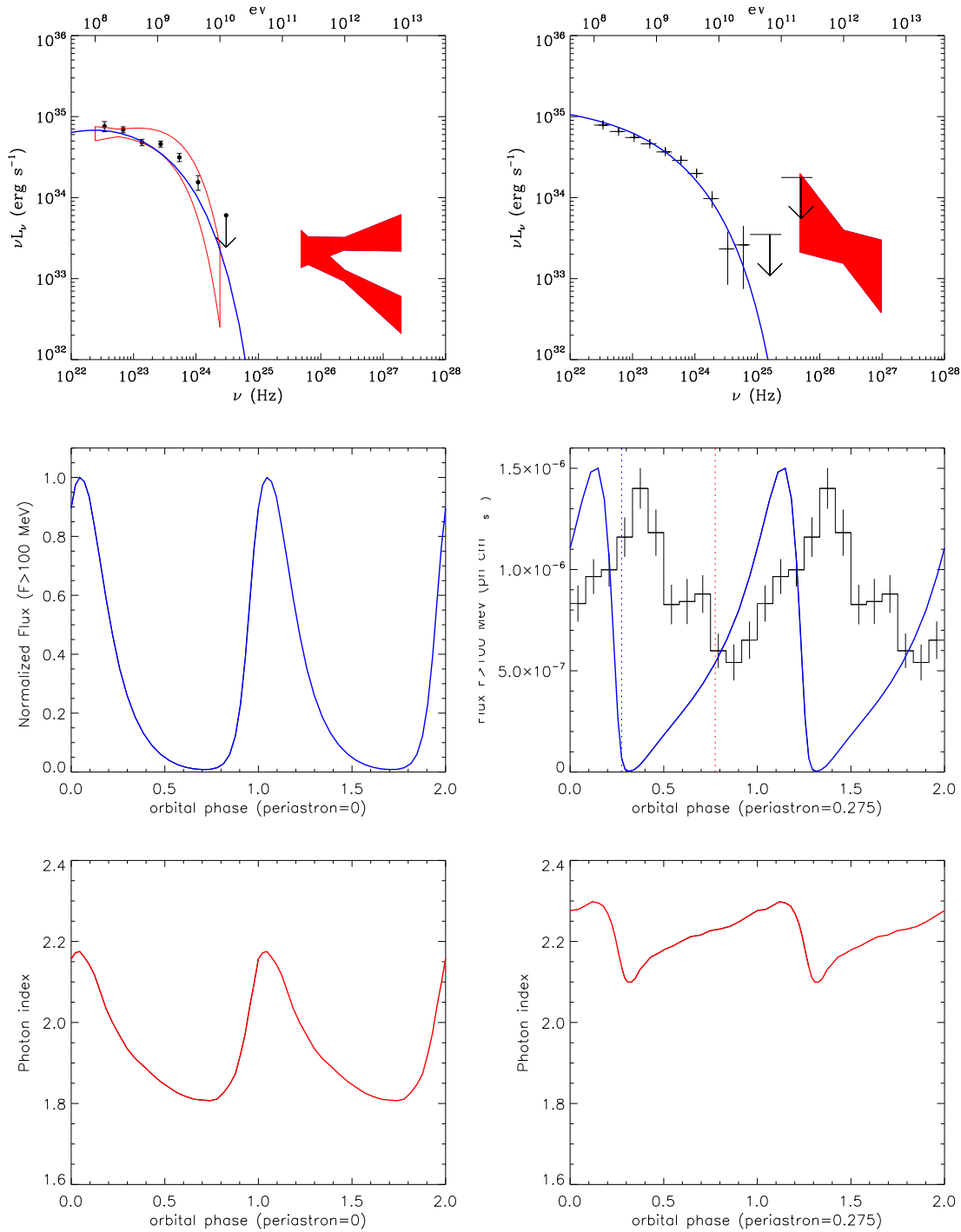


Fig. 48. Inverse Compton emission in the gamma-ray binaries LS 5039 (*left*) and LS I +61°303 from an unshocked pulsar wind. *Top*: Theoretical orbit-averaged spectrum (blue solid line) for an inclination $i = 60^\circ$. Bowties are HESS and MAGIC observations (red, Aharonian *et al.* 2006; Albert *et al.* 2006), black data points show *Fermi* measurements (Abdo *et al.* 2009a,b). *Middle*: Gamma-ray flux integrated over 100 MeV as a function of the orbital phase ϕ (two full orbits), the *Fermi* light curve is overplotted for LS I +61°303. *Bottom*: Expected spectral index in the GeV energy band along the orbit.

I had the opportunity to present these investigations in a contributed talk at the "2009 *Fermi* Symposium". The proceeding was published in Cerutti *et al.* (2009a).

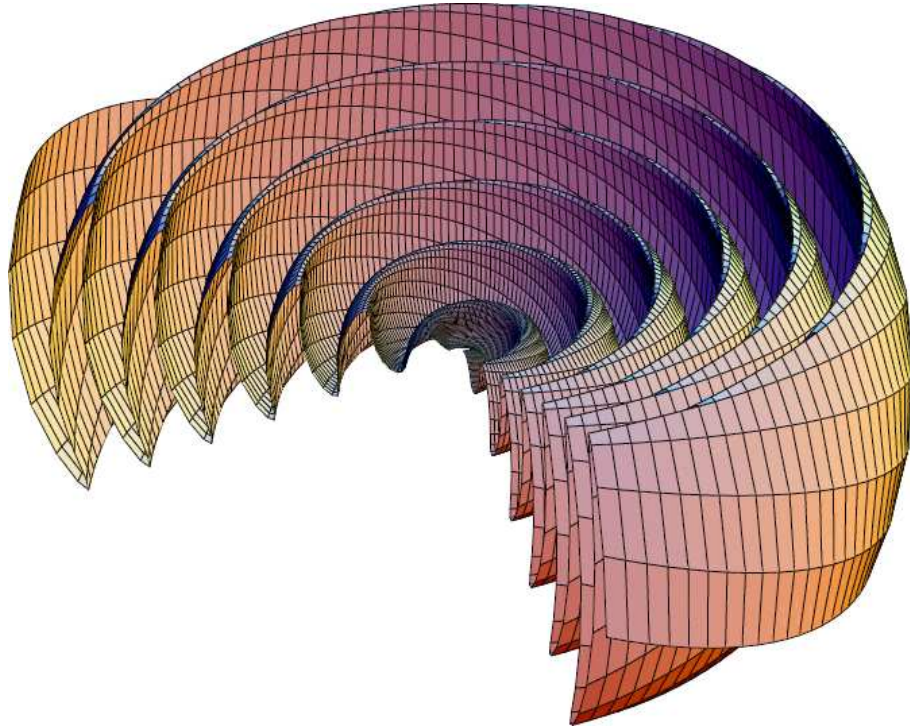
TAB. 2. Parameters used for the modeling of the Compton emission shown in Fig. 48.

Parameters	p	E_{cut} (GeV)	E_{min} (GeV)	L_p (erg s ⁻¹)	η
LS 5039	2.3	7.5	0.5	2×10^{36}	0.02
LS I +61°303	3.1	25	0.5	10^{37}	0.5

9. Striped pulsar wind

The production of the gamma-ray radiation in isolated pulsars is usually assumed to originate in the pulsar magnetosphere, inside the light cylinder. There are many models for the high-energy pulsed radiation in pulsars such as for instance the "polar cap" (Ruderman & Sutherland 1975) or "outer gap" (Cheng *et al.* 1986) models.

Alternatively, the emission could come from the pulsar wind, *i.e.* beyond the light cylinder. In the "striped pulsar wind" model for inclined rotators (Coroniti 1990; Michel 1994), a striped current sheet separates the magnetic field line (toroidal) coming from the opposite magnetic pole of the neutron star. This current sheet has a wave-like structure propagating close to the speed of light with a wavelength $\approx 2\pi R_L$, where R_L is the light cylinder radius (see Fig. 49).

**FIG. 49.** The striped current sheet produced by an oblique rotator obtained with the split monopole model by Bogovalov (1999). Picture extracted from Kirk *et al.* (2009).

The dissipation of this alternating magnetic field structure could accelerate particles in the wind up to very high-energy (*e.g. via* magnetic reconnection as suggested by Coroniti 1990). This possibility was originally proposed to explain the so-called " σ problem" *i.e.* the transition from a highly magnetized wind (close to the pulsar) to a low magnetized wind dominated by the

kinetic energy of relativistic particles (far from the light-cylinder). In this model, the dissipation of the striped structure occurs in the pulsar wind if the dissipation timescale is shorter than the timescale for a stripe to reach the termination shock. This condition provides the following upper-limit for the Lorentz factor of the wind (Arons 2008)

$$\Gamma_w < \left(\beta_{eff} \frac{R_s}{R_L} \right)^{1/2}, \quad (48.202)$$

where R_s is the termination shock radius and β_{eff} gives the efficiency of the dissipation process considered (not specified and taken equal to 1 here). In gamma-ray binaries $R_s/R_L \sim 10^4$. Hence, if $\Gamma_w > 100$ the pulsar wind does not have enough time to dissipate and remains highly magnetized up to the termination shock. Only a small fraction of energy would then be available for pairs, leading to a weak and undetectable gamma-ray signal. This scenario could explain why no such strong line-like component is not observed in LS 5039 and LS I +61°303. The conditions in the shocked pulsar wind should however remain unchanged. Particle-In-Cells (PIC) simulations indicate that the magnetic energy density can be dissipated and accelerate particles at the termination shock (Pétri & Lyubarsky 2007). I discussed about this scenario in a contributed talk at the "French Society of Astronomy and Astrophysics meeting 2008" (see the proceeding Cerutti *et al.* 2008a).

I think that it would be worthwhile to investigate the emission from a striped pulsar wind in gamma-ray binaries. The work done on the Geminga pulsar by Pétri (2009) is very encouraging and could be applied to LS 5039 and LS I +61°303. Some modifications should however be made to include external Compton scattering of stellar photons. This model could account for *Fermi* observations (spectrum and modulation). It is however not obvious whether this model could account for the correct GeV orbital modulation in LS I +61°303. Specific studies are necessary to answer this question.

10. What we have learned

The energetic electron-positron pairs in the pulsar wind upscatter the optical-UV photons from the massive star to high energy *via* inverse Compton scattering. For a mono-energetic Crab-like pulsar wind, the emitted spectrum is a sharp peak broadened by particle cooling, centered at an energy set by the Lorentz factor of the wind γ_0 . The amplitude of the peak depends on the extension of the pulsar wind zone and saturates when particles have enough time to radiate before they reach the termination shock. The maximum Compton line flux is given by the pulsar luminosity L_p . An anisotropic pulsar wind can also change the gamma-ray emission level, but this effect would be important only for very peculiar orientations.

In LS 5039 and LS I +61°303, the emission from the free pulsar wind is very strong along the orbit. We found that available observations at GeV and TeV energies undoubtedly rule out a mono-energetic pulsar wind with Lorentz factor $10^4 < \gamma_0 < 10^7$.

It is conceivable that the simple Crab-like assumption for the pulsar wind is incorrect in gamma-ray binaries. Pairs might be injected with a power-law energy distribution. In this case, the emission from the unshocked pulsar wind could explain the recent *Fermi* observations (Cerutti *et al.* 2009a). Nevertheless, this scenario cannot account for the correct gamma-ray modulation in LS I +61°303. Alternatively, the pulsar wind remains highly magnetized up to the termination shock. The wind may not have enough time to accelerate and transfer magnetic

energy into kinetic energy for pairs since the scales probed in these systems ($\sim 0.01\text{-}0.1$ AU) are about 5 orders of magnitude smaller than for isolated pulsars (~ 0.1 pc). The striped wind model appears as a promising alternative to explain the emission of the free pulsar wind and possibly the GeV component. This model has not been applied to gamma-ray binaries yet. Further theoretical investigations should be carried out in this direction.

11. [Français] Résumé du chapitre

§ 49. Contexte et objectifs

Les pulsars sont des étoiles compactes ($R_{NS} \sim 10$ km), en rotation rapide ($P_{NS} \lesssim 1$ s) hautement magnétisées. L'énorme champ électrique induit par la rotation de l'étoile à neutron extrait et accélère des particules chargées dans la magnétosphère. Ce plasma de particules est libéré sous la forme d'un vent relativiste au cylindre de lumière où les lignes de champ magnétique s'ouvrent, *i.e.* à une distance où la vitesse de corotation est égal à la vitesse de la lumière $R_L = cP_{NS}/2\pi$. Dans le modèle classique des pulsars isolés comme le Crabe (voir *e.g.* Rees & Gunn 1974; Kennel & Coroniti 1984a), une partie de l'énergie rotationnelle du pulsar est emportée par un vent relativiste constitué de paires électron-positron et probablement aussi d'ions. Ce vent est supposé radial, monoénergétique avec un facteur de Lorentz d'ensemble ultrarelativiste $\gamma_0 \sim 10^6$. La formation et la structure des vents de pulsar ne sont toujours pas bien contraintes et comprises aujourd'hui (le lecteur intéressé peut se référer aux revues par Gaensler & Slane 2006; Kirk *et al.* 2009). Le vent de pulsar s'étend librement jusqu'au choc terminal (rayon R_s , voir Fig. 31) où les paires sont isotropisées, réaccélérées et rayonnent par synchrotron et diffusent les photons ambiants de basse énergie à de hautes énergies.

En amont du choc terminal, les particules n'émettent pas de rayonnement synchrotron parce que le champ magnétique est gélé dans l'écoulement relativiste de paires. C'est pour cette raison que le vent non choqué de pulsar a été pendant longtemps considéré comme non observable. Néanmoins, la diffusion Compton inverse des photons ambiants de basse énergie par les paires reste possible dans cette zone. En raison du facteur de Lorentz élevé du vent, la signature spectrale du vent non choqué devrait être directement observable en gamma. Dans les pulsars isolés, le rayonnement ambiant peut provenir de la nébuleuse elle-même (synchrotron, ou émission thermique) ou du fond diffus cosmologique mais ces sources de photons sont trop ténues pour produire un signal gamma détectable. Bogovalov & Aharonian (2000) considèrent l'émission thermique en provenance de la surface de l'étoile à neutron dans la nébuleuse du Crabe et prédirent une raie Compton en gamma. Les auteurs ont mis des contraintes sur la taille de la zone où le vent est dominé par l'énergie cinétique des particules dans le vent.

Dans le scénario du vent de pulsar, les binaires gamma sont composées d'un pulsar jeune (voir Chapitre 1). Dans de tels systèmes, l'étoile compagne fournit une énorme quantité de photons cibles de basse énergie pour la diffusion Compton inverse ($n_\star \sim 10^{14}$ ph cm $^{-3}$ à la position de l'objet compact dans LS 5039). L'émission Compton inverse en provenance du vent non choqué du pulsar devrait être en conséquence très forte. La densité de photons du fond diffus cosmologique est très faible comparée à la densité stellaire ($n_{CMB} \sim 10^3$ ph cm $^{-3} \ll n_\star$) et pourra être négligée. La densité de photons X thermiques produite à la surface de l'étoile à neutron peut être aussi négligée ici ($n_{NS} < n_\star$ au cylindre de lumière si $R_L > R_{NS}/R_\star (T_{NS}/T_\star)^{3/2} d$, *i.e.* si $P_{NS} \gtrsim 75$ ms dans LS 5039). En plus, les collisions entre les

photons et les paires se produiraient par l'arrière dans le référentiel de l'observateur, autrement dit de manière très inefficace.

Les binaires gamma apparaissent comme des objets idéaux pour étudier la physique des vents de pulsar à de très courtes échelles spatiales (échelles sub UA, à comparer avec ~ 0.1 pc pour une nébuleuse de pulsar isolée typique). Nous allons regarder dans ce chapitre si une émission en provenance du vent non choqué de pulsar peut être attendue et observée aujourd'hui dans les binaires gamma. Ball & Kirk (2000) ont calculé cette émission dans les binaires PSR B1259–63 et PSR J0045–73. Nous nous proposons ici de calculer l'émission Compton dans des systèmes encore plus compacts que sont LS 5039 et LS I +61°303 dans lesquels le signal gamma devrait être encore plus intense. Le but de ce travail est de mettre des contraintes sur les paramètres du vent tels que l'énergie des paires, la taille et la structure du vent.

Ce chapitre est organisé comme suit. Je commence par quantifier le refroidissement des particules dans le vent par diffusion Compton inverse anisotrope (Sect. 3). Les équations pour calculer le spectre gamma émis vu par un observateur lointain sont dérivées (Sect. 4). Ensuite, je calcule le spectre gamma attendu en provenance du vent non choqué dans LS 5039 et LS I +61°303 (Sect. 7). Ces résultats sont discutés dans le contexte des observations *Fermi* (Sect. 8) et dans le contexte d'un modèle alternatif d'émission dans les vents de pulsar (Sect. 9). Les résultats et conclusions de cette étude sont présentés dans l'article Cerutti *et al.* (2008b), entièrement mis à la disposition du lecteur dans la Sect. 12.

§ 50. Ce que nous avons appris

Les paires d'électron-positron relativistes dans le vent de pulsar diffusent les photons optique-UV en provenance de l'étoile massive à haute énergie *via* la diffusion Compton inverse. Pour un vent de pulsar monoénergétique de type pulsar du Crabe, le spectre émis est une raie élargie par le refroidissement des particules, centrée à une énergie déterminée par le facteur de Lorentz du vent γ_0 . L'amplitude de la raie Compton dépend de la taille de la zone du vent non choqué et sature lorsque les particules ont suffisamment de temps pour rayonner avant qu'elles n'atteignent le choc terminal. Le flux maximum atteint est donné par la luminosité du pulsar L_p . Un vent anisotrope peut aussi changer le niveau d'émission gamma, mais cet effet est important seulement pour des orientations très particulières.

Dans LS 5039 et LS I +61°303, l'émission du vent non choqué est très forte tout au long de l'orbite. Nous avons trouvé que les observations dont nous disposons au GeV et au TeV permettent d'exclure un vent de pulsar monoénergétique avec un facteur de Lorentz $10^4 < \gamma_0 < 10^7$.

Il est tout à fait concevable que les hypothèses simplificatrices utilisées ici et dans les pulsars isolés soient incorrectes dans les binaires gamma. Les paires pourraient être injectées avec une loi de puissance. Dans ce cas, l'émission en provenance du vent non choqué de pulsar pourrait expliquer les récentes observations *Fermi* (Cerutti *et al.* 2009a). Cependant, ce scénario ne permet pas de rendre compte de la modulation gamma dans LS I +61°303. Une autre possibilité est d'imaginer que le vent de pulsar reste hautement magnétisé jusqu'au choc terminal. Le vent n'aurait alors pas assez de temps pour accélérer et convertir l'énergie magnétique en énergie cinétique dans les paires, étant donné que les échelles spatiales sondées dans ces systèmes (~ 0.01 - 0.1 AU) sont environ 5 ordres de grandeurs plus petites que dans le cas des pulsars isolés

(~ 0.1 pc). Le modèle du vent strié apparaît comme étant un scénario alternatif prometteur pour expliquer l'émission du vent non choqué du pulsar et peut-être même pour expliquer la composante au GeV. Ce modèle n'a cependant pas encore été appliqué aux binaires gamma. Des études théoriques supplémentaires devraient être menées dans cette direction.

**12. Paper: Spectral signature of a free pular wind in the
gamma-ray binaries LS 5039 and LS I +61 303**

Spectral signature of a free pulsar wind in the gamma-ray binaries LS 5039 and LSI +61°303

Benoît Cerutti, Guillaume Dubus, and Gilles Henri

Laboratoire d'Astrophysique de Grenoble, UMR 5571 CNRS, Université Joseph Fourier, BP 53, 38041 Grenoble, France

Draft July 7, 2008

ABSTRACT

Context. LS 5039 and LSI +61°303 are two binaries that have been detected in the TeV energy domain. These binaries are composed of a massive star and a compact object, possibly a young pulsar. The gamma-ray emission would be due to particle acceleration at the collision site between the relativistic pulsar wind and the stellar wind of the massive star. Part of the emission may also originate from inverse Compton scattering of stellar photons on the unshocked (free) pulsar wind.

Aims. The purpose of this work is to constrain the bulk Lorentz factor of the pulsar wind and the shock geometry in the compact pulsar wind nebula scenario for LS 5039 and LSI +61°303 by computing the unshocked wind emission and comparing it to observations.

Methods. Anisotropic inverse Compton losses equations are derived and applied to the free pulsar wind in binaries. The unshocked wind spectra seen by the observer are calculated taking into account the $\gamma - \gamma$ absorption and the shock geometry.

Results. A pulsar wind composed of monoenergetic pairs produces a typical sharp peak at an energy which depends on the bulk Lorentz factor and whose amplitude depends on the size of the emitting region. This emission from the free pulsar wind is found to be strong and difficult to avoid in LS 5039 and LSI +61°303.

Conclusions. If the particles in the pulsar are monoenergetic then the observations constrain their energy to roughly 10-100 GeV. For more complex particle distributions, the free pulsar wind emission will be difficult to distinguish from the shocked pulsar wind emission.

Key words. radiation mechanisms: non-thermal – stars: individual (LS 5039, LSI +61°303) – stars: pulsars: general – gamma rays: theory – X-rays: binaries

1. Introduction

Pulsars are fast rotating neutron stars that contain a large amount of rotational energy. A significant fraction of this energy is carried away by an ultra-relativistic wind of electrons/positrons pairs and possibly ions (see Kirk et al. 2007 for a recent review). In the classical model of the Crab nebula (Rees & Gunn 1974; Kennel & Coroniti 1984), the pulsar wind is isotropic, radial and monoenergetic with a bulk Lorentz factor $\gamma_0 \sim 10^6$ far from the light cylinder where the wind is kinetic energy-dominated ($\sigma \ll 1$). The cold relativistic wind expands freely until the ram pressure is balanced by the surrounding medium at the standoff distance R_s . In the termination shock region, the pairs are accelerated and their pitch angle to the magnetic field are randomized, producing an intense synchrotron source. Moreover, the inverse Compton scattering of the relativistic electrons on soft photons produces high energy (HE, GeV domain) and very high energy (VHE, TeV domain) gamma-rays.

The shocked pulsar wind is thought to be responsible for most of the emitted radiation and gives clues about the properties of this region. However, our knowledge of the unshocked pulsar wind region is limited and based on theoretical state-

ments. If the magnetic field is frozen into the pair plasma as it is usually assumed, there is no synchrotron radiation from the unshocked wind. Nevertheless, nothing prevents inverse Compton scattering of soft photons onto the cold ultra-relativistic pairs from occurring. The pulsar wind nebula (PWN) emission has two components: radiation from the shocked and the unshocked regions.

Bogovalov & Aharonian (2000) investigated the inverse Compton emission from the region upstream the termination shock of the Crab pulsar. Comparisons between calculated and measured fluxes put limits on the parameters of the wind, in particular the size of the kinetic energy dominated region. Ball & Kirk (2000) investigated emission from an unshocked freely expanding wind with no termination shock in compact binaries. They computed spectra and light curves in the gamma-ray binary PSR B1259-63, a system with a 48 ms pulsar and a Be star in a highly eccentric orbit. The resulting gamma-ray emission is a line-like spectrum.

In addition to PSR B1259-63, two other binaries have been firmly confirmed as gamma-ray sources: LS 5039 (Aharonian et al. 2005) and LSI +61°303 (Albert et al. 2006). They are composed of a massive O or Be star and a compact object in an eccentric orbit. The presence of a young pulsar was de-

2

Cerutti, Dubus and Henri: Spectral signature of a free pulsar wind in LS 5039 and LSI +61°303

tected only in PSR B1259-63 (Johnston et al. 1992). Radio pulses are detectable but vanish near periastron, probably due to free-free absorption and interaction with the Be disk wind. The compact PWN scenario is most probably at work in this system and investigations were carried out to model high and very high energy radiation (Kirk et al. 1999; Sierpowska & Bednarek 2005; Khangulyan et al. 2007; Sierpowska-Bartosik & Bednarek 2008). In LS 5039 and LSI +61°303 the nature of the compact object is still controversial but spectral and temporal similarities with PSR B1259-63 argue in favor of the compact pulsar wind nebula scenario (Dubus 2006b). The VHE radiation would therefore be produced by the interaction between the pulsar wind and the stellar companion wind. The massive star provides a huge density of seed photons for inverse Compton scattering with the ultra-relativistic pairs from the pulsar wind. Because of the relative position of the compact object, the companion star and the observer, the Compton emission is modulated on the orbital period. The vicinity of a massive star is an opportunity to probe the pulsar wind at small scales.

The component of the shocked pulsar wind was computed in Dubus et al. (2008) for LS 5039 and limits on the electron distribution, the pulsar luminosity and the magnetic field at the termination shock were derived. Sierpowska-Bartosik & Torres (2008) calculated the VHE emission in LS 5039 as well, assuming a power law injection spectrum for the pairs in the unshocked pulsar wind and pair cascading. In this paper, we investigate the anisotropic inverse Compton scattering of stellar photons on the unshocked pulsar wind within the compact PWN scenario for LS 5039 and LSI +61°303. Because of their tight orbits, the photon density is higher than in the Crab pulsar and PSR B1259-63. A more intense gamma-ray signal from the unshocked pulsar wind is expected. The main purpose of this work is to constrain the bulk Lorentz factor γ_0 of the pairs and the shock geometry. The next section presents the method and the main equations used in order to compute spectra in gamma-ray binaries. Section 3 describes and shows the expected spectra for LS 5039 and LSI +61°303 with different parameters. Section 4 discusses the spectral signature from the unshocked pulsar wind.

2. Anisotropic Compton losses in γ -binaries

2.1. The cooling of pairs

An electron of energy $E_e = \gamma_e m_e c^2$ in a given soft photon field of density n_0 ph cm⁻³ cools down through inverse Compton scattering (here the term ‘electrons’ refers indifferently to electrons and positrons). The power lost by the electron is given by (Jones 1965; Blumenthal & Gould 1970)

$$-\frac{dE_e}{dt} = \int_{\epsilon_-}^{\epsilon_+} (\epsilon_1 - \epsilon_0) n_0 \frac{dN}{dtd\epsilon_1} d\epsilon_1 \quad (1)$$

where ϵ_0 is the incoming soft photon energy, ϵ_1 the scattered photon energy and $dN/dtd\epsilon_1$ is the Compton kernel. ϵ_{\pm} boundaries are fixed by the relativistic kinematics of inverse Compton scattering. The cooling of the pairs e^+/e^- depends on the angular distribution and spectrum of the incoming photon field. In

the simple case of a monoenergetic and unidirectional beam of photons in the Thomson limit, the calculation of the Compton energy loss per electron is

$$-\frac{dE_e}{dt} = \sigma_T c n_0 \epsilon_0 (1 - \beta \mu_0) \left[(1 - \beta \mu_0) \gamma_e^2 - 1 \right] \quad (2)$$

where σ_T is the Thomson cross section, $\mu_0 = \cos \theta_0$ and θ_0 the angle between the incoming photon and the direction of the electron motion. This calculation is done using the Compton kernel calculated by Fargion et al. (1997). In the Thomson limit, the cooling of the electron follow a γ_e^2 power law and has a strong angular dependence. In a more general way and for $\gamma_e \gg 1$, the power lost per electron is calculated with the kernel derived in Dubus et al. (2008) Eq. (A.6).

2.2. Compton cooling of the free pulsar wind

The pulsar is considered as a point-like source of monoenergetic and radially expanding wind of relativistic pairs e^+/e^- . The pulsar wind momentum is assumed to be entirely carried away by the pairs. The companion star, with a typical luminosity of $10^{38} - 10^{39}$ ergs s⁻¹, provides seeds photons for inverse Compton scattering onto the radially expanding electrons from the pulsar. The electrons see a highly anisotropic photon field. Inverse Compton efficiency has a strong dependence on θ_0 as seen in Eq. (2). Depending of the relative position and direction motion of the electron with respect to the incoming photons direction, the cooling of the wind is anisotropic as well. Figure 1 sketches the geometry considered in the binary system to perform calculations.

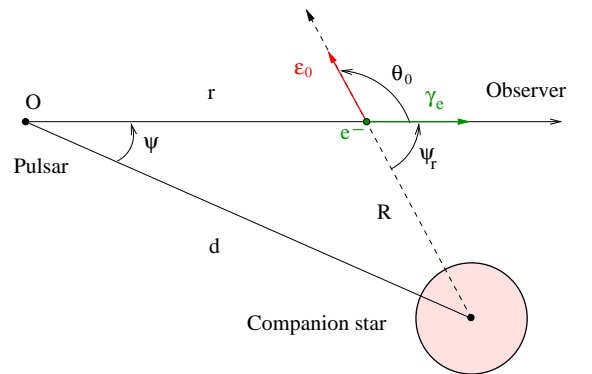


Fig. 1. Geometry of the binary system. Electrons of Lorentz factor γ_e are radially moving away at a distance r from the pulsar and R from the companion star. The angle ψ quantifies the relative position between the pulsar, the companion star and the observer. ψ_r measures the angle between the electron direction of motion and the line joining the companion star center to the electron position through its motion to the observer.

For ultra-relativistic electrons, the radial dependence of the electron Lorentz factor $\gamma_e(r)$ for a given viewing angle is obtained by solving the first order differential equation Eq. (1). Chernyakova & Illarionov (1999) found an analytical solution in the Thomson limit and Ball & Kirk (2000) derived a solution in the general case using the Jones (1965) results for a

point-like and monoenergetic star with $\gamma_e \gg 1$. In this approximation, the density of photons is $L_\star/(4\pi cR^2\bar{\epsilon}_0)$ ph cm⁻³, where L_\star is the star luminosity and $\bar{\epsilon}_0 = 2.7kT_\star$ the average energy photon from the star. The differential equation is then

$$\frac{d\gamma_e}{dr} = -\frac{1}{m_e c^3} \frac{L_\star}{4\pi cR^2} \int_{\epsilon_-}^{\epsilon_+} \left(\frac{\epsilon_1 - \bar{\epsilon}_0}{\bar{\epsilon}_0} \right) \frac{dN}{dt d\epsilon_1} d\epsilon_1 \quad (3)$$

where $R^2 = d^2 + r^2 - 2rd \cos \psi$. Calculations beyond the monoenergetic and point-like star approximation require two extra integrations, one over the star spectrum and the other onto the angular distribution of the incoming photons due to the finite size of the star. The complete differential equation is then given by

$$\frac{d\gamma_e}{dr} = -\frac{1}{m_e c^3} \iiint (\epsilon_1 - \epsilon_0) n_0 \frac{dN}{dt d\epsilon_1} d\epsilon_1 d\epsilon_0 d\Omega_0. \quad (4)$$

For a blackbody of temperature T_\star and a spherical star of radius R_\star , the incoming photon density n_0 is given by Eq. (13) in Dubus et al. (2008). It is more convenient to compute the calculation of the Lorentz factor as a function of ψ_r rather than r (see Fig. 1). These two variables are related through the relation

$$r = d \cos \psi \left(1 - \frac{\tan \psi}{\tan \psi_r} \right), \quad r \in [0, +\infty], \quad \psi_r \in [\psi, \pi]. \quad (5)$$

Figure 2 presents the numerical computed output solution $\gamma(\psi_r)$ applied to LS 5039 with an inclination of $i = 60^\circ$ for a neutron star where the viewing angle varies between $\pi/2 - i = 30^\circ$ and $\pi/2 + i = 150^\circ$. Here, the wind is assumed to have an injection Lorentz factor $\gamma(\psi_r, 0) = \gamma_0 = 10^5$ and to continue unimpeded to infinity (i.e. it is not contained by the stellar wind).

For small viewing angles ψ , the cooling of the wind is very efficient because the collision electron/photon is almost head-on and the electrons are moving in the direction of the star where the photon density increases. For viewing angles $\psi \gtrsim \pi/2$, the cooling of the pairs is limited. In all cases, most of the cooling occurs at $\psi_r \sim \psi$. For $\psi_r \gtrsim \pi/2$, the electron is moving away from the star and the scattering angle become small leading to a decrease in the wind energy loss. A comparison of Compton cooling between the point-like and finite size star is shown in Fig. 2. The effects of the finite size of the star are significant in two cases. The impact of the finite size of the star is important if the observer is within the cone defined by the star and the electron at apex (see Dubus et al. 2008 for more details). For viewing angles $\psi \lesssim \arcsin(R_\star/d)$, the cooling is less efficient whereas for $\psi \gtrsim \pi - \arcsin(R_\star/d)$ it is more efficient as it can be seen in the two extreme value of ψ in figure 2. The other situation occurs when the electrons travel close to the companion star surface, for $\psi \lesssim \pi/2$ and $\psi_r \gtrsim \pi/2$. In that case the angular distribution of the stellar photons is broad and close head-on scatterings are possible, leading to more efficient cooling compared with a point-like star. Nevertheless, these effects remain small for LS 5039 and LSI +61°303 and will be neglected in the following spectral calculations.

2.3. Unshocked pulsar wind spectra

The number of scattered photons per unit of time, energy and solid angle depends on three contributions: the density of the

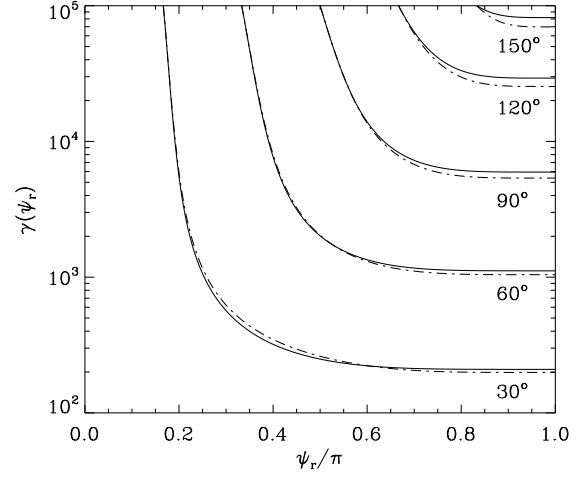


Fig. 2. Compton cooling of a monoenergetic, free pulsar wind with $\gamma_0 = 10^5$, $d = 2R_\star$ ($T_\star = 39\,000$ K, $R_\star = 9.3 R_\odot$). The different curves show the dependence with the viewing angle ψ on the cooling. ψ varies between 30° (bottom) and 150° (top) if $i = 60^\circ$. Each curve shows the evolution of the Lorentz factor γ with ψ_r as the electron moves along the line of sight. ψ_r is related to r by Eq. (5) so that $\psi_r = \psi$ at $r = 0$ and $\psi_r = \pi$ for $r = +\infty$. The calculation was carried out for a blackbody point like star (solid line) and taking into account the finite size of the star (dashed line).

incoming photons, the density of target electrons and the number of scattered photons per electron. The pulsar wind of luminosity L_p is assumed isotropic and monoenergetic, composed only of pairs and with a negligible magnetic energy density ($\sigma \ll 1$). The electrons density (e⁻ cm⁻³ erg⁻¹) is then proportional to $1/r^2$ if pair production is neglected. Here, the interesting quantity for spectral calculations is the number of electrons per unit of solid angle, energy and length, which is r^2 time the electrons density so that (Ball & Kirk 2000)

$$\frac{dN_e}{d\Omega_e d\gamma dr} = \frac{L_p}{4\pi c \beta_0 \gamma_0 m_e c^2} \delta(\gamma - \gamma_e(r)), \quad (6)$$

with δ the Dirac distribution. In deep Klein-Nishina regime, spectral broadening is expected because the continuous energy loss prescription fails ($\Delta E_e \sim E_e$). The complete kinetic equation must be used in order to describe accurately the electrons dynamics (see Blumenthal & Gould 1970 Eq. (5.7)). However, the δ approximation used here is reasonably good (Zdziarski 1989). The case of an anisotropic pulsar wind is discussed in §4. In the following, the pulsar wind will therefore be assumed to follow Eq. (6). Heating of the pulsar wind by the radiative drag is neglected (Ball & Kirk 2000).

In order to compute spectra, the emitted photons are supposed to be entirely scattered in the direction of the electron motion. Because of the ultra-relativistic motion of the electrons, most of the emission is within a cone of aperture angle of the order of $1/\gamma_e \ll 1$. In this classical approximation, the spectrum seen by the observer is the superposition of the contributions from the electrons along the line of sight pulsar-observer

4

Cerutti, Dubus and Henri: Spectral signature of a free pulsar wind in LS 5039 and LSI +61°303

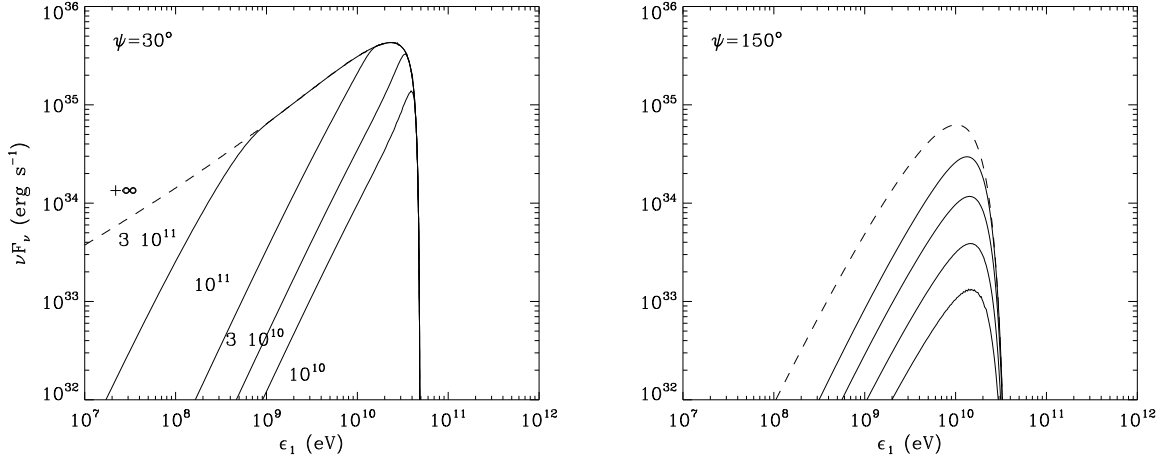


Fig. 3. Computed inverse Compton spectrum from the unshocked pulsar wind in LS 5039 and its dependence with the emitting region size R_s . The pulsar wind has $\gamma_0 = 10^5$, $L_p = 10^{36}$ erg s $^{-1}$ and the star is a point-like blackbody. Spectra are calculated at the superior (left) and inferior (right) conjunctions for different standoff distances $R_s = 10^{10}$ (bottom), $3 \cdot 10^{10}$, 10^{11} , $3 \cdot 10^{11}$ cm and $+\infty$ (dashed line).

in the solid angle $d\Omega_e$. The spectrum seen by the observer is obtained with the following formula

$$\frac{dN_{tot}}{dt d\epsilon_1 d\Omega_e} = \iiint n_0 \frac{dN}{dt d\epsilon_1} e^{-\tau_{\gamma\gamma}} \frac{dN_e}{d\Omega_e dy dr} dy d\epsilon_0 dr d\Omega_0 \quad (7)$$

where $\tau_{\gamma\gamma}$ takes into account the absorption of gamma-rays due to pair production with soft photons from the companion star and is calculated following Dubus (2006a).

2.4. The compact PWN geometry

The collision of the relativistic wind from the pulsar and the non-relativistic wind from the massive star produces two termination shock regions separated by a contact discontinuity (see Fig. 4). The geometry of the shock fronts are governed by the ratio of the flux wind momentum quantified by η and defined as (e.g. Stevens et al. 1992; Eichler & Usov 1993)

$$\eta = \frac{L_p}{c \dot{M}_w v_\infty} \quad (8)$$

where \dot{M}_w is the mass loss rate and v_∞ the stellar wind speed of the O/Be star. For two spherical winds, the standoff distance R_s depends on η and on the orbital separation d

$$R_s = \frac{\sqrt{\eta}}{1 + \sqrt{\eta}} d. \quad (9)$$

Bogovalov et al. (2008) have investigated the collision between the pulsar wind and the stellar wind in the binary PSR B1259-63, with a relativistic code and an isotropic pulsar wind in the hydrodynamical limit. They obtained the geometry for the relativistic and nonrelativistic shock fronts and the contact discontinuity. They find that the collision between the two winds produces an unclosed pulsar wind termination shock (in the backward facing direction) for $\eta > 1.25 \cdot 10^{-2}$.

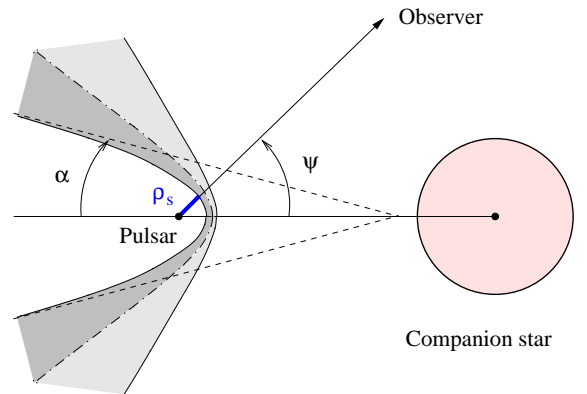


Fig. 4. Shock geometry considered for the wind collision. For $\eta > 1.25 \cdot 10^{-2}$, the pulsar wind region remains open with an asymptotic half-opening angle α . The dark region is the shocked relativistic pulsar wind and the light region is the shocked non-relativistic stellar wind, separated by a contact discontinuity (dot-dashed line). The size of the emitting zone seen by the observer ρ_s depends on the viewing angle ψ .

The size of the emitting region depends on the shock geometry and the viewing angle, which can therefore have a major impact on the emitted spectra. Ball & Dodd (2001) computed spectra from the unshocked pulsar wind in PSR B1259-63 for an hyperbolic shock front terminated close to the pulsar. They found a decrease in the spectra fluxes and a decrease in the light curve asymmetry and flux particularly near periastron compared with the spectra computed by Ball & Kirk (2000).

Figure 3 presents computed spectra, ignoring $\gamma\gamma$ absorption at this stage, applied to LS 5039 at the superior and inferior conjunctions for different standoff distances R_s and a pulsar wind with $\gamma_0 = 10^5$. At the superior conjunction where $\psi = 30^\circ$, the Compton cooling of the wind is efficient. The broadness in energy of the radiated spectra is related to the size

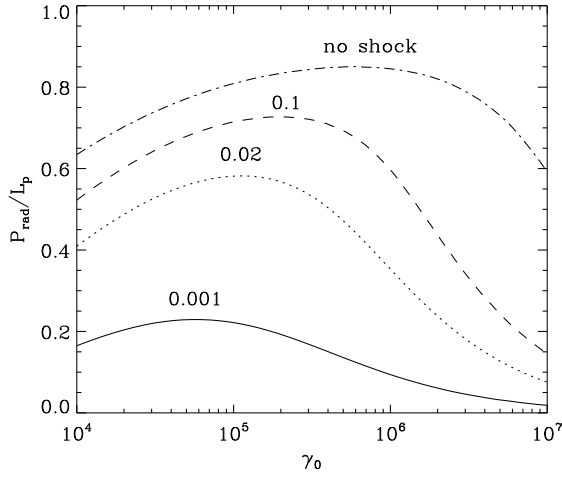


Fig. 5. Total radiated power by the unshocked pulsar wind P_{rad} in LS 5039 as a function of γ_0 . P_{rad} is computed at periastron for $\eta = 10^{-3}$ (solid line), $2 \cdot 10^{-2}$ (dotted line), 10^{-1} (dashed line) and with no termination shock (dotted-dashed line).

of the unshocked pulsar wind region. For small standoff distances $R_s \ll d$, spectra are truncated and sharp because the termination shock region is very close to the pulsar, so that the pairs do not have time to radiate before reaching the shock. For $R_s \gtrsim d$, the free pulsar wind region is extended and emission from cooled electrons starts contributing to the low energy tail in the scattered spectrum. The amplitude of the spectrum reaches a maximum when the injected particles can cool efficiently before reaching the shock. The spectral luminosity is then set by the injected power and is not affected anymore by the size of the emitting zone. At the inferior conjunction where $\psi = 150^\circ$, the cooling is less efficient and most of the emission occurs close to the pulsar where the photon density and θ_0 are greater, regardless of the size of the emitting region. The radiated flux then depends linearly on R_s . A complete investigation is presented in the next section where absorption and spectra along the orbit are computed and applied to LS 5039 and LSI +61°303, ignoring pair cascading.

3. Spectral signature of a monoenergetic pulsar wind in LS 5039 and LSI +61°303

In the following sections, the emission expected by the unshocked pulsar wind in LS 5039 and LSI +61°303 is compared with measured fluxes. Because spectra depends on the shock geometry and the injection Lorentz factor, spectra are calculated for various values of the two free parameters η and γ_0 .

3.1. LS 5039

The companion star and the pulsar winds are assumed isotropic and purely radial. The orbital parameters are those measured by Casares et al. (2005b) as used in Dubus et al. (2008).

Figure 5 gives the total power radiated by the electrons in the unshocked pulsar wind as a function of γ_0 at peri-

astron. Here, the shock front is assumed spherical of radius R_s . A maximum of efficiency is observed at about $\gamma_0 \sim 10^5$ which corresponds to the transition between the Thomson and Klein-Nishina regimes where the Compton timescale is shortest (Dubus 2006b). The fraction of the pulsar wind power radiated at periastron depends strongly on R_s . It is about 20% for $\eta = 10^{-3}$ and can reach 70% for $\eta = 0.1$. Hence, most of the spindown energy can be radiated directly by the unshocked pulsar wind.

Figure 6 presents computed spectra averaged along the orbit for different shock geometry and Lorentz factor with a pulsar spindown luminosity of $L_p = 10^{36}$ erg s $^{-1}$. The relativistic shock front is described by an hyperbolic equation. The hyperbola apex is set by Eq. (9) and the asymptotic half-opening angle α is taken from Eq. (27) in Bogovalov et al. (2008), both parameters depending only on η . Figure 4 sketches the shock morphology for $1.25 \cdot 10^{-2} < \eta < 1$ and presents the different shock fronts expected. The twist due to the orbital motion is ignored since most of the emission occurs in the vicinity of the pulsar. The size of the emitting zone ρ_s seen by the observer is thus set for any given viewing angle ψ . Note that it is always greater than R_s . The remaining free parameter γ_0 is chosen independently between 10^4 and 10^7 .

Computed spectra predict the presence of a narrow peak in the spectral energy distribution due to the presence of the free pulsar wind. The luminosity of this narrow peak can be comparable to or greater than the measured fluxes by EGRET and HESS (Hartman et al. 1999; Aharonian et al. 2006). For $\eta = 10^{-3}$, the pulsar wind termination shock is closed and the unshocked wind emission zone is small. For $\eta = 0.02$ and $\eta = 0.1$ the line spectra are well above both the limits imposed by the HESS observations. The extreme case with no termination shock shows little differences with the case where $\eta = 0.1$. Spectroscopic observations of LS 5039 constrains the O star wind parameters to $\dot{M}_w \sim 10^{-7} M_\odot \text{ yr}^{-1}$ and $v_\infty \sim 2400 \text{ km s}^{-1}$ (McSwain et al. 2004). Assuming $L_p = 10^{36}$ erg s $^{-1}$ then gives $\eta \sim 2 \cdot 10^{-2}$ (top right panel of Fig. 6) or $R_s \approx 2 \cdot 10^{11}$ cm as in (Dubus 2006b). In this case, almost half of the pulsar wind energy is lost to inverse Compton scattering before the shock is reached (Fig. 5). This is an upper limit since the reduced pulsar wind luminosity would bring the shock location closer to the pulsar than estimated from Eq. (9). HESS observations already rule out a monoenergetic pulsar wind with $\gamma_0 = 10^6$ or 10^7 and $L_p = 10^{36}$ erg s $^{-1}$ as this would produce a large component easily seen at all orbital phases (see Fig. 5 in Dubus et al. 2008). The EGRET observations probably also already rule out values of $\gamma \leq 10^5$.

3.2. LSI +61°303

In this system the stellar wind from the companion star is assumed to be composed of a slow dense equatorial disk and a fast isotropic polar wind. The stellar wind may be clumpy and Zdziarski et al. (2008) have proposed a model of the high-energy emission from LSI +61°303 that entails a mix between the stellar and the pulsar wind. The orbital parameters are those

6

Cerutti, Dubus and Henri: Spectral signature of a free pulsar wind in LS 5039 and LSI +61°303

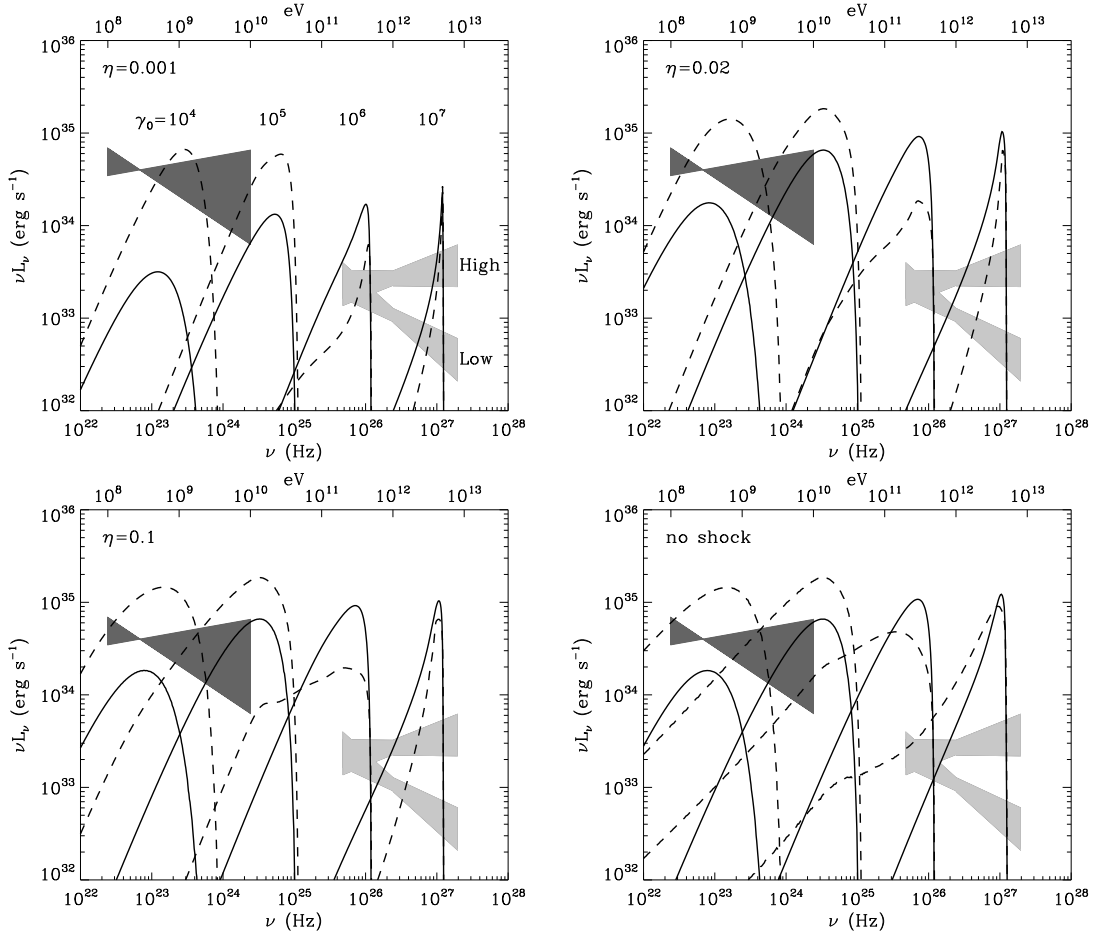


Fig. 6. Spectral signature from the unshocked pulsar wind expected in LS 5039 and dependence with γ_0 and η . Spectra are averaged on the orbital phases corresponding to the HESS ‘high state’ (solid line, $0.45 < \phi < 0.9$, with $\phi \equiv 0$ at periastron) and ‘low state’ (dashed line, $\phi < 0.45$ or $\phi > 0.9$). The spectra are compared with EGRET (dark bowtie) and HESS (light bowties) observations, adopting a distance of 2.5 kpc. In the top left panel, $\eta = 10^{-3}$ the shock is closed and the unshocked pulsar wind is assumed spherical. For $\eta = 2 \cdot 10^{-2}$ (top right panel) and $\eta = 0.1$ (bottom left panel) the shock is open with half-opening angles $\alpha \sim 2^\circ$ and $\alpha \sim 30^\circ$ respectively. The bottom right panel shows the extreme case with no termination shock.

measured by Casares et al. (2005a) (new orbital parameters were recently measured by Grundstrom et al. 2007).

Computed spectra applied to LSI +61°303 and averaged over the orbit to compare with EGRET and MAGIC luminosities (Hartman et al. 1999; Albert et al. 2006) are presented in Fig. 7. New data were recently reported by the MAGIC collaboration (Albert et al. 2008). They confirmed the measurements of the first observational campaign and found a periodicity in the gamma-ray flux close to the orbital period. The pulsar spin-down luminosity is set to $L_p = 10^{36}$ erg s $^{-1}$ and the injected Lorentz factor to 10^4 , 10^5 , 10^6 and 10^7 as for LS 5039. There is more uncertainty in η because of the complexity of the stellar wind. The polar outflow is usually modelled with $\dot{M}_w = 10^{-8} M_\odot \text{ yr}^{-1}$ and $v_\infty = 2000$ km s $^{-1}$ (Waters et al. 1988) leading to $\eta \sim 0.2 - 0.3$. Concerning the slow dense equatorial disk, the mass flux is typically one hundred times greater than the polar wind and the terminal velocity is a few hundred km s $^{-1}$ giving η compatible with $\sim 10^{-3} - 10^{-2}$.

The overall behaviour is similar to LS 5039. The spectral luminosities and the total power radiated by the unshocked pulsar wind (Fig. 8) are lower in LSI +61°303 than LS 5039 because the compact object is more distant to its companion star and the latter has a lower luminosity, leading to a decrease in the density of seed photons for inverse Compton scattering. If $\eta = 10^{-3}$, no constraints on γ_0 can be formulated as the spectrum is always below the observational limits. For larger values of η , the very high energy observations constrain γ_0 to be below 10^6 , assuming the pulsar wind is monoenergetic. Spectra were computed for $\eta = 0.53$ with $\dot{M}_w = 10^{-8} M_\odot \text{ yr}^{-1}$ and $v_\infty = 1000$ km s $^{-1}$ as used by Romero et al. (2007). In this case, the spectra are close to the freely propagating pulsar wind. The EGRET luminosity is slightly overestimated for $\gamma_0 \leq 10^5$ when $\eta = 0.53$.

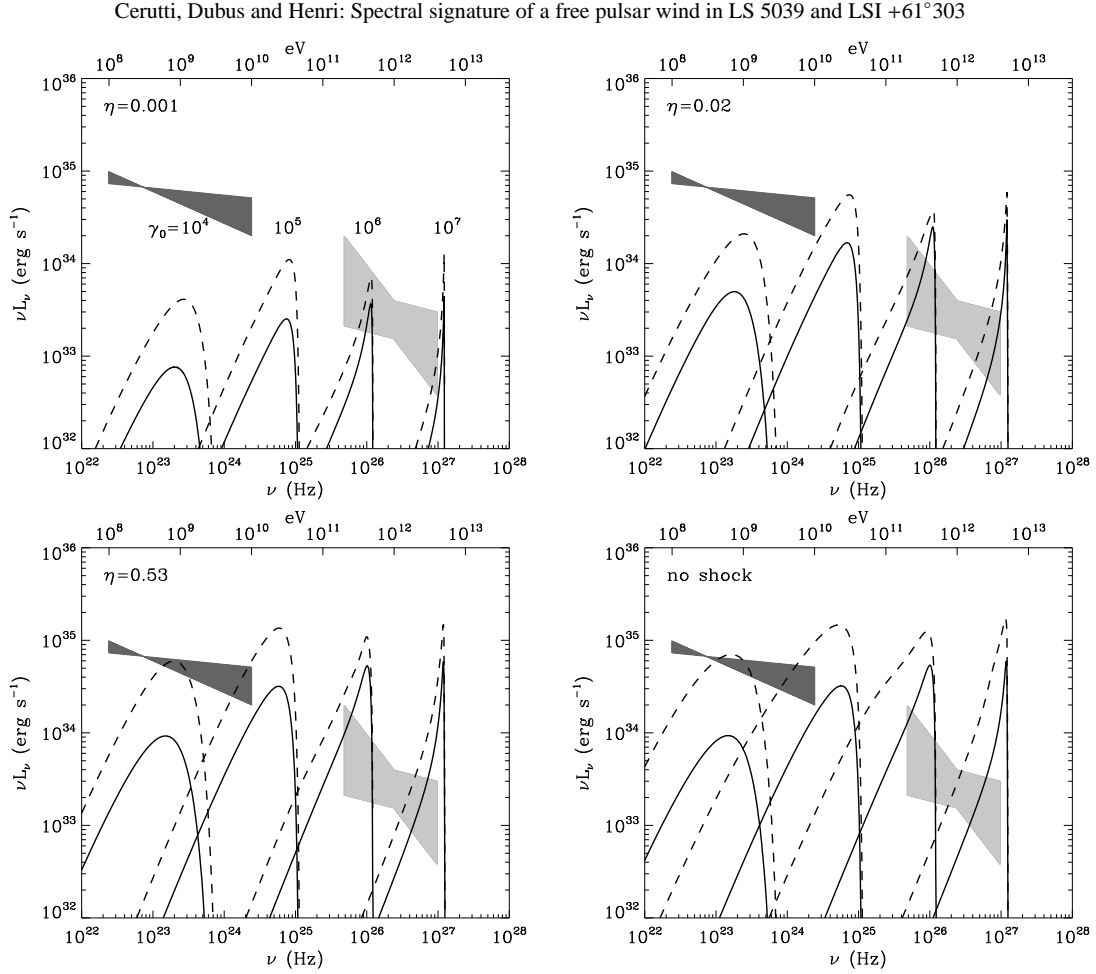


Fig. 7. Spectral signature from the unshocked pulsar wind expected in LSI +61°303 and dependence with γ_0 and η . Spectra are averaged between phase $0.4 < \phi < 0.7$ (solid line, at periastron $\phi \equiv 0.23$) and the complementary phases $\phi < 0.4$ or $\phi > 0.7$ (dashed line). Luminosities are compared with the EGRET (dark bowtie) and MAGIC (light bowtie) observations, adopting a distance of 2.3 kpc. In the top left panel, $\eta = 10^{-3}$ the shock is closed and the unshocked pulsar wind is assumed spherical. For $\eta = 2 \cdot 10^{-2}$ (top right panel) and $\eta = 0.53$ (bottom left panel) the shock is open with half-opening angles $\alpha \sim 2^\circ$ and $\alpha \sim 60^\circ$ respectively. The bottom right panel shows the extreme case with no termination shock.

4. Discussion

The proximity of the massive star in LS 5039 and LSI +61°303 provides an opportunity to directly probe the distribution of particles in the highly relativistic pulsar wind. The calculations show the inverse Compton emission from the unshocked wind should be a significant contributor to the observed spectrum. For a monoenergetic and isotropic pulsar wind the emission remains line-like, with some broadening due to cooling, as had been found previously for the Crab and PSR B1259-63 (Bogovalov & Aharonian 2000; Ball & Kirk 2000). However, here, such line emission can pretty much be excluded by the available very high energy observations of HESS or MAGIC, and (to a lesser extent) by the EGRET observations that show power-law spectra at lower flux levels.

4.1. Is the pulsar wind power overestimated?

Reducing the pulsar power (or, equivalently, increasing the distance to the object) would diminish the predicted unshocked wind emission relative to the observed emission. This is not viable as this would also reduce the level of the shocked pulsar wind emission. Similarly, the energy carried by the particles may represent only a small fraction of the wind energy. At distances of order of the pulsar light cylinder the energy is mostly electromagnetic. Evidence that this energy is converted to the kinetic energy of the particles comes from plerions, which probe distances of order 0.1 pc from the pulsar. It is therefore conceivable that this conversion is not complete at the distances under consideration here (0.01-0.1 AU). In this case the emission from the particle component would be reduced. However, the shocked emission would also be reduced as high σ shocks divert little of the energy into the particles (Kennel & Coroniti 1984). Furthermore, the high energy particles would preferentially emit synchrotron rather than inverse

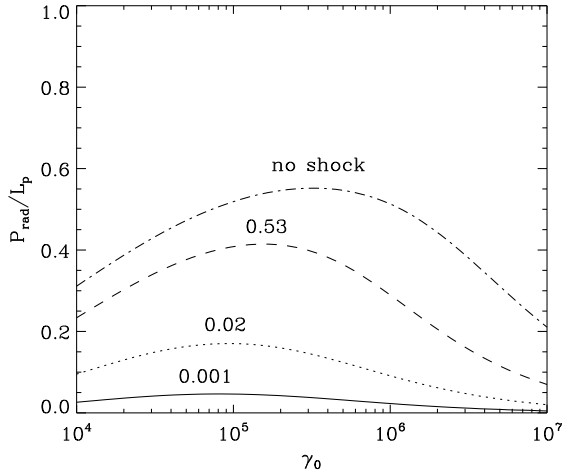


Fig. 8. Total radiated power by the unshocked pulsar wind P_{rad} in LSI +61°303 as a function of γ_0 . P_{rad} is computed at periastron for $\eta = 10^{-3}$ (solid line), $2 \cdot 10^{-2}$ (dotted line), 0.53 (dashed line) and with no termination shock (dotted-dashed line).

Compton due to the higher magnetic field. Hence, this possibility also seems unlikely.

Alternatively, the unshocked wind emission could be weaker compared to the shocked wind emission if the termination shock was closer to the pulsar, *i.e.* if one had a low η . In LS 5039 the unshocked wind emission is strong even with $\eta = 0.001$, which already implies a stronger stellar wind than optical observations seem to warrant. Furthermore, the value of the magnetic field would be high if the termination shock was close to the pulsar and this inhibits the formation of very high energy gamma-rays as the high energy electrons would then preferentially lose energy to synchrotron radiation (Dubus 2006b). Hence, it does not seem viable either to invoke a smaller zone for the free wind.

The conclusion is that the strong emission from the pulsar wind found in the previous section is robust against general changes in the parameters used. The following subsections examine how this emission can be made consistent with the observations.

4.2. Constrains on the pulsar wind Lorentz factor

The high level of unshocked emission is compatible with the observations only if it occurs around 10 GeV or above 10 TeV, *i.e.* outside of the ranges probed by EGRET and the current generation of Cherenkov telescopes. This poses stringent constraints on the energy of the particles in the pulsar wind. The Lorentz factor of the pulsar wind would be constrained to a few 10^5 or to more than 10^7 . The 1-100 GeV energy range will be partly probed by GLAST and HESS-2, and CTA in the more distant future. For instance, unshocked wind emission in LS 5039 would appear in the GLAST data as a spectral hardening at the highest energies. Nevertheless, that the free wind is

emitting in the least accessible spectral region may appear too fortuitous for comfort.

4.3. Anisotropic pulsar wind

The assumptions on the pulsar wind may be inaccurate. Pulsar winds are thought to be anisotropic (Begelman & Li 1992). Bogovalov & Khangoulyan (2002) interpreted the jet-torus structure revealed by X-ray Chandra observations of the Crab nebula, as a latitude dependence of the Lorentz factor $\gamma(\theta) = \gamma_i + \gamma_m \sin^2 \theta$ where γ_i is small (say 10^4) and γ_m is high (say 10^6). This hypothesis was corroborated by computational calculations in Komissarov & Lyubarsky (2004) where the synchrotron jet-torus was obtained. Here, the pulsar orientation to the observer is fixed (unless it precesses) so that the initial Lorentz factor of the pulsar wind along the line of sight would remain the same along the orbit. However, assuming the particle flux in the pulsar wind remains isotropic, the unshocked wind emission will appear at a lower energy and at a lower flux if the pulsar is seen more pole-on. The peak energy of the line-like spectral feature directly depends on $\gamma(\theta)$. Its intensity will also decrease in proportion as the pulsar power matches the latitude change in γ to keep the particle flux isotropic (see Eq. 6).

The shocked wind emission is set by the mean power and Lorentz factor of the wind and is insensitive to orientation. However, a more pole-on orientation will lower the contribution from the unshocked component. For instance, if $\gamma(\theta) = 10^4 + 10^6 \sin^2 \theta$ and $\theta = 17.5^\circ$ then the effective γ along the line-of-sight will be 10^5 and the observed luminosity of the unshocked emission will be lowered by a factor 10 compared to the mean pulsar power (Eq. 6). The probability to have an orientation corresponding to a value of $\gamma(\theta)$ of $0.1 \gamma_m$ or less is about $\frac{1}{5}$, assuming a uniform distribution of orientations. This would be enough to push the line emission to lower energies and to lower fluxes by a factor 10 or more, thereby relaxing the constraints on the mean Lorentz factor of the wind. Although this is not improbable, it would again require some fortuitous coincidence for the pulsars in both LS 5039 and LSI +61°303 to be seen close enough to the pole that their free wind emission is not detected.

4.4. The energy distribution of the pairs

The assumption of a monoenergetic wind may be incorrect, if only because the particles in the pulsar wind are bathed by a strong external photon field even as they accelerate and that this may lead to a significantly different distribution. Fig. 9 shows the emission from a pulsar wind where the particles have been assumed to have a power-law distribution with an index of -2 between γ of 10^3 and 10^8 . Obviously, a power-law distribution of pairs erases the line-like spectral feature. The emission properties are essentially identical to the emission from the shocked region with a harder and fainter *intrinsic* Compton spectrum when the pulsar is seen in front of the star compared to when it is behind. The emission from the shocked region is also shown, calculated as in Dubus et al. (2008). The par-

particle injection spectrum is the same in both regions. The particles are assumed to stay close to the pulsar and to escape from the shocked region after a time $t_{\text{esc}} = R_s/(c/3)$ (top) and $10R_s/(c/3)$ (bottom). Longer t_{esc} do not change the distribution any further. The longer escape timescale enables a harder particle distribution to emerge at high energies (where the radiative timescale is comparable to R_s/c , see Fig. 2 in Dubus 2006b). With $t_{\text{esc}} = R_s/(c/3)$, the shocked spectra is very close to the unshocked spectra. Generally, calculations show the spectra from the shocked and unshocked regions may be indistinguishable when the injected particles are taken to be the same in both regions. The only possible difference is that the longer residence time of particles in the shocked region allows for harder spectra.

4.5. Dominant emission from the unshocked wind

Emission from the unshocked wind could be the dominant contributor to the spectral energy distribution. In this case, the observations give the particle distribution in the pulsar wind. Sierpowska-Bartosik & Torres (2008) have considered such a scenario for LS 5039 and use a total energy in leptons of about 10^{35} erg s⁻¹ and a power-law distribution with an index around -2, both of which are adjusted to the observations and vary with orbital phase. The total pulsar power is much larger, 10^{37} erg s⁻¹, in order to have a big enough free wind emission zone. Most of the pulsar energy is then carried by nuclei. Such a large luminosity would make the pulsar very young, comparable to the Crab pulsar, implying a high birth rate for such systems. Fig. 10 shows the expected emission from a pulsar wind propagating to infinity and with a particle power law index of -1.5 from $\gamma = 10^3$ to 10^8 chosen to adjust the ‘high state’ of LS 5039. The injected power is 4×10^{35} erg s⁻¹. The injected spectrum gives a good fit of the ‘hard’ state. However, the ‘low’ state dominates the complete very high energy contribution ($\gtrsim 1$ TeV) due to the extended emitting region. Particles have enough time to radiate very high energy gamma-ray far away, where they are less affected by $\gamma - \gamma$ absorption.

A possible drawback of this scenario is that the synchrotron and inverse Compton emission are not tied by the shock conditions and that the total energy in leptons is low so that it is not clear how the radio, X-ray and gamma-ray observations below a few GeV would arise. It is also unclear how this can lead to a collimated radio outflow as seen in LSI +61°303. A possibility is emission from secondary pairs created in the stellar wind by cascading as suggested by Bosch-Ramon et al. (2008). More work is necessary to understand these different contributions and the signatures that may enable to distinguish them.

Another potential drawback of this scenario is that it does not explain why the very high energy gamma-ray flux is observed to peak close to apastron in LSI +61°303. If the inverse Compton scattering in the pulsar wind is responsible then the maximum should be around periastron, especially as gamma-gamma attenuation is very limited in LSI +61°303. On the other hand, if the emission arises from the shocked pulsar wind then synchrotron losses explain the lack of very high energy gamma-rays at periastron: the pulsar probes the dense equa-

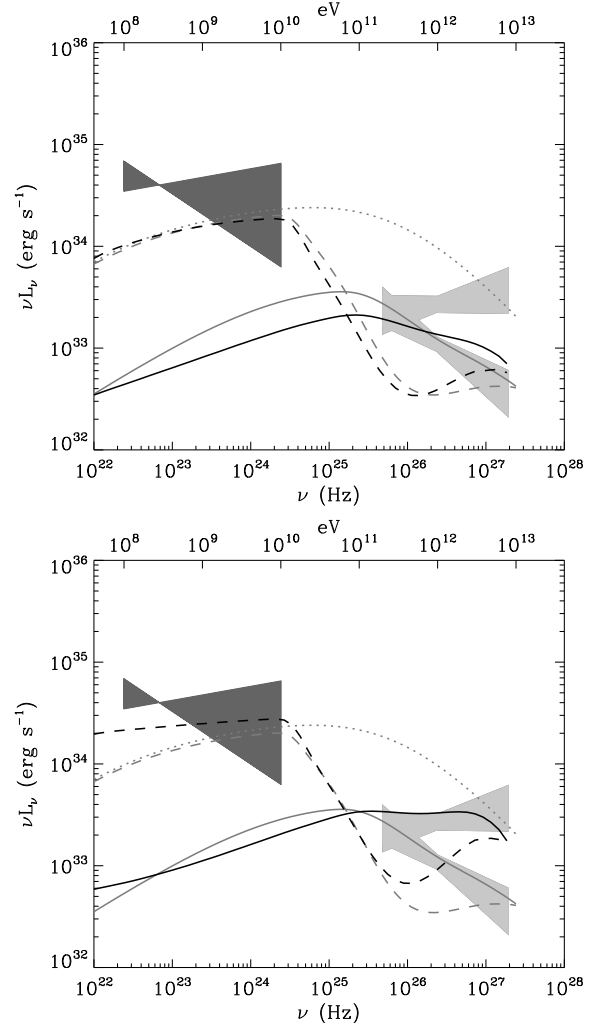


Fig. 9. Comparison between emission from the shocked and unshocked regions in LS 5039, taking the same particle injection for both regions. The distribution is a power-law of index -2 between $\gamma = 10^3$ and 10^8 with total power 10^{36} erg s⁻¹. Spectra are averaged to correspond to the HESS ‘high state’ (solid lines) and ‘low state’ (dashed lines) as in Fig. 6. The geometry is a sphere of radius 2×10^{11} cm. Grey lines show emission from the unshocked emission and dark lines show the emission from the shocked region. The orbital averaged *non-absorbed* spectrum from the unshocked pulsar wind is shown in grey dotted line. Particles escape from the shocked region on a timescale $t_{\text{esc}} = R_s/(c/3)$ (top) or $10R_s/(c/3)$ (bottom). The unshocked emission is the same in both panels.

torial wind from the Be star and the shock forms at a small distance, leading to a high magnetic field and a cutoff in the high-energy spectrum (see §6.2.2 in Dubus 2006b).

5. Conclusion

Gamma-ray binaries are of particular interest in the study of pulsar wind nebula at very small scales. The massive star radiates a large amount of soft seeds photons for inverse Compton scattering on relativistic electrons from the pulsar. One expects

10

Cerutti, Dubus and Henri: Spectral signature of a free pulsar wind in LS 5039 and LSI +61°303

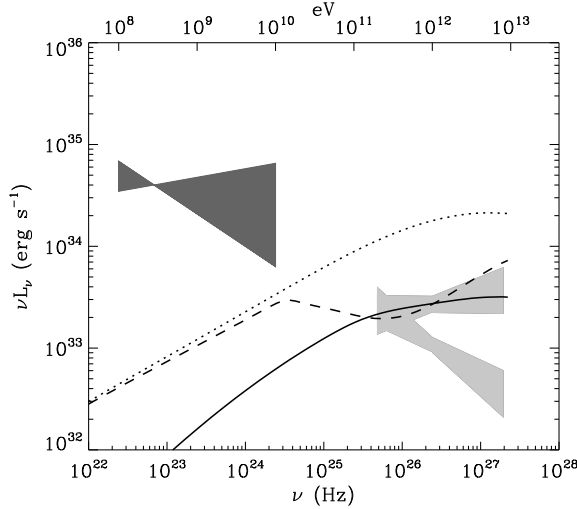


Fig. 10. Fit to the observations of LS 5039, assuming the dominant contribution comes from the unshocked region of the pulsar wind. The ‘high state’ of HESS corresponds to the solid line, the ‘low state’ to the dashed line and the dotted line to the orbital averaged non-absorbed spectrum. The injected particles had a power law distribution with an index of -1.5 between $\gamma = 10^3$ and 10^8 . The injected power is 4×10^{35} erg s^{-1} .

two contributions in the gamma-ray spectral energy distribution: one from the shocked pulsar wind and another from the unshocked pulsar wind. The spectral signature from the unshocked region is strong and depends on the shock geometry and the initial energy of the pairs in the pulsar wind. A significant fraction of the pulsar wind power can be lost to inverse Compton scattering before a shock forms with the stellar wind (Sierpowska & Bednarek 2005). The shock location will thus be slightly closer in to the neutron star than calculated without taking into account the losses in the pulsar wind, assuming the wind is composed only of e^+e^- pairs.

Significant emission from the free pulsar wind seems unavoidable. Inverse Compton losses in the free wind may be reduced if the shock occurs very close to the neutron star. This is unlikely as it would require a very strong stellar wind or a pulsar wind power that would be too low to produce the observed emission. If the pulsar wind is anisotropic then the orientation of the pulsar with respect to the observer can make the unshocked emission less conspicuous. This comes at the price of a peculiar orientation. If the pulsar wind is monoenergetic, then the line-like expected spectrum exceeds the observed very high energy power-laws for all geometries unless the pair energy is around 10 GeV or above 10 TeV. This pushes the direct emission from the wind in ranges where it may be constrained by future GLAST, HESS-2 or CTA measurements. The absence of any line emission will show that the assumption of a Crab-like monoenergetic, low σ pulsar wind was simplistic. If the pairs in the pulsar wind have a power-law distribution, then the unshocked emission is essentially indistinguishable from the shocked emission (Sierpowska-Bartosik & Torres 2008). A promising alternative is the *striped wind* model in which the wind remains highly magnetised up to the termination shock,

where the alternating field could be dissipated and accelerate particles (see Kirk et al. 2007 and references therein). Future theoretical studies on the generation of pulsar relativistic winds in the context of a strong source of photons may be able to yield the particle distribution to expect and lead to more accurate predictions.

Acknowledgements. GD acknowledges support from the *Agence Nationale de la Recherche*.

References

- Aharonian, F., Akhperjanian, A. G., Aye, K.-M., et al. 2005, *Science*, 309, 746
- Aharonian, F., Akhperjanian, A. G., Bazer-Bachi, A. R., et al. 2006, *A&A*, 460, 743
- Albert, J., Aliu, E., Anderhub, H., et al. 2006, *Science*, 312, 1771
- Albert, J., Aliu, E., Anderhub, H., et al. 2008, *ArXiv e-prints*, 0806.1865
- Ball, L. & Dodd, J. 2001, *Publications of the Astronomical Society of Australia*, 18, 98
- Ball, L. & Kirk, J. G. 2000, *Astroparticle Physics*, 12, 335
- Begelman, M. C. & Li, Z.-Y. 1992, *ApJ*, 397, 187
- Blumenthal, G. R. & Gould, R. J. 1970, *Reviews of Modern Physics*, 42, 237
- Bogovalov, S. V. & Aharonian, F. A. 2000, *MNRAS*, 313, 504
- Bogovalov, S. V. & Khangulyan, D. V. 2002, *Astronomy Letters*, 28, 373
- Bogovalov, S. V., Khangulyan, D. V., Koldoba, A. V., Ustyugova, G. V., & Aharonian, F. A. 2008, *MNRAS*, 570
- Bosch-Ramon, V., Khangulyan, D., & Aharonian, F. A. 2008, *A&A*, 482, 397
- Casares, J., Ribas, I., Paredes, J. M., Martí, J., & Allende Prieto, C. 2005a, *MNRAS*, 360, 1105
- Casares, J., Ribó, M., Ribas, I., et al. 2005b, *MNRAS*, 364, 899
- Chernyakova, M. A. & Illarionov, A. F. 1999, *MNRAS*, 304, 359
- Dubus, G. 2006a, *A&A*, 451, 9
- Dubus, G. 2006b, *A&A*, 456, 801
- Dubus, G., Cerutti, B., & Henri, G. 2008, *A&A*, 477, 691
- Eichler, D. & Usov, V. 1993, *ApJ*, 402, 271
- Fargion, D., Konoplich, R. V., & Salis, A. 1997, *Z. Phys. C.*, 74, 571
- Grundstrom, E. D., Caballero-Nieves, S. M., Gies, D. R., et al. 2007, *ApJ*, 656, 437
- Hartman, R. C., Bertsch, D. L., Bloom, S. D., et al. 1999, *ApJS*, 123, 79
- Johnston, S., Manchester, R. N., Lyne, A. G., et al. 1992, *ApJ*, 387, L37
- Jones, F. C. 1965, *Physical Review*, 137, 1306
- Kennel, C. F. & Coroniti, F. V. 1984, *ApJ*, 283, 694
- Khangulyan, D., Hnatic, S., Aharonian, F., & Bogovalov, S. 2007, *MNRAS*, 380, 320
- Kirk, J. G., Ball, L., & Skjaeraasen, O. 1999, *Astroparticle Physics*, 10, 31
- Kirk, J. G., Lyubarsky, Y., & Petri, J. 2007, *ArXiv Astrophysics e-prints*, 0703.116

- Komissarov, S. S. & Lyubarsky, Y. E. 2004, *MNRAS*, 349, 779
- McSwain, M. V., Gies, D. R., Huang, W., et al. 2004, *ApJ*, 600, 927
- Rees, M. J. & Gunn, J. E. 1974, *MNRAS*, 167, 1
- Romero, G. E., Okazaki, A. T., Orellana, M., & Owocki, S. P. 2007, *A&A*, 474, 15
- Sierpowska, A. & Bednarek, W. 2005, *MNRAS*, 356, 711
- Sierpowska-Bartosik, A. & Bednarek, W. 2008, *MNRAS*, 347
- Sierpowska-Bartosik, A. & Torres, D. F. 2008, *ArXiv e-prints*, 0801.3427
- Stevens, I. R., Blondin, J. M., & Pollock, A. M. T. 1992, *ApJ*, 386, 265
- Waters, L. B. F. M., van den Heuvel, E. P. J., Taylor, A. R., Habets, G. M. H. J., & Persi, P. 1988, *A&A*, 198, 200
- Zdziarski, A. A. 1989, *ApJ*, 342, 1108
- Zdziarski, A. A., Neronov, A., & Chernyakova, M. 2008, *ArXiv e-prints*, 0802.1174

Part III

Pair cascade emission in gamma-ray binaries

6	Anisotropic pair production	127
7	One-dimensional pair cascading	141
8	Three-dimensional pair cascading	169

6

Anisotropic pair production

Outline

1. What we want to know	127
2. Kinematics and threshold energy	128
3. Cross sections	129
4. Construction of the center-of-mass frame	130
§ 49. Geometrical construction	130
§ 50. Lorentz transform parameters	131
5. Rate of gamma-ray absorption	131
6. The spectrum of the produced pair	132
§ 51. General solution	132
§ 52. Anisotropic pair production kernel	133
§ 53. Integration over a power-law energy distribution and anisotropic effects	134
§ 54. Comparison with the isotropic and mono-energetic solution	134
§ 55. Comparison with Böttcher & Schlickeiser solution	135
7. The density of pairs	136
8. What we have learned	138
9. [Français] Résumé du chapitre	138
§ 56. Contexte et objectifs	138
§ 57. Ce que nous avons appris	138

PHOTON-PHOTON ANNIHILATION yields a pair electron-positron above the threshold energy for pair production. I investigate below the interaction between two mono-energetic beams of photons. I provide the equations for the detailed calculation of the spectrum of pairs produced in this interaction. This study is similar in scope than the one for anisotropic inverse Compton scattering presented in Chapter 3. In particular, I focus my investigations on the angular dependence of the spectrum of the created pairs. This work is based on previous studies by Gould & Schröder (1967); Bonometto & Rees (1971); Böttcher & Schlickeiser (1997). Comparisons with known formulae are also presented in this chapter.

1. What we want to know

- What is the spectrum of the e^-/e^+ pair created by photon-photon annihilation?

- What is the angular dependence?
- What is the density of pair produced?

2. Kinematics and threshold energy

We consider the annihilation process $\gamma(k_1) + \gamma(k_0) \rightarrow e^+(p_1) + e^-(p_2)$ (Fig. 50). Defining the 4-momentum of each particle in the observer frame

$$k_1 = \begin{pmatrix} \epsilon_1 \\ \mathbf{k}_1 \end{pmatrix} \quad k_0 = \begin{pmatrix} \epsilon_0 \\ \mathbf{k}_0 \end{pmatrix} \quad p_1 = \begin{pmatrix} E_e \\ \mathbf{p}_1 \end{pmatrix} \quad p_2 = \begin{pmatrix} E'_e \\ \mathbf{p}_2 \end{pmatrix}, \quad (50.203)$$

and in the center-of-mass frame (primed quantities) where $\mathbf{k}'_0 + \mathbf{k}'_1 = \mathbf{p}'_1 + \mathbf{p}'_2 = \mathbf{0}$, we have

$$k'_1 = \begin{pmatrix} \epsilon'_1 \\ \mathbf{k}'_1 \end{pmatrix} \quad k'_0 = \begin{pmatrix} \epsilon'_1 \\ -\mathbf{k}'_1 \end{pmatrix} \quad p'_1 = \begin{pmatrix} \epsilon_e \\ \mathbf{p}'_1 \end{pmatrix} \quad p'_2 = \begin{pmatrix} \epsilon_e \\ -\mathbf{p}'_1 \end{pmatrix}. \quad (50.204)$$

Using the Lorentz invariance of the total 4-momentum module, we can write

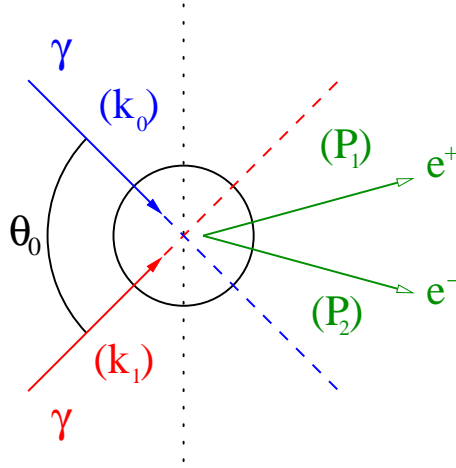


FIG. 50. Kinematics for pair production. The photons annihilate and produce a pair electron-positron if the total energy available in the center-of-mass frame is greater than the rest mass energy of the pair.

$$(k_1 + k_0)^2 = (p'_1 + p'_2)^2 \quad (50.205)$$

$$k_1^2 + k_0^2 + 2k_1 \cdot k_0 = p_1'^2 + p_2'^2 + 2p'_1 \cdot p'_2 \quad (50.206)$$

$$2\epsilon_1\epsilon_0(1 - \cos\theta_0) = 2m_e^2c^4 + 2(\epsilon_e^2 + |\mathbf{p}'_1|^2) \quad (50.207)$$

An electron-positron pair will be created if the total energy available in the center-of-mass (CM) frame is at least equal to the rest mass energy of the pair. At threshold, the pair is produced at rest in the CM frame, *i.e.* with no kinetic energy so that

$$p'_{1/2} = \begin{pmatrix} m_e c^2 \\ \mathbf{0} \end{pmatrix}. \quad (50.208)$$

It is useful in the following to define the Lorentz invariant quantity s

$$s = \frac{1}{4}(k_0 + k_1)^2 = \frac{\epsilon_0\epsilon_1}{2}(1 - \cos\theta_0). \quad (50.209)$$

Hence, a pair is created if

$$s \geq m_e^2 c^4. \quad (50.210)$$

Also, $s = \epsilon_e^2$ then the Lorentz factor of the pair in the CM frame can be expressed as

$$\gamma = \frac{\epsilon_e}{m_e c^2} = \frac{\sqrt{s}}{m_e c^2} \quad (50.211)$$

and since $\beta = (1 - 1/\gamma^2)^{1/2}$, we have

$$\beta = \left(1 - \frac{m_e^2 c^4}{s}\right)^{1/2}. \quad (50.212)$$

3. Cross sections

The differential cross section for pair production can be precisely computed by Quantum Electrodynamics with the perturbation theory. At the second order of the development, two Feynman diagrams interfere (Fig. 51).

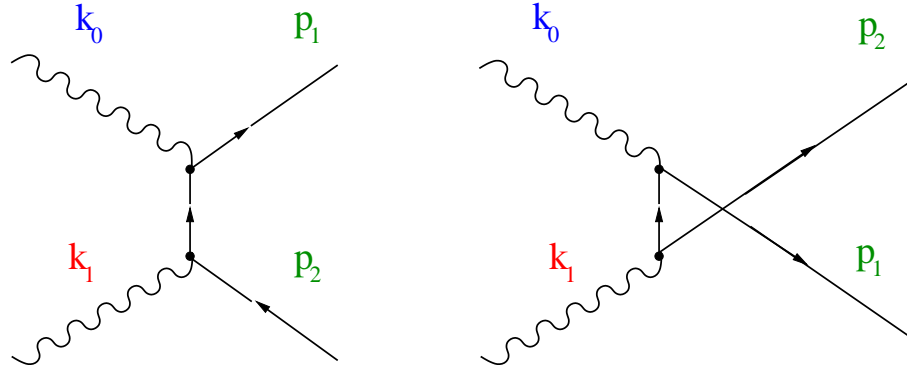


FIG. 51. Second order Feynman diagram for pair production.

The differential cross section in the CM frame is given by (see *e.g.* Bonometto & Rees 1971)

$$\frac{d\sigma_{\gamma\gamma}}{d(\beta \cos \theta'_1)} = \frac{\pi r_e^2}{2} (1 - \beta^2) \left\{ \frac{1 - (\beta \cos \theta'_1)^4 + 2(1 - \beta^2) [\beta^2 - (\beta \cos \theta'_1)^2]}{[1 - (\beta \cos \theta'_1)^2]^2} \right\}, \quad (50.213)$$

where β is the velocity of the created electron (or the positron) in the CM frame, and θ'_1 is the angle between the direction of the outgoing pair and the incoming photons direction in the CM frame. The differential cross section is maximum for $\cos \theta'_1 = \pm 1$ and minimum for $\cos \theta'_1 = 0$ (see Fig. 52). In other words, the pair is mostly created along the direction of the incoming radiation in the CM frame. Close to threshold ($\beta < 0.7$), the cross section is almost isotropic as it does not have a strong angular dependence. For $\beta > 0.7$, the angular dependence increases and the cross section degenerates into two symmetric peaks at $\cos \theta'_1 = \pm 1$ for $\beta \approx 1$.

The total pair production cross section given in Eq. (11.58) (see Chapter 2) is obtained by integrating Eq. (50.213) over the solid angle

$$\sigma_{\gamma\gamma} = \int_{-\beta}^{+\beta} \frac{d\sigma_{\gamma\gamma}}{d(\beta \cos \theta'_1)} d(\beta \cos \theta'_1). \quad (50.214)$$

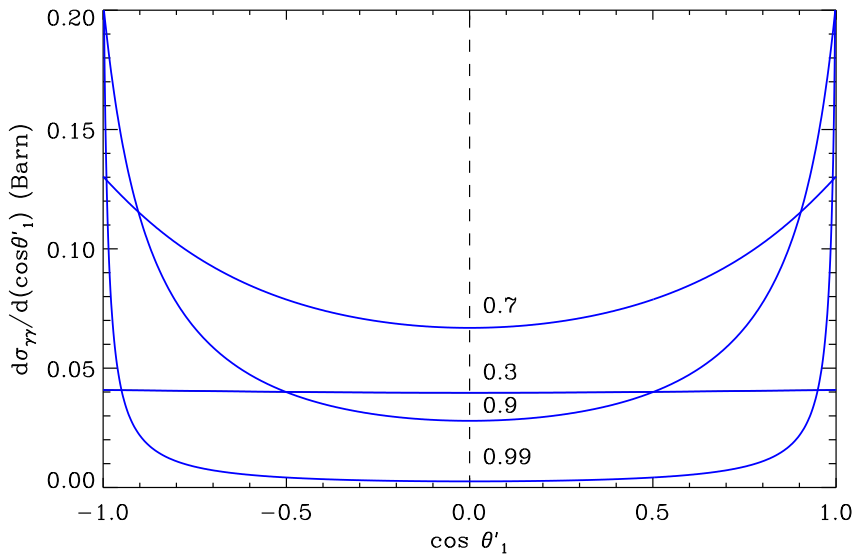


FIG. 52. Variation of the differential cross section $d\sigma_{\gamma\gamma}/d(\cos\theta'_1)$ for pair production as a function of $\cos\theta'_1$ for $\beta = 0.3, 0.7, 0.9$ and 0.99 .

4. Construction of the center-of-mass frame

In this section, we derive the parameters for the relativistic boost (β', γ') to connect the CM frame to the observer frame. First, we are going to use a simplifying approximation for the calculations.

§ 51. Geometrical construction

The CM frame is built from the condition $\mathbf{p}'_{tot} = \mathbf{k}'_0 + \mathbf{k}'_1 = \mathbf{0}$. The direction of motion of the center-of-mass in the observer frame is given by the sum of the two initial (or final) momenta vectors (Fig. 53).

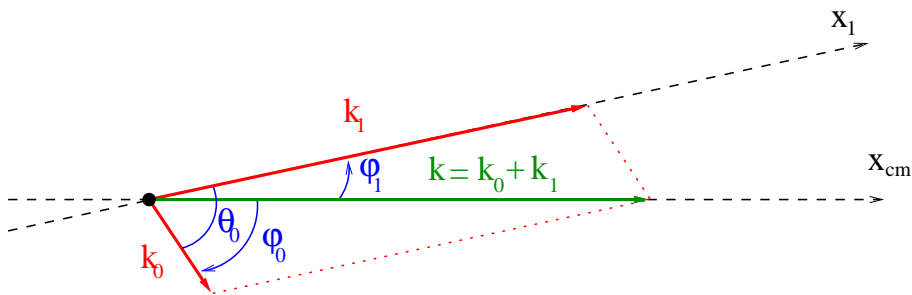


FIG. 53. Geometrical construction of the center-of-mass frame direction of motion (x_{cm} -axis).

If $\epsilon_1 \gg \epsilon_0$, the direction of motion of the CM frame coincides with the direction of the primary gamma-ray photon ϵ_1 . The angle between the gamma ray and the CM direction of motion ϕ_1 tends to 0. Indeed, we have

$$\mathbf{k}_1 \cdot \mathbf{k} = \mathbf{k}_1 \cdot \mathbf{k}_1 + \mathbf{k}_1 \cdot \mathbf{k}_0 \tag{51.215}$$

$$\Rightarrow \cos \phi_1 = \frac{\epsilon_1}{\sqrt{\epsilon_1^2 + \epsilon_0^2}} \left(1 + \frac{\epsilon_0}{\epsilon_1} \cos \theta_0 \right), \quad (51.216)$$

so that if $\epsilon_1 \gg \epsilon_0$, $\phi_1 \approx 0$. Also, the angle between the soft photon and the CM direction of motion ϕ_0 degenerates into θ_0 since

$$\mathbf{k}_0 \cdot \mathbf{k} = \mathbf{k}_0 \cdot \mathbf{k}_1 + \mathbf{k}_0 \cdot \mathbf{k}_0 \quad (51.217)$$

$$\Rightarrow \cos \phi_0 = \frac{\epsilon_1}{\sqrt{\epsilon_1^2 + \epsilon_0^2}} \left(\frac{\epsilon_0}{\epsilon_1} + \cos \theta_0 \right), \quad (51.218)$$

hence $\phi_0 \approx \theta_0$ if $\epsilon_1 \gg \epsilon_0$. In practice, this simplifying assumption will be always fulfilled in the context of this thesis since the target photons, generated by the massive star, have a few eV only. In this case, pair production will occur for photons above $\epsilon_1 \gtrsim 10 \text{ GeV} \gg \epsilon_0$ (Eq. 50.210).

§ 52. Lorentz transform parameters

With the simplifying assumption $\epsilon_1 \gg \epsilon_0$, the Doppler shift formulae between the CM frame and the observer frame are (see Eqs. 16.78-16.79)

$$\epsilon'_0 \approx \gamma' (1 - \beta' \cos \theta_0) \epsilon_0 \quad (52.219)$$

$$\epsilon'_1 \approx \gamma' (1 - \beta') \epsilon_1. \quad (52.220)$$

Both frames are linked *via* the parameters of the Lorentz boost β' and γ' . Because $\epsilon'_1 = \epsilon'_0$

$$\beta' = \frac{\epsilon_1 - \epsilon_0}{\epsilon_1 - \epsilon_0 \cos \theta_0}. \quad (52.221)$$

With Eq. (50.209) and because $\epsilon_1 \gg \epsilon_0$,

$$\beta' \approx \frac{1}{1 + 2s/\epsilon_1^2} \approx 1 - \frac{2s}{\epsilon_1^2}. \quad (52.222)$$

Writing $\beta' = (1 - 1/\gamma'^2)^{1/2} \approx 1 - 1/2\gamma'^2$, the Lorentz factor of the transform is then

$$\gamma' = \frac{\epsilon_1}{2\sqrt{s}}. \quad (52.223)$$

5. Rate of gamma-ray absorption

The rate of absorption of a gamma-ray photon of energy ϵ_1 bathed in a soft radiation field of density $dn/d\epsilon d\Omega$ per unit of path length l is (Gould & Schröder 1967)

$$\frac{d\tau_{\gamma\gamma}}{dl} = \iint \frac{dn}{d\epsilon d\Omega} (1 - \cos \theta) \sigma_{\gamma\gamma} d\epsilon d\Omega, \quad (52.224)$$

where θ is the angle between the soft photon of energy ϵ and the gamma-ray photon. Let's rewrite this equation performing the integration over the invariant s rather than over $\cos \theta$. With

$$d(\cos \theta) = -\frac{2}{\epsilon_1 \epsilon} ds, \quad (52.225)$$

the differential gamma-ray opacity is

$$\frac{d\tau_{\gamma\gamma}}{dl} = \frac{4}{\epsilon_1^2} \int_{\phi} \int_s \int_{\epsilon} \frac{s}{\epsilon^2} \frac{dn}{d\epsilon d\Omega} \sigma_{\gamma\gamma} d\epsilon ds d\phi. \quad (52.226)$$

This quantity tells us about the probability of absorption of a gamma ray but does not provide any information about the energy distribution of the pair produced.

6. The spectrum of the produced pair

§ 53. General solution

By analogy with the calculation of the rate of absorption Eq. (52.226), Bonometto & Rees (1971) suggested that the probability for a gamma ray of energy ϵ_1 to create an electron with an energy between E_e and $E_e + dE_e$ and a positron of energy $E'_e \approx \epsilon_1 - E_e$ (if $\epsilon_1 \gg \epsilon$, condition always fulfilled in our context) between l and $l + dl$ is

$$g_{\gamma\gamma} = \frac{4}{\epsilon_1^2} \int_{\phi} \int_s \int_{\epsilon} \frac{s}{\epsilon^2} \frac{dn}{d\epsilon d\Omega} \frac{d\sigma_{\gamma\gamma}}{dE_e} d\epsilon ds d\phi, \quad (53.227)$$

where the differential cross section $d\sigma_{\gamma\gamma}/dE_e$ can be expressed as

$$\frac{d\sigma_{\gamma\gamma}}{dE_e} = \frac{d\sigma_{\gamma\gamma}}{d(\beta \cos \theta'_1)} \frac{d(\beta \cos \theta'_1)}{dE_e}. \quad (53.228)$$

We need an extra equation with an explicit relation between E_e and $\beta \cos \theta'_1$. This link is given by the Lorentz transform of the electron energy from the observer to the CM frames which is

$$E_e = \gamma' \left[s^{1/2} + \beta' (s - m_e^2 c^4)^{1/2} \cos \theta'_1 \right]. \quad (53.229)$$

Defining $x = \gamma'^2$, β and $\beta \cos \theta'_1$ can be rewritten as

$$\beta(x) = \left(1 - \frac{4m_e^2 c^4 x}{\epsilon_1^2} \right)^{1/2} \quad (53.230)$$

$$\beta \cos \theta'_1(x) = \frac{2E_e - \epsilon_1}{\epsilon_1 (1 - \frac{1}{x})^{1/2}}. \quad (53.231)$$

Then,

$$\frac{d(\beta \cos \theta'_1)}{dE_e} = \frac{2}{\epsilon_1 (1 - \frac{1}{x})^{1/2}} \quad (53.232)$$

$$ds = -\frac{\epsilon_1^2}{4x^2} dx. \quad (53.233)$$

The general expression for $g_{\gamma\gamma}$ is

$$g_{\gamma\gamma} = \frac{\epsilon_1}{4} \int_{\phi} \int_x \int_{\epsilon} \frac{1}{\epsilon^2 x^3} \frac{2}{(1 - \frac{1}{x})^{1/2}} \frac{dn}{d\epsilon d\Omega} \frac{d\sigma_{\gamma\gamma}}{d(\beta \cos \theta'_1)} (\beta(x), \beta \cos \theta'_1(x)) d\epsilon dx d\phi, \quad (53.234)$$

This equation coincides with Eq. (2.14) in Bonometto & Rees (1971). Because $-1 \leq \cos \theta'_1 \leq +1$, we have $E_- \leq E_e \leq E_+$ with

$$E_{\pm}(x) = \frac{\epsilon_1}{2} \left[1 \pm \left(1 - \frac{1}{x} \right)^{1/2} \left(1 - \frac{4m_e^2 c^4 x}{\epsilon_1^2} \right)^{1/2} \right]. \quad (53.235)$$

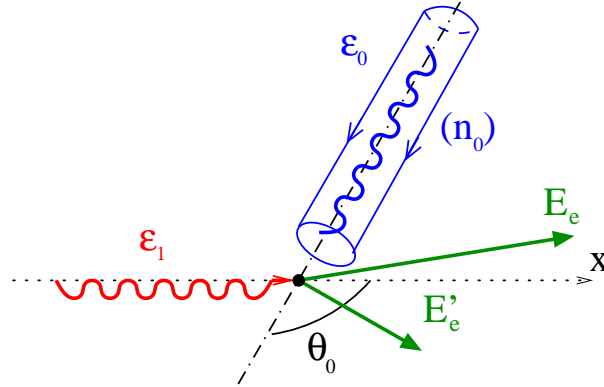


FIG. 54. Geometrical configuration for the computation of the anisotropic pair production kernel.

§ 54. Anisotropic pair production kernel

Similarly to what I have done for anisotropic inverse Compton scattering (see Sect. 4 in Chapter 3), I derive here from Eq. (53.234) the anisotropic pair production kernel. This is a convenient tool for spectral calculations where complex source of radiation are usually considered. Let's consider a mono-energetic beam of soft photons interacting with a gamma-ray photon with a pitch angle θ_0 (Fig. 54), where the condition $\epsilon_0 \ll \epsilon_1$ is fulfilled. The normalized soft photon density in the observer frame is

$$\frac{dn}{d\epsilon d\Omega} = \delta(\epsilon - \epsilon_0) \delta(\mu - \mu_0) \delta(\phi - \phi_0), \quad (54.236)$$

where $\mu_{(0)} \equiv \cos \theta_{(0)}$ and δ is the Dirac distribution. Transforming the Dirac on μ into a Dirac on x (using Eq. 17.90), we obtain

$$\delta(\mu - \mu_0) = \frac{\epsilon_1}{2\epsilon_0(1 - \mu_0)^2} \delta(x - x_0), \quad (54.237)$$

with

$$x_0 = \frac{\epsilon_1}{2\epsilon_0(1 - \mu_0)}. \quad (54.238)$$

Injecting Eq. (54.236) into Eq. (53.234) leads to the final expression for the anisotropic pair production kernel

$$g_{\gamma\gamma} = \frac{2(1 - \mu_0)}{\epsilon_1 \left(1 - \frac{1}{x_0}\right)^{1/2}} \frac{d\sigma_{\gamma\gamma}}{d(\beta \cos \theta'_1)} (\beta(x_0), \beta \cos \theta'_1(x_0)) \quad (54.239)$$

and with $E_-(x_0) \leq E_e \leq E_+(x_0)$. The pair production kernel has a dependence on the angle of interaction θ_0 and is symmetric with respect to $E_e = \epsilon_1/2$ (Fig. 55). $g_{\gamma\gamma}$ is peaked at $E_e = E_{\pm}$. Close to threshold ($s \approx m_e^2 c^4$), there is almost no angular dependence and the pair shares equally the energy of the primary gamma ray $E_e \approx E'_e \approx \epsilon_1/2$. Far from threshold ($s \gg m_e^2 c^4$), the kernel degenerates into two peaks where one lepton takes almost all the energy of the gamma-ray photon $E_e \approx \epsilon_1$ and $E'_e \approx 0$ (Fig. 55).

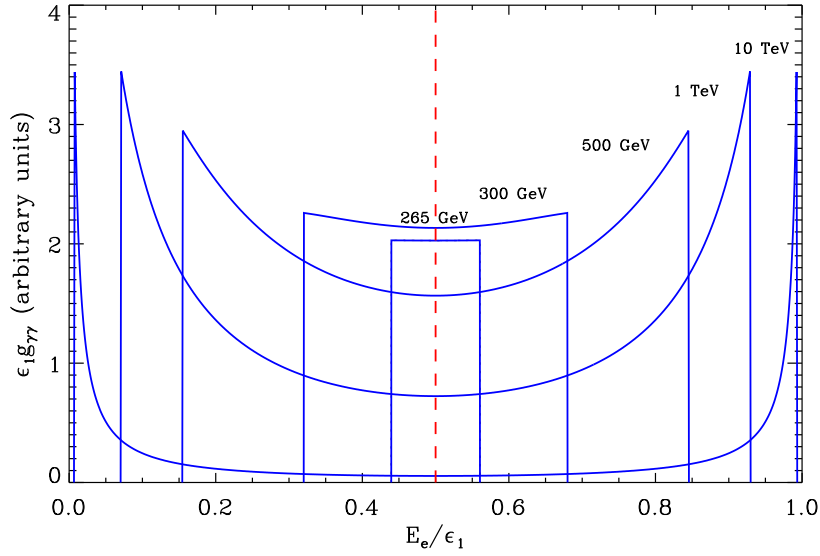


FIG. 55. Spectrum the pair produced in the interaction of a gamma-ray photon of energy $\epsilon_1 = 265$ GeV, 300 GeV, 500 GeV, 1 TeV and 10 TeV with a mono-energetic beam of soft radiation ($\epsilon_0 = 1$ eV). The collision is head-on here ($\theta_0 = \pi$). The threshold energy for pair production is ≈ 260 GeV in this configuration.

§ 55. Integration over a power-law energy distribution and anisotropic effects

The angular dependence of the kernel can be better appreciated if a power law energy distribution is considered for the primary gamma rays. If $dN/d\epsilon_1 \propto \epsilon_1^{-\alpha}$, $\epsilon_- < \epsilon_1 < \epsilon_+$ (with ϵ_{\pm} far from threshold), the spectrum of created pairs is

$$g_{\gamma\gamma}^{pl} \propto \int_{\epsilon_1} \epsilon_1^{-\alpha} g_{\gamma\gamma} d\epsilon_1. \quad (55.240)$$

In Fig. 56, the spectrum of pairs is shown for different values for the angle of interaction θ_0 . The low energy cut-off is due to threshold and depends on the angle (see Eq. 50.210). At very high-energy (*i.e.* far from threshold), the angular dependence decreases and pairs follow a power law distribution softer than the primary injection of photons. Pair production is more efficient for head-on collisions in the observer frame ($\theta_0 = 180^\circ$), as for inverse Compton scattering (see § 23). For rear-end collisions ($\theta_0 = 0^\circ$), no pairs are produced since the threshold energy for pair production becomes infinite.

§ 56. Comparison with the isotropic and mono-energetic solution

Aharonian *et al.* (1983) found an analytical formula for the pair production kernel for an isotropic distribution of soft radiation if $\epsilon_1 \gg \epsilon_0$. We would like here to compare our formula in Eq. (54.239) averaged over the solid angles with the analytical solution. The kernel averaged for an isotropic gas of photons can be computed by performing the following integrals

$$g_{\gamma\gamma}^{iso} = \frac{1}{4\pi} \iint g_{\gamma\gamma} \sin\theta_0 d\theta_0 d\phi_0. \quad (56.241)$$

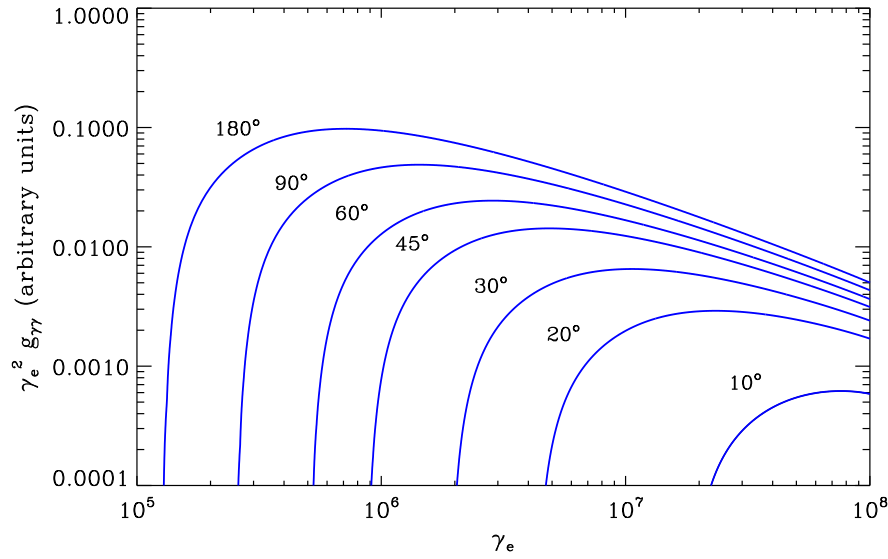


FIG. 56. Spectrum of pairs created by absorption of primary gamma rays following a power law energy distribution (photon index -2) and a mono-energetic beam of soft radiation (with $\epsilon_0 = 1$ eV). Spectra are computed for $\theta_0 = 10^\circ, 20^\circ, 30^\circ, 45^\circ, 60^\circ, 90^\circ$ and 180° .

The solution found by Aharonian *et al.* (1983) is (see the formula in *e.g.* Zdziarski 1988)

$$g_{\gamma\gamma}^{iso} = \frac{3\sigma_T}{4E\epsilon_1} \left[r - (2+r) \frac{E_\star}{E} + 2 \left(\frac{E_\star}{E} \right)^2 + 2 \frac{E_\star}{E} \ln \left(\frac{E}{E_\star} \right) \right], \quad (56.242)$$

where

$$E = \frac{\epsilon_1 \epsilon_0}{m_e^2 c^4} \quad E'_e = \epsilon_1 - E_e$$

$$E_\star = \frac{\epsilon_1^2}{4E_e E'_e} \quad r = \frac{1}{2} \left(\frac{E_e}{E'_e} + \frac{E'_e}{E_e} \right), \quad (56.243)$$

and with the boundaries given by the condition $E > E_\star > 1$. In other words, this condition implies that $E_e \geq \epsilon_1/2$ and $E_- < E_e < E_+$ with

$$E_\pm = \frac{\epsilon_1}{2} \left[1 \pm \left(1 - \frac{m_e^2 c^4}{\epsilon_1 \epsilon_0} \right)^{1/2} \right]. \quad (56.244)$$

The comparison between the numerical solution computed with Eq. (56.241) and the analytical solution gives compatible results (Fig. 57).

§ 57. Comparison with Böttcher & Schlickeiser solution

The kernel found in Eq. (54.239) is correct only if $\epsilon_1 \gg \epsilon_0$. Böttcher & Schlickeiser (1997) found the exact solution for the anisotropic pair production kernel. We would like here to compare our solution with the exact kernel. The exact solution is

$$g_{\gamma\gamma}^{BS} = (1 - \mu_0) \frac{d\sigma}{dE_e}, \quad (57.245)$$

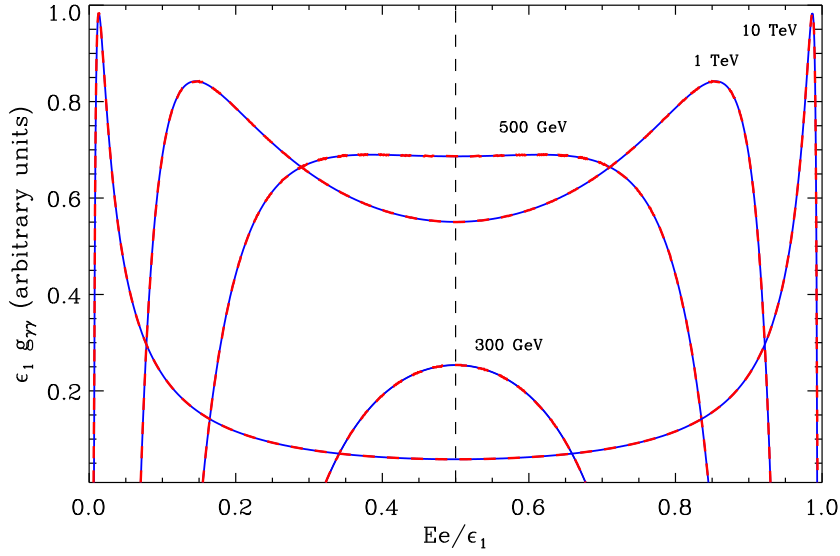


Fig. 57. Comparison between the analytical (blue line) and the numerically integrated (red dashed line) kernels for an isotropic source of soft radiation. $\epsilon_0 = 1$ eV and $\epsilon_1 = 300$ GeV, 500 GeV, 1 TeV and 10 TeV.

where

$$\frac{d\sigma}{dE_e} = \frac{\pi r_e^2 m_e c^2}{\epsilon_{cm}} \left[-\frac{m_e c^2}{N \epsilon_{cm}} + \frac{3 - \beta_{cm}^4}{4} (G_+ + G_-) - \frac{m_e^2 c^4}{8 \epsilon_{cm}^2} (F_+ + F_-) \right], \quad (57.246)$$

and, using the same notation as in Böttcher & Schlickeiser (1997),

$$\begin{aligned} \epsilon_{cm}^2 &= \frac{\epsilon_1 \epsilon_0}{2} (1 - \mu_0) & \gamma_{cm} &= \frac{\epsilon_{cm}}{m_e c^2} & E &= \epsilon_1 + \epsilon_0 \\ \gamma_c &= \frac{E}{2 \epsilon_{cm}} & N &= \sqrt{E^2 - 4 \epsilon_{cm}^2} & z &= \frac{\epsilon_1 - \epsilon_0}{N} \\ \epsilon_{1,0} &= \epsilon_{cm} \gamma_c (1 \pm \beta_c z) & c_{\pm} &= \left(\frac{\epsilon_{1,0}}{m_e c^2} - \gamma_e \right)^2 - 1 & d_{\pm} &= \epsilon_{1,0}^2 + \epsilon_1 \epsilon_0 \pm E_e (\epsilon_0 - \epsilon_1) \\ G_{\pm} &= \frac{1}{\sqrt{\epsilon_1 \epsilon_0 + \epsilon_{cm}^2 c_{\pm}}} & F_{\pm} &= \frac{d_{\pm} - 2 \epsilon_{cm}^2}{(\epsilon_1 \epsilon_0 + \epsilon_{cm}^2 c_{\pm})^{3/2}}. \end{aligned} \quad (57.247)$$

Relativistic kinematics gives

$$\gamma_{cm} \gamma_c (1 - \beta_{cm} \beta_c) < \gamma_e < \gamma_{cm} \gamma_c (1 + \beta_{cm} \beta_c). \quad (57.248)$$

Both kernels give similar results if $\epsilon_0 \ll \epsilon_1$ (Fig. 58). I have noted substantial differences between the two solutions if $\epsilon_0 \sim \epsilon_1$, in particular the exact spectrum of the pair becomes asymmetric with respect to the energy $\epsilon_1/2$.

7. The density of pairs

The pair production kernel does not give directly the density of pairs produced as we have to take into account of the past history of the primary gamma ray. Let's consider a gamma-ray photon of energy ϵ_1 in a given mono-energetic beam of soft radiation. The number of electrons and positrons created at the distance l from the source of gamma rays and $l + dl$ at an energy

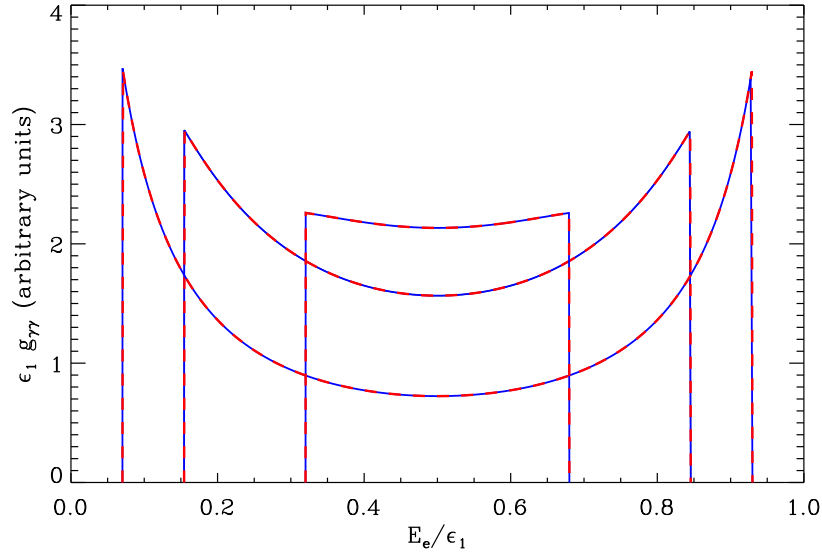


FIG. 58. Comparison between the kernel found in Eq. (54.239) and the kernel found by Böttcher & Schlickeiser (1997), Eq. (57.245) where $\epsilon_0 = 1$ eV, and $\epsilon_1 = 300$ GeV, 500 GeV and 1 TeV for a head-on collision.

between E_e and $E_e + dE_e$, depends on the probability to create a pair and on the probability for the primary gamma ray to remain unabsorbed so that

$$\frac{dN_e}{dl dE_e} = [g_{\gamma\gamma}(E_e) + g_{\gamma\gamma}(\epsilon_1 - E_e)] e^{-\tau_{\gamma\gamma}(l)}, \quad (57.249)$$

with

$$\tau_{\gamma\gamma}(l) = \int_0^l \frac{d\tau_{\gamma\gamma}}{dl'} dl', \quad (57.250)$$

where $\tau_{\gamma\gamma}(l)$ is the gamma-ray opacity integrated along the path from the source to the distance l . Because electrons and positrons cannot be distinguished in this process, it is not necessary to specify the nature of the particles in the equation. Also, we have (see Fig. 55)

$$g_{\gamma\gamma}(\epsilon_1 - E_e) = g_{\gamma\gamma}(E_e). \quad (57.251)$$

Hence, the density of pairs (in $\text{erg}^{-1} \text{cm}^{-1}$) is

$$\frac{dN_e}{dl dE_e} = 2g_{\gamma\gamma}(E_e) e^{-\tau_{\gamma\gamma}(l)}. \quad (57.252)$$

The integration over the energy of the electrons yields

$$\frac{dN_e}{dl} = \int_{E_e} \frac{dN_e}{dl dE_e} dE_e = 2 \left(\int_{E_e} g_{\gamma\gamma}(E_e) dE_e \right) e^{-\tau_{\gamma\gamma}(l)} = 2 \frac{d\tau_{\gamma\gamma}}{dl} e^{-\tau_{\gamma\gamma}(l)}, \quad (57.253)$$

and the integration over the length path l gives $N_e(r)$ the total density of pairs produced from the source up to the distance r

$$N_e(r) = \int_0^r \frac{dN_e}{dl} dl = 2 \int_0^r \frac{d\tau_{\gamma\gamma}}{dl} e^{-\tau_{\gamma\gamma}(l)} dl \quad (57.254)$$

$$N_e(r) = 2 \left[1 - e^{-\tau_{\gamma\gamma}(r)} \right]. \quad (57.255)$$

There is two interesting regime to note:

- For low opacity ($\tau_{\gamma\gamma} \ll 1$), $N(r) \approx 2\tau_{\gamma\gamma}(r) \ll 1$, no pair is produced.
- For high opacity ($\tau_{\gamma\gamma} \gg 1$), $N(r) \approx 2$, the gamma-ray photon has created one pair.

8. What we have learned

Following Bonometto & Rees (1971), I found a simple analytical expression for the anisotropic pair production kernel in the observer frame provided that $\epsilon_1 \gg \epsilon_0$. The latter assumption will be always fulfilled in the context of this thesis where target photons from the massive star have only a few eV. This formula (Eq. 54.239) provides the spectrum of the pair produced in the interaction between two photons at a given pitch angle θ_0 . Pairs are mostly produced close to threshold, with almost no kinetic energy in the CM frame. In the observer frame, the pair shares equally the energy of the primary high-energy photon close to threshold $E_e \approx E'_e \approx \epsilon_1/2$. Hence, pairs can be produced at high-energy. The spectrum of pairs depends strongly on the pitch angle between the two beams of photons. The solution derived in this chapter is compatible with previous published works such as Aharonian *et al.* (1983) (isotropic solution) and Böttcher & Schlickeiser (1997) (exact anisotropic solution).

The anisotropic pair production kernel is a key element for the computation of pair cascading in binaries for which two full chapters are dedicated in this manuscript (Chapter 7 and 8). The work presented in this chapter was partly published in the appendix of the paper Cerutti *et al.* (2009b), provided here in Chapter 7.

9. [Français] Résumé du chapitre

§ 58. Contexte et objectifs

L'annihilation de deux photons produit une paire électron-positron au delà de l'énergie seuil de production de paires. J'étudie dans ce chapitre l'interaction entre deux faisceaux de photons. Je donne l'ensemble des équations pour le calcul détaillé du spectre des paires produites dans cette interaction. Cette étude est similaire à celle menée sur la diffusion Compton inverse anisotrope présentée au Chapitre 3. Ce travail se concentre en particulier sur la dépendance angulaire du spectre de la paire créée. Cette étude est basée sur les recherches précédentes par Gould & Schröder (1967); Bonometto & Rees (1971); Böttcher & Schlickeiser (1997). Je compare également dans ce chapitre mes résultats avec les formules connues dans la littérature.

§ 59. Ce que nous avons appris

En suivant l'approche de Bonometto & Rees (1971), j'ai trouvé une expression analytique simple pour le noyau de production de paire anisotrope dans le référentiel de l'observateur si $\epsilon_1 \gg \epsilon_0$. Cette dernière hypothèse sera toujours réalisée dans le contexte de cette thèse où les photons cibles provenant de l'étoile massive n'ont que quelques eV seulement. Cette formule (Eq. 54.239) donne le spectre de la paire produite dans l'interaction entre deux photons avec un angle d'attaque donné θ_0 . Les paires sont essentiellement produites à proximité du seuil, avec presque aucune énergie cinétique dans le référentiel du centre de masse. Dans le référentiel de l'observateur, la paire partage de manière symétrique l'énergie du photon primaire de haute

énergie proche du seuil $E_e \approx E'_e \approx \epsilon_1/2$. Les paires peuvent donc être produites à haute énergie. Le spectre de la paire dépend fortement de l'angle d'attaque entre les deux faisceaux de photons. La solution obtenue dans ce chapitre est compatible avec les travaux publiés précédents comme ceux de Aharonian *et al.* (1983) (solution isotrope) et de Böttcher & Schlickeiser (1997) (solution anisotrope exacte).

Le noyau de production de paire est un élément de base pour le calcul de l'émission d'une cascade de paires dans les binaires pour lequel deux chapitres entiers sont dédiés dans ce manuscrit (Chapitres 7 et 8). Le travail présenté dans ce chapitre a été en partie publié dans l'appendice de l'article Cerutti *et al.* (2009b), donné ici au Chapitre 7.

7

One-dimensional pair cascading

Outline

1. What we want to know	142
2. Assumptions and approximations for 1D cascade	143
3. Equations for anisotropic 1D cascade	144
§ 58. Equation for photons	144
§ 59. Equation for pairs	145
§ 60. Numerical integration	147
4. The development of 1D pair cascade in binaries	147
5. Anisotropic effects	149
6. 1D cascade emission in LS 5039	149
7. The density of escaping pairs	151
8. Pair cascading in the free pulsar wind	152
9. What we have learned	154
10. [Français] Résumé du chapitre	154
§ 61. Contexte et objectifs	154
§ 62. Ce que nous avons appris	155
11. One dimensional pair cascade emission in gamma-ray binaries	157

AS WE ALREADY KNOW, a primary energetic photon going through a given radiation field can be annihilated to produce an electron-positron pair (Chapter 2). This new generation of particles interacts with the ambient soft radiation and scatters high-energy photons by inverse Compton scattering. If these new photons have high enough energy, they will produce a second generation of pairs in the system which could produce new gamma rays and so on (see Fig. 59). A cascade of pairs and gamma rays is produced. This process will continue as long as gamma rays are produced with energy beyond the threshold energy for pair production and before particles escape the system. Pair cascading often occurs in compact environment where the gamma-ray opacity is very high $\tau_{\gamma\gamma} \gg 1$.

In chapter 4 (Dubus *et al.* 2008), we modeled the gamma-ray modulation in LS 5039 as the combination of anisotropic inverse Compton emission and gamma-ray absorption on UV stellar photons, but we ignored the contribution from pair cascading. This model can explain correctly the modulation in the TeV energy band at every orbital phases ϕ (see Chapter 4, Fig. 26) except

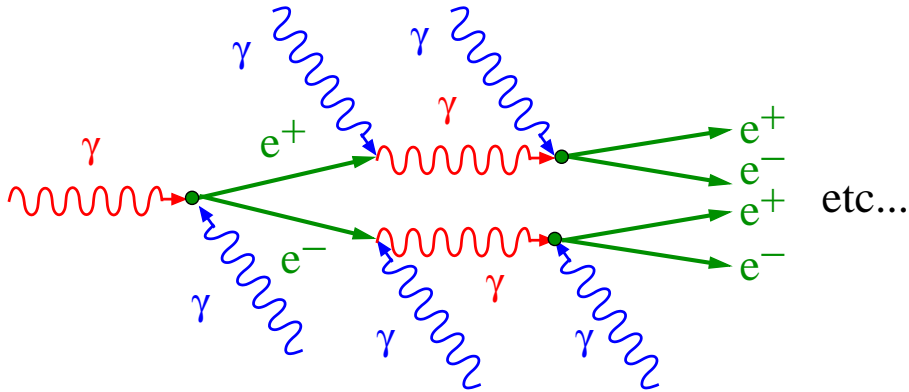


FIG. 59. Cascade of pairs initiated by a primary high-energy gamma ray propagating in a soft photon field.

close to superior conjunction ($\phi \approx 0.06$), *i.e.* where the compact object lies behind the massive star with respect to the observer. At this phase, the gamma-ray opacity is very high $\tau_{\gamma\gamma} \gg 1$. Hence we expect to have no detectable TeV flux with this model.

HESS observations (Aharonian *et al.* 2006) have shown that a significant excess is measured close to superior conjunction (6.1σ at phase 0.0 ± 0.05), in contradiction with our results. Undoubtedly, more gamma rays are able to escape from the system than expected. The solution for this discrepancy could be found in pair cascading. Indeed, the mismatch with observations occurs precisely where the gamma-ray opacity is very high. A significant amount of the absorbed energy is possibly efficiently reprocessed by a cascade of pairs in the system and contributes to the total high-energy flux. Alternatively, these observations would indicate that the primary source of gamma rays should not be localized close to the compact object but further away, for instance in a jet or backward in the pulsar wind. This possibility has been proposed by Bosch-Ramon *et al.* (2008b) in LS 5039 and by Zdziarski *et al.* (2009) for a similar issue in the microquasar Cygnus X–1. We will come back to this alternative in the next chapter.

In this chapter, I explore the effect of pair cascading in gamma-ray binaries and focus my investigations on LS 5039 where absorption is very high (see Dubus 2006a). As a first attempt, I model here the contribution from a 1D cascade, *i.e.* where pairs and gamma rays produced in the cascade stay along the same line. I give below the main conditions required to have a 1D cascade in LS 5039 and derive the full equations to describe the dynamics of the cascade. I apply this model to LS 5039 and LS I +61°303.

1. What we want to know

- What are the physical conditions for the development of 1D pair cascade in binaries?
- What is the contribution of a 1D cascade to the total TeV escaping emission in gamma-ray binaries?
- Can pair cascade account for the TeV flux observed close to superior conjunction in LS 5039?

2. Assumptions and approximations for 1D cascade

For simplicity, the massive star will be assumed monoenergetic of energy $\epsilon_0 \approx 2.7kT_*$ (with k the Boltzmann constant) and point-like. In LS 5039, pair production occurs if the energy of the primary gamma ray exceed the threshold energy $\epsilon_1 \geq \epsilon_0/m_e^2c^4 \approx 30$ GeV (see Eq. 50.210, for head-on collision). Created pairs are boosted in the direction of the primary gamma ray (in the observer frame) since most of the momentum is carried by the gamma-ray photon ($\epsilon_1 \gg \epsilon_0$). In addition, pairs produced in the cascade are ultra-relativistic with typical Lorentz factor of about $\gamma_e \sim 10^6 \gg 1$ (at threshold $E_e \approx \epsilon_1/2$). Their emission is then highly beamed within a cone of semi-aperture angle $\alpha \sim 1/\gamma_e \ll 1$, in the direction of motion of the pair. It is a good approximation to assume that all particles in the cascade remain on the same line, the line of sight (see Fig. 60) according to certain conditions that are investigated below.

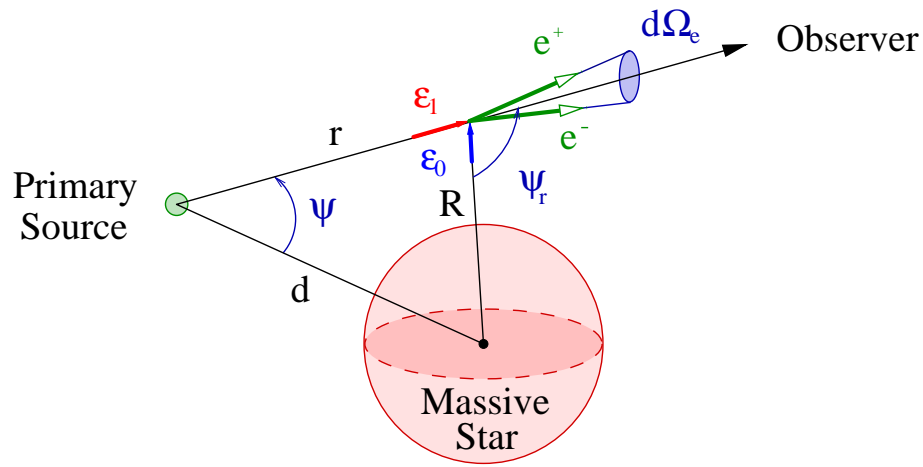


FIG. 60. Geometrical quantities used in the model. The primary source injects gamma rays of energy ϵ_1 at a viewing angle ψ . These photons are absorbed by the stellar photon of energy $\epsilon_0 \approx 2.7kT_*$ at a distance r from the source and yield electron positron pairs focused along the line of sight due to relativistic beaming effect.

The deviations on the electron trajectory by Compton collisions might be important. However, the electron loses most of its energy in one collision since the inverse Compton scattering would be in the Klein-Nishina regime. The cooled pairs will not contribute in the cascade radiation anymore. We will ignore this effect in the following.

The ambient magnetic field in the system can have an impact on the trajectories of pairs in the cascade. In this case, the pair would be sensitive to the magnetic field line structure in the system and the problem becomes complicated to solve (see for instance Sierpowska & Bednarek 2005). The cascade is one-dimensional if these deflections along the Compton interaction length $\lambda_{ic} \sim (n_*\sigma_{ic})^{-1}$ remain within the cone of emission of the electrons (see Fig. 61). This condition is fulfilled if

$$\frac{\lambda_{ic}}{2R_L} < \frac{1}{\gamma_e}, \quad (59.256)$$

with $R_L = E_e/eB$ is the Larmor radius of the electron. For TeV electrons in LS 5039, the magnetic field should not exceed 10^{-8} G. This value is probably unrealistically small. Nevertheless, the 1D cascade approximation provides an upper limit of the cascade radiation at orbital phases where absorption is very high. If the magnetic field is higher, pair will radiate in other directions.

This redistribution of pairs in the system affects orbital phases where many pairs are produced to the benefit of the phases where only few are produced. 1D cascade might also occur in the unshocked pulsar wind since the magnetic field is frozen into the flow of pairs (see Chapter 5). I investigate this possibility in Sect. 8.

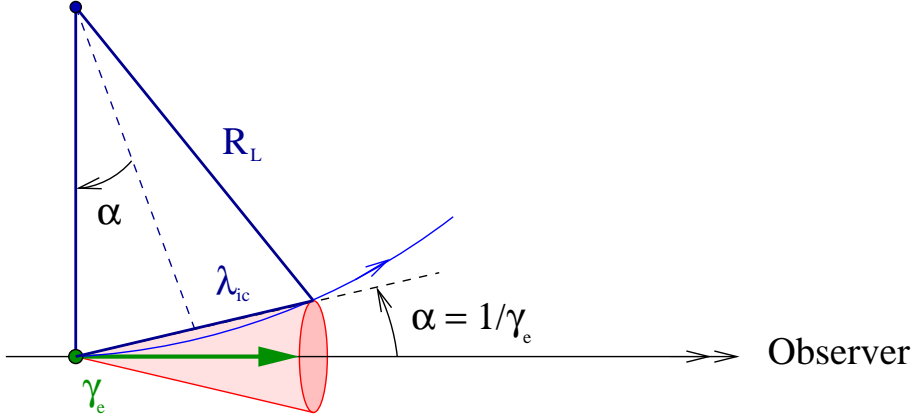


FIG. 61. If the trajectory of the electron deviated by the magnetic field along the Compton interaction length λ_{ic} remains within a cone of half opening angle $\alpha = 1/\gamma_e$, the cascade is one-dimensional.

The annihilation of electron-positron pairs is neglected here. This process might occur only far outside the system where pairs would have enough time to thermalize and annihilate in the interstellar medium (see the discussion in Sect. 7). Triplet pair production is also ignored (see Chapter 2). The interaction of high-energy gamma rays with the surrounding material can also produce pairs. With a cross section of about $0.04\sigma_T Z^2$ (with Z is the number of protons per nucleus, see e.g. Longair 1992) and with a typical column density of material $N_H \sim 10^{22} \text{ cm}^{-2}$ in gamma-ray binaries, very few interactions will occur in the propagation of gamma rays up to the observer. This process is neglected as well in the following.

Interactions between gamma rays and pairs in the cascade are ignored because the density of stellar photons is much greater than the gamma-ray density. The cascade can be considered as fully "linear" (Svensson 1987). In addition, such interaction would be very unlikely because it would occur in the very deep Klein-Nishina regime as noted by Zdziarski (1988). Also, particles would interact rear-end in the 1D cascade, making these collisions even less probable.

3. Equations for anisotropic 1D cascade

§ 60. Equation for photons

Let's consider a primary gamma-ray source injecting at $r \equiv 0$ a density of photons $n_\gamma(0) \equiv dN_\gamma(0)/dt d\epsilon_1 d\Omega$ (Fig. 62). At a distance $r + dr$ from the source, the density of gamma rays $n_\gamma(r + dr)$ is

$$n_\gamma(r + dr) = n_\gamma(r) - n_\gamma(r) \left(\frac{d\tau_{\gamma\gamma}}{dr} \right) dr + \left[\int_{E_e} n_e n_\star \frac{dN}{dt d\epsilon_1} dE_e \right] dr, \quad (60.257)$$

where $n_e \equiv dN_e/dr dE_e d\Omega_e$ is the density of pairs, $dN/dt d\epsilon_1$ is the anisotropic Compton kernel (see Eq. 25.135) and $n_\star = L_\star/4\pi c\epsilon_0 R^2$ is the density of stellar photon at r . This expression can be

rewritten as a differential equation for photons

$$\boxed{\frac{dn_\gamma}{dr} = -n_\gamma \left(\frac{d\tau_{\gamma\gamma}}{dr} \right) + \int_{E_e} n_e n_* \frac{dN}{dt d\epsilon_1} dE_e} \quad (60.258)$$

This is the radiative transfer equation for gamma rays, where the second term in the equation is a sink due to absorption and the last term a source of new photons due to pair production. If there is no source term, we find the pure absorbed spectrum formula as we used *e.g.* in our model for the shocked or for the unshocked pulsar wind (Eq. 32.152 and Eq. 44.184).

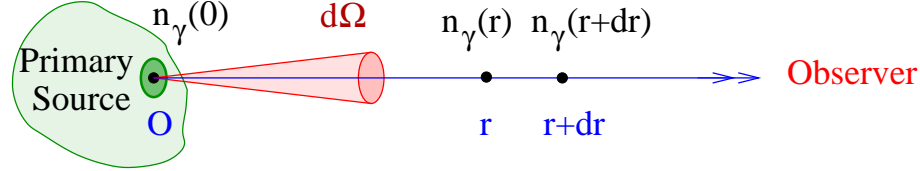


FIG. 62. The primary source injects a density of gamma rays n_γ . Between r and $r + dr$, part of these photons are absorbed and new are emitted by the pairs produced in the cascade.

§ 61. Equation for pairs

The dynamics of the density of pairs produced in the cascade is given by the kinetic equation. The evolution of the density of pairs $n_e \equiv dN_e/dr dE_e d\Omega_e$ is composed of a cooling term and a term of creation due to pair production. Because pairs cool down *via* inverse Compton scattering in the Klein-Nishina regime, electrons lose most of their energy in a single interaction with stellar photons ($\Delta E_e \approx E_e$). We propose to consider these catastrophic losses accurately in this study, even though the continuous losses approximation is still rather good (Zdziarski 1989).

- **Cooling term:** We can decompose the cooling term into two distinct components: the "population" and "depopulation" rate of a given energy level of the electron E_e . The general expression of these two terms is given for instance by Blumenthal & Gould (1970) and Zdziarski (1988). The depopulation rate of the level of energy E_e is given by

$$\int_{m_e c^2}^{E_e} n_e(E_e) \mathcal{P}(E_e, E'_e) dE'_e, \quad (61.259)$$

where $\mathcal{P}(E_e, E'_e)$ quantify the transition rate for an electron of energy E_e to jump into the level of energy $E'_e \leq E_e$. In the extreme case, the electron loses all of its kinetic energy hence the lower limit of the integral $E'_e = m_e c^2$. This term sums over all the possible energy levels available for the electron. Each transition is weighted by the probability $\mathcal{P}(E_e, E'_e)$ (Fig. 63).

Similarly, the populating rate can be written as

$$\int_{E_e}^{+\infty} n_e(E'_e) \mathcal{P}(E'_e, E_e) dE'_e, \quad (61.260)$$

where $\mathcal{P}(E'_e, E_e)$ is the transition rate for an electron of energy $E'_e \geq E_e$ to cool down at an energy E_e . From the point of view of the energy level E_e , the total number of electrons that will downscattered at this energy depends on the initial energy of the pairs E'_e but also of their density $n_e(E'_e)$ (Fig. 64).

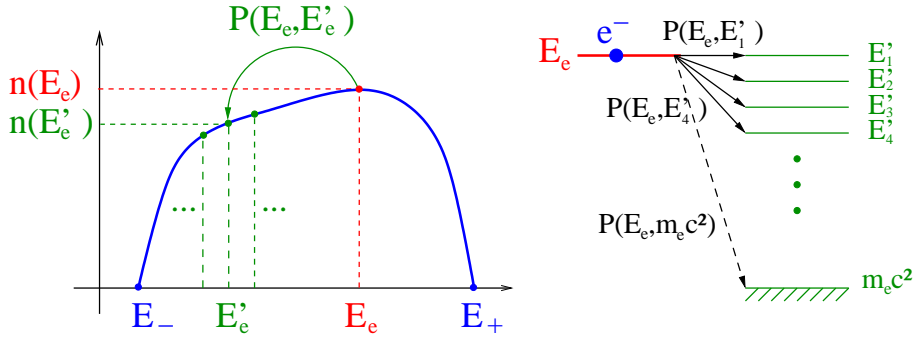


FIG. 63. This diagrams depicts qualitatively the depopulation of the energy level E_e to the benefit of lower energy levels $m_e c^2 < E'_e < E_e$.

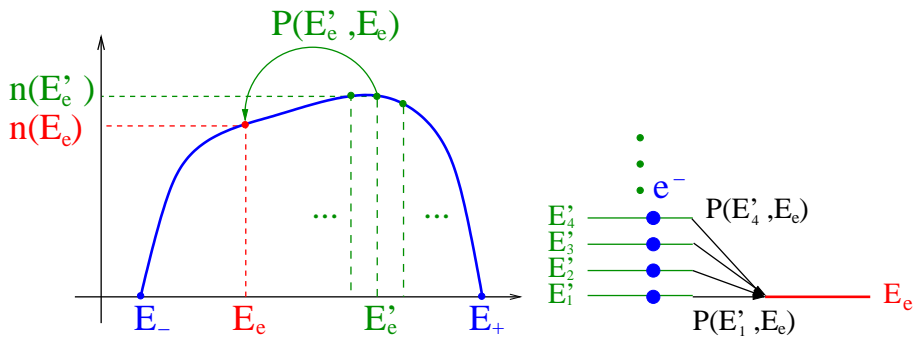


FIG. 64. This diagrams depicts qualitatively the population of the energy level E_e by higher energy levels $E'_e \geq E_e$.

There is a direct link between the transition rates and the Compton kernel. Indeed, the Compton kernel gives the scattering rate of photons of energy ϵ_1 per electron of energy E_e . Hence, the transition rates can be rewritten as

$$\mathcal{P}(E_e, E'_e) = n_\star(r) \frac{dN}{dt dE'_e}, \quad (61.261)$$

where $dN/dt dE'_e$ gives the spectrum of the scattered electrons rather than the spectrum of the scattered photon as in the Compton kernel $dN/dt d\epsilon_1$ provided that $\epsilon_1 \approx E_e - E'_e$. $\mathcal{P}(E'_e, E_e)$ has the same expression as in Eq. (61.261) with $\epsilon_1 \approx E'_e - E_e$. In this form, it appears that the depopulation term is the scattering rate weighted by the density of electron so that

$$\begin{aligned} \int_{m_e c^2}^{E_e} n_e(E_e) \mathcal{P}(E_e, E'_e) dE'_e &= n_e n_\star \int_{m_e c^2}^{E_e} \frac{dN}{dt dE'_e} dE'_e \\ &= n_e n_\star \frac{dN}{dt} \\ &= n_e n_\star \sigma_{ic} c (1 - \beta_e \mu_0), \end{aligned} \quad (61.262)$$

where θ_0 is the pitch angle between the particles in the cascade and the stellar photons. The full expression for σ_{ic} is given in Eq. (5.2). The cooling term for pairs in the cascade is then

$$\frac{dn_e}{dt} = -n_e n_\star \sigma_{ic} c (1 - \beta_e \mu_0) + \int_{E_e}^{+\infty} n_e(E'_e) \mathcal{P}(E'_e, E_e) dE'_e. \quad (61.263)$$

- **Source term:** The density of electrons and positrons created in the cascade is given by (see Chapter 6)

$$2 \int_{\epsilon_1} n_\gamma n_* g_{\gamma\gamma} d\epsilon_1, \quad (61.264)$$

where $g_{\gamma\gamma}$ is the anisotropic pair production kernel (see Eq. 54.239).

- **Full kinetic equation for pairs:**

$$\boxed{\frac{dn_e}{dt} = -n_e n_* \sigma_{ic} c (1 - \beta_e \mu_0) + \int_{E_e}^{+\infty} n_e(E'_e) \mathcal{P}(E'_e, E_e) dE'_e + 2 \int_{\epsilon_1} n_\gamma n_* g_{\gamma\gamma} d\epsilon_1}. \quad (61.265)$$

§ 62. Numerical integration

The differential equations for the cascade Eqs. (60.258, 61.265) are coupled. This system of equation should be solve together at every step of the computation. I used a simple Runge-Kutta of the fourth order to solve these equations. It is more relevant here to compute the cascade as a function of the distance to the source r rather than the time t with $dr = cdt$ for photons and $dr = \beta_e cdt \approx cdt$ for electrons. For practical reasons, I use the angular variable ψ_r (see Fig. 60) instead of r as for the computation of the Compton emission in the unshocked pulsar wind (see chapter 5).

4. The development of 1D pair cascade in binaries

Fig. 65 shows the development of pair cascading along the line of sight up to the observer (*i.e.* at infinity). The primary source of gamma rays is isotropic and injects photons with a -2 power law distribution in energy at $r = 0$. Spectra are computed in LS 5039 for a viewing angle $\psi = 30^\circ$.

At the vicinity of the primary source ($r \lesssim d$), pair production produces a deep and sharp dip in the spectrum. The emission from secondary pairs produced in the cascade starts to contribute at energies where absorption is strong and reduces the opacity of the source. An accumulation of radiation appears just below the minimum threshold energy since photons do not suffer from pair production. This is a well-known spectral feature of pair cascading. The energy distribution of pairs is peaked close to threshold and declines at very-high energy (for $E_e > 1$ TeV) due to the decline of the pair production cross section far from threshold. Almost no pair lies below threshold as electrons have not cooled down significantly yet (the propagation timescale is shorter than the Compton cooling timescale).

Far from the source ($r > d$), the cascade is the main contributor to the very-high energy gamma-ray flux that escapes the system. As the distance increases, the soft photon density and the interaction angle between the particles in the cascade and the stellar photons diminishes. The threshold energy for pair production shifts to higher and higher energy. Three zones appear distinctly in the cascade spectrum far from the primary source. Below the minimum threshold energy ($\epsilon_1 \lesssim 30$ GeV in LS 5039), the spectrum can be approximated as a hard power law of index ~ -1.5 . This is due to the Compton cooling of pairs in the Thomson regime. Above threshold, this is the energy domain where emission and absorption compete. At very-high energy ($\epsilon_1 > 10$ TeV), the emission from the cascade declines because both pair production and inverse Compton scattering (Klein-Nishina effects) become inefficient.

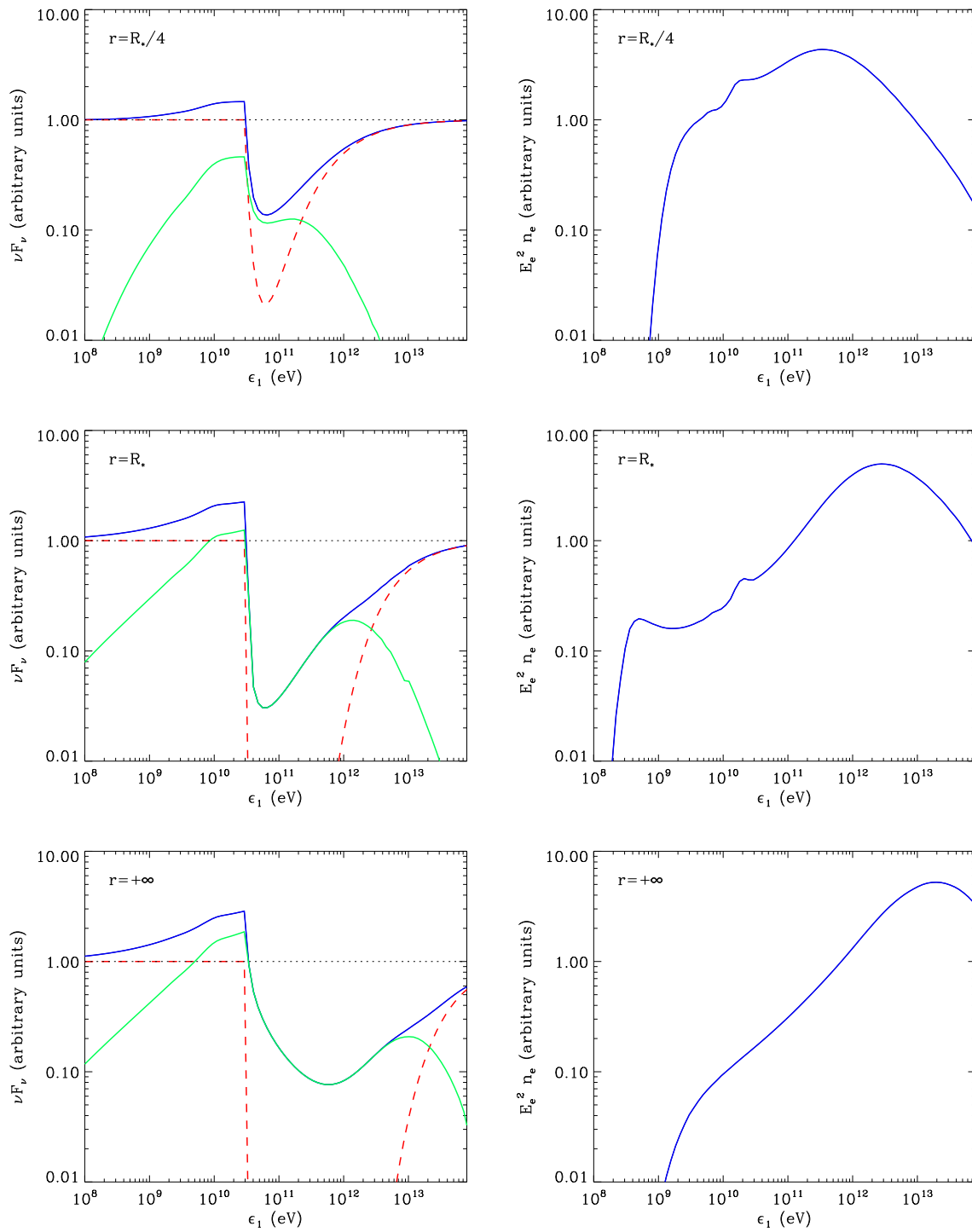


FIG. 65. Development of the 1D cascade along the line of sight joining the primary source to the observer. The primary source is point-like, isotropic and injects gamma rays with a -2 power law energy distribution between 100 MeV and 100 TeV at the location of the compact object in LS 5039. The viewing angle is $\psi = 30^\circ$. On the left panels are shown the full escaping gamma-ray spectra (blue line), the radiation from the cascade only (green line) and the pure absorbed spectrum (red dashed line) for $r = R_*/4$ (top), R_* (middle) and $+\infty$ (bottom). The corresponding total unabsorbed emission from the cascade pairs is shown in the right panels.

5. Anisotropic effects

The cascade emission has a strong angular dependence. Fig. 66 shows this dependence in LS 5039 of the spectrum observed by a distant observer for a constant and isotropic injection of primary gamma rays at the compact object location. The cascade radiation contributes significantly for small viewing angles ($\psi \lesssim 90^\circ$) where absorption is strong. For higher viewing angle, the cascade emission is small as gamma-ray photons and pairs escape directly from the system. For $\psi \gtrsim 150^\circ$, the cascade can be ignored. The angular dependence depicted here is very similar to the one described and analyzed in the emission of a free pulsar wind since pairs also propagate linearly in this case (see Chapter 5).

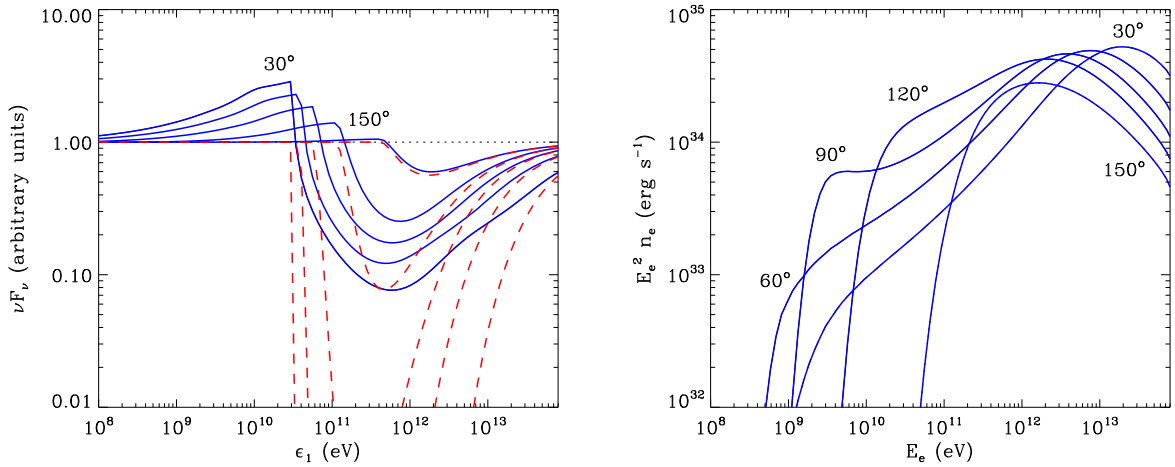


FIG. 66. The same as Fig. 65 with $r \rightarrow +\infty$ and $\psi = 30^\circ, 60^\circ, 90^\circ, 120^\circ,$ and 150° . The radiation from the cascade only is not shown for more readability.

Figs. 67, 68 allow a better appreciation of the anisotropic emission from the cascade in the binaries LS 5039 and LS I +61°303. These plots show the orbital modulation of the TeV flux from the cascade compared with the primary absorbed flux. In both binaries, the primary absorbed source and the cascade lightcurves are anticorrelated with extrema at conjunctions. In LS 5039, the cascade dominates the overall very-high energy flux close to superior conjunction ($\phi \approx 0.06$) between the orbital phases $\phi = 0.0 - 0.2$ and can be completely ignored elsewhere in the orbit. Note that there is a small dip in the pair cascade emission at superior conjunction in LS 5039 (see red curve in Fig. 67). At this phase, pair production is maximum and dominates slightly over Compton emission in the cascade. In LS I +61°303, the cascade flux peaks at superior conjunction ($\phi \approx 0.93$, see Fig. 68) as well but remains much smaller than the primary flux all along the orbit. Pair cascading may not play any role in the formation of the gamma-ray emission in this system.

6. 1D cascade emission in LS 5039

We investigate into more details the role of pair cascading in LS 5039. We would like to see whether 1D pair cascade emission can explain the residual flux detected by HESS close to superior conjunction in the TeV energy band. We assumed here that the primary source of gamma rays is produced by a cooled isotropic distribution of electrons located at the compact

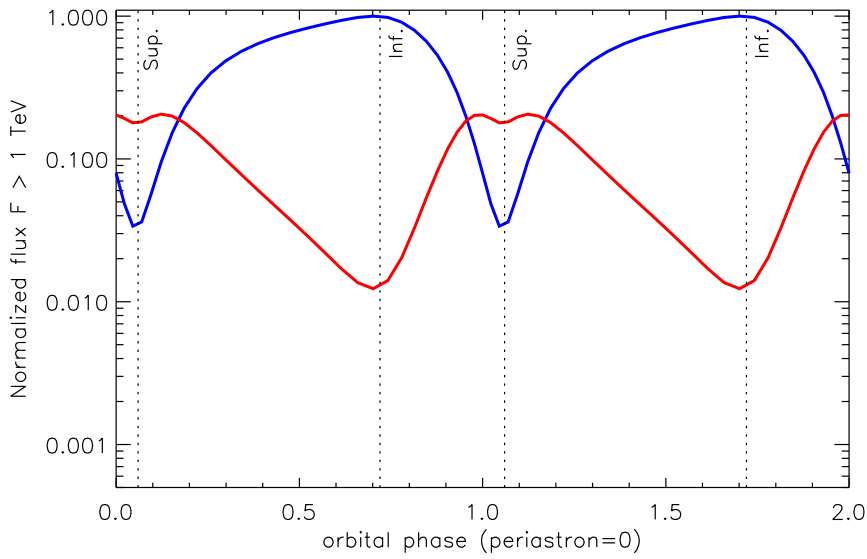


FIG. 67. TeV orbital modulation of 1D pair cascade emission in LS 5039 (red line) as a function of the orbital phase (two full orbits shown here), and comparison with the primary absorbed flux (blue line). The injection of primary gamma rays is isotropic and constant along the orbit. Both conjunctions are shown with vertical dashed lines (with the orbital parameters found by Casares *et al.* 2005b).

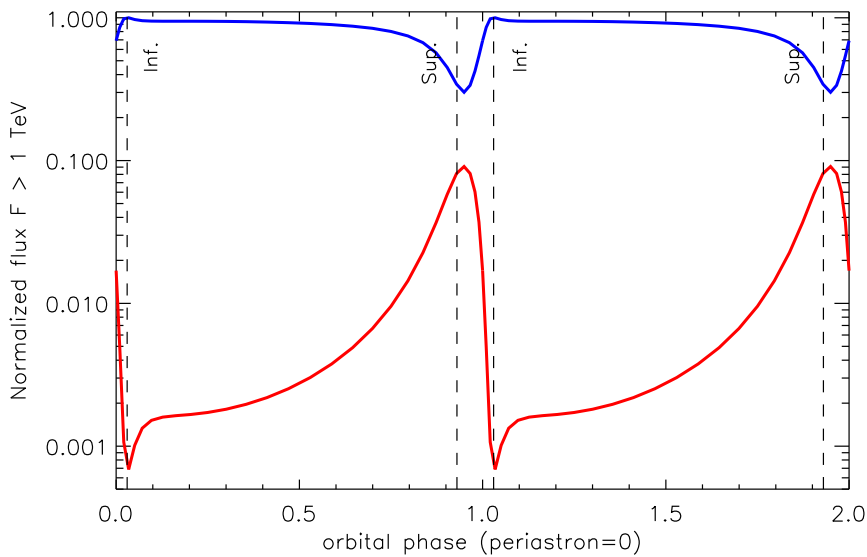


FIG. 68. Same as in Fig. 67 for LS I +61°303. The orbital parameters are taken from Casares *et al.* 2005a).

object location as in Dubus *et al.* (2008). The theoretical lightcurves are shown in Fig. 69, in the *Fermi* energy band (flux above 1 GeV) and in the HESS band (> 100 GeV) for an inclination of the orbit $i = 60^\circ$. At GeV energies, the cascade is correlated to the primary source and responsible for a third of the total flux. At TeV energies, the cascade flux definitively adds more flux close to superior conjunction as expected but this contribution is too strong to account for observation.

In addition, the sum of this component with the primary source produce a flat plateau in the light curve between $\phi \approx 0.1 - 0.7$ with a sharp peak around $\phi \approx 0.9$. The TeV modulation is not reproduced anymore. Changing the inclination does not help: the cascade radiation increases compared with the primary flux for lower inclination since there is more absorption on average along the orbit in this case as showed by Dubus (2006a). I think that the development of 1D cascade can be excluded in LS 5039. Nonetheless, this study provides a theoretical upper-limit of the cascade contribution in this system. A complex 3D cascade will contribute less close to superior conjunction and could possibly account for observations. This is the main purpose of the next chapter.

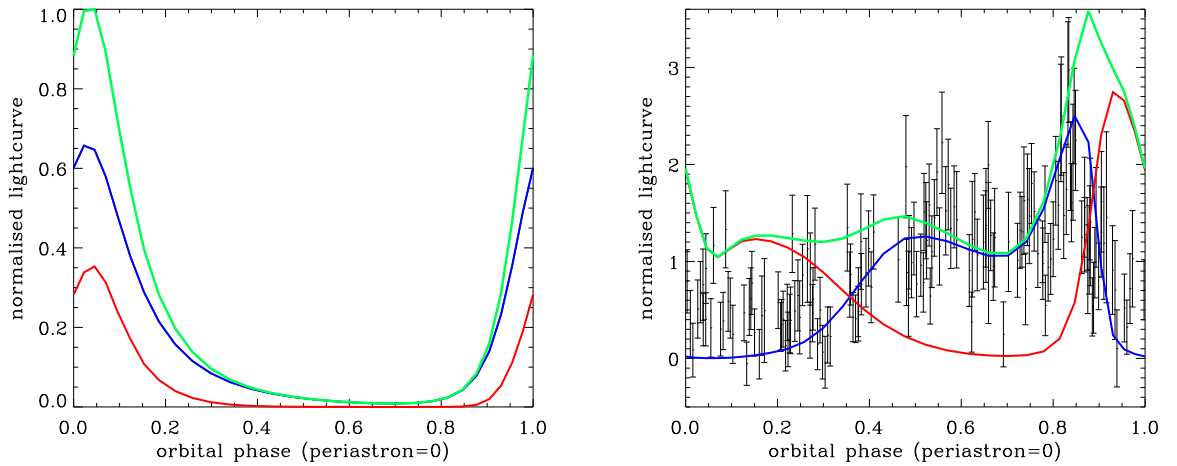


FIG. 69. Theoretical gamma-ray lightcurves in LS 5039, in the *Fermi* energy range (flux > 1 GeV *left* panel) and HESS energy range (flux > 100 GeV, *right* panel). HESS data points are taken from Aharonian *et al.* (2006). The 1D cascade component (red line) is compared with the primary absorbed contribution (blue line). The sum of both component is shown by the green line.

7. The density of escaping pairs

I estimate in this part the density of pairs produced in the cascade in LS 5039. The total density of pairs escaping the system is given by

$$\frac{dN_e^\infty}{dt} = \int_0^{2\pi} \int_{\alpha_*}^{\pi} \int_{E_e} \frac{dN_e^\infty}{dt dE_e d\Omega_e} \sin \psi dE_e d\psi d\phi, \quad (62.266)$$

where $dN_e^\infty / dt dE_e d\Omega_e$ is the spectrum of pairs produced in the cascade at infinity, and ψ , ϕ the spherical angles as defined in Fig. 70. α_* is the apparent angular extension of the star from the compact object location so that $\alpha_* = \arcsin(R_*/d)$. In LS 5039, the 1D cascade injects about 6×10^{35} electrons per second in the interstellar medium. This rate is pretty low, and gamma-ray binaries are probably very rare in the Galaxy. These objects are not strong emitters of 511 keV annihilation line emission. They are not responsible for the diffuse 511 keV emission observed by SPI on *INTEGRAL* (Knödlseeder *et al.* 2005) (see also the discussion in Cerutti *et al.* 2009b). The production of pairs is maximum at about $\psi = 70^\circ$. This is also where pairs escape with the lowest energy on average (Fig. 71).

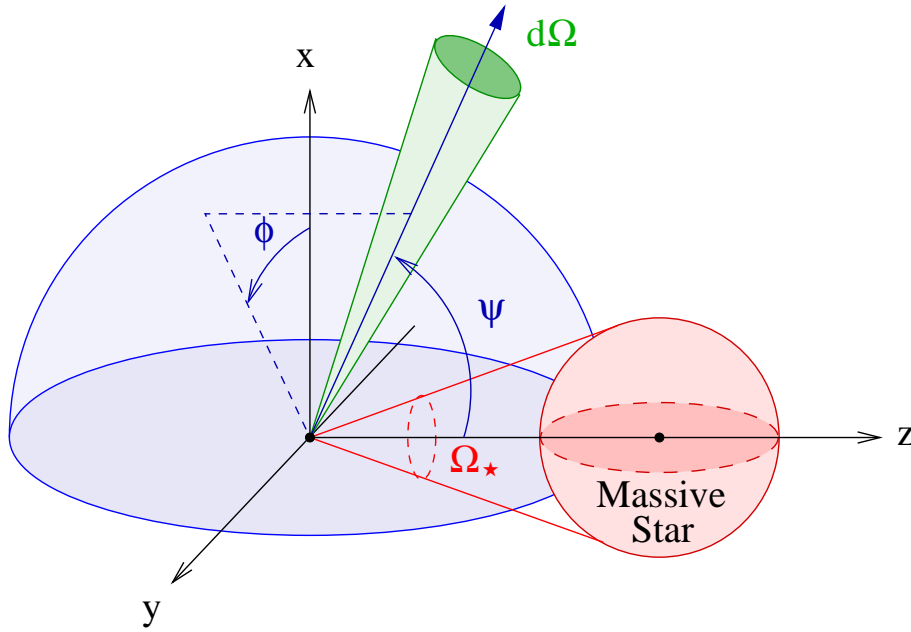


FIG. 70. Definition of the geometrical quantities useful for the computation of the density of escaping pairs in binaries. From the compact object point of view (origin), the massive star covers a solid angle Ω_* . Pairs propagating in the direction of the star (*i.e.* within Ω_*) are not considered in the calculation of the escaping density of pairs.

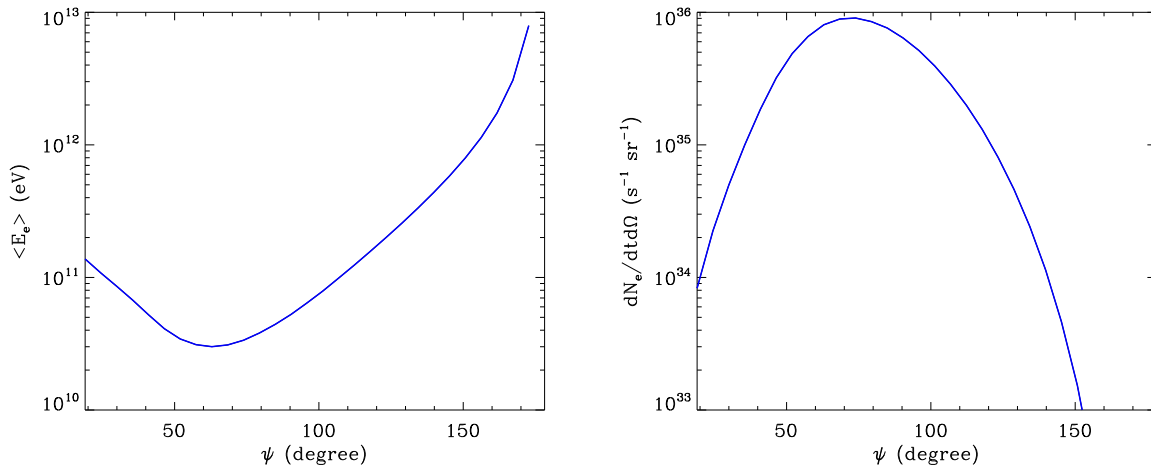


FIG. 71. *Left panel:* Mean energy of escaping pairs at infinity as a function of the viewing angle ψ . *Right panel:* Density of escaping pairs in the cone of semi-aperture angle ψ as a function of ψ .

8. Pair cascading in the free pulsar wind

I also investigated the contribution from pair cascading in the unshocked pulsar wind. This is also an opportunity here to check whether the continuous losses approximation used in Chapter 5 is correct or not, since I use the exact stochastic Compton losses in the 1D cascade calculation (see § 61). We assume that the primary source does not inject photons but electrons.

For a mono-energetic pulsar wind the density of pairs injected is

$$\frac{dN_e}{dt dE_e d\Omega_e}(0) = \frac{L_p}{4\pi\gamma_0 m_e c^2} \delta(E_e - E_0), \quad (62.267)$$

where $E_0 = \gamma_0 m_e c^2$ is the initial energy of the electrons in the wind. In practice, I approximate the δ distribution with a narrow log-normal distribution. For a mono-energetic pulsar wind of Lorentz factor $\gamma_0 = 10^6$, we observe significant spectral differences due to Klein-Nishina effects in the cooling of pairs. The spectrum is softer and less flux is expected compared with the continuous losses approximation (see Fig. 72). I tried also for $\gamma_0 = 10^4$ and found almost no differences with the approximate solution as expected since pairs cool down in the Thomson regime (Fig. 72), *i.e.* where pairs lose a small amount of energy per interaction with the stellar photons. Pair cascade emission contributes to decrease the gamma-ray opacity above threshold and increases significantly the flux below threshold (by a factor 20 in LS 5039 at superior conjunction, Fig. 72). If electrons are injected with a power law energy distribution, I have noticed only small differences between the exact and the approximate solution in agreement with the conclusions in Zdziarski (1989). In this case, pair cascading contributes also below and above the minimum energy for pair production. The effect of 1D pair cascade does not change our conclusions in Cerutti *et al.* (2009b), since it does not help to diminish the contribution from the pulsar wind. Hence, the model in Cerutti *et al.* (2009b) provides a lower limit to the emission from a free pulsar wind in gamma-ray binaries.

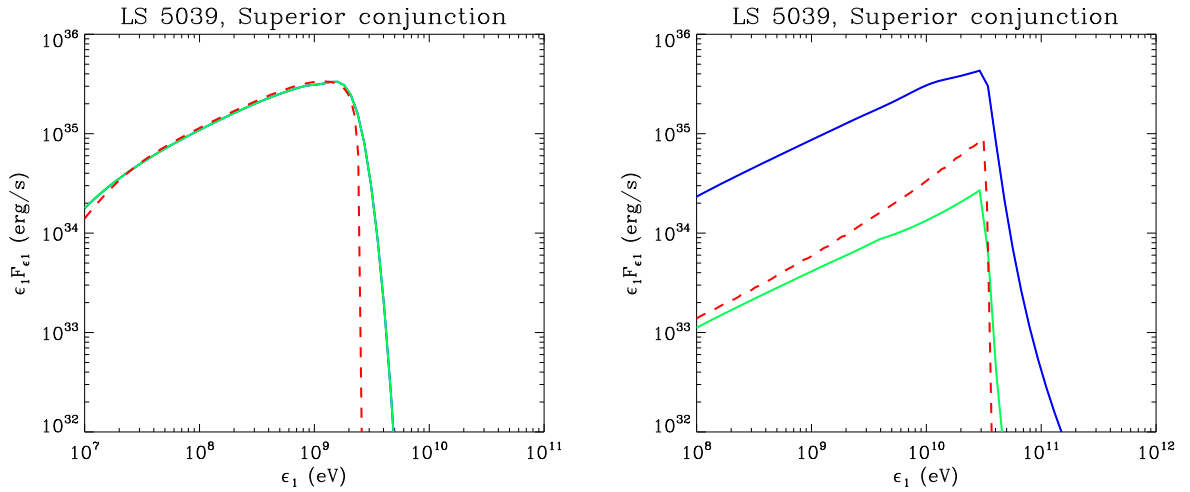


FIG. 72. Emission from a mono-energetic free pulsar wind in LS 5039 at superior conjunction ($\psi = 30^\circ$) for $\gamma_0 = 10^4$ (left) and 10^6 (right) with $L_p = 10^{36} \text{ erg s}^{-1}$. The exact solution (*i.e.* keeping track of stochastic losses for the electrons, green line) is compared with the approximate solution (continuous losses approximation, red dashed line). The solution with 1D pair cascading is shown by the blue line.

Sierpowska-Bartosik & Torres (2008) used a Monte Carlo code to compute the emission from a terminated free pulsar wind. In this model, the authors consider the development of 1D pair cascade emission in the unshocked pulsar wind only. Beyond the shock, the spectrum is just purely absorbed. I tried to compare my model with their solutions and found similar but not completely the same solutions in the mono-energetic pulsar wind case. For a power-law, I found compatible spectrum for the electrons but a different escaping gamma-ray spectrum (I found less

gamma rays above the threshold energy for pair production). I still do not know the reason of this discrepancy today but I suspect some differences in the absorption beyond the termination shock. Anyhow, both models lead qualitatively to the same results.

9. What we have learned

I found that pair cascade emission should be important in tight gamma-ray binaries such as LS 5039. In the one-dimensional limit, the dynamics of the cascade can be accurately computed with a semi-analytical approach. The 1D approximation is valid as long as the magnetic deviation on pair trajectories remains within the cone of emission of the pairs produced in the cascade. In LS 5039, the ambient magnetic field should be lower than 10^{-8} G. This value is probably unrealistically small for gamma-ray binaries. Nevertheless, this type of cascade maximizes the contribution that could be expected from pair cascading at orbital phases where the gamma-ray opacity is very high. In consequence, if the 1D cascade contribution is negligible at these phases then any type of cascade cannot be responsible for the TeV emission at these orbital phases. We would then have had to find other explanations (*e.g.* that the gamma-ray source is not within the system).

One-dimensional pair cascade emission has a strong angular dependence, and dominates the total gamma-ray flux above threshold for viewing angles where absorption is very high. In LS I +61°303, the contribution from a cascade does not play any role in the formation of the gamma-ray flux, since the 1D cascade emission is negligible. In LS 5039, the 1D cascade is significant and adds more flux close to superior conjunction as expected. However, the cascade contributes too much since HESS observations are overestimated. In addition, the TeV orbital modulation cannot be well reproduced. 1D cascade can be ruled out in LS 5039 but this study does not exclude the existence of a more complex 3D cascade. This possibility is fully explored in the next chapter (see Chapter 8).

I also investigate the contribution of pair cascading and the effect of Klein-Nishina cooling in the unshocked pulsar wind, but I found that these two effects do not change our previous conclusions exposed in Chapter 5, as this does not decrease the strong gamma-ray emission from the wind. Moreover, we have shown that gamma-ray binaries are probably not big contributors to the 511 keV Galactic diffuse emission.

This study was published in Cerutti *et al.* (2009b). I presented early results in a contributed talk at the "High energy phenomena in massive stars meeting 2009" (see the proceeding Cerutti *et al.* 2010a). I also had the opportunity to present our conclusions on 1D cascade in gamma-ray binaries in a contributed talk at the "French Society of Astronomy and Astrophysics meeting 2009" (see the proceeding Cerutti *et al.* 2009c).

10. [Français] Résumé du chapitre

§ 63. Contexte et objectifs

Comme nous le savons déjà, un photon gamma primaire de haute énergie traversant un champ de rayonnement peut être annihilé et produire une paire électron-positron (Chapitre 2). Cette nouvelle génération de particules interagit avec les photons mous ambiants et diffuse des photons gamma de haute énergie par Compton inverse. Si l'énergie de ces photons est plus

grande que le seuil de la production de paire, une seconde génération de paires est produite dans le système, paires qui peuvent à leur tour émettre de nouveaux photons gamma et ainsi de suite (voir Fig. 59). Une cascade de paires et de photons gamma est ainsi initiée. Ce processus continuera tant que les rayons gamma produits ont une énergie supérieure au seuil de production de paire et avant que les particules ne s'échappent du système. Une cascade de paires se développe souvent dans les environnements compacts où l'opacité gamma est très élevée $\tau_{\gamma\gamma} \gg 1$.

Au Chapitre 4 (Dubus *et al.* 2008), nous avons modélisé la modulation gamma dans LS 5039 en combinant l'émission Compton inverse anisotrope et l'absorption gamma sur les photons stellaires UV, mais nous avons négligé toute contribution en provenance d'une cascade de paires. Ce modèle permet d'expliquer correctement la modulation TeV à toutes les phases orbitales ϕ (voir Chapitre 4, Fig. 26) sauf à proximité de la conjonction supérieure ($\phi \approx 0.06$), *i.e.* lorsque l'objet compact se situe derrière l'étoile massive par rapport à l'observateur. A cette phase, l'opacité gamma est très forte $\tau_{\gamma\gamma} \gg 1$. Nous nous attendons donc à ce qu'aucun flux au TeV ne soit détectable avec ce modèle.

Les observations HESS (Aharonian *et al.* 2006) montrent qu'il existe un excès significatif de gamma proche de la conjonction supérieure (6.1σ à la phase 0.0 ± 0.05), contrairement à ce qu'indiquent nos résultats. Manifestement, plus de rayons gamma arrivent à s'échapper du système que prévu. La solution à ce problème pourrait se trouver dans la cascade de paires. En effet, le désaccord avec les observations se produit précisément où l'opacité gamma est très forte. Une partie importante de l'énergie absorbée pourrait être efficacement recyclée par une cascade de paires dans le système et contribuer au flux total de haute énergie. Il est aussi possible que la source primaire de rayons gamma ne coïncide pas avec la position de l'objet compact, mais qu'elle soit localisée plus loin comme par exemple dans un jet ou plus en arrière dans le vent du pulsar. Cette possibilité a été proposée par Bosch-Ramon *et al.* (2008b) dans LS 5039 et par Zdziarski *et al.* (2009) pour un problème similaire dans le microquasar Cygnus X-1. Nous reviendrons sur ce point au chapitre suivant.

Dans ce chapitre, j'étudie les effets d'une cascade de paires dans les binaires gamma en me concentrant plus particulièrement sur le cas de LS 5039 où l'absorption est très forte (voir Dubus 2006a). Ma première tentative est de modéliser la contribution d'une cascade 1D, *i.e.* où les paires et les photons gamma de la cascade restent le long de la même ligne. Je commence par exposer les conditions nécessaires pour avoir une cascade 1D dans LS 5039 et je dérive l'ensemble des équations qui décrit la dynamique de la cascade. J'applique ce modèle à LS 5039 et LS I +61°303.

§ 64. Ce que nous avons appris

J'ai trouvé que l'émission en provenance d'une cascade de paires est importante dans les systèmes binaires gamma compacts comme LS 5039. Dans la limite unidimensionnelle, la dynamique de la cascade peut être précisément calculée avec une approche semi-analytique. L'approximation 1D est valable tant que les déviations magnétiques sur les trajectoires des paires restent dans le cône d'émission des paires produites dans la cascade. Dans LS 5039, le champ magnétique ambiant ne doit pas dépasser 10^{-8} G. Cette limite supérieure est probablement irréaliste dans les binaires gamma. Néanmoins, ce type de cascade donne la contribution maximale attendue d'une cascade de paires aux phases orbitales où l'opacité gamma est très

importante. Par conséquent, si la contribution de la cascade 1D est trop faible à ces phases orbitales alors aucun autre type de cascade ne pourra être responsable de l'émission au TeV. Nous aurions alors à rechercher d'autres explications (*e.g.* la source gamma se situe plus loin du système).

L'émission produite dans une cascade 1D a une forte dépendance angulaire, et domine le flux gamma total au dessus du seuil pour des angles de vue où l'absorption est très forte. Dans LS I +61°303, la contribution d'une cascade ne joue aucun rôle significatif dans la formation du flux gamma puisque l'émission de la cascade 1D est négligeable. Dans LS 5039, la cascade 1D est importante et rajoute plus de flux autour de la conjonction supérieure comme attendu. Cependant, la cascade contribue trop et le modèle n'est alors plus en accord avec les observations HESS. De plus, la modulation orbitale au TeV n'est plus bien reproduite. La possibilité d'avoir une cascade 1D dans LS 5039 peut être écartée, mais cette étude n'exclue pas l'existence d'une cascade 3D plus complexe. Cette possibilité est considérée en détail au chapitre suivant (Chapitre 8).

J'ai également étudié la contribution d'une cascade de paires et l'effet du refroidissement Compton dans le régime Klein-Nishina dans le vent non choqué du pulsar, mais j'ai trouvé que ces deux effets ne changent pas les conclusions que nous avons formulé au Chapitre 5, puisqu'ils ne permettent pas de diminuer la forte émission gamma en provenance du vent. Par ailleurs, nous avons montré que les binaires gamma ne contribuent probablement pas beaucoup à l'émission diffuse galactique à 511 keV.

Ce travail a été publié dans Cerutti *et al.* (2009b). J'ai présenté des résultats préliminaires au cours d'une présentation orale à la conférence internationale "High energy phenomena in massive stars meeting 2009" (voir le compte rendu Cerutti *et al.* 2010a). Plus tard, j'ai aussi eu la chance de présenter nos conclusions sur la cascade 1D dans les binaires gamma dans une présentation orale à la réunion générale de la Société Française d'Astronomie et d'Astrophysique en 2009 (voir le compte rendu Cerutti *et al.* 2009c).

11. Paper: One dimensional pair cascade emission in gamma-ray binaries

One-dimensional pair cascade emission in gamma-ray binaries

An upper-limit to cascade emission at superior conjunction in LS 5039

B. Cerutti, G. Dubus, and G. Henri

Laboratoire d'Astrophysique de Grenoble, UMR 5571 CNRS, Université Joseph Fourier, BP 53, 38041 Grenoble, France

Draft September 29, 2009

ABSTRACT

Context. In gamma-ray binaries such as LS 5039, a large number of electron-positron pairs are created by the annihilation of primary very high-energy (VHE) gamma rays with photons from the massive star. The radiation from these particles contributes to the total high-energy gamma-ray flux and can initiate a cascade, decreasing the effective gamma-ray opacity in the system.

Aims. The aim of this paper is to model the cascade emission and investigate whether it can account for the VHE gamma-ray flux detected by HESS from LS 5039 at superior conjunction, where the primary gamma rays are expected to be fully absorbed.

Methods. A one-dimensional cascade develops along the line-of-sight if the deflections of pairs induced by the surrounding magnetic field can be neglected. A semi-analytical approach can then be adopted, including the effects of the anisotropic seed radiation field from the companion star.

Results. Cascade equations are numerically solved, yielding the density of pairs and photons. In LS 5039, the cascade contribution to the total flux is large and anti-correlated with the orbital modulation of the primary VHE gamma rays. The cascade emission dominates close to superior conjunction but is too strong to be compatible with HESS measurements. Positron annihilation does not produce detectable 511 keV emission.

Conclusions. This study provides an upper limit to cascade emission in gamma-ray binaries at orbital phases where absorption is strong. The pairs are likely to be deflected or isotropized by the ambient magnetic field, which will reduce the resulting emission seen by the observer. Cascade emission remains a viable explanation for the detected gamma rays at superior conjunction in LS 5039.

Key words. radiation mechanisms: non-thermal – stars: individual: LS 5039 – gamma rays: theory – X-rays: binaries

1. Introduction

The massive star in gamma-ray binaries plays a key role in the formation of very high-energy (VHE, >100 GeV) radiation. The large seed-photon density provided by the O or Be companion star, contributes to the production of gamma rays *via* inverse Compton scattering on ultra-relativistic electrons accelerated in the system (*e.g.* in a pulsar wind or a jet). The same photons annihilate with gamma rays, leading to electron-positron pairs production $\gamma + \gamma \rightarrow e^+ + e^-$. In some tight binaries such as LS 5039, this gamma-ray absorption mechanism is strong if the VHE emission occurs close to the compact object. Gamma-ray absorption can account for an orbital modulation in the VHE gamma-ray flux from LS 5039, as observed by HESS (Böttcher & Dermer 2005; Bednarek 2006; Dubus 2006).

A copious number of pairs may be produced in the surrounding medium as a by-product of the VHE gamma-ray absorption. If the number of pairs created is large enough and if they have enough time to radiate VHE photons before escaping, a sizeable electromagnetic cascade can be initiated. New generations of pairs and gamma rays are produced as long as the secondary particles have enough energy to boost stellar pho-

tons beyond the pair production threshold energy. Because of the anisotropic stellar photon field in the system, the inverse Compton radiation produced in the cascade has a strong angular dependence. The cascade contribution depends on the position of the primary gamma-ray source with respect to the massive star and a distant observer.

The VHE modulation in LS 5039 was explained in Dubus et al. (2008) using phase-dependent absorption and inverse Compton emission, ignoring the effect of pair cascading. This model did not predict any flux close to superior conjunction, *i.e.* where the massive star lies between the compact object and the observer. This is contradicted by HESS observations (Aharonian et al. 2006a). Interestingly, this mismatch intervenes at phases where $\gamma\gamma$ -opacity is known to be high $\tau_{\gamma\gamma} \gg 1$. The development of a cascade could contribute to the residual flux observed in the system, with secondary gamma-ray emission filling in for the highly absorbed primary gamma rays. This possibility has been proposed to explain this discrepancy (Aharonian et al. 2006a) and is quantitatively investigated in this article.

The ambient magnetic field strength has a critical impact on the development of pair cascading. If the magnetic field

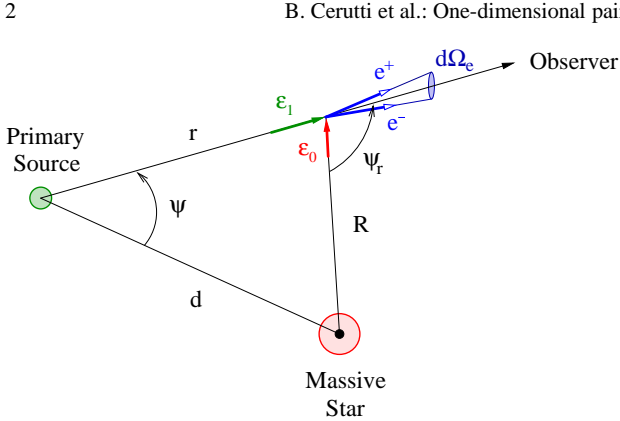


Fig. 1. This diagram describes the system geometry. A gamma-ray photon of energy ϵ_1 from the primary source (compact object) interacts with a soft photon of energy ϵ_0 at a distance r from the source and R from the massive star (assumed point-like and mono-energetic), producing a pair e^+/e^- boosted toward a distant observer. The system is seen at an angle ψ .

strength is low enough to neglect the induced deflections on pair trajectories then the cascade develops along the line of sight joining the primary source of gamma rays and a distant observer. The particles do not radiate synchrotron radiation. Cascade calculations are then reduced to a one-dimension problem. Such a situation would apply in an unshocked pulsar wind where the pairs are cold relative to the magnetic field carried in the wind. This paper explores the development of an one-dimensional pair cascade in a binary and its implications.

Previous computations of cascade emission in binary environment were carried out by Bednarek (1997); Sierpowska & Bednarek (2005); Aharonian et al. (2006b); Bednarek (2006, 2007); Orellana et al. (2007); Khangulyan et al. (2008); Sierpowska-Bartosik & Torres (2008); Zdziarski et al. (2009). Except for Aharonian et al. (2006b), all these works are based on Monte Carlo methods. One peculiarity of the gamma-ray binary environment is that the source of seed-photons for pair production and inverse Compton emission is the high luminosity companion star. This study proposes a semi-analytical model for one-dimensional cascades calculations, taking into account the anisotropy in the seed-photon field. The aim of the paper is to investigate and compute the total contribution from pair cascading in the system LS 5039, and see if it can account for the measured flux close to superior conjunction. The next section presents the main assumptions and equations for cascade computations. The development and the anisotropic effects of pair cascading in compact binaries are investigated. The density of escaping pairs and their rate of annihilation are also calculated in this part. The cascade contribution along the orbit in LS 5039 is computed and compared with the available observations in Section 3. The last section concludes on the implications of one-dimensional cascades in gamma-ray binaries. More details about pair production are available in the appendices.

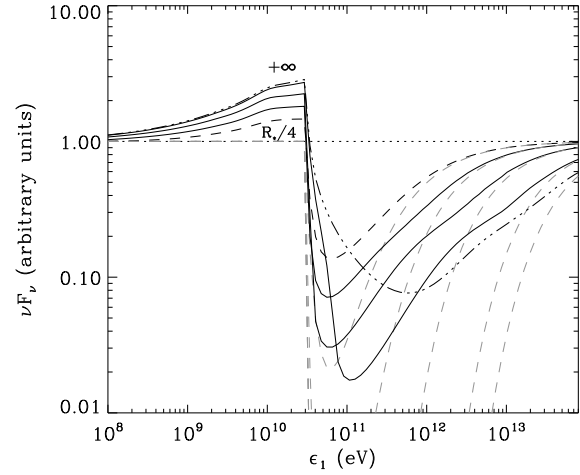


Fig. 2. Cascade development along the path to the observer. The primary source of photons, situated at the location of the compact object, has a power law spectral distribution with photon index -2 (dotted line). Spectra are computed using the parameters appropriate for LS 5039 at superior conjunction ($d \approx 2R_*$, $R_* = 9.3 R_\odot$, $T_* = 39\,000$ K) for $\psi = 30^\circ$. The transmitted spectrum, including cascade emission, is shown at various distances from the primary source: $r = R_*/4$ (black dashed line), $R_*/2$, R_* , $2R_*$ (solid lines) and $r = +\infty$ (dotted-dashed line). Pure absorbed spectra are shown for comparison (light dashed line).

2. Anisotropic pair cascading in compact binaries

2.1. Assumptions

This part examines one-dimensional cascading in the context of binary systems. The massive star sets the seed-photon radiation field for the cascade. For simplicity, the massive star is assumed point-like and mono-energetic. This is a reasonable approximation as previous studies on absorption (Dubus 2006) and emission (Dubus et al. 2008) have shown. The effects of the magnetic field and pair annihilation are neglected (see §2.5). Triplet pair production (TPP) due to the high-energy electrons or positrons propagating in a soft photon field ($\gamma + e^{+-} \rightarrow e^{+-} + e^+ + e^-$, Mastichiadis 1991) is not taken into account here. The cross section for this process becomes comparable to inverse Compton scattering when $E_e \epsilon_0 \gtrsim 250(m_e c^2)^2$ that is for electron energies $E_e \gtrsim 6$ TeV interacting with $\epsilon_0 \approx 10$ eV stellar photons. With a scattering rate of about $\sim 10^{-2} \text{ s}^{-1}$, only a few pairs can be created *via* TPP by each VHE electron, before it escapes or loses its energy in a Compton scattering. The created pairs have much lower energy than the primary electrons. TPP cooling remains inefficient compared to inverse Compton for VHE electrons with energy \lesssim PeV. HESS observations of LS 5039 show a break in the spectrum at a few TeV so few electrons are expected to interact by TPP in the cascade. Observations of other gamma-ray binaries also show steep spectra but this assumption will have to be revised if there is significant primary emission beyond ≈ 10 TeV. Pair production due to high-energy gamma rays interacting with the surrounding material is also neglected. This occurs for γ -rays > 1

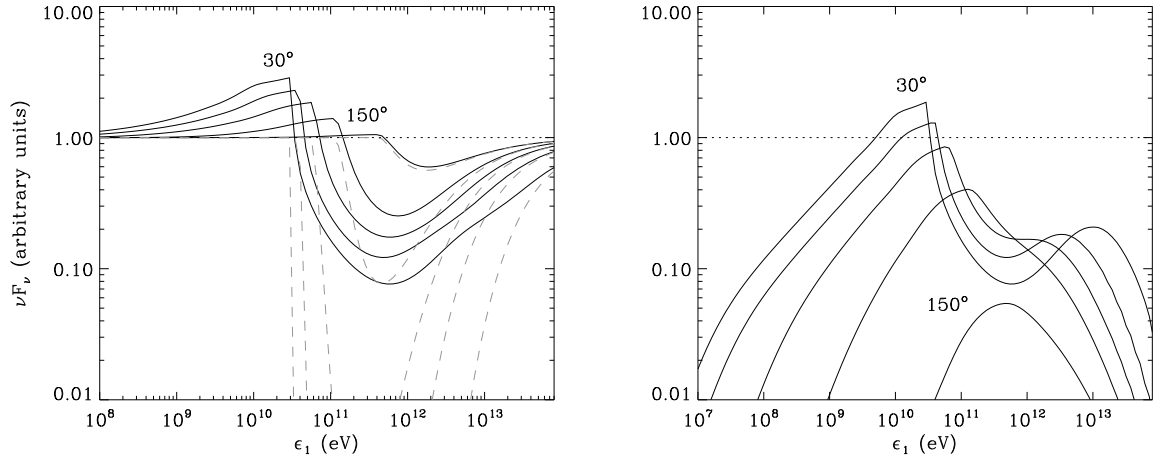


Fig. 3. Spectra as seen by an observer at infinity, taking into account the effect of cascading. Calculations are applied to LS 5039 at periastron for different viewing angle $\psi = 30^\circ, 60^\circ, 90^\circ, 120^\circ$ and 150° . *Left panel:* Complete spectra (solid line) are compared to the pure absorbed (light dashed line) and injected (dotted line) spectra. The contribution from the cascade is presented in the *right panel*.

MeV and the cross-section is of order $0.04\sigma_T Z^2 \text{ cm}^2$ (see *e.g.* Longair 1992), with σ_T the Thomson cross-section. Since the measured N_H is at most 10^{22} cm^{-2} in gamma-ray binaries, pair production on matter will not affect the propagation of gamma rays towards the observer.

Due to the high velocity of the center-of-mass (CM) frame in the observer frame, the direction of propagation of pairs created by $\gamma\gamma$ -absorption is boosted in the direction of the initial gamma ray. For a gamma ray of energy $\epsilon_1 = 1 \text{ TeV}$, the Lorentz factor of the CM to the observer frame transform is $\gamma' \sim \epsilon_1/2m_e c^2 = 10^6 \gg 1$ (see the appendix, Eq. A.2). Pairs produced in the cascade are ultra-relativistic with typical Lorentz factor $\gamma_e \sim 10^6 \gg 1$. Their emission is forward boosted within a cone of semi-aperture angle $\alpha \sim 1/\gamma_e \ll 1$ in the direction of electrons. The deviations on the electron trajectory due to scattering in the Thomson regime are $\sim \epsilon_0/m_e c^2 \ll 1/\gamma_e$. In the Klein-Nishina regime most of the electron energy is given to the photon. It is assumed here that electrons and photons produced in the cascade remain on the same line, a good approximation since γ' and $\gamma_e \gg 1$. This line joins the primary gamma-ray source to a distant observer (Fig. 1).

Pair cascading is one-dimensional as long as magnetic deviations of pairs trajectories along the Compton interaction length λ_{ic} remain within the cone of emission of the electrons. This condition holds if $\lambda_{ic}/(2R_L) < 1/\gamma_e$, with R_L the Larmor radius. For a typical interaction length $\lambda_{ic} \sim 1/(n_*\sigma_{ic}) \sim 10^{11} \text{ cm}$ for TeV pairs in LS 5039, the ambient magnetic field must be lower than $B \lesssim 10^{-8} \text{ G}$. If the magnetic field strength is much greater, pairs locally isotropize and radiate in all directions. In between, pairs follow the magnetic field lines and the dynamics of each pairs must be followed as treated in Sierpowska & Bednarek (2005). The above limit may appear unrealistically stringent. However, since deviations and isotropization will dilute the cascade flux, the one-dimensional approach can be seen as maximizing the cascade emission. More exactly, this redistribution induced by magnetic deflec-

tions would decrease the cascade flux at orbital phases where many pairs are produced to the benefit of phases where only a few are created. Hence, the one-dimensional approach gives an upper limit to the cascade contribution at phases where absorption is strong. If the flux calculated here using this assumption is lower than required by observations then cascading will be unlikely to play a role. Finally, one-dimensional cascading should hold in the free pulsar wind as long as the pairs move strictly along the magnetic field. In Sierpowska & Bednarek (2005) and Sierpowska-Bartosik & Torres (2008), the cascade radiation is computed up to the termination shock using a Monte Carlo approach. Sierpowska & Bednarek (2005) also include a contribution from the region beyond the shock. The cascade electrons in this region are assumed to follow the magnetic field lines (in contrast with the pulsar wind zone where the propagation is radial). There is no reacceleration at the shock and synchrotron losses are neglected. In the method expounded here, the cascade radiation is calculated semi-analytically from a point-like gamma-ray source at the compact object location up to infinity, providing the maximum possible contribution of the one-dimensional cascade in gamma-ray binaries.

2.2. Cascade equations

In order to compute the contribution from the cascade, the radiative transfer equation and the kinetic equation of the pairs have to be solved simultaneously.

The radiative transfer equation for the gamma-ray density $n_\gamma \equiv dN_\gamma/dtd\epsilon_1 d\Omega$ at a distance r from the source is

$$\frac{dn_\gamma}{dr} = -n_\gamma \left(\frac{d\tau_{\gamma\gamma}}{dr} \right) + \int n_* \frac{dN}{dtd\epsilon_1} n_e dE_e, \quad (1)$$

where $n_e \equiv dN_e/dr dE_e d\Omega_e$ is the electrons distribution, n_* the seed-photon density from the massive star and $dN/dtd\epsilon_1$ the Compton kernel. The kernel is normalized to the soft photon density and depends on the energy E_e of the electron and

the angle between the photon and the direction of motion of the electron (Dubus et al. 2008). In the mono-energetic and point-like star approximation the stellar photon density can be estimated as $L_\star/4\pi cR^2\bar{\epsilon}_0$, where L_\star is the stellar luminosity, $\bar{\epsilon}_0 \approx 2.7kT_\star$ the mean thermal photon energy and R the distance to the massive star (see Fig. 1). The absorption rate $d\tau_{\gamma\gamma}/dr$ is given by Eq. (B.8), convoluted to the soft photon density.

The kinetic equation for the pairs is given by the following integro-differential equation for $\gamma_e \gg 1$ (Blumenthal & Gould 1970; Zdziarski 1988; D’Avezac et al. 2007)

$$\frac{dn_e}{dt} = -n_e(E_e) \int_{m_e c^2}^{E_e} \mathcal{P}(E_e, E'_e) dE'_e + \int_{E_e}^{+\infty} n_e(E'_e) \mathcal{P}(E'_e, E_e) dE'_e + 2 \int n_\star g_{\gamma\gamma} n_\gamma d\epsilon_1, \quad (2)$$

where $\mathcal{P}(E_e, E'_e)$ is the transition rate for an electron of energy E_e down-scattered at an energy $E'_e \leq E_e$ at r . The first two terms on the right side of the equation describe the inverse Compton cooling of pairs, taking into account catastrophic losses in the deep Klein-Nishina regime. In this case, most of the electron energy is lost in the interaction and the scattered photon carries away most of its energy since $\epsilon_1 = E_e - E'_e \approx E_e$. A continuous losses equation inadequately describes sizeable stochastic losses in a single interaction (Blumenthal & Gould 1970; Zdziarski 1989).

Since the inverse Compton kernel gives the probability per electron of energy E_e to produce a gamma ray of energy ϵ_1 , the scattering rate can be rewritten as

$$\mathcal{P}(E_e, E'_e) = n_\star(r) \frac{dN}{dt dE'_e}. \quad (3)$$

The expression of $dN/dt dE'_e$ is the same as the Compton kernel as described before but gives the spectrum of scattered electrons instead of the outgoing photon. The first integral in Eq. (2) is the inverse Compton scattering rate and can be analytically expressed as

$$\int_{m_e c^2}^{E_e} \mathcal{P}(E_e, E'_e) dE'_e = \sigma_{ic} c n_\star(r) (1 - \beta_e \cos \theta_0), \quad (4)$$

where β_e is the electron velocity in the observer frame and σ_{ic} is the total inverse Compton cross-section (for the full expression see *e.g.* Rybicki & Lightman 1979, Eq. 7.5). The last term in the kinetic equation is a source of pairs from $\gamma\gamma$ -absorption coupled with the photon density (see the appendices). The pair production kernel $g_{\gamma\gamma}$ is normalized to the soft photon density.

The anisotropic cascade can be computed by inserting the anisotropic kernels for inverse Compton scattering (see Eq. A.6 in Dubus et al. 2008) and for pair production obtained in Eq. (B.5) in Eqs. (1-2). The following sections present cascade calculations applied to compact binaries, using a simple Runge-Kutta 4 integration method. It is more convenient to perform integrations over an angular variable rather than r . Here, calculations are carried out using ψ_r , the angle between the line joining the massive star to the observation point and the line of sight (see Fig. 1).

2.3. Cascade growth along the line of sight

Figure 2 presents cascade calculations for different distances r from the primary gamma-ray source. For illustrative purpose, the source is assumed isotropic and point-like, injecting a power-law distribution of photons with an index -2 at $r = 0$ but no electrons. The calculations were carried out for a system like LS 5039 and for a viewing angle $\psi = 30^\circ$. In this geometric configuration, absorption is known to be strong ($\tau_{\gamma\gamma} \approx 40$ for 200 GeV photons) and a significant fraction of the total absorbed energy is expected to be reprocessed in the cascade, inverse Compton scattering being also very efficient in this configuration.

Close to the source ($r \lesssim d$ with d the orbital separation), absorption produces a sharp and deep dip in the spectrum (light dashed line) but the cascade starts to fill the gap (black solid line). The angle ψ_r increases with the distance r to the primary source. Hence, the threshold energy for pair production increases as well. Cascading adds more flux to higher energy gamma rays where absorption is maximum. The cascade produces an excess of low energy gamma rays below the minimum threshold energy $\epsilon_1 \approx 30$ GeV. Because these new photons do not suffer from absorption, they accumulate at lower energies. This is a well-known feature of cascading.

2.4. Anisotropic effects

This section investigates anisotropic effects in the development of the cascade as seen by a distant observer. Cascades are computed for different viewing angle ψ at infinity, assuming an isotropic power-law spectrum for the primary gamma rays.

The *left panel* in figure 3 shows the complete spectrum taking into account cascading (solid line) compared to the pure absorbed power-law (dashed line). Due to the angular dependence in the pair production process, higher viewing angles shift the cascade contribution to higher energies and decrease its amplitude (Fig. 3, *right panel*). The cascade flux is low enough to be ignored for $\psi \gtrsim 150^\circ$.

Three different zones can be distinguished in the cascade spectra. First, below the pair production threshold energy, photons accumulate in a low energy tail (photon index ≈ -1.5) produced by inverse Compton cooling of pairs. For $\psi \lesssim 90^\circ$, a low energy cut-off is observed due to the pairs escaping the system (Ball & Kirk 2000; Cerutti et al. 2008). This low energy cut-off is at about 0.1 GeV for $\psi = 30^\circ$. The cutoff occurs when the cascade reaches a distance from the primary source corresponding to $\psi_r \approx 90^\circ$. Then, the electrons cannot cool effectively because the inverse Compton interaction angle diminishes and the stellar photon density decreases as they propagate. For $\psi \gtrsim 90^\circ$, particles escape right away from the vicinity of the companion star and no tail is produced. Second, above the threshold energy, there is a competition between absorption and gamma-ray production by reprocessed pairs, particularly for low angles where both effects are strong. Even if cascading increases the transparency for gamma rays, absorption still creates a dip in the spectrum. Third, well beyond the threshold energy, absorption becomes inefficient. Fewer pairs are created, producing a high-energy cut-off (≈ 10 TeV, for

Table 1. Mean energy of escaping pairs and radiated power efficiency of the cascade.

ψ	30°	60°	90°	120°	150°
$\langle E_e \rangle$ (GeV)	400	100	70	200	1000
P_r/P_a	80%	70%	60%	40%	15%

$\psi = 30^\circ$). Klein-Nishina effects also contribute to the decrease of the high-energy gamma-rays production.

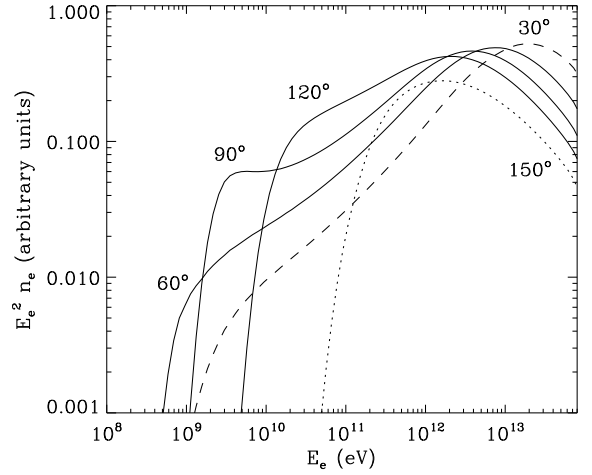
2.5. Escaping pairs

The spectrum of pairs produced in the cascade as seen at infinity is shown in figure 4. The density depends strongly on the viewing angle as expected, but the mean energy of pairs lies at very high energies ($\langle E_e \rangle \gtrsim 100$ GeV, see Table 1). The accumulation of very high-energy particles can be explained by two concurrent effects. Far from the massive star ($r \gg d$), most of the pairs are created at very high energy due to the high threshold energy (almost rear-end collision). The second effect is that inverse Compton losses are in deep Klein-Nishina regime for high-energy electrons. The cooling timescale increases and becomes longer than the propagation timescale of electrons close to the companion star, producing an accumulation of pairs at very high energies.

The distribution of pairs allows to assess the fraction of the total absorbed energy escaping the system in the form of kinetic energy in the pairs. This non-radiated power P_e can be compared to the radiated power released in the cascade P_r . Energy conservation yields the total absorbed power $P_a = P_e + P_r$.

The asymptotic radiated power reached by the cascade is compared to the total absorbed power integrated over energy in Table 1. The fraction of lost energy increases with the viewing angle. In fact, for $\psi > 90^\circ$ most of the power remains in kinetic energy. Once the electrons are created, only a few have time to radiate through inverse Compton interaction. Below ($\psi < 90^\circ$), the radiative power dominates and the cascade is very efficient (recycling efficiency up to 80% for $\psi = 30^\circ$). The cascade is fully linear, since the power re-radiated remains much lower than the star luminosity $P_r \ll L_\star$ (Svensson 1987). Self-interactions in the cascade are then negligible. This is also a consequence of Klein-Nishina cascading (Zdziarski 1988). In addition, interactions between particles in the cascade would be forcedly rear-end, hence highly inefficient.

The created positrons will annihilate and form a 511 keV line. However, the expected signal is very weak. The annihilation cross-section is $\sigma \sim \sigma_T \log \gamma/\gamma$ (see *e.g.* Longair 1992). The escaping positrons have a very high average Lorentz factor $\gamma \gtrsim 10^5$ (Tab. 1) so they are unlikely to annihilate within the system. They will thermalize and annihilate in the interstellar medium. Escaping positrons from gamma-ray binaries are unlikely to contribute much to the diffuse 511 keV emission. The average number of pairs created along the orbit in LS 5039 (based on the results to be discussed in the following section) is $\mathcal{N}_e \sim 5 \times 10^{35} \text{ s}^{-1}$. This estimate does not take into account contributions from triplet pair production or from the

**Fig. 4.** Distribution of escaping pairs seen by a distant observer, depending on the viewing angle $\psi = 30^\circ$ (dashed line), 60° , 90° , 120° and 150° (dotted line). The binary parameters are the same as in Fig. 3.

pulsar wind (for a pulsar injecting pairs with $\langle \gamma_e \rangle \sim 10^5$ and a luminosity of 10^{36} erg/s, about 10^{36} s^{-1} pairs are produced). Gamma-ray binaries have short lifetimes and it is unlikely there is more than a few hundred currently active in the Galaxy. Hence, the expected contribution is orders-of-magnitude below the positron flux required to explain the diffuse 511 keV emission ($\sim 10^{43} \text{ s}^{-1}$, Knödlseder et al. 2005). Even if the positrons thermalize close to or within the system (because magnetic fields contain them, see §5) then, following Guessoum et al. (2006), the expected contribution from a single source at 2 kpc would be at most $\sim 10^{-9} \text{ ph cm}^{-2} \text{ s}^{-1}$, which is currently well below detectability.

3. Cascading in LS 5039

LS 5039 was detected by HESS (Aharonian et al. 2005) and the orbital modulation of the TeV gamma-ray flux was later on reported in Aharonian et al. (2006a). Most of the temporal and spectral features can be understood as a result of anisotropic gamma-ray absorption and emission from relativistic electrons accelerated in the immediate vicinity of the compact object, *e.g.* in the pulsar wind termination shock (Dubus et al. 2008). However, this description fails to explain the residual flux observed close to superior conjunction where a significant excess has been detected (6.1σ at phase 0.0 ± 0.05). The primary gamma rays should be completely attenuated. The aim of this part is to find if cascading can account for this observed flux. The cascade is assumed to develop freely from the primary gamma-ray source up to the observer. The contribution of the cascade as a function of the orbital phase is also investigated.

The primary source of gamma rays now considered is the spectrum calculated in Dubus et al. (2008). Figure 5 shows phase-averaged spectra along the orbit at INFC (orbital phase $0.45 < \phi < 0.9$) and SUPC ($\phi < 0.45$ or $\phi > 0.9$) for the primary source, the cascade and the sum of both components. The orbital parameters and the distance (2.5 kpc) are taken from

6

B. Cerutti et al.: One-dimensional pair cascade emission in gamma-ray binaries

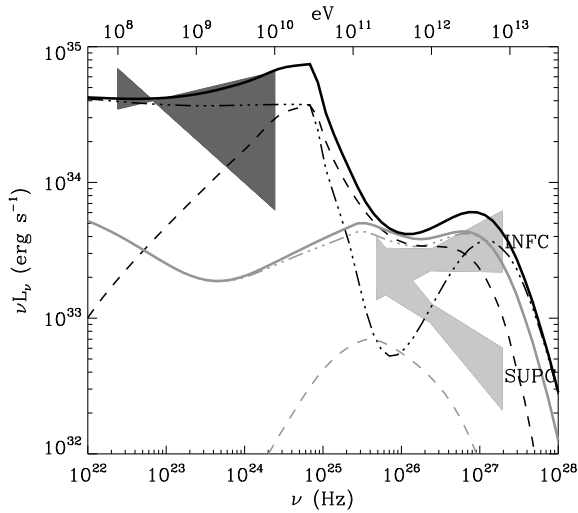


Fig. 5. Orbit-averaged spectra in LS 5039 at INFC ($0.45 < \phi < 0.9$, grey lines) and SUPC ($\phi < 0.45$ or $\phi > 0.9$, black lines) and comparisons with EGRET (dark) and HESS (light) bowties (Hartman et al. 1999; Aharonian et al. 2006a). Dotted-dashed lines represent the primary source of gamma rays with pure absorption, injected at $r \equiv 0$, computed with the model described in Dubus et al. (2008) for a monoenergetic and point-like star. Dashed lines show the contribution from the cascade and thick solid lines the sum of the primary absorbed source and the cascade contributions.

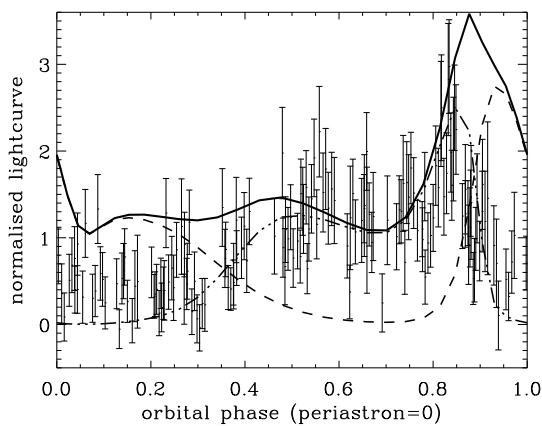


Fig. 6. Computed light-curves along the orbit in LS 5039, in the HESS energy band (flux ≥ 100 GeV). The cascade contribution (dashed line) is compared to the primary pure absorbed source (dotted-dashed line) and HESS observations. The thick solid line shows the sum of both components.

Casares et al. (2005) for an inclination $i = 60^\circ$ so ψ varies between $30^\circ - 150^\circ$. The cascade contribution is highly variable along the orbit and dominates at SUPC for $\epsilon_1 \geq 30$ GeV, where a high pair-production rate is expected. At INFC, cascading is negligible compared with the primary flux. With pair cascading the spectral differences between INFC and SUPC are very small at VHE, contrary to what is observed by HESS. In the

GeV band, cascades contribute to a spectral hardening at SUPC close to 10-30 GeV.

Orbital light-curves in the HESS energy band give a better appreciation of the contribution from both components (Fig. 6). The contribution from cascading is anti-correlated with the primary absorbed flux. The cascade light-curve is minimum at inferior conjunction ($\phi \approx 0.72$). The non trivial double peaked structure of the lightcurve at phases 0.85-0.35 is due to competition in the cascade between absorption and inverse Compton emission. Absorption has a slight edge at superior conjunction ($\phi \approx 0.06$), producing a dip at this phase. Elsewhere, the primary contribution dominates over the cascade emission. At lower energies ($\epsilon_1 < 10$ GeV), the cascade contribution is undistinguishable from the primary source.

In this configuration, the cascade does add VHE gamma-ray emission close to superior conjunction but the expected contribution overestimates HESS observations. Decreasing the inclination of the system does not help: the cascade flux in the TeV energy band increases, since the primary source is on average more absorbed along the orbit (see §3 in Dubus 2006). For $i \lesssim 30^\circ$, the cascade contribution dominates the primary flux at every orbital phases in the VHE band. One-dimension cascades can be ruled out by the current HESS observations of LS 5039.

4. Conclusion

This paper explored the impact of one-dimensional pair cascading on the formation of the very high-energy radiation from gamma-ray binaries in general, LS 5039 specifically. A significant fraction of the total absorbed energy can be reprocessed at lower energy by the cascade, decreasing the global opacity of the primary source. Anisotropic effects also play a major role on the cascade radiation spectrum seen by a distant observer.

A large contribution from cascading is expected in LS 5039, large enough that it significantly overestimates the flux observed by HESS. One-dimensional cascading is too efficient in redistributing the absorbed primary flux and can be ruled out. However, the fact that it overestimates the observed flux means a more general cascade cannot be ruled out (it would have been if the HESS flux had been underestimated). If the ambient magnetic field is high enough ($B \gg 10^{-8}$ G) the pairs will be deflected from the line-of-sight. For $B \geq 10^{-3}$ G the Larmor radius of a TeV electron becomes smaller than the LS 5039 orbital separation and the pairs will be more and more isotropized locally. All of this will tend to dilute cascade emission compared to the one-dimensional case, which should therefore be seen as an upper limit to the cascade contribution at orbital phases where absorption is strong, particularly at superior conjunction. The initiated cascade will be three-dimensional as pointed out by Bednarek (1997). Each point in the binary system becomes a potential secondary source able to contribute to the total gamma-ray flux at every orbital phases. Cascade emission can still be sizeable all along the orbit in LS 5039, yet form a more weakly modulated background in the light-curve on account of the cascade radiation redistribution at other phases. The strength and structure of the surrounding magnetic field (from both stars) has a strong influ-

ence on the cascade (Sierpowska & Bednarek 2005; Bosch-Ramon et al. 2008a,b). More realistic pair cascading calculations cannot be treated with the semi-analytical approach exposed here. Complementary investigations using a Monte Carlo approach are needed to better appreciate the cascade contribution in gamma-ray binaries.

Finally, the cascade will be quenched if the created pairs lose energy to synchrotron rather than inverse Compton scattering. This requires ambient magnetic fields $B \gtrsim 5$ G, as found by equating the radiative timescales for a 1 TeV electron at periastron in LS 5039. Such ambient magnetic field strengths could be reached close to the companion star. In this case an alternative explanation is needed to account for the flux at superior conjunction. A natural one to consider is that the primary gamma-ray source is farther from the massive star. The VHE source would not be coincident with the compact object location anymore and would suffer less from absorption. In the microquasar scenario, Bednarek (2007) can account for consistent flux with HESS observations at superior conjunction if some electrons are injected well above the orbital plane (jet altitude $z > 10 R_*$). In addition to LS 5039, this possibility was also considered for the system Cyg X-1 by Bosch-Ramon et al. (2008b) and Zdziarski et al. (2009).

In practice, reality may consist of a complex three-dimensional cascade partly diluted and partly quenched depending upon position, angle and magnetic field configuration.

Acknowledgements. GD thanks A. Mastichiadis for discussions of triplet pair production. This work was supported by the *European Community* via contract ERC-StG-200911.

Appendix A: Pair production

The main equations for the pair production process are briefly presented here. Detailed calculations can be found in Gould & Schröder (1967), Bonometto & Rees (1971) and Böttcher & Schlickeiser (1997).

A.1. Kinematics and cross-sections

The interaction of a gamma-ray photon of energy ϵ_1 and a soft photon of energy ϵ_0 in the observer frame leads to the production of an electron-positron pair if the total available energy in the center-of-mass (CM) frame is greater than the rest mass energy of the pair

$$2\epsilon_1\epsilon_0(1 - \cos\theta_0) \geq 4m_e^2c^4, \quad (\text{A.1})$$

where m_e is the electron mass and θ_0 the angle between the two incoming photons in the observer frame. It is useful to define the Lorentz invariant $s = \epsilon_1\epsilon_0(1 - \cos\theta_0)/2$. Pairs are produced if $s \geq m_e^2c^4$ and the velocity β of the electron-positron pair in the CM frame is $\beta = (1 - m_e^2c^4/s)^{1/2}$.

The differential cross-section $d\sigma_{\gamma\gamma}/d(\beta \cos\theta'_1)$ in the CM frame depends on β and the angle θ'_1 between the outgoing electron-positron pair and the incoming photons. The full expression can be found in *e.g.* Bonometto & Rees (1971), Eq. (2.7). The differential cross-section presents a symmetric structure, peaked at $\cos\theta'_1 = \pm 1$ and minimum for $\cos\theta'_1 = 0$.

Electrons are mostly created in the same and opposite direction with respect to the incoming hard photon direction in the CM frame. The double peaked structure is enhanced with increasing energy ($s \gg m_e^2c^4$) and becomes less pronounced close to the threshold ($s \sim m_e^2c^4$). The integration over the angles gives the total pair production cross-section $\sigma_{\gamma\gamma}$, maximum close to the threshold (see Eq. 1 in Gould & Schröder 1967).

The construction of the CM frame with respect to the observer frame can be simplified if one of the incoming photons carries most of the energy. This case is appropriate in the present context. For $\epsilon_1 \gg \epsilon_0$, the CM frame can be considered as propagating along the same direction as the high-energy photon. The velocity of the CM frame in the observer frame can be expressed as

$$\beta' = \left(1 - \frac{4s}{\epsilon_1^2}\right)^{1/2}. \quad (\text{A.2})$$

The total energy of say the electron E_e in the observer frame can then be formulated using the Lorentz transform from the CM to the observer frames

$$E_e = \gamma' \left[s^{1/2} + \beta' (s - m_e^2c^4)^{1/2} \cos\theta'_1 \right], \quad (\text{A.3})$$

providing a relation between E_e and $\cos\theta'_1$.

A.2. Rate of absorption and pair spectrum kernels

A gamma-ray photon going through a soft photon gas of density $dn/d\epsilon d\Omega$ is absorbed at a rate per unit of path length l

$$\frac{d\tau_{\gamma\gamma}}{dl} = \iint \frac{dn}{d\epsilon d\Omega} (1 - \cos\theta) \sigma_{\gamma\gamma} d\epsilon d\Omega. \quad (\text{A.4})$$

The absorption rate gives the probability for a gamma ray of energy ϵ_1 to be absorbed but does not give the energy of the pair created in the interaction.

Following Bonometto & Rees (1971), the probability for a gamma ray of energy ϵ_1 to be absorbed between l and $l + dl$ yielding an electron of energy between E_e and $E_e + dE_e$ (with a positron of energy $E_{e^+} \approx \epsilon_1 - E_e$ for $\epsilon_1 \gg \epsilon$) is

$$g_{\gamma\gamma} = \iint \frac{dn}{d\epsilon d\Omega} (1 - \cos\theta) \frac{d\sigma_{\gamma\gamma}}{dE_e} d\epsilon d\Omega. \quad (\text{A.5})$$

As with anisotropic inverse Compton scattering (Dubus et al. 2008), it is useful to consider the case of a monoenergetic beam of soft photons. The normalized soft photon density in the observer frame is

$$\frac{dn}{d\epsilon d\Omega} = \delta(\epsilon - \epsilon_0) \delta(\cos\theta - \cos\theta_0) \delta(\phi - \phi_0), \quad (\text{A.6})$$

where δ is the Dirac distribution. Injecting Eq. (A.6) into Eq. (A.5) gives the anisotropic pair production kernel, a convenient tool for spectral computations. The detailed calculation is presented in Appendix B and the complete expression given in Eq. (B.5). The pair production kernel has a strong angular dependence and a symmetric structure, centered at $E_e = \epsilon_1/2$ and peaked at $E_e = E_{\pm}$ (see Appendix B, Fig. B.1). The effect of the angle θ_0 is reduced close to the threshold where the particles share equally the energy of the primary gamma-ray photon

8

B. Cerutti et al.: One-dimensional pair cascade emission in gamma-ray binaries

$E_e \approx E_{e^+} \approx \epsilon_1/2$. Far from the threshold, one particle carries away almost all the available energy $E_e \approx \epsilon_1$.

The anisotropic kernel integrated over all the pitch angles, in the case of an isotropic gas of photons, is consistent with the kernel found by Aharonian et al. (1983). Note that a general expression for the anisotropic kernel valid beyond the approximation $\epsilon_1 \gg \epsilon_0$ is presented in Böttcher & Schlickeiser (1997).

A.3. Pair density

The number of pair created per unit of length path and electron energy depends on the probability to create a pair and on the probability for the incoming gamma ray to remain unabsorbed up to the point of observation so that

$$\frac{dN_e}{dl dE_e} = \{g_{\gamma\gamma}(E_e) + g_{\gamma\gamma}(\epsilon_1 - E_e)\} e^{-\tau_{\gamma\gamma}(l)}. \quad (\text{A.7})$$

Because of the symmetry in $g_{\gamma\gamma}$ and since electrons and positrons cannot be distinguished here, $g_{\gamma\gamma}(\epsilon_1 - E_e) = g_{\gamma\gamma}(E_e)$. The integration over electron energy yields

$$\frac{dN_e}{dl} = 2 \left(\int g_{\gamma\gamma}(E_e) dE_e \right) e^{-\tau_{\gamma\gamma}(l)} = 2 \frac{d\tau_{\gamma\gamma}}{dl} e^{-\tau_{\gamma\gamma}(l)}. \quad (\text{A.8})$$

The total number of pairs produced by a single gamma ray bathed in a soft radiation along the path l up to the distance r is then

$$N_e(r) = 2 \left(1 - e^{-\tau_{\gamma\gamma}(r)} \right). \quad (\text{A.9})$$

For low opacity $\tau_{\gamma\gamma} \ll 1$, pair production is inefficient and the number of particles produced tends to $\approx 2\tau_{\gamma\gamma}$. For high opacity $\tau_{\gamma\gamma} \gg 1$, a pair is always created.

Appendix B: Anisotropic pair production kernel

This section is dedicated to the calculation of the pair energy spectrum produced in the interaction between a single gamma-ray photon of energy ϵ_1 and a mono-energetic beam of soft photons. The general expression in Eq. (A.5) can be reformulated using the relativistic invariant s

$$g_{\gamma\gamma} = \frac{4}{\epsilon_1^2} \iiint \frac{s}{\epsilon_0^2} \frac{dn}{d\epsilon d\Omega} \frac{d\sigma_{\gamma\gamma}}{dE_e} d\epsilon ds d\phi. \quad (\text{B.1})$$

Combining the expression of β with the equations Eqs. (A.2-A.3) and defining $x \equiv \gamma^2$, the differential cross-section variables can be written as

$$\beta(x) = \left(1 - \frac{4m_e^2 c^4 x}{\epsilon_1^2} \right)^{1/2}, \quad \beta \cos \theta'_1(x) = \frac{2E_e - \epsilon_1}{\epsilon_1 \left(1 - \frac{1}{x} \right)^{1/2}}. \quad (\text{B.2})$$

The differential cross-section can then be expressed as

$$\begin{aligned} \frac{d\sigma_{\gamma\gamma}}{dE_e} &= \frac{d\sigma_{\gamma\gamma}}{d(\beta \cos \theta'_1)} \frac{d(\beta \cos \theta'_1)}{dE_e} \\ &= \frac{2}{\epsilon_1 \left(1 - \frac{1}{x} \right)^{1/2}} \frac{d\sigma_{\gamma\gamma}}{d(\beta \cos \theta'_1)}. \end{aligned} \quad (\text{B.3})$$

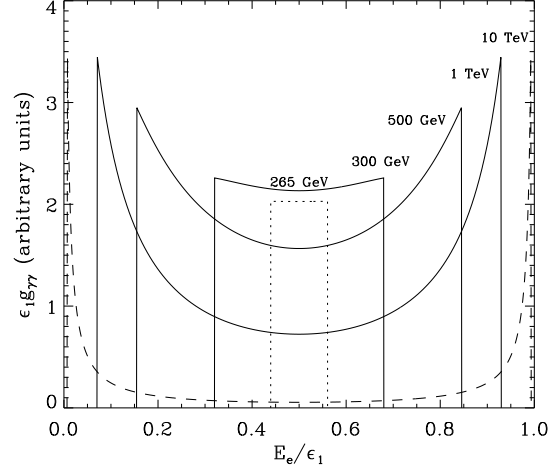


Fig. B.1. Anisotropic pair production kernel $g_{\gamma\gamma}$ with ϵ_0 set at 1 eV for a head-on collision ($\theta_0 = \pi$). The kernel is computed for $\epsilon_1 = 265$ GeV (dotted line), 300 GeV, 500 GeV, 1 TeV and 10 TeV (dashed line). The yielding of pairs occurs for $\epsilon_1 \geq 260$ GeV.

The complete general formula to compute the spectrum of the pair for a non-specified soft radiation field is

$$g_{\gamma\gamma} = \frac{\epsilon_1}{4} \iiint \frac{1}{\epsilon^2 x^3} \frac{2}{\left(1 - \frac{1}{x} \right)^{1/2}} \frac{dn}{d\epsilon d\Omega} \frac{d\sigma_{\gamma\gamma}}{d(\beta \cos \theta'_1)} d\epsilon dx d\phi, \quad (\text{B.4})$$

corresponding to Eq. (2.14) in Bonometto & Rees (1971). The injection of a mono-energetic and unidirectional soft photon density (Eq. A.6) in this last equation yields

$$g_{\gamma\gamma} = \frac{2(1 - \mu_0)}{\epsilon_1 \left(1 - \frac{1}{x_0} \right)^{1/2}} \frac{d\sigma_{\gamma\gamma}}{d(\beta \cos \theta'_1)} \{ \beta(x_0), \beta \cos \theta'_1(x_0) \}, \quad (\text{B.5})$$

where $\mu_0 \equiv \cos \theta_0$ and

$$x_0 = \frac{\epsilon_1}{2\epsilon_0(1 - \mu_0)}. \quad (\text{B.6})$$

This expression is valid for $\epsilon_1 \gg \epsilon_0$ and $s \geq m_e^2 c^4$. The minimum E_- and maximum E_+ energy reached by the particles is set by the kinematics of the reaction and given by

$$E_{\pm} = \frac{\epsilon_1}{2} \left[1 \pm \left(1 - \frac{1}{x_0} \right)^{1/2} \left(1 - \frac{4m_e^2 c^4 x_0}{\epsilon_1^2} \right)^{1/2} \right]. \quad (\text{B.7})$$

Figure B.1 presents the pair production kernel for different incoming gamma-ray energy ϵ_1 .

Note that a kernel can be calculated as well for the absorption rate. Injecting Eq. (A.6) into Eq. (A.4) is straightforward and gives

$$\frac{d\tau_{\gamma\gamma}}{dl} = (1 - \cos \theta_0) \sigma_{\gamma\gamma}(\beta). \quad (\text{B.8})$$

References

Aharonian, F., Akhperjanian, A. G., Aye, K.-M., et al. 2005, *Science*, 309, 746

- Aharonian, F., Akhperjanian, A. G., Bazer-Bachi, A. R., et al. 2006a, *A&A*, 460, 743
- Aharonian, F., Anchordoqui, L., Khangulyan, D., & Montaruli, T. 2006b, *Journal of Physics Conference Series*, 39, 408
- Aharonian, F. A., Atoian, A. M., & Nagapetian, A. M. 1983, *Astrofizika*, 19, 323
- Ball, L. & Kirk, J. G. 2000, *Astroparticle Physics*, 12, 335
- Bednarek, W. 1997, *A&A*, 322, 523
- Bednarek, W. 2006, *MNRAS*, 368, 579
- Bednarek, W. 2007, *A&A*, 464, 259
- Blumenthal, G. R. & Gould, R. J. 1970, *Reviews of Modern Physics*, 42, 237
- Bonometto, S. & Rees, M. J. 1971, *MNRAS*, 152, 21
- Bosch-Ramon, V., Khangulyan, D., & Aharonian, F. A. 2008a, *A&A*, 482, 397
- Bosch-Ramon, V., Khangulyan, D., & Aharonian, F. A. 2008b, *A&A*, 489, L21
- Böttcher, M. & Dermer, C. D. 2005, *ApJ*, 634, L81
- Böttcher, M. & Schlickeiser, R. 1997, *A&A*, 325, 866
- Casares, J., Ribó, M., Ribas, I., et al. 2005, *MNRAS*, 364, 899
- Cerutti, B., Dubus, G., & Henri, G. 2008, *A&A*, 488, 37
- D’Avezac, P., Dubus, G., & Giebels, B. 2007, *A&A*, 469, 857
- Dubus, G. 2006, *A&A*, 451, 9
- Dubus, G., Cerutti, B., & Henri, G. 2008, *A&A*, 477, 691
- Gould, R. J. & Schröder, G. P. 1967, *Physical Review*, 155, 1408
- Guessoum, N., Jean, P., & Prantzos, N. 2006, *A&A*, 457, 753
- Hartman, R. C., Bertsch, D. L., Bloom, S. D., et al. 1999, *ApJS*, 123, 79
- Khangulyan, D., Aharonian, F., & Bosch-Ramon, V. 2008, *MNRAS*, 383, 467
- Knödlseeder, J., Jean, P., Lonjou, V., et al. 2005, *A&A*, 441, 513
- Longair, M. S. 1992, *High energy astrophysics. Vol.1: Particles, photons and their detection*, ed. M. S. Longair
- Mastichiadis, A. 1991, *MNRAS*, 253, 235
- Orellana, M., Bordas, P., Bosch-Ramon, V., Romero, G. E., & Paredes, J. M. 2007, *A&A*, 476, 9
- Rybicki, G. B. & Lightman, A. P. 1979, *Radiative processes in astrophysics* (New York, Wiley-Interscience, 1979. 393 p.)
- Sierpowska, A. & Bednarek, W. 2005, *MNRAS*, 356, 711
- Sierpowska-Bartosik, A. & Torres, D. F. 2008, *Astroparticle Physics*, 30, 239
- Svensson, R. 1987, *MNRAS*, 227, 403
- Zdziarski, A. A. 1988, *ApJ*, 335, 786
- Zdziarski, A. A. 1989, *ApJ*, 342, 1108
- Zdziarski, A. A., Malzac, J., & Bednarek, W. 2009, *MNRAS*, L175+

8

Three-dimensional pair cascading

Outline

1. Assumptions on the ambient magnetic field.....	170
2. The first generation of pairs in binaries.....	171
§ 63. <i>Spectrum and energy of pairs</i>	172
§ 64. <i>Absorption and spatial distribution of pairs</i>	173
3. The first generation of gamma rays in binaries.....	174
§ 65. <i>Geometry</i>	174
§ 66. <i>Equations for the first generation of gamma rays in the cascade</i>	175
§ 67. <i>Anisotropic effects</i>	178
§ 68. <i>Spatial distribution in LS 5039</i>	179
4. Beyond the first generation approximation.....	180
§ 69. <i>Semi-analytical approach</i>	180
§ 70. <i>The Monte Carlo approach</i>	182
§ 71. <i>The effect of the magnetic field</i>	183
5. 3D pair cascade emission in LS 5039.....	184
§ 72. <i>Modulation and spectra</i>	185
§ 73. <i>The location of the TeV source</i>	185
§ 74. <i>The ambient magnetic field in LS 5039</i>	187
6. What we have learned.....	187
7. [Français] Résumé du chapitre.....	189
§ 75. <i>Contexte et objectifs</i>	189
§ 76. <i>Ce que nous avons appris</i>	191
8. Modeling the three-dimensional pair cascade in binaries.....	193

THREE DIMENSIONAL PAIR CASCADE develops in binaries if the ambient magnetic field is strong enough to deviate pairs produced in the cascade. In the general case, this problem is very complicated since pairs in the cascade would be sensitive to the magnetic field line structure in the system. If pairs are confined and isotropized by the magnetic field at their creation, the modeling of the 3D cascade becomes much simpler. Each

point in the binary system can then be considered as secondary steady source of radiation in all directions. I call here this type of 3D cascade "isotropic" (because pairs are assumed to be isotropized once created, even though their emission is anisotropic). Pairs cool down *via* inverse Compton scattering and synchrotron radiation. In this chapter, I compute the contribution of a 3D isotropic cascade in binaries using a new semi-analytical method. I investigate whether the 3D cascade can explain the amplitude of the TeV modulation observed by HESS in LS 5039 (Aharonian *et al.* 2006), precisely where the 1D cascade fails. For this study, I initiated a collaboration with Julien Malzac to benefit from his experience on Monte Carlo computation techniques. This powerful method is well adapted for the computation of multiple scattering problems like here.

1. Assumptions on the ambient magnetic field

Pairs are confined at their site of creation if the Larmor radius R_L is shorter than the Compton interaction length λ_{ic} and the size of the system, *i.e.* the orbital separation d . $R_L < d$ if

$$\begin{aligned} B &\gtrsim \frac{\gamma_e m_e c^2}{ed} \\ B &\gtrsim 10^{-3} \gamma_6 d_{0.1}^{-1} \text{ G}, \end{aligned} \quad (64.268)$$

where $\gamma_6 = \gamma_e/10^6$ and $d_{0.1} = d/0.1$ AU. In the Thomson limit, we have $\lambda_{ic}^{-1} \approx n_* \sigma_T$ then $R_L \leq \lambda_{ic}$ if

$$\frac{E_e}{eB} \leq \frac{1}{n_* \sigma_T}. \quad (64.269)$$

Assuming the companion star is point-like and mono-energetic, the density of stellar photons at the compact object location is $n_* = L_*/4\pi c \epsilon_0 d^2$ with $\epsilon_0 = 3\zeta(4) kT_*/\zeta(3)$ (the mean energy for a black body distribution) and $L_* = 4\pi R_*^2 \sigma_{SB} T_*^4$ is the stellar luminosity (with σ_{SB} the Stefan-Boltzmann constant). The above condition is valid in the Thomson limit if

$$\begin{aligned} B_T &\geq \frac{\zeta(3) m_e c \sigma_T \sigma_{SB}}{3\zeta(4) k e} \gamma_e T_*^3 \left(\frac{R_*}{d}\right)^2 \\ B_T &\geq 8 \times 10^{-5} \gamma_3 T_{*,4}^3 R_{*,10}^2 d_{0.1}^{-2} \text{ G}, \end{aligned} \quad (64.270)$$

writing $\gamma_3 = \gamma_e/10^3$, $T_{*,4} = T_*/40\,000$ K, and $R_{*,10} = R_*/10 R_\odot$. In the general case, the full cross section should be used to compute λ_{ic} (see Eq. 5.2). In the Klein-Nishina regime, the full expression can be simplified (see Eq. 5.3). Averaging over all the angles we have

$$\begin{aligned} \lambda_{ic} &\approx \frac{\gamma_e \epsilon_0}{\pi r_e^2 m_e c^2 n_*} \left[\ln \left(\frac{4\gamma_e \epsilon_0}{m_e c^2} \right) - \frac{1}{2} \right]^{-1} \\ \lambda_{ic} &\approx 10^{12} \gamma_6 T_{*,4}^{-2} R_{*,10}^{-2} d_{0.1}^2 [\ln(\gamma_6 T_{*,4}) + 3.79]^{-1} \text{ cm}. \end{aligned} \quad (64.271)$$

Pairs are confined by the magnetic field in the Klein-Nishina regime if

$$\begin{aligned} B_{KN} &\geq \frac{\pi [\zeta(3)]^2 r_e^2 m_e^2 c^3 \sigma_{SB}}{9 [\zeta(4)]^2 k^2 e} T_*^2 \left(\frac{R_*}{d}\right)^2 \left[\ln \left(\frac{12\zeta(4) k \gamma_e T_*}{\zeta(3) m_e c^2} \right) - \frac{1}{2} \right] \\ B_{KN} &\geq 1.6 \times 10^{-3} T_{*,4}^2 R_{*,10}^2 d_{0.1}^{-2} [\ln(\gamma_6 T_{*,4}) + 3.79] \text{ G}. \end{aligned} \quad (64.272)$$

In addition to this condition, the magnetic field strength should not be too high or pairs will emit mainly synchrotron radiation, *i.e.* photons with energy below threshold for pair production. The cascade is quenched in this case as soon as the first generation of pairs is produced. Electrons

will cool down *via* inverse Compton scattering rather than synchrotron radiation if $\dot{E}_{ic} \geq \dot{E}_{syn}$. In the Thomson limit, this condition gives (see Eqs. 5.9, 7.27)

$$\frac{4}{3}\sigma_T c \gamma_e^2 \epsilon_0 n_* \geq \frac{4}{3}\sigma_T c \gamma_e^2 \left(\frac{B^2}{8\pi}\right), \quad (64.273)$$

or

$$B_T \leq \left(\frac{8\pi\sigma_{SB}}{c}\right)^{1/2} T_*^2 \left(\frac{R_*}{d}\right)$$

$$B_T \leq 163 T_{*,4}^2 R_{*,10} d_{0.1}^{-1} \text{ G}. \quad (64.274)$$

In the Klein-Nishina regime, using the approximate formula in Eq. (5.10) for the Compton cooling (for a mono-energetic star), we have

$$B_{KN} \leq \left(\frac{\pi [\zeta(3)]^2 m_e^2 c^3 \sigma_{SB}}{4 [\zeta(4)]^2 k^2}\right)^{1/2} \gamma_e^{-1} T_* \left(\frac{R_*}{d}\right) \left[\ln\left(\frac{12\zeta(4) k \gamma_e T_*}{\zeta(3) m_e c^2}\right) - \frac{11}{6}\right]^{1/2}$$

$$B_{KN} \leq 4.7 \gamma_6^{-1} T_{*,4} R_{*,10} d_{0.1}^{-1} [\ln(\gamma_6 T_{*,4}) + 2.46]^{1/2} \text{ G}. \quad (64.275)$$

The combination of these constraints gives the domain where 3D isotropic cascade exists. Fig. 73 shows the domain where the 3D cascade is isotropic as a function the ambient magnetic field and the energy of pairs, in LS 5039 and in LS I +61°303 at periastron. These maps show that 3D isotropic pair cascade can be initiated in the TeV energy band for plausible magnetic field. At $E_e = 1$ TeV, the magnetic field is constrained between $\sim 10^{-2}$ -1 G for LS 5039 and $\sim 10^{-3}$ - 10^{-1} G in LS I +61°303.

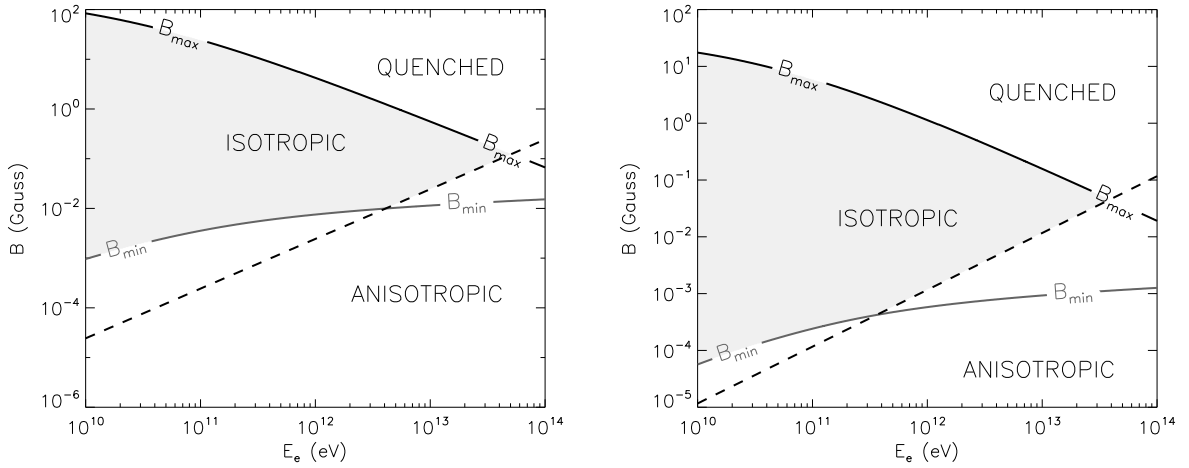


FIG. 73. Three-dimensional "isotropic" pair cascade (grey domain) is initiated if the magnetic field is strong enough to confine locally pairs $B > B_{min}$ or the cascade would be "anisotropic", but it should not exceed $B < B_{max}$ or pairs will emit mainly synchrotron radiation and the cascade would be "quenched". Pairs remain in the system if the magnetic field is above the dashed line. *Left:* LS 5039, *right:* LS I +61°303, at periastron for both systems.

2. The first generation of pairs in binaries

Contrary to 1D cascade, there is not a simple way to compute 3D pair cascade emission because no equation can be explicitly formulated to describe the dynamics of the full cascade. It is

however possible to treat this problem if the cascade is decomposed into discrete generations of pairs and gamma rays. I present in this section, a semi-analytical model to compute the first generation of pairs produced in the 3D isotropic cascade. We will show in the next section that the first generation catches the main features of the full 3D cascade.

§ 65. Spectrum and energy of pairs

We have shown in Chapter 6 that the density of pairs produced by a gamma-ray photon of energy ϵ_1 at a distance r from the source is (see Eq. 57.252)

$$\frac{dN_e}{drdE_e} = 2g_{\gamma\gamma} e^{-\tau_{\gamma\gamma}(r)}. \quad (65.276)$$

If the primary gamma rays are injected with a density $dN_{ph}^{(0)}/dtd\epsilon_1 d\Omega_{ph}$ in the direction given by the spherical angles θ and ϕ as defined in Fig. 74, the number of electrons produced per unit of time t , energy E_e and volume \mathcal{V} at a distance r from the source is

$$\boxed{\frac{dN_e^{(1)}}{dtdE_e d\mathcal{V}} = 2 \int_{\epsilon_1} \frac{1}{r^2} \frac{dN_{ph}^{(0)}}{dtd\epsilon_1 d\Omega_{ph}} g_{\gamma\gamma} e^{-\tau_{\gamma\gamma}(r)} d\epsilon_1}, \quad (65.277)$$

where $d\mathcal{V} = r^2 \sin\theta drd\theta d\phi$. The massive star is assumed point-like and mono-energetic here.

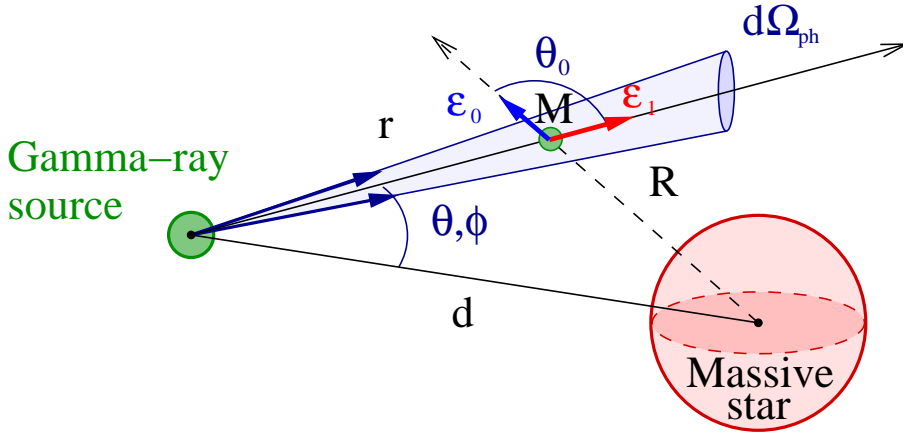


FIG. 74. Primary gamma rays injected at $r \equiv 0$ in the direction (θ, ϕ) produce pairs at r from the source and R from the massive star center.

Fig. 75 gives the numerically computed density of pairs produced (before cooling) in LS 5039 as a function of the angle θ at various distances r . The source injects gamma rays with a -2 power energy distribution in all directions. The spectrum of pairs has a strong angular dependence as depicted in Chapter 6. In a given direction, the mean energy of electrons increases with the separation to the gamma-ray source. As pairs escape the system, the angle between the stellar photons and the gamma rays θ_0 decreases and the threshold energy for pair production shifts to higher energies. Fig. 76 shows the mean energy of the first generation of pairs in the cascade.

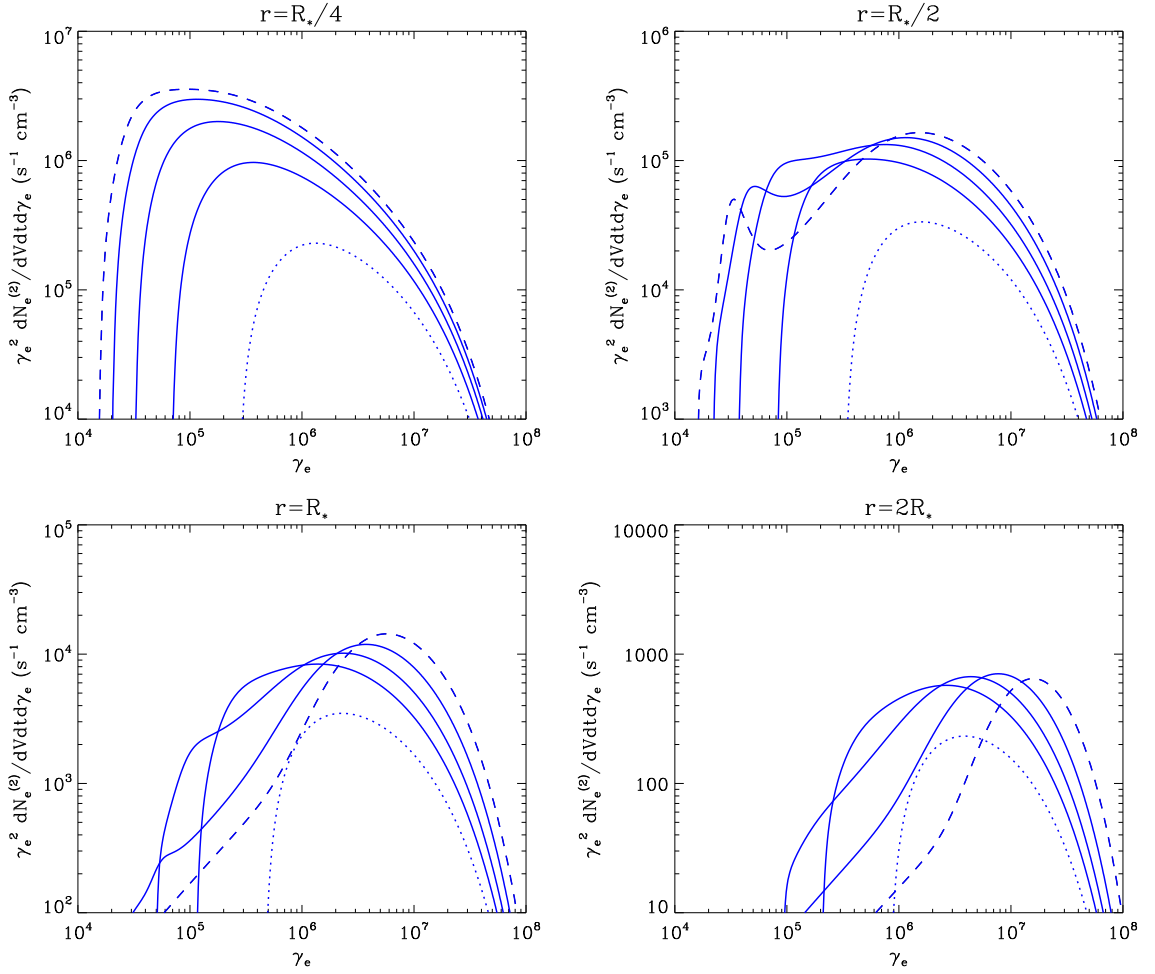


FIG. 75. Density of pairs produced by the annihilation of the primary gamma rays (injected at $r \equiv 0$ with a -2 power law energy distribution) with stellar photons at $r = R_*/4$ (top left), $R_*/2$, R_* and $2R_*$ (bottom right) in LS 5039. In each panel, the spectrum of pairs is computed for $\theta = 30^\circ$ (top, dashed line), 60° , 90° , 120° and 150° (bottom, dotted line).

§ 66. Absorption and spatial distribution of pairs

We propose here to compute the spatial distribution of secondary pairs in LS 5039 and LS I +61°303. Let's consider an isotropic and mono-energetic source of gamma-ray photons of energy ϵ_1 . The number of pairs produced per unit of time and volume is given by (see Eq. 57.253)

$$\frac{dN_e^{(1)}}{dt dV}(r, \theta) \propto \frac{1}{r^2} \left(\frac{d\tau_{\gamma\gamma}}{dr} \right) e^{-\tau_{\gamma\gamma}(r, \theta)}. \quad (66.278)$$

The integrated density of pairs created along the length path l up to the distance r is

$$\begin{aligned} \frac{dN_e^{(1)}}{dt d\Omega}(r, \theta) &\propto \int_0^r l^2 \frac{1}{l^2} \left(\frac{d\tau_{\gamma\gamma}}{dl} \right) e^{-\tau_{\gamma\gamma}(l, \theta)} dl \\ &\propto 1 - e^{-\tau_{\gamma\gamma}(r, \theta)}. \end{aligned} \quad (66.279)$$

Figs. 77-79 represent the gamma-ray opacity and spatial distribution of electrons injected in LS 5039 and LS I +61°303 at periastron. These maps are rotationally symmetric about the line

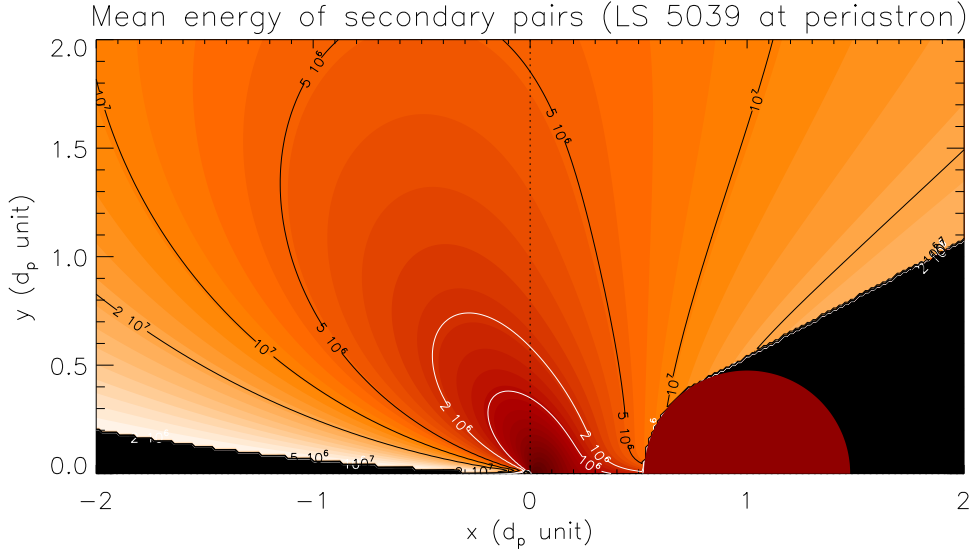


Fig. 76. This map gives the mean Lorentz factor of the pairs at their creation in LS 5039 at superior conjunction. The primary source is a -2 power law with a high energy cut-off at 100 TeV. The star (red disk) is assumed mono-energetic and point-like but the eclipse is taken into account (black region behind the star with respect to the source).

joining the companion star to the source. The massive star has a finite size for this calculation. The extension of this cloud of secondary pairs is significant compared with the binary separation d and depends on the gamma-ray energy ϵ_1 . Close to the minimum threshold energy, pairs are produced in a compact region around the source. For higher energies, the extension of the cloud of electrons increases because the cross section for pair production decreases beyond threshold. It is important to note at this stage that many pairs with very-high energy ($E_e \gtrsim 100$ GeV, see Fig. 76) are created at the outer edge of the system ($r \gtrsim d$). The radiation emitted by these particles will suffer less from absorption and will contribute to increase the transparency of the primary source, particularly at orbital phases where pair production is strong along the line of sight. The next generations of particles in the cascade would increase even more the extension of this cloud of pairs and would contribute even more to increase the escaping gamma-ray flux. We discuss about the role of the next generations below in Sect. 4.

3. The first generation of gamma rays in binaries

§ 67. Geometry

The primary gamma-ray source is assumed located at the compact object location. The photons propagating in the (θ, ϕ) direction create pairs at a distance r (Fig. 80). The angle between the massive star, the secondary electrons location and the observer ψ_{obs} can be defined as the product $\cos \psi_{obs} = -\mathbf{e}_* \cdot \mathbf{e}_{obs}$. Defining

$$\mathbf{e}_* = \begin{pmatrix} \sin(\psi_r - \theta) \cos \phi \\ \sin(\psi_r - \theta) \sin \phi \\ -\cos(\psi_r - \theta) \end{pmatrix} \quad \mathbf{e}_{obs} = \begin{pmatrix} \sin \psi \\ 0 \\ \cos \psi \end{pmatrix}, \quad (67.280)$$

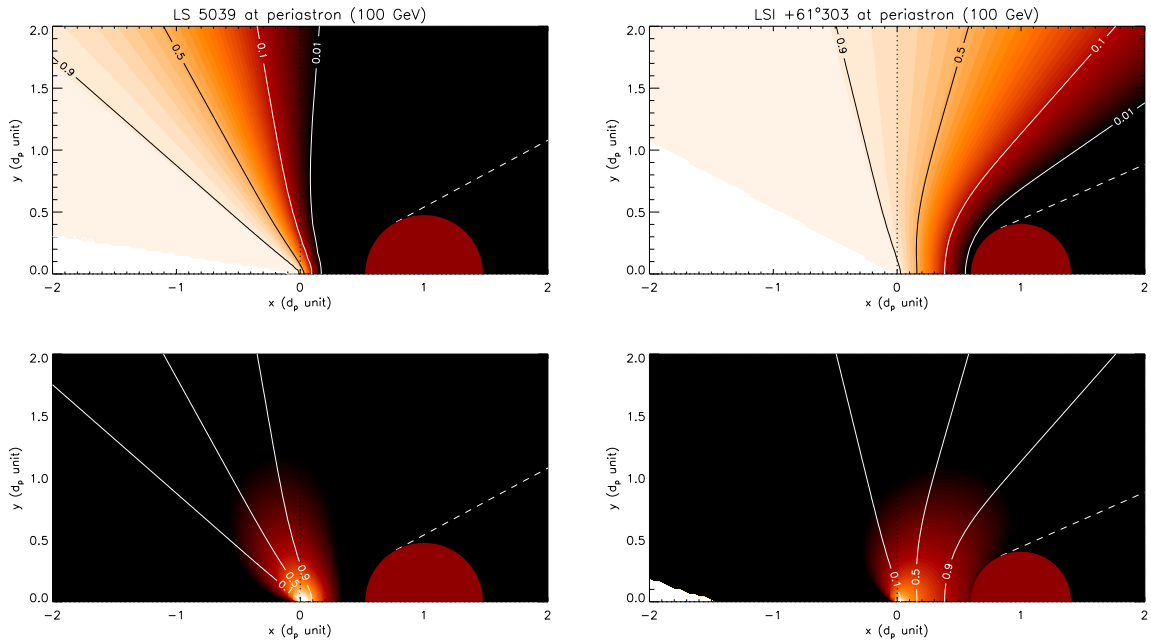


FIG. 77. *Top panels:* This map shows the fraction of the gamma-ray flux left after pair production $e^{-\tau_{\gamma\gamma}(r,\theta)}$. Bright regions are transparent and black regions are opaque. *Bottom panels:* Density of secondary pairs given by Eq. (66.278). The white lines give the fraction of the absorbed primary gamma-ray flux. In both maps, the primary source injects photons of energy $\epsilon_1 = 100$ GeV at the compact object location ($r \equiv 0$) in LS 5039 (*left panels*) and LSI +61°303 (*right panels*), at periastron for both systems. The eclipsed region by the massive star (red semi disk) is delimited by a white dashed line. Distances are normalized to the orbital separation d .

we have

$$\cos \psi_{obs} = -\cos \theta_0 = -\mathbf{e}_* \cdot \mathbf{e}_{obs} = \cos \psi \cos(\psi_r - \theta) - \sin \psi \sin(\psi_r - \theta) \cos \phi. \quad (67.281)$$

This angle is the viewing angle of the secondary source of radiation. Note that the position of the observer with respect to the system breaks the rotational symmetry about the line joining both stars. There is a ϕ -dependence in the expression of ψ_{obs} .

Even though we assume that the massive star is point-like for the computation of radiative processes in the following, it is important to take into account the effect of eclipses. Otherwise we overestimate the density of pairs and gamma rays produced by the cascade. The first zone to exclude is the cone behind the massive star with respect to the source (see Fig. 81). No pairs are produced (for the first generation only) if $\theta \leq \alpha_* = \arcsin(R_*/d)$ and if l is greater than

$$l_{max}(\theta) = d \left[\cos \theta - (\sin^2 \alpha_* - \sin^2 \theta)^{1/2} \right], \quad (67.282)$$

the gamma rays will hit the star surface in this case. The second volume to exclude is the cylinder of radius R_* behind the massive star with respect to the observer (see Fig. 81).

§ 68. Equations for the first generation of gamma rays in the cascade

The fresh electrons produced by the absorption of the primary gamma rays cool down *via* synchrotron radiation and inverse Compton scattering. We assume that pairs stay enough time at their site of creation to radiate before they escape (*i.e.* radiative timescales $t_{rad} \ll t_{esc}$, the

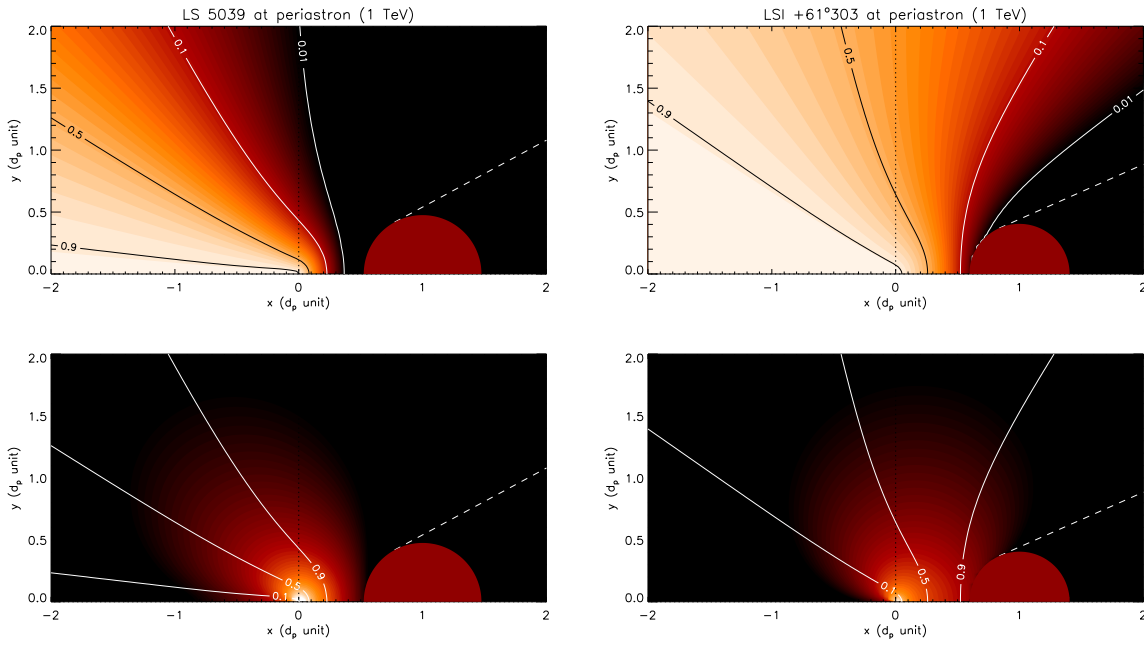


FIG. 78. Same as Fig. 77 with $\epsilon_1 = 1$ TeV.

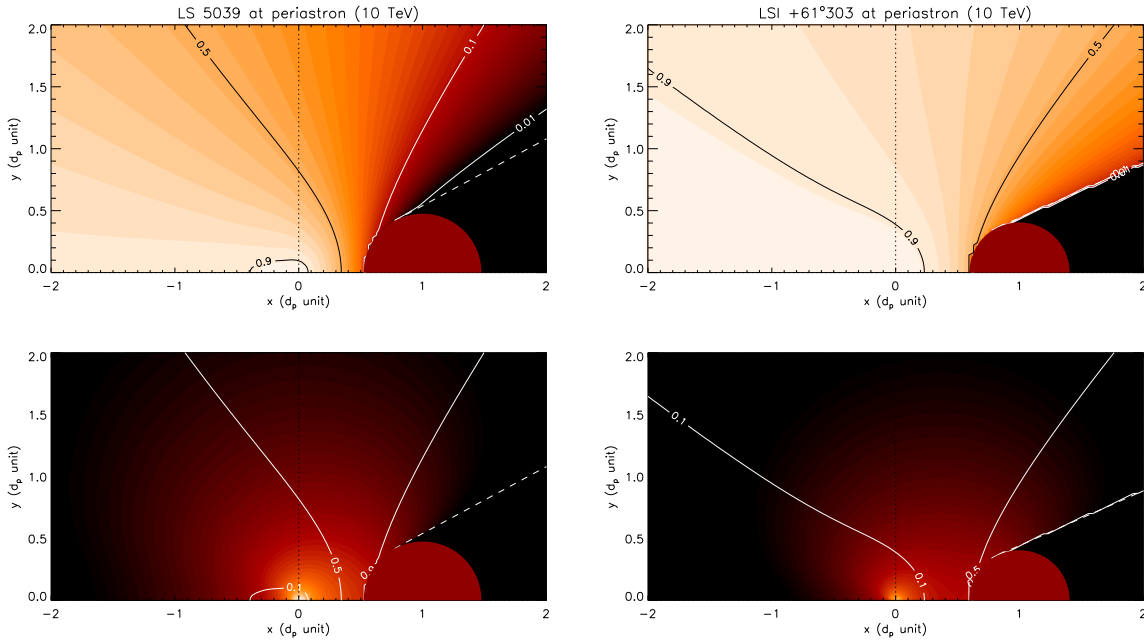


FIG. 79. Same as Fig. 77 with $\epsilon_1 = 10$ TeV.

escaping timescale). The advection of particles by the massive star wind is ignored as the Compton cooling timescale t_{ic} is much shorter than the typical advection time t_{ad} in LS 5039 for the very-high energy pairs we are interested in (see Bosch-Ramon *et al.* 2008a where this effect has been considered). Indeed, with a terminal velocity $v_\infty \approx 2400 \text{ km s}^{-1}$ (McSwain

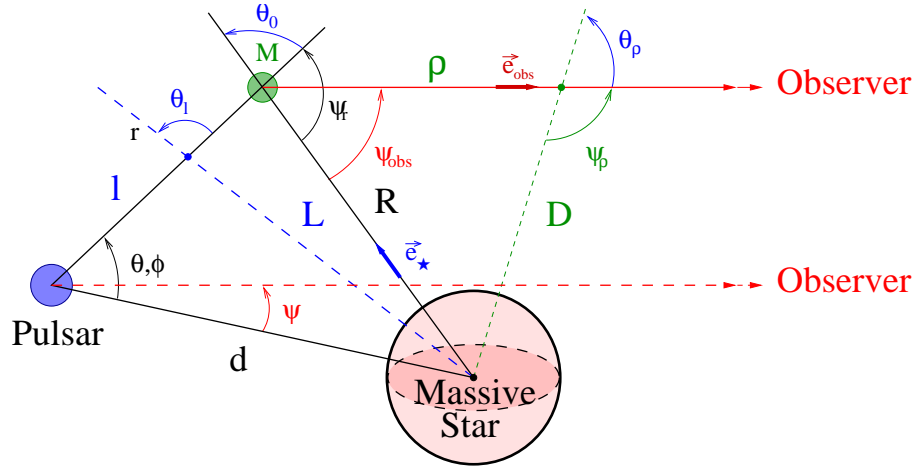


FIG. 80. The binary system is seen by a distant observer with a viewing angle ψ . Secondary pairs are secondary sources of gamma rays seen at an angle ψ_{obs} .

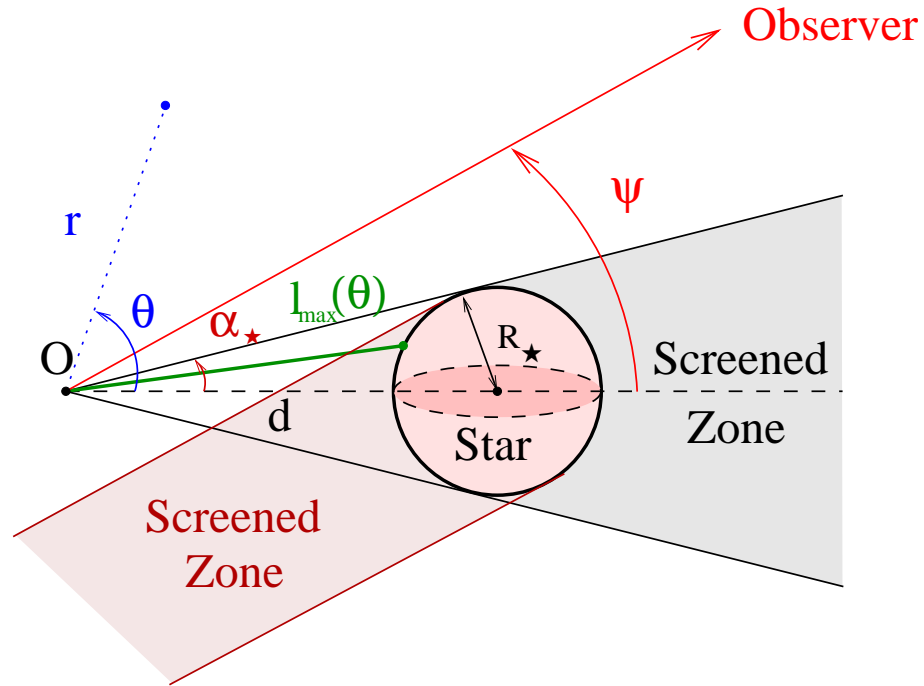


FIG. 81. The massive star excludes part of the volume to the primary gamma-ray source (grey area) and to the observer (red area).

et al. 2004) the massive star wind in LS 5039 advects electrons outside the system in about $t_{ad} = d/v_{\infty} \approx 6 \times 10^3 \text{ s} \gg t_{ic} \approx 20 \text{ s}$ for a 1 TeV electron.

Assuming that $t_{esc} \gg t_{ic}, t_{syn}$ and that pairs are isotropized, the steady state cooled distribution of secondary pairs is given by (see Eq. 13.69)

$$\frac{dN_e^{(1)}}{dE_e dV d\Omega_e} = \frac{1}{|\dot{E}_{ic} + \dot{E}_{syn}|} \int_{E_e}^{+\infty} \frac{1}{4\pi} \frac{dN_e^{(1)}}{dt dE'_e dV} dE'_e \quad (68.283)$$

where $dN_e^{(1)}/dt dE'_e dV$ is obtained with Eq. (65.277) and \dot{E}_{ic} and \dot{E}_{syn} given by Eqs. (5.8), (7.27). Note that we are using the continuous losses approximation for inverse Compton scattering, even in the Klein-Nishina regime. As I have shown in the previous chapter (see Chapter 7, Sect. 8), this is a good approximation particularly because the energy distribution of gamma rays considered here are broad (power law). The inverse Compton emission produced in the volume dV is

$$\frac{dN_{ic}^{(1)}}{dt d\epsilon_1 d\Omega_e dV} = \int_{E_e} \frac{dN_e^{(1)}}{dE_e dV d\Omega_e} n_* \frac{dN}{dt d\epsilon_1} e^{-\tau_{\gamma\gamma}} dE_e, \quad (68.284)$$

where $dN/dt d\epsilon_1$ is the anisotropic Compton kernel (see Eq. 25.135) and

$$\tau_{\gamma\gamma} = \int_0^{+\infty} \left(\frac{d\tau_{\gamma\gamma}}{d\rho} \right) d\rho \quad (68.285)$$

is the gamma-ray opacity from the secondary source location to the observer (see Fig. 80). The total escaping inverse Compton spectrum is then

$$\boxed{\frac{dN_{ic}^{(1)}}{dt d\epsilon_1 d\Omega_e} = \int_0^{2\pi} \int_0^\pi \int_0^{+\infty} \int_{E_e} \frac{dN_e^{(1)}}{dE_e dV d\Omega_e} n_* \frac{dN}{dt d\epsilon_1} e^{-\tau_{\gamma\gamma}} r^2 \sin\theta dE_e dr d\theta d\phi}. \quad (68.286)$$

In practice, secondary pairs do not contribute significantly to the total gamma-ray flux for r greater than 5 times the orbital separation. In the mono-energetic and point-like star approximation, the angle between stellar photons and the secondary electrons is $\theta_0 = \pi - \psi_{obs}$. Similarly to inverse Compton scattering, the synchrotron emissivity is

$$\boxed{\frac{dN_{syn}^{(1)}}{dt d\epsilon_1 d\Omega_e} = \iint \frac{dN_e^{(1)}}{dE_e dV d\Omega_e} \frac{dN_{syn}}{dt d\epsilon_1} dE_e dV}, \quad (68.287)$$

where $dN_{syn}/dt d\epsilon_1$ is the synchrotron kernel (see Eq. 7.22) averaged over an isotropic distribution of pitch angle to the magnetic field. Note that there is no absorption term $e^{-\tau_{\gamma\gamma}}$ in this equation because synchrotron radiation is emitted below the threshold energy for pair production here.

The annihilation of pairs and triplet pair production are ignored. In addition, self interactions between particles in the cascade are neglected (see the discussion in Chapter 7, Sect. 2).

§ 69. Anisotropic effects

The 3D cascade emission shares identical spectral feature with the 1D cascade (see Sect. 4 in Chapter 7). Fig. 82 gives the computed spectrum emitted by secondary pairs given by Eq. (68.286) in LS 5039 at periastron for different viewing angle ψ . The primary source is isotropic and injects a -2 power law energy distribution for gamma rays. The full complexity arising from anisotropic effects are considered (see § 67), but synchrotron radiation is ignored for now.

As for 1D cascade, the escaping spectrum can be decomposed into three zones. Below the minimum energy for pair production, gamma rays accumulates in a hard ~ -1.5 (photon index) power law tail where pairs cool down in the Thomson limit. Above threshold, the spectrum presents a dip where emission and absorption compete. At very-high energy ($\epsilon_1 \gtrsim 10$ TeV), the cascade emission decreases due to the decline of the inverse Compton and the pair production cross sections.

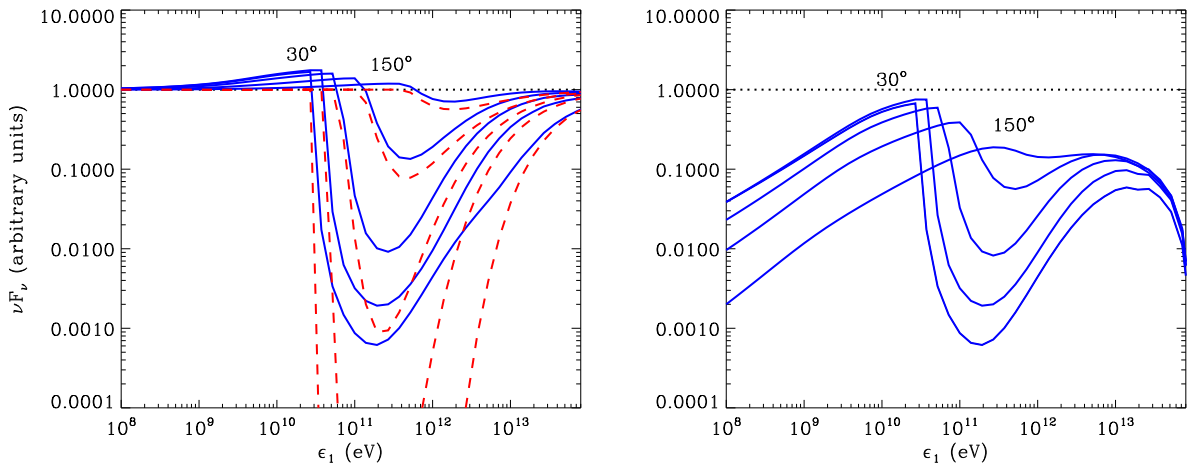


FIG. 82. *Left panel:* Escaping radiation spectrum (blue line) for $\psi = 30^\circ, 60^\circ, 90^\circ, 120^\circ$ and 150° . The primary source is point-like, isotropic and injects gamma rays with a -2 power law energy distribution between 100 MeV and 100 TeV at the location of the compact object in LS 5039 (dotted line). The radiation from the pure absorbed spectrum (red dashed line) is shown for comparison. The emission from secondary pairs only is shown in the *right panel*.

Contrary to 1D cascade, the angular dependence of the very-high energy emission in the 3D cascade is identical to the primary absorbed flux (see Fig. 83). The TeV flux is minimum at superior conjunction and maximum at inferior conjunction. The 3D cascade suffers more from absorption for small viewing angle than in the 1D cascade limit since pairs do not propagate. For higher viewing angles $\psi \gtrsim 90^\circ$, more flux is produced in the 3D cascade because the observed flux is emitted by pairs produced in other directions (particularly where $\theta < 90^\circ$, see Fig. 80). This effect has been called by Bednarek (1997) the "focusing of gamma rays by the soft radiation of a massive star". 3D cascade does not change the shape of the lightcurve and decreases the amplitude of the modulation since the cascade flux dominates slightly close to superior conjunction. This work is in agreement with similar results obtained by Bednarek (2006).

This first result indicates that 3D cascade could explain the shape and the amplitude of the modulation in LS 5039, but one generation seems insufficient to explain the flux at superior conjunction. The contribution from extra-generations is investigated below in Sect. 4.

§ 70. Spatial distribution in LS 5039

Fig. 84 gives the spatial distribution of the very-high energy radiation flux produced by the first generation of gamma rays in the cascade at both conjunctions (assuming an orbit inclined at $i = 60^\circ$). As shown in the previous section, more gamma rays escape at inferior conjunction than at superior conjunction. Also, and contrary to the distribution of pairs, the spatial distribution of photons received by the observer is not rotationally symmetric because of the ϕ -dependence in the angle of interaction between electrons and stellar photons (Eq. 67.281). Eclipsed regions are delimited by white dashed lines. At inferior conjunction, no gamma rays are produced along the line joining the star to the observer because the collision between the stellar photon and the

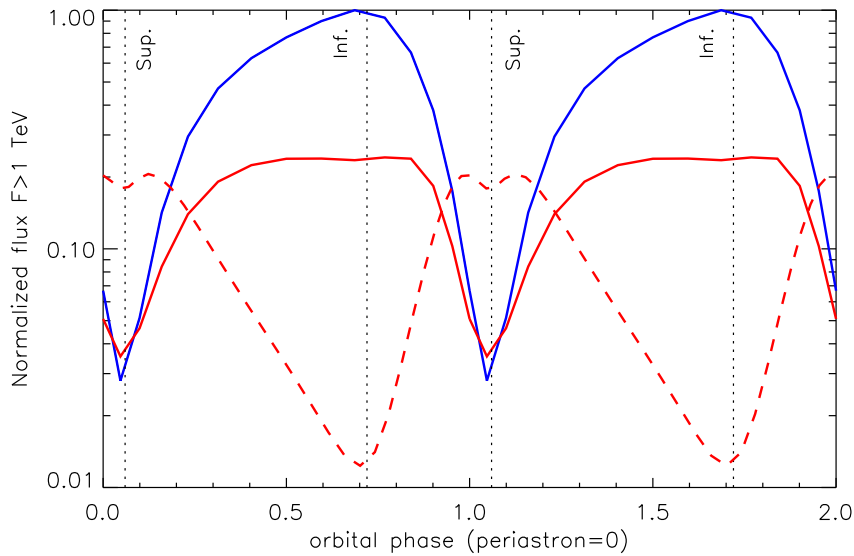


Fig. 83. TeV orbital modulation of 3D pair cascade emission in LS 5039 (red line) as a function of the orbital phase (two full orbits shown here), and comparison with the primary absorbed flux (blue line) and the full 1D cascade flux (red dashed line). The injection of primary gamma rays is isotropic and constant along the orbit. Both conjunctions are shown with vertical dashed lines (with the orbital parameters found by Casares *et al.* 2005b).

electrons is rear-end ($\theta_0 = 0^\circ$). This feature is particularly visible here because the massive star is assumed point-like for the computation of radiative processes.

4. Beyond the first generation approximation

We investigate in this section the role of the next generations of pairs on the total escaping gamma-ray flux in binaries.

§ 71. Semi-analytical approach

In principle, the semi-analytical method presented in the previous section can be extended to an arbitrary number of generations. It is possible to write formally a recursive relation between the generation n and the generation $n - 1$. For this, the new density of gamma rays found in Eq. (68.284) should be injected in Eq. (65.277) to compute the next generation of pairs which radiate inverse Compton and synchrotron radiation following Eqs. (68.286), (68.287), and so on. However, the computing time of this method increases very quickly with the number of generation considered. Although correct, this method cannot be used in practice to compute the full cascade radiation. I could explore only the second generation of pairs. Beyond, the computing time was unreasonably long on a simple desk computer.

The computation of the second generation of gamma rays still reveals interesting information. First, the angular dependence of the gamma-ray emission is similar to the first generation but dampened (see Fig. 85, *left* panel). Also, the second generation contributes more than the first generation to the total escaping very high-energy gamma-ray flux, interestingly for small viewing angle *i.e.* where the primary flux is highly absorbed (see Fig. 85, *right* panel).

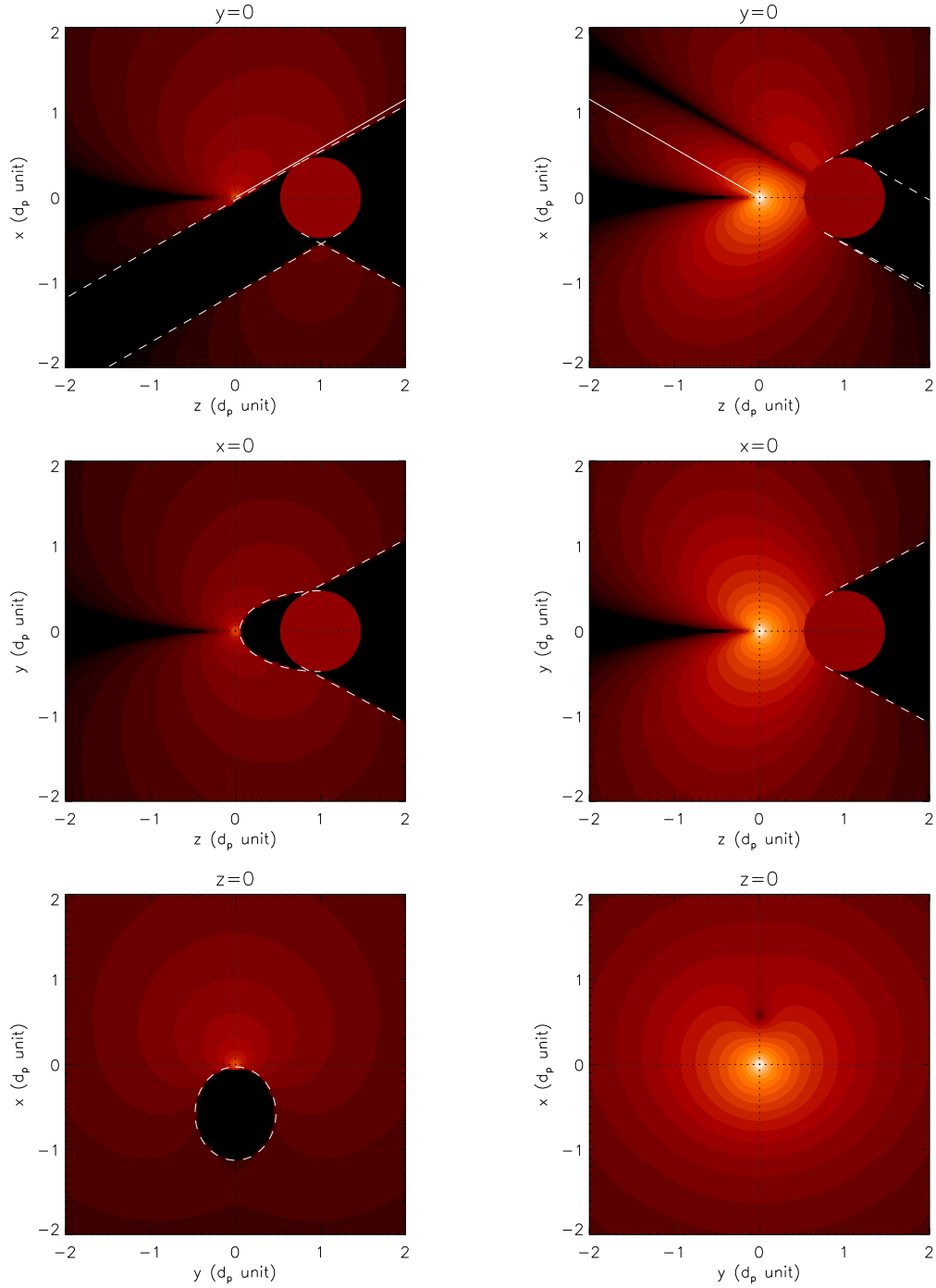


FIG. 84. Spatial distribution and intensity of the very high-energy (> 100 GeV) radiation produced by the first generation of pairs in the 3D cascade in LS 5039 as observed by a distant observer (whose direction is indicated by a white solid line, *top panels*). Distances are normalized to the orbital separation d . The system is viewed at superior (*left*) and inferior conjunctions (*right*). Each map is a slice of the 3D cloud of gamma rays in the three orthogonal planes: front view (plane containing the observer and both stars, *top panels*), top view (*middle*) and right view (*bottom*). The primary source lies at the origin. The eclipsed regions by the massive star (red disk) are delimited by white dashed lines. The injection of the primary gamma rays is the same as in Fig. 82.

Consequently, the lightcurve shape in Fig. 83 remains unchanged and more flux is expected at orbital phases where absorption is high. This calculation seems to indicate that the cascade may be composed of more than 2 generations of particles.

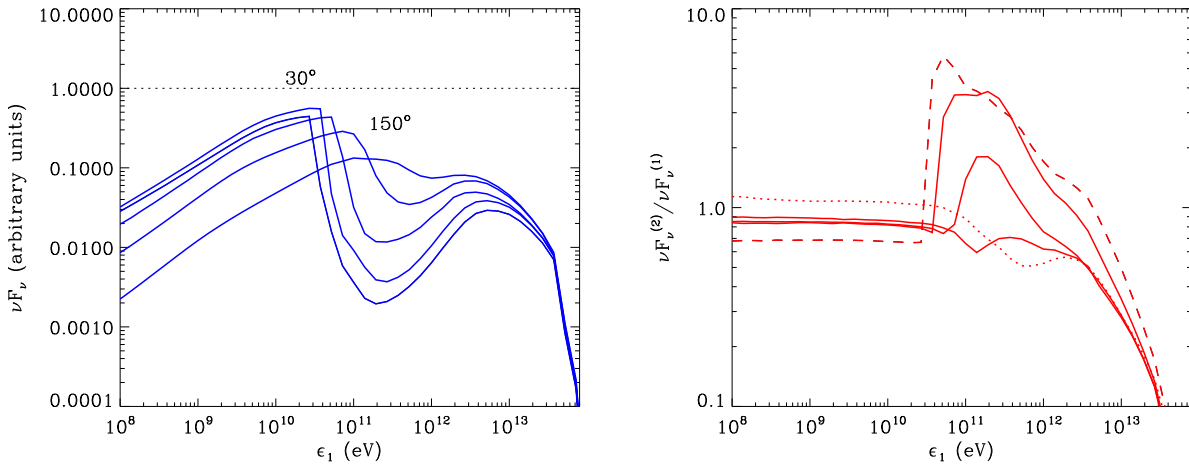


Fig. 85. *Left panel:* The same as in Fig. 82 (*right panel*) for the second generation of pairs in the cascade only. *Right panel:* ratio of the second generation to the first generation gamma-ray flux in the cascade as a function of energy.

§ 72. The Monte Carlo approach

In order to explore the contribution from extra-generations in the cascade (> 2), the best way is to use Monte Carlo techniques. This computation method is best suited for complex radiative transfer problems. I have not developed during my PhD thesis this kind of Monte Carlo code, but we decided to initiate a collaboration with Julien Malzac at the CESR in Toulouse to benefit from his expertise on Monte Carlo techniques. Julien adapted his code to the computation of 3D pair cascade in the microquasar Cygnus X–1 for a similar issue than in LS 5039 here (Zdziarski *et al.* 2009), *i.e.* the computation of pair cascading close to superior conjunction. For the present study, he added in his code synchrotron radiation from pairs in the cascade.

We first compared the Monte Carlo and the semi-analytical methods for the first generation of pairs. We found very similar results (see Fig. 86). Note that there are some slight differences where absorption is high due to statistical and binning effects in the Monte Carlo code. In addition, we have noticed that the spectrum given by the Monte Carlo code is slightly softer compared with the semi-analytical spectrum at very high-energy. This difference might be due to the differences in the treatment of particle cooling in the Klein-Nishina regime. In fact, the Monte Carlo code takes into account the effects of catastrophic Compton losses in the Klein-Nishina regime.

Extra-generations are of major importance for the total gamma-ray emission in LS 5039 at every orbital phases. In fact, the radiation from extra-generations adds a constant offset to the escaping TeV lightcurve (see Figs. 86, 87).

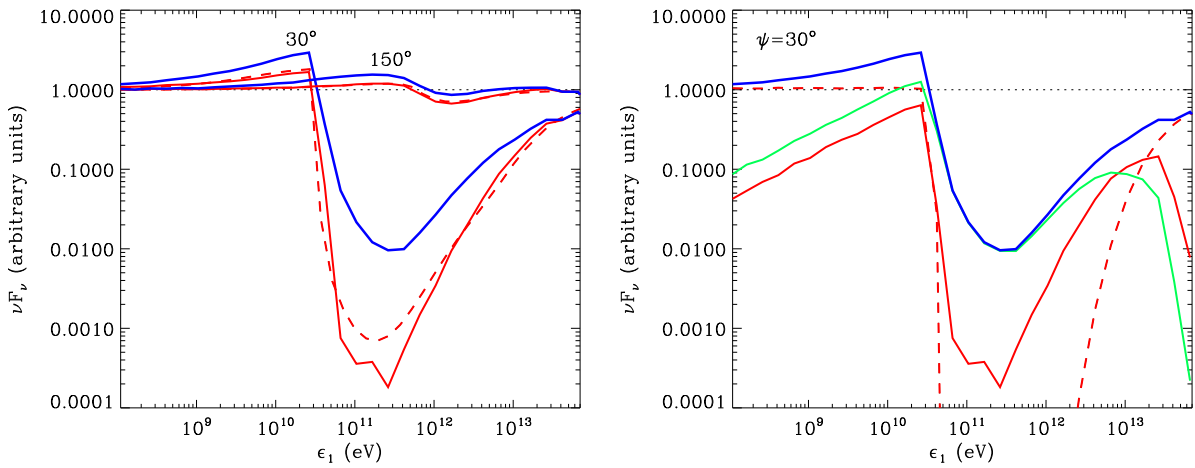


FIG. 86. *Left panel:* Full cascade emission computed with the Monte Carlo code (blue solid line) in LS 5039 for $\psi = 30^\circ$ and 150° . Comparison between the semi-analytical (red dashed line) and the Monte Carlo (red solid line) results for the first generation of gamma rays only. The primary source is shown with a dotted line. *Right panel:* This plot shows the relative contribution from the primary absorbed flux (red dashed line), the first generation (red solid line) and from extra-generations (*i.e.* > 1 , green line) to the total escaping gamma-ray flux (blue line) in LS 5039 for $\psi = 30^\circ$. The right panel uses only results from the Monte Carlo code. Synchrotron radiation is ignored.

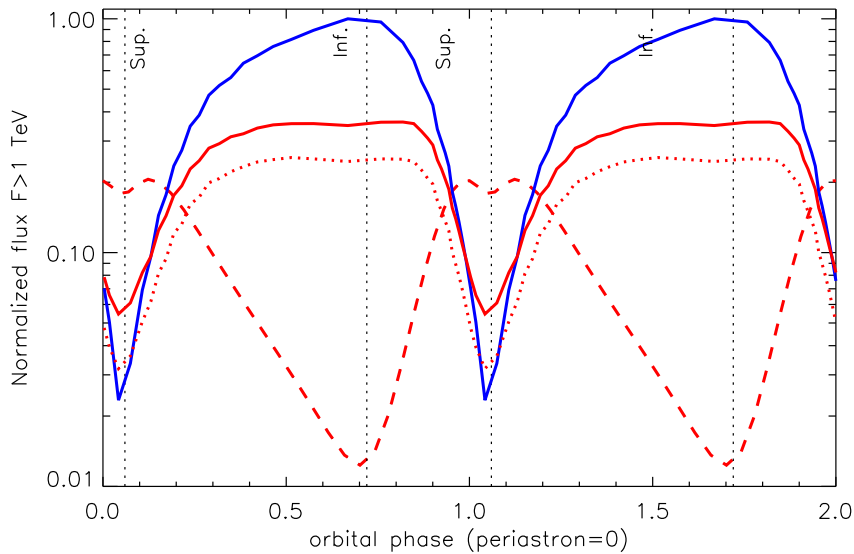


FIG. 87. The same as in Fig. 83 where the 3D cascade radiation is computed with the Monte Carlo approach for all the generations (red solid line). The radiation from the first generation (Monte Carlo result) is plotted as well for comparison (red dotted line).

§ 73. The effect of the magnetic field

The magnetic field strength has a major impact on the development of pair cascading as discussed in the first section in this chapter. If the magnetic field is too strong, pairs will emit

mainly synchrotron radiation whose energy is below the threshold for pair production. The absorbed energy is then fully radiated at low energy, *i.e.* in the X-ray and soft gamma-ray bands. The cascade is quenched. We propose here to quantify more precisely this effect on the full cascade emission.

The first effect is the decrease of the very-high energy gamma-ray flux in the cascade. An energy cut-off appears where the synchrotron cooling timescale becomes shorter than the inverse Compton cooling timescale ($t_{syn} < t_{ic}$). As the synchrotron cooling timescale depends on $1/B$ (see Chapter 2, Eq. 7.28), this energy cut-off shifts to lower energies with increasing magnetic field (see Fig. 88, *left* panel). Meanwhile, the synchrotron flux increases below threshold. If the magnetic field is too strong, the number of generations in the cascade is also affected. For $B \lesssim 5$ G, many generations contribute to the total gamma-ray flux. For $B \gtrsim 5$ G, the emission from the first generation of electrons only is sufficient to describe the full cascade radiation (see Fig. 88, *right* panel). In this case, the pairs will not have enough time to produce new high-energy photons for the next generation.

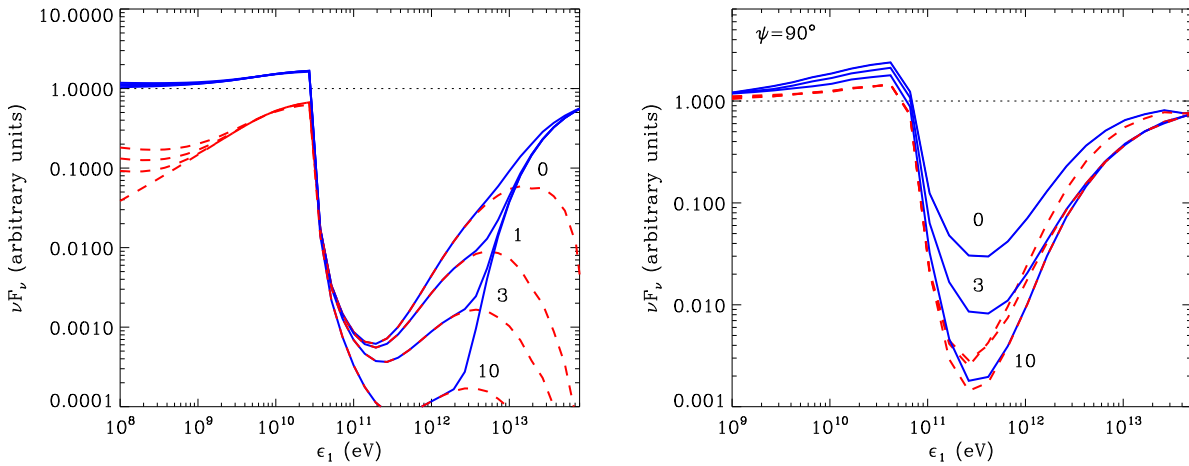


FIG. 88. *Left* panel: Effect of the ambient magnetic field on the cascade radiation (first generation). The cascade is computed with the same parameters (semi-analytical approach) as used in Fig. 82 for $\psi = 30^\circ$ with an uniform magnetic field $B = 0$ (top) , 1, 3, and 10 G (bottom). The cascade radiation (dashed red line) is compared with the injected (dotted line) and the full escaping gamma-ray spectra (blue solid line). *Right* panel: Effect of the magnetic field on the contribution from extra-generations in the cascade for $B = 0$, 3, and 10 G and $\psi = 90^\circ$. The full escaping gamma-ray spectrum (Monte Carlo approach) with all generation (solid blue line) is compared with the one-generation cascade approximation (red dashed line).

5. 3D pair cascade emission in LS 5039

We would like now to investigate whether 3D cascade explains both the amplitude and the shape of the TeV orbital modulation observed by HESS in LS 5039 (Aharonian *et al.* 2006). We assume that the primary source of gamma rays is emitted by a population of isotropic electrons and positrons located in a compact region considered here as point-like, *i.e.* as in Chapter 4.

§ 74. Modulation and spectra

The full 3D cascade emission is calculated with the Monte Carlo code along the orbit, considering the finite size and the black-body spectrum of the companion star. The primary source is located at the compact object location. Fig. 89 gives the very-high energy gamma-ray flux in LS 5039 as a function of the orbital phase ϕ for an inclination of the orbit $i = 60^\circ$ and 40° . Theoretical fluxes are averaged over a constant orbital phase interval of width $\Delta\phi = 0.1$ in order to compare with the HESS binned lightcurve.

With 3D pair cascading, the theoretical peaks and dips expected in the lightcurve remain at the same orbital phase than for the primary absorbed flux. The flux is minimum at superior conjunction ($\phi \approx 0.06$) and is maximum close to inferior conjunction ($\phi \approx 0.85$). The cascade emission dominates over the primary absorbed flux for $0.0 \lesssim \phi \lesssim 0.2$. The amplitude and the shape of the TeV modulation is consistent with observations only if $i = 40 \pm 5^\circ$. Taking a mass function $f = 2.61 \times 10^{-3} M_\odot$ (Casares *et al.* 2005b; Aragona *et al.* 2009) and $M_\star = 23 M_\odot$ for the companion star, the compact object mass should be $M_{co} = 1.8 \pm 0.3 M_\odot$. The compact object could still be a pulsar.

The GeV lightcurve is unchanged with pair cascading and remains anticorrelated with the TeV lightcurve due to pair production. For illustrative purposes, I computed the gamma-ray emission map as seen by a distant observer, *i.e.* projected on the sky, as a function of the orbital phase (Fig. 91). The GeV-TeV anticorrelation appears clearly in these maps. The gamma-ray spectral energy distribution is not significantly changed by the 3D pair cascade (Fig. 90). Still, the cascade produces a slight spectral hardening below threshold ($\epsilon_1 \lesssim 30$ GeV). In addition, the cascade contributes more in the TeV band than at GeV energies. HESS and *Fermi* fluxes cannot be both reproduced with this model. If the model fits HESS observations, the GeV flux is underestimated. The GeV component could have a different origin as discussed in Chapter 5, Sect. 8.

§ 75. The location of the TeV source

The amplitude of the TeV orbital modulation can be reduced also if the primary source of gamma rays does not lie at the compact object position. If particles radiate further away in the system, gamma rays will suffer less from absorption and more flux could escape the system close to superior conjunction.

One possibility would be to imagine that gamma rays are produced at larger distances in the orbital plane, for instance in the pulsar wind collimated by the massive star wind. We consider the simple case where the source is point-like and located at a distance d backward the compact object in the star-compact object direction (Fig. 92). For an inclination $i = 60^\circ$, a consistent amplitude of the TeV modulation is found if d' is greater than about 3 times the orbital separation but then the shape is incorrectly reproduced (see Fig. 93). The main peak shifts towards superior conjunction and the dip between $0 < \phi < 0.4$ is filled because the source suffers less from gamma-ray absorption. Electrons should remain close to the compact object if they are in the orbital plane.

Another possibility would be to imagine that particles radiate above the orbital plane, for instance in a jet. For illustrative purpose, the source of gamma rays is assumed point-like and

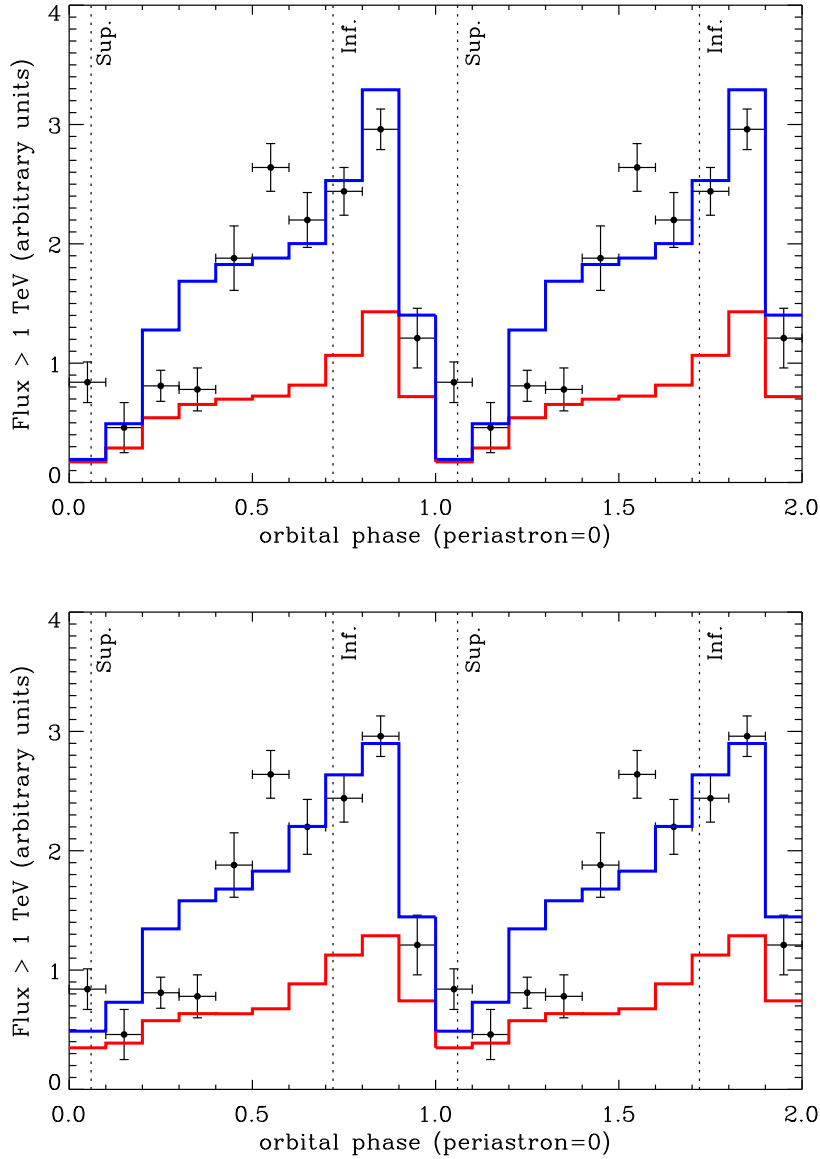


FIG. 89. Theoretical TeV lightcurve in LS 5039 (two full orbits, blue solid line) for $i = 60^\circ$ (top panel) and $i = 40^\circ$ (bottom panel), where 3D pair cascade radiation is computed with the Monte Carlo code for a finite-size and black-body companion star. The contribution from the cascade only (red solid line) and HESS data points are shown for comparison. Lightcurves are averaged in phase interval of width $\Delta\phi = 0.1$. The orbital parameters are taken from Casares *et al.* (2005b). Conjunctions are indicated by dotted lines.

located at an altitude h above and perpendicular to the orbital plane (Fig. 92). In this case, electrons are seen at an angle $\psi' = \pi/2 + \psi - \alpha$ with $\alpha = \arcsin \left[d / (d^2 + h^2)^{1/2} \right]$. If pairs are radiating at $h \gtrsim R_*$ for $i = 60^\circ$, the amplitude of the TeV modulation is correctly reproduced but not the shape of the lightcurve for similar reasons as the previous possibility (Fig. 93).

We find that particles emitting TeV radiation should be close to the compact object location or the TeV lightcurve modulation is not explained.

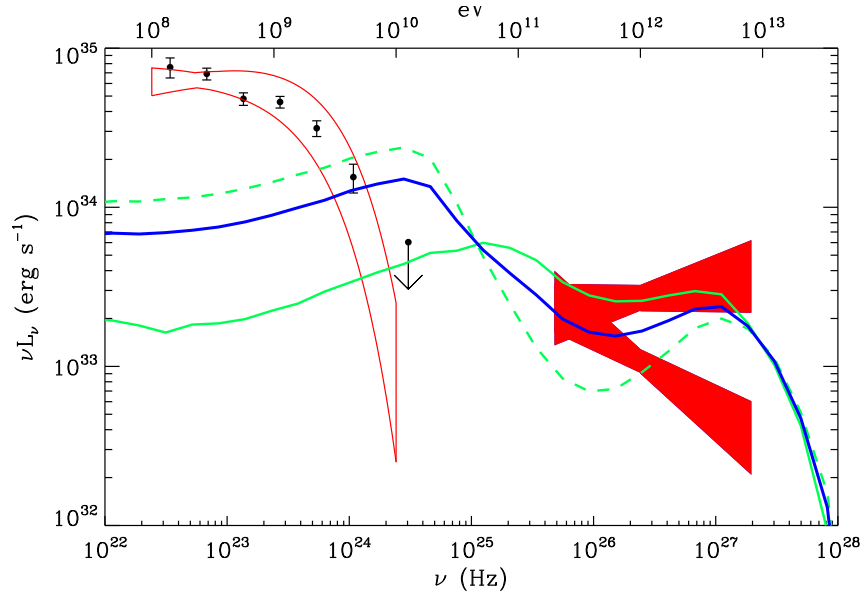


FIG. 90. Theoretical gamma-ray spectra in LS 5039 with $i = 40^\circ$. Spectra are averaged over the "SUPC" ($0.45 < \phi < 0.9$, green dashed line) and "INFC" ($\phi < 0.45$ or $\phi > 0.9$, green solid line) states as defined in Aharonian *et al.* (2006), and over the whole orbit (blue line). *Fermi* (data points and red contours) and HESS (red bowties) measurements are overlotted. The full 3D pair cascade emission is included (Monte Carlo calculations). The ambient magnetic field is chosen small $B < 1$ G.

§ 76. The ambient magnetic field in LS 5039

As discussed in § 73, the ambient magnetic field has a critical influence on the emitted spectrum in the cascade. First, the very high-energy flux is depleted due to the dominant synchrotron cooling. Second, synchrotron radiation from pairs in the cascade contributes in the X-ray and soft gamma-ray energy band (Fig. 94). The magnetic field cannot be too strong or the synchrotron emission from secondary pairs in the cascade would exceed the observed X-ray flux. The recent *Suzaku* measurements in the 2-10 keV band (Takahashi *et al.* 2009) constrains the magnetic field below 10 G in LS 5039 (see Fig. 94). For this calculation I computed the radiation from secondary pairs only since for high magnetic field ($B \gtrsim 5$ G), most of the cascade radiation is emitted by the first generation (see § 73).

6. What we have learned

We found that three-dimensional pair cascade emission increases significantly the very-high energy flux particularly where the primary photons are highly absorbed. If the ambient magnetic field is strong enough to confine and isotropize pairs where they are created, the computation of the cascade emission becomes much more simple. However, the magnetic field should not be too intense or the synchrotron cooling in the cascade would be too strong and the cascade quenched.

I developed a semi-analytical method to compute the radiation in the 3D cascade in which all the anisotropic effects are considered. In this approach, the cascade is decomposed into discrete generations of particles. An arbitrary number of generations can be in principle considered in the calculations, but in practice only the first generation can be computed in a

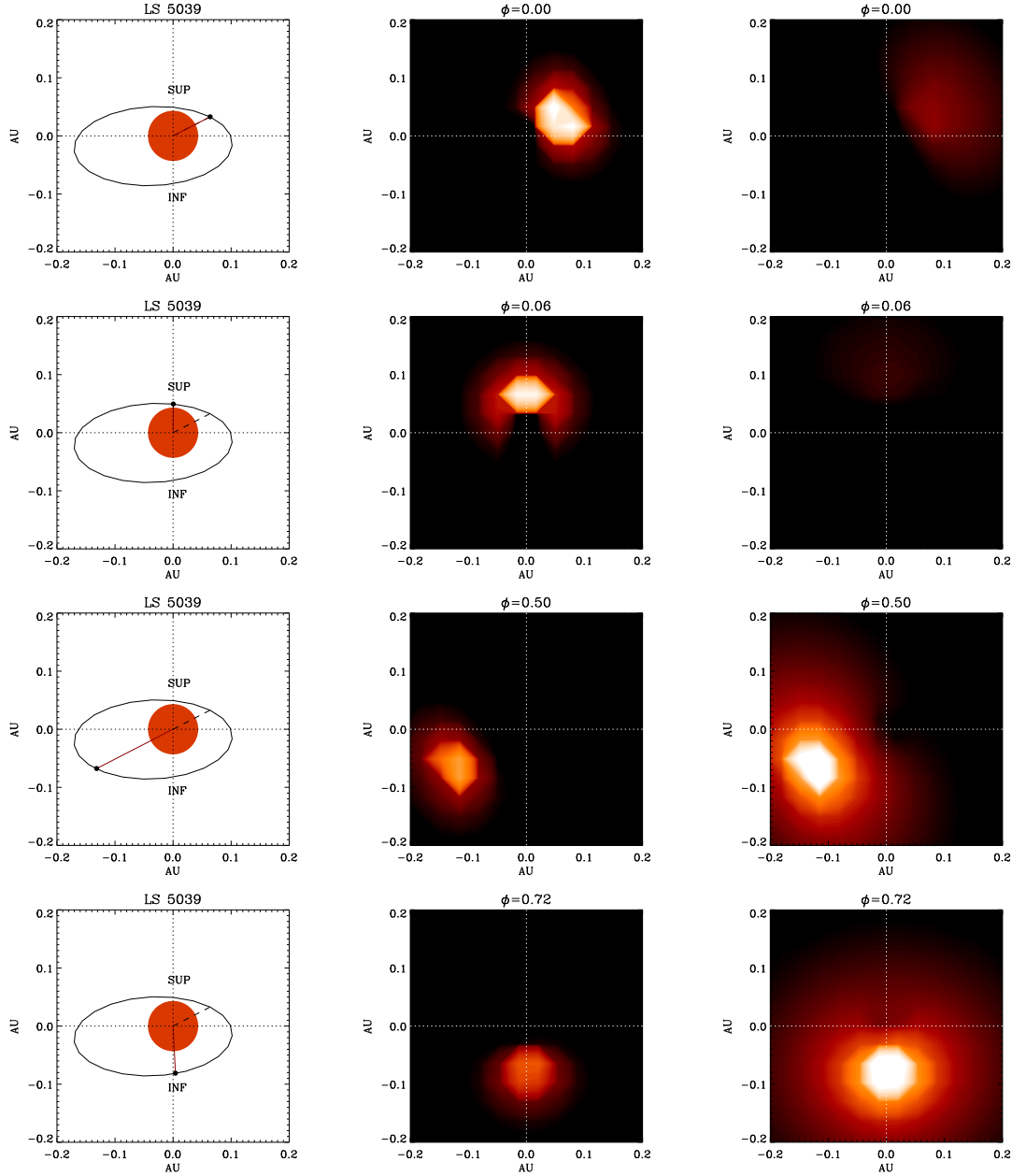


FIG. 91. Spatial distribution of the gamma-ray flux in LS 5039 at periastron (*top* panels), superior conjunction, apastron and inferior conjunction (*bottom* panels). These maps show the cascade gamma-ray emission in the high-energy (flux > 1 GeV, *middle* panels) and very-high energy bands (flux > 100 GeV, *right* panels) from the first generation only. These calculations were performed with the semi-analytical method. Each maps are centered to the massive star center. The orbit seen with an inclination $i = 60^\circ$ is shown on the left panel. The position of the compact object in the orbit is indicated by red solid line and a black dot.

reasonable amount of time. Nonetheless, we have shown that the first generation of particles in the cascade catches the main features of the full 3D cascade emission.

The Monte Carlo code developed by Julien Malzac gives compatible results with the semi-analytical approach for the first generation of particles in the cascade, and is best suited for the computation of the full cascade *i.e.* with all the generations. The radiation from extra-

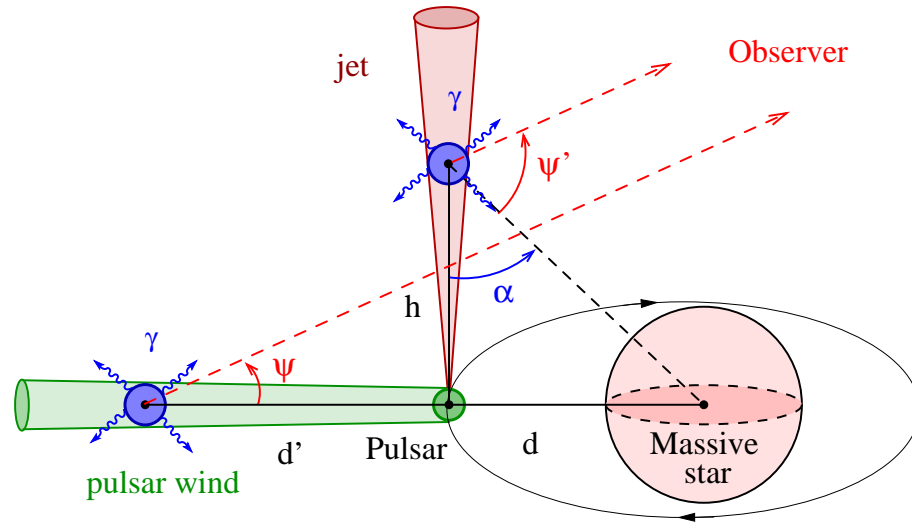


FIG. 92. The gamma-ray source may not coincide with the compact object location (green circle) but could be localized further away at a distance d' from the massive star center in the orbital plane (blue circle in the "pulsar wind"), or above the orbital plane at an altitude h (blue circle in the "jet").

generations (> 1) dominates over the first generation at orbital phases in binaries where the flux is almost fully absorbed. It is therefore of major importance to consider all the generations in our modeling.

The cascade emission in LS 5039 is significant at every orbital phases and dominates over the primary absorbed source close to superior conjunction. 3D and 1D cascade lightcurves are anti-correlated. In addition, 3D cascade contributes less than 1D cascade close to superior conjunction and provides a lower limit to the flux expected from a cascade at these phases. We found that the amplitude and the shape of the TeV modulation can be accurately reproduced if the system is inclined at $i \approx 40^\circ$ and if the primary source of gamma rays lies close to the compact object location. We found also that the ambient magnetic field should not exceed ~ 10 G, or the synchrotron radiation from the pairs in the cascade would overestimate the observed X-ray flux. This is a reasonable constraint since most O stars are thought to be non-magnetic (see the recent review by Donati & Landstreet 2009, and references therein).

This work have been accepted recently in the *Astronomy & Astrophysics* journal (Cerutti *et al.* 2010c) and is fully provided below. Early results shown in this chapter have also been presented in two contributed talks, at the "High energy phenomena in massive stars meeting 2009" (see the proceeding Cerutti *et al.* 2010a) and at the "French Society of Astronomy and Astrophysics meeting 2009" (see the proceeding Cerutti *et al.* 2009c).

7. [Français] Résumé du chapitre

§ 77. Contexte et objectifs

Une cascade de paires 3D peut se développer dans les binaires si le champ magnétique ambiant est suffisamment fort pour dévier les paires produites dans la cascade. Dans le cas général, ce problème est très compliqué puisque les paires sont sensibles à la structure des lignes de champ magnétique dans le système. Si les paires sont confinées et isotropisées par le champ

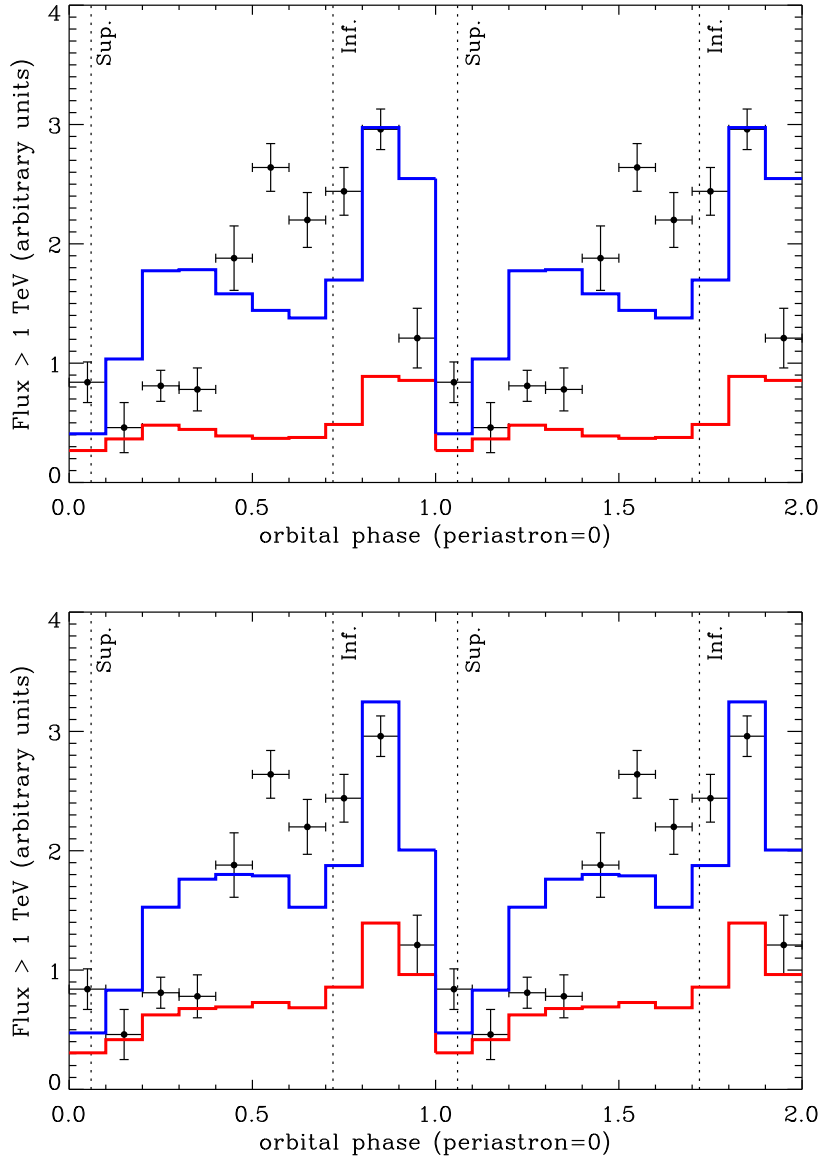


Fig. 93. Same as in Fig. 89 for $i = 60^\circ$, where the TeV primary source is located in the orbital plane with $d' = 3d$ (top panel) or above and perpendicular to the orbital plane at an altitude $h = R_*$ (bottom panel).

magnétique dès leur création, la modélisation de la cascade 3D devient bien plus simple. Chaque point du système binaire peut alors être considéré comme une source secondaire stationnaire de rayonnement dans toutes les directions. J'appellerai ici ce type de cascade 3D "isotrope" (parce que les paires sont supposées être isotropisées une fois créées, même si leur émission est anisotrope). Les paires se refroidissent par diffusion Compton inverse et par synchrotron. Dans ce chapitre, je calcule la contribution d'une cascade 3D isotrope dans les binaires en utilisant une nouvelle méthode semi-analytique. En particulier, j'aimerais voir si cette cascade 3D pourrait expliquer l'amplitude de la modulation TeV observée par HESS dans LS 5039 (Aharonian *et al.* 2006), précisément où la cascade 1D échoue. Pour mener à bien cette étude, j'ai initié une collaboration avec Julien Malzac pour bénéficier de son expertise sur les méthodes de calcul de

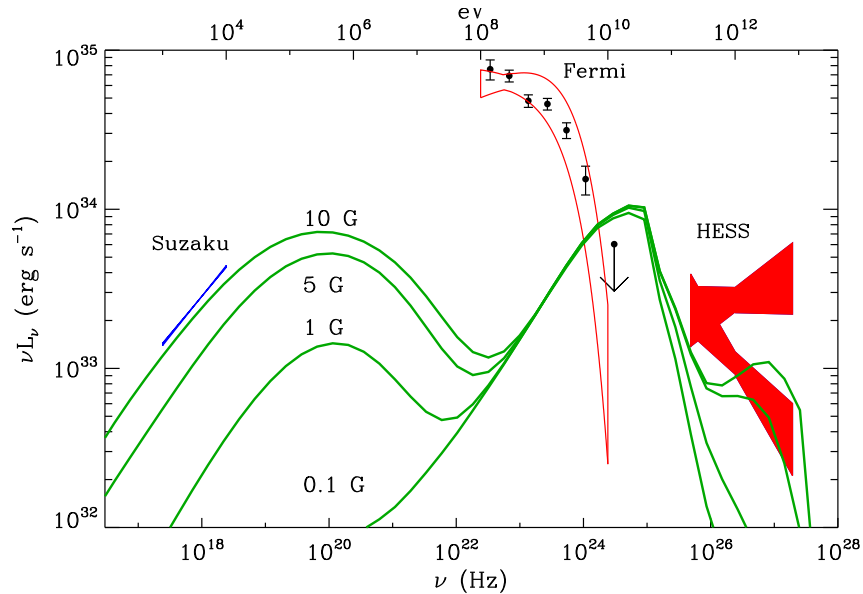


FIG. 94. Theoretical spectrum of the cascade radiation (first generation) averaged over the orbit with a uniform ambient magnetic field $B = 0.1, 1, 5$ and 10 G. Suzaku (Takahashi *et al.* 2009), *Fermi* (Abdo *et al.* 2009b) and HESS (Aharonian *et al.* 2006) observations are shown for comparison.

type Monte Carlo. Cette méthode est puissante et bien adaptée aux problèmes de diffusions multiples comme ici.

§ 78. Ce que nous avons appris

Nous avons trouvé que l'émission d'une cascade 3D de paires augmente substantiellement le flux gamma de très haute énergie en particulier où les photons primaires sont très absorbés. Si le champ magnétique ambiant est suffisamment fort pour confiner et isotropiser les paires à l'endroit où elles sont créées, le calcul de la cascade devient alors beaucoup plus simple. Cependant, le champ magnétique ne doit pas être trop intense ou le refroidissement synchrotron dans la cascade serait trop fort et la cascade inhibée.

J'ai développé une méthode semi-analytique pour calculer le rayonnement produit dans la cascade 3D dans laquelle tous les effets d'anisotropie sont pris en compte. Dans cette approche, la cascade est décomposée en générations discrètes de particules. Un nombre arbitraire de génération peut être en principe considéré dans les calculs, mais en pratique seule la première génération peut être calculée en un temps raisonnable. Malgré tout, nous avons montré que la première génération de particules dans la cascade permet de décrire les principales caractéristiques de l'émission totale de la cascade 3D.

Le code Monte Carlo développé par Julien Malzac donne des résultats compatibles avec l'approche semi-analytique pour la première génération de particules dans la cascade, et est bien mieux adaptée au calcul de la cascade totale *i.e.* avec toutes les générations. Le rayonnement émis par les générations supérieures (> 1) est plus important que celui produit par la première génération aux phases orbitales dans les binaires où le flux est presque totalement absorbé. Il est donc primordial de considérer toutes les générations dans notre modélisation de la cascade 3D.

L'émission de la cascade dans LS 5039 est importante à toutes les phases orbitales et domine le flux primaire absorbé autour de la conjonction supérieure. Les courbes de lumière de la cascade 1D et 3D sont anti-corrélées. De plus, la cascade 3D contribue moins que la cascade 1D autour de la conjonction supérieure et donne une limite inférieure au flux attendu d'une cascade à ces phases. Nous avons trouvé que l'amplitude et la forme de la modulation TeV peut être bien reproduite à condition que le système soit incliné à un angle $i \approx 40^\circ$ et si la source primaire de gamma se situe à proximité de l'objet compact. Nous avons trouvé également que le champ magnétique ambiant ne doit pas excéder ~ 10 G, ou le flux synchrotron produit par les paires dans la cascade dépasserait le flux X observé. C'est une contrainte raisonnable car la plupart des étoiles O ne semblent être pour la plupart pas ou peu magnétiques (voir la revue récente par Donati & Landstreet 2009 et les références qui s'y trouvent).

Ce travail a été accepté récemment dans le journal *Astronomy & Astrophysics* (Cerutti *et al.* 2010c), donné intégralement ci-dessous. Quelques résultats préliminaires présentés dans ce chapitre ont été exposés dans deux présentations orales, à la conférence "High energy phenomena in massive stars meeting 2009" (voir le compte rendu Cerutti *et al.* 2010a) et au cours de la réunion générale de la Société Française d'Astronomie et d'Astrophysique en 2009 (voir le compte rendu Cerutti *et al.* 2009c).

8. Paper: Modeling the three-dimensional pair cascade in binaries

Modeling the three-dimensional pair cascade in binaries

Application to LS 5039

B. Cerutti¹, J. Malzac², G. Dubus¹, and G. Henri¹

¹ Laboratoire d'Astrophysique de Grenoble, UMR 5571 CNRS, Université Joseph Fourier, BP 53, 38041 Grenoble, France

² Centre d'Etude Spatiale des Rayonnements, OMP, UPS, CNRS, 9 Avenue du Colonel Roche, BP 44346, 31028 Toulouse Cédex 4, France

Draft June 28, 2010

ABSTRACT

Context. LS 5039 is a Galactic binary system emitting high and very-high energy gamma rays. The gamma-ray flux is modulated on the orbital period and the TeV lightcurve shaped by photon-photon annihilation. The observed very-high energy modulation can be reproduced with a simple leptonic model but fails to explain the flux detected by HESS at superior conjunction, where gamma rays are fully absorbed.

Aims. The contribution from an electron-positron pair cascade could be strong and prevail over the primary flux at superior conjunction. The created pairs can be isotropized by the magnetic field, resulting in a three-dimensional cascade. The aim of this article is to investigate the gamma-ray radiation from this pair cascade in LS 5039. This additional component could account for HESS observations at superior conjunction in the system.

Methods. A semi-analytical and a Monte Carlo method for computing three-dimensional cascade radiation are presented and applied in the context of binaries. The cascade is decomposed into discrete generations of particles where electron-positron pairs are assumed to be confined at their site of creation. Both methods give similar results. The Monte Carlo approach remains best suited to calculation of a multi-generation cascade.

Results. Three-dimensional cascade radiation contributes significantly at every orbital phase in the TeV lightcurve, and dominates close to superior conjunction. The amplitude of the gamma-ray modulation is correctly reproduced for an inclination of the orbit of $\approx 40^\circ$. Primary pairs should be injected close to the compact object location, otherwise the shape of the modulation is not explained. In addition, synchrotron emission from the cascade in X-rays constrains the ambient magnetic field to below 10 G.

Conclusions. The radiation from a three-dimensional pair cascade can account for the TeV flux detected by HESS at superior conjunction in LS 5039, but the very-high energy spectrum at low fluxes remains difficult to explain in this model.

Key words. radiation mechanisms: non-thermal – stars: individual: LS 5039 – gamma rays: theory – X-rays: binaries

1. Introduction

LS 5039 was first identified as a high-mass X-ray binary by Motch et al. (1997). This binary system is composed of a massive O type star and an unknown compact object, possibly a young rotation-powered pulsar (Martocchia et al. 2005; Dubus 2006b). LS 5039 was detected as a very high-energy (> 100 GeV, VHE) gamma-ray source by HESS (Aharonian et al. 2005) modulated on the orbital period (Aharonian et al. 2006). In a leptonic scenario, the gamma-ray emission is produced by inverse Compton scattering of stellar photons on energetic electron-positron pairs injected and accelerated by a rotation-powered pulsar (pulsar wind nebula scenario) or in a relativistic jet powered by accretion on the compact object (microquasar scenario). Most of the VHE modulation is probably caused by absorption of gamma rays in the intense UV stellar radiation field set by the massive star (Böttcher & Dermer 2005; Bednarek 2006; Dubus 2006a).

Pairs produced in the system can upscatter a substantial fraction of the absorbed energy into a new generation of gamma rays and initiate a cascade of pairs. The radiation from the full cascade can significantly increase the transparency of the source, particularly at orbital phases where the gamma-ray opacity is high ($\tau_{\gamma\gamma} \gg 1$). A one-zone leptonic model applied to LS 5039 explains the lightcurve and the spectral features at VHE (Dubus et al. 2008), and yet, this model cannot account for the flux detected by HESS at superior conjunction where gamma rays should be fully absorbed. Pair cascading was mentioned as a possible solution for this disagreement (Aharonian et al. 2006).

The development of a cascade of pairs depends on the ambient magnetic field intensity. If the magnetic deviations on pair trajectories can be neglected, the cascade grows along the line joining the source to the observer. The cascade is one-dimensional. In this case, the cascade contribution is too strong close to superior conjunction in LS 5039. A one-dimensional

2

B. Cerutti et al.: Modeling the three-dimensional pair cascade in binaries. Application to LS 5039

cascade can be ruled out by HESS observations (Cerutti et al. 2009b) (see the model in Sierpowska-Bartosik & Torres 2008 for an alternative solution). If the magnetic field is strong enough to deviate and confine electrons in the system, pairs radiate in all directions and a three-dimensional cascade is initiated (Bednarek 1997). The development of a three-dimensional cascade in LS 5039 is possible and was investigated by Bednarek (2006, 2007) with a Monte Carlo method and by Bosch-Ramon et al. (2008a) with a semi-analytical method.

Bosch-Ramon et al. (2008a) derived the non thermal emission produced by the first generation of pairs in gamma-ray binaries. In their model, the density of secondary pairs is averaged over angles describing the mean behavior of the radiating pairs in the system. Here, we aim to investigate the detailed angular dependence in the gamma-ray emission from pairs in the cascade. In the microquasar scenario, Bednarek (2007) finds consistent flux at superior conjunction in LS 5039 if the emission originates farther along the jet ($> 10 R_*$) whose direction is assumed to be perpendicular to the orbital plane, including the synchrotron losses. The role of three-dimensional cascade is revisited here in the pulsar wind nebula scenario (Maraschi & Treves 1981; Dubus 2006b), where the VHE emitter is close to the compact object location. The aim of this article is to corroborate HESS observations of LS 5039 and to constrain the ambient magnetic field strength in the system, using a semi-analytical and a Monte Carlo computation methods. The Monte Carlo code used in the following was previously applied to the system Cygnus X-1 for similar reasons (Zdziarski et al. 2009).

The paper is divided as follows. Sect. 2 gives the main conditions to initiate a three-dimensional cascade in LS 5039. The semi-analytical approach and the Monte Carlo code for cascading calculations are presented in Sect. 3 and the main features of a three-dimensional pair cascade in binaries are discussed in Sect. 4. Sect. 5 is dedicated to the full calculation of a three-dimensional cascade in LS 5039. The effect of the ambient magnetic field intensity is also investigated in this part. The conclusions of the article are exposed in the last section.

In the following, we use the term “electrons” to refer indifferently to electrons and positrons.

2. The magnetic field for 3D cascade

The development of the cascade is dictated by the intensity of the ambient magnetic field in the binary environment. The main conditions for the existence of a three-dimensional cascades have been investigated by Bednarek (1997) and are reviewed here and applied to LS 5039.

The magnetic field B must be high enough to locally isotropize pairs once created. This condition is fulfilled if the Larmor radius of the pair R_L is shorter than the inverse Compton energy losses length given by $\lambda_{cool} = -\beta_e c \gamma_e / \dot{\gamma}_e$, where $\gamma_e = 1/(1 - \beta_e^2)^{1/2}$ is the Lorentz factor of the electron and $\dot{\gamma}_e \equiv d\gamma_e/dt$ is the Compton energy losses. This provides a lower-limit for the magnetic field. In the Thomson regime, this is given by

$$B_T \gtrsim 2 \times 10^{-6} \gamma_3^2 T_{\star,4}^4 R_{\star,10}^2 d_{0,1}^{-2} \text{ G}, \quad (1)$$

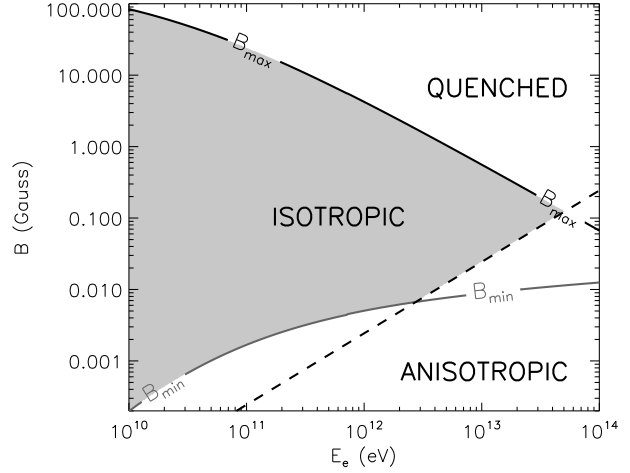


Fig. 1. This map shows the domain (gray surface, ‘ISOTROPIC’) where a three-dimensional isotropic cascade can be initiated as a function of the ambient magnetic field B and the energy of the electron E_e . This calculation is applied to LS 5039 at periastron (orbital separation $d \approx 0.1$ AU). The upper-limit is bounded by the black solid line labeled ‘ B_{max} ’ and the lower-limit by the gray solid line ‘ B_{min} ’. For $B > B_{max}$ (‘QUENCHED’), synchrotron losses dominate and the cascade is inhibited. For $B < B_{min}$ (‘ANISOTROPIC’) the cascade is not locally isotropized and depends on the magnetic field structure. The isotropic domain is truncated at VHE as the pairs escape from the system (below the dashed line).

writing $\gamma_3 = \gamma_e/10^3$, $T_{\star,4} = T_\star/40\,000$ K and $R_{\star,10} = R_\star/10 R_\odot$ the temperature and radius of the companion star, and $d_{0,1} = d/0.1$ AU the orbital separation. Using the approximate formula for Compton energy losses (Blumenthal & Gould 1970), the same condition in the extreme Klein-Nishina regime holds if

$$B_{KN} \gtrsim 1.6 \times 10^{-3} T_{\star,4}^2 R_{\star,10}^2 d_{0,1}^{-2} [\ln(\gamma_6 T_{\star,4}) + 2.46] \text{ G}. \quad (2)$$

If the Larmor radius is compared with the Compton mean free path given by $\lambda_{ic} \sim 1/n_\star \sigma_{ic}$, where n_\star is the stellar photon density and σ_{ic} the Compton cross section, the condition on the magnetic field is more restrictive. In the Thomson regime, the electron loses only a small fraction of its total energy per interaction, hence $\lambda_{cool} > \lambda_{ic}$. In the Klein-Nishina regime, most of the electron energy is lost in a single scattering and $\lambda_{cool} \approx \lambda_{ic}$. Because the cascade occurs mostly in the Klein-Nishina regime in gamma-ray binaries, both conditions lead approximately to the same lower limit for the ambient magnetic field.

In addition to this condition, pairs are assumed to be isotropized at their creation site for simplicity. Pairs will be randomized if the ambient magnetic field is disorganized. Isotropization of pairs in the cascade will also occur due to pitch angle scattering if the magnetic turbulence timescale is smaller than the energy loss timescale (e.g. if it is on the order of the Larmor timescale). For lower magnetic field intensity (‘anisotropic’ domain in Fig. 1), the cascade remains three-

dimensional but then pairs cannot be considered as locally isotropized. In this case, the trajectories of the particles should be properly computed as in *e.g.* Sierpowska & Bednarek 2005. For $B \lesssim 10^{-8}$ G, the cascade is one-dimensional (Cerutti et al. 2009b).

If the magnetic field is too strong, pairs locally isotropize but cool down via synchrotron radiation rather than by inverse Compton scattering. Most of the energy is then emitted in X-rays and soft gamma rays, *i.e.* below the threshold energy for pair production. The cascade is quenched as soon as the first generation of pairs is produced. This condition gives an upper-limit for the magnetic field. Synchrotron losses are smaller than inverse Compton losses $\dot{E}_{syn} < \dot{E}_{ic}$ for

$$B_T \lesssim 163 T_{\star,4}^2 R_{\star,10} d_{0.1}^{-1} \text{ G}, \quad (3)$$

in the Thomson regime and for

$$B_{KN} \lesssim 4.7 \gamma_6^{-1} T_{\star,4} R_{\star,10} d_{0.1}^{-1} [\ln(\gamma_6 T_{\star,4}) + 2.46]^{1/2} \text{ G} \quad (4)$$

in the deep Klein-Nishina regime (Blumenthal & Gould 1970). It can be noticed that the most relevant upper-limit for the magnetic field strength is given by the Thomson formula in Eq. (3), since high-energy particles ($E_e \gtrsim 1$ GeV) with $B_{KN} < B < B_T$ can cool down and get into the cascade domain.

Figure 1 shows the complete domain where a three-dimensional ‘isotropic’ cascade can be initiated in LS 5039, combining the lower and upper-limit for B . This domain encompasses plausible values for the ambient magnetic field in the system. It is worthwhile to note that for very high-energy electrons $E_e \gtrsim 45 d_{0.1} B_{0.1}$ TeV, where $B_{0.1} = B/0.1$ G, the Larmor radius becomes greater than the binary separation in LS 5039 (Fig. 1). In this case, the local magnetic confinement approximation of particles is not appropriate anymore. This is unlikely to happen in LS 5039 if the VHE emission has a leptonic origin since HESS observations shows an energy cut-off for photons at ≈ 10 TeV.

3. Computing methods

Contrary to the one-dimensional case, three-dimensional pair cascading cannot be explicitly computed. Nevertheless, it is possible to decompose the cascade into successive generations of particles. Two different approaches are presented below, one based on semi-analytical calculations and the other on a Monte Carlo code. In both models, the primary source of gamma rays is point-like and coincident with the compact object position as it is depicted in Fig. 2. The origin and the angular dependence of the primary gamma-ray flux are not specified at this stage. These methods are general and could be applied to any other astrophysical context involving 3D pair cascading.

3.1. Semi-analytical

A beam of primary gamma rays propagating in the direction defined by the spherical angles θ and ϕ (see Fig. 2), produces at a distance r to the primary source the first generation of pairs. In the point-like and mono-energetic star approximation, the den-

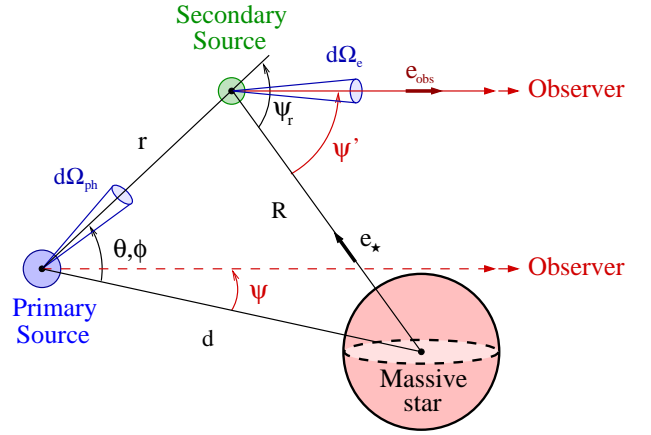


Fig. 2. In this figure is depicted the geometric quantities useful for three-dimensional pair cascading calculation in γ -ray binaries. The primary source is point-like and coincides with the compact object location. The system is viewed at an angle ψ by a distant observer. The absorption of primary gamma rays at the distance r in the (θ, ϕ) direction creates a secondary source of radiation, viewed at an angle ψ' by the observer.

sity of electrons and positrons injected per unit of time, energy and volume ($\text{s}^{-1} \text{erg}^{-1} \text{cm}^{-3}$) is

$$\frac{dN_e^{(1)}}{dt dE_e dV} = 2 \int_{\epsilon_1} \frac{1}{r^2} \frac{dN_{ph}^{(0)}}{dt d\epsilon_1 d\Omega_{ph}} g_{\gamma\gamma} e^{-\tau_{\gamma\gamma}(r)} d\epsilon_1, \quad (5)$$

where $dN_{ph}^{(0)}/dt d\epsilon_1 d\Omega_{ph}$ is the density of primary gamma rays of energy ϵ_1 , $g_{\gamma\gamma}$ the anisotropic pair production kernel (Bonometto & Rees 1971; Böttcher & Schlickeiser 1997; Cerutti et al. 2009b) and $\tau_{\gamma\gamma}(r)$ the $\gamma\gamma$ -opacity integrated from the source to the position r . This new density of pairs is spatially extended and anisotropic but is symmetric with respect to the line joining the star to the primary source. For a fixed stellar radiation field and a given steady source of primary gamma rays, pair production provides a continuous source of fresh electrons injected in the binary system environment.

Pairs are supposed to be immediately confined and isotropized by the local magnetic field at their creation site. The binary vicinity is surrounded by a plasma of isotropic pairs cooling *via* synchrotron radiation and inverse Compton scattering. For simplicity, electrons are assumed to have enough time to radiate before escaping their site of injection and the advection of particles by the massive star wind is ignored although this can have some impact (Bosch-Ramon et al. 2008a). For a 1 TeV electron, the radiative cooling timescales in LS 5039 are $t_{ic} \approx 20$ s (inverse Compton, at the compact object location) and $t_{syn} \approx 400$ s (synchrotron, for $B = 1$ G). The maximum escaping timescale is given by the advection time of pairs by the stellar wind. Taking a wind terminal velocity $v_\infty \approx 2400$ km s^{-1} for the massive star in LS 5039 (McSwain et al. 2004), $t_{esc} = d/v_\infty \approx 6 \times 10^3$ s $\gg t_{ic}$ and t_{syn} . In the case where pairs would escape the system at the speed of light, electrons have just enough time to radiate by inverse Compton scattering ($t_{esc} = d/c \approx 50$ s $\lesssim t_{ic}$). This extreme situation is unlikely

4

B. Cerutti et al.: Modeling the three-dimensional pair cascade in binaries. Application to LS 5039

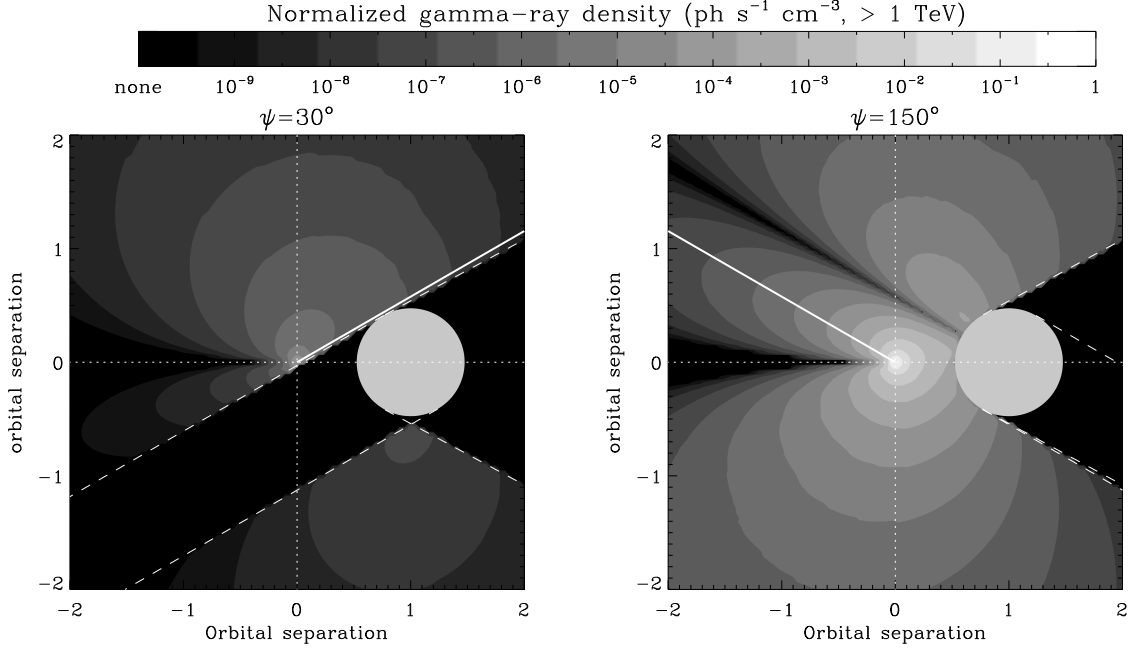


Fig. 3. Spatial distribution of the escaping (*i.e.* including the effect of gamma-ray absorption) VHE photon density ($\text{ph s}^{-1} \text{cm}^{-3}$) emitted by the first generation of electrons (isotropized) in the cascade as observed by a distant observer in LS 5039 at superior (*left*) and inferior (*right*) conjunction. These maps show the gamma-ray density in logarithmic scale (common for both maps), where bright and dark regions correspond respectively to high and low density. Each map is a slice of the 3D gamma-ray emission distribution in the plane that contains the observer (whose direction is indicated by the white solid line) and both stars, computed with the semi-analytical method. The primary source of gamma rays is isotropic and lies at the compact object location (origin). White dashed lines delimit the eclipsed regions (for the primary source and the observer) by the massive star (bright uniform disk). The massive star is assumed point like and mono-energetic in the calculations of radiative processes. Distances are normalized to the orbital separation.

since pairs are confined by the ambient magnetic field but provides a lower limit for the escaping timescale in the system. Assuming that $t_{esc} \gg t_{ic}$ and t_{syn} is a rather good approximation in LS 5039 for the high-energy particles.

The steady-state particle distribution in $\text{erg}^{-1} \text{cm}^{-3} \text{sr}^{-1}$ is (Ginzburg & Syrovatskii 1964)

$$\frac{dN_e^{(1)}}{dE_e d\mathcal{V} d\Omega_e} = \frac{1}{|\dot{E}_e|} \int_{E_e}^{+\infty} \frac{1}{4\pi} \frac{dN_e^{(1)}}{dt dE'_e d\mathcal{V}} dE'_e, \quad (6)$$

with $\dot{E}_e = \dot{E}_{ic} + \dot{E}_{syn}$ the inverse Compton and synchrotron losses and \mathcal{V} the volume encircling the binary. Note that the annihilation of pairs is not considered in this calculation since this effect would be important only for pairs that are almost thermalized. Triplet pair production $\gamma + e^\pm \rightarrow e^\pm + e^+ + e^-$ (see *e.g.* Mastichiadis 1991) is ignored too (see the discussion in Cerutti et al. 2009b, Sect. 2.1).

The total inverse Compton radiation produced by the first generation of pairs observed by a distant observer is given by

$$\frac{dN_{ic}^{(1)}}{dt d\epsilon_1 d\Omega_e} = \iint \frac{dN_e^{(1)}}{dE_e d\mathcal{V} d\Omega_e} n_\star \frac{dN_{ic}}{dt d\epsilon_1} e^{-\tau_{\gamma\gamma}} dE_e d\mathcal{V}, \quad (7)$$

where n_\star is the stellar photon density in cm^{-3} , $dN_{ic}/dt d\epsilon_1$ the anisotropic inverse Compton kernel (Dubus et al. 2008) and $\tau_{\gamma\gamma}$

the absorption from the secondary source up to the observer. Depending on the relative position of the secondary source, the massive star and the observer, inverse Compton emission is anisotropic though pairs are isotropic. The secondary source is seen at an angle ψ' with $\cos \psi' = -\mathbf{e}_\star \cdot \mathbf{e}_{obs}$ (Fig. 2) so that

$$\cos \psi' = \cos \psi \cos(\psi_r - \theta) - \sin \psi \sin(\psi_r - \theta) \cos \phi. \quad (8)$$

In the point-like star approximation, this viewing angle ψ' is related to the interaction angle θ_0 between photons and electrons such as $\cos \psi' = -\cos \theta_0$. Similarly to inverse Compton scattering, the total synchrotron radiation produced by the first generation of pairs is

$$\frac{dN_{syn}^{(1)}}{dt d\epsilon_1 d\Omega_e} = \iint \frac{dN_e^{(1)}}{dE_e d\mathcal{V} d\Omega_e} \frac{dN_{syn}}{dt d\epsilon_1} dE_e d\mathcal{V}, \quad (9)$$

with $dN_{syn}/dt d\epsilon_1$ the synchrotron kernel averaged over an isotropic distribution of pitch angles to the magnetic field (see *e.g.* Blumenthal & Gould 1970).

This semi-analytical method can be extended to an arbitrary number of generations. By replacing the primary density of gamma rays in Eq. (5) by the new density of created photons Eqs. (7)-(9), the second generation of pairs and gamma-rays in the cascade can be computed, and so on for the next generations.

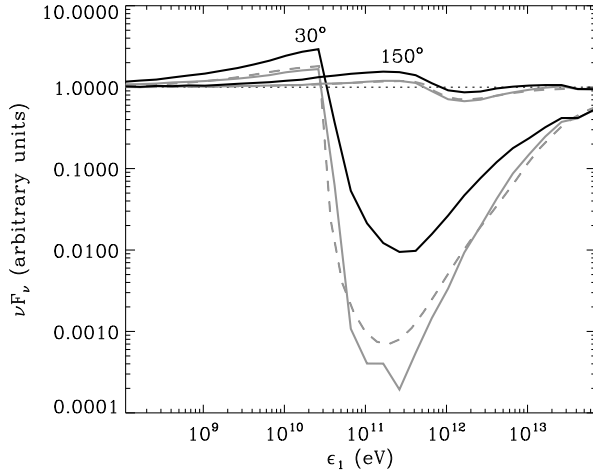


Fig. 4. The full cascade radiation (all generations) computed with the Monte Carlo code (black solid lines) and the primary injected gamma-ray source (isotropic, dotted line) are shown for $\psi = 30^\circ$ and 150° . The Monte Carlo output (solid gray lines) is compared with the semi-analytical calculations (dashed gray lines) in the one-generation cascade approximation. There is no magnetic field but pairs are still assumed to be confined and isotropized. The massive star is point like and mono-energetic.

3.2. Monte Carlo

We also used a Monte-Carlo code to simulate the development of the full electromagnetic pair cascade in the radiation field of the star. In this calculation the path and successive interactions of photons and leptons are tracked until they escape the system (in practice until they reach a distance about 10 times the binary separation). This code was previously used by Zdziarski et al. (2009) to model the TeV emission of Cygnus X-1. It is similar in scope and capabilities to the code of Bednarek (1997). The present code was developed completely independently, and most of the random number generation techniques used for computing photon path and simulating the interactions are very different from those used by Bednarek. Perhaps the most important difference is that the Compton interactions are simulated without any approximation, even in the deep Klein-Nishina regime. Also, in order to reduce the computing time required to achieve high accuracy at high energies, we use a weighting technique which avoids following every particle of the cascade down to low energies. The results of both codes were compared and found compatible (Zdziarski et al. 2009).

4. Three-dimensional pair cascade radiation

For illustrative purpose only, the primary source of gamma rays is assumed isotropic in this section. This assumption allows a better appreciation of the intrinsic anisotropic effects of the pair cascade emission in binaries. Primary gamma rays are injected with a -2 (photon index) power-law spectrum at the location of the compact object. For simplicity, the massive star is assumed

here point-like and mono-energetic. More realistic assumptions (injection of isotropic electrons, black body and finite size companion star) are considered for the calculation of the 3D cascade emission in LS 5039 in the next Section (Sect. 5).

4.1. Spatial distribution of gamma rays in the cascade

Figure 3 shows the spatial distribution of the first generation of escaping TeV gamma rays seen by a distant observer (*i.e.* including the effect of gamma-ray absorption) produced by the cascade in LS 5039 at both conjunctions (for an inclination of the orbit $i = 60^\circ$). These maps are computed with the semi-analytical approach. The massive star is assumed point-like for the computation of radiative processes but eclipses are considered. No pairs can be created behind the star with respect to the primary source of gamma rays. Also, gamma rays produced behind the star with respect to the observer are excluded from the overall cascade radiation (see black regions in Fig. 3). Synchrotron radiation is neglected in this part: pairs radiate only *via* inverse Compton scattering.

The spatial distribution of gamma rays is extended and is not rotationally symmetric about the line joining the two stars (contrary to pairs) since the observed inverse Compton emission depends on the peculiar orientation of the observer with respect to the binary system. No gamma rays are emitted along the line joining the star to the observer direction (see Fig. 3, *right panel*) because pairs undergo rear-end collisions with the stellar photons ($\mathbf{e}_* \cdot \mathbf{e}_{obs} = 1$). This effect is smoothed if the finite size of the massive star is considered. The escaping gamma-ray density at inferior conjunction is more important than at superior conjunction as TeV photons suffer less from absorption.

4.2. One and multi-generation cascade

The semi-analytical method is ideal to study the first generation of particles in the cascade as it provides quick and accurate solutions. In principle, this method can be extended to an arbitrary number of generation but the computing time increases tremendously. The Monte Carlo approach is well suited to treat complex three dimensional radiative transfer problems. With this method, the full cascade radiation (including all generations) can be computed with a reasonable amount of time but a large number of events is required to have enough statistics for accurate predictions.

Figure 4 gives the escaping gamma-ray spectra at both conjunctions in LS 5039. The Monte Carlo output is compared with the semi-analytical results in the same configuration as in Fig. 3 for $\psi = 30^\circ$ and 150° . Both approaches give similar results for the first generation of gamma rays. There are slight differences mainly due to statistical and binning effect in the Monte Carlo result, particularly at $\psi = 30^\circ$ where the absorption is high. The contribution from additional generations of pairs to the cascade radiation is of major importance as it dominates the overall escaping gamma-ray flux where the primary photons are fully absorbed. The Monte Carlo approach is needed to compute the cascade radiation where ab-

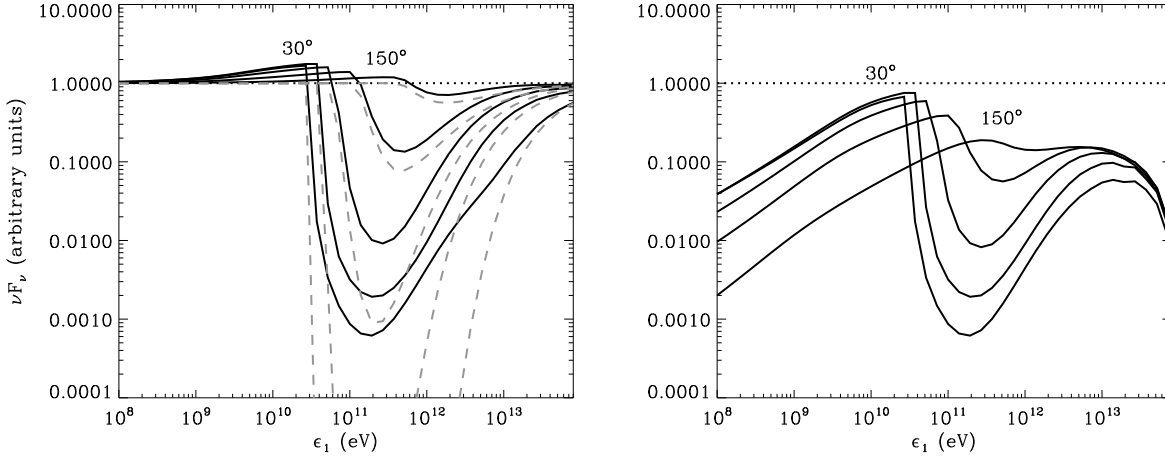


Fig. 5. Cascade radiation emitted by the first generation computed with the semi-analytical method in LS 5039 at periastron for $\psi = 30^\circ, 60^\circ, 90^\circ, 120^\circ$ and 150° . *Left:* The escaping gamma-ray spectrum (solid line) is compared to the pure-absorbed (dashed gray line) and injected (isotropic, dotted line) spectra. The radiation from the cascade only is shown on the *right panel*. Synchrotron radiation is ignored and the massive star is point like and mono-energetic.

sorption is strong *i.e.* at superior conjunction. In practice, the one-generation approximation catches the main features of the full three-dimensional pair cascade calculation elsewhere along the orbit.

4.3. Comparison with one-dimensional cascade

Three-dimensional cascade radiation presents identical spectral features to the one-dimensional limit (Cerutti et al. 2009b) (Fig. 5). Below the threshold energy for pair production, *i.e.* $\epsilon_1 < m_e^2 c^4 / 2\epsilon_0 (1 - \cos \theta_0)$ with ϵ_0 the stellar photon energy, pairs cool down *via* inverse Compton scattering in the Thomson regime and accumulate at lower energy in a ~ -1.5 photon index power-law tail. Above, emission and absorption compete, giving rise to a dip in the spectrum. At higher energies ($\epsilon_1 \gtrsim 10$ TeV), the gamma-ray production in the cascade declines due to Klein-Nishina effect in inverse Compton scattering and pair production becomes less efficient.

Three-dimensional cascade radiation has a strong angular dependence (Fig. 5) that differs significantly from the one-dimensional case. Figure 6 presents the modulation of the TeV radiation from a 1D and 3D cascade along the orbit in LS 5039 (the one-dimensional cascade radiation is calculated with the method described in Cerutti et al. 2009b). Bednarek (2006) found a similar modulation for the 3D cascade radiation. Both contributions are anti-correlated. Contrary to the one-dimensional cascade, the three-dimensional cascade radiation preserves the modulation of the primary absorbed source of gamma rays since pairs do not propagate. Peaks and dips remain at conjunctions. In both cases, the cascade radiation flux prevails at superior conjunction where the primary flux is highly absorbed. Note that a small dip in the 1D cascade radiation appears at superior conjunction because absorption slightly dominates over emission. The 3D cascade contributes

less (by a factor ≈ 3) than the 1D cascade to the total TeV flux at this orbital phase.

4.4. The effect of the ambient magnetic field

Synchrotron radiation has a significant impact on the cascade spectrum. Figure 7 shows the effects of a uniform ambient magnetic field on the cascade radiation for $B = 0, 3$ and 10 G. The VHE emission is quenched as synchrotron radiation becomes the dominant cooling channel for electrons produced in the cascade ($t_{ic} > t_{syn}$). The large contribution of the cascade in the TeV band is preserved if the magnetic field does not exceed a few Gauss (see Fig. 1). Synchrotron radiation contributes to the total flux in the X-ray to soft gamma-ray energy band. These photons do not participate to the cascade as their energy does not exceed 100 MeV, which is insufficient for pair production with the stellar photons.

Figure 7 compares also the contribution from the first generation of gamma rays with the full cascade radiation. For low magnetic field ($B \lesssim 5$ G), all generations should be considered in the calculation. For higher magnetic field ($B > 5$ G), the first generation of gamma rays dominates the total cascade radiation. Only a few pairs can radiate beyond the threshold energy for pair production and the cascade is quenched.

A non-uniform magnetic field was also investigated for a toroidal or dipolar magnetic structure generated by the massive star (*i.e.* with a R^{-1} or R^{-3} dependence). These configurations do not give different results compared with the uniform case. Most of the cascade radiation is produced close to the primary source (see Sect. 4.1) and depends mostly on the magnetic field strength at this location.

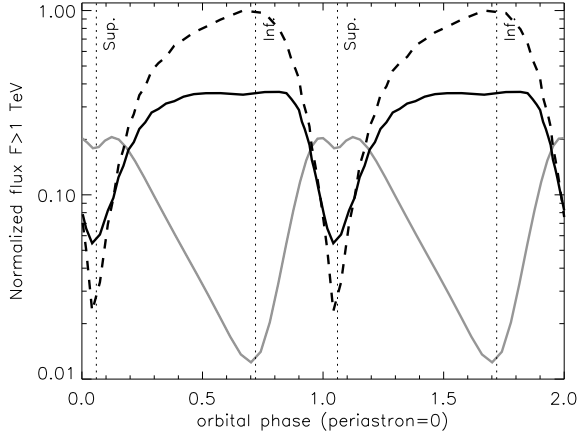


Fig. 6. Modulation of the TeV flux produced by a three-dimensional (Monte Carlo calculation, black solid line) and one-dimensional (semi-analytical calculation see Cerutti et al. 2009b, gray solid line) cascade in LS 5039 as a function of the orbital phase (two full orbits). Synchrotron radiation is ignored for the computation of 3D cascade radiation. The primary absorbed flux (identical injection as in Fig. 5, *i.e.* isotropic) is shown (dashed line) for comparison. Conjunctions are indicated by vertical dotted lines. Orbital parameters are taken from Casares et al. (2005) for an inclination $i = 60^\circ$. The companion star is point like and mono-energetic.

5. Three-dimensional cascades in LS 5039

The full cascade radiation calculation is applied to LS 5039 and discussed below. The black body spectrum and the spatial extension of the massive star are taken into account in this part. The primary source of gamma rays is computed here following the model described in Dubus et al. (2008) where the pulsar is assumed to inject energetic electron-positron pairs with an isotropic power-law energy distribution at the shock front, expected to lie at the vicinity of the compact star. Taking $v_\infty = 2400 \text{ km s}^{-1}$, $\dot{M} = 10^{-7} M_\odot \text{ yr}^{-1}$ for the massive star wind (McSwain et al. 2004), and a pulsar spin-down luminosity $L_p = 10^{36} \text{ erg s}^{-1}$, both wind momenta balance at a distance $r_{\text{shock}} \sim 0.1d$ from the pulsar. Pairs generated by the pulsar emit *via* inverse Compton scattering on stellar photons the primary gamma-ray photons. Contrary to the previous section, the primary gamma-ray source is highly anisotropic. The orbital parameters of the system are taken from Casares et al. (2005). New optical observations of LS 5039 have been carried out recently by Aragona et al. (2009) where slight corrections to the orbital parameters have been reported, but these do not change the results below.

5.1. TeV orbital modulation

The shape of the TeV light curve can be explained with a one-zone leptonic model (Dubus et al. 2008) that combines emission and absorption. However, it overestimates the amplitude of the modulation (by a factor $\gtrsim 50$ for $i = 60^\circ$). The TeV

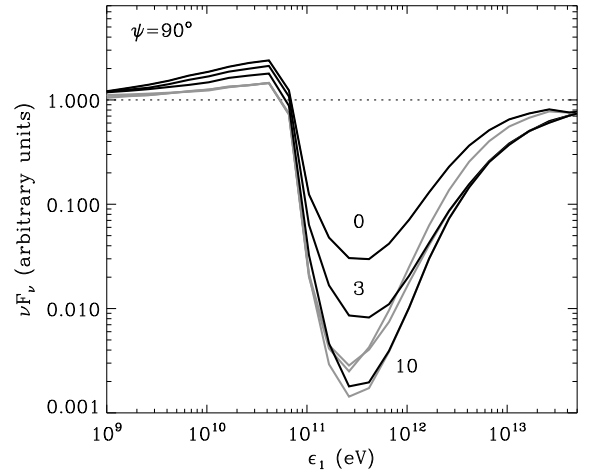


Fig. 7. Effect of the ambient magnetic field on the cascade radiation. The cascade is computed with the same parameters (Monte Carlo approach) as used in Fig. 4 for $\psi = 90^\circ$ with an uniform magnetic field $B = 0$ (top), 3 and 10 G (bottom). The full escaping gamma-ray spectra (all generations, black lines) is compared with the one-generation approximation (gray lines) and the injected isotropic spectra (dotted line). The companion star is point like and mono-energetic.

flux observed by HESS varies by about a factor 6 with a minimum at the orbital phases $\phi = 0.1-0.2$ and a maximum at $\phi = 0.8-0.9$ (Aharonian et al. 2006). The radiation from a three-dimensional cascade of pairs decreases the amplitude of the TeV modulation yet conserves the light curve pattern (see Sect. 4.3). The flux remains minimum at superior conjunction ($\phi \approx 0.06$) and maximum just after inferior conjunction ($\phi \approx 0.85$).

The amplitude of the modulation in LS 5039 can be reproduced for an inclination of the orbit $i = 40^\circ$ (Fig. 8, *top panel*), assuming a constant energy density of cooled particles along the orbit as in Dubus et al. (2008). This assumption implies that the injection of fresh particles depends (roughly) as d^{-2} . The ambient magnetic field is $\lesssim 1 \text{ G}$ (if uniform) otherwise emission up to 10 TeV cannot be sustained. For higher inclination ($i \gtrsim 50^\circ$), the flux at superior conjunction is too small to explain observations. For lower inclination ($i \lesssim 30^\circ$), the amplitude of the light curve becomes too small. If the injection rate of the uncooled primary pairs is instead kept constant along the orbit (Fig. 8, *bottom panel*), a lower inclination ($i \lesssim 30^\circ$) is required to reproduce an amplitude consistent with observations. Then, the light curve presents a broad peak centered at $\phi \approx 0.5$. The profile of the modulation is not explained to satisfaction in this case.

The cascade radiation contributes significantly at every orbital phase and dominates the overall gamma-ray flux close to superior conjunction ($0 < \phi < 0.15$), where the primary flux is highly absorbed. The residual flux observed at superior conjunction is explained by the cascade. The averaged spectra at high and very-high energy are not significantly changed com-

8

B. Cerutti et al.: Modeling the three-dimensional pair cascade in binaries. Application to LS 5039

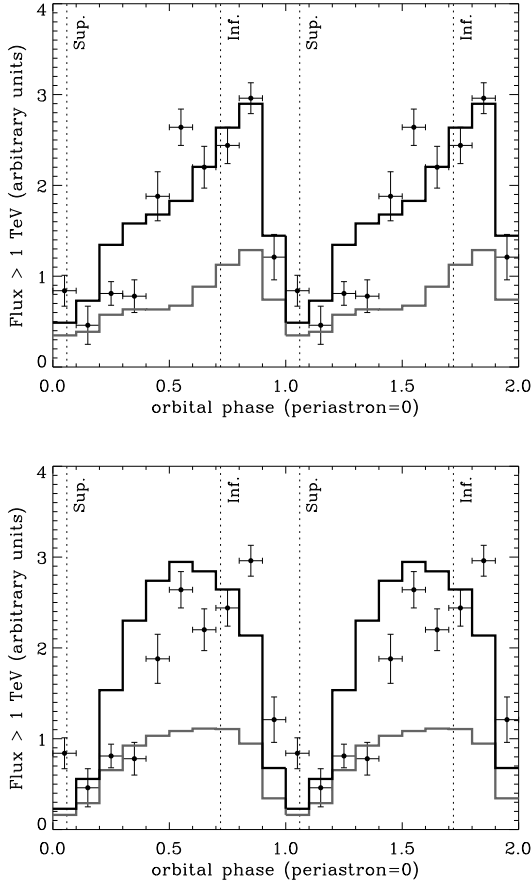


Fig. 8. Theoretical integrated flux above 1 TeV (black solid line) in LS 5039 as a function of the orbital phase (two orbits) with an inclination of the orbit $i = 40^\circ$ in both panels. The cascade radiation contribution (gray solid line) is computed with the Monte Carlo approach for a constant injection of energy in cooled particles (*top*) and for a constant injection of pairs (*bottom*) along the orbit. The black-body spectrum and the finite size of the companion star are taken into account. The ambient magnetic field is small ($B < 1$ G). Theoretical lightcurves are binned in phase interval of width $\Delta\phi = 0.1$ in order to compare with HESS observations (data points) taken from Aharonian et al. (2006). Both conjunctions (‘Sup.’ and ‘Inf.’) are indicated with dotted lines.

pared with the case without cascade (Fig. 9, see also Fig. 6 in Dubus et al. 2008). It should be noted that the ratio between the GeV and the TeV flux decreases if a three-dimensional pair cascading is considered. The cascade contributes more at TeV than at GeV energies with respect to the primary source. If spectra are fitted with HESS observations, then the flux expected at GeV energies is too low to explain observations. In addition, this model cannot account for the energy cutoff observed by *Fermi* at a few GeV (Abdo et al. 2009). Electrons radiating at GeV and TeV energies may have two different origins. An extra component, possibly from the pulsar itself (magnetospheric

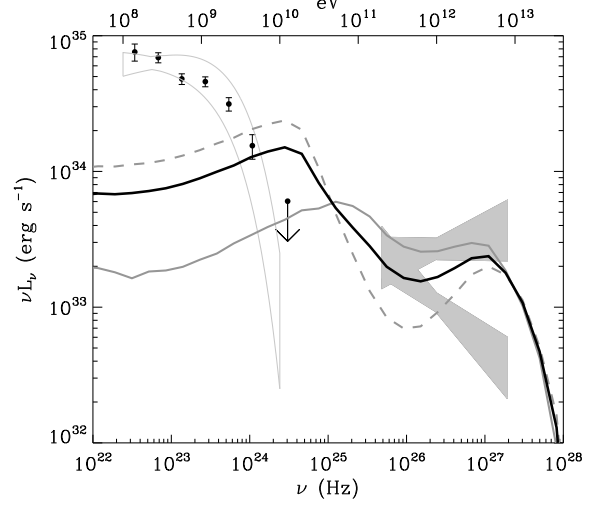


Fig. 9. Theoretical gamma-ray spectrum in LS 5039 for ‘SUPC’ (i.e. averaged over $0.45 < \phi < 0.9$, gray dashed line) and ‘INFC’ ($\phi < 0.45$ or $\phi > 0.9$, gray solid line) states as defined in Aharonian et al. (2006) and orbit averaged spectrum (black solid line). Comparison with *Fermi* (black data points, Abdo et al. 2009) and HESS (red bowties, Aharonian et al. 2006) observations.

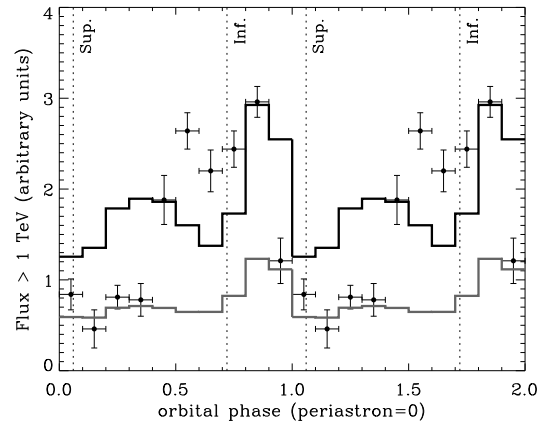


Fig. 10. Same as in Fig. 8 (*top panel*) for $i = 60^\circ$ with a primary source of gamma rays above the compact object and perpendicular to the orbital plane for an altitude $z = 2 R_\star$.

or free pulsar wind emission, see Cerutti et al. 2009a) might dominate at GeV energies.

5.2. Constraint on the location of the VHE emitter

The primary gamma-ray emitter position might not coincide with the compact object location. One possibility is to imagine that particles radiate VHE farther in the orbital plane, for instance backward in a shocked pulsar wind collimated by the massive star wind. In this case, the primary source is less absorbed along the orbit and more power into particles is re-

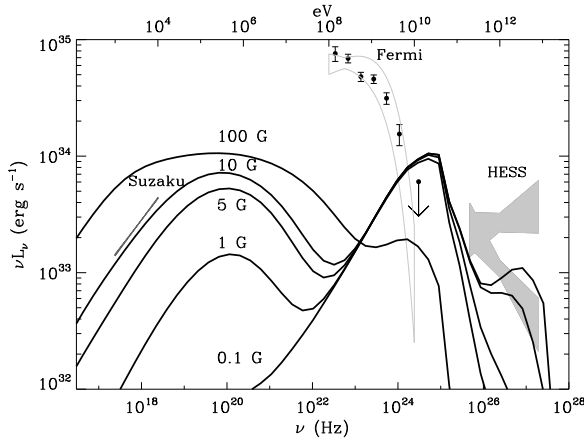


Fig. 11. Orbit averaged spectrum of the first generation of gamma rays in LS 5039 with a uniform magnetic field $B = 0.1, 1, 5, 10$ and 100 G. Comparison with observations from X-rays to TeV energies: *Suzaku* (Takahashi et al. 2009), *Fermi* (Abdo et al. 2009) and HESS (Aharonian et al. 2006) bowties.

quired to compensate for the decrease of the soft photon density from the companion star. A consistent amplitude could be obtained if the primary gamma rays originate from large distances ($\geq 10 d$), but then the TeV light curve shape is incorrectly reproduced as the tendency for the main peak is to shift towards superior conjunction. Another possibility is to assume that the VHE emitter stands above the orbital plane (*e.g.* in a jet). This situation does not differ significantly from the previous alternative. For altitudes $z > 2 R_{\star} \approx d$, the $\gamma\gamma$ -opacity decreases significantly and the escaping VHE gamma-ray flux increases at superior conjunction but the TeV modulation is not reproduced as well (Fig. 10). Regarding observations, it appears difficult with this model to push the gamma-ray emitter at the outer edge of the system. The primary source should still lie in the vicinity of the compact object (*i.e.* at distances smaller than the orbital separation).

5.3. Constraint on the ambient magnetic field

The synchrotron radiation produced by secondary pairs can be a dominant contributor to the overall X-ray luminosity as discussed by Bosch-Ramon et al. (2008a,b). Figure 11 presents the orbit-averaged spectrum of the first generation of gamma rays in LS 5039 with an inclination $i = 40^\circ$, using the semi-analytical approach for various magnetic field intensity. The comparison of the expected flux in the 2-10 keV band with the recent *Suzaku* observations (Takahashi et al. 2009) constrains the (uniform) magnetic field strength below 10 G. This result is in agreement with the development of a three-dimensional cascade (see Sect. 2). The one-generation approximation for the cascade is good in this case since for high magnetic field ($B > 5$ G), the contribution from extra-generations can be ignored (see Sect. 4.4). Note that the synchrotron peak energy emitted by secondary pairs barely changes with increasing magnetic field ($\epsilon_1 \approx 1$ MeV, see Fig. 11). This is due to

the effect of synchrotron losses on the cooled energy distribution of the radiating pairs in the cascade. Synchrotron cooling dominates over Compton cooling ($t_{\text{syn}} < t_{\text{ic}}$) at high energies and depletes the most energetic pairs in the steady-state distribution (see Eq. 6). In consequence, the mean energy of cooled pairs in the cascade diminishes with increasing magnetic field (for a fixed stellar radiation field). The non-trivial combination of both effects results in a (almost) constant synchrotron peak (the critical energy in synchrotron radiation is proportional to $\gamma_c^2 B$).

6. Conclusion

Three-dimensional pair cascade can be initiated in gamma-ray binaries provided that pairs are confined and isotropized by the ambient magnetic field in the system. In LS 5039, a three-dimensional pair cascade contributes significantly in the formation of the VHE radiation at every orbital phase. In particular, the cascade radiation prevails over the primary source of gamma rays close to superior conjunction (*i.e.* where the $\gamma\gamma$ -opacity is high) and gives a lower flux than the 1D cascade at this phase. The 3D cascade radiation is modulated differently compared with the 1D cascade and preserves the modulation of the primary absorbed flux because the pairs stay localized. In addition, the 3D cascade radiation decreases the amplitude of the observed TeV modulation. The amplitude of the HESS light curve is correctly reproduced for an inclination of $i \approx 40^\circ$.

The ambient magnetic field in LS 5039 cannot exceed 10 G (if uniform) or synchrotron radiation from pairs in the cascade would overestimate X-ray observations. This is a reasonable constraint as most of massive stars are probably non-magnetic, even though strong magnetic fields (> 100 G) have been measured for a few O stars at their surface (see Donati & Landstreet 2009 for a recent review and references therein). The VHE emitter should also remain very close to the compact object location, possibly at the collision site between both star winds, otherwise the TeV light curve shape is not reproduced although this does not rule out complex combinations.

The model described in this paper is not fully satisfying. The spectral shape of VHE gamma rays is still not reproduced close to superior conjunction. In addition, the light curve amplitude tends to be overestimated except for low inclinations but then the shape is not perfect. It remains difficult to explain both the shape and the amplitude of the modulation in LS 5039. A possible solution would be to consider a more complex injection of fresh pairs along the orbit or additional effects such as adiabatic losses or advection. A Doppler-boosted emission in the primary source can also change the spectrum seen by the observer, especially around superior conjunction (Dubus et al. 2010). The primary source of gamma rays might be extended, VHE photons would come from *e.g.* the shock front between the pulsar wind and the stellar wind or along a relativistic jet. The development of an anisotropic 3D cascade is not excluded as well. Nevertheless, the calculations show that a three dimensional pair cascading provides a plausible framework to understand the TeV modulation in LS 5039.

Acknowledgements. This work was supported by the *European Community* via contract ERC-StG-200911.

References

- Abdo, A. A., Ackermann, M., Ajello, M., et al. 2009, *ApJ*, 706, L56
- Aharonian, F., Akhperjanian, A. G., Aye, K.-M., et al. 2005, *Science*, 309, 746
- Aharonian, F., Akhperjanian, A. G., Bazer-Bachi, A. R., et al. 2006, *A&A*, 460, 743
- Aragona, C., McSwain, M. V., Grundstrom, E. D., et al. 2009, *ApJ*, 698, 514
- Bednarek, W. 1997, *A&A*, 322, 523
- Bednarek, W. 2006, *MNRAS*, 368, 579
- Bednarek, W. 2007, *A&A*, 464, 259
- Blumenthal, G. R. & Gould, R. J. 1970, *Reviews of Modern Physics*, 42, 237
- Bonometto, S. & Rees, M. J. 1971, *MNRAS*, 152, 21
- Bosch-Ramon, V., Khangulyan, D., & Aharonian, F. A. 2008a, *A&A*, 482, 397
- Bosch-Ramon, V., Khangulyan, D., & Aharonian, F. A. 2008b, *A&A*, 489, L21
- Böttcher, M. & Dermer, C. D. 2005, *ApJ*, 634, L81
- Böttcher, M. & Schlickeiser, R. 1997, *A&A*, 325, 866
- Casares, J., Ribó, M., Ribas, I., et al. 2005, *MNRAS*, 364, 899
- Cerutti, B., Dubus, G., & Henri, G. 2009a, *ArXiv e-prints*
- Cerutti, B., Dubus, G., & Henri, G. 2009b, *A&A*, 507, 1217
- Donati, J. & Landstreet, J. D. 2009, *ARA&A*, 47, 333
- Dubus, G. 2006a, *A&A*, 451, 9
- Dubus, G. 2006b, *A&A*, 456, 801
- Dubus, G., Cerutti, B., & Henri, G. 2008, *A&A*, 477, 691
- Dubus, G., Cerutti, B., & Henri, G. 2010, *ArXiv e-prints*
- Ginzburg, V. L. & Syrovatskii, S. I. 1964, *The Origin of Cosmic Rays*, ed. V. L. Ginzburg & S. I. Syrovatskii
- Maraschi, L. & Treves, A. 1981, *MNRAS*, 194, 1P
- Martocchia, A., Motch, C., & Negueruela, I. 2005, *A&A*, 430, 245
- Mastichiadis, A. 1991, *MNRAS*, 253, 235
- McSwain, M. V., Gies, D. R., Huang, W., et al. 2004, *ApJ*, 600, 927
- Motch, C., Haberl, F., Dennerl, K., Pakull, M., & Janot-Pacheco, E. 1997, *A&A*, 323, 853
- Sierpowska, A. & Bednarek, W. 2005, *MNRAS*, 356, 711
- Sierpowska-Bartosik, A. & Torres, D. F. 2008, *Astroparticle Physics*, 30, 239
- Takahashi, T., Kishishita, T., Uchiyama, Y., et al. 2009, *ApJ*, 697, 592
- Zdziarski, A. A., Malzac, J., & Bednarek, W. 2009, *MNRAS*, L175+

Part IV

High-energy emission from relativistic outflow

9	Anisotropic Doppler-boosted emission	207
10	Doppler-boosted emission in gamma-ray binaries	217
11	Doppler-boosted emission in the relativistic jet of Cygnus X-3	237

9

Anisotropic Doppler-boosted emission

Outline

1. What we want to know	207
2. Geometry and assumptions	208
3. Boosted synchrotron radiation	209
4. Boosted anisotropic inverse Compton scattering	210
§ 77. <i>Soft photon density in the comoving frame</i>	211
§ 78. <i>Doppler-boosted Compton spectrum</i>	212
5. What we have learned	214
6. [Français] Résumé du chapitre	215
§ 79. <i>Contexte et objectifs</i>	215
§ 80. <i>Ce que nous avons appris</i>	215

UP TO NOW, I have considered the emission from relativistic particles with no bulk velocities. If the plasma of pairs moves with a substantial fraction of the speed of light, the emitted radiation would be changed due to relativistic Doppler aberrations. My aim here is to quantify the beaming effects on synchrotron radiation and anisotropic inverse Compton scattering for relativistic bulk velocities (with a Lorentz factor $\Gamma > 1$). In this chapter, I compute the Doppler-boosted synchrotron and anisotropic inverse Compton spectrum, for an arbitrary orientation of the relativistic flow with respect to the observer and the source of soft radiation.

1. What we want to know

- What are the beaming patterns for synchrotron radiation and anisotropic inverse Compton scattering?
- What is the effect of the orientation of the flow with respect to the observer?

2. Geometry and assumptions

We consider a compact cloud moving with a bulk velocity $v_{flow} = \beta c$ and a bulk Lorentz factor $\Gamma = (1 - \beta^2)^{-1/2}$ in an arbitrary direction given by the unit vector \mathbf{e}_{flow} (see Fig. 95). The cloud contains a plasma of ultra-relativistic pairs of electrons and positrons isotropized in the comoving frame of the flow. Radiating pairs are assumed to be localized in a compact region, *i.e.* the spatial advection of the particles by the flow is ignored here.

Electrons emit *via* synchrotron radiation and inverse Compton scattering. The magnetic field is assumed to be desorganized and comoving with the flow. The source of soft radiation is *external* to the flow and is considered as monoenergetic and unidirectional, in the direction given by the unit vector \mathbf{e}_* . A distant observer sees photons escaping the moving cloud in the direction indicated by \mathbf{e}_{obs} (Fig. 95).

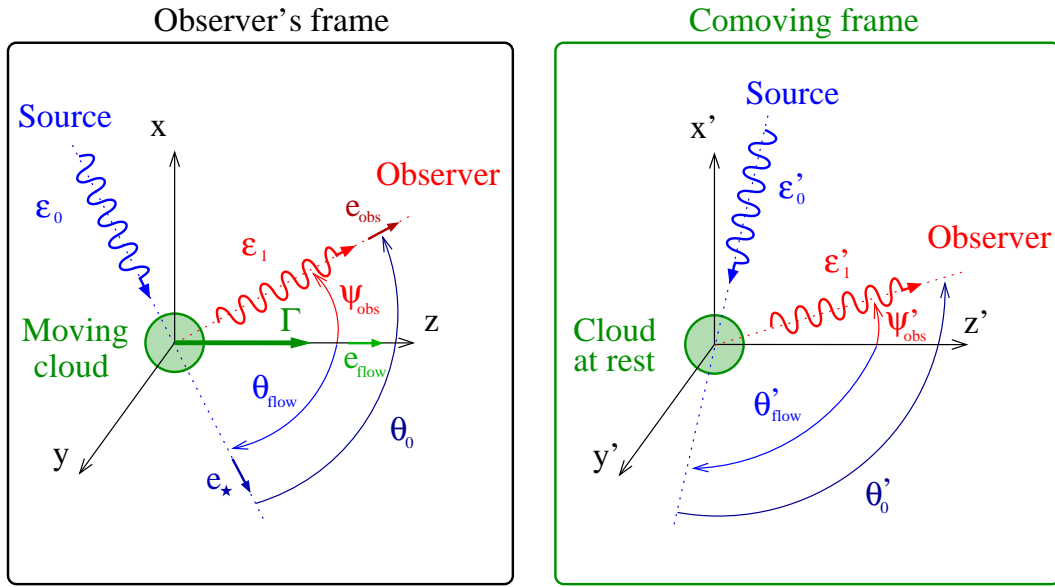


FIG. 95. Emission processes seen in the observer frame (*left panel*) and in the comoving frame of the flow (*right panel*). Waves represent photons and the green thick arrow shows the direction of motion of the flow with a bulk Lorentz factor $\Gamma > 1$. The boost from the observer to the comoving frame is along the z -axis.

The quantities defined in the comoving frame are primed. Energies are changed in the comoving frame as (see Eq. 16.78, 16.79)

$$\epsilon'_1 = \mathcal{D}_{obs}^{-1} \epsilon_1 \quad (78.288)$$

$$\epsilon'_0 = \mathcal{D}_*^{-1} \epsilon_0, \quad (78.289)$$

where we define the Doppler factors

$$\mathcal{D}_{obs} = \frac{1}{\Gamma (1 - \beta \mu_{obs})} \quad \mathcal{D}_* = \frac{1}{\Gamma (1 - \beta \mu_{flow})}, \quad (78.290)$$

with $\mu_{obs} \equiv \cos \psi_{obs} = \mathbf{e}_{obs} \cdot \mathbf{e}_{flow}$ and $\mu_{flow} \equiv \cos \theta_{flow} = \mathbf{e}_* \cdot \mathbf{e}_{flow}$. The angles defined with respect to the Lorentz boost direction, *i.e.* ψ_{obs} and θ_{flow} are changed into (see Eq. 16.80)

$$\mu'_{obs} = \frac{\mu_{obs} - \beta}{1 - \beta \mu_{obs}} \quad \mu'_{flow} = \frac{\mu_{flow} - \beta}{1 - \beta \mu_{flow}}. \quad (78.291)$$

If the angle is not defined to the boost direction, such as the angle θ_0 , the Lorentz transform is different. In this case, it is convenient to look how the unit vectors are changed by the boost. The general expression for the Lorentz transform matrix is

$$M = \begin{pmatrix} \Gamma & -\Gamma\boldsymbol{\beta} \\ -\Gamma\boldsymbol{\beta} & 1 + \frac{(\Gamma-1)}{\beta^2}\boldsymbol{\beta}\cdot\boldsymbol{\beta} \end{pmatrix}. \quad (78.292)$$

Let's consider the following 4-vector $V = \epsilon(1, \mathbf{e})$ for a photon of energy ϵ propagating in the direction given by the unit vector \mathbf{e} . This vector is transformed in the comoving frame as

$$V' = \epsilon' \begin{pmatrix} 1 \\ \mathbf{e}' \end{pmatrix} = MV = \begin{pmatrix} \Gamma(1 - \boldsymbol{\beta}\cdot\mathbf{e}) \\ -\Gamma\boldsymbol{\beta} + \mathbf{e} + \frac{(\Gamma-1)}{\beta^2}(\boldsymbol{\beta}\cdot\mathbf{e})\boldsymbol{\beta} \end{pmatrix}. \quad (78.293)$$

Hence, the unit vector \mathbf{e} in the comoving frame is changed into

$$\mathbf{e}' = \frac{1}{\Gamma(1 - \boldsymbol{\beta}\cdot\mathbf{e})} \left[-\Gamma\boldsymbol{\beta} + \mathbf{e} + \frac{(\Gamma-1)}{\beta^2}(\boldsymbol{\beta}\cdot\mathbf{e})\boldsymbol{\beta} \right]. \quad (78.294)$$

With $\boldsymbol{\beta} = \beta\mathbf{e}_{flow}$, we have

$$\mathbf{e}'_{\star} = \mathcal{D}_{\star} \{ \mathbf{e}_{\star} + [(\Gamma-1)\mu_{flow} - \Gamma\beta] \mathbf{e}_{flow} \} \quad (78.295)$$

$$\mathbf{e}'_{obs} = \mathcal{D}_{obs} \{ \mathbf{e}_{obs} + [(\Gamma-1)\mu_{obs} - \Gamma\beta] \mathbf{e}_{flow} \} \quad (78.296)$$

The cosine of the scattering angle θ_0 and after some simplifications, transforms as

$$\mu'_0 = \mathbf{e}'_{\star} \cdot \mathbf{e}'_{obs} = 1 - \mathcal{D}_{obs}\mathcal{D}_{\star}(1 - \mu_0). \quad (78.297)$$

Note that if $\theta_{flow} = 0$, then μ'_0 is changed as in Eq. (78.291).

3. Boosted synchrotron radiation

The computation of the boosted synchrotron radiation is straightforward as the magnetic field is assumed to be comoving with the relativistic flow. In the rest frame of the cloud, the magnetic field can be seen as an *internal* source of soft radiation interacting with pairs. Synchrotron flux F'_{syn} is first calculated with no modifications in the comoving frame. In the observer frame, the flux F_{syn} is boosted as

$$F_{syn}(\epsilon'_1) = \epsilon_1 \frac{dN_{syn}}{dt d\epsilon_1 d\Omega} = F'_{syn}(\epsilon'_1) \frac{\epsilon_1 dt' d\epsilon'_1 d\Omega'}{\epsilon'_1 dt d\epsilon_1 d\Omega}. \quad (78.298)$$

With $dt' = \mathcal{D}_{obs}dt$, $d\Omega' = \mathcal{D}_{obs}^2 d\Omega$ and $\epsilon'_1 = \mathcal{D}_{obs}\epsilon_1$, we have

$$F_{syn}(\epsilon'_1) = \mathcal{D}_{obs}^3 F'_{syn}(\epsilon'_1). \quad (78.299)$$

If synchrotron emission spectrum is an isotropic power law of index α in the comoving frame such as $F'_{syn}(\epsilon'_1) \propto \epsilon'^{-\alpha}$, then the flux in the observer frame is

$$\begin{aligned} F_{syn}(\epsilon_1) &\propto \mathcal{D}_{obs}^3 \epsilon_1'^{-\alpha} \\ &\propto \mathcal{D}_{obs}^{3+\alpha} \epsilon_1^{-\alpha}, \end{aligned} \quad (78.300)$$

where the extra component $\mathcal{D}_{obs}^{\alpha}$ accounts for the shift in energy of the scattered radiation. The relativistic boost does not change the spectral index (Fig. 96). Fig. 97 gives the variations of the Doppler factor \mathcal{D}_{obs} as a function of μ_{obs} . This plot shows that even for mildly relativistic flow ($\beta < 0.5$), the Doppler boost-deboost can be important. Fig. 98 presents also other interesting

properties of the boosted emission. If $\psi_{obs} \lesssim 60^\circ$, the emission will be boosted *i.e.* $\mathcal{D}_{obs} > 1$ as long as the bulk Lorentz factor $\Gamma \lesssim 1/\psi_{obs}$, beyond the emission is highly deboosted.

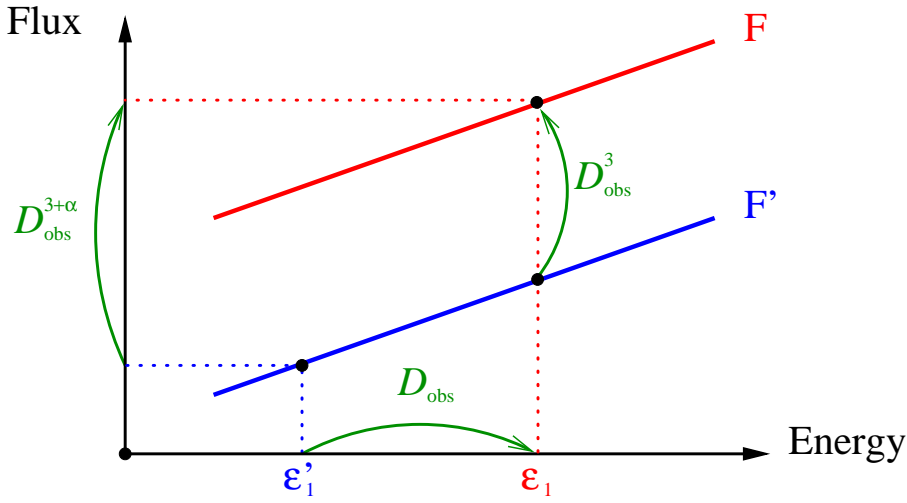


FIG. 96. Effect of the Doppler boost on synchrotron radiation flux for a power law spectrum. The flux is increased by a factor \mathcal{D}_{obs}^3 and the power law is shifted in energy by a factor \mathcal{D}_{obs} .

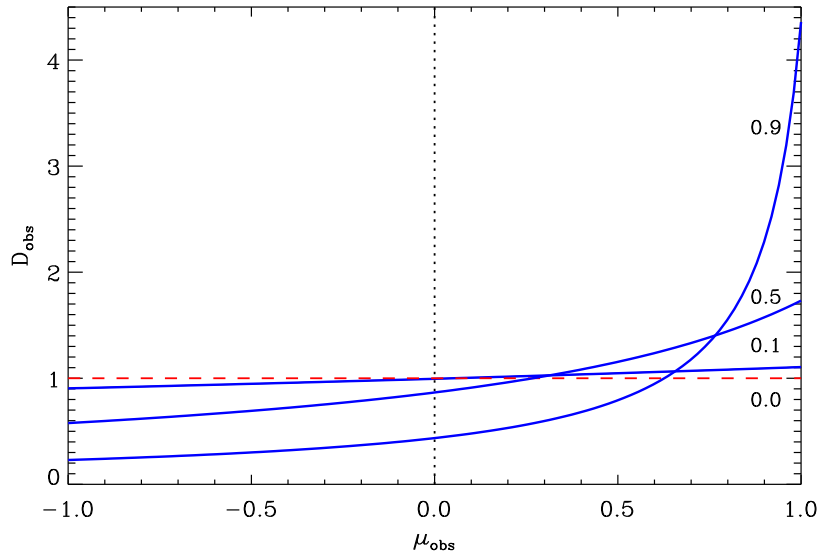


FIG. 97. Doppler factor \mathcal{D}_{obs} as a function of the cosine of the angle between the observer and the flow μ_{obs} for $\beta = 0$ (red dashed line), 0.1, 0.5 and 0.9 (top). The flux is forward boosted by the flow ($\mathcal{D}_{obs} > 1$) in a cone of semi aperture angle $\sim 1/\Gamma$, otherwise the flux is deboosted ($\mathcal{D}_{obs} < 1$).

4. Boosted anisotropic inverse Compton scattering

Inverse Compton emission is boosted differently compared with synchrotron radiation as the source of seed photons is *external* to the flow. The density of the soft radiation seen by the

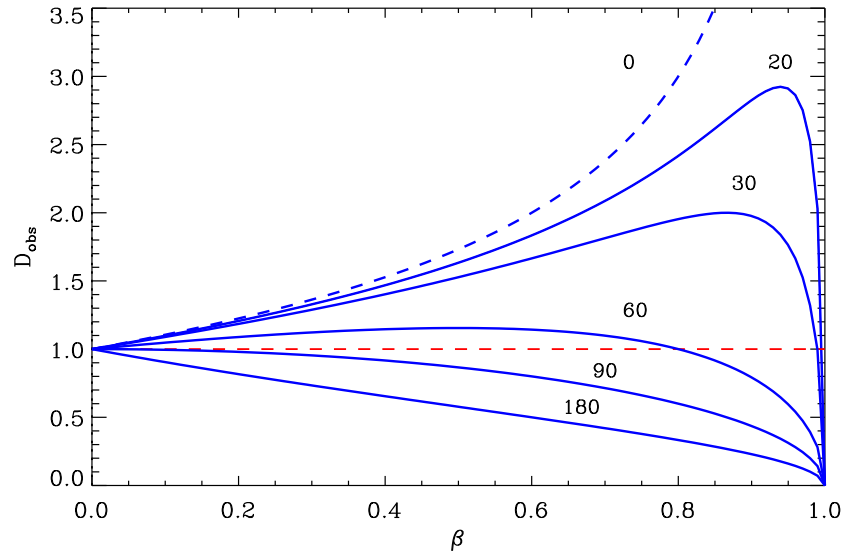


FIG. 98. Doppler factor \mathcal{D}_{obs} as a function of β for $\psi_{obs} = 0^\circ$ (dashed blue line) 20° , 30° , 60° , 90° and 180° . The flux is deboosted ($\mathcal{D}_{obs} < 1$) if $\Gamma \gtrsim 1/\psi_{obs}$.

particles in the comoving frame is modified. In addition, another complication arises because of the angular dependence in the Compton emitted spectrum. Photons will interact with a different angles θ'_0 in the comoving frame due to the relativistic motion of the frame. I aim here to consider all these effects for Compton scattering and I derive a simple expression in the Thomson regime.

There are two ways to compute anisotropic inverse Compton emission in the observer frame. The first possibility is to consider the inverse Compton interaction in the observer frame. In this case, the density of electrons should be changed in the observer frame according to relativistic beaming effects (the distribution of electrons is not isotropic in the observer frame, see *e.g.* Georganopoulos *et al.* 2001). The second possibility is to consider the interaction in the comoving frame. In this case, the density of electrons remains isotropic but the density of soft radiation should be changed due to relativistic Doppler effect. I have chosen to explore this possibility here as the situation is very similar to the calculation of anisotropic inverse Compton emission (see Chapter 3).

§ 79. Soft photon density in the comoving frame

For a mono-energetic and point-like star, the stellar photon density in the observer frame is (see Eq. 17.84)

$$\frac{dn}{d\epsilon d\Omega} = n_0 \delta(\epsilon - \epsilon_0) \delta(\mu - \mu_{flow}) \delta(\phi - \phi_{flow}), \quad (79.301)$$

where n_0 is the photon density (ph cm^{-3}). Using the invariance of the quantity dn/dc (Blumenthal & Gould 1970) as in § 17, this density in the comoving frame is changed into

$$\frac{dn'}{d\epsilon' d\Omega'} = \frac{dn}{d\epsilon d\Omega} \frac{d\Omega}{d\Omega'} = \mathcal{D}_*^{-2} \frac{dn}{d\epsilon d\Omega}. \quad (79.302)$$

The Dirac distributions change as

$$\delta(\epsilon - \epsilon_0) = \mathcal{D}_\star^{-1} \delta(\epsilon' - \epsilon'_0) \quad (79.303)$$

$$\delta(\mu - \mu_{flow}) = \mathcal{D}_\star^2 \delta(\mu' - \mu'_{flow}) \quad (79.304)$$

$$\delta(\phi - \phi_{flow}) = \delta(\phi' - \phi'_{flow}), \quad (79.305)$$

where

$$\epsilon'_0 = \mathcal{D}_\star^{-1} \epsilon_0 \quad \mu'_{flow} = \frac{\mu_{flow} - \beta}{1 - \beta \mu_{flow}}. \quad (79.306)$$

Hence, the density of stellar photons in the comoving frame is

$$\frac{dn'}{d\epsilon' d\Omega'} = n'_0 \delta(\epsilon' - \epsilon'_0) \delta(\mu' - \mu'_{flow}) \delta(\phi' - \phi'_{flow}), \quad (79.307)$$

with $n'_0 = \mathcal{D}_\star^{-1} n_0$.

§ 80. Doppler-boosted Compton spectrum

The computation of the anisotropic inverse Compton kernel $dN/dt d\epsilon_1$ found in the case with no boosting effect (see Eq. 25.135) is unchanged in the comoving frame but the following quantities have to be redefined as

$$\epsilon'_0 = \mathcal{D}_\star^{-1} \epsilon_0 \quad (80.308)$$

$$\epsilon'_1 = \mathcal{D}_{obs}^{-1} \epsilon_1 \quad (80.309)$$

$$n'_0 = \mathcal{D}_\star^{-1} n_0 \quad (80.310)$$

$$\mu'_0 = 1 - \mathcal{D}_{obs} \mathcal{D}_\star (1 - \mu_0). \quad (80.311)$$

In the observer frame, the flux of gamma rays received by the observer F_{ic} is boosted by a factor \mathcal{D}_{obs}^3 as for synchrotron radiation (see Eq. 78.299) so that

$$F_{ic}(\epsilon'_1) = \mathcal{D}_{obs}^3 F'_{ic}(\epsilon'_1). \quad (80.312)$$

In the Thomson limit, the anisotropic inverse Compton flux radiated by an isotropic population of ultra-relativistic electrons ($\gamma_e \gg 1$) in the comoving frame injected with a power-law distribution in energy so that

$$n_e \propto \gamma_e^{-p}, \quad \gamma_- \ll \gamma_e \ll \gamma_+, \quad (80.313)$$

is (see Eq. 22.119)

$$F'_{ic}(\epsilon'_1) \propto n'_0 (1 - \mu'_0)^{\frac{p+1}{2}} \epsilon'_0{}^{\frac{p-1}{2}} \epsilon'_1{}^{-\left(\frac{p-1}{2}\right)}. \quad (80.314)$$

Using Eqs. (80.308-80.311), and defining $\alpha = \frac{p-1}{2}$, the inverse Compton flux in the observer frame is

$$\boxed{F_{ic}(\epsilon_1) \propto \mathcal{D}_{obs}^{4+2\alpha} n_0 (1 - \mu_0)^{\alpha+1} \left(\frac{\epsilon_1}{\epsilon_0}\right)^{-\alpha}} \quad (80.315)$$

Hence, the anisotropic inverse Compton emission is boosted by a factor $\mathcal{D}_{obs}^{4+2\alpha}$ in the observer frame. Dermer *et al.* (1992) and Dermer & Schlickeiser (1993) found a similar pattern in AGN, but in the particular case where external photons (from the accretion disk) propagate in the same direction than the flow (jet), *i.e.* for $\theta_{flow} = 0^\circ$. We have just shown here that this result is valid for any orientation of the flow with respect to the soft photon direction of propagation.

We can extend the formula found in Eq. (80.315) to the case of a black-body star. Since the temperature of the massive star is changed into $T'_\star = \mathcal{D}_\star^{-1}T_\star$ and the fraction of the solid angle covered by the star $\Omega'_\star = \mathcal{D}_\star^2\Omega_\star$ in the comoving frame and using Eq. (23.124), the anisotropic inverse Compton emission in the Thomson regime for a point-like and a black body star is

$$F_{ic}(\epsilon_1) \propto \mathcal{D}_{obs}^{4+2\alpha} (kT_\star)^{\alpha+3} (1-\mu_0)^{\alpha+1} \epsilon_1^{-\alpha}. \quad (80.316)$$

Fig. 99 shows the effect of the Doppler boost on the emitted inverse Compton spectrum. Electrons are isotropized and injected with a power law energy distribution in the comoving frame. The analytical formula in the Thomson regime matches the numerically integrated solution at low energies. If $\psi_{obs} = 180^\circ$ and $\theta_{flow} = 0^\circ$, the observed emission is always debossed (see Fig. 99). For $0^\circ < \psi_{obs} \lesssim 90^\circ$, the emission is boosted if the bulk Lorentz factor $\Gamma \lesssim 1/\psi_{obs}$ and debossed for higher viewing angles as for synchrotron radiation (see Fig. 98).

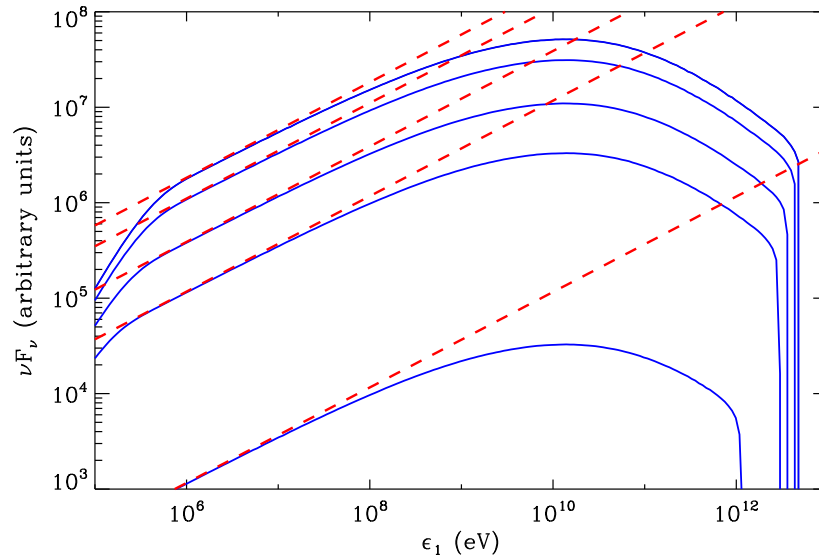


FIG. 99. Boosted anisotropic inverse Compton emission in the observer frame (blue solid lines) for $\psi_{obs} = 180^\circ$ and $\theta_{flow} = 0^\circ$ for a bulk velocity of the flow (from *top to bottom*) $\beta = 0, 0.1, 0.3, 0.5$ and 0.9 . Pairs are injected with an isotropic power law energy distribution with $\gamma_- = 10^2$ and $\gamma_+ = 10^7$, and with an index $p = 2$. The red dashed lines give the analytical solution found in Eq. (80.316) valid in the Thomson limit. The source of soft photon is point like with a black body spectrum of temperature $T_\star = 39\,000$ K in the observer frame.

The modulation of the gamma-ray spectrum is also changed by the relativistic motion of the flow. Fig. 100 gives the emitted GeV and TeV fluxes as a function of ψ_{obs} for different bulk velocities, in the simple case where $\theta_{flow} = 0^\circ$. The Compton flux is numerically computed in the comoving frame with Eq. (26.137) and transformed in the observer frame using the transformations in Eqs. (80.308)-(80.311). If $\beta = 0$, inverse Compton emission peaks where $\psi_{obs} = 180^\circ$ *i.e.* where soft photons and electrons collide head-on as expected (see Chapter 3). If $\beta > 0$, the peak splits into two symmetric peaks with respect to $\psi_{obs} = 180^\circ$ that shift towards $\psi_{obs} = 0^\circ$ (and 360°) with increasing bulk velocity of the flow. The debost is maximum for $\psi_{obs} = 180^\circ$ and the boost maximum at $\psi_{obs} = 0^\circ$ (and 180°). The intrinsic Compton emission and the Doppler boost factor interfere and anticorrelate in this simple case. Even for mildly

Lorentz boost ($\beta \sim 0.3$), the inverse Compton modulation is significantly modified. I would like also to stress here that the effect of the boost is very similar, though not identical, in the GeV and in the TeV energy band. The analytical solution found in the Thomson regime then depicts the main features of the Doppler boost on anisotropic inverse Compton scattering, even in the Klein-Nishina regime (see also the discussion in Georganopoulos *et al.* 2001 in the case where the soft photon density is isotropic in the observer frame).

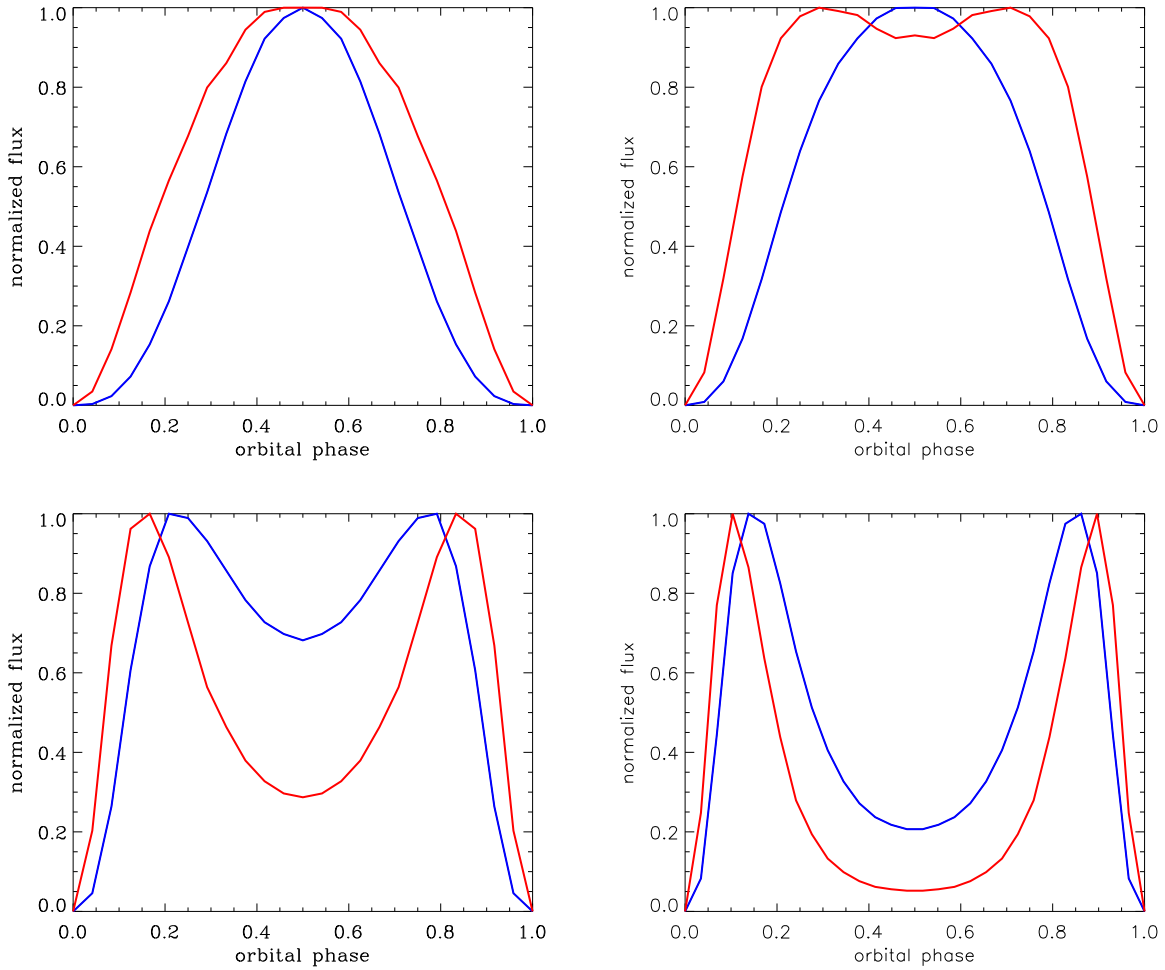


FIG. 100. Inverse Compton flux as a function of ψ_{obs} for $\theta_{flow} = 0^\circ$ and for a bulk velocity of the flow $\beta = 0$ (*top left* panel), 0.1 (*top right* panel), 0.3 (*bottom left* panel) and 0.5 (*bottom right* panel). The orbital phase is defined here as $\psi_{obs}/2\pi$ so that $\psi_{obs} = 180^\circ$ corresponds to 0.5. Curves are normalized and integrated over energies above 100 MeV (blue lines) and above 100 GeV (red lines), with $T_* = 39\,000$ K.

5. What we have learned

I have shown in this chapter that a Doppler-boost can significantly change the synchrotron and inverse Compton emission in compact binaries even for a mildly relativistic flow ($\beta \gtrsim 0.1$). Synchrotron radiation and inverse Compton scattering are affected differently by the relativistic motion of the flow. In the case where electrons are injected with a power law of index p in

the comoving frame, the synchrotron flux is changed by a factor $\mathcal{D}_{obs}^{3+\alpha}$ in the observer frame, where $\alpha = (p - 1)/2$. In the Thomson regime, I found that anisotropic inverse Compton flux is modified by the quantity $\mathcal{D}_{obs}^{4+2\alpha}$ in the observer frame, for any orientation of the flow with respect to the observer. I observed a similar, though not identical, pattern in the Klein-Nishina regime but the full calculation should be done numerically in this case.

6. [Français] Résumé du chapitre

§ 81. Contexte et objectifs

Jusqu'à maintenant, j'ai considéré l'émission en provenance de particules relativistes sans mouvement d'ensemble. Cependant, si le plasma de paires se déplace à une fraction non négligeable de la vitesse de la lumière, le rayonnement émis est alors modifié à cause du phénomène d'amplification Doppler relativiste. Mon objectif ici est de quantifier les effets de focalisation du rayonnement synchrotron et de la diffusion Compton inverse anisotrope pour des vitesses d'ensemble du plasma relativistes (avec un facteur de Lorentz $\Gamma > 1$). Dans ce chapitre, je calcule les spectres synchrotron et Compton inverse anisotrope amplifiés par effet Doppler relativiste, dans le cas d'une orientation arbitraire de l'écoulement relativiste par rapport à l'observateur et la source de photon mous.

§ 82. Ce que nous avons appris

J'ai montré dans ce chapitre que l'effet de l'amplification Doppler peut beaucoup changer l'émission synchrotron et Compton inverse dans les binaires compactes même pour des écoulement modérément relativistes ($\beta \gtrsim 0.1$). Le rayonnement synchrotron et la diffusion Compton inverse sont affectés différemment par le mouvement relativiste du flot. Dans le cas où les électrons sont injectés avec une loi de puissance d'indice p dans le référentiel comobile, le flux synchrotron est changé par un facteur $\mathcal{D}_{obs}^{3+\alpha}$ dans le référentiel de l'observateur, où $\alpha = (p - 1)/2$. Dans l'approximation Thomson, j'ai trouvé que le flux Compton inverse anisotrope est modifié par la quantité $\mathcal{D}_{obs}^{4+2\alpha}$ dans le référentiel de l'observateur, pour une orientation quelconque de l'écoulement par rapport à l'observateur. J'ai observé un comportement similaire, bien que non identique, dans le régime Klein-Nishina mais le calcul complet doit être effectué numériquement dans ce cas.

10

Doppler-boosted emission in gamma-ray binaries

Outline

1. Observational backdrop	217
2. The model and the geometry	218
3. LS 5039	218
4. LSI +61 303	219
5. PSR B1259-63	221
6. What we have learned	221
7. [Français] Résumé du chapitre	223
§ 81. Contexte et objectifs	223
§ 82. Ce que nous avons appris	224
8. Relativistic Doppler-boosted emission in gamma-ray binaries	225

1. Observational backdrop

OUR STUDIES OF THE DOPPLER-BOOSTED EMISSION in binaries presented in the previous chapter, were first motivated by the new X-ray observations by *INTEGRAL* and *Suzaku* satellites. Hoffmann *et al.* (2009) and Takahashi *et al.* (2009) found that the X-ray emission is orbital modulated and correlated with the TeV emission in LS 5039. Previous observations by *ASCA*, *Chandra* and *XMM* satellites show that the X-ray flux is also very stable on timescales of years (Kishishita *et al.* 2009). The averaged spectrum measured by *Suzaku* in the [0.6 – 70] keV band is consistent with a power law of spectral index $\alpha \sim 0.5$. The flux is maximum close to inferior conjunction and minimum at superior conjunction.

These observed features suggest that the X-ray emission is related to the position of the orbit with respect to the observer. In our model in Dubus *et al.* (2008) (see Chapter 4), the X-ray emission is dominated by synchrotron radiation but the expected orbital modulation is extremum close to periastron and apastron as the magnetic field $B \propto 1/d$ (see Eq. 30.140), which is inconsistent with observations. It would be possible to obtain a better fit with X-ray observations if, for instance, the magnetic field variations follows the X-ray modulation *i.e.*

maximum at inferior conjunction and minimum at superior conjunction. Although possible, this alternative seems very unlikely as there is no particular reasons for the magnetic field to peak at orbital phases defined only by the orientation of the observer with respect to the system. Takahashi *et al.* (2009) found that the X-ray modulation can be accurately reproduced with a one-zone leptonic model, if the adiabatic cooling timescale of leptons in X-rays dominates and peaks at inferior conjunction. Here again, this alternative is also not very convincing as there are no physical motivations to match the adiabatic cooling timescale variation with conjunctions. Instead, we propose a geometrical explanation for the X-ray modulation.

In the pulsar wind nebula scenario, the non-thermal emission is assumed to originate from energetic particles radiating in the pulsar wind shocked by the massive star wind (Chapter 1). In the MHD model of the crab nebula of Kennel & Coroniti (1984a), the post-shock velocity of the pulsar wind is $c/3$ (for a low magnetisation, $\sigma \ll 1$), *i.e.* mildly relativistic. If the stellar wind is strong ($\eta \ll 1$, see Chapter 5, Sect. 5), the pulsar wind could be confined and collimated in one direction. The non-thermal emission produced in the shocked pulsar wind should then be boosted due to the relativistic motion of the flow. The Doppler boost depends on the relative position of the observer to the system and could explain the X-ray modulation in LS 5039. Below, I briefly review the main results that we obtained in the modeling of the Doppler-boosted emission in the gamma-ray binaries LS 5039 (Sect. 3), LS I +61°303 (Sect. 4) and PSR B1259 – 63 (Sect. 5). More details about the models can be found in our paper (Dubus *et al.* 2010a), included here at the end of this chapter (Sect. 8). Note that Arons & Tavani (1993) expected an X-ray orbital modulation due to the Doppler boost in the "Black-widow" pulsar system PSR B1957 + 20. This prediction is in agreement with recent *XMM* observations by Huang & Becker (2007). Note also that the X-ray modulation could be due to absorption in the stellar wind, but the latter is not dense enough to produce a significant modulation (Szostek & Dubus 2010, submitted).

2. The model and the geometry

In this model, we consider the massive star as point-like with a black body spectrum. The flow is assumed to be contained in the orbital plane. Pairs are localized in a small region compared with the orbital separation at the pulsar location and have enough time to radiate before they escape. A distant observer sees the system at a viewing angle ψ_{obs} (see Fig. 101). If θ is the true anomaly, hence we have

$$\mu_{obs} = \mathbf{e}_{obs} \cdot \mathbf{e}_{flow} = -\sin(\theta + \theta_{flow}) \sin i, \quad (82.317)$$

and

$$\mu_0 = \mathbf{e}_* \cdot \mathbf{e}_{obs} = -\sin \theta \sin i, \quad (82.318)$$

where i is the inclination of the orbit.

3. LS 5039

We apply the Doppler-boost model described in Chapter 9 to LS 5039. Because the stellar wind terminal velocity ($v_\infty \sim 2400 \text{ km s}^{-1}$) is much greater than the orbital velocity of the pulsar ($v_{orb} \lesssim 400 \text{ km s}^{-1}$), we assume that the pulsar wind flow is radial, *i.e.* $\theta_{flow} = 0^\circ$ (see Fig. 102). The twist of the cometary tail due to the orbital motion is neglected here as the emission originates from a compact region at the vicinity of the compact object. In a more realistic model,

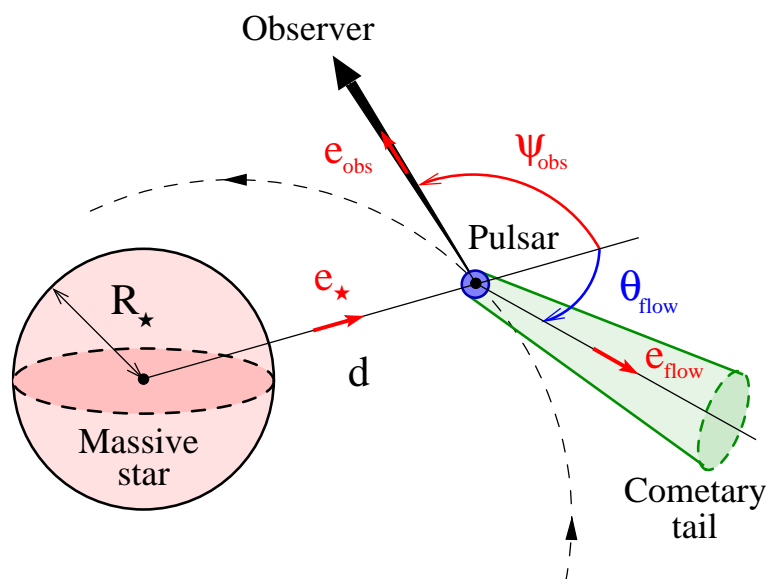


FIG. 101. Geometry in gamma-ray binaries for the calculation of the Doppler-boosted emission. The shocked pulsar wind is collimated, inclined at an angle θ_{flow} with respect to the massive star-pulsar direction and is contained in the orbital plane. A distant observer sees the system with a viewing angle ψ_{obs} . The emission originates from a very small region (blue disk) at the pulsar location.

the precise geometry and velocity of the flow should be considered as well as the radiation from cooled particles advected backward in the pulsar wind (multi-zone model).

The emission (both synchrotron and inverse Compton) is boosted at inferior conjunction and debossed at superior conjunction. Applying to our model Dubus *et al.* (2008) the Doppler boost, the X-ray modulation observed by *Suzaku* (shape and amplitude) can be well reproduced if $\beta \approx 1/3$ (Fig. 103). Note that the X-ray flux is not explained with this model. The emission from cooled particles advected in the pulsar wind probably contributes to increase the X-ray flux as done by Dubus (2006b). Alternatively, the magnetic field at the shock could be higher ($B > 1$ G) and increases the synchrotron emission in X-rays. This possibility seems unlikely as a higher magnetic field would suppress the TeV emission. Anyhow, the Doppler boost appears a viable explanation for the X-ray modulation in LS 5039.

The gamma-ray emission is also affected by the boost but the very-high energy lightcurve is almost unchanged since the TeV flux already peaks close to superior conjunction due to gamma-ray absorption. The amplitude of the TeV modulation is increased but the fit to HESS observations remains good. In the GeV energy band, the gamma-ray emission is significantly changed and cannot account for *Fermi* observations. As discussed in Sect. 8, Chapter 5, the GeV component might have a different origin and possibly comes from upstream the termination shock (unshocked wind or magnetospheric emission). Hence, the GeV emission might not be affected by the Doppler boost under consideration here.

4. LSI +61 303

In LSI +61°303, the structure of the wind is more complex and not well constrained. We assume that the pulsar wind moves in the dense equatorial disk wind of the Be companion star. This disk is thought to be almost Keplerian. Ignoring the eccentricity of the orbit, the pulsar would

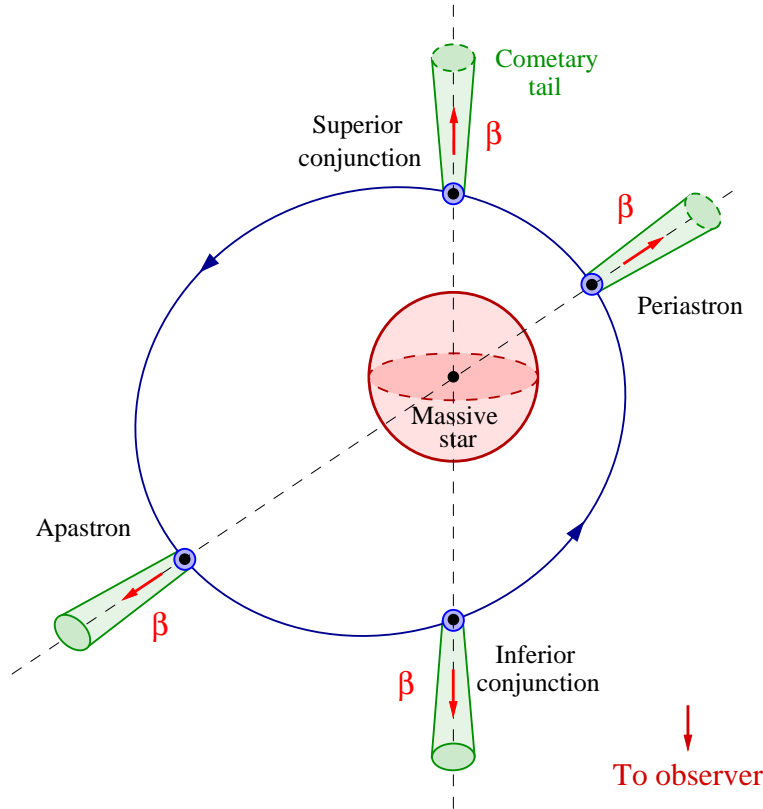


FIG. 102. Orientation of the shocked pulsar wind in LS 5039. In this system, the flow is assumed radial.

then move in a medium with no relative motion. In this case, the pulsar wind may be trailing backward in the orbit due to the orbital motion ($v_{orb} \gg v_{wind}$) and is not radial as in LS 5039. We assumed for simplicity that the shocked pulsar wind is tangent to the orbit at every orbital phase, *i.e.* $\theta_{flow} \neq 0$ (see Fig. 104).

We do not have a precise model for the non-thermal emission in LS I +61°303. As a first attempt and in order to quantify the effects of a Doppler-boost in this system, we inject electrons with a constant power law energy distribution $p = 2$ with a constant magnetic field along the orbit. If $\beta = 0$, synchrotron radiation is then constant along the orbit. Inverse Compton emission is maximum just after superior conjunction ($\phi = 0.081$ with $\phi = 0.275$ at periastron, Aragona *et al.* 2009) and is minimum at inferior conjunction ($\phi = 0.313$, see Fig. 105) as already noted in Chapter 5, Sect. 8. The Doppler-boost changes dramatically the X-ray and gamma-ray modulation (Fig. 105). If $\beta = 1/3$ and if the flow is tangent to the orbit, synchrotron and inverse Compton emission are both maximum around the orbital phase $\phi = 0.575 - 0.675$ *i.e.* close to apastron ($\phi = 0.775$), in agreement with X-ray (Anderhub *et al.* 2009) and TeV (Acciari *et al.* 2008; Albert *et al.* 2009) observations. As a result, the Doppler-boost could also provide a promising explanation for the X-ray/TeV correlation and the puzzling phasing of the maximum of the non-thermal high-energy emission in LS I +61°303.

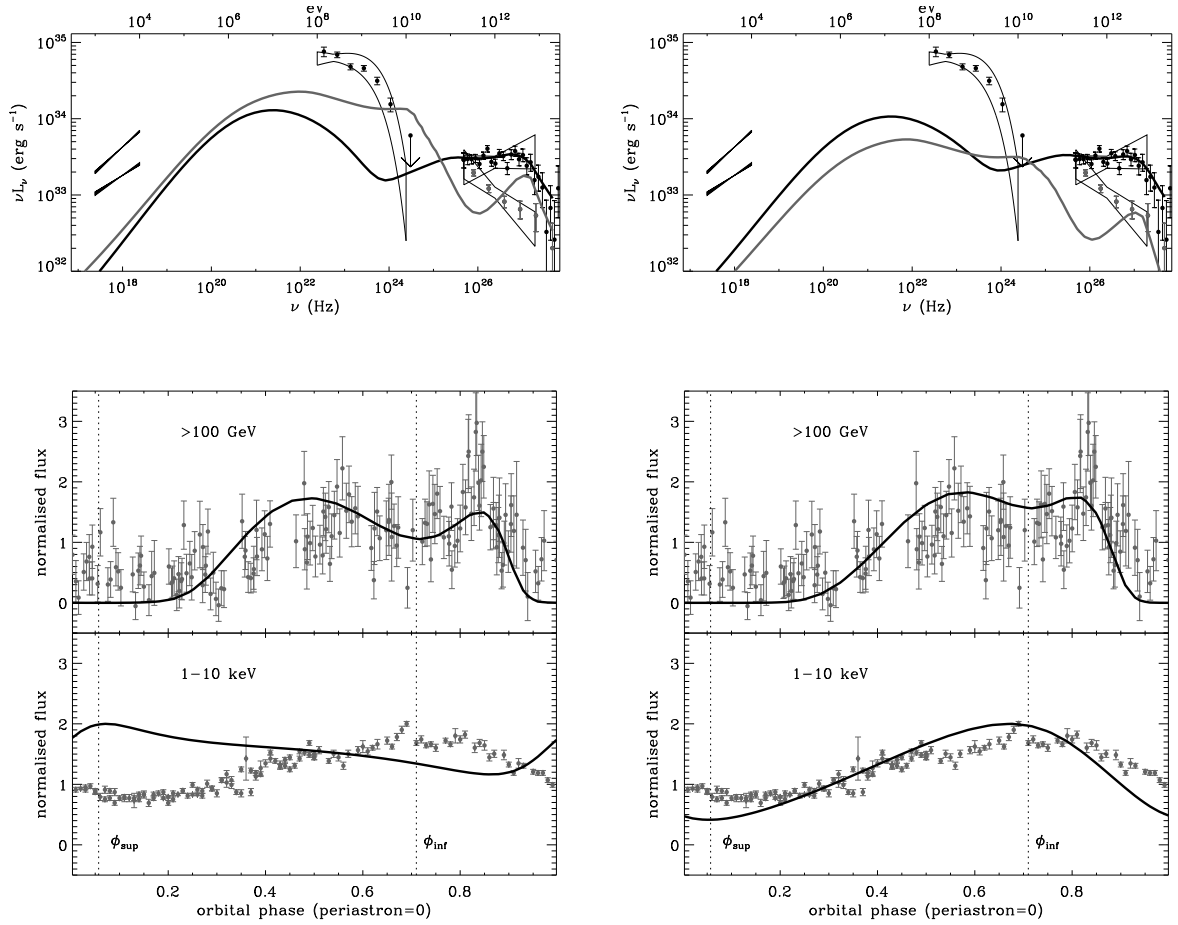


FIG. 103. *Left panels:* Theoretical non-thermal radiation expected in the one-zone leptonic model Dubus *et al.* (2008) with no Doppler boost $\beta = 0$. SUPC and INFC spectra are compared with *Suzaku* (Takahashi *et al.* 2009), *Fermi* (Abdo *et al.* 2009b) and HESS (Aharonian *et al.* 2006) bowties on the *top* panel. The expected very-high energy (*middle* panel) and X-ray (*bottom* panel) lightcurves are also shown. *Right panels:* The same as in the *left* panels with a Doppler boost $\beta = 1/3$ and $\theta_{flow} = 0^\circ$.

5. PSR B1259-63

We apply also the same model and the same assumptions as in LS I +61°303 to PSR B1259 – 63. Fig. 105 shows that the effect of a mildly relativistic Doppler boost $\beta = 1/3$ has a small impact on synchrotron and inverse Compton modulation. This is essentially because of the low inclination of the system ($i = 35^\circ$, Manchester *et al.* 1995). There is no apparent link between our results and the X-ray and gamma-ray observations. Other effects might dominate in this much elongated system.

6. What we have learned

We applied the effect of the Doppler-boosted emission in gamma-ray binaries, initially to explain the X-ray orbital modulation in LS 5039. In this model, the emission is produced by energetic pairs in a mildly relativistic shocked pulsar wind confined in the orbital plane. In LS 5039, the strong stellar wind may confine and collimate the pulsar wind flow radially. If the flow is mildly

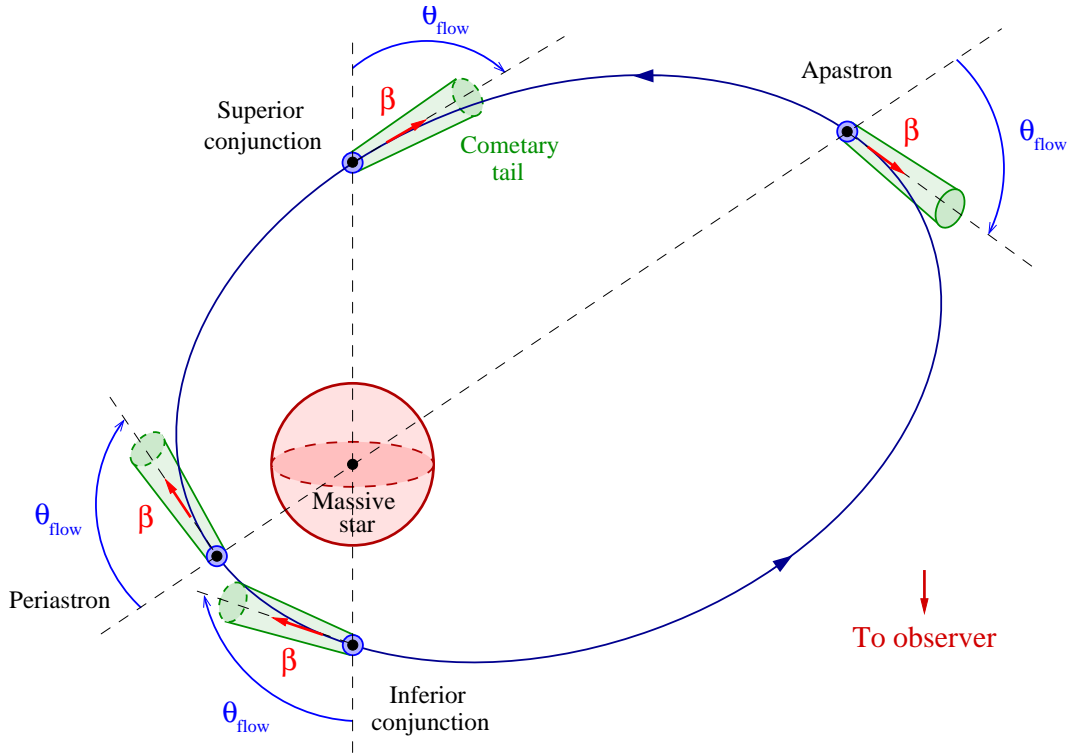


FIG. 104. Orientation of the shocked pulsar wind in LS I +61°303. In this system, the flow is assumed tangent to the orbit in the opposite direction of the orbital motion.

relativistic, the X-ray emission is boosted at conjunctions with a maximum at inferior conjunction and a minimum at superior conjunction. The shape and the amplitude of the X-ray modulation is explained if $\beta = 1/3$. The TeV emission is also affected by the Doppler-boost but the modulation is almost unchanged as the gamma-ray flux was already (*i.e.* with no boost) maximum at inferior conjunction due to pair production.

The effect of the Doppler-boost in LS I +61°303 leads to interesting results. If the pulsar moves in the slow equatorial wind of the Be companion star, the flow can be considered as tangent to the orbit. If the flow is not relativistic, the emission from electrons injected with a constant power law energy distribution along the orbit is maximum and minimum at conjunctions for inverse Compton and constant for synchrotron radiation if the magnetic field is constant. A mildly relativistic flow with $\beta = 1/3$ is sufficient to shift the maximum of synchrotron and inverse Compton emission at orbital phases around $\phi = 0.5 - 0.6$, *i.e.* close to apastron. This effect could provide a simple explanation for the observed correlation between the X-ray and the TeV emission in this system and explain also why the non-thermal flux is maximum at this non-trivial position in the orbit. This effect does not have a strong impact in PSR B1259 – 63. Other effects might dominate in this much elongated system.

This work have been accepted for publication in *Astronomy & Astrophysics* journal (Dubus *et al.* 2010a) (see Sect. 8). I presented this work in a contributed talk at the "ICREA Workshop on The High-Energy Emission from Pulsars and their Systems" (Cerutti *et al.* 2010b).

This study on the Doppler-boosted emission could also be used to compute the high-energy radiation produced in a striped pulsar wind where high-energy electrons upscatter the

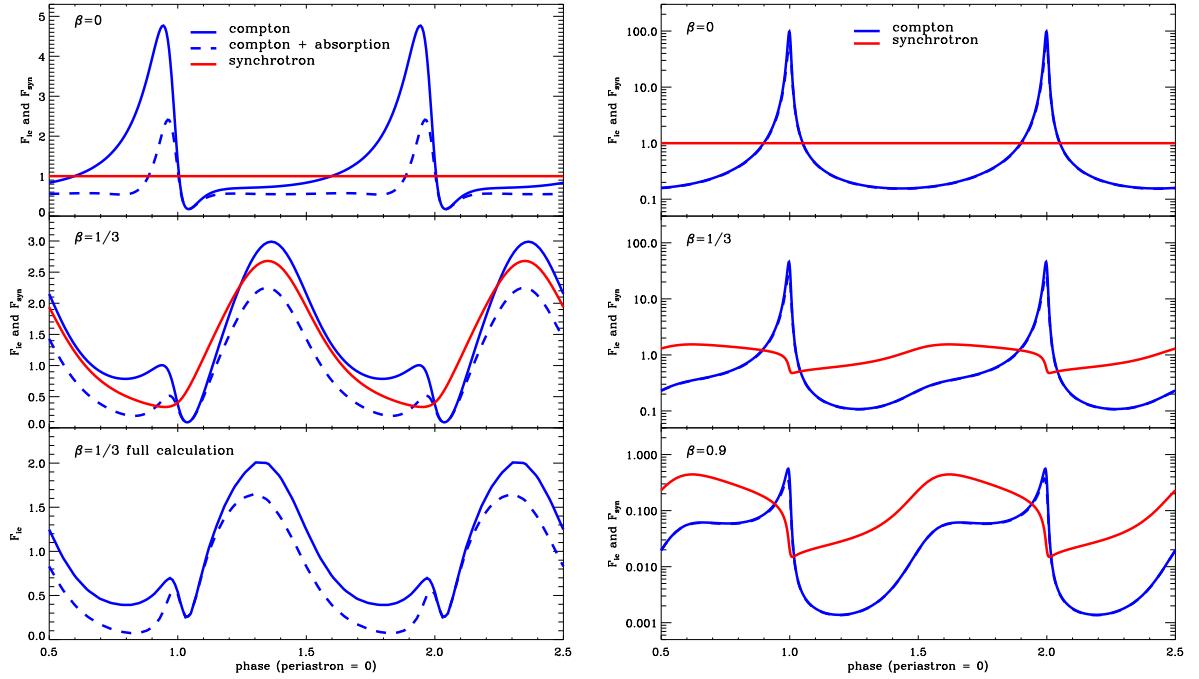


FIG. 105. *Left panels:* Theoretical synchrotron (red lines) and inverse Compton radiation (blue lines) expected in a one-zone leptonic model as a function of the orbital phase in LS I +61°303 (two full orbits). Electrons are injected with a constant power law energy distribution of index $p = 2$ and are bathed in a constant magnetic field along the orbit. In the *top* panel, synchrotron and the inverse Compton fluxes are calculated with $\beta = 0$. In the last two panels, $\beta = 1/3$ and the flow is assumed tangent to the orbit. Inverse Compton emission is computed with the analytical formula found in Eq. (80.316) (Thomson limit). The exact inverse Compton flux (with Klein-Nishina effects) computed above 100 GeV is shown in the *bottom* panel. The absorbed Compton gamma-ray lightcurve is shown with dashed line. The orbital parameters are taken from Aragona *et al.* (2009) and the origin $\phi = 0$ was chosen at periastron for this plot, *i.e.* 0.275 should be added to the phasing used in Aragona *et al.* (2009) and in the text. *Right panels:* Application to PSR B1259 – 63 with $\beta = 0$ (*top*), $1/3$ (*middle*) and 0.9 (*bottom*).

anisotropic UV flux from the stellar companion (see Chapter 5, Sect. 9). This is also another project I would be interested to work on in the future.

7. [Français] Résumé du chapitre

§ 83. Contexte et objectifs

Nos études sur l'émission amplifiée Doppler dans les binaires présentées dans le chapitre précédent, ont été motivées au départ par les nouvelles observations X par les satellites *INTEGRAL* et *Suzaku*. Hoffmann *et al.* (2009) et Takahashi *et al.* (2009) ont trouvé que l'émission X est modulée avec la période orbitale et est corrélée à l'émission au TeV dans LS 5039. Des observations précédentes par les satellites *ASCA*, *Chandra* et *XMM* montrent que le flux X est aussi très stable sur des échelles de temps s'étalant sur plusieurs années (Kishishita *et al.* 2009). Le spectre moyen mesuré par *Suzaku* dans la bande [0.6 – 70] keV s'apparente à une loi de puissance avec un indice spectral $\alpha \sim 0.5$. Le flux est maximum à proximité de la conjonction inférieure et minimum à la conjonction supérieure.

Ces caractéristiques observées suggèrent que l'émission X est reliée à la position de l'orbite par rapport à l'observateur. Dans notre modèle du vent choqué Dubus *et al.* (2008) (voir Chapitre 4), l'émission X est dominée par le rayonnement synchrotron mais la modulation orbitale attendue est extremum autour du périastre et de l'apoastre puisque le champ magnétique $B \propto 1/d$ (voir Eq. 30.140), ce qui est en désaccord avec les observations. Il serait possible d'obtenir un meilleur accord avec les observations X si, par exemple, les variations du champ magnétique suivaient la modulation X *i.e.* maximum à la conjonction inférieure et minimum à la conjonction supérieure. Même si cela est possible, un tel cas est très peu probable puisqu'il n'y a aucune raison pour que le champ magnétique pique à des phases orbitales définies uniquement par l'orientation de l'observateur par rapport au système. Takahashi *et al.* (2009) ont trouvé que la modulation X pouvait être correctement reproduite avec un modèle leptonique à une zone, si le temps de refroidissement adiabatique des leptons en X domine et pique à la conjonction inférieure. Une fois de plus, cette possibilité n'est pas très convaincante étant donné qu'il n'y a aucune motivation physique pour que les extrema du temps de refroidissement adiabatique coïncident avec les conjonctions. Nous privilégions et proposons plutôt une explication géométrique à la modulation X.

Dans le scénario du vent de pulsar, l'émission non-thermique est supposée provenir de particules relativistes rayonnant dans le vent du pulsar choqué par le vent de l'étoile massive (Chapitre 1). Dans le modèle MHD de Kennel & Coroniti (1984a) de la nébuleuse du Crabe, la vitesse du vent du pulsar en aval du choc est $c/3$ (pour une faible magnétisation, $\sigma \ll 1$), *i.e.* modérément relativiste. Si le vent stellaire est fort ($\eta \ll 1$, voir Chapitre 5, Sect. 5), le vent du pulsar peut être confiné et collimaté dans une direction. L'émission non-thermique produite dans le vent choqué du pulsar devrait alors être amplifiée due au mouvement relativiste de l'écoulement. L'amplification Doppler dépend de la position relative de l'observateur au système et pourrait expliquer la modulation X dans LS 5039. Ici, je passe en revue brièvement les principaux résultats que nous avons obtenu dans la modélisation de l'émission amplifiée Doppler dans les binaires gamma LS 5039 (Sect. 3), LS I +61°303 (Sect. 4) et PSR B1259 – 63 (Sect. 5). Plus de détails sur le modèle pourront être trouvés dans notre papier (Dubus *et al.* 2010a), inclus ici à la fin de ce chapitre (Sect. 8). Remarquons que Arons & Tavani (1993) s'attendaient à une modulation orbitale du flux X à cause de l'effet Doppler dans le système du pulsar "Black-widow" PSR B1957 + 20. Cette prédiction est en accord avec les observations récentes XMM par Huang & Becker (2007). Notons également que la modulation X pourrait être due à l'absorption dans le vent stellaire, mais ce dernier n'est pas suffisamment dense pour produire une modulation importante (Szostek & Dubus 2010, soumis).

§ 84. Ce que nous avons appris

Nous avons appliqué l'effet de l'amplification Doppler de l'émission dans les binaires gamma, initialement pour expliquer la modulation orbitale du flux X dans LS 5039. Dans ce modèle l'émission est produite par des particules énergétiques localisées dans le vent choqué modérément relativiste et confiné dans le plan orbital. Dans LS 5039, le puissant vent stellaire pourrait confiner et collimater le vent du pulsar radialement. Si l'écoulement est modérément relativiste, l'émission X est amplifiée aux conjonctions avec un maximum à la conjonction inférieure et un minimum à la conjonction supérieure. La forme et l'amplitude de la modulation

X est expliquée si $\beta = 1/3$. L'émission au TeV est également affectée par l'amplification Doppler mais la modulation est quasiment inchangée puisque le flux gamma était déjà (*i.e.* sans amplification) maximum à la conjonction inférieure en raison de la production de paires.

L'effet de l'amplification Doppler dans LS I +61°303 conduit à des résultats intéressants. Si le pulsar évolue dans le vent équatorial lent de l'étoile compagnon Be, le flot peut être considéré comme tangent à l'orbite. Si le flot n'est pas relativiste, l'émission produite par des électrons injectés avec une distribution en énergie en loi de puissance constante le long de l'orbite, est maximale et minimale aux conjonctions pour la diffusion Compton inverse et est constante pour le rayonnement synchrotron si le champ magnétique est constant. Un écoulement modérément relativiste avec $\beta = 1/3$ est suffisant pour décaler l'émission Compton inverse et synchrotron aux phases orbitale aux alentours de $\phi = 0.5 - 0.6$, *i.e.* autour de l'apoastre. Cet effet pourrait fournir une explication simple à la corrélation observée entre les X et l'émission au TeV dans ce système et expliquer aussi pourquoi le flux non-thermique est maximum à cet endroit non trivial de l'orbite. Cet effet n'a pas d'impact fort dans PSR B1259 – 63. D'autres effets pourraient dominer dans ce système bien plus allongé.

Ce travail a été accepté pour publication dans le journal *Astronomy & Astrophysics* (Dubus *et al.* 2010a) (voir Sect. 8). J'ai présenté ce travail dans une présentation orale à la conférence "ICREA Workshop on The High-Energy Emission from Pulsars and their Systems" (Cerutti *et al.* 2010b).

Cette étude sur l'amplification Doppler de l'émission pourrait être aussi utilisée pour calculer l'émission de haute énergie produite dans un vent strié de pulsar où des électrons de haute énergie diffusent le flux UV anisotrope en provenance de l'étoile compagnon (voir Chapitre 5, Sect. 9). Il s'agit d'un autre projet sur lequel je serais intéressé de travailler dans le futur.

8. Paper: Relativistic Doppler-boosted emission in gamma-ray binaries

Relativistic Doppler-boosted emission in gamma-ray binaries

Guillaume Dubus, Benoît Cerutti, and Gilles Henri

Laboratoire d'Astrophysique de Grenoble, UMR 5571 Université Joseph Fourier Grenoble I / CNRS, BP 53, 38041 Grenoble, France

Draft March 26, 2010

ABSTRACT

Context. Gamma-ray binaries could be compact pulsar wind nebulae formed when a young pulsar orbits a massive star. The pulsar wind is contained by the stellar wind of the O or Be companion, creating a relativistic comet-like structure accompanying the pulsar along its orbit.

Aims. The X-ray and the very high energy (>100 GeV, VHE) gamma-ray emission from the binary LS 5039 are modulated on the orbital period of the system. Maximum and minimum flux occur at the conjunctions of the orbit, suggesting that the explanation is linked to the orbital geometry. The VHE modulation has been proposed to be due to the combined effect of Compton scattering and pair production on stellar photons, both of which depend on orbital phase. The X-ray modulation could be due to relativistic Doppler boosting in the comet tail where both the X-ray and VHE photons would be emitted.

Methods. Relativistic aberrations change the seed stellar photon flux in the comoving frame so Doppler boosting affects synchrotron and inverse Compton emission differently. The dependence with orbital phase of relativistic Doppler-boosted (isotropic) synchrotron and (anisotropic) inverse Compton emission is calculated, assuming that the flow is oriented radially away from the star (LS 5039) or tangentially to the orbit (LS I +61°303, PSR B1259-63).

Results. Doppler boosting of the synchrotron emission in LS 5039 produces a lightcurve whose shape corresponds to the X-ray modulation. The observations imply an outflow velocity of 0.15–0.33c consistent with the expected flow speed at the pulsar wind termination shock. In LS I +61°303, the calculated Doppler boosted emission peaks in phase with the observed VHE and X-ray maximum.

Conclusions. Doppler boosting is not negligible in gamma-ray binaries, even for mildly relativistic speeds. The boosted modulation reproduces the X-ray modulation in LS 5039 and could also provide an explanation for the puzzling phasing of the VHE peak in LS I +61°303.

Key words. radiation mechanisms: non-thermal — stars: individual (LS 5039, LS I +61°303, PSR B1259-63) — gamma rays: theory — X-rays: binaries

1. Introduction

Gamma-ray binaries display non-thermal emission from radio to very high energy gamma rays (VHE, >100 GeV). Their spectral luminosities peak at energies greater than a MeV. At present, three such systems are known: PSR B1259-63 (Aharonian et al. 2005b), LS 5039 (Aharonian et al. 2005a) and LS I +61°303 (Albert et al. 2006). A fourth system, HESS J0632+057 may also be a gamma-ray binary (Hinton et al. 2009). The systems are composed of a O or Be massive star and a compact object, identified as a young radio pulsar in PSR B1259-63. All gamma-ray binaries could harbour young pulsars (Dubus 2006).

Electrons accelerated in the binary system upscatter UV photons from the companion to gamma-ray energies. The Compton scattered radiation received by the observer is anisotropic because the source of seed photons is the companion star. VHE gamma-rays will also

produce e^+e^- pairs as they propagate through the dense radiation field, absorbing part of the primary emission. This is also anisotropic. Both effects combine to produce an orbital modulation of the gamma-ray flux if the electrons are in a compact enough region. This modulation depends only on the geometry. Orbital modulations of the high-energy (HE, >100 MeV) and VHE fluxes have indeed been observed. The modulations unambiguously identify the gamma-ray source with the binary (Aharonian et al. 2006; Albert et al. 2006; Acciari et al. 2008).

Synchrotron emission can dominate over inverse Compton scattering at X-ray energies, providing additional information to disentangle geometrical effects from intrinsic variations of the source. *Suzaku* and *INTEGRAL* observations of LS 5039 have revealed a stable modulation of the X-ray flux (Takahashi et al. 2009; Hoffmann et al. 2009). Possible interpretations are discussed in §2. None are satisfying. The key point is that the X-ray flux

2

Dubus, Cerutti, Henri: Relativistic Doppler-boosted emission in gamma-ray binaries

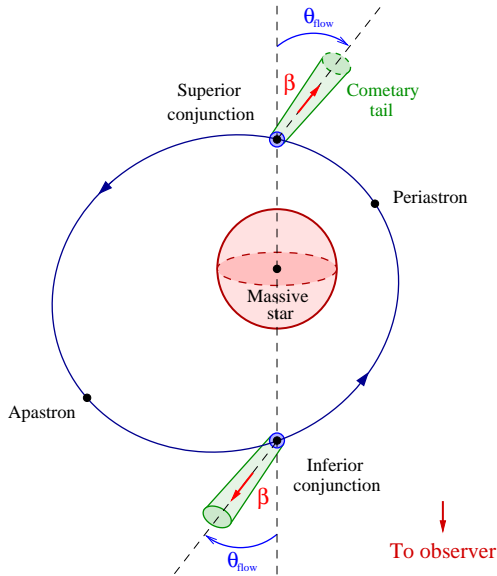


Fig. 1. Geometry of Doppler boosted emission from a collimated shock pulsar wind nebula. The orbit is that of LS 5039 (to scale). The comet tail moves away from the pulsar with a speed $\beta = v/c$ at an angle θ_{flow} . If $\theta_{\text{flow}} = 0$ then intrinsic emission in the co-moving frame is boosted in the observer frame at inferior conjunction and deboosted at superior conjunction.

is maximum and minimum at conjunctions and that this excludes any explanation unrelated to the system’s geometry as seen by the observer.

In the pulsar wind scenario, the synchrotron emission is expected to arise in shocked pulsar wind material collimated by the stellar wind. This creates a cometary tail with a mildly relativistic bulk motion (Fig. 1). Relativistic Doppler boosting of the emission due to this bulk motion is calculated in §3 with details given in Appendix A. The orbital motion leads to a modulation of the Doppler boost, as previously proposed in the context of black widow pulsars (Arons & Tavani 1993; Huang & Becker 2007). The calculated synchrotron modulation is similar to that seen in X-rays in LS 5039. Although this is not formally confirmed due to their long orbital periods, LS I +61°303 and PSR B1259-63 also appear to have modulated X-ray emission (Chernyakova et al. 2006, 2009; Acciari et al. 2009; Anderhub et al. 2009). The application to these gamma-ray binaries is discussed in §4.

2. The X-ray modulation in LS 5039

2.1. X-ray observations

LS 5039 has shown steady, hard X-ray emission since its discovery (Motch et al. 1997; Ribó et al. 1999; Reig et al. 2003; Martocchia et al. 2005; Bosch-Ramon et al. 2005, 2007). *RXTE* observations hinted at orbital variability (Bosch-Ramon et al. 2005) but confirmation had to wait the *Suzaku* and *INTEGRAL* observations (Takahashi et al. 2009; Hoffmann et al. 2009). The average spectrum seen

by *Suzaku* from 0.6 keV to 70 keV is an absorbed power-law with spectral index $\alpha = 0.51 \pm 0.02$ ($F_\nu \sim \nu^{-\alpha}$) and $N_{\text{H}} = 7.7 \pm 0.2 \times 10^{21} \text{ cm}^{-2}$ and $F_{1-10 \text{ keV}} = 8 \times 10^{-12} \text{ erg cm}^{-2} \text{ s}^{-1}$, consistent with previous observations. There is no evidence for a cutoff up to 70 keV.

Variability in *Suzaku* is dominated by a well-resolved modulation followed over an orbit and a half. The X-ray flux varies by a factor 2 with a minimum at $\phi \approx 0.1$, slightly after superior conjunction ($\phi_{\text{sup}} = 0.05$ based on Aragona et al. 2009) and a maximum at inferior conjunction ($\phi_{\text{inf}} = 0.67$). The 1–10 keV photon index is also modulated, varying between 1.61 ± 0.04 at minimum flux and 1.46 ± 0.03 at maximum flux. The comparison with *Chandra* and *XMM* measurements suggests the modulation is stable on timescales of years (Kishishita et al. 2009). The column density is constant with orbital phase, as if there were only absorption from the ISM. The lack of significant wind absorption suggests that the X-ray source is located far from the system or that the wind is highly ionised and/or has a mass-loss rate $\lesssim 10^{-7} M_{\odot} \text{ yr}^{-1}$ (Bosch-Ramon et al. 2007). Here, we assume that the X-ray source is situated within the orbital system.

2.2. Inverse Compton X-ray emission?

The phases of X-ray and VHE maximum (minimum) are identical. If both are due to inverse Compton scattering off stellar photons then maximum emissivity is at superior conjunction. Subsequent in-system absorption due to pair production moves the observed VHE maximum flux to the inferior conjunction. X-ray photons are too weak for pair production but could be absorbed in the stellar wind with a similar result. This can be ruled out since the modulation is seen in hard X-rays above 10 keV and N_{H} is constant with orbital phase. Thomson scattering of the hard X-rays is unlikely as it would require a column density of scattering electrons $\approx 10^{24} \text{ cm}^{-2}$ (e.g. a Wolf-Rayet wind as in Cyg X-3 rather than an O star wind), two orders-of-magnitude above the observed absorbing column density and plausible stellar wind column densities.

2.3. Synchrotron X-ray emission?

Alternatively, the X-ray emission is synchrotron radiation from the same electrons that emit HE and VHE γ -rays. In Dubus et al. (2008), we proposed that several features of the VHE observations could be explained by assuming continuous injection of a E^{-2} power-law of electrons at the location of the compact object in a zone with a homogeneous magnetic field B of order 1 G (Dubus et al. 2008). The synchrotron X-ray spectrum expected in this model¹ is shown in Fig. 2. It is hard with $\alpha \approx 0.5$. The

¹ Here, the injected number of fresh particles is kept constant along the orbit whereas the energy density of cooled particles had been kept constant in Dubus et al. (2008). With the energy density constant, the particle distribution varied very little with orbital phase, which highlighted the impact of

Dubus, Cerutti, Henri: Relativistic Doppler-boosted emission in gamma-ray binaries

3

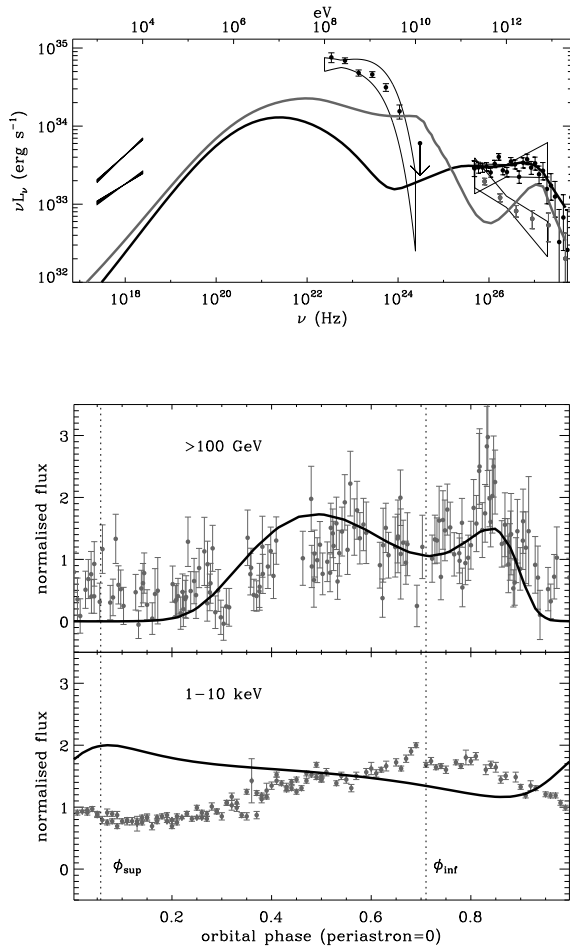


Fig. 2. Comparison of the model for LS 5039 described in §2.3 with observations. Top panel: spectral energy distribution showing the *Suzaku* 1-10 keV maximum and minimum spectra (Takahashi et al. 2009), the 100 MeV - 10 GeV average *Fermi* spectrum (Abdo et al. 2009b) and the VHE spectra averaged over phases INFC (dark points) and SUPC (grey points) as defined in Aharonian et al. (2006). The model spectra averaged over INFC and SUPC are shown as dark and grey curves. Middle and bottom panels: expected VHE gamma-ray and X-ray orbital modulation compared to the HESS and *Suzaku* observations.

electrons producing this X-ray synchrotron emission have energies between 10 GeV and 1 TeV, for which the dominant cooling mechanism is inverse Compton scattering in the Klein-Nishina regime. This keeps the steady-state distribution close to the E^{-2} power law (Fig. 3 in Dubus et al. 2008). Synchrotron cooling takes over at higher energies, causing a break to $\alpha \approx 1$. In fact, the spectral index

anisotropic scattering. However, a constant injection in number of particles is probably more realistic (at least for a pulsar wind). It has no noticeable influence on the spectra but it slightly changes the VHE lightcurve from that shown in Dubus et al. (2008). The VHE lightcurve remains compatible with the HESS results.

seen by *INTEGRAL* up to 200 keV is softer ($\alpha = 1 \pm 0.2$) than the average index measured by *Suzaku* up to 70 keV ($\alpha = 0.51 \pm 0.02$).

Whereas it is promising to have the hard X-ray spectral shape correctly reproduced, the level of X-ray emission is too low and, more importantly, the orbital X-ray lightcurve from the model is inconsistent with the observed modulation. The expected 1-10 keV lightcurve shows only a very modest change with a peak at periastron (Fig. 2). The reason is that the variations in particle and magnetic energy densities (a factor 4) compensate to keep the synchrotron emission almost constant.

2.4. Variations in parameters?

A better fit is possible by treating B or particle injection as free functions of orbital phase or by taking adiabatic losses into account. Takahashi et al. (2009) argued that the X-ray spectrum necessarily implies dominant adiabatic cooling of an E^{-2} electron distribution (this is sufficient but not necessary: as discussed above, Klein-Nishina cooling also keeps the distribution hard). The X-ray and VHE observations were then fitted by adjusting the adiabatic timescale t_{ad} with orbital phase. The derived variation in t_{ad} mirrors the X-ray lightcurve with t_{ad} reaching a maximum at ϕ_{inf} . There is no obvious reason why t_{ad} should peak at this phase. Takahashi et al. (2009) expect the variation in t_{ad} to reflect variations in the size of the emitting zone, itself modulated by the external pressure of the wind. The relevant phases are those of apastron (low pressure) and periastron (high pressure), but not inferior conjunction which is an observer-dependent phase unrelated to wind pressure. In LS 5039, ϕ_{inf} is significantly different from the phases of periastron and apastron passage. Hence, it would require a coincidence for any intrinsic change in the source (B , number of particles, t_{ad} , size, etc) to result in a peak at this conjunction.

The link between the extrema of the X-ray lightcurve and conjunctions calls for a *geometrical* explanation related to how the observer views the X-ray source. Doppler boosting (see Fig. 1) is a possible solution to this puzzle.

3. Relativistic Doppler boosting

In the interacting winds scenario, the X-ray emission is expected to occur beyond the shock where the ram pressures balance (Bignami et al. 1977; Maraschi & Treves 1981; Tavani et al. 1994; Dubus 2006). Particles in the shocked pulsar wind are randomized and accelerated. MHD jump conditions for a perpendicular shock and a low magnetisation pulsar wind give a post-shock flow speed of $c/3$ (Kennel & Coroniti 1984). If the ratio of wind momenta $\eta = (\dot{E}_{\text{p}}/c)/(\dot{M}_{\star}v_{\star})$ is small then the shocked pulsar wind is confined by the stellar wind. The shocked wind flows away from the companion star forming a comet-like tail of emission. Relativistic hydrodynamical calculations show

4

Dubus, Cerutti, Henri: Relativistic Doppler-boosted emission in gamma-ray binaries

the flow is conical with an opening angle set by η and can reach highly relativistic speeds (Bogovalov et al. 2008). High energy electrons emit VHE gamma-rays and synchrotron X-rays close to the pulsar and lose energy as they flow out, emitting in the radio band far from the system (Dubus 2006). Here, the relativistic electrons radiating X-rays (by synchrotron) and VHE γ -rays (by inverse Compton) are assumed to be localized at the compact object location. The calculation of the relativistic Doppler boosting in the flow is general and can also be applied e.g. to the case of a relativistic jet in a binary (Dubus et al. 2010).

3.1. Synchrotron

Even if the flow is only mildly relativistic, Doppler boosting can introduce a geometry-dependent modulation of emission that is isotropic in the comoving frame (Fig. 1). This will be the case for synchrotron emission. The relativistic boost is given by

$$\mathcal{D}_{\text{obs}} = \frac{1}{\Gamma(1 - \beta \mathbf{e}_{\text{obs}} \cdot \mathbf{e}_{\text{flow}})} \quad (1)$$

where \mathbf{e}_{flow} is the unit vector along the direction of the flow and \mathbf{e}_{obs} is the unit vector from the emission site, assumed to be the compact object location, to the observer. The flow will be assumed to be in the orbital plane where it makes an angle θ_{flow} to the star - compact object direction.

The outgoing energy will be modified by $\epsilon = \mathcal{D}_{\text{obs}} \epsilon'$ and the outgoing flux will be $F_{\nu}(\epsilon) = \mathcal{D}_{\text{obs}}^3 F'_{\nu}(\epsilon')$, with primed quantities referring to the comoving frame. In the case of a constant synchrotron power-law spectrum in the comoving frame with index α then

$$F_{\text{syn}} \propto \mathcal{D}_{\text{obs}}^{3+\alpha} \quad (2)$$

The ratio of maximum to minimum flux is (see also Pelling et al. 1987)

$$\frac{F_{\text{max}}}{F_{\text{min}}} = \left(\frac{1 + \beta \sin i}{1 - \beta \sin i} \right)^{3+\alpha} \approx 8 \quad (3)$$

for $\beta=1/3$, $i=60^\circ$, $\alpha=0.5$. Relativistic boosting can significantly change the theoretical X-ray lightcurve discussed in §2. In the case of a purely radial flow ($\theta_{\text{flow}}=0^\circ$), maximum (minimum) boost occurs at the inferior (superior) conjunction ($\psi_{\text{obs}} = \pi/2 - i$ or $\pi/2 + i$) where the flow is directed towards (away from) the observer.

3.2. Inverse Compton

Inverse Compton emission will also be modified by relativistic aberration. The spectrum of the target photons seen in a given solid angle in the comoving flow frame will be changed according to a different relativistic transform. If the star is assumed to be point-like, the relativistic boost involved is

$$\mathcal{D}_{\star} = \frac{1}{\Gamma(1 - \beta \mathbf{e}_{\star} \cdot \mathbf{e}_{\text{flow}})} \quad (4)$$

The total energy density from the star in the flow frame is

$$u_{\star} = \mathcal{D}_{\star}^{-2} \pi \left(\frac{R_{\star}}{d} \right)^2 \frac{a_{\text{SB}} T_{\star}^4}{4\pi} \quad (5)$$

with the Stefan-Boltzmann constant $a_{\text{SB}} = 7.56 \cdot 10^{-15} \text{ erg cm}^{-3} \text{ K}^{-4}$. The angle ψ under which scattering occurs will also be changed. This angle ($\cos \psi' = \mathbf{e}'_{\star} \cdot \mathbf{e}'_{\text{obs}}$) is given in Appendix A. The inverse Compton spectrum is then calculated in the comoving frame as in Dubus et al. (2008). The resulting spectrum is then transformed back to the observer frame as in §3.1.

Because of this double transform, and because of the intrinsic orbital phase dependence of scattering on stellar photons, the Doppler-boosted inverse Compton flux variability can be quite different from the Doppler-boosted synchrotron variability. In the case of Thomson scattering off a power-law of electrons $dN \propto \gamma^{-p} d\gamma$ (see Appendix A)

$$F_{\text{ic}} \propto \mathcal{D}_{\text{obs}}^{3+p} (1 - \mathbf{e}_{\star} \cdot \mathbf{e}_{\text{obs}})^{\frac{p+1}{2}} d^{-2} \quad (6)$$

Note that F_{ic} takes into account the decrease in target photon density with distance d to the star since the orbits are not circular. Test calculations show this approximation captures the main features of the full calculation at high energies, including in the Klein-Nishina regime (see also Georganopoulos et al. 2001). It will be used to discuss the behaviour of the inverse Compton emission.

4. Discussion

The Doppler-boosted synchrotron (F_{syn} , Eq. 2) and inverse Compton (F_{ic} , Eq. 6) intensity variations were calculated for the three gamma-ray binaries and are discussed here. Full calculations were also carried out for LS 5039 and LS I +61°303. The orbital parameters are taken from Manchester et al. (1995) for PSR B1259-63 and from Aragona et al. (2009) for LS 5039 and LS I +61°303. The inclination i is assumed to be $i=30^\circ$ for PSR B1259-63, and 60° for both LS 5039 and LS I +61°303 (Dubus 2006).

4.1. LS 5039

LS 5039 has a stellar wind velocity ($v_w \approx 2500 \text{ km s}^{-1}$) significantly greater than the compact object orbital velocity ($v_{\text{orb}} \leq 400 \text{ km s}^{-1}$) so that the cometary flow is assumed to be purely radial ($\theta_{\text{flow}} = 0$). Doppler boosting leads to peaks and troughs for the synchrotron emission F_{syn} at conjunctions as outlined in §3 (Fig. 3). The amplitude of the inverse Compton flux (F_{ic}) is reduced as the increased scattering rate at superior conjunction is compensated by a deboost of \mathcal{D}_{obs} (and vice-versa at inferior conjunction). The shape of the modulation does not change much. The bottom panel shows that F_{syn} follows well the *Suzaku* data when β is adjusted to 0.15 in order to match the X-ray modulation amplitude. The spectral

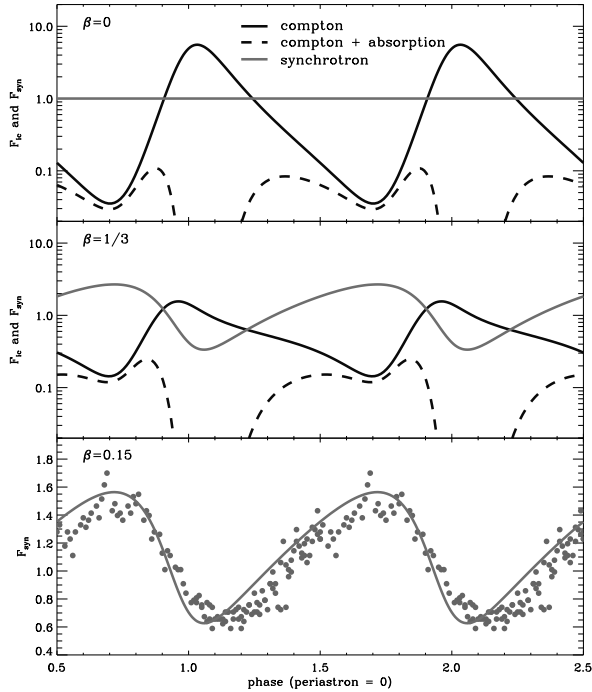


Fig. 3. Doppler-boosted synchrotron (F_{syn} , Eq. 2) and inverse Compton (F_{ic} , Eq. 6) intensity variations for LS 5039 assuming $\beta=0$ (top), $\beta=1/3$ (middle), $\beta=0.15$ (bottom). In all panels α is 0.5 (equivalent to $p=2$) as given by the X-ray spectrum. The flow direction is radial ($\theta_{\text{flow}} = 0^\circ$). Dashed lines show F_{ic} after attenuation due to pair production at 1 TeV. The bottom panel shows a comparison of F_{syn} with the *Suzaku* X-ray measurements of Takahashi et al. (2009). The X-ray data is multiplied by a constant renormalization factor and $\beta=0.15$ to match the X-ray amplitude.

index is fixed to the value observed by *Suzaku*, $\alpha = 0.5$ (equivalent to $p=2$ for the electron distribution). However, this assumes the intrinsic synchrotron emission is constant with orbital phase, unlike what happens in the model discussed in §2 and shown in Fig. 2.

The precise relativistic corrections were applied to the model discussed in §2 (Fig. 2), assuming $\beta = 1/3$. No other changes were made. The average level of X-ray emission is not changed much. However, the relativistic corrections move the peak X-ray flux to superior conjunction and increase the amplitude of the variations, bringing the model X-ray lightcurve very close to the observations (shown in the bottom panel of Fig. 2). The spectral shape is slightly harder than the observed one by about 0.15 in the index α . The orbital modulation of α follows the X-ray lightcurve with a hardening of α from 0.42 (superior conjunction) to 0.30 (inferior conjunction), which is similar in amplitude to the hardening observed by *Suzaku* (§2.1). However, the average level of X-ray emission is systematically too low compared to the observations. Increasing the magnetic field by a factor 3 would be sufficient to raise the level of X-ray flux but this would also modify the VHE spectrum,

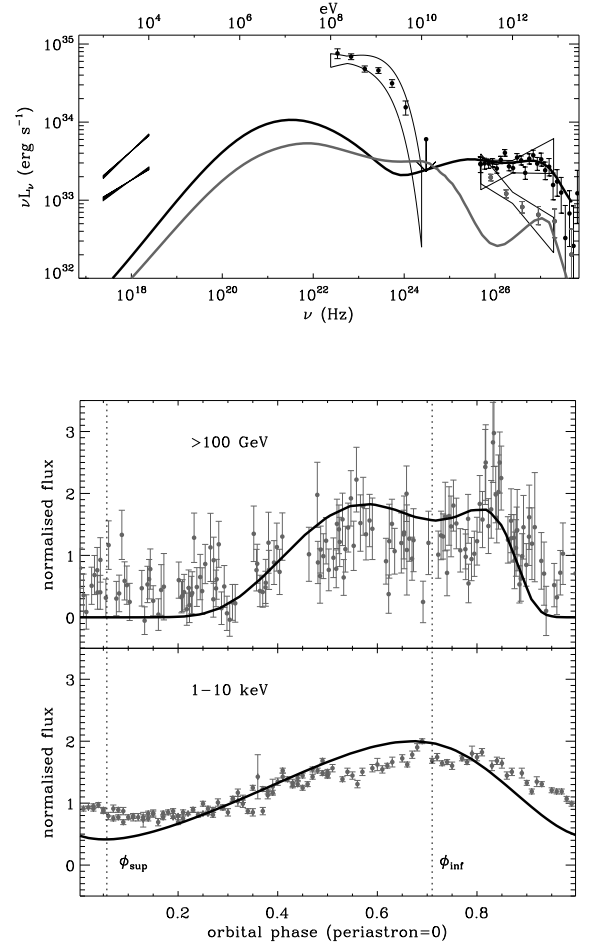


Fig. 4. Same as Fig. 1 but with the corrections due to relativistic motion taken into account. The flow is assumed to originate at the compact object location with $\beta = 1/3$ and to point radially outwards from the star.

bringing the break at a few TeV to energies that are too low. The model assumes all the emission arises within a single zone and this could explain this shortcoming. The X-ray (and GeV) emission come from electrons that have significantly cooled since their injection and, thus, this emission would be more likely to be affected by a more detailed model where particle cooling is followed along the flow, as done in Dubus (2006) based on the Kennel & Coroniti (1984) model for pulsar wind nebula. Numerical simulations are needed to provide detailed constraints on the geometry and physical conditions in the post-shock flow.

As expected, the VHE gamma-ray lightcurve is not affected much by the corrections because most of the escaping VHE gamma-rays are emitted close to inferior conjunction (as a result of the $\gamma\gamma$ opacity). The modified VHE spectrum for SUPC phases is actually better than the original model that overestimated the VHE flux at a few TeV. Pair cascading can fill in the flux between 30 GeV and a few TeV at this phase (Cerutti et al., submitted). At

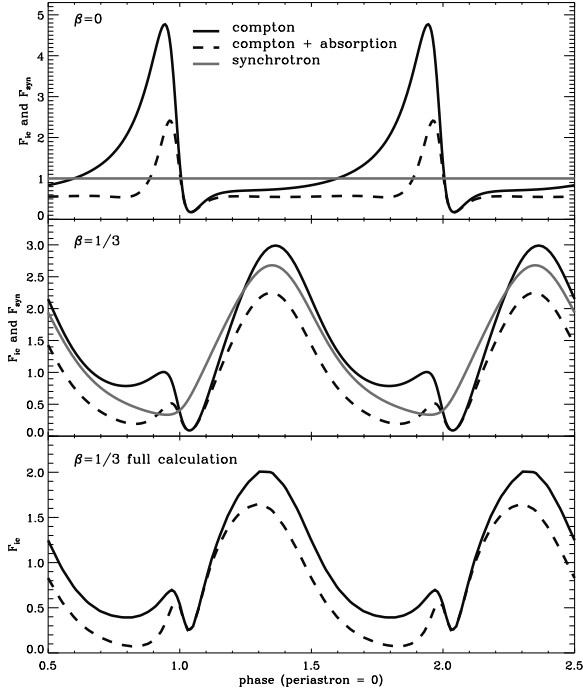


Fig. 5. Doppler-boosted synchrotron (F_{syn} , Eq. 2) and inverse Compton (F_{ic} , Eq. 6) intensity variations for LS I +61°303 assuming $\beta=0$ (top) and $1/3$ (middle). Here, the direction of the flow is assumed to be tangent to the orbit ($\theta_{\text{flow}} \neq 0$). The bottom panel shows the inverse Compton emission above 100 GeV using the full calculation instead of Eq. 6. Dashed lines show the inverse Compton emission after absorption due to pair production. In all panels a $p=2$ power-law of electrons, corresponding to $\alpha=0.5$ for synchrotron, is assumed. An offset of 0.275 should be added to the above phases to compare with the radio-based ephemeris of LS I +61°303.

HE gamma-ray energies, in the *Fermi* range, the average flux level is reduced significantly because most of the HE gamma rays arise at superior conjunction where the flow deboosts the emission. *Fermi* observations of LS 5039 and LS I +61°303 show that the HE gamma-ray emission cuts off exponentially at a few GeV, suggesting the emission in the *Fermi* range (100 MeV - 10 GeV) is a distinct component from the shocked flow (Abdo et al. 2009a,b). This could be due to pulsar magnetospheric emission, in which case the relativistic corrections and model discussed here will not apply to the GeV component.

4.2. LS I +61°303

The impact of the relativistic Doppler corrections in LS I +61°303 (and PSR B1259-63) is more difficult to assess because the orientation of the cometary flow is uncertain. The wind of the Be stellar companion is thought to be composed of a fast, tenuous polar wind and, more prominently, a slow, dense equatorial wind. These equatorial winds are effectively Keplerian discs with a small out-

flow velocity (compared to their angular velocity). If the compact object moves through this disc, then (neglecting corrections due to the orbital eccentricity) it is essentially moving through a static medium in the corotating frame, suggesting the outcome is more likely to be cometary flow trailing the orbit rather than directed radially away from the companion star. This will have to be confirmed by numerical simulations of the interaction.

VHE observations by the MAGIC and VERITAS collaborations consistently find that the peak VHE emission occurs at phases 0.6-0.7 using the historical radio ephemeris (Acciari et al. 2008; Albert et al. 2009). The best estimation of the periastron passage phase in this ephemeris is 0.275 (Aragona et al. 2009), hence there is an offset of 0.275 between the radio ephemeris used by observers and the one used here. As outlined in §2, the phases of periastron/apastron passage or the conjunctions are the natural phases where the physical conditions or the configuration of the system would be expected to produce minima or maxima in the lightcurves. The peak VHE flux occurs 2 to 5 days before apastron and is clearly not associated with any of those phases, making it difficult to interpret only with anisotropic inverse Compton emission and pair production.

Superior conjunction in LS I +61°303 occurs slightly before periastron passage, and inferior conjunction slightly after. The inverse Compton peak and trough match exactly with the conjunctions when there is no correction (top panel, Fig. 5). Doppler corrections have a strong impact on the inverse Compton lightcurve. Figure 5 shows the correction factors for LS I +61°303 if the flow velocity vector is taken to be exactly tangent to the orbit. The maximum boost is around phases 0.3-0.4 and the emission is deboosted around periastron passage. The effect is strong enough to push the maximum of F_{ic} and F_{syn} at phases 0.57-0.67, using the radio ephemeris, as observed. The correlated behaviour is also consistent with the X-ray and VHE observations reported in Anderhub et al. (2009). These conclusions also hold when doing a full calculation (bottom panel, Fig. 5) to properly take into account the Klein-Nishina cross-section. The calculation assumed a constant power-law distribution of electrons with $p=2$. The VHE spectrum is $F_{\nu} \sim \nu^{-2}$ because of Klein-Nishina effects and the X-ray spectrum is $F_{\nu} \propto \nu^{-0.5}$, both of which agree with observations.

4.3. PSR B1259-63

The case of PSR B1259-63 was also explored under the same assumption as LS I +61°303 (Fig. 6). The inclination is relatively low $i = 30^\circ$ so that F_{ic} is almost symmetric without Doppler corrections (top panel). Looking at the top two panels, it can be seen that the Doppler corrections have little impact on the overall lightcurve because of the low inclination. The bottom panel shows that high Doppler factors can strongly deboost the overall lightcurve even though the morphology remains roughly the same.

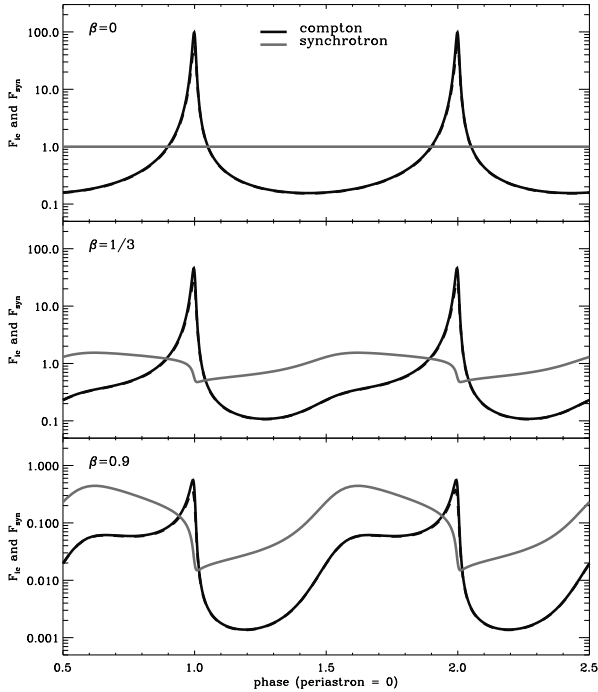


Fig. 6. Doppler-boosted synchrotron (F_{syn} , Eq. 2) and inverse Compton (F_{ic} , Eq. 6) intensity variations for PSR B1259-63 assuming $\beta=0$ (top), $1/3$ (middle) and 0.9 (bottom). The direction of the flow is assumed to be tangent to the orbit ($\theta_{\text{flow}} \neq 0$). Note the logarithmic y-axis scale. Gamma-ray absorption is negligible here.

There is no obvious relationship between these curves and the (sparse) X-ray or VHE observations. Other variability factors probably dominate in this much wider binary system.

Bogovalov et al. (2008) carried out relativistic hydrodynamical simulations of a pulsar wind interacting with a stellar wind with the specific case of PSR B1259-63 in mind. They found that the shocked pulsar wind can accelerate from bulk Lorentz factors ≈ 1 close to the termination shock up to 100 far away. Emission from such highly relativistic flows is not compatible with observations: the emission would be strongly deboosted (bottom panel, Fig. 6) except where (and if) the line-of-sight crosses the relativistic beaming angle where it would produce a flare. The observed X-ray and VHE modulations in gamma-ray binaries suggest modest boosting. The X-ray and VHE emission is more likely to originate close to the termination shock where the jump conditions for an unmagnetized relativistic flow give $\beta = 1/3$ (Kennel & Coroniti 1984).

5. Conclusion

The X-ray orbital modulation of LS 5039 peaks and falls at conjunctions, suggesting that the underlying mechanism is related to the geometry seen by the observer. Phase-

dependent Doppler boosting of emission from a mildly relativistic flow provides a viable explanation. The underlying assumption is that the flow direction changes with orbital phase, so that even constant intrinsic emission becomes variable as seen by the observer. The peaks and troughs are at conjunctions for a flow directed radially away from the star, as expected if the emission arises from a shocked pulsar wind confined by the fast stellar wind of its companion (Dubus 2006). A moderate relativistic speed of $\beta = 0.15$ or $1/3$ is enough to reproduce the morphology of the observed X-ray lightcurve assuming (resp.) either constant intrinsic emission or the model of Dubus et al. (2008). Note that these values of β allow for quite large values of the opening angles. More detailed calculations assuming a conical geometry for the flow confirmed that the results were unchanged as long as the angular size of the flow is smaller than $1/\Gamma$ (if larger, the modulation is dampened). Reproducing the level of X-ray emission is difficult with a one-zone model as it requires values of the magnetic field that are a factor 3 above current values, leading to cutoff in the VHE spectra at energies that are too low. A more complex multi-zone model of the post-shock flow might resolve this discrepancy.

Inverse Compton scattering in the flow of external stellar photons will be modulated differently than intrinsic emission from the flow. In the case of a radial outflow, the external seed photon flux will be deboosted at all phases. However, a flow tangent to an eccentric orbit, as might arise in LS I +61°303 and PSR B1259-63, can lead both to boosts and deboosts in the comoving frame depending on orbital phase and thus give rise to complex modulations. The calculated Doppler corrected emission in LS I +61°303 peaks in phase with the observed VHE maximum. This is noteworthy since a simple explanation had not yet been proposed for the phase of VHE (and X-ray) maximum in LS I +61°303. This explanation requires that the shocked pulsar wind flows along the orbit, which appears compatible with the radio VLBI images on larger scales shown in Dhawan et al. (2006).

The present work assumed a pulsar relativistic wind in the orbital plane but microquasar models have also been proposed for both LS 5039 and LS I +61°303. In this case, the emission arises from a relativistic jet. The jet angle to the observer remains constant along the orbit and so do \mathcal{D}_{obs} and F_{syn} . Hence, no orbital modulation of intrinsic (synchrotron) X-ray emission due to Doppler boosting would be expected, apart from the possible impact of jet precession on timescales longer than the orbital period (Kaufman Bernadó et al. 2002). Doppler boosting in a relativistic jet cannot explain the X-ray modulation in LS 5039 or LS I +61°303. However, unless the electrons are far from the system or the system is seen pole-on, the angle of interaction between photons and electrons $\mathbf{e}_* \cdot \mathbf{e}_{\text{obs}}$ will change with orbital phase. A modulation in F_{ic} is unavoidable. This variation in inverse Compton emission can explain the orbital modulation seen in high-energy gamma-rays from the microquasar Cygnus X-3 by *Fermi*

Gamma-ray Space Telescope (Abdo et al. 2009c; Dubus et al. 2010).

Acknowledgements. We thank T. Takahashi for sharing the data points plotted in Fig. 2. The authors acknowledge support from the European Community via contract ERC-StG-200911.

References

- Abdo, A. A., Ackermann, M., Ajello, M., et al. 2009a, *ApJ*, 701, L123
- Abdo, A. A., Ackermann, M., Ajello, M., et al. 2009b, *ApJ*, 706, L56
- Abdo, A. A., Ackermann, M., Ajello, M., et al. 2009c, *Science*, 326, 1512
- Acciari, V. A., Aliu, E., Arlen, T., et al. 2009, *ApJ*, 700, 1034
- Acciari, V. A., Beilicke, M., Blaylock, G., et al. 2008, *ApJ*, 679, 1427
- Aharonian, F., Akhperjanian, A. G., Aye, K.-M., et al. 2005a, *Science*, 309, 746
- Aharonian, F., Akhperjanian, A. G., Aye, K.-M., et al. 2005b, *A&A*, 442, 1
- Aharonian, F., Akhperjanian, A. G., Bazer-Bachi, A. R., et al. 2006, *A&A*, 460, 743
- Albert, J., Aliu, E., Anderhub, H., et al. 2009, *ApJ*, 693, 303
- Albert, J., Aliu, E., Anderhub, H., et al. 2006, *Science*, 312, 1771
- Anderhub, H., Antonelli, L. A., Antoranz, P., et al. 2009, *ApJ*, 706, L27
- Aragona, C., McSwain, M. V., Grundstrom, E. D., et al. 2009, *ApJ*, 698, 514
- Arons, J. & Tavani, M. 1993, *ApJ*, 403, 249
- Bignami, G. F., Maraschi, L., & Treves, A. 1977, *A&A*, 55, 155
- Bogovalov, S. V., Khangulyan, D. V., Koldoba, A. V., Ustyugova, G. V., & Aharonian, F. A. 2008, *MNRAS*, 387, 63
- Bosch-Ramon, V., Motch, C., Ribó, M., et al. 2007, *A&A*, 473, 545
- Bosch-Ramon, V., Paredes, J. M., Ribó, M., et al. 2005, *ApJ*, 628, 388
- Chernyakova, M., Neronov, A., Aharonian, F., Uchiyama, Y., & Takahashi, T. 2009, *ArXiv e-prints*
- Chernyakova, M., Neronov, A., & Walter, R. 2006, *MNRAS*, 372, 1585
- Dermer, C. D. & Schlickeiser, R. 1993, *ApJ*, 416, 458
- Dermer, C. D., Schlickeiser, R., & Mastichiadis, A. 1992, *A&A*, 256, L27
- Dhawan, V., Mioduszewski, A., & Rupen, M. 2006, in *VI Microquasar Workshop: Microquasars and Beyond*, Vol. MQW6 (Proceedings of Science), 52
- Dubus, G. 2006, *A&A*, 456, 801
- Dubus, G., Cerutti, B., & Henri, G. 2008, *A&A*, 477, 691
- Dubus, G., Cerutti, B., & Henri, G. 2010, *MNRAS*, accepted, arXiv1002.3888D
- Georganopoulos, M., Kirk, J. G., & Mastichiadis, A. 2001, *ApJ*, 561, 111

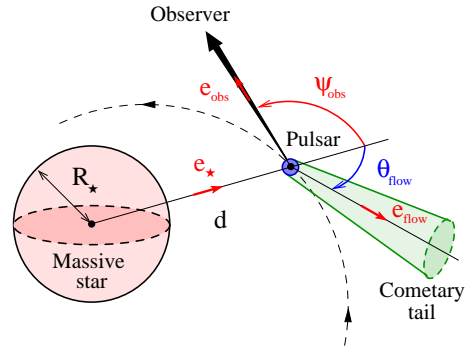


Fig. A.1. Geometry of the binary + pulsar wind nebula flow system. The calculations assume that the massive star is point-like and that emission in the tail is limited to a small region at the pulsar location.

- Hinton, J. A., Skilton, J. L., Funk, S., et al. 2009, *ApJ*, 690, L101
- Hoffmann, A. D., Klochkov, D., Santangelo, A., et al. 2009, *A&A*, 494, L37
- Huang, H. H. & Becker, W. 2007, *A&A*, 463, L5
- Kaufman Bernadó, M. M., Romero, G. E., & Mirabel, I. F. 2002, *A&A*, 385, L10
- Kennel, C. F. & Coroniti, F. V. 1984, *ApJ*, 283, 694
- Kishishita, T., Tanaka, T., Uchiyama, Y., & Takahashi, T. 2009, *ApJ*, 697, L1
- Manchester, R. N., Johnston, S., Lyne, A. G., et al. 1995, *ApJ*, 445, L137
- Maraschi, L. & Treves, A. 1981, *MNRAS*, 194, 1P
- Martocchia, A., Motch, C., & Negueruela, I. 2005, *A&A*, 430, 245
- Motch, C., Haberl, F., Dennerl, K., Pakull, M., & Janot-Pacheco, E. 1997, *A&A*, 323, 853
- Pelling, R. M., Paciesas, W. S., Peterson, L. E., et al. 1987, *ApJ*, 319, 416
- Reig, P., Ribó, M., Paredes, J. M., & Martí, J. 2003, *A&A*, 405, 285
- Ribó, M., Reig, P., Martí, J., & Paredes, J. M. 1999, *A&A*, 347, 518
- Takahashi, T., Kishishita, T., Uchiyama, Y., et al. 2009, *ApJ*, 697, 592
- Tavani, M., Arons, J., & Kaspi, V. M. 1994, *ApJ*, 433, L37

Appendix A: Doppler boosted inverse Compton emission on stellar photons

The star is approximated as a point source of photons and the electrons are confined in a very small region. The overall geometry and vectors are shown in Fig. A.1. In the point-like and mono-energetic approximation, the stellar photon density in the observer frame is

$$\frac{dn}{ded\Omega} = n_0 \delta(\epsilon - \epsilon_0) \delta(\mu - \mu_0) \quad (\text{A.1})$$

where ϵ_0 is the incoming photon energy and μ_0 is the cosine of the angle between the incoming photon and the

electron direction. Applying relativistic transforms to go to the comoving frame gives

$$\frac{dn'}{d\epsilon'd\Omega'} = \Gamma^2 (1 - \beta \mathbf{e}_\star \cdot \mathbf{e}_{\text{flow}})^2 \frac{dn}{d\epsilon d\Omega} = \mathcal{D}_\star^{-2} \frac{dn}{d\epsilon d\Omega} \quad (\text{A.2})$$

Developing the Dirac functions leads to

$$\frac{dn'}{d\epsilon'd\Omega'} = n'_0 \delta(\epsilon' - \epsilon'_0) \delta(\mu' - \mu'_0) \quad (\text{A.3})$$

with $n'_0 = \mathcal{D}_\star^{-1} n_0$ and $\epsilon'_0 = \mathcal{D}_\star^{-1} \epsilon_0$. For inverse Compton scattering on an isotropic distribution of electrons in the comoving frame, $\mu'_0 \approx \mathbf{e}'_\star \cdot \mathbf{e}'_{\text{obs}}$ (Dubus et al. 2008). The unit vector \mathbf{e}'_\star transforms in the comoving frame as

$$\mathbf{e}'_\star = \frac{\mathbf{e}_\star + [(\Gamma - 1)(\mathbf{e}_\star \cdot \mathbf{e}_{\text{flow}}) - \Gamma\beta] \mathbf{e}_{\text{flow}}}{\Gamma(1 - \beta \mathbf{e}_\star \cdot \mathbf{e}_{\text{flow}})} \quad (\text{A.4})$$

The transform giving \mathbf{e}'_{obs} is simply given by replacing \mathbf{e}_\star with \mathbf{e}_{obs} above. The dot product of the two vectors in the comoving frame simplifies to

$$1 - \mathbf{e}'_\star \cdot \mathbf{e}'_{\text{obs}} = \mathcal{D}_{\text{obs}} \mathcal{D}_\star (1 - \mathbf{e}_\star \cdot \mathbf{e}_{\text{obs}}) \quad (\text{A.5})$$

The anisotropic inverse Compton scattering kernel in Dubus et al. (2008) can then be used, with the photon density given in Eq. A.3 and with the direction given by $\mathbf{e}'_\star \cdot \mathbf{e}'_{\text{obs}}$. The resulting outgoing spectrum is then transformed back to the observer frame by using $\epsilon_1 = \mathcal{D}_{\text{obs}} \epsilon'_1$ and $F_\nu(\epsilon_1) = \mathcal{D}_{\text{obs}}^3 F'_\nu(\epsilon'_1)$ as discussed in §3.1. \mathcal{D}_{obs} is defined in Eq. 1 and ϵ_1 is the outgoing photon energy.

For inverse Compton emission by a power-law distribution of electrons in the Thomson regime, the spectrum in the comoving frame is given by

$$F'_\nu(\epsilon'_1) = K n'_0 (1 - \mathbf{e}'_\star \cdot \mathbf{e}'_{\text{obs}})^{\frac{p+1}{2}} \left(\frac{\epsilon'_1}{\epsilon'_0} \right)^{\frac{1-p}{2}} \quad (\text{A.6})$$

where p is the power-law index and K is a constant. In this case, the spectrum seen by the observer is

$$F_\nu(\epsilon_1) = K n_0 \mathcal{D}_\star^{-1-\alpha} \mathcal{D}_{\text{obs}}^{3+\alpha} (1 - \mathbf{e}'_\star \cdot \mathbf{e}'_{\text{obs}})^{\alpha+1} \left(\frac{\epsilon_1}{\epsilon_0} \right)^{-\alpha} \quad (\text{A.7})$$

so that, using the dot product in Eq. A.5,

$$F_\nu(\epsilon_1) = K n_0 \mathcal{D}_{\text{obs}}^{4+2\alpha} (1 - \mathbf{e}_\star \cdot \mathbf{e}_{\text{obs}})^{\alpha+1} \left(\frac{\epsilon_1}{\epsilon_0} \right)^{-\alpha} \quad (\text{A.8})$$

where $\alpha \equiv (p - 1)/2$. This is identical to the expression found by Dermer et al. (1992) and Dermer & Schlickeiser (1993) in the case of external scattering by a jet propagating away from the seed photon source (an accretion disc). The formula in Eq. A.6-A.8 are formally only valid for Thomson scattering on an infinite power-law of electrons.

For completeness, the orbital separation d is given by

$$d = \frac{a(1 - e^2)}{1 + e \cos(\theta - \omega)} \quad (\text{A.9})$$

with the semi-major axis $a = (GMP_{\text{orb}}^2/4\pi^2)^{1/3}$, M the total mass, e the eccentricity, θ the true anomaly and ω the periastron angle of the compact object. If the flow is

in the orbital plane where it makes an angle θ_{flow} to the star - pulsar direction then

$$\mathbf{e}_{\text{obs}} \cdot \mathbf{e}_{\text{flow}} = -\sin(\theta + \theta_{\text{flow}}) \sin i \quad (\text{A.10})$$

$$\mathbf{e}_\star \cdot \mathbf{e}_{\text{obs}} = -\sin \theta \sin i \quad (\text{A.11})$$

where i is the inclination of the system.

Doppler-boosted emission in the relativistic jet of Cygnus X–3

Outline

1. Observational backdrop	237
2. The model and the geometry	238
3. Results	240
4. Absorption and location of the gamma-ray source	240
§ 83. <i>Soft photon density from the disk</i>	241
§ 84. <i>Gamma-ray absorption and application to Cygnus X-3</i>	244
5. What we have learned	245
6. [Français] Résumé du chapitre	247
§ 85. <i>Contexte et objectifs</i>	247
§ 86. <i>Ce que nous avons appris</i>	248
7. The relativistic jet of Cygnus X-3 in gamma rays	249

1. Observational backdrop

CYGNUS X–3 IS AN ACCRETING BINARY SYSTEM with relativistic jets, *i.e.* a microquasar (see Chapter 1). This system is composed of a luminous Wolf-rayet star (see *e.g.* van Kerkwijk *et al.* 1996) and a compact object of unknown nature, possibly a black hole, in a 4.8 hours orbit (Parsignault *et al.* 1972) and at a distance of about 7 kpc from Earth (Ling *et al.* 2009).

The gamma-ray space telescopes *AGILE* and *Fermi* detected gamma-ray flares from Cygnus X–3 (Tavani *et al.* 2009; Fermi LAT Collaboration 2009). This detection is secure because an orbital modulation of the gamma-ray flux was found in the *Fermi* data. This result is the first firm detection ever of high-energy gamma rays from a microquasar. The detected gamma-ray flares are all coincident with powerful radio flares which are known to be associated with episodes of major ejections in Cygnus X–3. The gamma-ray emission might occur in the relativistic jet.

The gamma-ray emission is almost anticorrelated with X-rays. Both lightcurves are shifted by $\Delta\phi = 0.3\text{--}0.4$ in phase. The X-ray modulation is very stable over time, minimum at superior

conjunction and maximum at inferior conjunction. This modulation is probably due to the absorption of X-rays by the dense Wolf-Rayet star wind. The gamma-ray modulation would be due to boosted anisotropic inverse Compton scattering of stellar photons on relativistic electron-positron pairs accelerated in the jet. We explore whether this scenario can explain the gamma-ray emission in Cygnus X–3. I briefly review below the model and the main results presented in our paper Dubus *et al.* (2010b) (see Sect. 7).

GeV gamma rays produced in the jet could be absorbed by soft X-rays emitted by the inner regions of an accretion disk around the compact object. I investigate also the gamma-ray opacity in Cygnus X–3 and put constraints on the location of the high-energy source of radiation.

2. The model and the geometry

We build a simple-minded model where pairs are located in two compact and symmetric zones with respect to the compact object position, at an altitude H in the jet and counter-jet (see Fig. 106). The jet is relativistic (with a bulk velocity $\beta > 0$) and is inclined in an arbitrary direction along the unit vector \mathbf{e}_j and the spherical angles ϕ_j (polar angle) and θ_j (azimuth angle) such as

$$\mathbf{e}_j = \begin{pmatrix} \sin \phi_j \cos \theta_j \\ \sin \phi_j \sin \theta_j \\ \cos \phi_j \end{pmatrix} \quad \mathbf{e}_{cj} = \begin{pmatrix} \sin (\phi_j + \pi) \cos \theta_j \\ \sin (\phi_j + \pi) \sin \theta_j \\ \cos (\phi_j + \pi) \end{pmatrix} = -\mathbf{e}_j, \quad (84.319)$$

where \mathbf{e}_{cj} is the unit vector in the counter-jet direction. Angles are defined with respect to the (x,y,z) axis defined in Fig. 106, the orbit is in the (x,y) plane. The orbit is assumed circular with an orbital separation $d = 3 \times 10^{11}$ cm. The star-compact object direction is indicated by the unit vector \mathbf{e}_c given by

$$\mathbf{e}_c = \begin{pmatrix} \cos \theta \\ \sin \theta \\ 0 \end{pmatrix}, \quad (84.320)$$

where θ is the mean anomaly, so that $\theta = 0$ where $y = 0$. The orbital phase in Cygnus X–3 are directly given here by $\phi = \theta/2\pi$. We define at $\phi = 0.25$ superior conjunction, then $\phi = 0.75$ corresponds to inferior conjunction (see Fig. 106). If the system is inclined at an angle i , the unit vector along the line joining the electrons to the observer \mathbf{e}_{obs} is then

$$\mathbf{e}_{obs} = \begin{pmatrix} 0 \\ -\sin i \\ \cos i \end{pmatrix}. \quad (84.321)$$

The Wolf-Rayet star has an effective temperature of about $T_\star = 10^5$ K and a radius $R_\star \approx R_\odot$ but the star will be considered as point-like for simplicity. The star provides also a large density of seed photons ($n_\star \gtrsim 10^{14}$ ph cm $^{-3}$ at the compact object) for inverse Compton scattering on pairs in the jet. Stellar photons come from the direction indicated by \mathbf{e}_\star along the line joining the star to the electrons, such as

$$\mathbf{e}_\star = \frac{d\mathbf{e}_c + H\mathbf{e}_j}{R}, \quad (84.322)$$

with $R^2 = d^2 + H^2 + 2dH\mathbf{e}_c \cdot \mathbf{e}_j$ the distance between the star center and the electrons in the jet.

Electrons are isotropized and injected with a constant power-law energy distribution in the comoving frame of the jet, so that $dn_e/d\gamma_e = K_e\gamma_e^{-p}$ with K_e a normalization constant. In the

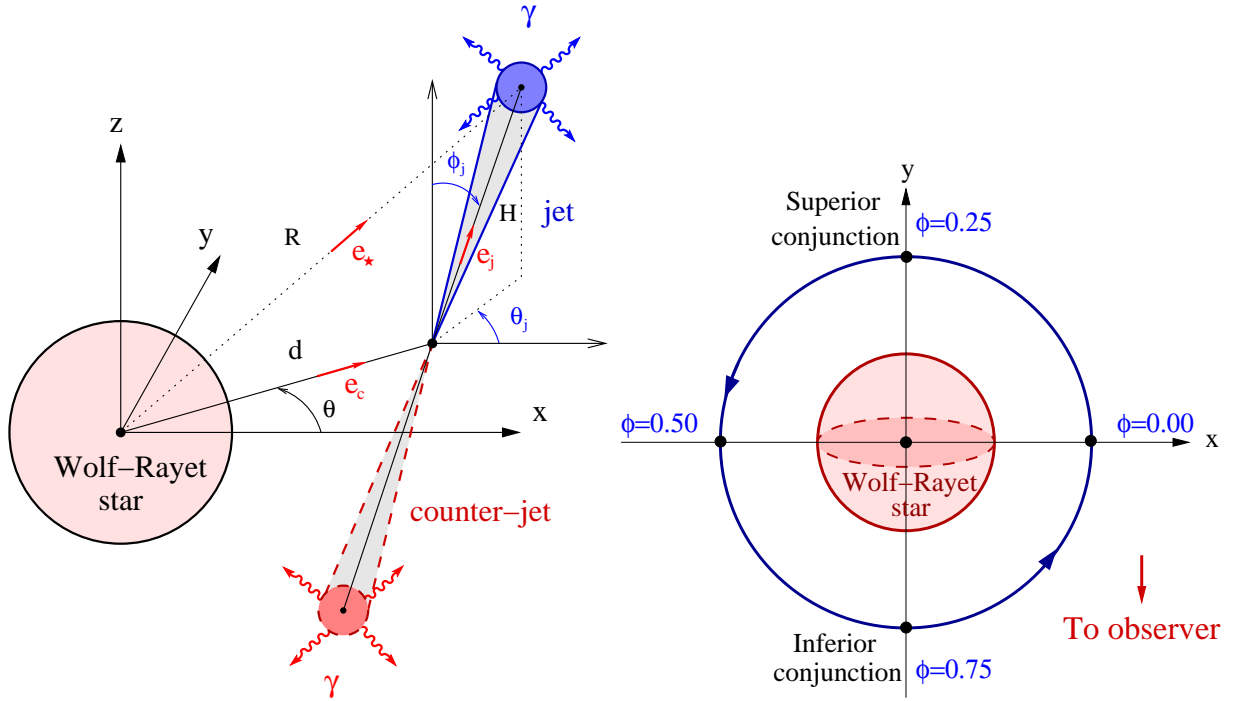


FIG. 106. *Left panel:* Geometry of the jet in Cygnus X-3. The compact object produce a two-sided inclined jet with a relativistic velocity $\beta = \pm\beta\mathbf{e}_j$. Stellar photons are upscattered to high energies by energetic electrons localized at two symmetric positions at an altitude H in the jet (blue disk) and counter-jet (red dashed disk). *Right panel:* Top view of the compact object orbit.

Thomson regime, the emitted flux F_V in the observer frame (from the jet component) is given by (see Eq. 80.316)

$$F_V^{jet}(\epsilon_1) = \mathcal{D}_{obs}^{4+2\alpha} C(p) K_e \pi \left(\frac{R_\star}{R}\right)^2 (kT_\star)^{\alpha+3} (1 - \mathbf{e}_\star \cdot \mathbf{e}_{obs})^{\alpha+1} \epsilon_1^{-\alpha}, \quad (84.323)$$

with (see Eq. 23.124)

$$C(p) = \frac{\pi r_e^2 c^2 2^{\frac{p+5}{2}} (p^2 + 4p + 11) \Gamma\left(\frac{p+5}{2}\right) \zeta\left(\frac{p+5}{2}\right)}{h^3 c^3 (p+1)(p+3)(p+5)}, \quad (84.324)$$

and $\alpha = (p-1)/2$. The Doppler factor \mathcal{D}_{obs} is given in this context by

$$\mathcal{D}_{obs} = \frac{1}{\Gamma(1 - \beta \mathbf{e}_{obs} \cdot \mathbf{e}_j)}. \quad (84.325)$$

Similarly, the contribution from the counter-jet $F_V^{cjet}(\epsilon_1)$ is found by changing \mathbf{e}_j into $-\mathbf{e}_j$ in Eq. (84.323). The Thomson approximation is good in the *Fermi* energy band. Klein-Nishina effects should slightly change the spectrum above 1 GeV but we know that all the relevant patterns of boosted inverse Compton emission are well reproduced by Eq. (84.323) (see Chapter 9).

Seed photons for inverse Compton scattering could also come from the accretion disk around the compact object. As the orientation of the disk to the observer remains constant along the orbit (unless it precesses), the orbital gamma-ray modulation cannot be due to inverse Compton scattering with these photons, but could instead contribute to the DC gamma-ray component.

Nevertheless, these photons could be important for the gamma-ray opacity in the system. This is investigated and discussed below in Sect. 4.

Apart from the uncertainties in the orbital parameters of the system, we have a set of five free parameters proper to our model, which are β , H , θ_j , ϕ_j , K_e . Thanks to the analytical formula given in Eq. (84.323), an exhaustive exploration of the space parameter is possible.

3. Results

We apply the model described above to Cygnus X–3 and we chose to use two extreme orbital solutions for this system as suggested in Szostek & Zdziarski (2008). The first solution is consistent with a $20 M_\odot$ black-hole orbiting a $50 M_\odot$ Wolf-Rayet star of radius $R_\star = 2.3 R_\odot$ for an inclination $i = 30^\circ$. The second possibility is a $1.4 M_\odot$ neutron star with a $5 M_\odot$ Wolf-Rayet star of radius $R_\star = 0.6 R_\odot$ with $i = 70^\circ$. The *Fermi* spectrum is a power law of spectral index $\alpha = 1.7$. The index for electrons should then be chosen as $p \approx 4.4$ (in the Thomson limit) with $\gamma_- = 10^3$ for electrons.

We explore the parameter space and compare the theoretical lightcurve with observations. The χ^2 defined as

$$\chi^2(K_e, \beta, \theta_j, \phi_j, H) = \sum_j \frac{(d_j - Km_j)^2}{\sigma_j^2}, \quad (84.326)$$

is computed for each set of parameters, where j is the number of data-point, d_j the measured flux, σ_j the error on the measured flux d_j , m_j the normalized theoretical flux and K a normalization constant. The best fit to observations is given by the minimum χ^2 solution. Many solutions fit correctly observations. Fig. 107 shows one of them. Fig. 108 presents the distribution of the models for which the fit to *Fermi* observation is good (90% of confidence region) for all the parameters.

This study reveals that the jet should be inclined and mildly relativistic $\beta \lesssim 0.9$. Note that the "microblazar" solution is likely. This solution corresponds to the case where the jet is aligned to the line of sight *i.e.* $\phi_j \approx i$ and $\theta_j \approx -90^\circ$ (the equivalent of "blazar" for microquasars). In addition, the location of the gamma-ray source should not lie at the compact object location ($0.5d \lesssim H \lesssim 10d$) but should still remain within the system. Energetically speaking, the black hole solution is favored as the total power in pairs required to explain observations should be a significant fraction of the Eddington luminosity in the neutron star solution. In other words, it means that most of the total accretion power should be injected into non-thermal pairs in the relativistic jet.

We predict also with this model that the precession of the jet would change significantly the modulation and the flux of the gamma-ray emission in the GeV energy band (Fig. 109). It is then possible that Cygnus X–3 was previously brighter or fainter than it is today. The negative results by *COS B* (Hermsen *et al.* 1987) and *EGRET* (Mori *et al.* 1997) may be due to a non-favorable orientation of the jet with respect to the observer. The controversial detection by the gamma-ray satellite *SAS-2* (Lamb *et al.* 1977) in the early seventies might actually be a real detection.

4. Absorption and location of the gamma-ray source

High-energy gamma rays produced in the jet can be absorbed by the stellar photons and by thermal photons produced in the accretion disk around the compact object. With stellar photons

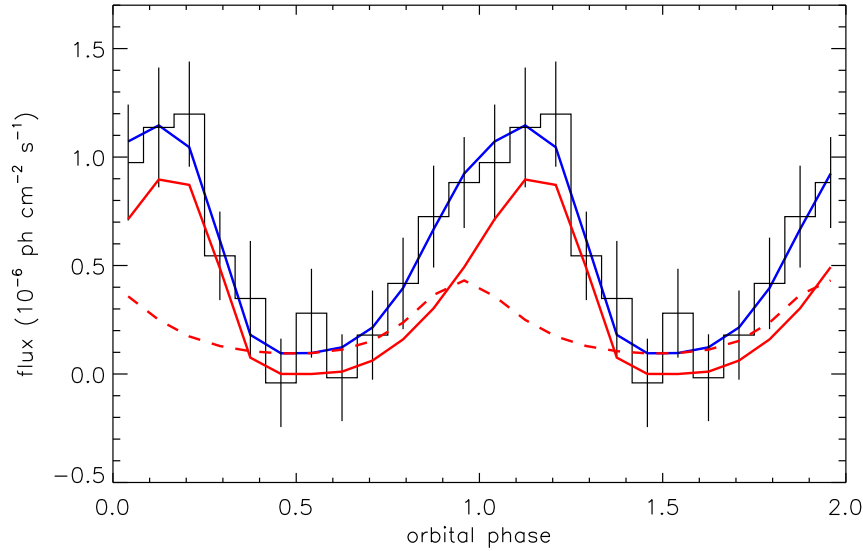


FIG. 107. High-energy gamma-ray flux (> 100 MeV) in Cygnus X-3 as a function of the orbital phase (two full orbits here) for the black hole solution. The solution shown (blue solid line) has a $\chi^2 = 2.9$ for a set of parameters $\beta = 0.45$, $H = 8.5 \times 10^{11}$ cm, $\phi_j = 12^\circ$, $\theta_j = 106^\circ$ and with a total power in electrons $P_e = 1.12 \times 10^{38}$ erg s $^{-1}$ (where $\gamma_- = 10^3$). The contributions from the jet (red solid line) and the counter-jet (red dashed line) are shown as well for comparison. The folded *Fermi* lightcurve data points are taken from Fermi LAT Collaboration (2009).

of energy $\epsilon_0 \approx 23$ eV in Cygnus X-3, gamma rays are absorbed if $\epsilon_1 \gtrsim 20$ GeV. Hence, gamma-ray absorption with photons from the Wolf-Rayet star is not really relevant in the *Fermi* energy band. Accretion disk are known to emit thermal radiation up to soft X-rays. A 1 GeV gamma-ray photon can be absorbed by a 0.1 keV photon from the accretion disk. Carraminana (1992) showed that this effect is important in the GeV energy band and affects the escaping gamma-ray spectrum in microquasars. In this study, the author did the simplifying assumption that soft photons are emitted only perpendicular to the accretion disk. Bednarek (1993) considered the full geometrical complexity of the accretion disk where gamma rays are postulated to be produced. Later, Zhang & Cheng (1997) carried out the exact calculation for the gamma-ray opacity as in Bednarek (1993) but where the gamma-ray source is located above the accretion disk in AGN. Following Zhang & Cheng (1997), I quantitatively investigate pair production in the radiation field produced by a standard accretion disk in Cygnus X-3.

§ 85. Soft photon density from the disk

The disk is assumed steady, optically thick, flat and geometrically thin with an inner radius R_{in} and outer radius R_{out} . The compact object lies at the center of the accretion disk in the point O (see Fig. 110). Doppler effects due to the Keplerian rotation of the disk is ignored. The gamma-ray source is point-like and located above the accretion disk at an altitude $H = (r^2 + z^2)^{1/2}$. Let's consider the absorption of a gamma ray propagating towards a distant observer whose line of sight is inclined at an angle ψ with the disk (Fig. 110). First, I consider a single gamma ray of

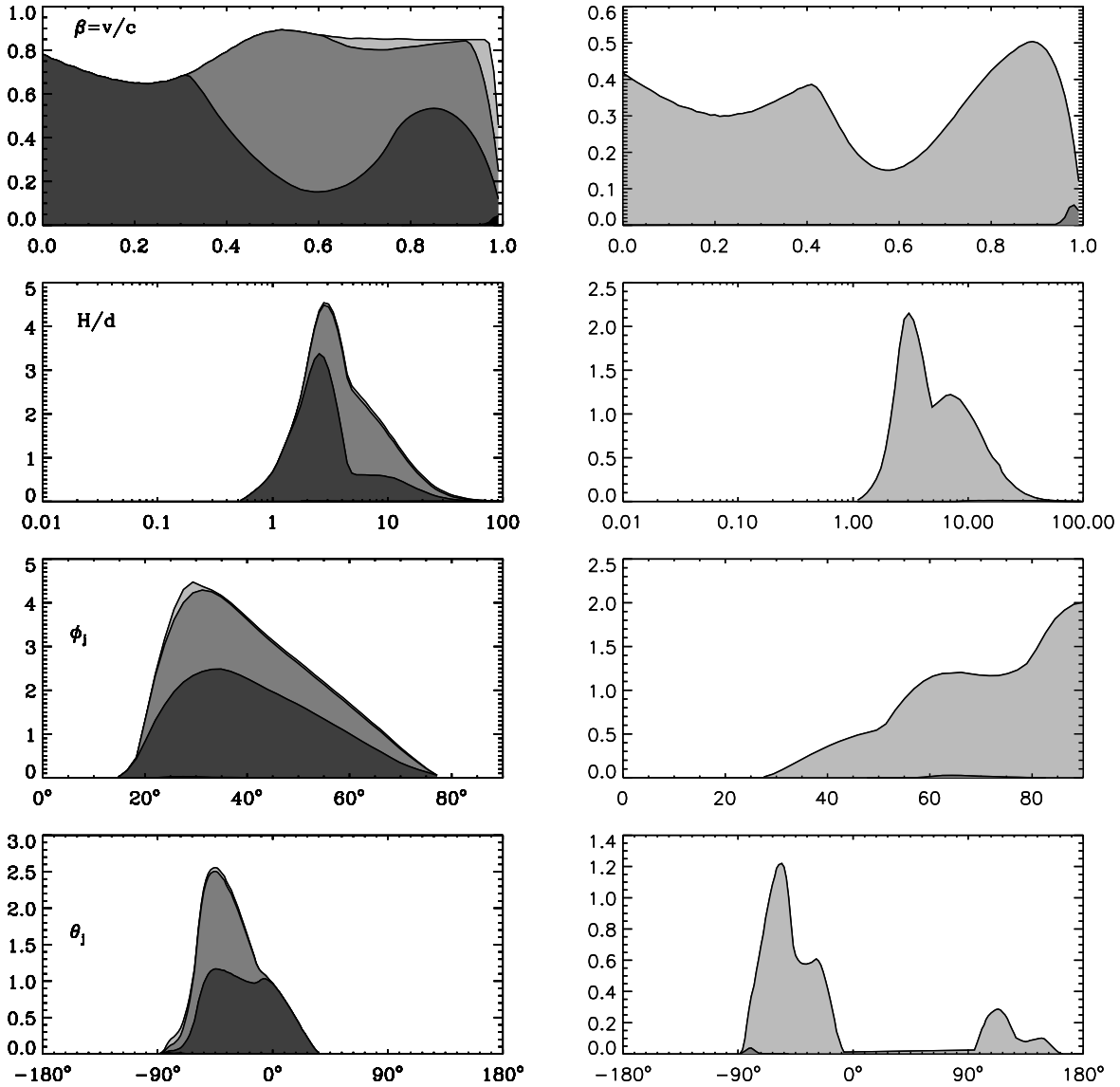


FIG. 108. Distribution of good fit models in the 90% of confidence region of the χ^2 statistics for the black hole solution (*left panels*) and for the neutron star solution (*right panels*) for the parameters β (*top panels*), H , ϕ_j and θ_j (*bottom panels*). The filled regions gives the number of model such as the total power injected into pairs P_e is $\lesssim L_{edd}$ (light grey region), $\lesssim 10^{-1}L_{edd}$ (grey region) and $\lesssim 10^{-2}L_{edd}$ (dark grey region). The Eddington luminosity is $L_{edd} = 2 \times 10^{39}$ erg s^{-1} for the black hole and $L_{edd} = 2 \times 10^{38}$ erg s^{-1} for the neutron star.

energy ϵ_1 at the point P interacting with photons from the elementary surface $dS = R dR d\phi$ in the point M. R is the radial distance in the disk plane to the center and ϕ is the polar angle.

In the standard model, the accretion disk is formed by concentric annuli in thermal equilibrium emitting a black body spectrum (see *e.g.* Pringle 1981). The profile of temperature in the disk T is then given by (Shakura & Sunyaev 1973)

$$T(R) = T_{co} \left(\frac{R}{R_{co}} \right)^{-3/4}, \quad (85.327)$$

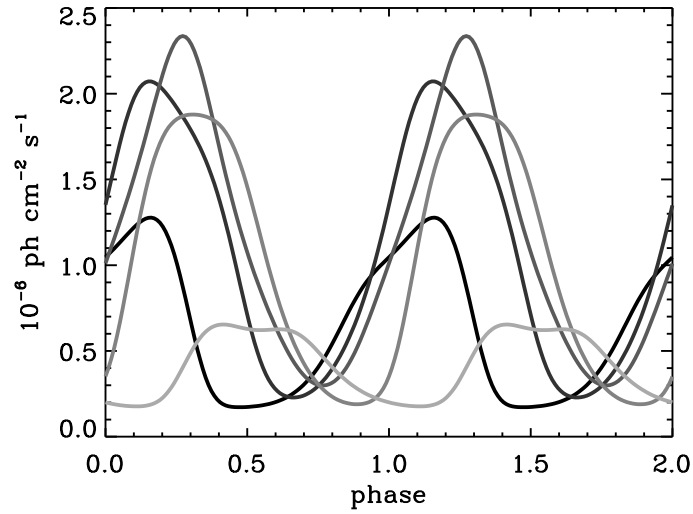


FIG. 109. Effect of the precession of the jet on the high-energy emission and modulation in Cygnus X-3. From the best fit solution (black solid line) with $\theta_j = 319^\circ$, only the azimuth angle is changed to (from dark to light grey line) $\theta_j = 31^\circ, 103^\circ, 175^\circ$ and 247° .

where

$$T_{co} = \left(\frac{3GM\dot{M}_{co}}{8\pi\sigma_{SB}R_{co}^3} \right)^{1/4} \quad (85.328)$$

is the characteristic temperature of the disk, where \dot{M} is the accretion rate, M_{co} and R_{co} the mass and radius of the accreting compact object. Each surface element dS of the disk produces a soft photon density per unit of volume, energy and solid angle

$$\frac{dn}{d\epsilon d\Omega} = \frac{2}{h^3 c^3} \frac{\epsilon^2}{\exp\left(\frac{\epsilon}{kT(R)}\right) - 1}. \quad (85.329)$$

The fraction of the solid angle covered by the surface dS as seen by a gamma-ray photon propagating towards the observer is (Fig. 110)

$$d\Omega = \frac{\mathbf{e}_x \cdot \mathbf{dS}}{D^2} = \frac{R\rho \cos\theta}{D^3} dR d\phi, \quad (85.330)$$

where \mathbf{e}_x is the unit vector along the MP direction. The distance D is given by

$$D^2 = R^2 + \rho^2 - 2R\rho \sin\theta \cos\phi, \quad (85.331)$$

and

$$\rho^2 = z^2 + r^2 + l^2 + 2l(z \cos\psi + r \sin\psi). \quad (85.332)$$

l is the length path of the gamma-ray photon from the source to P. We have also

$$\cos\theta = \frac{z + l \cos\psi}{\rho} \quad \sin\theta = \frac{r + l \sin\psi}{\rho} \quad (85.333)$$

$$\cos\alpha = \frac{z + l \cos\psi}{D} \quad \sin\alpha = \frac{\delta}{D} \quad (85.334)$$

$$\delta^2 = D^2 - (z + l \cos\psi)^2 \quad \cos\omega = \frac{r + l \sin\psi - R \cos\phi}{\delta}. \quad (85.335)$$

The angle between both photons in P is then

$$\cos \theta_0 = \mathbf{e}_{\text{obs}} \cdot \mathbf{e}_* = \sin \psi \sin \alpha \cos \omega + \cos \psi \cos \alpha. \quad (85.336)$$

§ 86. Gamma-ray absorption and application to Cygnus X-3

The total gamma-ray opacity $\tau_{\gamma\gamma}$ integrated along the length path l from the source to the observer, over the geometrical extension and over the thermal photon spectrum of the accretion disk is (Eq. 11.60)

$$\tau_{\gamma\gamma}(r, z, \psi) = \int_0^{+\infty} \int_0^{2\pi} \int_{R_{\text{in}}}^{R_{\text{out}}} \int_{\epsilon} \frac{dn}{d\epsilon d\Omega} (1 - \cos \theta_0) \sigma_{\gamma\gamma} \frac{R\rho \cos \theta}{D^3} d\epsilon dR d\phi dl. \quad (86.337)$$

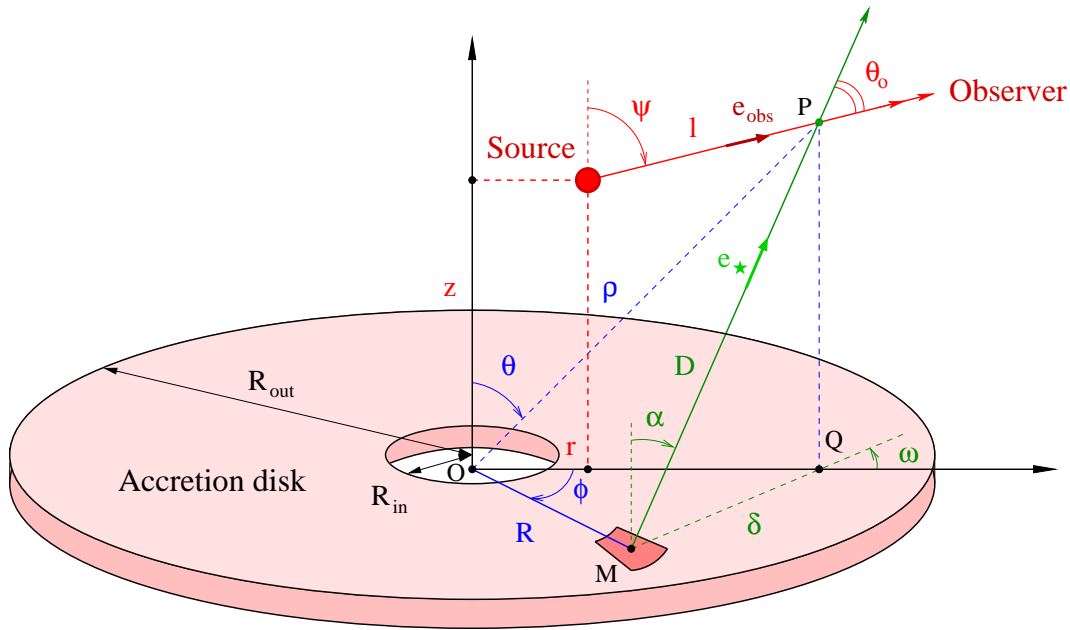


FIG. 110. Geometry of a standard accretion disk. The compact object is located at the origin and the gamma-ray source above the accretion disk. Gamma-ray photons propagating towards the observer can be absorbed by thermal photons from the disk.

The inner radius of the accretion disk is usually set at the last stable orbit *i.e.* $R_{\text{in}} = 3r_g$ with $r_g = 2GM_{\text{co}}/c^2 \approx R_{\text{co}} \approx 6 \times 10^6$ cm for a $20 M_{\odot}$ black hole. The value of the external radius does not really matter here since external regions of the disk emit low energy photons. I chose $R_{\text{ext}} = 10^{11}$ cm. The accretion rate is given by the luminosity of the disk if

$$L_{\text{disk}} = \frac{GM\dot{M}_{\text{co}}}{2R_{\text{co}}}. \quad (86.338)$$

Assuming that $L_{\text{disk}} \approx L_X$ with $L_X \approx 10^{38}$ erg s^{-1} in Cygnus X-3 (see *e.g.* Vilhu *et al.* 2009), we have $\dot{M} \approx 10^{-8} M_{\odot} \text{yr}^{-1}$.

Fig. 111 shows the probability for a gamma ray of energy $\epsilon_1 = 1$ GeV to escape from the accretion disk radiation field towards the observer, *i.e.* $\exp(-\tau_{\gamma\gamma})$. The gamma-ray source is on the axis of the disk at an altitude z and seen for different viewing angle ψ . This study shows that gamma-ray photons are significantly absorbed by the accretion disk only if the source lies

very close to the compact object $z \lesssim 100R_{in} \ll d$. If the primary source is not located on the axis of the disk, the gamma-ray opacity is high only in a compact region around the compact object (z or $r \lesssim 100R_{in} \ll d$, see Fig. 112). Only photons produced in the inner regions of the accretion disk are energetic enough to annihilate with a 1 GeV gamma-ray photon. Fig. 113 gives the gamma-ray opacity as a function of the gamma-ray photon energy. Note that similar maps were obtained by Sitarek & Bednarek (2010) and applied to the AGN Centaurus A.

We conclude that the gamma-ray emitter should not be localized too close to the compact object ($z \gtrsim 100R_{in} \ll d$) or photons will be highly absorbed. This study supports the results found above to explain the GeV modulation in Cygnus X-3.

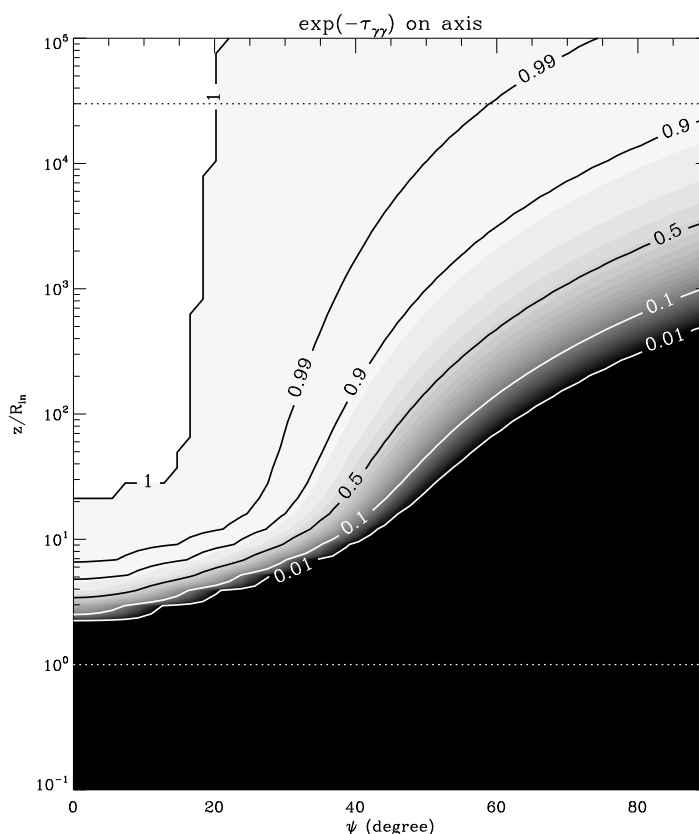


FIG. 111. Gamma-ray opacity map $\exp(-\tau_{\gamma\gamma})$ as a function of the viewing angle ψ and the altitude of the gamma-ray source z in the jet, for $r = 0$ (along the axis of the accretion disk). Bright regions indicate low opacity $\tau_{\gamma\gamma} \ll 1$ and dark regions high opacity ($\tau_{\gamma\gamma} \gg 1$). The gamma-ray photons have an energy $\epsilon_1 = 1$ GeV and propagate above an accretion of inner radius $R_{in} = 10^7$ cm and external radius $R_{ext} = 10^{11}$ cm with $\dot{M} = 10^{-8}M_{\odot} \text{ yr}^{-1}$. The white dotted line indicates $z = R_{in}$ and the black dotted line $z = d$.

5. What we have learned

Boosted anisotropic inverse Compton emission could also be at work in the relativistic jet of microquasars. We built a simple model where energetic electrons are localized and boosted in a relativistic jet, and applied this model to explain the gamma-ray orbital modulation observed in the system Cygnus X-3. An exhaustive exploration of the space parameters reveals that the fit to the observed lightcurve is good if the jet is inclined close to the line of sight and if pairs are

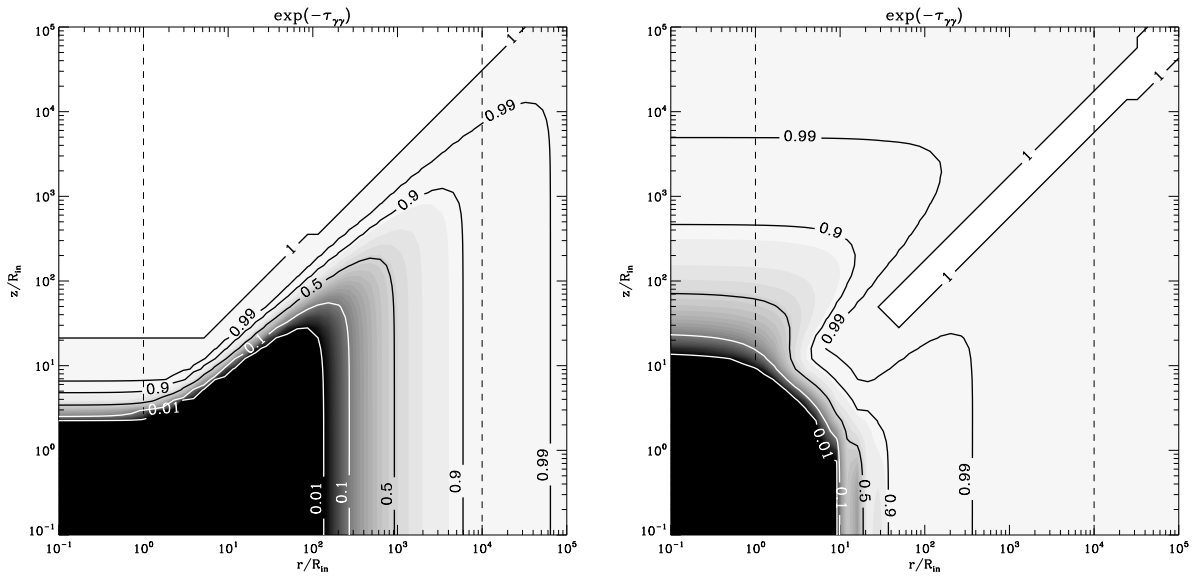


FIG. 112. Same as in Fig. 111 in the (r, z) plane for a viewing angle $\psi = 0^\circ$ (left panel) and $\psi = 45^\circ$ (right panel). The black dashed lines indicate $r = R_{in}$ and $r = R_{ext}$.

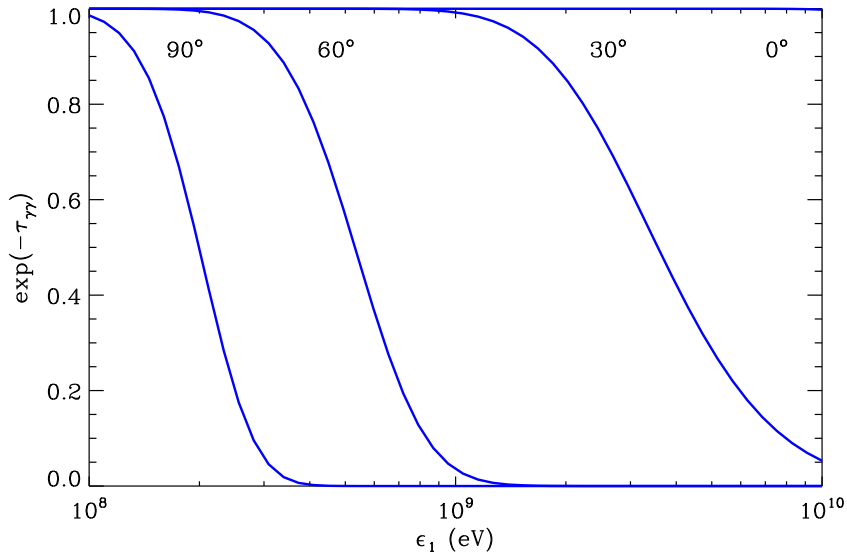


FIG. 113. Gamma-ray opacity as a function of the gamma-ray energy ϵ_1 for $z = 100R_{in}$ on axis ($r = 0$) and $\psi = 0^\circ, 30^\circ, 60^\circ,$ and 90° .

not localized too close to the compact object. Particles should then be accelerated at a specific location in the jet. This acceleration site could be related with recollimation shocks in the jet as observed in some AGN such as for instance in M 87 (Stawarz *et al.* 2006). Such recollimation shocks could be produced by the interaction of the jet with the dense Wolf-Rayet wind. This idea is supported by recent MHD simulations in compact High-mass X-ray binaries (Perucho *et al.* 2010). Our solutions favor also a massive compact object (*i.e.* a black hole) as a lower fraction of

the total accretion power is required to explain the observed gamma-ray luminosity. In addition, we predict that the precession of the jet, probably with super-orbital periodicity, has a dramatic influence on the gamma-ray modulation and flux. Hence, the detection of Cygnus X–3 during the next radio flares by *Fermi* in gamma rays is not guaranteed if the orientation of the jet is not favorable. These results were published in Dubus *et al.* (2010b) (see Sect. 7).

Gamma-ray photons could be absorbed by the thermal photons from the accretion disk. For a standard, optically thick and geometrically thin disk, high-energy gamma rays escape the system if the source is not too close to the compact object ($\gtrsim 1000 r_g$ in Cygnus X–3). Absorption with stellar photons is not really relevant in the energy band probed by *Fermi* as it would be maximum around ~ 20 GeV. Nevertheless, this study on absorption is still incomplete to me. Indeed, observations in X-rays show a bright thermal component in soft X-rays, probably related to the disk emission, and also a non-thermal tail in hard X-rays (see *e.g.* Szostek *et al.* 2008). This non-thermal component could be due to the emission from comptonized hot electrons in a corona above the accretion disk (see *e.g.* Coppi 1999). These photons could also contribute significantly to the absorption of MeV-GeV gamma rays produced in the jet. This is a possible extension of this work on the gamma-ray absorption in Cygnus X–3.

I will present and discuss the main results of this work in a contributed talk at the "French Society of Astronomy and Astrophysics meeting 2010".

6. [Français] Résumé du chapitre

§ 87. Contexte et objectifs

Cygnus X–3 est un système binaire accrétant avec des jets relativistes, *i.e.* un microquasar (voir Chapitre 1). Ce système est composé d'une étoile lumineuse de type Wolf-Rayet (voir *e.g.* van Kerkwijk *et al.* 1996) et d'un objet compact de nature inconnue, probablement un trou noir, sur une orbite de 4.8 heures (Parsignault *et al.* 1972) et se situe à une distance d'environ 7 kpc de la Terre (Ling *et al.* 2009).

Les télescopes spatiaux gamma *AGILE* et *Fermi* ont détecté des éruptions gamma en provenance de Cygnus X–3 (Tavani *et al.* 2009; Fermi LAT Collaboration 2009). Cette détection est solide puisque la période orbitale a été retrouvée dans les données de *Fermi*. Ce résultat est la première détection ferme d'un rayonnement gamma de haute énergie en provenance d'un microquasar. Les éruptions gamma détectées coïncident toutes avec de puissantes éruptions radio qui sont connues pour être associées à des épisodes d'éjection importantes dans Cygnus X–3. L'émission gamma pourrait donc se produire dans le jet relativiste.

L'émission gamma est presque anti-corrélée avec les X. Les deux courbes de lumière sont décalées en phase de $\Delta\phi = 0.3-0.4$. La modulation X est très stable au cours du temps, est minimale à la conjonction supérieure et maximale à la conjonction inférieure. Cette modulation est probablement due à l'absorption des rayons X par le vent dense de l'étoile Wolf-Rayet. La modulation gamma pourrait être due à de l'émission Compton inverse anisotrope entre les photons de l'étoile et des paires électron-positron accélérées dans le jet dont l'émission est amplifiée par effet Doppler relativiste. Nous étudions ici si ce scénario pourrait expliquer l'émission gamma dans Cygnus X–3. Je décris brièvement le modèle ci-dessous et les principaux résultats présentés dans notre article Dubus *et al.* (2010b) (voir Sect. 7).

Les photons gamma du GeV produit dans le jet pourraient être absorbés par les X mous émis par les régions internes d'un disque d'accrétion autour de l'objet compact. J'étudie aussi l'opacité gamma dans Cygnus X–3 et mets des contraintes sur la localisation de la source de rayonnement de haute énergie.

§ 88. Ce que nous avons appris

L'amplification Doppler de l'émission Compton inverse pourrait être à l'oeuvre dans les jets relativistes des microquasars. Nous avons construit un modèle simple où des électrons énergétiques sont localisés dans un jet relativiste. Nous avons ensuite appliqué ce modèle pour expliquer la modulation orbitale observée du flux gamma dans le système Cygnus X–3. Une exploration exhaustive de l'espace des paramètres révèle que l'ajustement à la courbe de lumière observée est bon si le jet est incliné dans une direction proche de la ligne de visée et si les paires ne sont pas localisées trop près de l'objet compact. Les particules devraient donc être accélérées à des endroits précis dans le jet. Ces lieux de réaccélération pourraient être reliés à des chocs de recollimation dans le jet observé dans certains AGN comme par exemple dans M 87 (Stawarz *et al.* 2006). De tels chocs de recollimation pourraient être produits dans l'interaction du jet avec le vent dense de l'étoile Wolf-Rayet. Cette idée est soutenue par de récentes simulations MHD dans les binaires X compactes de grandes masses (Perucho *et al.* 2010). Nos solutions favorisent aussi un objet compact massif (*i.e.* un trou noir) car une plus faible fraction de la puissance totale d'accrétion est nécessaire pour expliquer la luminosité gamma observée. De plus, nous prédisons que la précession du jet, probablement avec une période super orbitale, a une grande influence sur la modulation et le flux gamma observés. Par conséquent, la détection de Cygnus X–3 au cours des prochaines éruptions radio par *Fermi* en gamma n'est pas garantie si l'orientation du jet n'est pas favorable. Ces résultats ont été publiés dans Dubus *et al.* (2010b) (voir Sect. 7).

Les photons gamma peuvent être absorbés par les photons thermiques en provenance du disque d'accrétion. Pour un disque standard, optiquement épais et géométriquement mince, les photons gamma de haute énergie s'échappent du système si la source n'est pas trop près de l'objet compact ($\gtrsim 1000 r_g$ dans Cygnus X–3). L'absorption avec les photons stellaires n'est pas vraiment pertinente dans la bande d'énergie sondée par *Fermi* puisque la production de paires n'est maximale qu'autour de ~ 20 GeV. Néanmoins, cette étude sur l'absorption reste à mes yeux incomplète. En effet, les observations X montrent une brillante composante thermique en X mous, probablement reliée à l'émission du disque, mais aussi une queue non-thermique en X durs (voir *e.g.* Szostek *et al.* 2008). Cette composante non-thermique pourrait être due à l'émission en provenance d'une couronne d'électrons chauds comptonisés au-dessus du disque d'accrétion (voir *e.g.* Coppi 1999). Ces photons pourraient contribuer significativement à l'absorption des photons gamma du MeV-GeV produits dans le jet. C'est une piste possible de recherche future sur l'absorption gamma dans Cygnus X–3.

Je présenterai et discuterai des principaux résultats de ce travail lors d'une présentation orale à la prochaine réunion générale de la Société Française d'Astronomie et d'Astrophysique 2010.

7. Paper: The relativistic jet of Cygnus X-3 in gamma rays

The relativistic jet of Cygnus X-3 in gamma rays

G. Dubus, B. Cerutti and G. Henri

Laboratoire d'Astrophysique de Grenoble, UMR 5571 Université Joseph Fourier Grenoble I / CNRS, BP 53, 38041 Grenoble, France

Accepted . Received ; in original form 26 March 2010

ABSTRACT

High energy gamma-rays have been detected from Cyg X-3, a system composed of a Wolf-Rayet star and a black hole or neutron star. The gamma-ray emission is linked to the radio emission from the jet launched in the system. The flux is modulated with the 4.8 hr orbital period, as expected if high energy electrons are upscattering photons emitted by the Wolf-Rayet star to gamma-ray energies. This modulation is computed assuming that high energy electrons are located at some distance along a relativistic jet of arbitrary orientation. Modelling shows that the jet must be inclined and that the gamma ray emitting electrons cannot be located within the system. This is consistent with the idea that the electrons gain energy where the jet is recollimated by the stellar wind pressure and forms a shock. Jet precession should strongly affect the gamma-ray modulation shape at different epochs. The power in non-thermal electrons represents a small fraction of the Eddington luminosity only if the inclination is low *i.e.* if the compact object is a black hole.

Key words: radiation mechanisms: non-thermal — stars: individual (Cygnus X-3) — ISM: jets and outflows — gamma rays: theory — X-rays: binaries

1 INTRODUCTION

Cyg X-3 is a high-mass X-ray binary composed of a compact object in a 4.8 hr orbit around a Wolf-Rayet (WR) star at a distance of about 7 kpc (see Bonnet-Bidaud & Chardin 1988; van Kerkwijk et al. 1996; Ling et al. 2009, and references therein). The system is a bright X-ray source with $L_X \approx 10^{38}$ erg s $^{-1}$. Cyg X-3 is also well-known for radio flaring (up to 20 Jy) when the source has a soft X-ray spectra (Szostek et al. 2008). The radio source is resolved into a relativistic jet with an expansion speed of 0.3-0.7c. The strong stellar wind from the WR companion ($\dot{M}_w \approx 10^{-5} M_\odot \text{yr}^{-1}$, $v_w \approx 1000$ km s $^{-1}$) has a major impact on the environment of the high-energy source. Scattering in the wind is probably responsible for washing out rapid X-ray variability timescales and also for modulating the X-ray emission. It acts as a veil that has made it difficult to identify the nature of the compact object, black hole or neutron star. Despite the differences caused by the WR wind, Cyg X-3 is firmly established as a trademark accreting binary with relativistic jet *i.e.* a microquasar.

The *AGILE* and the *Fermi Gamma-ray Space Telescope* collaborations have recently reported the detection of high-energy gamma rays (HE, >100 MeV) from Cyg X-3 (Tavani et al. 2009; Abdo et al. 2009). The identification is firm because the detections occur exclusively when Cyg X-3 is flaring in radio and because *Fermi* observations show the HE gamma-ray flux is modulated with the orbital period. The gamma-ray modulation is almost in anti-phase with

the X-ray modulation, with the gamma-ray minimum occurring about 0.3-0.4 in phase after X-ray minimum. The modulation amplitude is close to 100% after background subtraction. The spectrum is consistent with a power law $F_\nu \sim \nu^{-\alpha}$ with $\alpha = 1.7$. The luminosity above 100 MeV is a few $10^{36} (d/7 \text{ kpc})^2$ erg s $^{-1}$.

Inverse Compton (IC) scattering of photons from the WR star on high energy electrons is a natural candidate to explain the gamma-ray emission. The high temperature of the WR star ($R_* \approx 1 R_\odot$, $T_* \approx 10^5$ K) and tight orbit ($d \approx 3 \cdot 10^{11}$ cm) imply that the radiation density in photons from the star is $u_* \approx 10^5$ erg cm $^{-3}$ at the location of the compact object, which is at least an order-of-magnitude higher than any other X-ray binary. Electrons with Lorentz factors of a few 10^3 upscatter 20 eV stellar photons above 100 MeV very efficiently in such a radiation field. IC scattering directly produces a modulation of the flux because of the orbital motion. The maximum occurs when stellar photons are backscattered towards the observer. The accretion disc can also provide seed photons if the HE electrons are close enough. This does not lead to a modulation unless the HE electrons - disk geometry seen by the observer changes with orbital phase (Meszaros et al. 1977). Pion production is possible if there are high energy protons. However, even in this dense environment, it is less efficient than IC so that its energy requirements are higher.

The link between gamma-ray and radio flares suggests that the HE electrons are located in the relativistic jet. Observations of knots in active galactic nuclei show that

2 *G. Dubus, B. Cerutti and G. Henri*

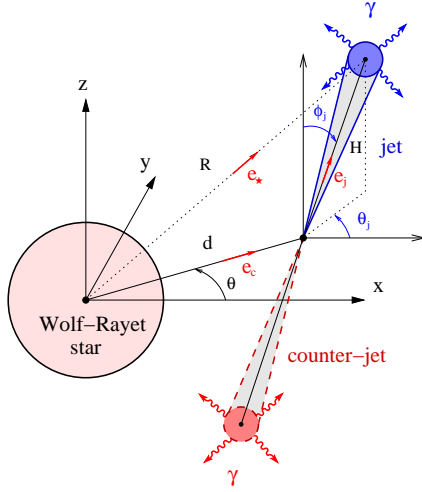


Figure 1. Geometry of the jet model. The scattering electrons are situated at symmetric locations in a jet with relativistic speed β . The seed photon source is the star.

particles may be accelerated at specific locations along the jet, linked *e.g.* to recollimation shocks (Stawarz et al. 2006). Assuming the electrons mainly upscatter stellar photons at some location along the jet, the expected IC emission will depend upon the distance to the star, the bulk velocity of the jet and its orientation. This orientation is not necessarily perpendicular to the orbital plane if *e.g.* the inner accretion disc is warped or it depends on the black hole spin axis. However, the jet orientation is fixed as seen by the observer (changing only if the jet precesses).

The goal here is to test quantitatively whether the *Fermi* gamma-ray modulation can be reproduced in this framework and to see if constraints can be derived on the jet parameters.

2 JET INVERSE COMPTON EMISSION

2.1 Emission spectrum

The HE electrons are assumed to be located at a distance H from the compact object along a jet with a bulk velocity $\beta = v/c$ (Fig. 1). The stellar emission is approximated as a point-like blackbody of temperature T_* and luminosity $4\pi R_*^2 \sigma_{SB} T_*^4$. The electron Lorentz factors γ_e are distributed as a power-law $dN_e = K_e \gamma_e^{-p} d\gamma_e$. In the Thompson regime, the inverse Compton emission spectrum at a photon energy ϵ (in ergs) is given by (Dubus et al. 2010)

$$F_{IC} \equiv \epsilon \frac{dN}{dt d\epsilon} = C(p) K_e \pi \left(\frac{R_*}{R} \right)^2 (kT_*)^{\alpha+3} \times \mathcal{D}_{obs}^{4+2\alpha} (1 - \mathbf{e}_* \cdot \mathbf{e}_{obs})^{\alpha+1} \epsilon^{-\alpha} \quad (1)$$

where: the flux index is related to the electron power law index through $\alpha = (p - 1)/2$, R is the distance from the star to the electron location; \mathbf{e}_* and \mathbf{e}_{obs} are unit vectors along, respectively, the star-to-electrons and the electrons-to-observer directions;

$$\mathcal{D}_{obs} = \frac{(1 - \beta^2)^{1/2}}{(1 - \beta \mathbf{e}_{obs} \cdot \mathbf{e}_{jet})} \quad (2)$$

defined the Doppler boost of the jet, \mathbf{e}_{jet} being the unit vector along the jet direction; $C(p)$ is given by

$$C(p) = \frac{\pi r_e^2 c^2 2^{\frac{p+5}{2}} (p^2 + 4p + 11) \Gamma\left(\frac{p+5}{2}\right) \zeta\left(\frac{p+5}{2}\right)}{h^3 c^3 (p+1)(p+3)(p+5)} \quad (3)$$

with Γ the gamma function and ζ the Riemann function. This formula is valid in the Thompson regime, that is when $\gamma_e \epsilon_0 < m_e c^2$ where ϵ_0 is the characteristic energy of the seed photons. For a blackbody with $T_* = 10^5$ as in Cyg X-3, $\epsilon_0 \approx 2.7 kT_* \approx 23$ eV so the limit occurs for $\gamma_e \approx 2 \cdot 10^4$ (neglecting the Doppler boost). IC emission from 100 MeV to a few GeV (the relevant *Fermi* range) occurs in the Thompson regime.

The model geometry is shown in Fig. 1. The jet has an azimuth θ_j and polar angle ϕ_j ($=0$ when perpendicular to orbital plane). With the origin set at the location of the WR star,

$$R^2 = d^2 + H^2 + 2dH(\mathbf{e}_c \cdot \mathbf{e}_{jet}) \quad (4)$$

where \mathbf{e}_c is the unit vector along the star to compact object direction, and the unit vectors are given by

$$\begin{aligned} \mathbf{e}_* &= (d\mathbf{e}_c + H\mathbf{e}_{jet})/R \\ \mathbf{e}_{jet} &= (\cos \theta_j \sin \phi_j, \sin \theta_j \sin \phi_j, \cos \phi_j) \\ \mathbf{e}_c &= (\cos \theta, \sin \theta, 0) \\ \mathbf{e}_{obs} &= (0, -\sin i, \cos i) \end{aligned} \quad (5)$$

with θ the true anomaly, d the orbital separation and i the inclination. Here, the true anomaly is defined so that $\theta = \pm \pi/2$ at conjunctions.

2.2 Main properties

The inverse Compton emission has an orbital modulation because of the dependence of \mathbf{e}_c on the true anomaly ($=$ orbital phase for a circular orbit). Developing $\partial F_{IC}/\partial \theta = 0$, the emission maximum and minimum along the orbit verify:

$$(\alpha+1)(\mathbf{e}_c \times \mathbf{e}_{obs}) \cdot \mathbf{e}_z = \frac{H}{R} ((\alpha+3)\mathbf{e}_* \cdot \mathbf{e}_{obs} - 2)(\mathbf{e}_c \times \mathbf{e}_{jet}) \cdot \mathbf{e}_z \quad (6)$$

If $H \ll d$, or if the jet is perpendicular to the orbital plane, then the maxima and minima are at conjunctions as outlined in §1. Otherwise, they occur at orbital phases that can be very different.

The IC flux will be equal to zero if $\mathbf{e}_* \cdot \mathbf{e}_{obs} = 1$ somewhere along the orbit. Having a 100% modulation can be translated into a necessary condition on H for given i , d , ϕ_j and θ_j . Similarly, although the seed photon density decreases with H , the maximum of the IC flux for a given jet geometry does not necessarily occur for $H=0$ because of the dependence of \mathbf{e}_* on H .

The jet speed only appears in \mathcal{D}_{obs} and $\mathbf{e}_{obs} \cdot \mathbf{e}_{jet}$ is constant along the orbit: changing β will only impact the flux normalisation and not the shape of the modulation. The maximum flux occurs when $\beta = \mathbf{e}_{obs} \cdot \mathbf{e}_{jet}$. Emission from a jet oriented away from the observer will always be weak for highly relativistic speeds because of the deboost.

3 APPLICATION TO CYG X-3

The observed modulation is plotted in Figure 2. The background level in diffuse gamma rays of $3.6 \cdot 10^{-6}$ ph cm $^{-2}$ s $^{-1}$ was subtracted to the *Fermi* lightcurve (Abdo et al.

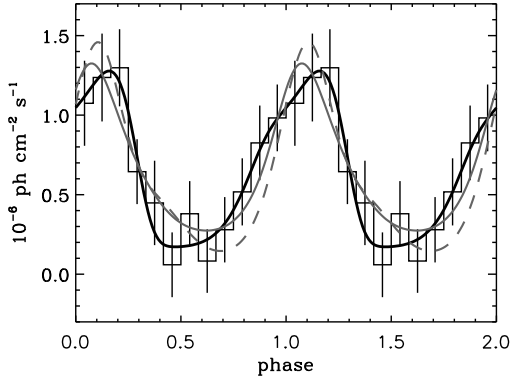


Figure 2. Model fits to the observed > 100 MeV gamma-ray modulation in Cyg X-3. Conjunctions are at phases 0.25 and 0.75 for the conventions adopted in this work. The models shown assumed an orbit with a black hole (O1). The best model is shown with a black solid line. A model with $\beta = 0$ is shown with a grey solid line. The model with minimum P_e ($3 \times 10^{33} \text{ erg s}^{-1}$) is shown with a grey dashed lines. All of these models are statistically acceptable fits to the data (see §3 for details).

2009). There is not absolute phasing of the orbit of Cyg X-3. The *Fermi* observations have been phased so that the well-defined minimum X-ray flux occurs at superior conjunction i.e. phase 0.25 with the conventions adopted in this paper (Fig. 1). This phasing is justified if the X-ray modulation is due to Thompson scattering in the stellar wind (Pringle 1974). It is independently supported by infrared spectroscopy (Hanson et al. 2000).

The orbital parameters of Cyg X-3 are not determined precisely (Hanson et al. 2000; Vilhu et al. 2009) so two extreme solutions are adopted following Szostek & Zdziarski (2008). Orbit 1 (O1) has a $M_1=20 M_\odot$ black hole around a $50 M_\odot$ WR star of radius $2.3 R_\odot$ and is seen with an inclination of 30° . Orbit 2 (O2) has a $M_1=1.4 M_\odot$ neutron star around a $5 M_\odot$ WR star of radius $0.6 R_\odot$ with $i = 70^\circ$. The *Fermi* spectrum $\alpha = 1.7$ sets the electron power-law index $p = 4.4$. The emission arise from two symmetric sites: the jet and the counterjet. The counterjet has $\phi_{cj} = \pi + \phi_j$.

3.1 Parameter exploration

The jet is parametrised by β , H , ϕ_j , θ_j and K_e . The expected modulation in the *Fermi* band is calculated using the equation in §2 for the jet and the counterjet. The evaluation of Eq. 1 is very fast and allows an exhaustive exploration of the parameter space. The jet angle ϕ_j was varied between 0 and $\pi/2$; θ_j varied between 0 and 2π . The emission height H was varied between $0.01d$ and $100d$ in logarithmic steps (d is the orbital separation). The jet speed β was varied linearly from 0 to 0.99 (bulk Lorentz factor ≈ 7).

The model K_e is adjusted to minimize the χ^2 goodness-of-fit to the observed modulation. The normalisation K_e is converted into a power in HE electrons P_e assuming a distance of 7 kpc and a minimum HE electron Lorentz factor $\gamma_{e,\min} = 1000$. P_e is highly sensitive to $\gamma_{e,\min}$ because of the very steep electron spectrum. IC emission above 100 MeV

The relativistic jet of Cyg X-3 in gamma rays 3

requires that $\gamma_{e,\min} \leq 1000$ so P_e is a lower limit on the non-thermal power.

Good fits can be obtained for both O1 ($\chi^2_{\min} = 2.7$ for 12 data points - 5 parameters = 7 degrees of freedom) and O2 ($\chi^2_{\min} = 4.2$). The best model for O1 is plotted in Figure 2. It has $\beta = 0.41$, $H = 8 \times 10^{11} \text{ cm}$, $\phi_j = 39^\circ$, $\theta_j = 319^\circ$, $P_e = 10^{38} \text{ erg s}^{-1}$. The 90% confidence range for the parameters was determined by adding 9.24 to the minimum χ^2 (Lampton et al. 1976). Only models that had P_e lower than the Eddington luminosity $L_{\text{Edd}} \approx 10^{38} (M_1/M_\odot) \text{ erg s}^{-1}$ were kept. Besides being physically implausible, models with larger P_e are associated with high values of β or large H . The high P_e then compensates for Doppler deboosting or low IC efficiency (see §3.3).

3.2 Jet orientation

Figure 3 shows the distributions of β , H , ϕ_j and θ_j for the black hole case (O1). The figure also shows the distributions for various limits on P_e . In all cases, the HE electrons distance H is between 0.5 and 30 times the orbital separation (i.e. between 2×10^{11} and 10^{13} cm). A location very close to the compact object is excluded. The orientation of the jet is constrained to be $20^\circ \lesssim \phi_j \lesssim 80^\circ$ with a preference for values comparable to the system inclination ($i = 30^\circ$). A jet perpendicular to the orbital plane does not fit the data. The azimuth θ_j is less constrained: there is a well defined peak in the distribution (bottom panel, Fig. 3) but, contrary to H or ϕ_j , there are good models all over the range even if in small numbers (not visible on a linear scale).

Moderate relativistic speeds β are favoured but this is not strongly constrained. The speed is closely linked to the power in HE electrons. There is a tendency to have lower values of β when the allowed P_e gets smaller, accompanied by a smaller H . A model in the 90% confidence region with $\beta=0$ is shown in Figure 2. It has $\chi^2 = 7.1$, $H = 7 \times 10^{11} \text{ cm}$, $\phi_j = 31^\circ$, $\theta_j = 9^\circ$, $P_e = 2 \times 10^{37} \text{ erg s}^{-1}$. This trend on β reverses for low values of $P_e \lesssim 0.001 L_{\text{Edd}}$. These do not appear in Figure 3 as there are comparatively very few such models. The minimum P_e in the 90% confidence region is $4 \times 10^{33} \text{ erg s}^{-1}$, a very modest fraction of L_{Edd} . This model is also shown in Figure 2. It has $\chi^2 = 11.3$, $\beta = 0.99$, $H = 10^{12} \text{ cm}$, $\phi_j = 32^\circ$ and $\theta_j = 275^\circ$. These low P_e models all have $\phi_j \approx i$ and $\theta_j \approx -90^\circ$: they are almost aligned with the observer ($\mathbf{e}_{\text{jet}} \cdot \mathbf{e}_{\text{obs}} \approx 1$) at superior conjunction. The slight difference in θ_j accounts for the phase difference of the maximum. Here, Doppler boosting compensates for the low P_e . There is some degeneracy between the two parameters up to some (large) value of the Lorentz factor ≈ 20 where good models cannot be found anymore. These are effectively microblazar models.

The constraints in the neutron star case (orbit O2, not shown here) are similar. The jet orientation is well constrained with $25^\circ \lesssim \phi_j \lesssim 65^\circ$, $-60^\circ \lesssim \theta_j \lesssim -10^\circ$ and $2 \times 10^{11} \text{ cm} \lesssim H \lesssim 6 \times 10^{11} \text{ cm}$ (H/d from 1 to 3), comparable to the values found with O1. However, in all cases β is $\lesssim 0.2$. Interestingly, P_e is constrained to be rather large with $P_e \gtrsim 0.2 L_{\text{Edd}}$ (about $3 \times 10^{37} \text{ erg s}^{-1}$). The large inclination (70°) required for a neutron star primary is the reason for the difference with the black hole case. Arbitrarily setting $i = 30^\circ$ with the orbit O2 gives results for β and P_e that are

4 *G. Dubus, B. Cerutti and G. Henri*

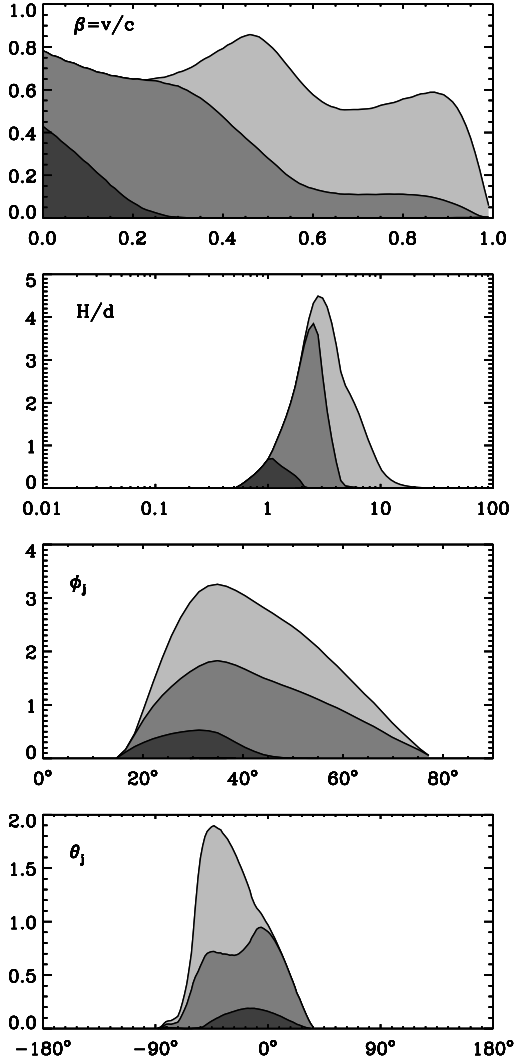


Figure 3. Distribution of jet parameters for models in the 90% confidence region given by χ^2 statistics. Orbit O1 ($20 M_{\odot}$ black hole, $i=30^\circ$) is assumed. The various regions correspond to a power in high energy electrons $P_e \leq L_{\text{Edd}}$ (light grey), $\leq 0.1L_{\text{Edd}}$ (grey), $\leq 0.01L_{\text{Edd}}$ (dark grey). Here, L_{Edd} is $2 \cdot 10^{39} \text{ erg s}^{-1}$.

consistent with those of O1. Large inclinations do not allow good fits for small values of P_e or large values of β .

These results were obtained for a steep power-law distribution of electrons with an index $p = 4.4$, because of the soft gamma-ray flux index and the assumption of Thompson scattering. Taking $p = 2$ or $p = 3$ does not affect the conclusions. A few tests calculations using the full IC cross section (done as explained in Dubus et al. 2010) showed that a slightly harder electron index ($p \approx 4$) is required to match the spectrum. Again, this does not change the results. The steep spectrum may not directly reflect an electron power-law distribution but represent the best fit to *e.g.* a cutoff in the 100 MeV – 1 GeV range. To test this, a lightcurve

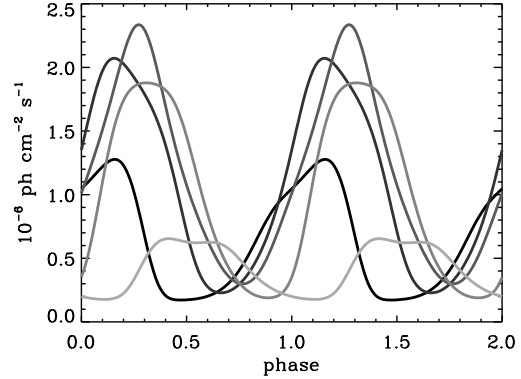


Figure 4. Impact of jet precession on the gamma-ray lightcurve for the best-fit model shown in Figure 2. The jet azimuth θ_j is rotated in steps of 72° from its best fit value of 319° , with lighter lines as θ_j moves away from this value.

was calculated (including the full IC cross section) for a jet with the parameters of the best fit shown in Fig. 2 but assuming a power law distribution $p = 3$ from $\gamma_e = 100$ up to $\gamma_{e,\text{cutoff}} \approx 3 \cdot 10^3$. (A $p = 3$ slope is expected for a steady state distribution of electrons injected with the canonical $p = 2$ power law in the presence of strong Thompson IC cooling.) The >100 MeV lightcurve was indistinguishable from the one in Fig. 2, even though the cutoff energy changed significantly along the orbit due to Doppler boosting. Hence, the results obtained here are likely to extend when more complex spectral shapes and Klein-Nishina effects are taken into account.

3.3 Jet precession

The preceding section showed that the jet must be inclined in order to obtain good fits to the gamma-ray modulation. There is evidence for jet inclination in Cyg X-3 as well as other microquasars (Maccarone 2002). An inclined jet is likely to undergo precession on a timescale longer than the orbital period. There is currently no evidence for or against jet precession in Cyg X-3. Here, jet precession will manifest itself as a change in the gamma-ray modulation since θ_j will sample the full range from 0 to 2π in a full precession. Both the shape and amplitude are affected as shown in Figure 4. The peak flux phase and amplitude can vary dramatically from one precession phase to another.

The *Fermi* data already show a hint for a change in the phasing of the modulation between the two epochs during which Cyg X-3 was detected. In addition, the first reported detection of Cyg X-3 at 100 MeV from SAS-2 showed a gamma-ray orbital modulation correlated (instead of roughly anti-correlated) with the X-ray modulation (Lamb et al. 1977). Later observations by *Cos B* and EGRET failed to re-detect the source unambiguously (Mori et al. 1997). A possible explanation is that the jet orientation had changed in between these observations. Future *Fermi* observations of Cyg X-3 may find a different modulation lightcurve or may actually fail to detect the source

because of its low flux, even though Cyg X-3 shows the right radio and X-ray state.

The comparison between gamma-ray lightcurves can serve as a very powerful diagnostic of the jet geometry. For instance, in the microblazar models discussed in §3.2, the near perfect alignment of a jet with the line-of-sight and the high β means that the gamma-ray flux is detectable only during the very short interval in precession phase where it is Doppler boosted. The gamma-ray flux will be deboosted most of the time — so that the *Fermi* and *AGILE* detections would have required very special circumstances.

4 CONCLUSIONS

The orbital modulation of the >100 MeV flux from Cyg X-3 can be very well fitted by a simple-minded model in which the emission is due to HE electrons up-scattering stellar photons. The HE electrons are situated in two symmetric locations in a relativistic jet with an arbitrary orientation.

The fitting procedure reveals that the jet is necessarily inclined to the orbital plane normal. The most likely value is close to the line-of-sight ($\phi_j \approx i$, in agreement with the conclusions based on radio imaging of the jet (Mioduszewski et al. 2001). The HE electrons cannot be close to the compact object. They are outside of the system at distances of at least one orbital separation, possibly up to $10d$. IC scattering of accretion disc photons is then irrelevant. If the compact object in Cyg X-3 is a neutron star, the required power in HE electrons is a significant fraction of the Eddington luminosity. For a black hole, because of the lower system inclination implied, the power required can be as low as $10^{-3} L_{\text{Edd}}$. These conclusions appear robust even when more complex electron distributions and the full IC cross-section are taken into account. Precession can be expected from an inclined jet. It should cause a change in the shape and amplitude of the gamma-ray modulation in the future.

The IC cooling timescale is $t_{\text{ic}} \approx 0.5(\gamma_e/10^3)^{-1}(R/d)^2$ seconds (scaled to the orbital separation d and for orbit O1). The size of the gamma ray emitting region is roughly $s \approx \beta c t_{\text{ic}}$, giving $s/R \lesssim 0.04\beta(\gamma_e/10^3)^{-1}(R/d)$ when scaled to R . Hence, the assumption that the emission in the *Fermi* energy range is localised holds up to distances $\approx 10d$ from the star. Cooling slows down at lower energies and electrons emit synchrotron radio beyond the γ -ray emission zone on much larger scales.

The γ -ray emission zone could be related to electron acceleration at a recollimation shock as the jet pushes its way through the stellar wind. The jet is initially over-pressured compared to its environment. It expands freely until its pressure p_j matches that of the environment p_e . Here, p_e is the ram pressure of the supersonic wind $\rho_w v_w^2$. The jet pressure is $p_j \sim L_j/(\pi c \Theta^2 l^2)$ where L_j is the jet power, Θ is its opening angle and l is the distance along the jet (e.g. Bednarek & Protheroe 1997). The pressures equilibrate at

$$\frac{l}{R} \sim 0.5 \Theta^{-1} L_{38}^{1/2} \dot{M}_{-5}^{-1/2} v_{1000}^{-1/2} \quad (7)$$

with $L_j = 10^{38}$ erg s $^{-1}$, $\dot{M}_w = 10^{-5} M_{\odot}$ yr $^{-1}$ and $v_w = 1000$ km s $^{-1}$. A jet recollimation shock forms beyond l . The shock crosses the jet axis after a further distance of order l

when the external pressure is constant (Stawarz et al. 2006). This is roughly the case here since the jet does not extend very far from the system and the dependence of p_w with l remain shallow (unless it is pointed directly away from the star). The location is consistent with the values of H derived above, suggesting this is where jet kinetic or magnetic energy is channeled into particle acceleration. This should be verified by calculations taking into account the non-radial nature of the jet-wind interaction. The shock occurs in the wind only because \dot{M}_w is very large (WR star) and the orbit very tight. Most microquasar jets will actually break out of the immediate vicinity of the system and interact much further away when their pressure matches that of the ISM. Any HE particles there will find a much weaker radiation environment and will be less likely to produce a (modulated) IC gamma-ray flux detectable by *Fermi* or *AGILE*.

The emerging picture is that of a jet launched around a black hole, with a moderate bulk relativistic speed, oriented not too far from the line-of-sight, interacting with the WR stellar wind to produce a shock at a distance of $1-10d$ from the system, where electrons are accelerated to GeV energies and upscatter star photons.

ACKNOWLEDGMENTS

The authors thank S. Corbel, J.-P. Lasota, L. Stawarz and A. Szostek for comments. This work was supported by the European Community via contract ERC-StG-200911.

REFERENCES

- Abdo A. A., et al. (*Fermi*-LAT collaboration) 2009, *Science*, 326, 1512
- Bednarek W., Protheroe R. J., 1997, *MNRAS*, 287, L9
- Bonnet-Bidaud J. M., Chardin G., 1988, *Phys. Rep.*, 170, 326
- Dubus G., Cerutti B., Henri G., 2010, *A&A*, submitted
- Hanson M. M., Still M. D., Fender R. P., 2000, *ApJ*, 541, 308
- Lamb R. C., Fichtel C. E., Hartman R. C., Kniffen D. A., Thompson D. J., 1977, *ApJ*, 212, L63
- Lampton M., Margon B., Bowyer S., 1976, *ApJ*, 208, 177
- Ling Z., Zhang S. N., Tang S., 2009, *ApJ*, 695, 1111
- Maccarone T. J., 2002, *MNRAS*, 336, 1371
- Meszáros P., Meyer F., Pringle J. E., 1977, *Nature*, 268, 420
- Mioduszewski A. J., Rupen M. P., Hjellming R. M., Pooley G. G., Waltman E. B., 2001, *ApJ*, 553, 766
- Mori M., et al. 1997, *ApJ*, 476, 842
- Pringle J. E., 1974, *Nature*, 247, 21
- Stawarz L., Aharonian F., Kataoka J., Ostrowski M., Siemiginowska A., Sikora M., 2006, *MNRAS*, 370, 981
- Szostek A., Zdziarski A. A., 2008, *MNRAS*, 386, 593
- Szostek A., Zdziarski A. A., McCollough M. L., 2008, *MNRAS*, 388, 1001
- Tavani M., et al. (*AGILE* collaboration) 2009, *Nature*, 462, 620
- van Kerkwijk M. H., Geballe T. R., King D. L., van der Klis M., van Paradijs J., 1996, *A&A*, 314, 521

6 *G. Dubus, B. Cerutti and G. Henri*

Vilhu O., Hakala P., Hannikainen D. C., McCollough M.,
Koljonen K., 2009, A&A, 501, 679

Part V

Conclusion

12

Conclusion

Outline

1. What we have learned	259
§ 87. <i>Gamma-ray emission in gamma-ray binaries</i>	259
§ 88. <i>Pair cascade emission in gamma-ray binaries</i>	260
§ 89. <i>High-energy emission from relativistic outflows</i>	261
2. Open questions and looking forwards	262

GAMMA-RAY BINARIES AND MICROQUASARS provide novel environments for the study of pulsar winds and relativistic jets at very small spatial scales (AU scales). I have shown in this thesis that a simple modeling of the high-energy gamma-ray emission can put tight constraints on the physical parameters in these systems. I briefly summarize below the main results obtained and give some possible research directions addressed to future investigations.

1. What we have learned

The main objective of this thesis was to understand why the gamma-ray emission is orbital modulated in gamma-ray emitting binaries. This issue lead me to explore the gamma-ray emission mechanisms in gamma-ray binaries (§ 89), pair cascade radiation (§ 90) and Doppler-boosted emission in relativistic outflows (pulsar winds and jets) (§ 91).

§ 89. Gamma-ray emission in gamma-ray binaries

My investigations on the modeling of the high-energy radiation from binaries were first triggered by the intriguing orbital modulation of the TeV gamma-ray flux uncovered by HESS in LS 5039. The stability of the lightcurve suggests that the modulation is mainly due to geometrical effects. In the pulsar wind nebula scenario, gamma rays are produced by inverse Compton scattering of low-energy photons from the massive star on ultra-relativistic pairs injected by a young pulsar. Because of the well-known angular dependence of the Compton emissivity, the gamma-ray emission depends on the relative position of the observer with respect to both stars, hence on

the orbital phase. I studied the angular dependence of inverse Compton scattering and derived new analytical formulae convenient for spectral calculations, for a given anisotropic source of seed photons, in the Thomson approximation and in the general case including Klein-Nishina effects. I first applied these equations to gamma-ray binaries.

As a first attempt to model the gamma-ray orbital modulation in gamma-ray binaries, I built a simple model where ultra-relativistic electron-positron pairs are injected in a small region compared with the orbital separation. This is a prototype model of the shocked pulsar wind. Pairs cool down *via* inverse Compton scattering and synchrotron radiation. The subtle interplay between anisotropic Compton emission and pair production can reproduce correctly the TeV lightcurve observed by HESS in LS 5039. The comparison with observations constrains several key parameters in the system such as the strength of the magnetic field, the injected particle distribution and the total power in pairs. The modulation in the GeV energy band, where *Fermi* is operating, was also predicted but the spectral features (flux and cut-off) cannot be explained. I applied also this model to LS I +61°303 and PSR B1259 – 63 but the gamma-ray orbital modulation cannot be reproduced. The pulsar evolves in a more complex environment than in LS 5039. The physical conditions in the shocked pulsar wind region may vary dramatically along the orbit (*Be* wind, highly eccentric orbit). Other processes might dominate the gamma-ray modulation in these two systems (adiabatic cooling, interaction with the *Be* equatorial wind, pulsar-stellar wind mixing, ...).

According to the classical model of pulsar winds, high-energy emission should also be emitted by the Compton cooling of a mono-energetic plasma of pairs in the free pulsar wind, *i.e.* upstream the termination shock. In gamma-ray binaries, the shock front between the pulsar wind and the stellar wind is expected to lie very close to the pulsar (~ 0.1 AU) compared with isolated pulsars (~ 0.1 pc). Gamma-ray binaries are the best objects known today to probe the free pulsar wind. I performed a detailed study on the spectral signature expected from an unshocked pulsar wind in LS 5039 and LS I +61°303. The emission from the free pulsar wind is very strong along the orbit. GeV and TeV observations exclude such emission line. This non-detection leads to an important result: the classical Crab-like model for pulsar winds is too simplistic. It is conceivable that the wind may still be highly magnetized up to the termination shock. The wind may not have enough time to accelerate and transfer magnetic energy into kinetic energy for pairs regarding the small spatial scales probed in these systems. The "striped wind" model provides an interesting theoretical framework to interpret this possibility. In addition, this model could account for the GeV component observed by *Fermi* in LS 5039 and LS I +61°303. Specific studies should be carried out in this direction.

§ 90. Pair cascade emission in gamma-ray binaries

The modeling of the high-energy orbital modulation in LS 5039 provides a simple and good explanation for the orbital modulation of the TeV flux, but fails to explain HESS observations at orbital phases where the flux is highly absorbed. Pairs produced by gamma-ray absorption can reprocess a significant fraction of the absorbed energy in the TeV band and initiate a cascade of pairs. I aimed to quantify accurately the contribution from pair cascade emission in LS 5039 to see whether this process could explain the observed emission close to superior conjunction. In

order to compute pair cascade emission, I derived a new analytical solution for the spectrum of the pair created by photon-photon annihilation in an anisotropic radiation field.

As a first attempt to quantify the cascade emission, I developed a full semi-analytical model for one-dimensional pair cascade in binaries. This type of cascade develops as long as the magnetic deviations on pairs trajectories remains within the cone of emission of the pairs produced in the cascade. Applied to gamma-ray binaries, I found that 1D-cascade emission has a strong angular dependence and could dominate the primary absorbed gamma-ray flux at orbital phases where pair production is very high. In LS I +61°303, the 1D cascade does not contribute significantly to the gamma-ray flux all along the orbit. In LS 5039, the situation is quite different: the 1D cascade emission is important and add more flux close to superior conjunction as expected but contributes too much to be compatible with TeV observations. The development of this type of cascade in LS 5039 should be discarded. Nevertheless, this study provides the maximum contribution of the cascade possible at orbital phases where absorption is high. The development of a more general cascade cannot be excluded in LS 5039. In LS I +61°303 and PSR B1259 – 63, the cascade does not play any role in the formation of the high-energy emission.

The ambient magnetic field (pulsar and massive star) may deviate the pairs produced in the cascade. Hence, the cascade becomes tree-dimensional. If the magnetic field is high enough to confine and isotropize locally pairs, the 3D cascade radiation can be computed accurately with no additional assumptions and the problem becomes much more simple. The ambient magnetic field should not exceed a few Gauss or the cascade radiation will be quenched. In this thesis, I developed an original semi-analytical approach to calculate the cascade radiation generation by generation. In practice, only the first two generations can be computed in a reasonable amount of time. I initiated a collaboration with Julien Malzac to benefit from his experience on Monte Carlo methods, a powerful tool well adapted for multiple scattering problems. We found compatible results between both approaches for the first generation of particules. Applied to LS 5039, I found that the TeV gamma-ray modulation (amplitude and shape) is reasonably explained if the inclination of the system is rather low ($i \approx 40^\circ$), and if the primary emitter remains at the vicinity of the compact object. 3D pair cascade appears as a viable explanation for the TeV emission close to superior conjunction in LS 5039, even though it is difficult to explain precisely the shape and the amplitude of the modulation. We are probably reaching the limit of this simple model.

§ 91. High-energy emission from relativistic outflows

The intriguing X-ray orbital modulation observed in LS 5039 triggered my studies on the high-energy emission from relativistic outflow. We propose that the X-ray modulation in LS 5039 is related to the Doppler-boosting effect of the emitted radiation in the shocked pulsar wind. I found a new analytical solution to quantify correctly the Doppler-boosting effect on the anisotropic Compton emission in the Thomson regime, for an arbitrary orientation of the flow with respect to the observer. Assuming that the shocked pulsar wind is collimated in the orbital plane by the stellar wind, we found that a mildly relativistic motion of the shocked pulsar wind can change significantly the emitted non-thermal radiation. In LS 5039, the X-ray orbital modulation is reproduced by Doppler-boosted synchrotron radiation with a bulk velocity of the flow $\sim c/3$. The shape of the gamma-ray modulation is almost unchanged. In LS I +61°303, the puzzling phasing of the TeV maximum emission and the correlation with the

X-ray emission could be explained by the Doppler-boosting effects. In PSR B1259 – 63, the effect of a mildly relativistic motion of the flow does not play a significant in the X-ray and gamma-ray modulation.

My theoretical studies on the high-energy Doppler-boosted emission, initially developed for gamma-ray binaries, can be applied to the emission from relativistic jets in microquasars. We found that Doppler-boosted Compton emission explains the gamma-ray orbital modulation in Cygnus X–3 observed by *Fermi*. Assuming that the gamma-ray emission originates from two symmetric (with respect to the compact object) point-like locations in the jet, we constrained the orientation of the jet, the altitude of the gamma-ray source in the jet, the total energy in the pairs and the bulk velocity of the jet. The gamma-ray modulation is reproduced if the jet is oriented close to the line of sight. The pairs should not be localized too close to the compact object. In addition, GeV photons would be absorbed by the thermal radiation produced by a standard accretion disk if injected at the vicinity of the compact star. Energetically speaking, this study favors a massive compact object (black hole) in the system. This simple model predicts that the gamma-ray emission (flux, modulation) may change significantly with time if the jet precesses.

2. Open questions and looking forwards

In this manuscript, I have tried to answer to the list of questions presented in the introduction concerning the physics at work in gamma-ray emitting binaries. My investigations and new observations have brought new elements of response to these questions and have aroused also new ones addressed to future investigations. Here are some possible research directions:

- What is the origin of the GeV component (spectrum and modulation) in LS 5039 and LS I +61°303? This puzzling feature was not predicted by models. It appears clear today that an extra component of particles is necessary to explain the GeV emission. This may come from the pulsar itself in the system. Current models for the gamma-ray emission in the pulsar magnetosphere cannot account for the observed modulation. These models may have to be revisited in the case where there is a strong, external and anisotropic source of radiation (generated by the companion star). Alternative models such as the striped wind should be developed for gamma-ray binaries as well.
- What is the origin of the TeV gamma-ray modulation in LS I +61°303 and PSR B1259 – 63? In particular, how to explain the puzzling phasing of the gamma-ray flux maximum in LS I +61°303? These questions may be related to our poor knowledge of the interaction of a pulsar wind with the complex environment of a Be wind. Global relativistic MHD simulations should help in answering this question.
- How high-energy particles are accelerated in microquasar jets? Our studies revealed that high-energy pairs should not be accelerated close to the compact object, but further away at specific locations in the jet in Cygnus X–3. Particles may be accelerated at the recollimation shock generated by the interaction of the jet with the dense stellar wind. Global relativistic MHD simulations should also help in answering this question.

I have developed during this thesis an expertise in the modeling of the high-energy processes, particularly in those emitting gamma rays. The theoretical results obtained in this work concerning anisotropic inverse Compton scattering, pair production and Doppler-boosted

emission are general and could be applied to the modeling of other sources of non-thermal radiation such as *e.g.* blazars, gamma-ray bursts or pulsars/magnetars.

The study of gamma-ray binaries provides an opportunity to explore a new class of Galactic objects. The number of gamma-ray binaries present in our Galaxy is unknown but this number may not exceed a hundred. How do these systems evolve with time is also an important issue. Gamma-ray binaries could be the progenitors of the current population of high-mass X-ray binaries. *Fermi* and the future Cherenkov Telescope Array (CTA) may detect a dozen new systems (Cerutti *et al.* 2009d), allowing populations studies and more detailed modeling of these objects.

[Français] Conclusion

Les binaires gamma et les microquasars fournissent des environnements nouveaux à l'étude des vents de pulsar et des jets relativistes à de très courtes échelles spatiales (UA). J'ai montré dans cette thèse qu'un modèle simple de l'émission gamma de haute énergie permet de mettre des contraintes fortes sur les paramètres physiques dans ces systèmes. Je résume brièvement ici les principaux résultats obtenus et donne quelques pistes de recherche possibles destinées à de futures recherches.

3. Ce que nous avons appris

Le principal objectif de cette thèse était de comprendre pourquoi l'émission gamma est modulée à la période orbitale dans les binaires émettant en gamma. Cette question m'a conduit à étudier les mécanismes d'émission gamma dans les binaires gamma (§ 92), le rayonnement produit dans une cascade de paires (§ 93) et l'émission amplifiée dans les écoulements relativistes (vents de pulsars et jets) (§ 94).

§ 92. L'émission gamma dans les binaires gamma

Mes recherches sur la modélisation du rayonnement de haute énergie en provenance des binaires ont au départ été initiées par la curieuse modulation orbitale du flux gamma au TeV découverte par HESS dans LS 5039. La stabilité de la courbe de lumière suggère que la modulation est essentiellement due à des effets géométriques. Dans le scénario du vent de pulsar, les rayons gamma sont produits par diffusion Compton inverse de photons stellaires sur des paires ultra relativistes injectées par un pulsar jeune. En raison de la dépendance angulaire bien connue de l'émissivité Compton, l'émission gamma dépend de la position relative de l'observateur par rapport aux deux étoiles, donc de la phase orbitale. J'ai étudié la dépendance angulaire de la diffusion Compton inverse et dérivé de nouvelles formules analytiques très utiles pour les calculs spectraux, pour une source anisotrope de photon cible donnée, dans l'approximation Thomson et dans le cas général en incluant les effets Klein-Nishina. J'ai d'abord appliqué ces équations aux binaires gamma.

Dans un premier temps, j'ai construit un modèle simple où des paires électron-positron sont injectées dans une région petite par rapport à la séparation orbitale. C'est un modèle prototype pour l'émission du vent choqué du pulsar. Les paires se refroidissent par diffusion Compton inverse et par rayonnement synchrotron. Le jeu subtil entre l'émission Compton anisotrope et la production de paires peut reproduire correctement la courbe de lumière TeV observée par HESS dans LS 5039. La comparaison aux observations permet de contraindre plusieurs paramètres clés dans le système tels que l'intensité du champ magnétique, la distribution de particules injectée et la puissance totale dans les paires. La modulation GeV observée par *Fermi*, a également été

prédite mais les caractéristiques spectrales (flux et coupure) ne peuvent pas être expliquées. J'ai appliqué ce modèle à LS I +61°303 et PSR B1259 – 63 mais la modulation gamma ne peut pas être reproduite. Le pulsar évolue dans un environnement bien plus complexe que dans LS 5039. Les conditions physiques dans la région du vent choqué du pulsar peuvent varier énormément le long de l'orbite (vent étoile B_e , orbite très excentrique). D'autres processus pourraient dominer la modulation gamma dans ces deux systèmes (refroidissement adiabatique, interaction avec le vent équatorial de l'étoile B_e , mélange des vents pulsar-étoile, ...).

D'après les modèles classiques des vents de pulsar, de l'émission de haute énergie devrait aussi être émise lors du refroidissement Compton d'un plasma monoénergétique de paires dans le vent libre du pulsar, *i.e.* en amont du choc terminal. Dans les binaires gamma, le front de choc entre le vent du pulsar et le vent stellaire est attendu comme étant très proche du pulsar (~ 0.1 UA) comparé aux pulsars isolés (~ 0.1 pc). Les binaires gamma sont les meilleurs objets connus aujourd'hui pour sonder le vent non choqué du pulsar. J'ai réalisé une étude détaillée de la signature spectrale attendue d'un vent non choqué de pulsar dans LS 5039 et LS I +61°303. L'émission du vent libre du pulsar est très forte tout au long de l'orbite. Les observations au GeV et au TeV excluent une telle raie d'émission. Cette non détection conduit à un résultat important: le modèle classique du vent de pulsar type pulsar du Crabe est trop simpliste. Il est concevable que le vent soit encore hautement magnétisé lorsqu'il atteint le choc terminal. Le vent n'aurait peut-être pas suffisamment de temps pour accélérer et transférer l'énergie magnétique en énergie cinétique dans les paires étant donné les courtes échelles spatiales sondées dans ces systèmes. Le modèle du "vent strié" constitue un cadre théorique intéressant pour explorer cette piste. De plus, ce modèle pourrait aussi expliquer la composante au GeV observée par *Fermi* dans LS 5039 et LS I +61°303. Des études spécifiques devraient être menées sur cette voie.

§ 93. Emission d'une cascade de paires dans les binaires gamma

La modélisation de la modulation orbitale de haute énergie dans LS 5039 apporte une explication simple et correcte de la modulation du flux au TeV, mais ne permet pas d'expliquer les observations HESS aux phases orbitales où le flux est fortement absorbé. Les paires produites par absorption gamma peuvent recycler une fraction significative de l'énergie absorbée au TeV et initier une cascade de paires. Mon but était de quantifier précisément la contribution en provenance de l'émission d'une cascade de paires dans LS 5039 et de voir si un tel processus pouvait expliquer l'émission observée autour de la conjonction supérieure. Avec pour objectif de calculer l'émission de la cascade, j'ai dérivé une nouvelle solution analytique du spectre de la paire créée par annihilation photon-photon dans un champ de rayonnement anisotrope.

Dans un premier temps, j'ai développé un modèle semi-analytique complet pour le calcul de l'émission d'une cascade unidimensionnelle dans les binaires. Ce type de cascade se développe si les déviations magnétiques sur les trajectoires des paires restent dans le cône d'émission des paires une fois produites dans la cascade. En appliquant ce modèle aux binaires gamma, j'ai trouvé que l'émission de la cascade 1D a une forte dépendance angulaire et qu'elle domine le flux primaire absorbé aux phases orbitales où la production de paire est très élevée. Dans LS I +61°303, la cascade 1D ne contribue pas significativement au flux gamma tout au long de l'orbite. Dans LS 5039, la situation est tout autre: l'émission de la cascade 1D est importante et ajoute plus de flux autour de la conjonction supérieure comme attendu mais contribue trop pour

être compatible avec les observations TeV. Le développement de ce type de cascade dans LS 5039 peut être écarté. Néanmoins, cette étude donne la contribution maximale possible de la cascade aux phases orbitales où l'absorption est forte. Le développement d'une cascade plus générale ne peut pas être exclue dans LS 5039. Dans LS I +61°303 et PSR B1259 – 63, la cascade ne joue pas de rôle important dans la formation de l'émission de haute énergie.

Le champ magnétique ambiant (pulsar et étoile massive) peut dévier les paires produites dans la cascade. Si tel est le cas, la cascade devient alors tridimensionnelle. Si le champ magnétique est suffisamment fort pour confiner et isotropiser localement les paires, le rayonnement de la cascade 3D peut être précisément calculé sans hypothèses supplémentaires et le problème devient alors beaucoup plus simple. Le champ magnétique ambiant ne doit pas excéder quelques Gauss ou l'émission de la cascade sera inhibée. Dans cette thèse, j'ai développé une approche semi-analytique originale pour calculer le rayonnement de la cascade génération par génération. En pratique, seules les deux premières générations peuvent être calculées en un temps raisonnable. J'ai initié une collaboration avec Julien Malzac pour bénéficier de son expérience sur les méthodes de calcul Monte Carlo, un outil puissant bien adapté aux problèmes de diffusions multiples. Nous avons trouvé des résultats compatibles entre les deux approches pour la première génération de particules. En appliquant le modèle à LS 5039, j'ai trouvé que la modulation gamma au TeV (forme et amplitude) est raisonnablement expliquée si l'inclinaison du système est plutôt faible ($i \approx 40^\circ$), et si l'émetteur primaire reste au voisinage de l'objet compact. La cascade 3D de paires apparaît comme une explication possible de l'émission TeV autour de la conjonction supérieure dans LS 5039, même si il est difficile de reproduire précisément à la fois la forme et l'amplitude de la modulation. Nous atteignons probablement les limites du modèle.

§ 94. Emission de haute énergie dans les écoulement relativistes

L'étonnante modulation orbitale du flux X observée dans LS 5039 a initié mes recherches sur l'émission de haute énergie dans les écoulement relativistes. Nous proposons que la modulation orbitale X dans LS 5039 est reliée à l'amplification Doppler de l'émission rayonnée dans le vent choqué du pulsar. J'ai trouvé une nouvelle solution analytique pour quantifier correctement les effets d'amplification Doppler de l'émission Compton inverse anisotrope dans l'approximation Thomson, et pour une orientation arbitraire de l'écoulement par rapport à l'observateur. En supposant que le vent choqué du pulsar est collimaté dans le plan de l'orbite par le vent stellaire, nous avons trouvé qu'un mouvement modérément relativiste du vent choqué suffit pour changer significativement le rayonnement non-thermique émis. Dans LS 5039, la modulation orbitale X est reproduite par le rayonnement synchrotron amplifié Doppler pour une vitesse d'ensemble du flot $\sim c/3$. La forme de la modulation gamma reste presque inchangée. Dans LS I +61°303, la position étonnante du maximum de l'émission au TeV et la corrélation avec l'émission X pourraient être expliqués par les effets d'amplification Doppler. Dans PSR B1259 – 63, l'effet d'un mouvement modérément relativiste de l'écoulement ne joue pas de rôle essentiel dans la modulation X ou gamma.

Mes études théoriques sur l'émission amplifiée Doppler de haute énergie, initialement développées pour les binaires gamma, peuvent être appliquées à l'émission des jets relativistes dans les microquasars. Nous avons trouvé que de l'émission Compton amplifiée par effet

Doppler permet d'expliquer la modulation orbitale gamma de Cygnus X-3 observée par *Fermi*. En supposant que l'émission gamma provient de deux régions symétriques (par rapport à l'objet compact) et ponctuelles dans le jet, nous pouvons contraindre l'orientation du jet, l'altitude de la source gamma dans le jet, l'énergie totale dans les paires et la vitesse du jet. La modulation gamma est reproduite si le jet est orienté dans une direction proche de la ligne de visée. Les paires ne doivent être localisées trop près de l'objet compact. De plus, les photons du GeV seraient absorbés par le rayonnement thermique produit par un disque d'accrétion standard si injectés à proximité de l'étoile compacte. Energétiquement parlant, cette étude favorise un objet compact massif (trou noir) dans le système. Ce modèle simple prédit que l'émission gamma (flux, modulation) pourrait changer significativement au cours du temps si le jet précède.

4. Questions ouvertes et perspectives

Dans ce manuscrit, j'ai essayé de répondre à la liste de questions présentée dans l'introduction concernant la physique en jeu dans les binaires émettant en gamma. Mes recherches et les nouvelles observations ont apporté de nouveaux éléments de réponse à ces questions et ont aussi suscité de nouvelles, destinées à des recherches futures. Voici quelques pistes de recherches possibles:

- Quelle est l'origine de la composante GeV (spectre et modulation) dans LS 5039 et LS I +61°303? Cette caractéristique étonnante n'a pas été prédite par les modèles. Il apparaît clair aujourd'hui qu'une composante supplémentaire de particules est nécessaire pour expliquer l'émission au GeV. Elle pourrait provenir directement du pulsar présent dans le système. Les modèles actuels d'émission gamma dans la magnétosphère du pulsar ne permettent pas de rendre compte de la modulation observée. Ces modèles devraient peut-être être revus dans le cas où il existe une source externe intense et anisotrope de rayonnement (générée par l'étoile compagne). D'autres modèles tels que le vent strié devraient être développés dans les binaires gamma.
- Quelle est l'origine de la modulation gamma TeV dans LS I +61°303 et PSR B1259 – 63? En particulier, comment expliquer la position étonnante (sur l'orbite) du pic d'émission gamma dans LS I +61°303? Ces questions sont probablement liées à notre mauvaise connaissance de l'interaction entre un vent de pulsar et l'environnement complexe d'un vent d'étoile Be. Des simulations MHD relativistes globales devraient aider à répondre à ces questions.
- Comment des particules de haute énergie sont accélérées dans les jets de microquasar? Nos études ont révélées que les paires de haute énergie ne devraient pas être accélérées trop près de l'objet compact, mais plus loin à des endroits bien précis dans le jet de Cygnus X-3. Les particules pourraient être accélérées dans un choc de recollimation généré par l'interaction entre le jet et le dense vent stellaire. Des simulations MHD relativistes globales devraient également contribuer à répondre à cette question.

J'ai développé au cours de cette thèse une expertise dans la modélisation des processus de haute énergie, en particulier dans ceux qui émettent des rayons gamma. Les résultats théoriques obtenus dans ce travail concernant la diffusion Compton inverse anisotrope, la production de paire et l'amplification Doppler de l'émission sont généraux et pourraient être appliqués à la

modélisation d'autres sources de rayonnement non-thermique telles que *e.g.* les blazars, les sursauts gamma ou encore les pulsars/magnétars.

Etudier les binaires gamma, c'est aussi la chance de découvrir une nouvelle classe d'objets galactiques. Le nombre de binaires gamma présentes dans notre galaxie est inconnu mais ce nombre se dépasse sans doute pas une centaine. Comment ces systèmes évoluent au cours du temps est aussi une question importante. Les binaires gamma pourraient être les ancêtres de la population des binaires X massives actuelles. *Fermi* et le futur réseau de télescope Cherenkov CTA pourraient détecter une douzaine de nouveaux systèmes (Cerutti *et al.* 2009d), permettant ainsi des études de populations et une modélisation plus détaillée de ces objets.

Part VI

References

Bibliography

- Abdo, A. A., Ackermann, M., Ajello, M., Atwood, W. B. *et al.* 2009a, Fermi LAT Observations of LS I +61 303: First Detection of an Orbital Modulation in GeV Gamma Rays, *Astrophysical Journal, Letters* **701**, L123.
- Abdo, A. A., Ackermann, M., Ajello, M., Atwood, W. B. *et al.* 2009b, Fermi/LAT observations of LS 5039, *Astrophysical Journal, Letters* **706**, L56.
- Abramowitz, M. et Stegun, I. A. 1972, *Handbook of Mathematical Functions*.
- Acciari, V. A., Aliu, E., Arlen, T., Beilicke, M. *et al.* 2009, Evidence for Long-Term Gamma-Ray and X-Ray Variability from the Unidentified TeV Source HESS J0632+057, *Astrophysical Journal, Letters* **698**, L94.
- Acciari, V. A., Beilicke, M., Blaylock, G., Bradbury, S. M. *et al.* 2008, VERITAS Observations of the γ -Ray Binary LS I +61 303, *Astrophysical Journal* **679**, 1427.
- Aharonian, F., Akhperjanian, A. G., Anton, G., Barres de Almeida, U. *et al.* 2009, Very high energy γ -ray observations of the binary PSR B1259-63/SS2883 around the 2007 Periastron, *Astron. & Astrophys.* **507**, 389.
- Aharonian, F., Akhperjanian, A. G., Aye, K., Bazer-Bachi, A. R. *et al.* 2005a, Discovery of Very High Energy Gamma Rays Associated with an X-ray Binary, *Science* **309**, 746.
- Aharonian, F., Akhperjanian, A. G., Aye, K., Bazer-Bachi, A. R. *et al.* 2005b, Discovery of the binary pulsar PSR B1259-63 in very-high-energy gamma rays around periastron with HESS, *Astron. & Astrophys.* **442**, 1.
- Aharonian, F., Akhperjanian, A. G., Bazer-Bachi, A. R., Beilicke, M. *et al.* 2006, 3.9 day orbital modulation in the TeV γ -ray flux and spectrum from the X-ray binary LS 5039, *Astron. & Astrophys.* **460**, 743.
- Aharonian, F. A., Akhperjanian, A. G., Bazer-Bachi, A. R., Behera, B. *et al.* 2007, Discovery of a point-like very-high-energy γ -ray source in Monoceros, *Astron. & Astrophys.* **469**, L1.
- Aharonian, F. A., Atoian, A. M. et Nagapetian, A. M. 1983, Photoproduction of electron-positron pairs in compact X-ray sources, *Astrofizika* **19**, 323.
- Aharonian, F. A. et Atoyan, A. M. 2000, Broad-band diffuse gamma ray emission of the galactic disk, *Astron. & Astrophys.* **362**, 937.
- Albert, J., Aliu, E., Anderhub, H., Antonelli, L. A. *et al.* 2009, Periodic Very High Energy γ -Ray Emission from LS I +61 303 Observed with the MAGIC Telescope, *Astrophysical Journal* **693**, 303.
- Albert, J., Aliu, E., Anderhub, H., Antoranz, P. *et al.* 2006, Variable Very-High-Energy Gamma-Ray Emission from the Microquasar LS I +61 303, *Science* **312**, 1771.
- Albert, J., Aliu, E., Anderhub, H., Antoranz, P. *et al.* 2007, Very High Energy Gamma-Ray Radiation from the Stellar Mass Black Hole Binary Cygnus X-1, *Astrophysical Journal, Letters* **665**, L51.

- Anderhub, H., Antonelli, L. A., Antoranz, P., Backes, M. *et al.* 2009, Correlated X-Ray and Very High Energy Emission in the Gamma-Ray Binary LS I +61 303, *Astrophysical Journal, Letters* **706**, L27.
- Anguelov, V., Petrov, S., Gurdev, L. et Kourtev, J. 1999, On the numerical analysis of triplet pair production cross-sections and the mean energy of produced particles for modelling electron-photon cascade in a soft photon field, *Journal of Physics G Nuclear Physics* **25**, 1733.
- Aragona, C., McSwain, M. V., Grundstrom, E. D., Marsh, A. N. *et al.* 2009, The Orbits of the γ -Ray Binaries LS I +61 303 and LS 5039, *Astrophysical Journal* **698**, 514.
- Arons, J. 2008, Filamentation Instability of Interacting Current Sheets in Striped Relativistic Winds: The Origin of Low Sigma?, dans C. Bassa, Z. Wang, A. Cumming, & V. M. Kaspi (éditeur), *40 Years of Pulsars: Millisecond Pulsars, Magnetars and More*, vol. 983 de *American Institute of Physics Conference Series*, pp. 200–206.
- Arons, J. et Tavani, M. 1993, High-energy emission from the eclipsing millisecond pulsar PSR 1957+20, *Astrophysical Journal* **403**, 249.
- Ball, L. et Kirk, J. G. 2000, Probing pulsar winds using inverse compton scattering, *Astroparticle Physics* **12**, 335.
- Bednarek, W. 1993, Can high-energy gamma-ray photons escape from the radiation field emitted by an accretion disk?, *Astron. & Astrophys.* **278**, 307.
- Bednarek, W. 1997, Cascade initiated by VHE γ -rays in the radiation field of a close massive companion., *Astron. & Astrophys.* **322**, 523.
- Bednarek, W. 2006, Propagation of very high energy γ -rays inside massive binaries LS 5039 and LSI +61 303, *Mon. Not. of the Royal Astron. Soc.* **368**, 579.
- Bednarek, W. 2007, GeV-TeV γ -ray light curves expected in the IC e^\pm pair cascade model for massive binaries: application to LS 5039, *Astron. & Astrophys.* **464**, 259.
- Begelman, M. C. et Li, Z. 1992, An axisymmetric magnetohydrodynamic model for the Crab pulsar wind bubble, *Astrophysical Journal* **397**, 187.
- Bethe, H. A. et Mott, N. F. 1934, The influence of screening on the creation and stopping of electrons, dans *Proceedings of the Cambridge Philosophical Society*, vol. 30 de *Proceedings of the Cambridge Philosophical Society*, pp. 524–+.
- Bignami, G. F., Maraschi, L. et Treves, A. 1977, Cyg X-3: a young pulsar in a binary system?, *Astron. & Astrophys.* **55**, 155.
- Blumenthal, G. R. et Gould, R. J. 1970, Bremsstrahlung, Synchrotron Radiation, and Compton Scattering of High-Energy Electrons Traversing Dilute Gases, *Reviews of Modern Physics* **42**, 237.
- Bogovalov, S. V. 1999, On the physics of cold MHD winds from oblique rotators, *Astron. & Astrophys.* **349**, 1017.
- Bogovalov, S. V. et Aharonian, F. A. 2000, Very-high-energy gamma radiation associated with the unshocked wind of the Crab pulsar, *Mon. Not. of the Royal Astron. Soc.* **313**, 504.
- Bogovalov, S. V. et Khangulyan, D. V. 2002a, On the origin of the torus and jet-like structures in the centre of the Crab Nebula, *Mon. Not. of the Royal Astron. Soc.* **336**, L53.
- Bogovalov, S. V. et Khangulyan, D. V. 2002b, The Crab Nebula: Interpretation of Chandra Observations, *Astronomy Letters* **28**, 373.

- Bogovalov, S. V., Khangulyan, D. V., Koldoba, A. V., Ustyugova, G. V. *et al.* 2008, Modelling interaction of relativistic and non-relativistic winds in binary system PSR B1259-63/SS2883 - I. Hydrodynamical limit, *Mon. Not. of the Royal Astron. Soc.* **387**, 63.
- Bonometto, S. et Rees, M. J. 1971, On possible observable effects of electron pair-production in QSOs, *Mon. Not. of the Royal Astron. Soc.* **152**, 21.
- Bosch-Ramon, V. et Khangulyan, D. 2009, Understanding the Very-High Emission from Microquasars, *International Journal of Modern Physics D* **18**, 347.
- Bosch-Ramon, V., Khangulyan, D. et Aharonian, F. A. 2008a, Non-thermal emission from secondary pairs in close TeV binary systems, *Astron. & Astrophys.* **482**, 397.
- Bosch-Ramon, V., Khangulyan, D. et Aharonian, F. A. 2008b, The magnetic field and the location of the TeV emitter in Cygnus ;X-1 and LS ;5039, *Astron. & Astrophys.* **489**, L21.
- Böttcher, M. et Schlickeiser, R. 1997, The pair production spectrum from photon-photon annihilation., *Astron. & Astrophys.* **325**, 866.
- Brainerd, J. J. et Petrosian, V. 1987, Analytic and numerical calculations of quantum synchrotron spectra from relativistic electron distributions, *Astrophysical Journal* **320**, 703.
- Breit, G. et Wheeler, J. A. 1934, Collision of Two Light Quanta, *Physical Review* **46**, 1087.
- Brown, R. W., Hunt, W. F., Mikaelian, K. O. et Muzinich, I. J. 1973, Role of $\gamma+\gamma \rightarrow e^+ + e^- + e^+ + e^-$ in Photoproduction, Colliding Beams, and Cosmic Photon Absorption, *Phys. Rev. D* **8**, 3083.
- Bucciantini, N., Amato, E. et Del Zanna, L. 2005, Relativistic MHD simulations of pulsar bow-shock nebulae, *Astron. & Astrophys.* **434**, 189.
- Carraminana, A. 1992, Pair absorption of TeV gamma-rays in accreting binaries, *Astron. & Astrophys.* **264**, 127.
- Casares, J., Ribas, I., Paredes, J. M., Martí, J. *et al.* 2005a, Orbital parameters of the microquasar LS I +61 303, *Mon. Not. of the Royal Astron. Soc.* **360**, 1105.
- Casares, J., Ribó, M., Ribas, I., Paredes, J. M. *et al.* 2005b, A possible black hole in the γ -ray microquasar LS 5039, *Mon. Not. of the Royal Astron. Soc.* **364**, 899.
- Cerutti, B., Dubus, G. et Henri, G. 2007, Anisotropic inverse Compton scattering in gamma-ray binaries, dans J. Bouvier, A. Chalabaev, & C. Charbonnel (éditeur), *SF2A-2007: Proceedings of the Annual meeting of the French Society of Astronomy and Astrophysics held in Grenoble, France, July 2-6, 2007*, Eds.: J. Bouvier, A. Chalabaev, and C. Charbonnel, p.158, pp. 158–+.
- Cerutti, B., Dubus, G. et Henri, G. 2008a, Probing pulsar winds with gamma-ray binaries, dans C. Charbonnel, F. Combes, & R. Samadi (éditeur), *SF2A-2008*, pp. 187–+.
- Cerutti, B., Dubus, G. et Henri, G. 2008b, Spectral signature of a free pulsar wind in the gamma-ray binaries LS 5039 and LSI +61 303, *Astron. & Astrophys.* **488**, 37.
- Cerutti, B., Dubus, G. et Henri, G. 2009a, Modeling the high-energy radiation in gamma-ray binaries, *ArXiv e-prints* .
- Cerutti, B., Dubus, G. et Henri, G. 2009b, One-dimensional pair cascade emission in gamma-ray binaries. An upper-limit to cascade emission at superior conjunction in LS 5039, *Astron. & Astrophys.* **507**, 1217.
- Cerutti, B., Dubus, G. et Henri, G. 2009c, Pair cascading in gamma-ray binaries, dans M. Heydari-Malayeri, C. Reylé, & R. Samadi (éditeur), *SF2A-2009: Proceedings of the Annual*

meeting of the French Society of Astronomy and Astrophysics, held 29 June - 4 July 2009 in Besançon, France. Eds.: M. Heydari-Malayeri, C. Reylé and R. Samadi, p.139, pp. 139–+.

- Cerutti, B., Dubus, G. et Henri, G. 2010a, Anisotropic Pair Cascading in Gamma-Ray Binaries, dans J. Martí, P. L. Luque-Escamilla, & J. A. Combi (éditeur), *Astronomical Society of the Pacific Conference Series*, vol. 422 de *Astronomical Society of the Pacific Conference Series*, pp. 41–+.
- Cerutti, B., Dubus, G. et Henri, G. 2010b, Anisotropic pair cascading in gamma-ray binaries, dans N. Rea & D. F. Torres (éditeur), *ICREA Workshop on The High-Energy Emission from Pulsars and their Systems*, *Astrophysics and Space Science Proceedings*.
- Cerutti, B., Dubus, G., Henri, G., Hill, A. B. *et al.* 2009d, What Can Simbol-X Do for Gamma-ray Binaries?, dans J. Rodriguez & P. Ferrando (éditeur), *American Institute of Physics Conference Series*, vol. 1126 de *American Institute of Physics Conference Series*, pp. 263–266.
- Cerutti, B., Malzac, J., Dubus, G. et Henri, G. 2010c, Modeling the three-dimensional pair cascade in binaries. Application to LS 5039, *ArXiv e-prints* .
- Cheng, K. S., Ho, C. et Ruderman, M. 1986, Energetic radiation from rapidly spinning pulsars. I - Outer magnetosphere gaps. II - VELA and Crab, *Astrophysical Journal* **300**, 500.
- Chernyakova, M. A. et Illarionov, A. F. 1999, Non-pulsed gamma radiation from a binary system with a pulsar, *Mon. Not. of the Royal Astron. Soc.* **304**, 359.
- Coppi, P. S. 1999, The Physics of Hybrid Thermal/Non-Thermal Plasmas, dans J. Poutanen & R. Svensson (éditeur), *High Energy Processes in Accreting Black Holes*, vol. 161 de *Astronomical Society of the Pacific Conference Series*, pp. 375–+.
- Corbel, S., Fender, R. P., Tzioumis, A. K., Tomsick, J. A. *et al.* 2002, Large-Scale, Decelerating, Relativistic X-ray Jets from the Microquasar XTE J1550-564, *Science* **298**, 196.
- Coroniti, F. V. 1990, Magnetically striped relativistic magnetohydrodynamic winds - The Crab Nebula revisited, *Astrophysical Journal* **349**, 538.
- Dermer, C. D. 1986, Secondary production of neutral pi-mesons and the diffuse galactic gamma radiation, *Astron. & Astrophys.* **157**, 223.
- Dermer, C. D. et Böttcher, M. 2006, Gamma Rays from Compton Scattering in the Jets of Microquasars: Application to LS 5039, *Astrophysical Journal* **643**, 1081.
- Dermer, C. D. et Schlickeiser, R. 1991, Effects of triplet pair production on ultrarelativistic electrons in a soft photon field, *Astron. & Astrophys.* **252**, 414.
- Dermer, C. D. et Schlickeiser, R. 1993, Model for the High-Energy Emission from Blazars, *Astrophysical Journal* **416**, 458.
- Dermer, C. D., Schlickeiser, R. et Mastichiadis, A. 1992, High-energy gamma radiation from extragalactic radio sources, *Astron. & Astrophys.* **256**, L27.
- Donati, J. et Landstreet, J. D. 2009, Magnetic Fields of Nondegenerate Stars, *Annual Review of Astron and Astrophys* **47**, 333.
- Dubus, G. 2006a, Gamma-ray absorption in massive X-ray binaries, *Astron. & Astrophys.* **451**, 9.
- Dubus, G. 2006b, Gamma-ray binaries: pulsars in disguise?, *Astron. & Astrophys.* **456**, 801.
- Dubus, G., Cerutti, B. et Henri, G. 2008, The modulation of the gamma-ray emission from the binary LS 5039, *Astron. & Astrophys.* **477**, 691.

- Dubus, G., Cerutti, B. et Henri, G. 2010a, Relativistic Doppler-boosted emission in gamma-ray binaries, *ArXiv e-prints* .
- Dubus, G., Cerutti, B. et Henri, G. 2010b, The relativistic jet of Cygnus X-3 in gamma-rays, *Mon. Not. of the Royal Astron. Soc.* pp. L35+.
- Duncan, R. C. 2000, Physics in ultra-strong magnetic fields, dans R. M. Kippen, R. S. Mallozzi, & G. J. Fishman (éditeur), *Gamma-ray Bursts, 5th Huntsville Symposium*, vol. 526 de *American Institute of Physics Conference Series*, pp. 830–841.
- Duncan, R. C. et Thompson, C. 1992, Formation of very strongly magnetized neutron stars - Implications for gamma-ray bursts, *Astrophysical Journal, Letters* **392**, L9.
- Eichler, D. et Usov, V. 1993, Particle acceleration and nonthermal radio emission in binaries of early-type stars, *Astrophysical Journal* **402**, 271.
- Erber, T. 1966, High-Energy Electromagnetic Conversion Processes in Intense Magnetic Fields, *Reviews of Modern Physics* **38**, 626.
- Fargion, D., Konoplich, R. V. et Salis, A. 1997, Inverse Compton scattering on laser beam and monochromatic isotropic radiation, *Z. Phys. C.* **74**, 571.
- Fermi LAT Collaboration 2009, Modulated High-Energy Gamma-Ray Emission from the Microquasar Cygnus X-3, *Science* **326**, 1512.
- Fermi LAT collaboration 2009, The First Fermi Large Area Telescope Catalog of Gamma-ray Pulsars, *ArXiv e-prints* .
- Gaensler, B. M. et Slane, P. O. 2006, The Evolution and Structure of Pulsar Wind Nebulae, *Annual Review of Astron and Astrophys* **44**, 17.
- Gaisser, T. K. 1990, *Cosmic rays and particle physics*.
- Georganopoulos, M., Kirk, J. G. et Mastichiadis, A. 2001, The Beaming Pattern and Spectrum of Radiation from Inverse Compton Scattering in Blazars, *Astrophysical Journal* **561**, 111.
- Ginzburg, V. L. et Syrovatskii, S. I. 1964, *The Origin of Cosmic Rays*.
- Ginzburg, V. L. et Syrovatskii, S. I. 1965, Cosmic Magnetobremstrahlung (synchrotron Radiation), *Annual Review of Astron and Astrophys* **3**, 297.
- Gould, R. J. 1969, High-Energy Bremsstrahlung in Collisions of Electrons with One- and Two-Electron Atoms, *Physical Review* **185**, 72.
- Gould, R. J. et Schröder, G. P. 1967, Pair Production in Photon-Photon Collisions, *Physical Review* **155**, 1404.
- Heitler, W. 1954, *Quantum theory of radiation*.
- Hermsen, W., Bloemen, J. B. G. M., Jansen, F. A., Bennett, K. *et al.* 1987, High-energy gamma-ray and hard X-ray observations of CYG X-3, *Astron. & Astrophys.* **175**, 141.
- Hinton, J. A., Skilton, J. L., Funk, S., Brucker, J. *et al.* 2009, HESS J0632+057: A New Gamma-Ray Binary?, *Astrophysical Journal, Letters* **690**, L101.
- Hoffmann, A. D., Klochkov, D., Santangelo, A., Horns, D. *et al.* 2009, INTEGRAL observation of hard X-ray variability of the TeV binary LS 5039/RX J1826.2-1450, *Astron. & Astrophys.* **494**, L37.
- Holder, J. f. t. V. C. 2009, VERITAS Observations of LS I +61 303 in the Fermi Era, *ArXiv e-prints* .

- Huang, H. H. et Becker, W. 2007, XMM-Newton observations of PSR B1957+20, *Astron. & Astrophys.* **463**, L5.
- Jarp, S. et Mork, K. J. 1973, Differential Cross Sections for Pair Production by Photons on Electrons, *Phys. Rev. D* **8**, 159.
- Johnston, S., Manchester, R. N., Lyne, A. G., Bailes, M. *et al.* 1992, PSR 1259-63 - A binary radio pulsar with a Be star companion, *Astrophysical Journal, Letters* **387**, L37.
- Jones, F. C. 1965, Inverse Compton Scattering of Cosmic-Ray Electrons, *Physical Review* **137**, 1306.
- Jones, F. C. 1968, Calculated Spectrum of Inverse-Compton-Scattered Photons, *Physical Review* **167**, 1159.
- Joseph, J. et Rohrlich, F. 1958, Pair Production and Bremsstrahlung in the Field of Free and Bound Electrons, *Reviews of Modern Physics* **30**, 354.
- Kelner, S. R., Aharonian, F. A. et Bugayov, V. V. 2006, Energy spectra of gamma rays, electrons, and neutrinos produced at proton-proton interactions in the very high energy regime, *Phys. Rev. D* **74**, 3, 034018.
- Kennel, C. F. et Coroniti, F. V. 1984a, Confinement of the Crab pulsar's wind by its supernova remnant, *Astrophysical Journal* **283**, 694.
- Kennel, C. F. et Coroniti, F. V. 1984b, Magnetohydrodynamic model of Crab nebula radiation, *Astrophysical Journal* **283**, 710.
- Khangulyan, D., Aharonian, F. et Bosch-Ramon, V. 2008, On the formation of TeV radiation in LS 5039, *Mon. Not. of the Royal Astron. Soc.* **383**, 467.
- Khangulyan, D., Hnatic, S., Aharonian, F. et Bogovalov, S. 2007, TeV light curve of PSR B1259-63/SS2883, *Mon. Not. of the Royal Astron. Soc.* **380**, 320.
- Kirk, J. G., Ball, L. et Skjaeraasen, O. 1999, Inverse Compton emission of TeV gamma rays from PSR B1259-63, *Astroparticle Physics* **10**, 31.
- Kirk, J. G., Lyubarsky, Y. et Petri, J. 2009, The Theory of Pulsar Winds and Nebulae, dans W. Becker (éditeur), *Astrophysics and Space Science Library*, vol. 357 de *Astrophysics and Space Science Library*, pp. 421–+.
- Kishishita, T., Tanaka, T., Uchiyama, Y. et Takahashi, T. 2009, Long-Term Stability of Nonthermal X-Ray Modulation in the Gamma-Ray Binary LS 5039, *Astrophysical Journal, Letters* **697**, L1.
- Knödlseeder, J., Jean, P., Lonjou, V., Weidenspointner, G. *et al.* 2005, The all-sky distribution of 511 keV electron-positron annihilation emission, *Astron. & Astrophys.* **441**, 513.
- Lamb, R. C., Fichtel, C. E., Hartman, R. C., Kniffen, D. A. *et al.* 1977, Observation of gamma rays with a 4.8 hour periodicity from Cygnus X-3, *Astrophysical Journal, Letters* **212**, L63.
- Ling, Z., Zhang, S. N. et Tang, S. 2009, Determining the Distance of Cyg X-3 with its X-Ray Dust Scattering Halo, *Astrophysical Journal* **695**, 1111.
- Longair, M. S. 1992, *High energy astrophysics. Vol.1: Particles, photons and their detection.*
- Manchester, R. N., Johnston, S., Lyne, A. G., D'Amico, N. *et al.* 1995, Period evolution of PSR B1259-63: Evidence for propeller-torque spindown, *Astrophysical Journal, Letters* **445**, L137.
- Maraschi, L. et Treves, A. 1981, A model for LSI61 deg 303, *Mon. Not. of the Royal Astron. Soc.* **194**, 1P.

- Mastichiadis, A. 1986, The implications of ultra-high-energy activity in X-ray binary systems, *Astron. & Astrophys.* **169**, 373.
- Mastichiadis, A. 1991, Relativistic electrons in photon fields - Effects of triplet pair production on inverse Compton gamma-ray spectra, *Mon. Not. of the Royal Astron. Soc.* **253**, 235.
- Mastichiadis, A., Marscher, A. P. et Brecher, K. 1986, Electron-positron pair production by ultrarelativistic electrons in a soft photon field, *Astrophysical Journal* **300**, 178.
- McSwain, M. V., Gies, D. R., Huang, W., Wiita, P. J. et al. 2004, The N Enrichment and Supernova Ejection of the Runaway Microquasar LS 5039, *Astrophysical Journal* **600**, 927.
- Michel, F. C. 1969, Relativistic Stellar-Wind Torques, *Astrophysical Journal* **158**, 727.
- Michel, F. C. 1994, Magnetic structure of pulsar winds, *Astrophysical Journal* **431**, 397.
- Moderski, R., Sikora, M., Coppi, P. S. et Aharonian, F. 2005, Klein-Nishina effects in the spectra of non-thermal sources immersed in external radiation fields, *Mon. Not. of the Royal Astron. Soc.* **363**, 954.
- Mori, M., Bertsch, D. L., Dingus, B. L., Esposito, J. A. et al. 1997, Cygnus X-3 and EGRET Gamma-Ray Observations, *Astrophysical Journal* **476**, 842.
- Mork, K. J. 1967, Pair Production by Photons on Electrons, *Physical Review* **160**, 1065.
- Motz, J. W., Olsen, H. A. et Koch, H. W. 1969, Pair Production by Photons, *Reviews of Modern Physics* **41**, 581.
- Paredes, J. M., Bosch-Ramon, V. et Romero, G. E. 2006, Spectral energy distribution of the γ -ray microquasar LS 5039, *Astron. & Astrophys.* **451**, 259.
- Parsignault, D. R., Gursky, H., Kellogg, E. M., Matilsky, T. et al. 1972, No X-ray flare seen by Uhuru, *Nature* **239**, 123.
- Particle Data Group, Amsler, C., Doser, M., Antonelli, M. et al. 2008, Review of Particle Physics, *Physics Letters B* **667**, 1.
- Perucho, M., Bosch-Ramon, V. et Khangulyan, D. 2010, 3D simulations of wind-jet interaction in massive X-ray binaries, *ArXiv e-prints* .
- Pétri, J. 2009, High-energy pulses and phase-resolved spectra by inverse Compton emission in the pulsar striped wind. Application to Geminga, *Astron. & Astrophys.* **503**, 13.
- Pétri, J. et Lyubarsky, Y. 2007, Magnetic reconnection at the termination shock in a striped pulsar wind, *Astron. & Astrophys.* **473**, 683.
- Pringle, J. E. 1981, Accretion discs in astrophysics, *Annual Review of Astron and Astrophys* **19**, 137.
- Ram, M. et Wang, P. Y. 1971, Calculation of the Total Cross Section for Double Compton Scattering, *Physical Review Letters* **26**, 476.
- Rees, M. J. et Gunn, J. E. 1974, The origin of the magnetic field and relativistic particles in the Crab Nebula, *Mon. Not. of the Royal Astron. Soc.* **167**, 1.
- Romero, G. E., Okazaki, A. T., Orellana, M. et Owocki, S. P. 2007, Accretion vs. colliding wind models for the gamma-ray binary LS I +61 303: an assessment, *Astron. & Astrophys.* **474**, 15.
- Romero, G. E., Torres, D. F., Kaufman Bernadó, M. M. et Mirabel, I. F. 2003, Hadronic gamma-ray emission from windy microquasars, *A&A* **410**, L1.

- Ruderman, M. A. et Sutherland, P. G. 1975, Theory of pulsars - Polar caps, sparks, and coherent microwave radiation, *Astrophysical Journal* **196**, 51.
- Rybicki, G. B. et Lightman, A. P. 1979, *Radiative processes in astrophysics*.
- Sabatini, S., Tavani, M., Striani, E., Bulgarelli, A. et al. 2010, Episodic Transient Gamma-ray Emission from the Microquasar Cygnus X-1, *Astrophysical Journal, Letters* **712**, L10.
- Shakura, N. I. et Sunyaev, R. A. 1973, Black holes in binary systems. Observational appearance., *Astron. & Astrophys.* **24**, 337.
- Sierpowska, A. et Bednarek, W. 2005, γ -rays from cascades in close massive binaries containing energetic pulsars, *Mon. Not. of the Royal Astron. Soc.* **356**, 711.
- Sierpowska-Bartosik, A. et Bednarek, W. 2008, γ -rays from binary system with energetic pulsar and Be star with aspherical wind: PSR B1259-63/SS2883, *Mon. Not. of the Royal Astron. Soc.* **385**, 2279.
- Sierpowska-Bartosik, A. et Torres, D. F. 2008, Pulsar wind zone processes in LS 5039, *Astroparticle Physics* **30**, 239.
- Sierpowska-Bartosik, A. et Torres, D. F. 2009, γ -Ray Emission from LS I +61 303: The Impact of Basic System Uncertainties, *Astrophysical Journal* **693**, 1462.
- Sitarek, J. et Bednarek, W. 2010, Gamma-rays from the IC electron-positron pair cascade in the radiation field of an accretion disc: application to Cen A, *Mon. Not. of the Royal Astron. Soc.* **401**, 1983.
- Slane, P., Helfand, D. J., van der Swaluw, E. et Murray, S. S. 2004, New Constraints on the Structure and Evolution of the Pulsar Wind Nebula 3C 58, *Astrophysical Journal* **616**, 403.
- Stawarz, Ł., Aharonian, F., Kataoka, J., Ostrowski, M. et al. 2006, Dynamics and high-energy emission of the flaring HST-1 knot in the M 87 jet, *Mon. Not. of the Royal Astron. Soc.* **370**, 981.
- Stecker, F. W. 1966, The Production of Cosmic Gamma Rays in Interstellar and Intergalactic Cosmic-Ray Collisions. I the Kinematics of p-p Interactions and Secondary Meson and Hyperon Decay and the Cosmic Gamma-Ray Spectral Source Function, *SAO Special Report* **220**.
- Sturrock, P. A. 1971, A Model of Pulsars, *Astrophysical Journal* **164**, 529.
- Svensson, R. 1987, Non-thermal pair production in compact X-ray sources - First-order Compton cascades in soft radiation fields, *Mon. Not. of the Royal Astron. Soc.* **227**, 403.
- Szostek, A. et Zdziarski, A. A. 2008, Effects of the stellar wind on X-ray spectra of Cygnus X-3, *Mon. Not. of the Royal Astron. Soc.* **386**, 593.
- Szostek, A., Zdziarski, A. A. et McCollough, M. L. 2008, A classification of the X-ray and radio states of Cyg X-3 and their long-term correlations, *Mon. Not. of the Royal Astron. Soc.* **388**, 1001.
- Takahashi, T., Kishishita, T., Uchiyama, Y., Tanaka, T. et al. 2009, Study of the Spectral and Temporal Characteristics of X-Ray Emission of the Gamma-Ray Binary LS 5039 with Suzaku, *Astrophysical Journal* **697**, 592.
- Takata, J. et Taam, R. E. 2009, Probing the Pulsar Wind in the γ -ray Binary System PSR B1259-63/SS 2883, *Astrophysical Journal* **702**, 100.
- Tavani, M., Arons, J. et Kaspi, V. M. 1994, Regimes of high-energy shock emission from the Be star/pulsar system PSR 1259-63, *Astrophysical Journal, Letters* **433**, L37.

-
- Tavani, M., Bulgarelli, A., Piano, G., Sabatini, S. *et al.* 2009, Extreme particle acceleration in the microquasar CygnusX-3, *Nature* **462**, 620.
 - The Fermi-LAT Collaboration 2010, Fermi Large Area Telescope First Source Catalog, *ArXiv e-prints* .
 - van Kerkwijk, M. H., Geballe, T. R., King, D. L., van der Klis, M. *et al.* 1996, The Wolf-Rayet counterpart of Cygnus X-3., *Astron. & Astrophys.* **314**, 521.
 - Vilhu, O., Hakala, P., Hannikainen, D. C., McCollough, M. *et al.* 2009, Orbital modulation of X-ray emission lines in Cygnus X-3, *Astron. & Astrophys.* **501**, 679.
 - Waters, L. B. F. M., van den Heuvel, E. P. J., Taylor, A. R., Habets, G. M. H. J. *et al.* 1988, Evidence for low-velocity winds in Be/X-ray binaries, *Astron. & Astrophys.* **198**, 200.
 - Weisskopf, M. C., Hester, J. J., Tennant, A. F., Elsner, R. F. *et al.* 2000, Discovery of Spatial and Spectral Structure in the X-Ray Emission from the Crab Nebula, *Astrophysical Journal, Letters* **536**, L81.
 - Zdziarski, A. A. 1988, Saturated pair-photon cascades on isotropic background photons, *Astrophysical Journal* **335**, 786.
 - Zdziarski, A. A. 1989, Gamma rays from relativistic electrons undergoing Compton losses in isotropic photon fields, *Astrophysical Journal* **342**, 1108.
 - Zdziarski, A. A., Malzac, J. et Bednarek, W. 2009, A model of the TeV flare of Cygnus X-1: electron acceleration and extended pair cascades, *Mon. Not. of the Royal Astron. Soc.* pp. L175+.
 - Zdziarski, A. A., Neronov, A. et Chernyakova, M. 2010, A compact pulsar wind nebula model of the γ -ray-loud binary LS I +61 303, *Mon. Not. of the Royal Astron. Soc.* pp. 227+.
 - Zhang, L. et Cheng, K. S. 1997, Escape of TeV Gamma Rays from Anisotropic Thermal Photon Fields in Active Galactic Nuclei, *Astrophysical Journal* **475**, 534.

High-energy gamma-ray emission in compact binaries

Benoît CERUTTI

Abstract

Four gamma-ray sources have been associated with binary systems in our Galaxy: the microquasar Cygnus X-3 and the gamma-ray binaries LS I +61°303, LS 5039 and PSR B1259 – 63. These systems are composed of a massive companion star and a compact object of unknown nature, except in PSR B1259 – 63 where there is a young pulsar. I propose a comprehensive theoretical model for the high-energy gamma-ray emission and variability in gamma-ray emitting binaries. In this model, the high-energy radiation is produced by inverse Compton scattering of stellar photons on ultra-relativistic electron-positron pairs injected by a young pulsar in gamma-ray binaries and in a relativistic jet in microquasars. Considering anisotropic inverse Compton scattering, pair production and pair cascade emission, the TeV gamma-ray emission is well explained in LS 5039. Nevertheless, this model cannot account for the gamma-ray emission in LS I +61°303 and PSR B1259 – 63. Other processes should dominate in these complex systems. In Cygnus X-3, the gamma-ray radiation is convincingly reproduced by Doppler-boosted Compton emission of pairs in a relativistic jet. Gamma-ray binaries and microquasars provide a novel environment for the study of pulsar winds and relativistic jets at very small spatial scales.

Keywords: Gamma rays, Gamma-ray binaries, Pulsars, Microquasars, Relativistic jets

Résumé

Quatre sources de rayons gamma ont été associées à des systèmes binaires dans notre galaxie: le microquasar Cygnus X-3 et les binaires gamma LS I +61°303, LS 5039 et PSR B1259 – 63. Ces systèmes sont composés d'une étoile compagnon massive et d'un objet compact de nature inconnue, sauf dans PSR B1259 – 63 où un pulsar jeune a été détecté. Je propose ici un modèle théorique complet pour expliquer l'émission et la variabilité gamma de haute énergie dans les binaires émettant en gamma. Dans ce modèle, le rayonnement de haute énergie est produit par la diffusion Compton inverse des photons stellaires sur des paires électron-positron ultrarelativistes injectées par un pulsar jeune dans les binaires gamma et dans un jet relativiste dans les microquasars. La modulation du flux TeV dans LS 5039 est bien reproduite en combinant les effets d'émission, d'absorption et du recyclage de l'émission par une cascade de paires. Néanmoins, ce modèle ne permet pas d'expliquer l'émission gamma dans LS I +61°303 et PSR B1259 – 63. D'autres processus doivent dominer dans ces systèmes plus complexes. Dans Cygnus X-3, le rayonnement gamma peut être reproduit de manière convaincante avec l'émission Compton amplifiée Doppler de paires dans un jet relativiste. Les binaires gamma et les microquasars offrent un environnement nouveau permettant l'étude des vents de pulsar et des jets relativistes à de très petites échelles spatiales.

Mots clés: Rayons gamma, Binaires gamma, Pulsars, Microquasars, Jets relativistes.